Frank B. Sachse

Tutorial

LNCS 2966

Computational Cardiology

Modeling of Anatomy, Electrophysiology, and Mechanics

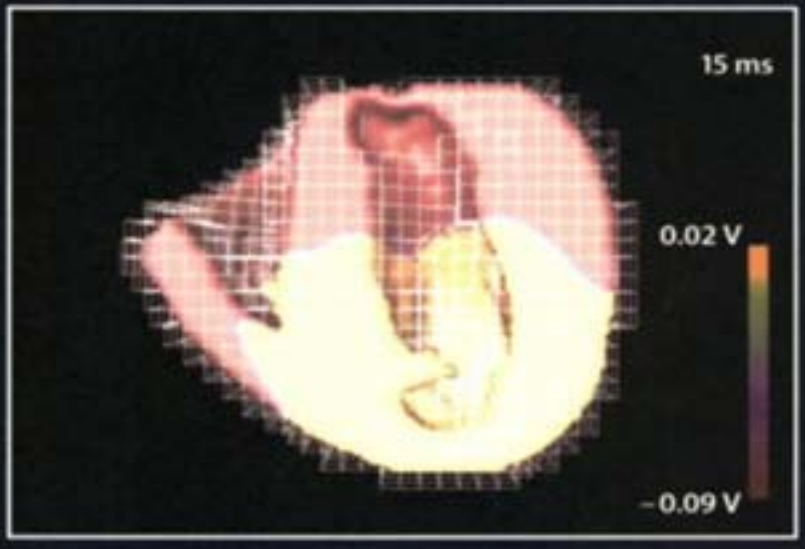

Springer

Lecture Notes in Computer Science 2966

Edited by G. Goos, J. Hartmanis, and J. van Leeuwen

Frank B. Sachse

Computational Cardiology

Modeling of Anatomy, Electrophysiology, and Mechanics

Springer

Author

Frank B. Sachse
University of Utah
Nora Eccles Harrison Cardiovascular Research and Training Institute
95 South 2000 East, Salt Lake City, UT 84112-5000, USA
E-mail: fs@cvrti.utah.edu

Library of Congress Control Number: 2004104242

CR Subject Classification (1998): I.7, I.4, G.1, J.3, J.2

ISSN 0302-9743
ISBN 3-540-21907-2 Springer-Verlag Berlin Heidelberg New York

Springer-Verlag is a part of Springer Science+Business Media

springeronline.com

Printed in Germany

Typesetting: Camera-ready by author, data conversion by Olgun Computergrafik
Printed on acid-free paper SPIN: 10996478 06/3142 5 4 3 2 1 0

Preface

Biomedical research is at a critical point at present. The research has led to an enormous amount of data and models describing these data, but approaches for application, formalization and integration of this knowledge from the molecular to the system level are still topics of ongoing research and certainly far from fully developed.

Also in cardiology the different anatomical and physiological constituents as well as the coupling between them are being researched in increasing detail and are often described using computer-based models. But for this domain an integrative framework is still missing.

The application of computer-based modeling as a research, development and clinical tool often necessitates the coupling of various models from different levels. Describing the interactions between these models, which are both physically sound and computationally efficient, determines the applicability of such promising computer-based attempts.

My hope is that this book will contribute to the comprehension, spread and impact of computer-based modeling in cardiology, both from a teaching point of view and by summarizing knowledge from several, commonly delimited topics relating to the cardiac manifoldness.

The book evolved from revision and extension of my professorial dissertation (Habilitationsschrift) "Mathematical Modeling of the Mammalian Heart" written in 2002. This dissertation was based on notes for the lectures "Computational Biology: Bioelectromagnetism and Biomechanics," "Simulation of Physical Fields in the Human Body," and "Anatomical, Physical and Functional Models of the Human Body," which I gave at the Universität Karlsruhe (TH) from 1998 to 2003.

Salt Lake City, 1 February 2004 Frank B. Sachse

Acknowledgement

Many people merit my gratitude for their assistance and support in this work. I appreciate the scientific opportunities offered by the Institut für Biomedizinische Technik at the Universität Karlsruhe (TH), Germany, and the Nora Eccles Harrison Cardiovascular Research and Training Institute at the University of Utah, USA. Prof. Dr. Olaf Dössel, Prof. Dr. Karsten Meyer-Waarden and Prof. Dr. Bruno Taccardi provided me with an excellent platform for my 'hobby.'

I am thankful that this work has been supported by the Richard A. and Nora Eccles Fund for Cardiovascular Research and awards from the Nora Eccles Treadwell Foundation as well as several funds from the Deutsche Forschungsgemeinschaft. Also, I am grateful to the Rechenzentrum at the Universität Karlsruhe (TH), particularly Rolf Mayer, and the Scientific Computing and Imaging Institute, University of Utah, which made the necessary computing and visualization resources available.

Particularly, I want to express my gratitude to Leo Blümcke, Rotraut Frech, Matthias Mohr, Prof. Dr. Carlos Sansour, Gunnar Seemann, Dr. Jeroen Stinstra, and Oleg Skipa for their numerous comments and proof-readings of this work. A large thanks must be given to Dr. Christian Werner with whom I enjoyed working for more than 5 years. Many highlights of our project wouldn't have been possible without his various contributions. I'd like to extend this gratitude to Dr. Ingo de Boer, Nils H. Busch, Heiko Jausel, Rong Liu, Steffen Mang, Claudia Riedel, Manfred Schroll, Lars Thomas, Daniel Weiß, Markus Wolf and many students who influenced this work significantly. Further thanks go to Matti Stenroos from Finland as well as Nuno Sa Couto and Sergio Barros from Portugal, who not only added some international flavor, but also provided important contributions.

I'm grateful to my parents, my brother Jochen and nephew Jan, because they demonstrated that there are important things in life other than work. My friends Reza and Dawud deserve special thanks for not losing patience even though I neglected so many of our appointments. Finally, a huge thanks to Denise, who not only tolerated my particularities resulting from this work, but also encouraged and supported me in the best possible manner.

Contents

List of Figures

List of Tables

1

Introduction

1.1 Motivation

Modeling of the heart allows the gain of knowledge concerning the interplay of anatomical structures and physical phenomena, which contribute to cardiac physiological and pathophysiological behavior. Applications of this knowledge are found in biomedical research, education and training as well as in development and approval of drugs and medical devices.

An important application of modeling in biomedical research is to understand mechanisms of heart failure, which is a leading cause of death in humans. Usage of appropriate models simplifies development and validation of drugs and medical devices. Modeling allows the exploration of a product's side effects, which is of particular importance for the product's approval.

Cardiac models provide a simplified description of the heart and can exist in a physical and mathematical representation. E.g. in clinical research the modeling of human hearts commonly refers an animal's heart, which is applied in an experiment. Mathematical models are commonly computer-based and applied in numerical simulations.

Modeling of the heart is subject of manifold, often interdisciplinary research activities undertaken in academic and commercial fields. The activities range from the description of molecular structures and interactions to reconstruction of gross anatomy and whole heart electro-mechanic behavior.

Explorations of the heart were performed as early as in the middle ages and the renaissance. Initially, the explorations consisted of anatomical studies by dissection of animals. First models of cardiac anatomy and physiology were constructed (Fig. 1.1), which are now considered as outdated resulting from new insights. Nevertheless, over centuries mediaeval graphical reconstructions of the heart served as foundation for medical education parallel to or substituting dissection of cadavers.

In recent decades new insights in the function and structure of the heart have been gained by the availability of new measurement techniques. The molecular structure and arrangement of cardiac cells have been explored e.g.

F.B. Sachse: LNCS 2966, pp. 1–4, 2004.

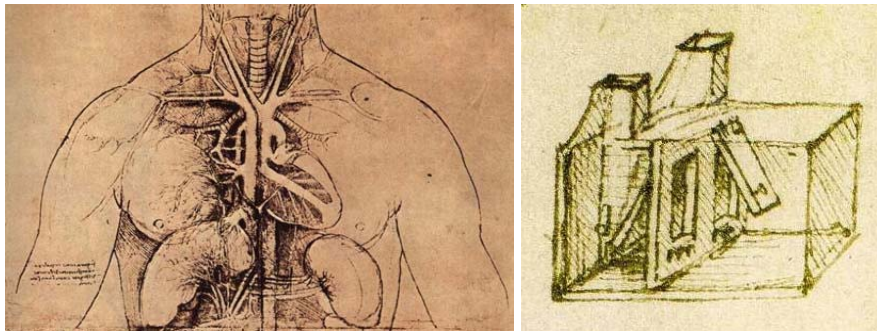

(a) (b)

Fig. 1.1. Drawings of Leonardo da Vinci. (a) Upper part of anatomical drawing of woman's torso with heart, blood vessels and kidneys [1]. The heart is divided into two chambers connected to blood vessels. (b) Model of heart's function [2]. The heart was considered as a furnace with inlets and outlets. An exchange of air is performed through connections to the lungs, which are viewed as chimney. The transport of heat to the body is made by blood flowing through the vessels. The model was subsequently modified by Leonardo da Vinci to incorporate new perceptions.

with new imaging techniques. Electrophysiological behavior has been measured at levels ranging from molecular, cellular to whole hearts. Mechanical properties and cardiac mechanics have been scanned by a variety of experiments. In recent time data concerning gene and protein expression in cardiac cells is raised under physiological and variant pathophysiological circumstances.

Many of these measurements have been used to describe mathematically the properties and behavior of cardiac tissue. Mathematical descriptions can be applied to simulate tissue behavior. The increase in computing capability in recent years has simplified and speeded up significantly the realization of simulations. On the one hand, these simulations offer the possibility of reconstruction of previously performed measurements. On the other hand, a-priori unknown behavior can be predicted and complex phenomena can be studied.

The topic of this work is the computer-based, mathematical modeling of the heart. The application of modeling as a research, development and clinical tool is stressed as a promising attempt to address many problems in cardiology, heart surgery and biomedical engineering.

The modeling includes the areas of anatomy, electrophysiology, excitation propagation, force development and mechanics as well as the coupling of these areas (Fig. 1.2). The work shows knowledge at molecular, cellular and macroscopic level, how these areas can be studied with measurements, and how these areas can be modeled with mathematical methods. Detailed informa-

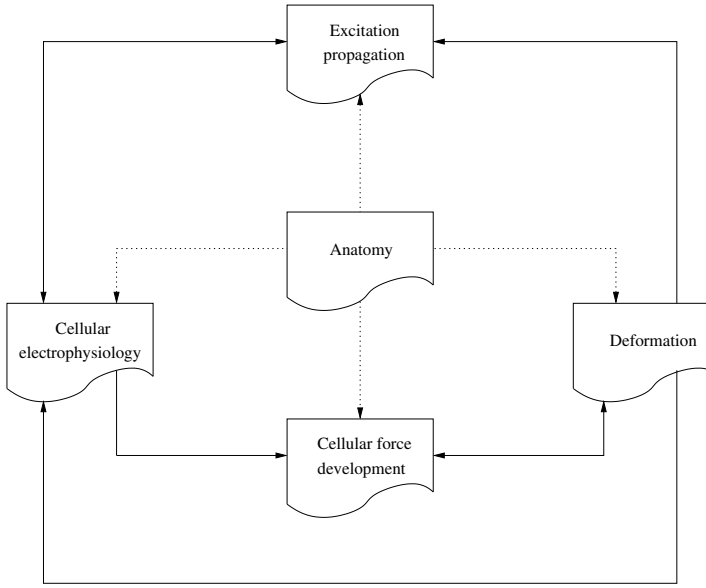

Fig. 1.2. Overview of modeling of cardiac electro-mechanics. Anatomical information determines modeling of cellular electrophysiology, excitation propagation, force development and deformation. The influence of the different areas to each other is depicted by arrows.

tion of phenomena on each of these levels is necessary to understand the ideas behind the modeling.

Special attention is given to macroscopic and integrative modeling with the aim of reconstruction of whole heart behavior. At macroscopic level anatomical models provide a basis for electrophysiological and mechanical models. Of particular interest is the assessment of influence of cardiac deformation to initiation and propagation of electrical excitation and to the force development. Variant simulation studies are demonstrated, which provide information about this assessment.

1.2 Organization

In the first section of this work a foundation of mathematics and numerics is provided. Mathematical definitions and formulations as well as numerical techniques are explained, which are relevant for modeling of cardiac electrophysiology and mechanics. The focus is particularly on the finite element and finite differences method, which are the standard techniques for solving many tasks in mechanical and electrical engineering. With the next two sections the theory of electric fields and continuum mechanics is introduced regarding the numerical calculation in anisotropic biological media, particularly with the

finite element method. In the following section an overview of digital image processing techniques is given, which are of pragmatic importance in conjunction with data from medical imaging systems. The section 'cardiac anatomy' offers detailed information of molecular and cellular structures as well as of gross anatomy. Models are introduced resulting from the application of digital image processing to images of human and animal hearts. The next section gives an introduction to cardiac electrophysiology at different levels. A multitude of cellular and excitation propagation models is introduced. The section 'cardiac mechanics' presents experiments concerning deformation and models of mechanical properties of myocardium. Simulations illustrate the connection between arrangement of cardiac fibers and deformation. The final section concerns the coupling of electrophysiology and mechanics. The modeling of cardiac electro-mechanics is presented at different levels and with various techniques. Simulations depict the phenomena of coupled electro-mechanics and are contrasted with results from non-coupled models.

2

Mathematical and Numerical Foundation

2.1 Overview

The mathematical modeling of biological systems is a subtopic of computational biology. This kind of modeling permits new insights into biological systems with the aid of numerical methods and computer systems. The modeling necessitates knowledge concerning useful mathematical notation and efficient numerical treatment of the occurring equations. The topic of this chapter is to give a summary and description of these mathematical fields, which are of importance in the context of this work for the mechanical and electrophysiological modeling of a specific biological system, i.e. the mammalian heart.

The Einstein summation convention is introduced, which allows a concise notation for equation systems comprising summations. The usage of the summation convention is useful, e.g. in continuum mechanics. An introduction to tensor algebra is given because many of the physical quantities in electromagnetism and mechanics are represented as tensors, to incorporate the effects of coordinate transformations.

Methods for the numerical solving of linear equation systems are presented in detail. A focus of the description is given to methods, which allow the solution of very large, sparse systems. The numerical integration of equations is described, which is an important technique e.g. for the application of the finite element and finite differences method.

The theory of differential equations is presented in conjunction with numerical methods convenient for solving large, coupled equation systems. Ordinary differential equations are used in the context of this work to describe the electrophysiological behavior of cells. Commonly, five to seventy coupled differential equations of first order are combined to a system and numerically solved. The solvability of these systems strongly depends on the efficiency of the solving methods. Partial differential equations are the mathematical foundation for modeling of electromagnetic fields and mechanical behavior. The differential equations can be numerically handled using the finite element and finite differences method.

F.B. Sachse: LNCS 2966, pp. 5–48, 2004.

2.2 Einstein Summation Convention

The Einstein summation convention was introduced by Albert Einstein in the formulation of the theory of relativity [3]. The convention reduces the complexity of equations by omitting the traditional sign Σ for summation. Instead of this sign twice occurring indices designate the summation. Both, subscripts and superscripts, are taken into account, e.g.:

$$\sum_i a_i x_i \equiv a_i x_i$$
$$\sum_i a^i x_i \equiv a^i x_i$$
$$\sum_i a_i x^i \equiv a_i x^i$$
$$\sum_i a^i x^i \equiv a^i x^i$$
$$\sum_i \sum_j a_{ij} x_i y_j \equiv a_{ij} x_i y_j$$

The range of summation as well as the differentiation between superscripts and exponents are context dependent. The repeated indices are so-called dummy indices, which can be renamed arbitrarily taking already existing names into account.

The handling of equation systems is simplified by the usage of free indices. These occur solitary in the equations and the range of free indices is context dependent. Commonly, the same range as for the summation of the dummy indices is assumed, e.g.:

$$y_i = a_{ij} x_j \text{ with } i, j = 1, 2, 3 \equiv \begin{aligned} y_1 &= a_{11}x_1 + a_{12}x_2 + a_{13}x_3 \\ y_2 &= a_{21}x_1 + a_{22}x_2 + a_{23}x_3 \\ y_3 &= a_{31}x_1 + a_{32}x_2 + a_{33}x_3 \end{aligned}$$

2.3 Tensor Algebra

Definition. Tensors are introduced to describe mathematical and physical quantities under coordinate transformations. Depending on the type and order of a tensor specific laws for the transformation of tensor coefficients have to be obeyed.

Coordinate Transformation. A transformation in a region of $\mathbb{R}^n$ from one coordinate system to another is given by:

$$\bar{x}^i = \bar{x}^i(x^1, x^2, \ldots, x^n) \tag{2.1}$$

with $1 \leq i \leq n$. The Jacobian matrix J of the coordinate transformation combines its first-order partial derivatives and is given by:

$$J = \left[\frac{\partial \bar{x}^i}{\partial x^j} \right]$$

The determinant of the Jacobian matrix is named the Jacobian of the coordinate transformation. If the Jacobian $\mathcal{J}$ does not vanish, the coordinate transformation is called bijective. Then, an inverse coordinate transformation can be defined as:

$$x^i = x^i(\bar{x}^1, \bar{x}^2, \ldots, \bar{x}^n) \tag{2.2}$$

with an attributed inverse Jacobian matrix $\bar{J}$:

$$\bar{J} = \left[\frac{\partial x^i}{\partial \bar{x}^j} \right]$$

The determinant of the inverse Jacobian matrix $\bar{J}$ is referred to as the inverse Jacobian $\bar{\mathcal{J}}$.

The coordinate systems of the transformation in equations 2.1 and 2.2 are arbitrary, e.g. Cartesian, affine and curvilinear. A coordinate system is called rectangular or Cartesian if the distance d between any two desired points A and B is determined by:

$$d = \sqrt{\Delta^i \Delta^i}$$

with $\Delta \equiv B - A$. An affine coordinate system is constructed if a linear transformation is used in equation 2.1. Nonlinear transformations lead to curvilinear coordinate systems, e.g. polar, cylindrical and spherical systems. In this work specific coordinate transformations are described in the area of continuum mechanics (Sect. 4.2.1) and digital image processing (Sect. 5.3.2).

First Order Tensors. A vector T^i associated to a point x is called a contravariant tensor of first order or contravariant vector, if it changes its coefficients under the coordinate transformation in equation 2.1 according to the following laws of transformation:

$$\bar{T}^i = T^j \frac{\partial \bar{x}^i}{\partial x^j}$$

Similarly, a vector T_i is called a covariant tensor of first order or covariant vector, if it changes its coefficients under coordinate transformations according to the following laws of transformation:

$$\bar{T}_i = T_j \frac{\partial x^j}{\partial \bar{x}^i}$$

Tensors of Arbitrary Order. Tensors with order higher than one can be of mixed type, i.e. contravariant of order p and covariant of order q. A definition of tensors of arbitrary order $n = p + q$ is given by [3]:

$$\bar{T}^{i_1 \ldots i_p}_{j_1 \ldots j_q} = T^{k_1 \ldots k_p}_{l_1 \ldots l_q} \frac{\partial \bar{x}^{i_1}}{\partial x^{k_1}} \cdots \frac{\partial \bar{x}^{i_p}}{\partial x^{k_p}} \frac{\partial x^{l_1}}{\partial \bar{x}^{j_1}} \cdots \frac{\partial x^{l_q}}{\partial \bar{x}^{j_q}}$$

Table 2.1. Tensors of different order and type. A tensor T is transformed to the tensor $\bar{T}$ obeying a type and order specific law of transformation.

Order	Type	Law
0	invariant	$\bar{T} = T$
1	contravariant	$\bar{T}^i = T^j \frac{\partial \bar{x}^i}{\partial x^j}$
1	covariant	$\bar{T}_i = T_j \frac{\partial x^j}{\partial \bar{x}^i}$
2	contravariant	$\bar{T}^{ij} = T^{kl} \frac{\partial \bar{x}^i}{\partial x^k} \frac{\partial \bar{x}^j}{\partial x^l}$
2	covariant	$\bar{T}_{ij} = T_{kl} \frac{\partial x^k}{\partial \bar{x}^i} \frac{\partial x^l}{\partial \bar{x}^j}$
2	mixed	$\bar{T}^i_j = T^k_l \frac{\partial \bar{x}^i}{\partial x^k} \frac{\partial x^l}{\partial \bar{x}^j}$
4	contravariant	$\bar{T}^{ijkl} = T^{mnop} \frac{\partial \bar{x}^i}{\partial x^m} \frac{\partial \bar{x}^j}{\partial x^n} \frac{\partial \bar{x}^k}{\partial x^o} \frac{\partial \bar{x}^l}{\partial x^p}$
4	covariant	$\bar{T}_{ijkl} = T_{mnop} \frac{\partial x^m}{\partial \bar{x}^i} \frac{\partial x^n}{\partial \bar{x}^j} \frac{\partial x^o}{\partial \bar{x}^k} \frac{\partial x^p}{\partial \bar{x}^l}$

The index position indicates the tensor type. A superscript denotes a contravariant tensor, a subscript a covariant tensor. Exemplary definitions of tensors with orders zero up to four, which are the relevant cases in the context of this work, are given in table 2.1.

Symmetry Properties. A tensor is symmetric concerning some indices, if the interchange of the indices does not change the tensor coefficients. The tensor is anti-symmetric or skew-symmetric, if the interchange of indices leads to a change of the sign of tensor coefficients. E.g. a second order tensor T_{ij} is symmetric, if $T_{ij} = T_{ji}$. The tensor is anti-symmetric, if $T_{ij} = -T_{ji}$.

Affine and Cartesian Tensors. Affine tensors are subject to linear coordinate transformations resulting in a Jacobian matrix J given by:

$$J = \left[\frac{\partial \bar{x}^i}{\partial x^j} \right] = \left[a^i_j \right]$$

with constant, scalar coefficients a^i_j. The Jacobian $\mathcal{J}$ does not vanish, i.e. $|a^i_j| \neq 0$.

Cartesian tensors are resulting from orthogonal coordinate transformations. These take a Cartesian system into another, where the origins of the Cartesian systems remain the same. Hereby, the Jacobian matrix of the transformation J and its inverse Jacobian matrix $\bar{J}$ are connected by:

$$\bar{J} = J^{-1} = J^T$$

Therefore, the transformation laws of contravariant Cartesian tensors T^i and covariant Cartesian tensors T_i are equal, e.g. for tensors of first order:

$$\bar{T}^i = T^j \frac{\partial \bar{x}^i}{\partial x^j} = T^j a^i_j$$

$$\bar{T}_i = T_j \frac{\partial x^j}{\partial \bar{x}^i} = T_j a_i^j$$

Because of the equality the notation of these tensors can be simplified. Commonly, Cartesian tensors are notated using subscripts.

Invariants of Second-Order Tensors. The eigenvalues λ of symmetric, real tensors of second order T_{ij} are given by:

$$|T_{ij} - \lambda \delta_{ij}| = 0$$

The definition of the determinant allows to formulate the characteristic polynomial:

$$\lambda^3 - I_T \lambda^2 + II_T \lambda - III_T \lambda = 0$$

with the invariants I_T, II_T and III_T of the symmetric, real tensors of second order T_{ij} defined as:

$$\begin{aligned} I_T &= tr(T_{ij}) = T_{ii} \\ II_T &= \frac{1}{2}(T_{ii}T_{jj} - T_{ij}T_{ij}) \\ III_T &= det(T_{ij}) \end{aligned}$$

The invariants are independent of the chosen coordinate system.

2.4 Numerics of Systems of Linear Equations

2.4.1 Definition

The efficient numerical solution of systems of linear equations is a fundamental task in different areas of computational physics and biology. A system of linear equations is defined as:

$$\begin{aligned} a_{11}x_1 + a_{12}x_2 + \cdots + a_{1N}x_N + b_1 &= 0 \\ a_{21}x_1 + a_{22}x_2 + \cdots + a_{2N}x_N + b_2 &= 0 \\ &\vdots \\ a_{M1}x_1 + a_{M2}x_2 + \cdots + a_{MN}x_N + b_M &= 0 \end{aligned}$$

with the a-priori known coefficients a_{ij} and b_i as well as the unknowns x_j. The number of lines is M and the number of unknowns equals N.

The system of linear equations can be described using another notation:

$$\sum_{j=1}^{N} a_{ij}x_j + b_i = 0 \text{ with } i = 1, \ldots, M \quad \text{summation convention}$$

$$a_{ij}x_j + b_i = 0 \quad \text{Einstein Summation convention}$$

$$\boldsymbol{A}\boldsymbol{x} + \boldsymbol{b} = \boldsymbol{0} \quad \text{matrix formulation}$$

with the matrix $\boldsymbol{A} = [a_{ij}]$ as well as the vectors $\boldsymbol{b} = [b_i]$ and $\boldsymbol{x} = [x_j]$.

A matrix $\boldsymbol{A}$ is named symmetric if it is equal to its transpose:

$$\boldsymbol{A} = \boldsymbol{A}^{\boldsymbol{T}}$$

with $\boldsymbol{A}^{\boldsymbol{T}} = [a_{ji}]$. A matrix $\boldsymbol{A}$ is quadratic if its number of rows M equals the number of columns N, i.e. $M = N$. A matrix $\boldsymbol{A}$ is called positive-definite, if

$$\underset{\boldsymbol{x}\neq\boldsymbol{0}}{\forall} \boldsymbol{x}^T A\boldsymbol{x} > 0$$

Positive-definiteness of a matrix $\boldsymbol{A}$ is ensured, if the 'larger' condition is weakened to a 'larger equal' condition. Diagonal dominance of a matrix is fulfilled, if

$$|a_{ii}| > \sum_{i=0, i\neq j}^{N} |a_{ij}|$$

Often, matrices with only a small number of elements not equal to zero are subject to numerical treatment. This kind of matrix is called sparse. Efficient methods for storing and numerical solution were developed [4, 5].

A special class of sparse matrices is band diagonal, where nonzero elements are found only in some diagonal lines parallel to the main diagonal [5]. The bandwidth of a band diagonal matrix m is given by:

$$\underset{i\in\{1,..,N\}, j\in\{1,..,N\}, |i-j|>m}{\forall} a_{ij} = 0$$

Direct and iterative methods are distinguished to solve systems of linear equations. Direct methods are based on the successive elimination of the unknown, e.g. with Gauss and Cholesky algorithm. Iterative methods use an iterative refinement of approximate solutions. Representatives of iterative methods are the steepest descent and conjugate gradient techniques as well as the more historical approaches of Jacobi, Gauss-Seidel and successive overrelaxation. Further representatives are the multigrid methods.

2.4.2 Direct Methods

Gauss Algorithm. The Gauss Algorithm is a well-known representative of the direct methods and can be described by factorization of the positive definite, symmetric matrix $\boldsymbol{A}$ into the diagonal matrix left $\boldsymbol{D}$, the lower triangular matrix $\boldsymbol{L}$ and its transpose, upper triangular matrix $\boldsymbol{L}^T$:

$$\boldsymbol{A} = \boldsymbol{L}\boldsymbol{D}\boldsymbol{L}^T$$

The matrix $\boldsymbol{L}$ is given by:

$$\boldsymbol{L} = \begin{pmatrix} 1 & 0 & \dots & \dots & \dots & 0 \\ l_{2\,1} & 1 & 0 & \dots & \dots & 0 \\ l_{3\,1} & l_{3\,2} & 1 & 0 & \dots & 0 \\ \dots & \dots & \dots & \dots & \dots & \dots \\ l_{N-1\,1} & l_{N-1\,2} & l_{N-1\,3} & \dots & 1 & 0 \\ l_{N\,1} & l_{N\,2} & l_{N\,3} & \dots & l_{N\,N-1} & 1 \end{pmatrix}$$

The matrices $\boldsymbol{D}$ and $\boldsymbol{L}$ result from the so-called Gaussian elimination, where the elements below the main diagonal of the matrix $\boldsymbol{A}$ are eliminated successively. This leads to the upper triangular matrix $\boldsymbol{R}$:

$$\boldsymbol{A} = \boldsymbol{L}\boldsymbol{R}$$

with following shape

$$\boldsymbol{R} = \begin{pmatrix} r_{1\,1} & r_{1\,2} & r_{1\,3} & \dots & r_{1\,N-1} & r_{1\,N} \\ 0 & r_{2\,2} & r_{2\,3} & \dots & r_{2\,N-1} & r_{2\,N} \\ 0 & 0 & r_{3\,3} & \dots & r_{3\,N-1} & r_{3\,N} \\ \dots & \dots & \dots & \dots & \dots & \dots \\ 0 & 0 & 0 & \dots & r_{N-1\,N-1} & r_{N-1\,N} \\ 0 & 0 & 0 & \dots & 0 & r_{N\,N} \end{pmatrix}$$

The matrix $\boldsymbol{R}$ can be expressed by the diagonal matrix $\boldsymbol{D}$ and the transpose of the lower triangular matrix $\boldsymbol{L}$:

$$\boldsymbol{D}\boldsymbol{L}^T = \boldsymbol{R}$$

The solution of the equation system is achieved in three steps using two auxiliary vectors. In each step one of the matrix factors is applied. In the first step the auxiliary vector $\boldsymbol{z}$ is determined by:

$$-\boldsymbol{L}\boldsymbol{z} + \boldsymbol{b} = 0$$

The second step serves to calculate the auxiliary vector $\boldsymbol{y}$:

$$-\boldsymbol{D}\boldsymbol{y} + \boldsymbol{z} = 0$$

The third step delivers the solution vector $\boldsymbol{x}$:

$$\boldsymbol{L}^T\boldsymbol{x} + \boldsymbol{y} = 0$$

A disadvantage of the Gauss algorithm is the destruction of band diagonal properties. Commonly, the matrix $\boldsymbol{L}$ is filled with nonzero elements in the whole lower triangular area and the matrix $\boldsymbol{R}$ in the whole upper triangular area.

Cholesky Algorithm. The Cholesky algorithm uses a factorization of the matrix $\boldsymbol{A}$ into the lower triangular matrix $\boldsymbol{L}$ and its transpose $\boldsymbol{L}^T$:

$$\boldsymbol{A} = \boldsymbol{L}\boldsymbol{L}^T$$

The matrix $\boldsymbol{L}$ is given by:

$$\boldsymbol{L} = \begin{pmatrix} l_{1\,1} & 0 & \dots & \dots & \dots & 0 \\ l_{2\,1} & l_{2\,2} & 0 & \dots & \dots & 0 \\ l_{3\,1} & l_{3\,2} & l_{3\,3} & 0 & \dots & 0 \\ \dots & \dots & \dots & \dots & \dots & \dots \\ l_{N-1\,1} & l_{N-1\,2} & l_{N-1\,3} & \dots & l_{N-1\,N-1} & 0 \\ l_{N\,1} & l_{N\,2} & l_{N\,3} & \dots & l_{N\,N-1} & l_{N\,N} \end{pmatrix}$$

The matrix $\boldsymbol{L}$ results from a process, the so-called 'taking the square root' [5], where line-wise its elements are calculated. At first for each line the i-th diagonal element l_{ii} is determined with:

$$l_{ii} = (a_{ii} - \sum_{k=1}^{i-1} l_{ik}^2)^{1/2}$$

The non-diagonal element l_{ij} of the i-th line and j-th column is given by:

$$l_{ij} = \frac{1}{l_{jj}} \, (a_{ij} - \sum_{k=1}^{j-1} l_{ik} l_{jk})$$

The solution of the equation system is achieved in two steps using a single auxiliary vector. In each step one of the two matrix factors, $\boldsymbol{L}$ and $\boldsymbol{L}^T$, is applied. In the first step the auxiliary vector $\boldsymbol{y}$ is determined:

$$-\boldsymbol{L}\boldsymbol{y} + \boldsymbol{b} = 0$$

The second step delivers the solution vector $\boldsymbol{x}$:

$$\boldsymbol{L}^T\boldsymbol{x} + \boldsymbol{y} = 0$$

The Cholesky algorithm necessitates positive-definiteness and symmetry of the matrix $\boldsymbol{A}$ as well as respects the band diagonal properties. The numerical expense of the Cholesky method is found to be half of the expense of the Gauss algorithm.

2.4.3 Iterative Methods

Definition. Iterative methods use an iterative refinement of approximate solution $\boldsymbol{x}^{(k)}$. The 0-th approximate solution $\boldsymbol{x}^{(0)}$ or so-called start vector is

given, e.g. set with a random and zero vector as well as with results from pre-calculations with similar and simplified matrices. A sequence of approximate solutions is calculated:

$$\boldsymbol{x}^{(0)} \rightarrow \boldsymbol{x}^{(1)} \rightarrow \cdots \rightarrow \boldsymbol{x}^{(n)}$$

The error of an approximate solutions $\boldsymbol{e}^{(k)}$ is defined as:

$$\boldsymbol{e}^{(k)} = \boldsymbol{x} - \boldsymbol{x}^{(k)}$$

with the exact solution $\boldsymbol{x}$. The error $\boldsymbol{e}^{(k)}$ is also called the correction. The common goal of iterative methods is to reduce the error iteratively.

The residuum of an approximate solutions $\boldsymbol{r}^{(k)}$ is defined as:

$$\boldsymbol{r}^{(k)} = \boldsymbol{A}\boldsymbol{x}^{(k)} + \boldsymbol{b}$$

An iterative method is called convergent if the same solution is found independently of the start-vector $\boldsymbol{x}^{(0)}$ for $k \rightarrow \infty$. A method shows linear convergence if the following inequation is fulfilled for all but finite k:

$$\|\boldsymbol{e}^{(k+1)}\| \leq \xi \|\boldsymbol{e}^{(k)}\|$$

where $\|\cdot\|$ denotes some norm and ξ the contraction number. The contraction number is larger or equal to the convergence rate. The term convergence rate is also referred to as the velocity of convergence and the velocity of iteration [6]. Because the error $\boldsymbol{e}^{(k)}$ is commonly not known during a solution process, an approximate convergence rate defined with the residuum is frequently applied.

Steepest Descent Method. The steepest descent method applies a minimization of the quadratic form F:

$$F(\boldsymbol{x}) = \frac{1}{2}\boldsymbol{x}^T\boldsymbol{A}\boldsymbol{x} + \boldsymbol{b}^T\boldsymbol{x}$$

concerning the vector $\boldsymbol{x}$ to solve the equation $\boldsymbol{A}\boldsymbol{x} + \boldsymbol{b} = 0$ (Fig. 2.1). A minimum is found if the gradient of the quadratic form F equals zero:

$$\nabla F(\boldsymbol{x}) = \boldsymbol{A}\boldsymbol{x} + \boldsymbol{b} = 0$$

The minimization is performed iteratively starting with the approximate solution $\boldsymbol{x}^{(0)}$. The k-th solution $\boldsymbol{x}^{(k)}$ is calculated using the gradient of the quadratic function $\boldsymbol{r}^{(k-1)}$ at the previous solution $\boldsymbol{x}^{(k-1)}$:

$$\boldsymbol{r}^{(k-1)} = \nabla F(\boldsymbol{x}^{(k-1)}) = \boldsymbol{A}\boldsymbol{x}^{(k-1)} + \boldsymbol{b}$$

The k-th solution $\boldsymbol{x}^{(k)}$ is determined by moving from the previous solution $\boldsymbol{x}^{(k-1)}$ in direction of the gradient $\boldsymbol{r}^{(k-1)}$:

$$\boldsymbol{x}^{(k)} = \boldsymbol{x}^{(k-1)} + \alpha^{(k)}\boldsymbol{r}^{(k-1)} \tag{2.3}$$

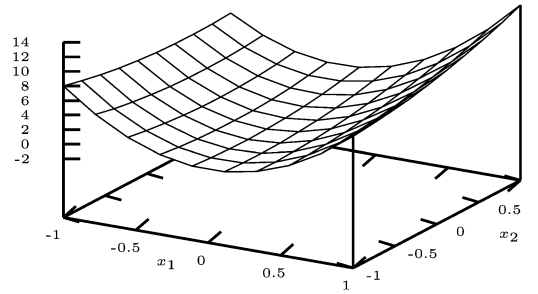

Fig. 2.1. Exemplary quadratic form in two dimensions. The value of the function $F(\boldsymbol{x}) = \frac{1}{2}\boldsymbol{x}^T\boldsymbol{A}\boldsymbol{x} + \boldsymbol{b}^T\boldsymbol{x}$ with the vector $\boldsymbol{x} = \begin{pmatrix} x_1 \\ x_2 \end{pmatrix}$, the matrix $\boldsymbol{A} = \begin{pmatrix} 8 & 1 \\ 1 & 1 \end{pmatrix}$, and the vector $\boldsymbol{b} = \begin{pmatrix} 2 \\ 1 \end{pmatrix}$ is plotted in the domain $[-1, 1][-1, 1]$. The minimum of the function F corresponds to the solution of the equation system $\boldsymbol{A}\boldsymbol{x} + \boldsymbol{b} = 0$.

where the scalar factor $\alpha^{(k)}$ is chosen by a minimization of the quadratic form F:

$$\frac{\partial F}{\partial \alpha^{(k)}}(\boldsymbol{x}^{(k)}) = 0 \tag{2.4}$$

Hence, the factor $\alpha^{(k)}$ is determined by:

$$\alpha^{(k)} = -\frac{\boldsymbol{r}^{(k-1)T}\boldsymbol{r}^{(k-1)}}{\boldsymbol{r}^{(k-1)T}\boldsymbol{A}\boldsymbol{r}^{(k-1)}}$$

The iteration is commonly stopped, if some norm of the residuum $\|\boldsymbol{r}^{(k)}\|$ becomes smaller than a given threshold or the iteration number k is larger than a given value.

The steepest descent method necessitates positive-definiteness of the matrix $\boldsymbol{A}$. Commonly, the method shows a small convergence rate [5]. The matrix $\boldsymbol{A}$ is unchanged during the solving process. Vector-vector and matrix-vector multiplications are the principle operations.

Conjugate Gradient Method. The conjugate gradient method uses like the steepest descent method a minimization of the quadratic function F:

$$F(\boldsymbol{x}) = \frac{1}{2}\boldsymbol{x}^T\boldsymbol{A}\boldsymbol{x} + \boldsymbol{b}^T\boldsymbol{x}$$

to determine a solution of the system of linear equations $\boldsymbol{A}\boldsymbol{x} + \boldsymbol{b} = 0$. The matrix $\boldsymbol{A}$ has to be symmetric and positive-definite.

The first step of the conjugate gradient method is the determination of the quadratic function's gradient $\boldsymbol{r}^{(0)}$ at a given initial solution $\boldsymbol{x}^{(0)}$:

$$\boldsymbol{r}^{(0)} = \nabla F(\boldsymbol{x}^{(0)}) = \boldsymbol{A}\boldsymbol{x}^{(\mathbf{0})} + \boldsymbol{b}$$

The minimization in direction of the gradient $\boldsymbol{r}^{(0)}$ delivers a new approximate solution $\boldsymbol{x}^{(1)}$ similar to the steepest descent method (equations 2.3 and 2.4). A secondary vector $\boldsymbol{p}^{(k)}$ is used in the conjugate gradient method to determine the direction of a correction. Initially, the vector $\boldsymbol{p}^{(1)}$ is set to the negative of the residuum $\boldsymbol{r}^{(0)}$.

In the k-th step the solution $\boldsymbol{x}^{(k)}$ is determined by

$$\boldsymbol{x}^{(k)} = \boldsymbol{x}^{(k-1)} + \alpha^{(k)}\boldsymbol{p}^{(k)}$$

where the minimization of the function F in direction of $\boldsymbol{p}^{(k)}$ delivers the scalar factor $\alpha^{(k)}$:

$$\frac{\partial}{\partial\alpha^{(k)}}F(\boldsymbol{x}^{(k)}) = 0$$

The factor $\alpha^{(k)}$ is calculated with the residual $\boldsymbol{r}^{(k-1)}$ and the direction $\boldsymbol{p}^{(k)}$:

$$\alpha^{(k)} = -\frac{\boldsymbol{r}^{(k-1)T}\boldsymbol{r}^{(k-1)}}{\boldsymbol{p}^{(k)T}\boldsymbol{A}\boldsymbol{p}^{(k)}}$$

The k-th direction $\boldsymbol{p}^{(k)}$ is determined with the residual $\boldsymbol{r}^{(k-1)}$, the direction $\boldsymbol{p}^{(k-1)}$ and the scalar factor $\beta^{(k-1)}$.

$$\boldsymbol{p}^{(k)} = -\boldsymbol{r}^{(k-1)} + \beta^{(k-1)}\boldsymbol{p}^{(k-1)}$$

The factor $\beta^{(k-1)}$ results from the condition that the directions $\boldsymbol{p}^{(k)}$ and $\boldsymbol{p}^{(k+1)}$ should be conjugate, i.e.:

$$\boldsymbol{p}^{(k)}\boldsymbol{A}\boldsymbol{p}^{(k+1)} = 0$$

Therefore, the factor $\beta^{(k-1)}$ is given by:

$$\beta^{(k-1)} = \frac{\boldsymbol{r}^{(k-1)T}\boldsymbol{A}\boldsymbol{p}^{(k-1)}}{\boldsymbol{p}^{(k-1)T}\boldsymbol{A}\boldsymbol{p}^{(k-1)}}$$

The k-th residual is defined by:

$$\boldsymbol{r}^{(k)} = \boldsymbol{r}^{(k-1)} + \alpha^{(k)}\boldsymbol{A}\boldsymbol{p}^{(k)}$$

The process constructs a sequence of directions, which are pairwise conjugated, and residuals, which are orthogonal [4]. Therefore, the process terminates theoretically after N steps. Although numerical problems may increase the iteration number, in many practical cases a prior termination is possible, e.g. when a sufficient accuracy is achieved.

Different variants of the conjugate gradient methods are developed, e.g. the biconjugate gradient method allows the treatment of systems with non-definite as well as asymmetric matrices [5].

Jacobi Method. The Jacobi method converges if the matrix $\boldsymbol{A}$ is diagonally dominant. The method is performed by decomposition of the matrix $\boldsymbol{A}$ into the sum of the lower triangular matrix $\boldsymbol{L}$, the diagonal matrix $\boldsymbol{D}$ and the upper triangular matrix $\boldsymbol{U}$:

$$\boldsymbol{A} = \boldsymbol{L} + \boldsymbol{D} + \boldsymbol{U}$$

Starting with a given vector $\boldsymbol{x}^{(0)}$ the k-th approximate solution $\boldsymbol{x}^{(k)}$ is determined with the scheme:

$$\boldsymbol{x}^{(k)} = \boldsymbol{D}^{-1}(-(\boldsymbol{L} + \boldsymbol{U})\boldsymbol{x}^{(k-1)} + \boldsymbol{b})$$

Alternatively, the equation system can be described in summation formulation, where the i-th coefficient of the solution vector x_i is given by:

$$x_i = -\frac{1}{a_{ii}} \left(b_i + \sum_{j=0, j \neq i}^{n-1} a_{ij} x_j \right)$$

The coefficients of the first approximate solution vector $x_i^{(1)}$ are determined by:

$$x_i^{(1)} = -\frac{1}{a_{ii}} \left(b_i + \sum_{j=0, j \neq i}^{n-1} a_{ij} x_j^{(0)} \right)$$

with the coefficients of the initial solution vector $x_j^{(0)}$. Similarly, the k-th solution vector's coefficients $x_i^{(k)}$ can be achieved using the previous solution vector $x_i^{(k-1)}$:

$$x_i^{(k)} = -\frac{1}{a_{ii}} \left(b_i + \sum_{j=0, j \neq i}^{n-1} a_{ij} x_j^{(k-1)} \right)$$

Similar to the other iterative methods, the iteration is commonly stopped, if some norm of the residuum $\boldsymbol{r}^{(k)}$ becomes smaller or the iteration number k becomes larger than a given value. The method is only of theoretical interest because the convergence rate is small. E.g. with $N \times N$ matrices resulting from finite difference approximations (Sect. 2.7.4) of a partial differential equation, i.e. the Poisson equation, the number of iterations r to reduce the error by the factor 10^{-p} is given by [5]:

$$r \simeq \frac{1}{2} p N^2$$

Gauss-Seidel Method. The Gauss-Seidel method is closely related to the Jacobi method. In contrast to the Jacobi method where the new solution takes knowledge only of the previous solution, the Gauss-Seidel method takes already calculated coefficients of the new solution into account. The matrix decomposition is given by:

$$(\boldsymbol{L}+\boldsymbol{D})\boldsymbol{x}^{(k)} = -\boldsymbol{U}\boldsymbol{x}^{(k-1)} + \boldsymbol{b}$$

In summation formulation the k-th step the new coefficients $x_i^{(k)}$ are determined by:

$$x_i^{(k)} = -\frac{1}{a_{ii}}\left(b_i + \sum_{j=0}^{i-1} a_{ij}x_j^{(k)} + \sum_{j=i+1}^{n-1} a_{ij}x_j^{(k-1)}\right)$$

The method increases the convergence in comparison with the Jacobi method. In the upper example the number of iterations r is halved. A further advantage is that the new and previous solution can share their storage. Nevertheless, the Gauss-Seidel method is unemployable for large problems because of its small convergence rate.

Successive Overrelaxation. Successive overrelaxation improves the Jacobi and Gauss-Seidel method. Successive overrelaxation applies a weighting on the difference Δ between the previous solution $\boldsymbol{x}^{(k-1)}$ and an approximation obtained with the methods. The weighted difference is added to the previous solution to achieve the new solution $\boldsymbol{x}^{(k)}$:

$$\boldsymbol{x}^{(k)} = \boldsymbol{x}^{(k-1)} + \omega\Delta$$

The weighting is done with a factor ω. The differences Δ_J and Δ_{GS} for the Jacobi and Gauss-Seidel method, respectively, are given by:

$$\Delta_J = \boldsymbol{D}^{-1}(-(\boldsymbol{L}+\boldsymbol{U})\boldsymbol{x}^{(k-1)} + \boldsymbol{b}) - \boldsymbol{x}^{(k-1)}$$
$$\Delta_{GS} = (\boldsymbol{L}+\boldsymbol{D})^{-1}(-\boldsymbol{U}\boldsymbol{x}^{(k-1)} + \boldsymbol{b}) - \boldsymbol{x}^{(k-1)}$$

In matrix formulation the k-th step the new coefficients $x_i^{(k)}$ are determined by:

$$x_i^{(k)} = x_i^{(k-1)} + \omega\left(-\frac{1}{a_{ii}}\left(b_i + \sum_{j=0, j\neq i}^{n-1} a_{ij}x_j^{(k-1)}\right) - x_i^{(k-1)}\right)$$

$$x_i^{(k)} = x_i^{(k-1)} + \omega\left(-\frac{1}{a_{ii}}\left(b_i + \sum_{j=0}^{i-1} a_{ij}x_j^{(k-1)} + \sum_{j=i+1}^{n-1} a_{ij}x_j^{(k-1)}\right) - x_i^{(k-1)}\right)$$

for the Jacobi and Gauss-Seidel method, respectively.

The successive overrelaxation converges if the matrix $\boldsymbol{A}$ is positive-definite and the weighting factor ω in the interval $]0:2[$. The appropriate selection of the factor ω is of importance to obtain large convergence rates. The optimal setting of the factor ω depends on the matrix properties. For a factor ω less than one the method performs a so-called underrelaxation, which is of interest for example in the multigrid methods. For a factor ω equal to one

the successive overrelaxation reduces to the Jacobi or Gauss-Seidel method. Commonly, the factor ω is determined by numerical experiments. For some classes of matrices an analytical determination of the optimal factor exists.

Optimal parameterization delivers a number of iterations r to reduce the error by the factor 10^{-p} in the upper problem, which is linearly dependent on the number of unknowns N. The number r is given by:

$$r \simeq \frac{1}{3} pN$$

Multigrid Method. Multigrid methods are applied for the solution of systems of linear equations resulting from discretization of partial differential equation [7, 6], e.g. with the finite element (Sect. 2.7.3) and finite differences method (Sect. 2.7.4). The methods necessitate the generation of different approximations of the linear equation systems, which can be achieved e.g. by simplification and coarsening of the spatial discretization. The h-th approximation of the linear equation system is given by:

$$\boldsymbol{A}_h \boldsymbol{x}_h + \boldsymbol{b}_h = 0$$

The motivation of multigrid methods can be understood by an frequency analysis of approximate solution's errors. Depending on their frequency the errors are reduced differently. E.g. the Jacobi and Gauss-Seidel methods decrease rapidly errors of high frequency while neglecting errors of low frequency. Therefore, it can be of advantage to reduce the errors in an appropriate spatially discretization.

Three types of operators are used in multigrid methods:

- Restriction
- Prolongation
- Smoothing

The restriction operator transfers values from fine to coarse discretized domains. The prolongation operator transfers values from coarse to fine domains. Commonly, the restriction as well as the prolongation operator are linear and global. The smoothing operator has the task of reducing efficiently high frequency errors in the different domains.

Two-Grid Method. The simplest multigrid method is the two-grid method. At first, the residuum $\boldsymbol{r}_h^{(0)}$ in the fine discretized domain is determined:

$$\boldsymbol{r}_h^{(0)} = \boldsymbol{A}_h \boldsymbol{x}_h^{(0)} + \boldsymbol{b}_h$$

with the startvector $\boldsymbol{x}_h^{(0)}$. The residuum is then transferred to the coarse domain using a restriction operator. The restriction operator performs an averaging and resampling of the residuum. In a three-dimensional domain, each of the following two operators $\boldsymbol{R}_{\mathbf{3\times3\times3}}$ and $\boldsymbol{R}_{\mathbf{2\times2\times2}}$ can be applied to

generate a coarse approximation $\boldsymbol{r}_{h-1}^{(0)}$. The operators are represented by a matrix:

$$\boldsymbol{R}_{\mathbf{2\times2\times2}} = \frac{1}{8}\begin{pmatrix}\begin{pmatrix}1&1\\1&1\end{pmatrix}\\\begin{pmatrix}1&1\\1&1\end{pmatrix}\end{pmatrix}$$

$$\boldsymbol{R}_{\mathbf{3\times3\times3}} = \frac{1}{8}\begin{pmatrix}\begin{pmatrix}0.125&0.25&0.125\\0.25&0.5&0.25\\0.125&0.25&0.125\end{pmatrix}\\\begin{pmatrix}0.25&0.5&0.25\\0.5&1&0.5\\0.25&0.5&0.25\end{pmatrix}\\\begin{pmatrix}0.125&0.25&0.125\\0.25&0.5&0.25\\0.125&0.25&0.125\end{pmatrix}\end{pmatrix}$$

The expense of the operator is determined by the type and sparsity of the matrix. The coarse residuum $\boldsymbol{r}_{h-1}^{(0)}$ is used as the right hand side of the equation system:

$$\boldsymbol{A}_{h-1}\boldsymbol{v}_{h-1}^{(0)} = -\boldsymbol{r}_{h-1}^{(0)}$$

The equation system is solved exactly, e.g. with direct methods, to determine the coarse correction $\boldsymbol{v}_{h-1}^{(0)}$. The correction $\boldsymbol{v}_{h-1}^{(0)}$ is transferred to the fine discretized domain by a prolongation operator resulting in the correction $\boldsymbol{v}_{h}^{(0)}$. Each of the following operators represented by the matrices $\boldsymbol{P}_{\mathbf{2\times2\times2}}$ and $\boldsymbol{P}_{\mathbf{3\times3\times3}}$ can be used to perform the transfer, which can be understood as interpolation starting from a coarse domain into a fine domain.

$$\boldsymbol{P}_{\mathbf{2\times2\times2}} = \begin{pmatrix}\begin{pmatrix}1&1\\1&1\end{pmatrix}\\\begin{pmatrix}1&1\\1&1\end{pmatrix}\end{pmatrix}$$

$$\boldsymbol{P}_{\mathbf{3\times3\times3}} = \begin{pmatrix}\begin{pmatrix}0.125&0.25&0.125\\0.25&0.5&0.25\\0.125&0.25&0.125\end{pmatrix}\\\begin{pmatrix}0.25&0.5&0.25\\0.5&1&0.5\\0.25&0.5&0.25\end{pmatrix}\\\begin{pmatrix}0.125&0.25&0.125\\0.25&0.5&0.25\\0.125&0.25&0.125\end{pmatrix}\end{pmatrix}$$

The expense of a prolongation operator is determined by type and sparcity of the transfer matrix. The correction $\boldsymbol{v}_{h}^{(0)}$ is added to the start vector to obtain the new approximation $\boldsymbol{x}_{h}^{(1)}$:

$$\boldsymbol{x}_h^{(1)} = \boldsymbol{x}_h^{(0)} + \boldsymbol{v}_h^{(0)}$$

Additionally, the new approximation $\boldsymbol{x}_h^{(1)}$ is smoothed to reduce high frequency error, e.g. with the Jacobi and Gauss-Seidel method.

The scheme of the two-grid method consists of residuum calculation, restriction, exact solution, prolongation and smoothing. This scheme is repeated until some stop criterion is fulfilled.

Multigrid Method. The crucial point concerning the efficiency of the two-grid method is the exact solution in the coarse domain. Substituting the step of exact solution by a recursive application leads to multigrid methods. Multigrid methods can be classified by the number of domains and by the strategy traversing through these domains [5].

Full-Multigrid Method. The full-multigrid method starts with the solution in the coarsest domain, e.g. by direct methods. The solution is transferred to the next finer domain with an appropriate prolongation operator. Here, the two-grid method is applied. The scheme is iteratively applied until a solution in the finest domain is achieved. In each domain the multigrid method is applied. The solutions in the different domains are transferred with a prolongation operator. The full-multigrid method offers the advantage that the determination of an appropriate start vector is automatically performed.

2.4.4 Singular Value Decomposition

The singular value decomposition is a further technique to solve systems of linear equations, which is commonly applied in cases where the upper direct and iterative methods fail. These methods fail e.g. if the matrix $\boldsymbol{A}$ is not square, if the rank of the matrix $\boldsymbol{A}$ is not maximal and if the column vectors are nearly linear dependent [8].

Any $M \times N$ matrix $\boldsymbol{A}$ with $M > N$ can be decomposed in a column-orthonormal $M \times N$ matrix $\boldsymbol{U}$, a diagonal $N \times N$ matrix $\boldsymbol{D}$ and the transpose of a column-orthonormal $N \times N$ matrix $\boldsymbol{V}$ [5]:

$$\boldsymbol{A} = \boldsymbol{U}\boldsymbol{D}\boldsymbol{V}^T$$

Column-orthogonality of the matrices $\boldsymbol{U}$ and $\boldsymbol{V}$ is defined as:

$$\boldsymbol{U}^T\boldsymbol{U} = I$$
$$\boldsymbol{V}^T\boldsymbol{V} = I$$

with the identity matrix I. Caused by the column-orthonormality of the matrices $\boldsymbol{V}$ and $\boldsymbol{U}$ their inverses are equal to their transpose:

$$\boldsymbol{U}^T = \boldsymbol{U}^{-1}$$
$$\boldsymbol{V}^T = \boldsymbol{V}^{-1}$$

The diagonal matrix $\boldsymbol{D}$ has the following form:

$$D = \begin{pmatrix} \lambda_1 & 0 & \cdots & \cdots & 0 \\ 0 & \lambda_2 & \ddots & & \vdots \\ \vdots & \ddots & \ddots & \ddots & \vdots \\ \vdots & & \ddots & \lambda_{N-1} & 0 \\ 0 & \cdots & \cdots & 0 & \lambda_N \end{pmatrix}$$

The diagonal elements $\lambda_1 \ldots \lambda_N$, the so-called singular values, are positive or zero.

If the matrix $\boldsymbol{A}$ is square and the singular values are positive, the decomposition allows to determine the inverse of the matrix $\boldsymbol{A}$:

$$\boldsymbol{A}^{-1} = \boldsymbol{V}\boldsymbol{D}^{-1}\boldsymbol{U}^T$$

In the case of a square, symmetric matrix $\boldsymbol{A}$, the orthogonal matrices are identical:

$$\boldsymbol{U} = \boldsymbol{V}$$

Different numerical techniques are used to perform a singular value decomposition depending on the numbers of columns versus the numbers of rows [5, 9].

2.5 Numerical Integration of Functions

2.5.1 Definition

The numerical integration of functions, the so-called quadrature, is an integral part of many numerical methods, e.g. of the finite element method to solve partial differential equations as well as of the Runge-Kutta method applied to solve ordinary differential equations [9]. The task of a numerical integration of an integrable function f in the interval $[a, b]$ is to determine an approximate solution for the integral I:

$$I = \int_a^b f(x)\ dx$$

An approximate solution $\tilde{I}$ can be calculated by the summation of weighted function values:

$$\tilde{I} = \sum_{i=1}^{N} w_i f(x_i) \tag{2.5}$$

with the weighting factors w_i, the integration points $x_i \in [a, b]$ and their number N. These parameters are variables and their choice is specific to the numerical technique for the integration of functions.

The numerical techniques can be classified by the positions of the integration points as well as on the assumptions and demands on the properties of the function f. Methods are distinguished with equidistant and non-equidistant integration points. The equidistance of integration points restricts the free variables in equation 2.5 to the weighting factors w_i and the number of integration points N.

2.5.2 Trapezoidal Rule

The trapezoidal rule uses an equidistant decomposition of the interval I [9]. In each partial interval the integral I is approximated by the values of the function f at the interval limits:

$$I = \int_a^b f(x)\ dx \approx \frac{1}{2}(b-a)\,(f(a)+f(b))$$

with the limits a and b as well as the length of the partial interval $b-a$. Summation over the whole integral delivers the approximate integral $\tilde{I}$:

$$\tilde{I} = h\left(\frac{1}{2}f(x_0) + \sum_{i=1}^{N-1} f(x_i) + \frac{1}{2}f(x_N)\right)$$

with the distance between sampling points $h = \frac{b-a}{N}$ and the sampling points $x_i = a + ih$.

The approximation neglects components of the function f resulting from its derivatives with order greater or equal than two. The neglect can be shown by Taylor series expansion [8, 9]. The approximation can be improved by increasing the number of integration points N.

2.5.3 Simpson's Rule

An equidistant decomposition of the interval I is used in the Simpson's rule [9]. Each partial interval is approximated with the values at the interval limits and center:

$$\int_a^b f(x)\ dx \approx \frac{1}{6}(b-a)\left(f(a) + 4f(\frac{a+b}{2}) + f(b)\right)$$

The formula for numerical integration by Simpson's rule with a number N of equidistant integration points x_i is given by:

$$\begin{aligned}\tilde{I} = h\Big(&\frac{1}{6}f(x_0) + \frac{4}{6}f(x_1) + \frac{2}{6}f(x_2) + \ldots \\ &+\frac{2}{6}f(x_{N-2}) + \frac{4}{6}f(x_{N-1}) + \frac{1}{6}f(x_N)\Big)\end{aligned}$$

with the distance between sampling points h.

The approximation by Simpson's Rule does not take into account components of the function f resulting from its derivatives with order greater or equal to four [8, 9].

Table 2.2. Gauss quadrature. Dependent on the domain and the polynomial order the integration points and weights are determined.

Domain	Polynomial Order	Points	Weights
$[-1,1]$	1	0.0	2
$[0,1]$	1	0.5	1
$[-1,1]$	3	± 0.57735	1, 1
$[0,1]$	3	$0.211325, 0.788675$	0.5, 0.5
$[-1,1]$	5	$\pm 0.77459, 0.0$	$0.\overline{5}, 0.\overline{5}, 0.\overline{8}$
$[0,1]$	5	$0.112705, 0.887295, 0.5$	$0.2\overline{7}, 0.2\overline{7}, 0.\overline{4}$

2.5.4 Gauss Quadrature

The Gauss quadrature uses non-equidistant integrations points x_i. In contrast to the former methods all parameters in equation 2.5 are variables and their values are determined by the assumption underlying the Gauss quadrature.

The Gauss quadrature uses N integration points x_i and N weights w_i to determine exactly a polynomial q of order $2N-1$. In the interval $[-1,1]$ the integration points x_i are uniquely defined as zero points of the Legendre-polynomial P_N (table 2.2):

$$P_N(x) = \frac{1}{2^N N!} \frac{d^N}{dx^N} \left(x^2 - 1\right)^N$$

The weights w_i are determined by:

$$w_i = \int_{-1}^{1} \prod_{j=1, j\neq i}^{N} \left(\frac{x - x_j}{x_i - x_j} \right)^2 dx$$

The Gauss quadrature is not restricted to the domain $[-1,1]$. It can be extended for the calculation of integrals in arbitrary one-dimensional domains (table 2.2) as well as in multidimensional domains. E.g. an integration in triangular-, tetrahedron-, quadrilateral- and hexahedron-shaped domains can be performed.

2.6 Numerics of Ordinary Differential Equations

2.6.1 Definition

An ordinary differential equation of order n is defined as:

$$\frac{d^n y}{dx^n} = f(x, y, \frac{dy}{dx}, \frac{d^2 y}{dx^2}, \ldots, \frac{d^{n-1} y}{dx^{n-1}}) \tag{2.6}$$

with the function y depending only on one variable x, i.e. $y = y(x)$. The order n indicates the maximal order of the derivatives of the function y. Commonly, the function f is nonlinear.

A so-called initial value problem consists of solving the equation 2.6 concerning the unknown function y with initially given values $b_0, \ldots, b_{n-1}$:

$$y(x_0) = b_0, \ \ldots, \ \frac{d^{n-1}y(x_0)}{dx^{n-1}} = b_{n-1}$$

The equation 2.6 can always be transformed to a system of first order differential equations introducing the new functions $y_0, \ldots, y_n$ [5, 9]:

$$y_0 \equiv y, \ y_1 \equiv \frac{dy}{dx}, \ y_2 \equiv \frac{d^2y}{dx^2}, \ \ldots, \ y_n \equiv \frac{d^ny}{dx^n}$$

The resulting system of first order differential equations is given by:

$$\begin{aligned}
\frac{dy_0}{dx} &= y_1 \\
\frac{dy_1}{dx} &= y_2 \\
&\vdots \\
\frac{dy_{n-2}}{dx} &= y_{n-1} \\
\frac{dy_{n-1}}{dx} &= f(x, y_0, \ldots, y_{n-2})
\end{aligned}$$

The initial values $b_0, \ldots, b_{n-1}$ are attributed to the new functions $y_0, \ldots, y_{n-1}$:

$$y_0(x_0) = b_0, \ \ldots, \ y_{n-1}(x_0) = b_{n-1}$$

The following overview of methods for numerical solving of ordinary differential equations is reduced to the treatment of first order equations. This reduction is motivated both by the availability of the upper transformation and by the common occurrence of the first order equation type.

2.6.2 Euler Method

The Euler method solves the first order differential equation:

$$\frac{dy}{dx} = f(x, y)$$

with the initial value $y(x_0) = b_0$ by propagation through successive points, where the step-size h is constant. The solving scheme works iteratively using the known value of the function $y_n \approx y(x_n)$ at x_n to calculate the next value $y_{n+1} \approx y(x_{n+1})$ at x_{n+1}:

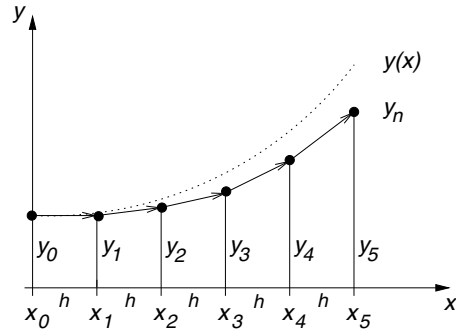

Fig. 2.2. Euler method for numerical solution of ordinary differential equations. The exact solution $y(x)$ is indicated by a dotted line. The numerical solution y_n is shown as a solid line. The solution function y_n is given by the values $y_0, \ldots, y_5$ which are calculated sequentially at points $x_0, \ldots, x_5$. The distance between the points h is constant during the propagation.

$$y_{n+1} = y_n + hf(x_n, y_n) \tag{2.7}$$

with the distance h between x_n and x_{n+1}. The distance h is kept constant during the progress (Fig. 2.2).

The properties of the Euler method can be studied using the Taylor series expansion for the function y [8, 9]:

$$y(x+h) = y(x) + h\frac{1}{1!}\frac{dy}{dx}(x) + h^2\frac{1}{2!}\frac{d^2y}{dx^2}(x) + h^3\frac{1}{3!}\frac{d^3y}{dx^3}(x) + \ldots \tag{2.8}$$

A comparison with the upper scheme (equation 2.7) shows that the Euler method neglects terms with derivatives of order greater or equal to two. The truncation error E is given by:

$$E = y(x+h) - y_{n+1} = h^2\frac{1}{2}\frac{d^2y}{dx^2}(x) + h^3\frac{1}{6}\frac{d^3y}{dx^3}(x) + \ldots \tag{2.9}$$

The truncation error E can be quadratically reduced by bisection of the distance h. Alternatively, a reduction of this error can be achieved by introduction of higher order terms in equation 2.7.

Another source of error is the inaccuracy of floating point arithmetic, e.g. by non-representability of numbers. This so-called rounding error is not limited to the application of the Euler method but inherent in the floating point arithmetic. The error can be reduced by careful selection of distance values, data type and implementation of the function f.

2.6.3 Runge-Kutta Method

The Runge-Kutta method allows like the Euler method the numerical solution of the first order ordinary differential equation:

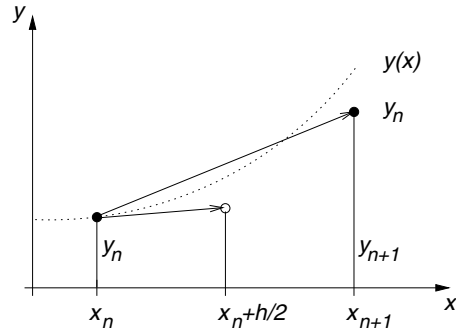

Fig. 2.3. Second order Runge-Kutta method for numerical solution of ordinary differential equations. The solution function y_n is determined by the values y_n and y_{n+1}. The distance h between the points x_n and x_{n+1} is constant during the propagation. The numerical solution y_n is shown as a solid line. The exact solution $y(x)$ is indicated by a dotted line.

$$\frac{dy}{dx} = f(x, y) \tag{2.10}$$

by propagation through different points, where the step-size h is constant. The method uses the value y_n and multiple evaluations of the function f to determine the new value y_{n+1} at x_{n+1}. The number of evaluations determines the order the Runge-Kutta method.

The idea behind the Runge-Kutta method is an integration of equation 2.10 in the interval $[x_n, x_{n+1}]$:

$$y_{n+1} - y_n = \int_{x_n}^{x_{n+1}} f(x, y)dx$$

with the known value y_n and the unknown value y_{n+1}. The right hand side of the equation is treated with numerical integration methods similar to the quadrature methods (Sect. 2.5). The integration points and the weighting values are optimized to minimize approximation errors.

The properties of the Runge-Kutta method can be examined by applying the Taylor series expansion for the function y [9], in a similar way like the study of the properties of the Euler method (equation 2.8).

The second order Runge-Kutta method uses a first evaluation of the function f at the point x_n, which is afterwards used at the point $x_n + \frac{1}{2}h$ for a second evaluation (Fig. 2.3):

$$\begin{aligned} k_1 &= hf(x_n, y_n) \\ k_2 &= hf(x_n + \frac{1}{2}h, y_n + \frac{1}{2}k_1) \\ y_{n+1} &= y_n + k_2 \end{aligned}$$

Using the Taylor series expansion it can be shown that the second order Runge-Kutta method neglects terms with derivatives of order greater or equal to three.

A third order Runge-Kutta method uses three evaluations of the function f at the points x_n, $x_n + \frac{1}{3}h$ and $x_n + \frac{2}{3}h$ to determine the value of y_{n+1}:

$$\begin{aligned} k_1 &= hf(x_n, y_n) \\ k_2 &= hf(x_n + \frac{1}{3}h, y_n + \frac{1}{3}k_1) \\ k_3 &= hf(x_n + \frac{2}{3}h, y_n + \frac{2}{3}k_2) \\ y_{n+1} &= y_n + \frac{1}{4}(k_1 + 3k_3) \end{aligned}$$

A fourth order method, the so-called classical Runge-Kutta method, is given by:

$$\begin{aligned} k_1 &= hf(x_n, y_n) \\ k_2 &= hf(x_n + \frac{1}{2}h, y_n + \frac{1}{2}k_1) \\ k_3 &= hf(x_n + \frac{1}{2}h, y_n + \frac{1}{2}k_2) \\ k_4 &= hf(x_n + h, y_n + k_3) \\ y_{n+1} &= y_n + \frac{h}{6}(k_1 + 2k_2 + 2k_3 + k_4) \end{aligned}$$

Four evaluations are necessary to proceed from the point x_n to the point x_{n+1}.

Commonly, Runge-Kutta methods with an order higher than four are not applied because of their large numerical expense. An extension of the Runge-Kutta method allows adaptive control over the propagation process by changing of the step-size h [5, 9]. The extension uses an estimation of the truncation error (equation 2.9) to increase or decrease the step-size. The truncation error can be estimated by comparing the results achieved by Runge-Kutta methods of different order.

2.7 Numerics of Partial Differential Equations

2.7.1 Definition

In contrast to an ordinary differential equation, where the unknown is a function y of only one variable x, i.e. $y = y(x)$, a partial differential equation describes a function u of two or more variables $x_1, x_2, \ldots$, e.g. in the two-dimensional case $u = u(x_1, x_2)$. Similarly, the order n of a partial differential equation indicates the maximal order of the derivative of the function.

As an example, a second order linear partial differential equation in the region $\Omega \subset \mathbb{R}^2$ is given by [9]:

$$A(x_1, x_2)\frac{\partial^2 u}{\partial {x_1}^2} + 2B(x_1, x_2)\frac{\partial^2 u}{\partial x_1 \partial x_2} + C(x_1, x_2)\frac{\partial^2 u}{\partial {x_2}^2} + D(x_1, x_2)\frac{\partial u}{\partial x_1} + E(x_1, x_2)\frac{\partial u}{\partial x_2} + F(x_1, x_2)\ u = G(x_1, x_2)$$

with the functions A, B, C, D, E, F, and G. Depending on the values of these functions and assuming that $A^2 + B^2 + C^2 \neq 0$ in Ω, this equation is classified into three types:

- $AC - B^2 > 0$: elliptic
- $AC - B^2 < 0$: hyperbolic
- $AC - B^2 = 0$: parabolic

The classification influences the choice of numerical treatment of the partial differential equation.

A representative of an elliptic differential equation is the so-called Poisson equation. In a two-dimensional formulation the equation is given by:

$$\frac{\partial^2 u}{\partial {x_1}^2} + \frac{\partial^2 u}{\partial {x_2}^2} = G(x_1, x_2) \tag{2.11}$$

If the right hand side of the equation is equal to zero, the Poisson equation reduces to the Laplace equation:

$$\frac{\partial^2 u}{\partial {x_1}^2} + \frac{\partial^2 u}{\partial {x_2}^2} = 0 \tag{2.12}$$

The Poisson and Laplace equations are frequently applied to describe stationary and quasi-stationary physical phenomena, e.g. time independent electric, magnetic and temperature fields. For this purpose the equations are extended to represent three-dimensional fields and to incorporate material specific behavior.

A prototypical hyperbolic differential equation is the wave equation:

$$\frac{\partial^2 u}{\partial t^2} = v^2 \frac{\partial^2 u}{\partial x^2} \tag{2.13}$$

with the constant velocity of wave propagation v. The wave equation can be used to describe instationary processes, e.g. the propagation of electromagnetic waves and acoustical resonance phenomena. Appropriate initial values must be given to ensure uniqueness.

A representative of a parabolic differential equation is the diffusion equation:

$$\frac{\partial u}{\partial t} = D\frac{\partial^2 u}{\partial x^2} \tag{2.14}$$

with the constant diffusion coefficient D. The diffusion equation models instationary phenomena, which are found for heat and mass transfer processes. The solution depends on given initial values.

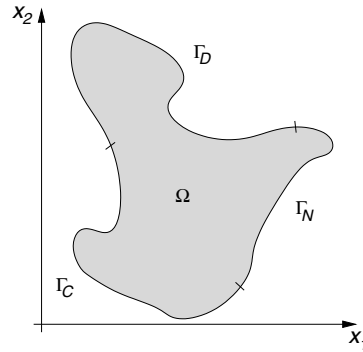

Fig. 2.4. Exemplary two-dimensional boundary value problem. The partial differential equation is defined in the region Ω with the boundary Γ. The boundary Γ is sub-divided in three partial boundaries Γ_D, Γ_N, and Γ_C. For each of these a specific type of boundary condition is defined.

2.7.2 Initial Values and Boundary Conditions

The solution of partial differential equations is dependent on the definition of initial values and boundary conditions. E.g. the uniqueness of the solution of elliptical equations is ensured only if appropriate boundary conditions are attributed [4, 9].

Initial values specify the solution function u and its derivatives for the time $t = 0$ (Sect. 2.6). Initial values can be applied everywhere in the region Ω and at its boundary Γ.

Boundary conditions specify the solution function u at the boundary Γ of the region Ω (Fig. 2.4). The boundary Γ is split up in three partial boundaries Γ_D, Γ_N, and Γ_C:

$$\Gamma = \Gamma_D \cup \Gamma_N \cup \Gamma_C$$

where different types of boundary conditions are defined, i.e. Dirichlet, Neumann and Cauchy conditions.

A Dirichlet condition specifies the values at parts of the boundary $\Gamma_D \subset \Gamma$ with the function ϕ:

$$u(\boldsymbol{x}) = \phi(\boldsymbol{x}) \text{ for } \boldsymbol{x} \in \Gamma_D$$

A Neumann condition defines the values of gradients in normal direction $\boldsymbol{n}$ of the partial boundary $\Gamma_N \subset \Gamma$ with the function γ:

$$\frac{\partial u}{\partial \boldsymbol{n}}(\boldsymbol{x}) = \gamma(x) \text{ for } \boldsymbol{x} \in \Gamma_N$$

The Cauchy condition is the general formulation of boundary conditions:

$$\frac{\partial u}{\partial \boldsymbol{n}}(\boldsymbol{x}) + \alpha(\boldsymbol{x})u(\boldsymbol{x}) = \beta(\boldsymbol{x}) \text{ for } \boldsymbol{x} \in \Gamma_C$$

with the functions α and β defined at the partial boundary $\Gamma_C \subset \Gamma$. The Cauchy condition includes the Dirichlet and Neumann condition as special cases.

2.7.3 Finite Element Method

Overview. The finite element method is one of the numerical methods used to solve partial differential equations. The ideas underlying the finite element method are introduced with the classical work of Ritz and Galerkin.

The method can be subdivided into consecutive steps:

- Discretization of the spatial domain
- Element-wise interpolation of the solution function
- Determination of element equations
- Assembling of system equations
- Incorporation of boundary conditions
- Solution of system equations

The name of the method comes from the first step of the proceeding, where the spatial domain is discretized in finite elements. Appropriate interpolation methods of the solution function dependent on element type are assigned. The element equations characterize the element's contribution to the equations describing the whole system. Each element's contribution is determined as a function of variables and assembled into the system equations. These equations are modified to incorporate boundary conditions and solved to determine the unknown function.

Classical Work

Ritz Method. The Ritz method is a historical approach to indirectly solve partial differential equations. The method approximates the unknown function u by a linear combination of $N+1$ orthogonal functions ϕ_i weighted with the factors a_i:

$$u = \phi_0 + \sum_{i=1}^{N} a_i \phi_i \tag{2.15}$$

The functions ϕ_i are defined over the whole spatial domain Ω as well as they are chosen appropriately in dependence of the application and boundary conditions. E.g. the Dirichlet conditions have to be respected by the function ϕ_0 and the other functions ϕ_i have to be zero.

The approximation in equation 2.15 substitutes the unknown function u in a functional Π which is equivalent to the differential equation. The factors a_i are determined in such a way that the functional is stationary:

$$\frac{\partial \Pi}{\partial a_i} = 0 \tag{2.16}$$

Example. The Ritz method is applied to solve the elliptical differential equation (equation 2.11) in the domain Ω with consideration of boundary conditions:

$$\frac{\partial^2 u}{\partial {x_1}^2} + \frac{\partial^2 u}{\partial {x_2}^2} = G(x_1, x_2)$$

The equivalent function Π is given by:

$$\Pi = \iint_\Omega \frac{1}{2} \left(\frac{\partial u}{\partial x_1} \right)^2 + \frac{1}{2} \left(\frac{\partial u}{\partial x_2} \right)^2 + G(x_1, x_2) u \; dx_1 \, dx_2$$

This equation is modified by substitution with the linear combination of weighted orthogonal functions ϕ_i (equation 2.15). The stationary condition, i.e. derivation of Π by the weighting factors a_i (equation 2.16), constructs a system of equations, which can be solved either exactly or approximately delivering the weighting values a_i for the determination of the unknown function u.

Galerkin Method. The Galerkin method, which is also known as the method of weighted residuals [4, 10], is a further classical method to indirectly solve partial differential equations. The method is based on the Ritz approach by using the approximation of the unknown function u with a linear combination of weighted orthogonal functions (equation 2.15).

An approximate solution $\tilde{u}$ of an arbitrary differential equation $D(u) = 0$ with the exact solution u is analyzed introducing the residuum R:

$$R = D(\tilde{u}) \tag{2.17}$$

Herewith, the Galerkin method consists of solving the system of integrals:

$$\int_\Omega \phi_i R \; d\Omega = 0 \tag{2.18}$$

The dimension of the system is $N + 1$. The residuum R is weighted with the approximation functions ϕ_i.

Example. The Galerkin method is applied to solve the elliptical differential equation (equation 2.11) in consideration of boundary conditions:

$$\frac{\partial^2 u}{\partial {x_1}^2} + \frac{\partial^2 u}{\partial {x_2}^2} = G(x_1, x_2)$$

which can be reformulated for simplicity as:

$$\mathbb{L}u = G(x_1, x_2) \tag{2.19}$$

with the elliptical operator $\mathbb{L}$ given by:

$$\mathbb{L} \equiv \left(\frac{\partial}{\partial x_1} \quad \frac{\partial}{\partial x_2} \right) \begin{pmatrix} \frac{\partial}{\partial x_1} \\ \frac{\partial}{\partial x_2} \end{pmatrix}$$

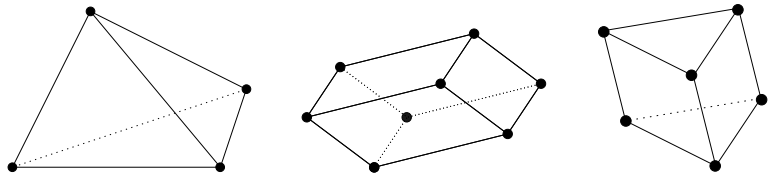

Fig. 2.5. Exemplary three-dimensional finite elements. The spatial domain Ω is subdivided in appropriate elements with assigned node points indicated by black spheres. Commonly, in three-dimensional domains (a) tetrahedron, (b) hexahedrons and (c) prisms are used.

The residuum R derived from equation 2.19 is defined as:

$$R = G(x_1, x_2) - \mathbb{L}u \tag{2.20}$$

The equation is modified by substitution with the linear combination of weighted orthogonal approximation functions ϕ_i:

$$R = G(x_1, x_2) - \mathbb{L}\left(\phi_0 + \sum_{i=1}^{n} a_i \phi_i\right)$$

This equation is substituted in equation 2.18. The resulting equation system can be solved either exactly or approximately to give the weighting values a_i.

Discretization of the Spatial Domain. The spatial discretization or meshing step in the finite element method consists of subdividing the domain Ω with appropriate elements occupying the domains $\Omega^{(m)}$:

$$\Omega = \bigcup_{m \in \{1,\ldots,N\}} \Omega^{(m)}$$

with N as the number of elements. The elements are non-intersecting:

$$\Omega^{(m)} \cap \Omega^{(n)} = 0$$

for $m, n \in \{1, \ldots, N\}$ and $m \neq n$.

Commonly, geometrically simple elements of varying size and shape are applied (Fig. 2.5). In three-dimensional domains tetrahedrons, hexahedrons and prisms are frequently employed. In two-dimensional domains triangles and quads are used. A distinction between structured and unstructured subdivisions is made leading to meshes with homogeneously distributed, uniform elements and arbitrary elements, respectively.

The node points are assigned to the elements and mostly lie at their corners. Further element types include node points inside or located at edges. Attributed to the node points are node variables, which describe the values of

the solution function. E.g. node variables represent potentials of electric fields, spatial displacements in structure mechanics, and velocities in fluid mechanics. Commonly, adjoining elements share node points and the attributed node variables.

The spatial discretization is a determinant for the accuracy of a finite element analysis. The decrease of element size by increasing the element number can lead to a higher accuracy. This kind of refinement of the discretization is known as the h-method. The shape of the elements has to be taken into account, e.g. elements with very large or small angles can lead to ill-conditioned equation systems. An adaptation to spatial and field particularities is of advantage, e.g. an increase of elements in regions with large inhomogeneity of geometry and with large alteration of the solution function will improve the accuracy of the analysis.

Element-Wise Interpolation of the Solution Function. The interpolation allows the determination of the solution function u at an arbitrary point $\boldsymbol{x}$ in the domain Ω. In contrast to the Ritz approach (equation 2.15), where the approximation functions ϕ_i are defined over the whole domain Ω and weighted by factors a_i, the interpolation functions used in the finite element methods are local. Interpolation functions are defined only inside the domain $\Omega^{(m)}$ of each m-th element and weighted by the values of the node variables $u_i^{(m)}$ assigned to node points $\boldsymbol{x}_i^{(m)}$. The element-wise interpolation is commonly carried out by summation of shape-functions $H_i^{(m)}$:

$$u(\boldsymbol{x}) = \sum_{i=1}^{N} H_i^{(m)}(\boldsymbol{x})\ u_i^{(m)}$$

with the node variables number N. The choice of appropriate shape-functions is influenced by the aspired order of interpolation, the dimension of the spatial domain and the traits of the solution function.

In the following section the description primarily treats the most common type of node variable. This type of node variable specifies directly the value of the unknown function u at the node points $\boldsymbol{x}_i^{(m)}$:

$$u(\boldsymbol{x}_i^{(m)}) = u_i^{(m)}$$

with the node variables $u_i^{(m)}$. Node variables specifying derivatives of the unknown function u are discussed in detail e.g. in [4].

The assumption leads to requirements for the shape-functions $H_i^{(m)}$ determining their values at the node points $\boldsymbol{x}_i^{(m)}$:

$$H_i^{(m)}(\boldsymbol{x}) = \begin{cases} 1 & : \quad \boldsymbol{x} = \boldsymbol{x}_i^{(m)} \\ 0 & : \quad \boldsymbol{x} = \boldsymbol{x}_j^{(m)}, j \neq i \end{cases} \tag{2.21}$$

A further, pragmatic requirement is, that the sum of the shape-functions $H_i^{(m)}$ at an arbitrary point is given by:

$$\sum_{i=1}^{N} H_i^{(m)}(\boldsymbol{x}) = 1 \tag{2.22}$$

Definition of Shape-Functions. These requirements allow a definition of shape-functions assuming an interpolation operator $\mathbb{P}$ for the solution function u:

$$u(\boldsymbol{x}) = \mathbb{P}(\boldsymbol{x}, \boldsymbol{a}^{(m)}) \tag{2.23}$$

with the a-priori unknown parameter vector $\boldsymbol{a}^{(m)}$. Commonly, the interpolation operator $\mathbb{P}$ is polynomial, e.g. linear, quadratic and cubic.

Substituting the requirements (equation 2.21) for the node variables $u_i^{(m)}$ at the given node points $\boldsymbol{x}_i^{(m)}$ allows an equation system for the m-th element to be set up:

$$u_i^{(m)} = \mathbb{P}(\boldsymbol{x}_i^{(m)}, \boldsymbol{a}^{(m)})$$

The equation system is transformed in such a way, that the parameter vector $\boldsymbol{a}^{(m)}$ is determined as a function of the node variables $u_i^{(m)}$. These parameter functions are substituted in the equation 2.23. The resulting equation is rearranged to separate the coefficients of the node variables $u_i^{(m)}$. The coefficients are identical to the shape-functions.

Example for Line Element. In a one-dimensional domain $\Omega = [0, 1]$ a linear interpolation at point x is given by:

$$u(x) = a_0^{(m)} + a_1^{(m)} x \tag{2.24}$$

with the two scalar constants $a_0^{(m)}$ and $a_1^{(m)}$. The scalar constants are a-priori unknown. The following equation system is set up from the requirements (equation 2.21) for the node variables $u_0^{(m)}$ and $u_1^{(m)}$ at the node points $x_0^{(m)} = 0$ and $x_1^{(m)} = 1$.

The requirements are substituted in the interpolation function (equation 2.24):

$$\begin{aligned} u_0^{(m)} &= a_0^{(m)} \\ u_1^{(m)} &= a_0^{(m)} + a_1^{(m)} \end{aligned}$$

which can be represented in matrix notation as:

$$\begin{pmatrix} u_0^{(m)} \\ u_1^{(m)} \end{pmatrix} = A \begin{pmatrix} a_0^{(m)} \\ a_1^{(m)} \end{pmatrix} \text{ with } A = \begin{pmatrix} 1 & 0 \\ 1 & 1 \end{pmatrix}$$

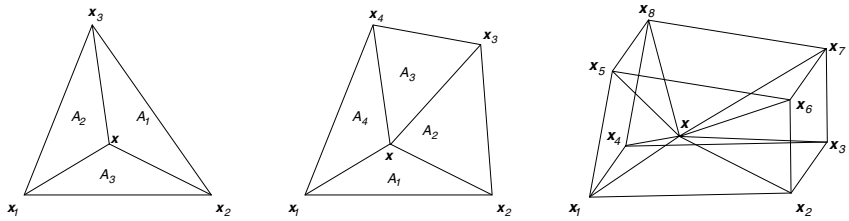

Fig. 2.6. Natural coordinates in (a) triangle, (b) quadrilateral and (c) tetrahedron. The coordinates describe uniquely a point $\boldsymbol{x}$ inside the element by areas constructed with the node points $\boldsymbol{x_i}$ and the point $\boldsymbol{x}$.

Inversion of the matrix A delivers the equation system:

$$A^{-1}\begin{pmatrix} u_0^{(m)} \\ u_1^{(m)} \end{pmatrix} = \begin{pmatrix} a_0^{(m)} \\ a_1^{(m)} \end{pmatrix} \text{ with } A^{-1} = \begin{pmatrix} 1 & 0 \\ -1 & 1 \end{pmatrix}$$

which describes the constants as a product of the matrix A^{-1} and the vector of node variables $\boldsymbol{u}^{(m)}$. Substitution of the constants in equation 2.24 and rearrangement:

$$\begin{aligned} u(x) &= u_0^{(m)} + (u_1^{(m)} - u_0^{(m)})x \\ &= u_0^{(m)}(1-x) + u_1^{(m)}x \end{aligned}$$

allows the determination of the shape-functions $H_0^{(m)}$ and $H_1^{(m)}$, which are given by:

$$\begin{aligned} H_0^{(m)}(x) &= 1 - x \\ H_1^{(m)}(x) &= x \end{aligned}$$

These shape-functions fulfill obviously the second requirement (equation 2.22).

Natural Coordinates. Shape-functions can alternatively be derived using natural coordinates of an element [4, 10]. Natural coordinates serve to describe uniquely a point $\boldsymbol{x}$ inside of the element (Fig. 2.6). The dimension of the natural coordinate system depends on the number of node points, e.g. three natural coordinates describe a point inside a triangle, four coordinates describe a point inside of a quadrilateral and a tetrahedron, eight coordinates are attributed in a hexahedron. In two- and three-dimensional elements shape-functions are identified by the ratio of areas and volumina, respectively. In two-dimensional elements the natural coordinates are also known as area coordinates [10].

In a triangle three areas A_i are constructed with the point $\boldsymbol{x}$ and the three corner points (Fig. 2.6 a). The ratio ξ_i of these areas to the whole triangle area A is given by [4]:

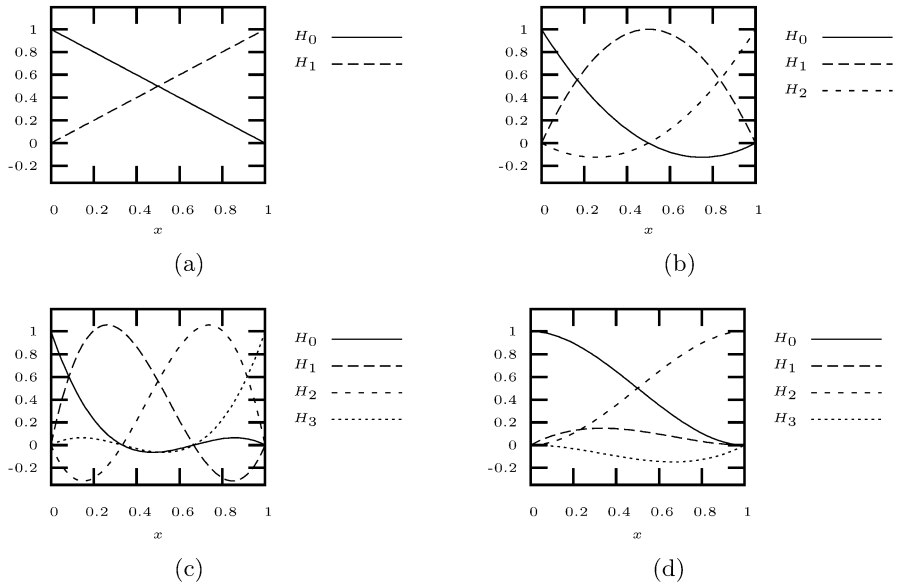

Fig. 2.7. One-dimensional shape-functions. (a) Linear, (b) quadratic, and (c,d) cubic shape-functions allow the determination of the solution function u at an arbitrary point $\boldsymbol{x}$ in a one-dimensional domain Ω starting from values of node variables u_i. The shape-functions shown in (a), (b) and (c) result from node variables specifying the function u at two, three and four, respectively, node points. The shape-functions depicted in (d) accrues from nodes variables defining the functions u as well as its first derivatives at two node points.

$$\xi_i = \frac{A_i}{A}$$

Obviously, the ratios fulfill the requirements for a shape-function (equation 2.21). Concerning a unit triangle, the shape-functions H_i are identical to the area ratios ξ_i:

$$H_i = \xi_i$$

Similar approaches serve to determine the shape-functions of polygons and polyhedrons.

One-Dimensional Shape-Functions. The determination of shape-functions can be achieved by taking into account the requirements (equation 2.21) or by the approach of the natural coordinates. Linear shape-functions for unit line elements result from the first order polynomial as interpolation function for the solution function u:

$$u(x) = a_0 + a_1 x$$

with the constant parameters a_0 and a_1. Two node variables, one assigned to each of the two node points, specify the solution function u. The shape-functions H_0 and H_1 are given by (Fig. 2.7 a):

$$H_0(x) = 1 - x \qquad (2.25)$$
$$H_1(x) = x$$

Quadratic shape-functions for line elements use a second order polynomial:

$$u(x) = a_0 + a_1 x + a_2 x^2$$

with three constant parameters a_i. The solution function u is determined with one node variable at three node points. The shape-functions H_i are given by (Fig. 2.7 b):

$$H_0(x) = (x-1)(2x-1)$$
$$H_1(x) = -4x(x-1)$$
$$H_2(x) = x(2x-1)$$

A third order polynomial is applied to determine cubic shape-functions:

$$u(x) = a_0 + a_1 x + a_2 x^2 + a_3 x^3$$

with four parameters a_i. Hereby, four node variables specify the solution function u. The cubic approach leads to the shape-functions (Fig. 2.7 c):

$$H_0(x) = -\frac{1}{2}(x-1)(3x-2)(3x-1)$$
$$H_1(x) = \frac{9}{2}(x-1)x(3x-2)$$
$$H_2(x) = -\frac{9}{2}(x-1)x(3x-1)$$
$$H_3(x) = \frac{1}{2}x(3x-2)(3x-1)$$

Alternatively, an element can be defined with two node points, where at each point a node variable fixes the value of the function u and a secondary node variable defines the derivative of the function u:

$$H_0(x) = (1-x)^2(1+2x)$$
$$H_1(x) = x(1-x)^2$$
$$H_2(x) = x^2(3-2x)$$
$$H_3(x) = -x^2(1-x)$$

The usage of this element type is recommended if the continuity of the first derivative at the node points is required.

Two-Dimensional Shape-Functions. Bilinear shape-functions for unit quadrilaterals result from the following polynomial as interpolation function for the solution function u:

$$u(x_1, x_2) = a_0 + a_1 x_1 + a_2 x_2 + a_3 x_1 x_2$$

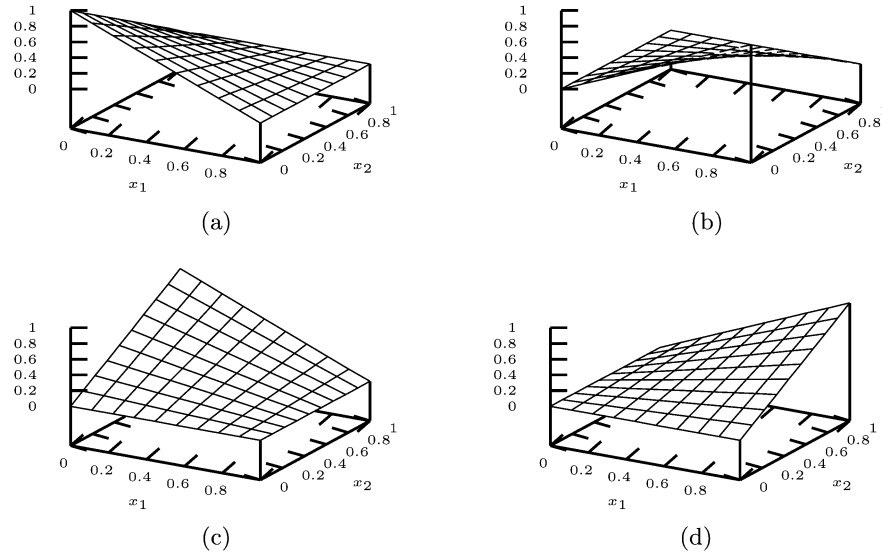

Fig. 2.8. Two-dimensional shape-functions in quadrilaterals. The bilinear shape-functions (a) H_0, (b) H_1, (c) H_2 and (d) H_3 allow the interpolation of function u at an arbitrary point $\boldsymbol{x}$ in a two-dimensional domain $\Omega = [0,1][0,1]$. The interpolation uses values of node variables u_i located at the vertices of the quadrilaterals.

with the constant parameters a_i. The shape-functions H_i are given by (Fig. 2.8):

$$\begin{aligned} H_0(x_1,x_2) &= (1-x_1)(1-x_2) \\ H_1(x_1,x_2) &= x_1(1-x_2) \\ H_2(x_1,x_2) &= (1-x_1)x_2 \\ H_3(x_1,x_2) &= x_1x_2 \end{aligned} \tag{2.26}$$

Three-Dimensional Shape-Functions. Trilinear shape-functions for unit hexahedrons result from the following polynomial as interpolation function for the solution function u:

$$\begin{aligned} u(x_1,x_2,x_3) = a_0 &+ a_1x_1 + a_2x_2 + a_3x_1x_2 + a_4x_3 + a_5x_1x_3 \\ &+ a_6x_2x_3 + a_7x_1x_2x_3 \end{aligned}$$

with the constant parameters a_i. The shape-functions H_i are given by:

$$\begin{aligned} H_0(x_1,x_2,x_3) &= (1-x_1)(1-x_2)(1-x_3) \\ H_1(x_1,x_2,x_3) &= x_1(1-x_2)(1-x_3) \\ H_2(x_1,x_2,x_3) &= (1-x_1)x_2(1-x_3) \\ H_3(x_1,x_2,x_3) &= x_1x_2(1-x_3) \end{aligned}$$

$$H_4(x_1, x_2, x_3) = (1 - x_1)(1 - x_2)x_3$$
$$H_5(x_1, x_2, x_3) = x_1(1 - x_2)x_3$$
$$H_6(x_1, x_2, x_3) = (1 - x_1)x_2x_3$$
$$H_7(x_1, x_2, x_3) = x_1x_2x_3$$

Determination of Element Equations. The element equations are commonly derived for each element applying the Galerkin method to transform partial differential equations into an integral or using the stationarity condition of a functional Π analog to the Ritz approach. Because these methods require the integration over an element's domain $\Omega^{(m)}$, an interpolation of the solution function u based on the variables at the node points is performed. The shape-functions serve to interpolate the solution function u. The interpolation can be expressed as vector multiplication:

$$u = \boldsymbol{u}^{(m)\,T}\ \boldsymbol{H}^{(m)} \tag{2.27}$$

with the vector of node variables $\boldsymbol{u}^{(m)}$ and the vector of shape-functions $\boldsymbol{H}^{(m)}$. The interpolation is substituted into the integrals. The integrals are transformed in such a way that a linear system of the node variables results. In the following description, element equations for exemplary elements and equations are derived.

Line Elements. Different functionals $\Pi^{(m)}$ for line elements with the domain $\Omega^{(m)}$ are frequently occurring both as part of a complex functional and as sole contribution [4]:

$$\Pi_1^{(m)} = \int_{\Omega^{(m)}} u\ dx$$
$$\Pi_2^{(m)} = \int_{\Omega^{(m)}} u^2\ dx$$
$$\Pi_3^{(m)} = \int_{\Omega^{(m)}} \left(\frac{\partial u}{\partial x}\right)^2 dx$$

The integrals are transformed to the unit interval $\Omega_0 = [0, 1]$:

$$\Pi_1^{(m)} = \int_{\Omega_0} u\,\mathcal{J}\,d\eta$$
$$\Pi_2^{(m)} = \int_{\Omega_0} u^2\,\mathcal{J}\,d\eta$$
$$\Pi_3^{(m)} = \int_{\Omega_0} \left(\frac{\partial u}{\partial \eta}\frac{\partial \eta}{\partial x}\right)^2 \mathcal{J}\,d\eta$$

with the Jacobian of the coordinate transformation $\mathcal{J}$. The substitution with the approximation of the solution functions (equation 2.27) delivers:

$$\Pi_1^{(m)} = \int_{\Omega_0} \boldsymbol{u}^{(m)\,T}\, \boldsymbol{H}^{(m)}\, \mathcal{J}\, d\eta = \boldsymbol{u}^{(m)\,T} \int_{\Omega_0} \boldsymbol{H}^{(m)}\, J\, d\eta$$

$$\Pi_2^{(m)} = \int_{\Omega_0} (\boldsymbol{u}^{(m)\,T}\, \boldsymbol{H}^{(m)})^2\, \mathcal{J}\, d\eta = \boldsymbol{u}^{(m)\,T} \int_{\Omega_0} \boldsymbol{H}^{(m)\,T\,2}\, J\, d\eta\; \boldsymbol{u}^{(m)}$$

$$\Pi_3^{(m)} = \int_{\Omega_0} \left(\frac{\partial (\boldsymbol{u}^{(m)\,T}\, \boldsymbol{H}^{(m)})}{\partial \eta} \frac{\partial \eta}{\partial x} \right)^2 \mathcal{J}\, d\eta$$

$$= \boldsymbol{u}^{(m)\,T} \int_{\Omega_0} \left(\frac{\partial \boldsymbol{H}^{(m)}}{\partial \eta} \frac{\partial \eta}{\partial x} \right)^{T\,2} \mathcal{J}\, d\eta\; \boldsymbol{u}^{(m)}$$

The superscript $T\,2$ denotes the transposition of the vector followed by squaring. A quadratic, symmetric matrix results in these cases. The derivatives of the shape-functions $H_i^{(m)}$ are directly derived from their definition (equation 2.25).

The integrals can be expressed as linear or quadratic form of the node variables $u_i^{(m)}$:

$$\Pi_1^{(m)} = \boldsymbol{u}^{(m)\,T} \boldsymbol{b}^{(m)}$$
$$\Pi_2^{(m)} = \boldsymbol{u}^{(m)\,T} \boldsymbol{M}^{(m)} \boldsymbol{u}^{(m)}$$
$$\Pi_3^{(m)} = \boldsymbol{u}^{(m)\,T} \boldsymbol{S}^{(m)} \boldsymbol{u}^{(m)}$$

with the vector $\boldsymbol{b}^{(m)}$, the mass element matrix $\boldsymbol{M}^{(m)}$ and the stiffness matrix $\boldsymbol{S}^{(m)}$. Using linear shape-functions (equation 2.25) in an element of length l the element vectors and matrices are given by [4]:

$$\boldsymbol{b}^{(m)} = \frac{l}{2} \begin{pmatrix} 1 \\ 1 \end{pmatrix}$$
$$\boldsymbol{M}^{(m)} = \frac{l}{6} \begin{pmatrix} 2 & 1 \\ 1 & 2 \end{pmatrix}$$
$$\boldsymbol{S}^{(m)} = \frac{1}{l} \begin{pmatrix} 1 & -1 \\ -1 & 1 \end{pmatrix}$$

The final step in the derivation of the element equations for a line element uses the stationarity condition analog to the Ritz approach. Therefore, the upper functionals $\Pi_i^{(m)}$ are either combined or used alone.

Quadrilaterals with Poisson Equation. The functional $\Pi^{(m)}$ for the m-th element is given by (Sect. 2.7.3):

$$\Pi^{(m)} = \iint_{\Omega^{(m)}} \frac{1}{2} \left(\frac{\partial u}{\partial x_1} \right)^2 + \frac{1}{2} \left(\frac{\partial u}{\partial x_2} \right)^2 + G(x_1, x_2)\; u\, dx_1\, dx_2$$

The integral is transformed to the unit interval $\Omega_0 = [0,1][0,1]$:

$$\Pi^{(m)} = \iint_{\Omega_0} \left(\frac{1}{2} \left(\frac{\partial u}{\partial \eta_1} \frac{\partial \eta_1}{\partial x_1} + \frac{\partial u}{\partial \eta_2} \frac{\partial \eta_2}{\partial x_1} \right)^2 + \frac{1}{2} \left(\frac{\partial u}{\partial \eta_1} \frac{\partial \eta_1}{\partial x_2} + \frac{\partial u}{\partial \eta_2} \frac{\partial \eta_2}{\partial x_2} \right)^2 + G(\eta_1, \eta_2)\, u \right) \mathcal{J}\, d\eta_1\, d\eta_2$$

with the Jacobian of the coordinate transformation $\mathcal{J}$. The substitution with the approximation of the solution functions (equation 2.27) delivers the quadratic form:

$$\Pi^{(m)} = \boldsymbol{u}^{(m)\,T} \frac{1}{2} \boldsymbol{S}^{(m)} \boldsymbol{u}^{(m)} + \boldsymbol{u}^{(m)\,T} \boldsymbol{b}^{(m)}$$

with the matrix $\boldsymbol{S}^{(m)}$ determined:

$$\boldsymbol{S}^{(m)} = \iint_{\Omega_0} \left(\left(\frac{\partial \boldsymbol{H}^{(m)}}{\partial \eta_1} \frac{\partial \eta_1}{\partial x_1} + \frac{\partial \boldsymbol{H}^{(m)}}{\partial \eta_2} \frac{\partial \eta_2}{\partial x_1} \right)^{T\,2} + \left(\frac{\partial \boldsymbol{H}^{(m)}}{\partial \eta_1} \frac{\partial \eta_1}{\partial x_2} + \frac{\partial \boldsymbol{H}^{(m)}}{\partial \eta_2} \frac{\partial \eta_2}{\partial x_2} \right)^{T\,2} \right) \mathcal{J}\, d\eta_1\, d\eta_2$$

and the vector $\boldsymbol{b}^{(m)}$ given by:

$$\boldsymbol{b}^{(m)} = \iint_{\Omega_0} G(\eta_1, \eta_2) \boldsymbol{H}^{(m)} \mathcal{J}\, d\eta_1\, d\eta_2$$

The derivatives of the shape-functions $H_i^{(m)}$ are determined by their definition (equation 2.26). The matrix $\boldsymbol{S}^{(m)}$ and the vector $\boldsymbol{b}^{(m)}$ are commonly determined with numerical integration methods, e.g. Gauss quadrature (Sect. 2.5). For simple element geometries, e.g. quadrat and parallelogram, an analytical solution is derivable [4].

Using bilinear shape-functions (equation 2.26) in a unit element and assuming $G(x_1, x_2) \equiv 1$, the element matrix $\boldsymbol{S}^{(m)}$ and vector $\boldsymbol{b}^{(m)}$ are given by:

$$\boldsymbol{S}^{(m)} = \frac{1}{3} \begin{pmatrix} 4 & -1 & -1 & -2 \\ -1 & 4 & -2 & -1 \\ -1 & -2 & 4 & -1 \\ -2 & -1 & -1 & 4 \end{pmatrix}$$

$$\boldsymbol{b}^{(m)} = \frac{1}{4} \begin{pmatrix} 1\ 1\ 1\ 1 \end{pmatrix}^T$$

The final step in the derivation of the element equations for a Poisson equation uses the stationarity condition of the equivalent functional $\Pi^{(m)}$. The condition delivers the linear equation system:

$$\frac{\partial \Pi^{(m)}}{\partial \boldsymbol{u}^{(m)}} = \boldsymbol{S}^{(m)} \boldsymbol{u}^{(m)} + \boldsymbol{b}^{(m)} = 0$$

Assembling of System Equations. The element matrices and vectors are assembled to generate the system equations describing the whole domain. These equations are commonly linear consisting of the so-called system matrix $\boldsymbol{A}$ and the system vector $\boldsymbol{b}$:

$$\boldsymbol{A}\boldsymbol{u} + \boldsymbol{b} = 0 \tag{2.28}$$

in conjunction with the vector of node variables $\boldsymbol{u}$. The values of the node variables u_i describe the solution function u and are a-priori unknown.

The system matrix $\boldsymbol{A}$ and system vector $\boldsymbol{b}$ result from a summation of the element matrices $\boldsymbol{A}^{(m)}$ and element vectors $\boldsymbol{b}^{(m)}$, where the coefficients are properly sorted:

$$\boldsymbol{A} = \sum_{m=1}^{N} \boldsymbol{A}^{(m)}$$

$$\boldsymbol{b} = \sum_{m=1}^{N} \boldsymbol{b}^{(m)}$$

The sorting of the coefficients is dependent on the sorting of the node variables. Element matrices can consist of stiffness and mass as well as further matrices.

The properties of the system matrix depend on the properties of the element matrices. E.g. the assembling of symmetric, positive-definite element matrices leads to a symmetric, positive-definite system matrix. The system matrix $\boldsymbol{A}$ is commonly sparse, where the application of efficient storing schemes is of advantage. Mostly, the system matrix $\boldsymbol{A}$ is quadratic, but its shape depends on the shape of the element matrices and the sorting of the node variables.

Incorporation of Boundary Conditions. The incorporation of boundary conditions can be performed on element or system level by modification of the corresponding equation systems. Element level modifications influence generally a group of element equations, e.g. by changing the shape-functions or replacing equations. System level incorporation can be realized by changing appropriate equations of the system equations.

If the differential equation is described by a system of linear equations (equation 2.28) boundary conditions can be created by reducing the dimension of the system matrix $\boldsymbol{A}$ and system vector $\boldsymbol{b}$ as well as by replacing coefficients of the system matrix $\boldsymbol{A}$ and the system vector $\boldsymbol{b}$ with appropriate values. E.g. a Dirichlet condition specifying the value of the node variable u_k located at node point x_k is represented by:

$$u_k = c$$

This substitution changes the vector $\boldsymbol{b}$ to the modified system vector $\boldsymbol{b}'$ by adding of the c-fold of the k-th column of the system matrix $\boldsymbol{A}$. The k-th element of the vector $\boldsymbol{b}'$ is removed. The system matrix $\boldsymbol{A}'$ results from the matrix $\boldsymbol{A}$ by deleting of the k-th row and column.

A similar approach can be chosen to represent Neumann conditions. This method changes the system's type. The sacrifice of the matrix's type and vector's dimension obstructs a numerical treatment.

Alternatively, boundary conditions can be incorporated with a method preserving the systems dimension [4]. Preservation is achieved by adding the c-fold of the k-th column of the system matrix $\boldsymbol{A}$ to the vector $\boldsymbol{b}$. The k-th element of the resulting vector $\boldsymbol{b}'$ is set to c. The k-th row and column of the system matrix $\boldsymbol{A}$ are filled with zeros. Finally, the k-th diagonal element of the resulting matrix $\boldsymbol{A}'$ is set to one.

Solution of System Equations. Depending on the type of differential equation different types of equation systems can arise. Stationary problems, e.g. on basis of the Poisson equation, commonly deliver a system of linear equations (equation 2.28), which is solved with the methods described in Sect. 2.4. The symmetry, positive-definiteness and sparcity of the system matrix are of advantage on behalf of the performance of solution and feasibility of numerical methods. Oscillation problems often result in eigenvalue problems, wherefore numerical methods beyond the scope of this work are enlisted. An overview of these methods is given in [4, 5, 9].

2.7.4 Finite Differences Method

The finite differences method can be applied to solve partial differential equations in a similar way like the finite element method. The method's name is motivated by the proceeding, where differential terms are substituted by approximations primarily consisting of differences. Commonly, in the finite differences method, the partial differential equations are solved directly at the node points which are regularly distributed over the spatial domain Ω. The method can be subdivided into a sequence of steps:

- Discretization of the spatial domain
- Determination of node equations
- Assembling of system equations
- Incorporation of boundary conditions
- Solution of system equations

The finite differences method can be seen as a subclass of the finite element method, which differs primarily in the first two steps, discretization and determination of the element matrices. In particular the final steps, incorporation of boundary conditions and solution of system equations, are equal in the finite element method and described in Sect. 2.7.3 and 2.7.3, respectively.

Discretization of the Spatial Domain. The spatial domain Ω is sampled with node points x_i. Commonly, rectangular, isotropic and equidistant lattices are applied, where the node points x_i are located at the vertices (Fig. 2.9).

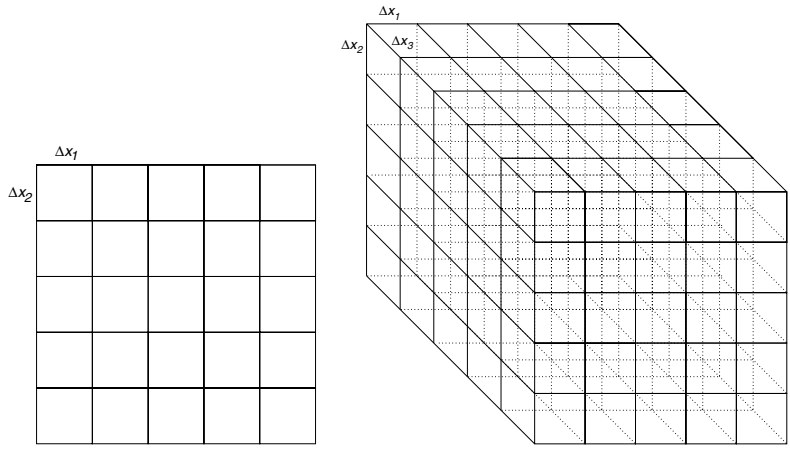

Fig. 2.9. Exemplary finite differences meshes in (a) two and (b) three dimensions. The spatial domain Ω is subdivided in a rectangular lattice, where node variables are assigned to the vertices. The distance between vertices Δx_i in direction of the edges is equal in isotropic, equidistant lattices.

The regularity of the node point distribution simplifies the discretization of the partial differential equations.

Adapted meshes were created for specific applications. The adaptation concerns both geometry as well as node variable assignment. Geometrical adapted meshes are in use e.g. for spherically and cylindrically shaped domains. An example for adaptation with regard to node variables is the dual mesh for electromagnetic problems of Yee [11], where node points and attributed variables of the electric and magnetic fields are shifted to each other.

Determination of Node Equations. The node equations result from a node-wise discretization of the partial differential equations. The differential terms are substituted by discrete approximations. Depending on the equation type spatial and temporal derivatives of different order have to be replaced. These approximations are simplified in equidistant, isotropic, orthogonal lattices. In irregular meshes approximations can be achieved by appropriate transformations.

An approximation of the first order spatial derivative in a one-dimensional domain Ω at the node point x_i can be achieved with different schemes. These schemes differ in the locations of the node variables taken into account. The schemes are the so-called central, forward and backward difference:

$$\frac{\partial u}{\partial x}(x_i) \approx \frac{u_{i+1} - u_{i-1}}{2\Delta x} \quad \text{central} \tag{2.29}$$

$$\frac{\partial u}{\partial x}(x_i) \approx \frac{u_{i+1} - u_i}{\Delta x} \quad \text{forward} \tag{2.30}$$

$$\frac{\partial u}{\partial x}(x_i) \approx \frac{u_i - u_{i-1}}{\Delta x} \quad \text{backward} \tag{2.31}$$

with the distance between node points Δx. The node variables u_{i-1}, u_i and u_{i+1} correspond to the node points x_{i-1}, x_i and x_{i+1}, respectively. In unequally spaced meshes this distance differs locally, i.e. a function of the location: $\Delta x \equiv \Delta x(x)$.

The second order spatial derivative in a one-dimensional domain Ω can be deduced by twice derivation with the upper schemes (equations 2.29-2.31). Using two-fold central differences the second order derivative at the node point x_i is given by:

$$\frac{\partial^2 u}{\partial x^2}(x_i) \approx \frac{u_{i+1} - 2u_i + u_{i-1}}{\Delta x^2}$$

The first order temporal derivative at time step t_i can be approximated similar to the upper schemes:

$$\begin{aligned}
\frac{\partial u}{\partial t}(t_i) &\approx \frac{u_{i+1} - u_{i-1}}{2\Delta t} \quad \text{central} \\
\frac{\partial u}{\partial t}(t_i) &\approx \frac{u_{i+1} - u_i}{\Delta t} \quad \text{forward} \\
\frac{\partial u}{\partial t}(t_i) &\approx \frac{u_i - u_{i-1}}{\Delta t} \quad \text{backward}
\end{aligned}$$

with the distance between time steps Δt. The backward scheme is comparable with the Euler method for solving of ordinary differential equations (Sect. 2.6.2). The second order temporal derivative can be deduced in a similar way to the upper deduction of the second order spatial derivative.

The derivatives in a two-dimensional domain Ω can be derived straightforwardly from the one-dimensional derivatives. In a rectangular, equidistant mesh, the first order derivatives at the node point $\boldsymbol{x}_{i,j}$ are approximated by:

$$\begin{aligned}
\frac{\partial u}{\partial x_1}(\boldsymbol{x}_{i,j}) &\approx \frac{u_{i+1,j} - u_{i-1,j}}{2\Delta x_1} \\
\frac{\partial u}{\partial x_2}(\boldsymbol{x}_{i,j}) &\approx \frac{u_{i,j+1} - u_{i,j-1}}{2\Delta x_2}
\end{aligned}$$

with the distance between the node points Δx_1 and Δx_2 in x_1 and x_2 direction, respectively. The node variables $u_{i+1,j}$, $u_{i-1,j}$, $u_{i,j+1}$ and $u_{i,j-1}$ correspond to the node points $\boldsymbol{x_{i+1,j}}$, $\boldsymbol{x_{i-1,j}}$, $\boldsymbol{x_{i,j+1}}$ and $\boldsymbol{x_{i,j-1}}$, respectively (Fig. 2.10).

The second order derivatives are given by:

$$\frac{\partial^2 u}{\partial x_1^2}(\boldsymbol{x}_{i,j}) \approx \frac{u_{i+1,j} - 2u_{i,j} + u_{i-1,j}}{\Delta x_1^2} \tag{2.32}$$

$$\frac{\partial^2 u}{\partial x_2^2}(\boldsymbol{x}_{i,j}) \approx \frac{u_{i,j+1} - 2u_{i,j} + u_{i,j-1}}{\Delta x_2^2} \tag{2.33}$$

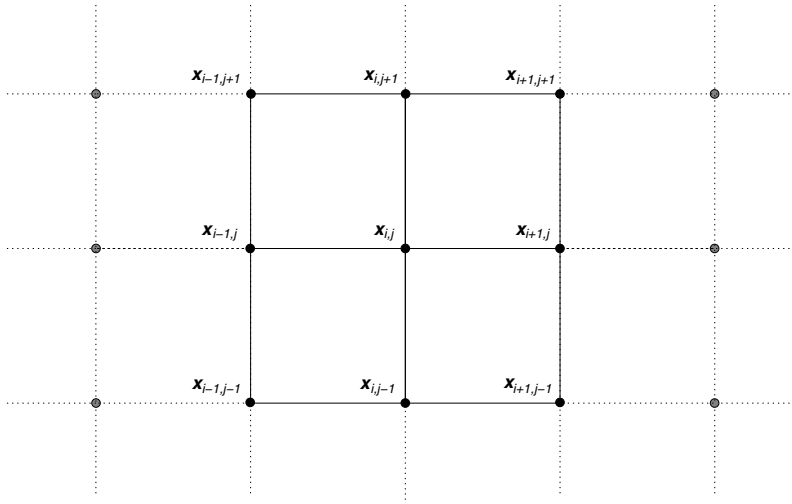

Fig. 2.10. Exemplary numbering of node points in two-dimensional, rectangular, equidistant mesh. A subarea of a two-dimensional spatial domain Ω is shown, which is subdivided in a rectangular lattice with quad-shaped cells. The center of the subarea is node point $\boldsymbol{x}_{i,j}$. The mesh can be applied in conjunction with the finite differences method for discretization of Poisson's equation. Node points are indicated by black closed circles.

$$\frac{\partial^2 u}{\partial x_1 \partial x_2}(\boldsymbol{x}_{i,j}) \approx \frac{u_{i+1,j+1} - u_{i-1,j+1} - u_{i+1,j-1} + u_{i-1,j-1}}{4\Delta x_1 \Delta x_2} \tag{2.34}$$

The second order derivatives are determined by two-fold central differences.

Derivatives in domains of dimension three and larger can be constructed by applying the upper strategy. The principle of the finite differences method is not restricted to spatial and temporal derivatives of the node variables, but can also be applied for derivation of material properties, e.g. electrical conductivity tensors.

Two-Dimensional Poisson Equation. The Poisson equation can be approximated in an equidistant, isotropic lattice by substituting the second order derivatives (equation 2.32 and 2.33). At the point $\boldsymbol{x}_{i,j}$ the Poisson equation is given by:

$$\frac{\partial^2 u}{\partial {x_1}^2}(\boldsymbol{x}_{i,j}) + \frac{\partial^2 u}{\partial {x_2}^2}(\boldsymbol{x}_{i,j}) = G(\boldsymbol{x}_{i,j})$$

Its finite differences approximation leads to:

$$\frac{u_{i+1,j} - 2u_{i,j} + u_{i-1,j}}{\Delta x_1^2} + \frac{u_{i,j+1} - 2u_{i,j} + u_{i,j-1}}{\Delta x_2^2} = G(\boldsymbol{x}_{i,j})$$

which can be simplified taking the isotropy of the lattice into account, i.e. $\Delta x_1^2 = \Delta x_2^2$, to:

$$\frac{-4u_{i,j} + u_{i+1,j} + u_{i-1,j} + u_{i,j+1} + u_{i,j-1}}{\Delta x^2} = G(\boldsymbol{x}_{i,j})$$

with the distance between node points Δx. In this equation all quantities are known except the node variables. The equation can be expressed using a vector product:

$$\boldsymbol{a}_{i,j}^T \boldsymbol{u}_{i,j} = G(\boldsymbol{x}_{i,j}) \tag{2.35}$$

with the vector of weightings of node variables $\boldsymbol{a}_{i,j}$:

$$\boldsymbol{a}_{i,j}^T = \frac{1}{\Delta x^2} \begin{pmatrix} -4 & 1 & 1 & 1 & 1 \end{pmatrix}$$

and the vector of node variables $\boldsymbol{u}_{i,j}$:

$$\boldsymbol{u}_{i,j}^T = \begin{pmatrix} u_{i,j} & u_{i+1,j} & u_{i-1,j} & u_{i,j+1} & u_{i,j-1} \end{pmatrix}$$

Error Estimation. The properties of the finite differences method can be examined, similar to the study of the properties of the Euler method (equation 2.8), using the Taylor series expansion for the function u [8, 9]:

$$u(x + \Delta x) = u(x) + \Delta x \frac{1}{1!} \frac{\partial u}{\partial x}(x) + \Delta x^2 \frac{1}{2!} \frac{\partial^2 u}{\partial x^2}(x) + \Delta x^3 \frac{1}{3!} \frac{\partial^3 u}{\partial x^3}(x) + \ldots$$

A comparison with the upper approximation for first order derivatives (equations 2.29-2.31) shows that the finite differences method neglects terms with derivatives of order greater and equal to two for forward and backward differences. Hereby, the truncation error E is given by:

$$E = u(x + \Delta x) - u_{n+1} = \Delta x^2 \frac{1}{2} \frac{\partial^2 u}{\partial x^2}(x) + \Delta x^3 \frac{1}{6} \frac{\partial^3 u}{\partial x^3}(x) + \ldots$$

The truncation error E can be quadratically reduced by bisection of the distance Δx. For central differences terms with derivatives of order greater and equal to three are neglected:

$$E = u(x + \Delta x) - u_{n+1} = \Delta x^3 \frac{1}{6} \frac{\partial^3 u}{\partial x^3}(x) + \ldots$$

The truncation error E can be cubically reduced regarding the distance Δx. Alternatively, a reduction of this error can be achieved by introduction of higher order terms in equations 2.29-2.31.

Assembling of System Equations. The element equations are assembled to generate the system equations describing the whole domain. Similar to the finite element method, these equations are commonly linear consisting of the so-called system matrix $\boldsymbol{A}$ and the system vector $\boldsymbol{b}$:

$$\boldsymbol{A}\boldsymbol{u} + \boldsymbol{b} = 0$$

in conjunction with the vector of node variables $\boldsymbol{u}$. The values of the node variables u_i represent the solution function u of the underlying partial differential equation and are a-priori unknown.

The system matrix $\boldsymbol{A}$ and system vector $\boldsymbol{b}$ result from a collection of sorted vectors $\boldsymbol{a}_i$ and coefficients b_i corresponding to a node variable:

$$\boldsymbol{A} = \begin{pmatrix} \boldsymbol{a}_1^T \\ \vdots \\ \boldsymbol{a}_N^T \end{pmatrix}, \quad \boldsymbol{b} = \begin{pmatrix} b_1 \\ \vdots \\ b_N \end{pmatrix}$$

The sorting of the coefficients is dependent on the sorting of the node variables.

The properties of the system matrix depend on the properties of the element equations. The system matrix $\boldsymbol{A}$ consists commonly of diagonal blocks, which can be efficiently stored.

3

Theory of Electric Fields

3.1 Introduction

A physically based modeling of electrophysiology at level of whole heart as well as of single muscle and nerve cells necessitates knowledge of electric fields. Changes of the electric field permit the propagation of excitation through the heart, from excitable cell to excitable cell, and over a single cell. The electrical excitation triggers mechanical contraction in muscle cells. Moreover electrical excitation is a carrier of information over nerve cells.

The theoretical foundation of electromagnetism is established by Maxwell's equations in conjunction with material equations and continuity laws. The Maxwell's equations integrate electric and magnetic quantities. A derivation of these equations under geometrically, physically and physiologically motivated neglects leads to Poisson's equation.

The modeling of electromagnetic properties of biological tissue plays an import role in the application of Maxwell's and Poisson's equations. Commonly, material properties are nonlinear and anisotropic, reflecting molecular and microscopic organization of cells and tissues. The representation of material properties as tensors allows an efficient treatment, both from a theoretical and numerical point of view. The coefficients of the tensors are dependent e.g. on the tissue type and arrangement of cells.

A numerical handling of Poisson's equation is the foundation for different aspects of electrophysiological modeling of muscle and nerve cells. The modeling includes not only propagation, initiation and manipulation of excitation, but also the reconstruction of electric and magnetic field distributions resulting from occurring electrical sources. The geometrical representation of the model is of importance referred to the numerical treatment of the model.

Two different strategies for a numerical treatment of electrical tasks are commonly applied, i.e. finite differences and finite element methods. Both methods are capable of handling nonlinear and anisotropic material properties. For both methods a sound mathematical framework exists to determine the solution. The determination of the underlying equations is influenced by

F.B. Sachse: LNCS 2966, pp. 49–67, 2004.

the representation of the model domain, which includes the distribution of node variables and of electrical quantities as well as geometrical properties.

3.2 Physical Laws

3.2.1 Maxwell's Equations

The Maxwell's equations describe the connection between the electric field $\boldsymbol{E}$, the electric flux density $\boldsymbol{D}$, the electric current density $\boldsymbol{J}$, the magnetic field $\boldsymbol{H}$, the magnetic flux density $\boldsymbol{B}$, and the electric free charge density ρ. In a differential or local formulation Maxwell's equations are given by [12]:

$$\nabla \times \boldsymbol{E} = -\frac{\partial \boldsymbol{B}}{\partial t} \tag{3.1}$$

$$\nabla \times \boldsymbol{H} = \boldsymbol{J} + \frac{\partial \boldsymbol{D}}{\partial t} \tag{3.2}$$

$$\nabla \cdot \boldsymbol{D} = \rho \tag{3.3}$$

$$\nabla \cdot \boldsymbol{B} = 0 \tag{3.4}$$

Material equations couple the electric field with the electric flux density and electric current density, as well as the magnetic field with the magnetic flux density, respectively. Thereto, the permeability in vacuum μ_0, the permittivity in vacuum ϵ_0, and the electric conductivity σ are utilized [12]:

$$\boldsymbol{B} = \mu_0(\boldsymbol{H} + \boldsymbol{M})$$
$$\boldsymbol{D} = \epsilon_0 \boldsymbol{E} + \boldsymbol{P}$$
$$\boldsymbol{J} = \sigma \boldsymbol{E}$$

with the magnetization $\boldsymbol{M}$ and electric polarization $\boldsymbol{P}$. The values of the physical constants μ_0 and ϵ_0 are specified in table A.2.

Often, the electric polarization $\boldsymbol{P}$ and the magnetization $\boldsymbol{M}$ are linear functions of the electric field $\boldsymbol{E}$ and the magnetic field $\boldsymbol{H}$, respectively. In non-ferromagnetic materials the connection between magnetic field $\boldsymbol{H}$ and flux density $\boldsymbol{B}$ can be reduced to:

$$\boldsymbol{B} = \mu \boldsymbol{H}$$

with the permeability μ. The connection between electric field $\boldsymbol{E}$ and flux density $\boldsymbol{D}$ can be simplified in linear, isotropic materials:

$$\boldsymbol{D} = \epsilon \boldsymbol{E}$$

with the permittivity ϵ. Thereto, the permeability μ and permittivity ϵ are expressed by the product of a material specific factor μ_r and ϵ_r, respectively, with the permeability in vacuum μ_0 and the permittivity in vacuum ϵ_0, respectively:

$$\mu = \mu_0 \ \mu_r$$
$$\epsilon = \epsilon_0 \ \epsilon_r$$

In a more general manner, the permeability, permittivity, and electric conductivity are described by tensors.

Neglect of Time Dependencies. In static electric and magnetic fields the physical quantities are constant over time. Maxwell's equations (equations 3.1-3.4) can be simplified if time dependencies are negligible:

$$\begin{aligned} \nabla \times \boldsymbol{E} &= 0 \\ \nabla \times \boldsymbol{H} &= \boldsymbol{J} \\ \nabla \cdot \boldsymbol{D} &= \rho \\ \nabla \cdot \boldsymbol{B} &= 0 \end{aligned} \tag{3.5}$$

Therewith, a scalar electric potential function ϕ can be introduced with the electric field $\boldsymbol{E}$ as the negative gradient [13]:

$$\boldsymbol{E} = -\nabla\phi \tag{3.6}$$

A similar interdependence can be constructed for the magnetic field $\boldsymbol{H}$ under the assumption that the electric current density $\boldsymbol{J}$ vanishes. Here, the magnetic field $\boldsymbol{H}$ can be described by the negative gradient of a scalar magnetic potential function ϕ_m [13]:

$$\boldsymbol{H} = -\nabla\phi_m \tag{3.7}$$

3.2.2 Poisson's Equation for Stationary Current Fields

The Poisson's equation for stationary current fields describes phenomena resulting solely from the flow of electric current in materials owning electric conductivity. Further material properties are ignored. A detailed description of the applicability of the equation in conjunction with biological materials is given in [14].

The derivation starts with the Maxwell's equations, whereby time dependencies are neglected. The divergence of equation 3.5 delivers:

$$\nabla \cdot (\nabla \times \boldsymbol{H}) = \nabla \cdot \boldsymbol{J}$$

The left hand side reduces to zero, because the divergence of a curl operator vanishes:

$$\nabla \cdot \boldsymbol{J} = 0 \tag{3.8}$$

In many cases and particularly in bioelectric tasks, the current density $\boldsymbol{J}$ is decomposed in two parts: the current density resulting from local sources $\boldsymbol{J}_s$ and the ohmic current density $\boldsymbol{J}_o$:

$$\boldsymbol{J} = \boldsymbol{J_s} + \boldsymbol{J_o} \tag{3.9}$$

The divergence of the current density $\boldsymbol{J}_s$ is given by:

$$f = \nabla \cdot \boldsymbol{J_s} \tag{3.10}$$

The quantity f is scalar and named current source density. The ohmic current density $\boldsymbol{J}_o$ consists of the product of the conductivity tensor σ and the electric field $\boldsymbol{E}$. Combining the equations 3.6, 3.8-3.10 yields Poisson's equation for stationary current fields:

$$\nabla \cdot (\sigma \nabla \phi) = f \tag{3.11}$$

Depending on the properties of the distribution of conductivity and current source density, different simplifications of Poisson's equation can be applied. Assuming that the conductivity is homogeneously distributed and can be described by a zero-th order tensor, i.e. scalar, yields:

$$\sigma \Delta \phi = f$$

with the Laplace operator $\Delta \equiv \nabla^2$. Assuming absence of sources leads to the Laplace equation for stationary current fields:

$$\nabla \cdot (\sigma \nabla \phi) = 0$$

3.2.3 Electromagnetic Properties of Biological Tissues

Biological tissues show electromagnetic properties, which are dependent on the species, tissue type and arrangement of tissue constituents as well as on measurement conditions. A multitude of measurements of electric conductivity σ, permittivity ϵ, and permeability μ in macroscopic tissue probes and in cell suspensions were performed since the exploration of electromagnetic phenomena and the availability of suitable technical equipment. Collections of measurement data and of experimental descriptions are frequently published [15, 16, 17, 18, 19, 20, 21].

Electromagnetic properties of tissues are determined by its microscopic anatomy and its molecular organization. On the one hand classes of tissues show significant consistence of their principal molecular organization, on the other hand tissues can vary widely concerning their microscopic anatomy (Sect. 6.2). Biological tissues like muscle, fat and blood consist of cells surrounded by extracellular fluids. Each cell is enclosed by a membrane, which is made up of a phospholipid bilayer with pore forming proteins. These pores connect the intracellular space with the extracellular space, just as they connect in specific cases, e.g. myocardium, the intracellular space of adjoining cells. The intracellular space includes organelles, which are encapsulated by a phospholipid bilayer.

This section is focused on macroscopic conductivities. Microscopic anatomical details are blurred and averaged conductivities are assigned to tissues.

The electromagnetic properties of tissues, i.e. electric conductivity σ, permittivity ϵ, and permeability μ, can be represented in a generalized approach by symmetric tensors of second order T (Sect. 2.3):

$$T = \begin{pmatrix} T_{11} & T_{12} & T_{13} \\ T_{21} & T_{22} & T_{23} \\ T_{31} & T_{32} & T_{33} \end{pmatrix}$$

whereby the coefficients of the tensor T_{ij} are dependent on tissue type and measurement conditions.

The general approach of representing electromagnetic properties of tissues by the tensor T allows the representation of anisotropic properties, which are resulting from the arrangement of tissue constituents, e.g. fiber orientation, indicated by the averaged principal axis of cells, and lamination, indicated by the striation of cell clusters. The arrangement is reflected by an appropriate coordinate transformation of the tensor. The coordinate transformation takes one Cartesian system into another, whereby the origins of the Cartesian systems are equal. Commonly, the transformation consists of a sequence of rotations. The tensor T in an arbitrary coordinate system spanned by the vectors $\boldsymbol{x}$, $\boldsymbol{y}$, and $\boldsymbol{z}$ can be described by an orthogonal coordinate transformation of a tensor T_{local} in a local system spanned by the vectors $\boldsymbol{a_1}$, $\boldsymbol{a_2}$, and $\boldsymbol{a_3}$:

$$T_{ij} = A_{ik}\ A_{jl}\ T_{local,kl}$$

with the constant, scalar coefficients A_{ij} of the rotation matrix $\boldsymbol{A}$.

Important simplifications of the tensor T are commonly performed in specific tasks. Usually, in bioelectric tasks an isotropy or transversal isotropy of the material properties is assumed. Thus, specific tensors and coordinate transformations of these are applied in the tasks.

Anisotropy. In the anisotropic case the tensor T_{aniso} can be represented in a local coordinate system built up by the orthonormal vectors $\boldsymbol{a_1}$, $\boldsymbol{a_2}$ and $\boldsymbol{a_3}$ by a diagonal matrix:

$$T_{aniso} = \begin{pmatrix} T_{a1} & 0 & 0 \\ 0 & T_{a2} & 0 \\ 0 & 0 & T_{a3} \end{pmatrix}$$

with the electromagnetic properties T_{a1}, T_{a2}, and T_{a3}. Theses properties describe the material in direction of the vectors $\boldsymbol{a_1}$, $\boldsymbol{a_2}$ and $\boldsymbol{a_3}$, respectively.

Transversal Isotropy. In case of transversal isotropy two scalar values, T_{fiber} and T_{trans}, are sufficient to define the tensor T_{tiso} of material properties in a local coordinate system:

$$T_{tiso} = \begin{pmatrix} T_{fiber} & 0 & 0 \\ 0 & T_{trans} & 0 \\ 0 & 0 & T_{trans} \end{pmatrix}$$

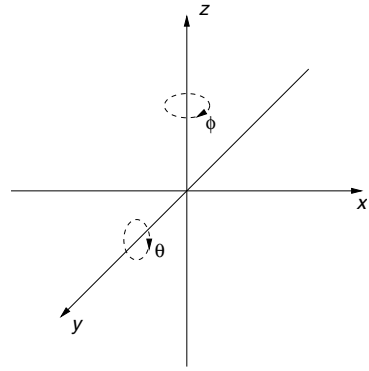

Fig. 3.1. Rotation in local coordinate system. In case of transversal isotropy the rotation of a tensor can be defined by two angles, ϕ and θ. The angles describe a rotation around the $\boldsymbol{z}$- and $\boldsymbol{y}$-axis, respectively.

The first property T_{fiber} describes the material in fiber orientation. The second property T_{trans} describes the material perpendicular to the fiber orientation. In the local system the $\boldsymbol{a_1}$-axis is aligned with fiber orientation. The $\boldsymbol{a_2}$- and $\boldsymbol{a_3}$-axis are chosen to be orthogonal to the $\boldsymbol{a_1}$-axis.

In case of transversal isotropy a matrix $\boldsymbol{A}$, describing the coordinate transformation, can be defined as product of two rotation matrices:

$$\boldsymbol{A} = \boldsymbol{R}_{xz}\boldsymbol{R}_{xy}$$

The two rotation matrices $\boldsymbol{R}_{xy}$ and $\boldsymbol{R}_{xz}$ are:

$$\boldsymbol{R}_{xy} = \begin{pmatrix} cos\ \phi & sin\ \phi & 0 \\ -sin\ \phi & cos\ \phi & 0 \\ 0 & 0 & 1 \end{pmatrix}$$

$$\boldsymbol{R}_{xz} = \begin{pmatrix} cos\ \theta & 0 & sin\ \theta \\ 0 & 1 & 0 \\ -sin\ \theta & 0 & cos\ \theta \end{pmatrix}$$

with the angles ϕ and θ defining a rotation around the $\boldsymbol{z}$- and $\boldsymbol{y}$-axis of the global coordinate system, respectively (Fig. 3.1). An extension for fully anisotropic cases follows straightforwardly by adding a further angle describing the orientation around the $\boldsymbol{x}$-axis.

Isotropy. In the isotropic case the tensor T_{iso} can be represented by a diagonal matrix:

$$T_{iso} = \begin{pmatrix} c & 0 & 0 \\ 0 & c & 0 \\ 0 & 0 & c \end{pmatrix}$$

whereby the diagonal coefficients T_{ii} are filled with a single value c describing the electromagnetic property. The tensor is independent of coordinate transforms and its order can be reduced to zero.

Electric Conductivity. The conductivity of biological tissues can be described by a symmetric tensor σ of second order. It has the following form in a local coordinate system with axes $\boldsymbol{a_1}$, $\boldsymbol{a_2}$ and $\boldsymbol{a_3}$:

$$\sigma_{local} = \begin{pmatrix} \sigma_{a1} & 0 & 0 \\ 0 & \sigma_{a2} & 0 \\ 0 & 0 & \sigma_{a3} \end{pmatrix}$$

with a scalar conductivity σ_{a1}, σ_{a2}, and σ_{a3} in axes direction. In the transversal isotropic case the diagonal element σ_{a2} is equal to σ_{a3}. The vector $\boldsymbol{a_1}$ is commonly aligned with the fiber orientation. Thereto perpendicular are the vectors $\boldsymbol{a_2}$ and $\boldsymbol{a_3}$. In the isotropic case all diagonal elements are equal: $\sigma_{a1} = \sigma_{a2} = \sigma_{a3}$. Here, the tensor σ can be substituted by a scalar conductivity.

Presently only the cases of transversal isotropy and isotropy are reported in macroscopic measurements of tissue conductivities. Transversal isotropy is documented for some types of tissue, e.g. muscle and nervous tissue. The conductivity is found to be significantly larger in fiber orientation. E.g. in low frequency measurements anisotropy factors $f = \frac{\sigma_{fiber}}{\sigma_{trans}}$ are reported for skeletal muscles in the range from 2–10 [19], for extracellular conductivity of myocardium in the range of 1.4–2.6, and for intracellular conductivity of myocardium in the range of 5.6–12 [22, 23, 24].

Depending on the frequency content of electrical sources used in measurements different spaces of composite tissue contribute to the conductivity (Fig. 3.2). E.g. if sources are located extracellularly, low frequency sources lead to current flow primarily in extracellular space. An increase of frequency enhances the current flow through the cell membrane and the contribution of intracellular space. Therefore, the macroscopic conductivity is enlarged. A further increase results from the contribution of intracellular structures encapsulated by a membrane.

Permittivity. The permittivity of biological tissues can be described by a symmetric tensor ϵ of second order. It has the following form in a local coordinate system:

$$\epsilon_{local} = \begin{pmatrix} \epsilon_{a1} & 0 & 0 \\ 0 & \epsilon_{a2} & 0 \\ 0 & 0 & \epsilon_{a3} \end{pmatrix}$$

with a scalar permittivity ϵ_{a1}, ϵ_{a2}, and ϵ_{a3} in the different axis directions.

Presently, only the cases of transversal isotropy and isotropy are documented in macroscopic measurements of tissue permittivities. The transversal isotropy is reported for tissues, which also show an anisotropic conductivity, e.g. muscle and nervous tissue. The permittivity is significantly smaller in fiber orientation, e.g. in low frequency measurements the anisotropy factor $f = \frac{\epsilon_{trans}}{\epsilon_{fiber}}$ ranges from 4–10 for skeletal muscles [19].

In biological materials the permittivity is found to be frequency dependent. Typically, a decrease is reported for increasing frequency (Fig. 3.3).

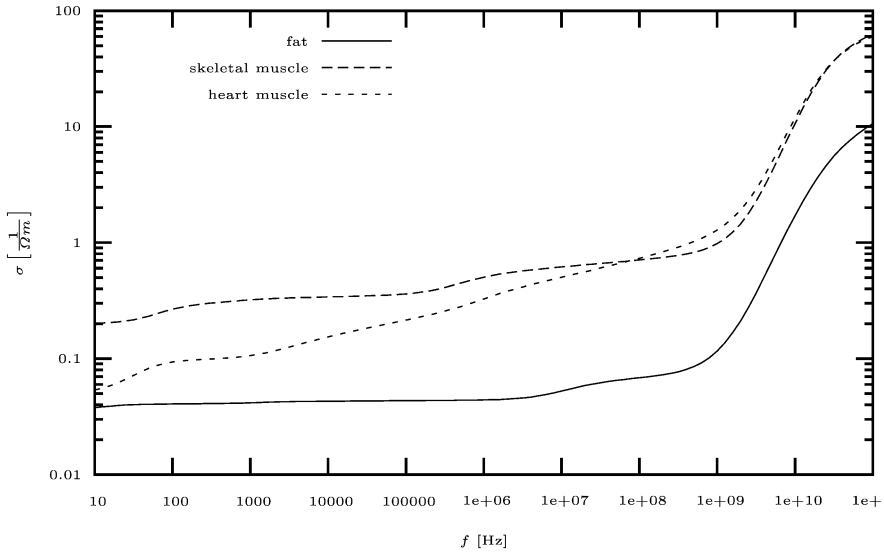

Fig. 3.2. Conductivity of exemplary biological tissues in dependency on frequency (data from [21]). The conductivity σ of fat, skeletal and heart muscle is shown in the range from 10^1 to 10^{11} Hz.

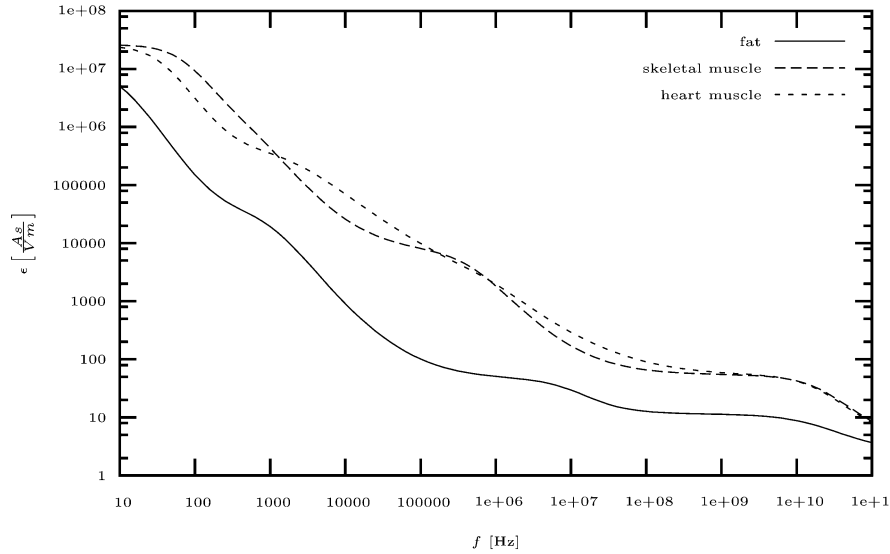

Fig. 3.3. Permittivity of exemplary biological tissues in dependency on frequency (data from [21]). The permittivity ϵ of fat, skeletal and heart muscle is shown in the range from 10^1 to 10^{11} Hz.

Permeability. The permeability of biological tissue resembles the permeability of its principal constituent water. Water shows only weak diamagnetic properties. Commonly, the permeability in vacuum μ_0 is used to describe the permeability of biological tissues.

3.3 Numerical Solution of Poisson's Equation

3.3.1 Finite Element Method

The application of the finite element method to solve Poisson's equations for electrical current fields starts with a subdivision of the spatial domain into finite elements (Sect. 2.7.3). An interpolation of the solution function, the electrical potential ϕ, is performed via shape-functions, which are selected dependent on the element's geometry and the order of interpolation. For each element a system of linear equations is derived, whereby the unknowns are the node variables, i.e. the values of the solution function at node points. The derivation of the linear system commences commonly with the setting up of an equivalent integral, which describes the power of the stationary electrical current field. This power is defined as the energy transformed by the conductivity of the medium into heat per time. The stationary condition delivers the system of linear equations. Finally, the element-wise linear equations are assembled into the system equations, boundary conditions are incorporated and the system is solved with iterative techniques (Sect. 2.4.3).

Interpolation via Shape-Functions. The solution function ϕ is interpolated in the domain $\Omega^{(m)}$ of the m-th element:

$$\phi = \boldsymbol{H}^{(m)\,T}\ \boldsymbol{\phi}^{(m)}$$

with the N-dimensional vector of node variables $\boldsymbol{\phi}^{(m)}$:

$$\boldsymbol{\phi}^{(m)} = \begin{pmatrix} \phi_0^{(m)} \\ \vdots \\ \phi_N^{(m)} \end{pmatrix}$$

and the N-dimensional vector of shape-functions $\boldsymbol{H}^{(m)}$:

$$\boldsymbol{H}^{(m)} = \begin{pmatrix} H_0^{(m)} \\ \vdots \\ H_N^{(m)} \end{pmatrix}$$

Shape-functions result from the polynomial interpolation of the solution function ϕ in the domain $\Omega^{(m)}$ of an element (Sect. 2.7.3).

The gradient of the potential $\nabla\phi$ can be defined with the upper shape-functions:

$$\nabla\phi = \nabla\left(\boldsymbol{H}^{(m)\,T}\boldsymbol{\phi}^{(m)}\right) = \left(\nabla\boldsymbol{H}^{(m)\,T}\right)\boldsymbol{\phi}^{(m)}$$

with the gradient of the shape-function's vector $\nabla\boldsymbol{H}^{(m)}$:

$$\nabla\boldsymbol{H}^{(m)} = \begin{pmatrix} \nabla H_0^{(m)} \\ \vdots \\ \nabla H_N^{(m)} \end{pmatrix} = \begin{pmatrix} \begin{pmatrix} \frac{\partial H_0^{(m)}}{\partial x} \\ \frac{\partial H_0^{(m)}}{\partial y} \\ \frac{\partial H_0^{(m)}}{\partial z} \end{pmatrix} \\ \vdots \\ \begin{pmatrix} \frac{\partial H_N^{(m)}}{\partial x} \\ \frac{\partial H_N^{(m)}}{\partial y} \\ \frac{\partial H_N^{(m)}}{\partial z} \end{pmatrix} \end{pmatrix}$$

The shape-functions $\boldsymbol{H}^{(m)}$ can also serve as the interpolation of the current source density f:

$$f = \boldsymbol{H}^{(m)\,T}\ \boldsymbol{f}^{(m)}$$

starting from the vector of current source densities at node points $\boldsymbol{f}^{(m)}$. Similarly, an interpolation of the conductivity σ in the element's domain can be performed:

$$\sigma = \boldsymbol{H}^{(m)\,T}\ \boldsymbol{\sigma}^{(m)}$$

with the vector of conductivity tensors $\boldsymbol{\sigma}^{(m)}$ at node points.

Exemplary Shape-Functions in Hexahedron. Trilinear shape-functions for unit hexahedrons H_i are given by:

$$\begin{aligned} H_0(x,y,z) &= (1-x)(1-y)(1-z) \\ H_1(x,y,z) &= x(1-y)(1-z) \\ H_2(x,y,z) &= (1-x)y(1-z) \\ H_3(x,y,z) &= xy(1-z) \\ H_4(x,y,z) &= (1-x)(1-y)z \\ H_5(x,y,z) &= x(1-y)z \\ H_6(x,y,z) &= (1-x)yz \\ H_7(x,y,z) &= xyz \end{aligned}$$

The gradient of the shape-function's vector $\nabla\boldsymbol{H}^{(m)}$ is defined by:

$$\nabla \boldsymbol{H}^{(m)} = \begin{pmatrix} \nabla H_0^{(m)} \\ \nabla H_1^{(m)} \\ \nabla H_2^{(m)} \\ \nabla H_3^{(m)} \\ \nabla H_4^{(m)} \\ \nabla H_5^{(m)} \\ \nabla H_6^{(m)} \\ \nabla H_7^{(m)} \end{pmatrix} = \begin{pmatrix} \begin{pmatrix} \frac{\partial H_0^{(m)}}{\partial x} \\ \frac{\partial H_0^{(m)}}{\partial y} \\ \frac{\partial H_0^{(m)}}{\partial z} \end{pmatrix} \\ \begin{pmatrix} \frac{\partial H_1^{(m)}}{\partial x} \\ \frac{\partial H_1^{(m)}}{\partial y} \\ \frac{\partial H_1^{(m)}}{\partial z} \end{pmatrix} \\ \begin{pmatrix} \frac{\partial H_2^{(m)}}{\partial x} \\ \frac{\partial H_2^{(m)}}{\partial y} \\ \frac{\partial H_2^{(m)}}{\partial z} \end{pmatrix} \\ \begin{pmatrix} \frac{\partial H_3^{(m)}}{\partial x} \\ \frac{\partial H_3^{(m)}}{\partial y} \\ \frac{\partial H_3^{(m)}}{\partial z} \end{pmatrix} \\ \begin{pmatrix} \frac{\partial H_4^{(m)}}{\partial x} \\ \frac{\partial H_4^{(m)}}{\partial y} \\ \frac{\partial H_4^{(m)}}{\partial z} \end{pmatrix} \\ \begin{pmatrix} \frac{\partial H_5^{(m)}}{\partial x} \\ \frac{\partial H_5^{(m)}}{\partial y} \\ \frac{\partial H_5^{(m)}}{\partial z} \end{pmatrix} \\ \begin{pmatrix} \frac{\partial H_6^{(m)}}{\partial x} \\ \frac{\partial H_6^{(m)}}{\partial y} \\ \frac{\partial H_6^{(m)}}{\partial z} \end{pmatrix} \\ \begin{pmatrix} \frac{\partial H_7^{(m)}}{\partial x} \\ \frac{\partial H_7^{(m)}}{\partial y} \\ \frac{\partial H_7^{(m)}}{\partial z} \end{pmatrix} \end{pmatrix} = \begin{pmatrix} \begin{pmatrix} -(1-y)(1-z) \\ -(1-x)(1-z) \\ -(1-x)(1-y) \end{pmatrix} \\ \begin{pmatrix} (1-y)(1-z) \\ -x(1-z) \\ -x(1-y) \\ -y(1-z) \\ (1-x)(1-z) \\ -(1-x)y \end{pmatrix} \\ \begin{pmatrix} y(1-z) \\ x(1-z) \\ -xy \end{pmatrix} \\ \begin{pmatrix} -(1-y)z \\ -(1-x)z \\ (1-x)(1-y) \end{pmatrix} \\ \begin{pmatrix} (1-y)z \\ -xz \\ x(1-y) \\ -yz \\ (1-x)z \\ (1-x)y \end{pmatrix} \\ \begin{pmatrix} yz \\ xz \\ xy \end{pmatrix} \end{pmatrix}$$

Equivalent Integral. The equivalent integral Π describes the electrical power in the domain Ω:

$$\Pi = \int_{\Omega} \frac{1}{2} (\nabla \phi)^T \sigma (\nabla \phi) + f\phi \; d\Omega \tag{3.12}$$

with the conductivity tensor σ, the electrical source density current f, and the electrical potential ϕ. The integrand is subdivided in two parts: one representing the conductivity ("ohmic") part of the electrical power and a second representing a part resulting from impressed currents.

Commonly, only the equivalent integral $\Pi^{(m)}$ of the domain of a finite element is of interest. This integral $\Pi^{(m)}$ is transformed into the unit domain Ω_0 using the rules of integral transformations to simplify the evaluation (Fig. 3.4).

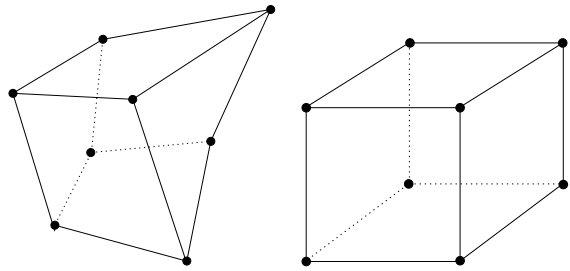

Fig. 3.4. Exemplary coordinate transformation of hexahedron from (a) original domain $\Omega^{(m)}$ to (b) unit domain Ω_0. The coordinate transformation is characterized by its Jacobian matrix J and leads to a transformation of the integral defined over the domain. Node variables are assigned at the node points indicated by black closed circles.

The transformation is determined by the underlying coordinate transformation, which is generally a spatially variant function and characterized by its first-order partial derivatives combined in the Jacobian matrix J. With the Jacobian of the coordinate transformation $\mathcal{J}$ the integral $\Pi^{(m)}$ is determined by:

$$\Pi^{(m)} = \int_{\Omega_0} \left(\frac{1}{2} (\nabla_0 \phi)^T \sigma (\nabla_0 \phi) + f\phi \right) \mathcal{J} \, d\Omega_0$$

whereby the transformed gradient operator ∇_0 is given

$$\nabla_0 = J^{-1} \nabla$$

Linear System of Equations. The equivalent integral $\Pi^{(m)}$ is transformed to a quadratic form:

$$\Pi^{(m)} = \frac{1}{2} \boldsymbol{\phi}^{(m)\,T} \boldsymbol{S}^{(m)} \boldsymbol{\phi}^{(m)} + \boldsymbol{\phi}^{(m)\,T} \boldsymbol{b}^{(m)} \tag{3.13}$$

with the vector of electrical potentials $\boldsymbol{\phi}^{(m)}$, the stiffness matrix $\boldsymbol{S}^{(m)}$ and the vector $\boldsymbol{b}^{(m)}$. The stationary condition is applied to the integral [25]:

$$\frac{\partial \Pi}{\partial \phi_i^{(m)}} = 0$$

and used to create the linear system of equations:

$$\boldsymbol{S}^{(m)} \boldsymbol{\phi}^{(m)} + \boldsymbol{b}^{(m)} = 0$$

In the following the derivation of integral formulations for stiffness matrices and vectors occurring in equation 3.13 is presented for different spatial arrangements of the potentials, conductivities and current source densities. The evaluation of the formulations is performed by analytical or numerical techniques (Sect. 2.5), e.g. Gauss Quadrature, depending on the complexity of the integrals.

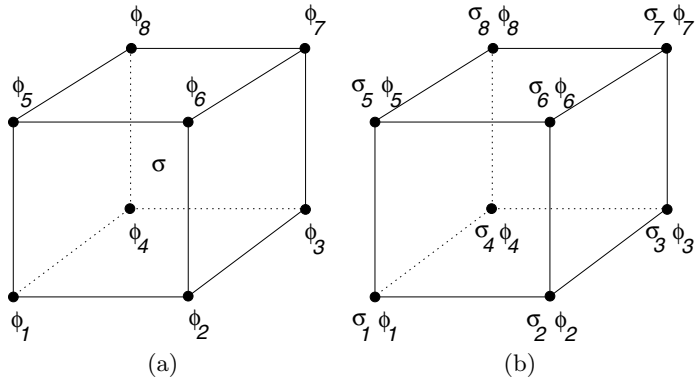

Fig. 3.5. Exemplary finite element with interpolation of potentials. Node variables ϕ_i describing electrical potentials are assigned at the node points indicated by black closed circles. (a) A conductivity σ is assigned to the whole element. (b) The conductivity is interpolated starting from conductivities at node points σ_i.

Stiffness Matrix for Interpolation of Potential and Constant Conductivity. The derivation of a stiffness matrix $\boldsymbol{S}^{(m)}$ in the domain Ω_m for the integral $\Pi^{(m)}$ starts with the substitution of the function ϕ in the integrand of equation 3.12 with the product of the shape-functions $\boldsymbol{H}^{(m)}$ and the node variables $\boldsymbol{\phi}^{(m)}$ (Fig. 3.5 a):

$$\Pi^{(m)} = \int_{\Omega_0} \frac{1}{2} (\nabla_0 \boldsymbol{H}^{(m)\,T} \boldsymbol{\phi}^{(m)})^T \sigma (\nabla_0 \boldsymbol{H}^{(m)\,T} \boldsymbol{\phi}^{(m)}) \; \mathcal{J} \; d\Omega_0$$

Here, the conductivity σ is assumed to be constant in the domain Ω_m of the m-th element:

$$\sigma(x, y, z) = \sigma_{const}$$

The integral is transformed in such a way that the node variables are taken out:

$$\begin{aligned} \Pi^{(m)} &= \int_{\Omega_0} \frac{1}{2} (\boldsymbol{\phi}^{(m)\,T} \nabla_0 \boldsymbol{H}^{(m)}) \sigma (\nabla_0 \boldsymbol{H}^{(m)\,T} \boldsymbol{\phi}^{(m)}) \; \mathcal{J} \; d\Omega_0 \\ &= \frac{1}{2} \; \boldsymbol{\phi}^{(m)\,T} \left(\int_{\Omega_0} (\nabla_0 \boldsymbol{H}^{(m)}) \sigma (\nabla_0 \boldsymbol{H}^{(m)\,T}) \; \mathcal{J} \; d\Omega_0 \right) \boldsymbol{\phi}^{(m)} \end{aligned}$$

The stiffness matrix $\boldsymbol{S}^{(m)}$ is defined by comparison with equation 3.13:

$$\boldsymbol{S}^{(m)} = \int_{\Omega_0} (\nabla_0 \boldsymbol{H}^{(m)}) \sigma (\nabla_0 \boldsymbol{H}^{(m)\,T}) \; \mathcal{J} \; d\Omega_0$$

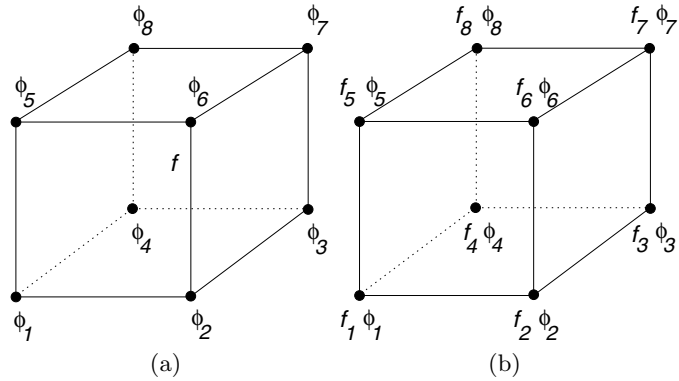

Fig. 3.6. Exemplary finite element with interpolation of current density sources. Node variables ϕ_i describing electrical potentials are assigned at the node points indicated by black closed circles. (a) A current density source f is assigned to the whole element. (b) The current density source is interpolated starting from the conductivities at the node points f_i.

Stiffness Matrix for Interpolation of Potential and Conductivity. In a similar manner a stiffness matrix $\boldsymbol{S}^{(m)}$ can be derived for the integral $\mathit{\Pi}^{(m)}$, whereby the conductivity σ is a spatial function (Fig. 3.5 b). The integral $\mathit{\Pi}^{(m)}$ is transformed after the substitution:

$$\begin{aligned}\mathit{\Pi}^{(m)} &= \int_{\Omega_0} \frac{1}{2} (\nabla_0 \boldsymbol{H}^{(m)\,T} \boldsymbol{\phi}^{(m)})^T \boldsymbol{H}^{(m)\,T} \boldsymbol{\sigma}^{(m)} (\nabla_0 \boldsymbol{H}^{(m)\,T} \boldsymbol{\phi}^{(m)}) \mathcal{J}\, d\Omega_0 \\ &= \frac{1}{2}\, \boldsymbol{\phi}^{(m)\,T} \left(\int_{\Omega_0} (\nabla_0 \boldsymbol{H}^{(m)}) \boldsymbol{H}^{(m)\,T} \boldsymbol{\sigma}^{(m)} (\nabla_0 \boldsymbol{H}^{(m)\,T}) \mathcal{J}\, d\Omega_0 \right) \boldsymbol{\phi}^{(m)}\end{aligned}$$

The stiffness matrix $\boldsymbol{S}^{(m)}$ results from comparison with equation 3.13:

$$\boldsymbol{S}^{(m)} = \int_{\Omega_0} (\nabla_0 \boldsymbol{H}^{(m)}) \boldsymbol{H}^{(m)\,T} \boldsymbol{\sigma}^{(m)} (\nabla_0 \boldsymbol{H}^{(m)\,T}) \mathcal{J}\, d\Omega_0$$

Vector for Constant Current Source Density. The inclusion of a current density source in the equations system of a finite element necessitates the transformation of the integral $\mathit{\Pi}^{(m)}$. The factor ϕ is replaced with the product of shape-functions $\boldsymbol{H}^{(m)}$ and node variables $\boldsymbol{\phi}^{(m)}$:

$$\begin{aligned}\mathit{\Pi}^{(m)} &= \int_{\Omega_0} f\ \boldsymbol{H}^{(m)\,T}\ \boldsymbol{\phi}^{(m)} \mathcal{J}\, d\Omega_0 \\ &= f \left(\int_{\Omega_0} \boldsymbol{H}^{(m)\,T} \mathcal{J}\, d\Omega_0 \right) \boldsymbol{\phi}^{(m)}\end{aligned}$$

Here, the current density source f is assumed to be constant in the domain Ω_m of the m-th element (Fig. 3.6 a):

$$f(x, y, z) = f_{const}$$

The vector $\boldsymbol{b}^{(m)}$ is defined taking equation 3.13 into account:

$$\boldsymbol{b}^{(m)} = f \int_{\Omega_0} \boldsymbol{H}^{(m)\,T} \mathcal{J}\; d\Omega_0$$

Vector for Trilinear Interpolation of Current Source Density. In a similar manner a vector $\boldsymbol{b}^{(m)}$ can be derived for the integral $\mathit{\Pi}^{(m)}$, whereby the current source density f is a spatial function (Fig. 3.6 b):

$$\begin{aligned}\mathit{\Pi}^{(m)} &= \int_{\Omega_0} \boldsymbol{H}^{(m)\,T}\; \boldsymbol{f}^{(m)}\; \boldsymbol{H}^{(m)\,T}\; \boldsymbol{\phi}^{(m)} \mathcal{J}\; d\Omega_0 \\ &= \boldsymbol{f}^{(m)\,T} \left(\int_{\Omega_0} \boldsymbol{H}^{(m)}\; \boldsymbol{H}^{(m)\,T} \mathcal{J}\; d\Omega_0 \right) \boldsymbol{\phi}^{(m)}\end{aligned}$$

The vector $\boldsymbol{b}^{(m)}$ is given by:

$$\boldsymbol{b}^{(m)} = \boldsymbol{f}^{(m)\,T} \int_{\Omega_0} \boldsymbol{H}^{(m)}\; \boldsymbol{H}^{(m)\,T} \mathcal{J}\; d\Omega_0$$

3.3.2 Finite Differences Method

The application of the finite differences method to solve Poisson's equation for electrical current fields starts with a discretization of the spatial domain by node points (Sect. 2.7.4). The application necessitates the symbolic evaluation of Poisson's equation. Poisson's equation is a partial differential equation, which combines the symmetric conductivity tensor of second order $\sigma = [\sigma_{ij}]$, the electrical potential ϕ and the current source density f:

$$\nabla \cdot (\sigma \nabla \phi) = f$$

In general all quantities are a function of space and defined everywhere in the domain Ω. The terms resulting from the symbolic evaluation are discretized using differences of the upper electrical quantities at specific locations to approximate the derivatives.

The node point-wise application of the finite differences method leads to a system of linear equations, where for each point a corresponding linear equation is generated [5, 26]. The further steps of the method are the assembling of the point-wise linear equations into the system equations, the incorporation of boundary conditions and the solving of the system commonly with iterative techniques (Sect. 2.4.3).

Symbolic Evaluation of Poisson's Equation. In general, the symbolic evaluation results in a sum of terms with first and second order spatial derivatives of the electrical potential as well as first order spatial derivatives of the components of the conductivity tensor:

$$\begin{aligned}
&\sigma_{11}\frac{\partial^2\phi}{\partial x^2} + \sigma_{22}\frac{\partial^2\phi}{\partial y^2} + \sigma_{33}\frac{\partial^2\phi}{\partial z^2} \\
&+ 2\sigma_{12}\frac{\partial^2\phi}{\partial x\partial y} + 2\sigma_{13}\frac{\partial^2\phi}{\partial x\partial z} + 2\sigma_{23}\frac{\partial^2\phi}{\partial y\partial z} \\
&+ \frac{\partial\sigma_{11}}{\partial x}\frac{\partial\phi}{\partial x} + \frac{\partial\sigma_{12}}{\partial y}\frac{\partial\phi}{\partial x} + \frac{\partial\sigma_{13}}{\partial z}\frac{\partial\phi}{\partial x} \\
&+ \frac{\partial\sigma_{12}}{\partial x}\frac{\partial\phi}{\partial y} + \frac{\partial\sigma_{22}}{\partial y}\frac{\partial\phi}{\partial y} + \frac{\partial\sigma_{23}}{\partial z}\frac{\partial\phi}{\partial y} \\
&+ \frac{\partial\sigma_{13}}{\partial x}\frac{\partial\phi}{\partial z} + \frac{\partial\sigma_{23}}{\partial y}\frac{\partial\phi}{\partial z} + \frac{\partial\sigma_{33}}{\partial z}\frac{\partial\phi}{\partial z} \\
&= f
\end{aligned} \tag{3.14}$$

Assumptions about the distribution and character of the conductivity tensor allow a simplification of the general formula. In the case of an inhomogeneous distribution of isotropic conductivity, the conductivity tensor σ can be represented by a diagonal matrix with $\sigma_{ii} \equiv \sigma_{inh}$. Therefore, terms vanish with off-diagonal components of the conductivity tensor σ. From the general formula (equation 3.14) remains:

$$\sigma_{inh}\left(\frac{\partial^2\phi}{\partial x^2} + \frac{\partial^2\phi}{\partial y^2} + \frac{\partial^2\phi}{\partial z^2}\right) + \frac{\partial\sigma_{inh}}{\partial x}\frac{\partial\phi}{\partial x} + \frac{\partial\sigma_{inh}}{\partial y}\frac{\partial\phi}{\partial y} + \frac{\partial\sigma_{inh}}{\partial z}\frac{\partial\phi}{\partial z} = f$$

In the case of a homogeneous distribution of isotropic conductivity the conductivity tensor σ is constant in the domain Ω and can be represented by a diagonal matrix with $\sigma_{ii} \equiv \sigma_{hom}$. Therefore, terms vanish with first order spatial derivatives and off-diagonal components of the conductivity tensor σ. The general formula (equation 3.14) reduces to:

$$\sigma_{hom}\left(\frac{\partial^2\phi}{\partial x^2} + \frac{\partial^2\phi}{\partial y^2} + \frac{\partial^2\phi}{\partial z^2}\right) = f$$

The discretization of the differential terms in the domain Ω is given by the model representation. Commonly, the domain Ω is decomposed in rectangular lattice consisting of cubic voxels. Each voxel is homogeneous concerning its conductivity. The voxel's centers serve as node points with associated node variables describing potentials and conductivity tensors (Fig. 3.7 a). The derivatives can be approximated by differences using the rules described in Sect. 2.7.4.

Exemplary Approximations of Derivatives. In a three-dimensional, rectangular, equidistant mesh a numbering of node points is defined (Fig. 3.8). Using this numbering the first order derivatives of the potential ϕ at the node point $\boldsymbol{x}_{i,j,k}$ are approximated by:

$$\frac{\partial\phi}{\partial x}(\boldsymbol{x}_{i,j,k}) \approx \frac{\phi_{i+1,j,k} - \phi_{i-1,j,k}}{2h}$$

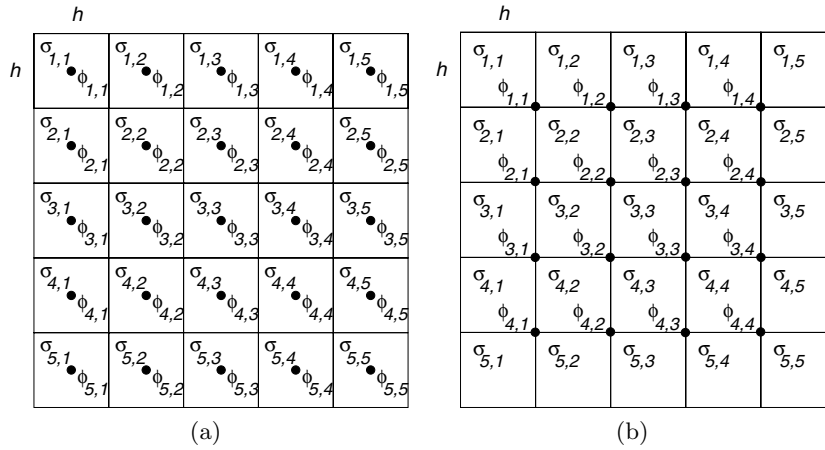

Fig. 3.7. Exemplary finite differences meshes for discretization of Poisson's equation. The two-dimensional spatial domain Ω is subdivided in a rectangular lattice with quad-shaped cells of length h. A conductivity $\sigma_{i,j}$ is assigned to each cell. The lattice is isotropic and equidistant. Node variables describing electrical potentials indicated by black closed circles are assigned. (a) The node variables $\phi_{i,j}$ are located at centers of cells. (b) The node variable $\phi_{i,j}$ are placed at the vertices of cells.

$$\frac{\partial \phi}{\partial y}(\boldsymbol{x}_{i,j,k}) \approx \frac{\phi_{i,j+1,k} - \phi_{i,j-1,k}}{2h}$$
$$\frac{\partial \phi}{\partial z}(\boldsymbol{x}_{i,j,k}) \approx \frac{\phi_{i,j,k+1} - \phi_{i,j,k-1}}{2h}$$

with the distance between node points h in x- as well as in y-direction. The second order derivatives of the potential ϕ are given by:

$$\frac{\partial^2 \phi}{\partial x^2}(\boldsymbol{x}_{i,j,k}) \approx \frac{\phi_{i+1,j,k} - 2\phi_{i,j,k} + \phi_{i-1,j,k}}{h^2}$$
$$\frac{\partial^2 \phi}{\partial y^2}(\boldsymbol{x}_{i,j,k}) \approx \frac{\phi_{i,j+1,k} - 2\phi_{i,j,k} + \phi_{i,j-1,k}}{h^2}$$
$$\frac{\partial^2 \phi}{\partial z^2}(\boldsymbol{x}_{i,j,k}) \approx \frac{\phi_{i,j,k+1} - 2\phi_{i,j,k} + \phi_{i,j,k-1}}{h^2}$$
$$\frac{\partial^2 \phi}{\partial x \partial y}(\boldsymbol{x}_{i,j,k}) \approx \frac{\phi_{i+1,j+1,k} - \phi_{i-1,j+1,k} - \phi_{i+1,j-1,k} + \phi_{i-1,j-1,k}}{4h^2}$$
$$\frac{\partial^2 \phi}{\partial x \partial z}(\boldsymbol{x}_{i,j,k}) \approx \frac{\phi_{i+1,j,k+1} - \phi_{i-1,j,k+1} - \phi_{i+1,j,k-1} + \phi_{i-1,j,k-1}}{4h^2}$$
$$\frac{\partial^2 \phi}{\partial y \partial z}(\boldsymbol{x}_{i,j,k}) \approx \frac{\phi_{i,j+1,k+1} - \phi_{i,j+1,k-1} - \phi_{i,j-1,k+1} + \phi_{i,j-1,k-1}}{4h^2}$$

In the general formulation of Poisson's equation (equation 3.14) first order derivatives of the conductivity tensor σ occur. The necessary components at

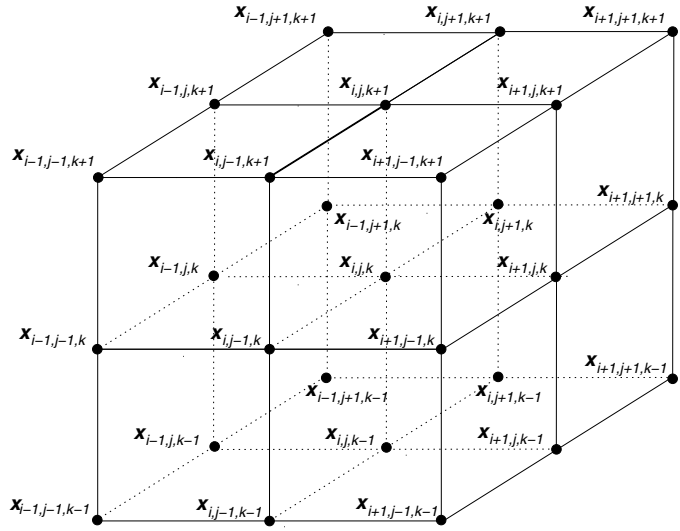

Fig. 3.8. Exemplary numbering of node points in three-dimensional, rectangular, equidistant mesh. A sub-volume of a three-dimensional spatial domain Ω is shown, which is subdivided in a rectangular lattice with cubic cells. The center of the sub-volume is node point $\boldsymbol{x}_{i,j,k}$. The mesh is applied in conjunction with the finite differences method for discretization of Poisson's equation. Node points are indicated by black closed circles.

the node point $\boldsymbol{x}_{i,j,k}$ can be taken from the following approximations:

$$\begin{aligned}
\frac{\partial \sigma}{\partial x}(\boldsymbol{x}_{i,j,k}) &\approx \frac{\sigma_{i+1,j,k} - \sigma_{i-1,j,k}}{2h} \\
\frac{\partial \sigma}{\partial y}(\boldsymbol{x}_{i,j,k}) &\approx \frac{\sigma_{i,j+1,k} - \sigma_{i,j-1,k}}{2h} \\
\frac{\partial \sigma}{\partial z}(\boldsymbol{x}_{i,j,k}) &\approx \frac{\sigma_{i,j,k+1} - \sigma_{i,j,k-1}}{2h}
\end{aligned}$$

An alternative to the upper technique with a voxel-centered placement of node variables is the placement at the vertices of voxels (Fig. 3.7 b). In this case the conductivity at a node point can be calculated by averaging of adjoint conductivities. An averaging in a three-dimensional, rectangular, equidistant mesh is given by:

$$\begin{aligned}
\sigma(\boldsymbol{x}_{i,j,k}) = \tfrac{1}{8} \, (&\sigma_{i,j,k} + \sigma_{i+1,j,k} + \sigma_{i,j+1,k} + \sigma_{i+1,j+1,k} \\
&+\sigma_{i,j,k+1} + \sigma_{i+1,j,k+1} + \sigma_{i,j+1,k+1} + \sigma_{i+1,j+1,k+1})
\end{aligned}$$

Applying this operation, the approximation of derivatives of conductivities can be performed straightforward. A disadvantage of this strategy is the large periphery around a node point $\boldsymbol{x}_{i,j,k}$, which has to be taken into account for

the derivative approximation. A more local strategy consists of the following approximations:

$$\begin{aligned}
\frac{\partial \sigma}{\partial x}(\boldsymbol{x}_{i,j,k}) &\approx \frac{\sigma_{i+1,j,k} - \sigma_{i,j,k}}{h} \\
\frac{\partial \sigma}{\partial y}(\boldsymbol{x}_{i,j,k}) &\approx \frac{\sigma_{i,j+1,k} - \sigma_{i,j,k}}{h} \\
\frac{\partial \sigma}{\partial z}(\boldsymbol{x}_{i,j,k}) &\approx \frac{\sigma_{i,j,k+1} - \sigma_{i,j,k}}{h}
\end{aligned}$$

A rearrangement of Poisson's equation is performed after the substitution of derivatives with the approximations by differences. The rearrangement of this node point-wise created equation leads to an equation, where main parts are combined as vector product:

$$\boldsymbol{a}_{i,j,k}^T \boldsymbol{\phi}_{i,j,k} = f(\boldsymbol{x}_{i,j,k})$$

with the vector of weightings of node variables $\boldsymbol{a}_{i,j,k}$ for the node point $\boldsymbol{x}_{i,j,k}$. The components of the vector $\boldsymbol{a}_{i,j,k}$ are a function of the conductivity distribution and the mesh properties.

4

Theory of Continuum Mechanics

4.1 Introduction

Continuum mechanics is a field of physics, which deals with deformation and flow in a continuous medium under the influence of forces. The continuous medium occupies a spatial region with boundaries and an assigned volume. Boundaries and volume may be a function of time. Whereas the term deformation describes a change of the medium's shape starting from an initial configuration to a subsequent configuration, the term flow describes the continuing state of the medium's motion [27].

In the context of a mathematical, mechanical modeling of biological materials, particularly of tissues found in the heart, a subregion of the theory of continuum mechanics is of specific importance, i.e. the elasticity theory. This theory allows a quantitative description of finite deformations of inhomogeneous, anisotropic cardiac tissues under the influence of external forces, e.g. at boundaries to the atrial and ventricular cavities caused by blood pressure, and of internal forces generated by contractile elements inside of myocytes.

In the following sections the theory of continuum mechanics is introduced, focusing on its underlying definitions and physical laws as well as on numerical approaches to describe deformation of materials. The introduction uses tensor algebra (Sect. 2.3) and Einstein summation convention (Sect. 2.2), which allows a habile description of equations and physical quantities.

The physical quantities strain and stress are illuminated in different configurations. Different formulations of stress equilibrium are deduced assuming a balance of forces and moments. Particularly, the principle of virtual displacements in Lagrangian formulation is introduced, which provides an efficient scheme for a numerical solution. Medium dependent relationships between strain and stress, the so-called constitutive relationships, are pointed out by using elasticity theory. Linear and non-linear relationships are introduced, e.g. Hooke's law, hyper-, hypo- and viscoelasticity.

The finite element method is presented as an approach for numerical simulation of deformation. The presentation focuses on the discretization of equa-

F.B. Sachse: LNCS 2966, pp. 69–90, 2004.

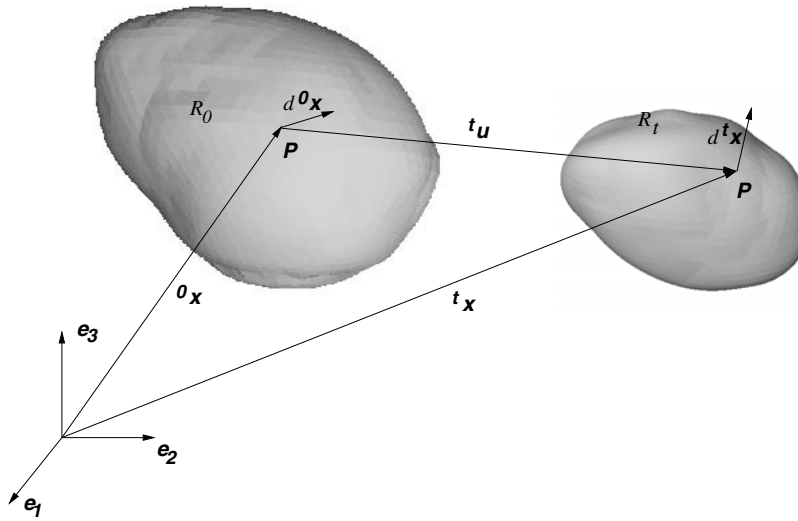

Fig. 4.1. Deformation in finite continuous medium. The point $\boldsymbol{P}$ with coordinates ${}^0\boldsymbol{x}$ in the Lagrangian configuration R_0 moves to the coordinates ${}^t\boldsymbol{x}$ in the Eulerian configuration R_t. The elementary segment $d\,{}^0\boldsymbol{x}$ at point P is transformed to the segment $d\,{}^t\boldsymbol{x}$.

tions derived from the total Lagrangian formulation and hyperelastic description of materials. Efficient types of finite elements are described and recipes are given for the handling of systems of equations resulting from the application of the finite element method.

4.2 Definitions and Physical Laws

4.2.1 Deformation Gradient

The finite continuous medium Ω is deformed starting from the reference configuration R_0 at time $t = 0$ [28]. The following configurations R_t are defined at time t. The reference configuration is named Lagrangian configuration, the following configurations are so-called Eulerian configurations (Fig. 4.1).

The coordinates of a point $\boldsymbol{P}$ in Ω are described in the Lagrangian configuration R_0 by the vector ${}^0\boldsymbol{x}$. At time t the motion of point $\boldsymbol{P}$ is defined by:

$$ {}^t\boldsymbol{x} = {}^t\boldsymbol{x}({}^0\boldsymbol{x}, t) $$

Alternatively, the coordinates of the point $\boldsymbol{P}$ in the Eulerian configurations are described by the vector ${}^t\boldsymbol{x}$. At time t the corresponding Lagrangian coordinates of the point $\boldsymbol{P}$ are defined by:

$$ {}^0\boldsymbol{x} = {}^0\boldsymbol{x}({}^t\boldsymbol{x}, t) $$

The displacement vector ${}^t\boldsymbol{u}$ joining the coordinates ${}^\mathbf{0}\boldsymbol{x}$ and ${}^\mathbf{t}\boldsymbol{x}$ of the point $\boldsymbol{P}$ is defined as:

$$ {}^t\boldsymbol{u} = {}^t\boldsymbol{x} - {}^0\boldsymbol{x} $$

The deformation gradient ${}^t_0\boldsymbol{X}$ can be defined by differentiating ${}^t\boldsymbol{x}({}^0\boldsymbol{x}, t)$ with respect to the reference configuration coordinates ${}^0\boldsymbol{x}$ [29] in a cartesian system:

$$ {}^t_0\boldsymbol{X} = \left[\frac{\partial\, {}^t x_i}{\partial\, {}^0 x_j}\right] = \begin{pmatrix} \frac{\partial\, {}^t x_1}{\partial\, {}^0 x_1} & \frac{\partial\, {}^t x_1}{\partial\, {}^0 x_2} & \frac{\partial\, {}^t x_1}{\partial\, {}^0 x_3} \\ \frac{\partial\, {}^t x_2}{\partial\, {}^0 x_1} & \frac{\partial\, {}^t x_2}{\partial\, {}^0 x_2} & \frac{\partial\, {}^t x_2}{\partial\, {}^0 x_3} \\ \frac{\partial\, {}^t x_3}{\partial\, {}^0 x_1} & \frac{\partial\, {}^t x_3}{\partial\, {}^0 x_2} & \frac{\partial\, {}^t x_3}{\partial\, {}^0 x_3} \end{pmatrix} $$

The deformation gradient ${}^t_0\boldsymbol{X}$ is a tensor of second order. The tensor converts an elementary segment $d\,{}^0\boldsymbol{x}$ of the reference configuration R_0 into a segment $d\,{}^t\boldsymbol{x}$ in the configuration R_t:

$$ d\,{}^t\boldsymbol{x} = {}^t_0\boldsymbol{X}\, d\,{}^0\boldsymbol{x} $$

Alternatively, the deformation gradient can be described by the displacement vector ${}^t\boldsymbol{u}$:

$$ {}^t_0\boldsymbol{X} = \left[\frac{\partial\, {}^t u_i}{\partial\, {}^0 x_j} + \delta_{ij}\right] = \begin{pmatrix} \frac{\partial\, {}^t u_1}{\partial\, {}^0 x_1} + 1 & \frac{\partial\, {}^t u_1}{\partial\, {}^0 x_2} & \frac{\partial\, {}^t u_1}{\partial\, {}^0 x_3} \\ \frac{\partial\, {}^t u_2}{\partial\, {}^0 x_1} & \frac{\partial\, {}^t u_2}{\partial\, {}^0 x_2} + 1 & \frac{\partial\, {}^t u_2}{\partial\, {}^0 x_3} \\ \frac{\partial\, {}^t u_3}{\partial\, {}^0 x_1} & \frac{\partial\, {}^t u_3}{\partial\, {}^0 x_2} & \frac{\partial\, {}^t u_3}{\partial\, {}^0 x_3} + 1 \end{pmatrix} $$

with the Kronecker delta δ.

The reverse deformation gradient ${}^0_t\boldsymbol{X}$ can be defined by differentiating ${}^0\boldsymbol{x}({}^t\boldsymbol{x}, t)$ with respect to the Eulerian configuration coordinates ${}^t\boldsymbol{x}$ in a cartesian system:

$$ {}^0_t\boldsymbol{X} = \left[\frac{\partial\, {}^0 x_i}{\partial\, {}^t x_j}\right] = \begin{pmatrix} \frac{\partial\, {}^0 x_1}{\partial\, {}^t x_1} & \frac{\partial\, {}^0 x_1}{\partial\, {}^t x_2} & \frac{\partial\, {}^0 x_1}{\partial\, {}^t x_3} \\ \frac{\partial\, {}^0 x_2}{\partial\, {}^t x_1} & \frac{\partial\, {}^0 x_2}{\partial\, {}^t x_2} & \frac{\partial\, {}^0 x_2}{\partial\, {}^t x_3} \\ \frac{\partial\, {}^0 x_3}{\partial\, {}^t x_1} & \frac{\partial\, {}^0 x_3}{\partial\, {}^t x_2} & \frac{\partial\, {}^0 x_3}{\partial\, {}^t x_3} \end{pmatrix} $$

The reverse deformation gradient ${}^0_t\boldsymbol{X}$ is a tensor of second order. The tensor converts an elementary segment $d\,{}^t\boldsymbol{x}$ of the Eulerian configuration R_t into a segment $d\,{}^0\boldsymbol{x}$ in the reference configuration R_0:

$$ d\,{}^0\boldsymbol{x} = {}^0_t\boldsymbol{X}\, d\,{}^t\boldsymbol{x} $$

Volume and Surface Changes. The elementary volume d^0V in the Lagrangian configuration R_0 is transformed to the elementary volume d^tV in the Eulerian configuration R_t by:

$$d^tV = {}^tJ \; d^0V \tag{4.1}$$

with the Jacobian ${}^tJ$ as the determinant of the deformation gradient ${}^t_0\boldsymbol{X}$. Therefore, a volume change resulting from a deformation can be quantified by the Jacobian ${}^tJ$. The volume change can also be determined with the mass conservation principle:

$${}^tJ = \frac{{}^0\rho}{{}^t\rho}$$

with the mass density ${}^0\rho$ in the Lagrangian configuration R_0 and the mass density ${}^t\rho$ in the Eulerian configuration R_t. A Jacobian ${}^tJ$ equal to one indicates an isovolumetric deformation, which can result e.g. by the incompressibility of a medium. Values of the Jacobian ${}^tJ$ smaller than or equal to zero are not common.

The elementary surface d^0S in the reference configuration R_0 is transformed to the elementary surface d^tS in the current configuration R_t by:

$${}^t\boldsymbol{n} \; d^tS = {}^tJ \, {}^0_t\boldsymbol{X}^T \, {}^0\boldsymbol{n} \; d^0S$$

with the surface normals ${}^t\boldsymbol{n}$ and ${}^0\boldsymbol{n}$.

Polar Decomposition. A deformation gradient $\boldsymbol{X}$ can be decomposed in a rotation tensor $\boldsymbol{R}$ and a right stretch tensor $\boldsymbol{U}$:

$$\boldsymbol{X} = \boldsymbol{R}\,\boldsymbol{U}$$

The right stretch tensor $\boldsymbol{U}$ can be represented by a symmetric, positive semidefinite matrix, the rotation tensor $\boldsymbol{R}$ by an orthonormal matrix.

The decomposition of the deformation gradient $\boldsymbol{X}$ can be achieved with the following transformations. The square of the tensor $\boldsymbol{X}$ delivers the square of the right stretch tensor $\boldsymbol{U}$:

$$\boldsymbol{X}^T \; \boldsymbol{X} = (\boldsymbol{R}\,\boldsymbol{U})^T(\boldsymbol{R}\,\boldsymbol{U}) = \boldsymbol{U}^T \; \boldsymbol{U}$$

A diagonalization of $\boldsymbol{U}^T \; \boldsymbol{U} = \boldsymbol{V}\boldsymbol{D}\boldsymbol{V}^T$ delivers the orthonormal matrix $\boldsymbol{V}$ and the positive semidefinite, diagonal matrix $\boldsymbol{D}$. With the transformation

$$\boldsymbol{U}^T \; \boldsymbol{U} = \boldsymbol{V}\boldsymbol{D}\boldsymbol{V}^T = \boldsymbol{V}\boldsymbol{D}^{\frac{1}{2}}\boldsymbol{D}^{\frac{1}{2}}\boldsymbol{V}^T = (\boldsymbol{V}\boldsymbol{D}^{\frac{1}{2}}\boldsymbol{V}^T)(\boldsymbol{V}\boldsymbol{D}^{\frac{1}{2}}\boldsymbol{V}^T)$$

the stretch tensor $\boldsymbol{U}$ can be constructed taking its symmetry into account:

$$\boldsymbol{U} = \boldsymbol{V}\boldsymbol{D}^{\frac{1}{2}}\boldsymbol{V}^T$$

The rotation tensor $\boldsymbol{R}$ is determined by:

$$\boldsymbol{R} = \boldsymbol{X} \; \boldsymbol{U}^{-1}$$

4.2.2 Strain Tensors

Cauchy-Green Right Dilation Tensor. The Cauchy-Green right dilation tensor ${}^t_0\boldsymbol{C}$ describes the changes of squared lengths in the Eulerian configuration. Here, the stretch ${}^t\lambda$ of an elementary segment $d^0\boldsymbol{x}$ can be determined by:

$$\begin{aligned} {}^t\lambda &= \sqrt{d^t\boldsymbol{x}^2} \\ &= \sqrt{({}^t_0\boldsymbol{X} d^0\boldsymbol{x})^2} \\ &= \sqrt{d^0\boldsymbol{x}^T({}^t_0\boldsymbol{X}^T\,{}^t_0\boldsymbol{X}) d^0\boldsymbol{x}} \\ &= \sqrt{d^0\boldsymbol{x}^T\,{}^t_0\boldsymbol{C}\; d^0\boldsymbol{x}} \end{aligned}$$

with the symmetric, second order Cauchy-Green right dilation tensor ${}^t_0\boldsymbol{C}$ defined as:

$${}^t_0\boldsymbol{C} = {}^t_0\boldsymbol{X}^T\,{}^t_0\boldsymbol{X}$$

Symmetrically, the Cauchy-Green left dilation or Finger strain tensor is constructed by:

$${}^t_0\boldsymbol{B} = {}^t_0\boldsymbol{X}\,{}^t_0\boldsymbol{X}^T$$

Cauchy Strain Tensor. The Cauchy strain tensor ${}^0_t\boldsymbol{C}$ describes the changes of squared lengths in the Lagrangian configuration:

$$d^0\boldsymbol{x}^2 = ({}^0_t\boldsymbol{X} d^t\boldsymbol{x})^2 = d^t\boldsymbol{x}^T\,{}^0_t\boldsymbol{C}\; d^t\boldsymbol{x}$$

The Cauchy strain tensor ${}^0_t\boldsymbol{C}$ is of second order with:

$${}^0_t\boldsymbol{C} = {}^0_t\boldsymbol{X}^T\,{}^0_t\boldsymbol{X} = {}^t_0\boldsymbol{B}^{-1}$$

Lagrangian Strain Tensor. The Green, Green-Lagrange or Lagrangian strain tensor can be introduced by the difference of the squared lengths of elementary segments in the Eulerian and Lagrangian configuration:

$$\begin{aligned} d^t\boldsymbol{x}^2 - d^0\boldsymbol{x}^2 &= d^0\boldsymbol{x}^T({}^t_0\boldsymbol{C} - \boldsymbol{I})\; d^0\boldsymbol{x} \\ &= d^0\boldsymbol{x}^T 2\,{}^t_0\boldsymbol{E}\; d^0\boldsymbol{x} \end{aligned}$$

with the symmetric, second order Lagrangian strain tensor ${}^t_0\boldsymbol{E}$ defined as:

$${}^t_0\boldsymbol{E} = \frac{1}{2}\left({}^t_0\boldsymbol{C} - \boldsymbol{I}\right)$$

Euler-Almansi Strain Tensor. Similarly, the Almansi, Euler-Almansi or Eulerian strain tensor can be introduced by the difference of the squared lengths of elementary segments in the Lagrangian and Eulerian configuration:

$$\begin{aligned} d^t\boldsymbol{x}^2 - d^0\boldsymbol{x}^2 &= d^t\boldsymbol{x}^T(\boldsymbol{I} - {}^0_t\boldsymbol{C})\; d^t\boldsymbol{x} \\ &= d^t\boldsymbol{x}^T 2\,{}^0_t\boldsymbol{e}\; d^t\boldsymbol{x} \end{aligned}$$

with the symmetric, second order Eulerian tensor ${}^0_t\boldsymbol{e}$ defined as:

$${}^0_t\boldsymbol{e} = \frac{1}{2}\left(\boldsymbol{I} - {}^0_t\boldsymbol{C}\right)$$

Linear Strain Tensor. The definition of the linear strain tensor ${}^{t}_{0}\boldsymbol{\epsilon}$ assumes small displacements and displacement gradients:

$$ {}^{t}_{0}\boldsymbol{\epsilon} = \left[\frac{1}{2}\left(\frac{\partial\, {}^{t}u_i}{\partial\, {}^{0}x_j} + \frac{\partial\, {}^{t}u_j}{\partial\, {}^{0}x_i}\right)\right] = \left[\frac{1}{2}\left(\frac{\partial\, {}^{t}u_i}{\partial\, {}^{t}x_j} + \frac{\partial\, {}^{t}u_j}{\partial\, {}^{t}x_i}\right)\right] $$

Here, the product terms of the Lagrangian and Eulerian strain tensors concerning the displacement gradients are neglected. The linear strain tensor ${}^{t}_{0}\boldsymbol{\epsilon}$ is used in the classical linear elasticity theory [27].

4.2.3 Stress Tensors

Cauchy Stress Tensor. The Cauchy stress tensor ${}^{t}\boldsymbol{\tau}$ is defined at every point in the continuous medium Ω and describes the forces per unit surface in the Eulerian configuration R_t. The stress tensor allows the assignment of a stress vector ${}^{t}\boldsymbol{t}^{<\boldsymbol{n}>}$ for an arbitrary oriented surface element with unit normal vector $\boldsymbol{n}$:

$$ {}^{t}\boldsymbol{t}^{<\boldsymbol{n}>} = {}^{t}\boldsymbol{\tau}\ \boldsymbol{n} \tag{4.2} $$

If stress vectors of three mutually perpendicular surfaces are known, the tensor ${}^{t}\boldsymbol{\tau}$ is uniquely defined (Fig. 4.2). Commonly, the stress vectors, which are also known as traction vectors and surface tension vectors, are different depending on the orientation of the corresponding surface elements, e.g.:

$$ {}^{t}\boldsymbol{t}^{<\boldsymbol{n}>} = -\,{}^{t}\boldsymbol{t}^{<-\boldsymbol{n}>} $$

The Cauchy stress tensor ${}^{t}\boldsymbol{\tau}$ is a second order tensor [3]:

$$ {}^{t}\boldsymbol{\tau} = \begin{pmatrix} {}^{t}\tau_{11} & {}^{t}\tau_{12} & {}^{t}\tau_{13} \\ {}^{t}\tau_{21} & {}^{t}\tau_{22} & {}^{t}\tau_{23} \\ {}^{t}\tau_{31} & {}^{t}\tau_{32} & {}^{t}\tau_{33} \end{pmatrix} $$

The diagonal elements of ${}^{t}\boldsymbol{\tau}$ are called normal stresses. The off-diagonal elements are called shear stresses.

The stress tensor is symmetric:

$$ {}^{t}\boldsymbol{\tau} = {}^{t}\boldsymbol{\tau}^{T} $$

First Piola-Kirchhoff Stress Tensor. The first Piola-Kirchhoff stress tensor or Lagrange stress tensor ${}^{t}_{0}\boldsymbol{T}$ is a non-symmetric second order tensor, which refers stresses to the Lagrangian configuration. The stress tensor ${}^{t}_{0}\boldsymbol{T}$ is derived from the Cauchy stress tensor ${}^{t}\boldsymbol{\tau}$:

$$ {}^{t}_{0}\boldsymbol{T} = {}^{t}J\ {}^{0}_{t}\boldsymbol{X}\ {}^{t}\boldsymbol{\tau} $$

with the Jacobian ${}^{t}J$ and the reverse deformation gradient ${}^{0}_{t}\boldsymbol{X}$.

For the deduction of the tensor the mass conservation principle is assumed. The tensor is used e.g. in measurements of mechanical parameters of a specimen, whereby stresses are referred to the specimen's initial cross section [28].

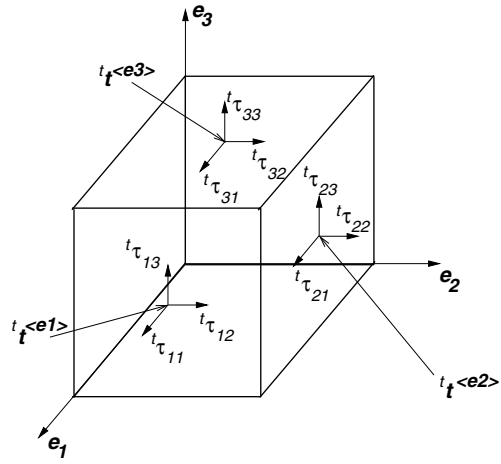

Fig. 4.2. Stresses on faces of cube. The stress vectors ${}^t\boldsymbol{t}^{<e1>}$, ${}^t\boldsymbol{t}^{<e2>}$, and ${}^t\boldsymbol{t}^{<e3>}$ are applied to three faces of an infinitesimal cube with the unit normal vectors $\boldsymbol{e_1}$, $\boldsymbol{e_2}$, and $\boldsymbol{e_3}$. The corresponding components of the Cauchy stress tensor ${}^t\boldsymbol{\tau}$ are indicated on the faces.

Second Piola-Kirchhoff Stress Tensor. The second Piola-Kirchhoff stress tensor ${}^t_0\boldsymbol{S}$ is a symmetric tensor of second order, which refers stresses to the Lagrangian configuration. The stress tensor ${}^t_0\boldsymbol{S}$ is defined by extension of the first Piola-Kirchhoff stress tensor ${}^t_0\boldsymbol{T}$:

$$ {}^t_0\boldsymbol{S} = {}^t_0\boldsymbol{T}\ {}^0_t\boldsymbol{X}^T = {}^tJ\ {}^0_t\boldsymbol{X}\ {}^t\boldsymbol{\tau}\ {}^0_t\boldsymbol{X}^T $$

with the Jacobian ${}^tJ$, the reverse deformation gradient ${}^0_t\boldsymbol{X}$ and the Cauchy stress tensor ${}^t\boldsymbol{\tau}$.

4.2.4 Stress Equilibrium

Equations of Motion. The balance of forces in a moving continuum in the configuration R_t can be described by [27, 28] (Fig. 4.3):

$$ \int_{{}^tV} \rho\, {}^t\boldsymbol{a}\ d\,{}^tV = \int_{{}^tV} {}^t\boldsymbol{f}^{\boldsymbol{B}}\ d\,{}^tV + \int_{{}^tS} {}^t\boldsymbol{t}^{<\boldsymbol{n}>}\ d\,{}^tS $$

with an arbitrary volume ${}^tV$ enclosed by the surface ${}^tS$, the mass density ρ, the acceleration ${}^t\boldsymbol{a}$, the volume force density ${}^tf^B$, and the surface stress vector ${}^t\boldsymbol{t}^{<\boldsymbol{n}>}$. A substitution as described in equation 4.2, i.e. ${}^t\boldsymbol{t}^{<\boldsymbol{n}>} = {}^t\boldsymbol{\tau}\,{}^t\boldsymbol{n}$ with the unit normal ${}^t\boldsymbol{n}$ of surface ${}^tS$, the symmetry of the Cauchy stress tensor ${}^t\boldsymbol{\tau}$, and the application of the divergence theorem of Gauss leads to:

$$ \int_{{}^tV} \rho\, {}^t\boldsymbol{a}\ d\,{}^tV = \int_{{}^tV} {}^t\boldsymbol{f}^{\boldsymbol{B}}\ d\,{}^tV + \int_{{}^tV} div\,{}^t\boldsymbol{\tau}\ d\,{}^tV $$

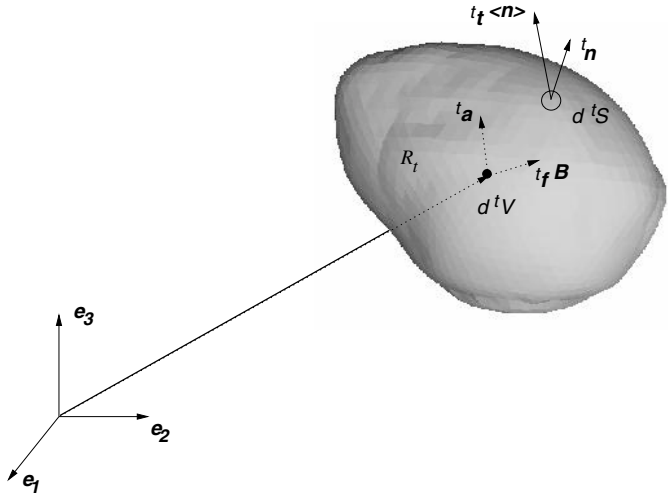

Fig. 4.3. Balance of forces. The equations of motion are determined assuming the balance of forces in a moving continuum in the configuration R_t. Therefore, the surface stress vector $^t\boldsymbol{t}^{<n>}$ at the differential surface element $d\,^tS$ with normal $^t\boldsymbol{n}$ as well as the volume force density $^t\boldsymbol{f}^B$, and the acceleration $^t\boldsymbol{a}$ at the differential volume element $d\,^tV$ are taken into account.

The volume ^tV was assumed to be arbitrary and therefore, the integrands vanish. The resulting system of equations is known as the equations of motion:

$$\rho\,^t\boldsymbol{a} = {}^t\boldsymbol{f}^{\boldsymbol{B}} + div\,^t\boldsymbol{\tau}$$

Principle of Virtual Displacements. Whereas the assumption for the deduction of the equations of motion is the balance of force, the principle of virtual displacements states that the equilibrium of a body is achieved if a small virtual displacement leads to an equality of the total internal virtual work and the total external virtual work [29]. The internal work results from strains and stresses in the medium. The external work is given by forces and displacements at the surface and inside of the medium. The principle of virtual displacements is also known as the principle of virtual work.

In the Eulerian configuration at time t the equilibrium of a body can be expressed using the principle of virtual displacements:

$$\int_{^tV} {}^t\tau_{ij}\,\delta\,{}_te_{ij}\;d\,^tV = {}^tR \tag{4.3}$$

with the volume ^tV, the components of the Cauchy stress tensor $^t\tau_{ij}$, the variation of the strain tensor $\delta_t e_{ij}$, and the external virtual work ^tR. The variation of the strain tensor is defined as

$$\delta\,{}_te_{ij} = \frac{1}{2}\left(\frac{\partial\delta u_i}{\partial^t x_j} + \frac{\partial\delta u_j}{\partial^t x_i}\right)$$

with the components of the virtual displacement vector δu_i. The external virtual work R is subdivided in applied force densities ${}^t f_i^B$ and surface tensions ${}^t f_i^S$:

$$ {}^t R = \int_{{}^t V} {}^t f_i^B \, \delta \, u_i \; d^t V + \int_{{}^t S_f} {}^t f_i^S \, \delta \, u_i^S \; d^t S_f $$

with the surface ${}^t S_f$ and the components of the virtual displacement vector at the surface δu_i^S.

Total Lagrangian Incremental Formulation. The total Lagrangian incremental formulation uses the principle of virtual displacements in conjunction with the second Piola-Kirchhoff stress tensor ${}^{t+\Delta t}_{\ 0}\boldsymbol{S}$ and the Green-Lagrange strain tensor ${}^{t+\Delta t}_{\ 0}\boldsymbol{E}$. Equivalent to equation 4.3, the equilibrium at time $t + \Delta t$ can be defined by [29]:

$$ \int_{{}^0 V} {}^{t+\Delta t}_{\ 0} S_{ij} \, \delta \, {}^{t+\Delta t}_{\ 0} E_{ij} \; d^0 V = {}^{t+\Delta t} R $$

with the external virtual work ${}^{t+\Delta t} R$. The integration is performed over the volume ${}^0 V$ at time $t = 0$, to which all quantities are referred. The external virtual work ${}^{t+\Delta t} R$ is decomposed in applied force densities ${}^{t+\Delta t}_{\ 0} f_i^B$ and surface tensions ${}^{t+\Delta t}_{\ 0} f_i^S$:

$$ {}^{t+\Delta t} R = \int_{{}^0 V} {}^{t+\Delta t}_{\ 0} f_i^B \, \delta \, u_i \; d^0 V + \int_{{}^0 S_f} {}^{t+\Delta t}_{\ 0} f_i^S \, \delta \, u_i^S \; d^0 S_f $$

with the surface ${}^0 S_f$.

Each coefficient of the stress tensor ${}^{t+\Delta t}_{\ 0}\boldsymbol{S}$ is decomposed in a coefficient of the stress tensor ${}^t_0\boldsymbol{S}$ and of the incremental stress tensor ${}_0\boldsymbol{S}$:

$$ {}^{t+\Delta t}_{\ 0} S_{ij} = {}^t_0 S_{ij} + {}_0 S_{ij} $$

Similarly, each coefficient of the strain tensor ${}^{t+\Delta t}_{\ 0}\boldsymbol{E}$ is decomposed in a coefficient of the strain tensor ${}^t_0\boldsymbol{E}$ and of the incremental strain tensor ${}_0\boldsymbol{E}$:

$$ {}^{t+\Delta t}_{\ 0} E_{ij} = {}^t_0 E_{ij} + {}_0 E_{ij} \tag{4.4} $$

Furthermore, each coefficient of the incremental strain tensor ${}_0\boldsymbol{E}$ is decomposed in a linear component ${}_0 e_{ij}$ and a nonlinear component ${}_0 \eta_{ij}$:

$$ {}_0 E_{ij} = {}_0 e_{ij} + {}_0 \eta_{ij} \tag{4.5} $$

These components are defined corresponding to the Green-Lagrange strain tensor:

$$ {}_0 e_{ij} = \frac{1}{2} ({}_0 u_{i,j} + {}_0 u_{j,i} + {}^t_0 u_{k,i} \, {}_0 u_{k,j} + {}_0 u_{k,i} \, {}^t_0 u_{k,j}) $$

$$ {}_0 \eta_{ij} = \frac{1}{2} ({}_0 u_{k,i} \, {}_0 u_{k,j}) $$

whereby the subindex of the coefficients of the incremental displacement vector ${}_0\boldsymbol{u}$ and displacement vector ${}^t_0\boldsymbol{u}$ following the comma denotes the differentiation with respect to the reference configuration coordinates ${}^0\boldsymbol{x}$.

Using the decompositions a nonlinear equation of motion with incremental decompositions is derived:

$$\int_{{}_0V} {}_0S_{ij}\,\delta\,{}_0E_{ij}\;d^0V + \int_{{}_0V} {}^t_0S_{ij}\,\delta\,{}_0\eta_{ij}\;d^0V = {}^{t+\Delta t}R - \int_{{}_0V} {}^t_0S_{ij}\,\delta\,{}_0e_{ij}\;d^0V$$

whereby the right hand side of the equation includes only components with known values at time t. The unknown parameters are found on the left hand side of the equation. The linearized equation of motion is obtained by using the approximations ${}_0C_{ijkl}\;{}_0e_{rs} = {}_0S_{ij}$ and $\delta\,{}_0e_{ij} = \delta\,{}_0E_{ij}$:

$$\int_{{}_0V} {}_0C_{ijkl}\;{}_0e_{rs}\,\delta\,{}_0e_{ij}\;d^0V + \int_{{}_0V} {}^t_0S_{ij}\,\delta\,{}_0\eta_{ij}\;d^0V = {}^{t+\Delta t}R - \int_{{}_0V} {}^t_0S_{ij}\,\delta\,{}_0e_{ij}\;d^0V$$

whereby the incremental stress-strain tensor ${}_0\boldsymbol{C}$ is dependent on the stress-strain relationship of the material:

$${}_0C_{ijkl} = \frac{\partial\,{}^t_0S_{ij}}{\partial\,{}^t_0\epsilon_{rs}}$$

4.2.5 Constitutive Relationships

Elasticity and Viscoelasticity. The theory of elasticity assumes that the relationship between stress and strain in a material is local and history independent [28]. Depending on the relationship a distinction between

- linear elastic
- nonlinear elastic

materials is made. Import representatives of nonlinear elastic materials are:

- hyperelastic
- hypoelastic

If strains are small nearly all materials can be sufficiently described with linear and nonlinear elasticity. Large deformations in rubber-like and concrete materials are commonly analyzed assuming hyper- and hypoelasticity.

An extension of the theory of elasticity results from the observation that materials can also show history dependent behavior [30]. Materials exhibiting this behavior are said to be viscoelastic.

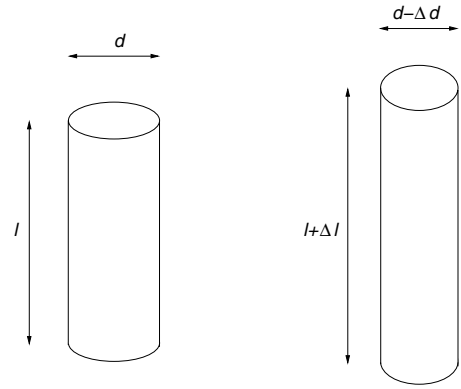

Fig. 4.4. Hooke's law. A bar with initial length l is strained to the length $l + \Delta l$ resulting from applied stresses. The initial bar's diameter d changes to the diameter $d - \Delta d$. The relationship between stress and strain is described by Hooke's law.

Linear Elasticity

Hooke's Law and Material Constants. According to Hooke's law the linear relationship between a strain ϵ and a stress τ in a bar is defined by [31]:

$$\tau = \frac{1}{E}\epsilon$$

with the elasticity modulus or Young's modulus E. The strain ϵ is a one-dimensional equivalent to the second order linear tensor ${}^{t}_{0}\boldsymbol{\epsilon}$ and describes the ratio between the change of the bar's length Δl and the initial length l (Fig. 4.4):

$$\epsilon = \frac{\Delta l}{l}$$

The stress τ is a one-dimensional equivalent to the Cauchy stress tensor ${}^{t}\boldsymbol{\tau}$ and describes the force F per surface A:

$$\tau = \frac{F}{A}$$

The change of the bar's diameter Δd resulting from the strain is quantified with Poisson's ratio ν by:

$$\nu = \frac{-\Delta d}{d}\frac{l}{\Delta l}$$

with the bar's length l and the bar's diameter d (Fig. 4.4).

The bulk modulus κ describes the volume change resulting from a pressure p:

$$\frac{\Delta V}{V} = -\frac{1}{\kappa}p$$

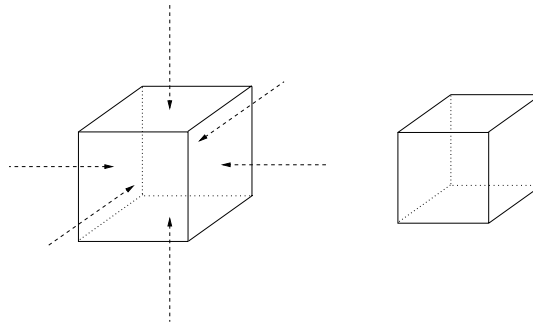

Fig. 4.5. Bulk modulus. The left cube is deformed by pressure indicated by dashed arrows. The volume change resulting from the deformation depends on the bulk modulus κ.

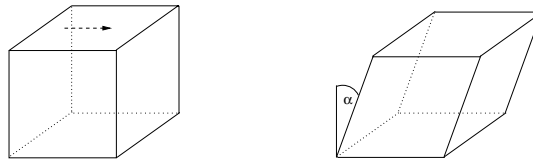

Fig. 4.6. Shear modulus. The left cube is deformed by forces indicated by the dashed arrows. The angle α resulting from the deformation depends on the shear modulus G.

The bulk modulus can be determined with the elasticity modulus E and the Poisson's ratio ν under the assumption that the pressure p acts in different directions in the same manner (Fig. 4.5), i.e. leading to same volume reduction:

$$\kappa = \frac{1}{3}\frac{E}{1-2\nu}$$

The shear modulus G couples the shear tension τ with the angle α of a plane perpendicular to the applied forces (Fig. 4.6):

$$\tau = G\alpha$$

The shear modulus G is determined with the elasticity modulus E and the Poisson's ratio ν as follows:

$$G = \frac{E}{2(1+\nu)}$$

Hooke's Law in three-dimensional space. A generalization of Hooke's law delivers the relationship between the Cauchy stress tensor ${}^t\boldsymbol{\tau}$ and the linear strain tensor ${}^t_0\boldsymbol{\epsilon}$:

$${}^t\tau_{ij} = C_{ijkl}\ {}^t_0\epsilon_{kl} \tag{4.6}$$

with the fourth order elasticity tensor $\boldsymbol{C}$. The elasticity tensor is also known as material tensor and comprises 81 coefficients. Regarding of symmetries allows the reduction of the number of independent coefficients of the elastic tensor to 36. The equation 4.6 can be rewritten in a simplified representation:

$$ {}^{t}\boldsymbol{\tau}_i = C_{ij}\, {}^{t}_{0}\boldsymbol{\epsilon}_j $$

with the Cauchy stress vector ${}^{t}\boldsymbol{\tau}$, the linear strain vector ${}^{t}_{0}\boldsymbol{\epsilon}$ and the elasticity matrix $\boldsymbol{C}$. The Cauchy stress vector ${}^{t}\boldsymbol{\tau}$ is derived from the Cauchy stress tensor ${}^{t}\boldsymbol{\tau}$ by:

$$ {}^{t}\boldsymbol{\tau} = \left({}^{t}\tau_{11}\ {}^{t}\tau_{22}\ {}^{t}\tau_{33}\ {}^{t}\tau_{12}\ {}^{t}\tau_{13}\ {}^{t}\tau_{23} \right) $$

The linear strain vector ${}^{t}_{0}\boldsymbol{\epsilon}$ is transformed from the linear strain tensor ${}^{t}_{0}\boldsymbol{\epsilon}$ by:

$$ {}^{t}\boldsymbol{\epsilon} = \left({}^{t}\epsilon_{11}\ {}^{t}\epsilon_{22}\ {}^{t}\epsilon_{33}\ 2\,{}^{t}\epsilon_{12}\ 2\,{}^{t}\epsilon_{13}\ 2\,{}^{t}\epsilon_{23} \right) $$

In case of isotropic media the elasticity matrix $\boldsymbol{C}$ is symmetric and of following shape:

$$ \boldsymbol{C} = \frac{E}{(\nu+1)(1-2\nu)} \begin{pmatrix} 1-\nu & \nu & \nu & 0 & 0 & 0 \\ \nu & 1-\nu & \nu & 0 & 0 & 0 \\ \nu & \nu & 1-\nu & 0 & 0 & 0 \\ 0 & 0 & 0 & \frac{1}{2}(1-2\nu) & 0 & 0 \\ 0 & 0 & 0 & 0 & \frac{1}{2}(1-2\nu) & 0 \\ 0 & 0 & 0 & 0 & 0 & \frac{1}{2}(1-2\nu) \end{pmatrix} $$

depending on the elasticity modulus E and the Poisson's ratio ν.

Alternatively, the elasticity matrix $\boldsymbol{C}$ can be expressed with Lamé constants λ and μ:

$$ \boldsymbol{C} = \begin{pmatrix} \lambda+2\mu & \lambda & \lambda & 0 & 0 & 0 \\ \lambda & \lambda+2\mu & \lambda & 0 & 0 & 0 \\ \lambda & \lambda & \lambda+2\mu & 0 & 0 & 0 \\ 0 & 0 & 0 & \mu & 0 & 0 \\ 0 & 0 & 0 & 0 & \mu & 0 \\ 0 & 0 & 0 & 0 & 0 & \mu \end{pmatrix} $$

The Lamé constants can be derived from the elasticity modulus E and the Poisson's ratio ν:

$$ \lambda = \frac{\nu E}{(1+\nu)(1-2\nu)} $$
$$ \mu = \frac{E}{2(1+\nu)} $$

Generalized Hooke's Law for Large Deformations. A further generalization of Hooke's law is used to describe the stress-strain relationship of large deformations. The second Piola-Kirchhoff stress tensor ${}^t_0\boldsymbol{S}$ is calculated with the material tensor $\boldsymbol{C}$ and the Green-Lagrange strain tensor ${}^t_0\boldsymbol{E}$:

$$ {}^t_0S_{ij} = C_{ijkl}\, {}^t_0E_{kl} $$

Alternatively, the stress-strain relationship for large deformations can be established with the deformation gradient ${}^t_0\boldsymbol{X}$ and the Cauchy-Green right dilation tensor ${}^t_0\boldsymbol{C}$.

Nonlinear Elasticity. Whereas the material tensor $\boldsymbol{C}$ is constant in linear elasticity, the tensor is a function of strain in nonlinear elasticity:

$$ \boldsymbol{C} = \boldsymbol{C}({}^t_0\epsilon) $$

The applied strain tensor depends on the type of deformation. E.g. for small displacements and displacement gradients commonly the linear strain tensor ${}^t_0\boldsymbol{\epsilon}$ is used. For large deformations the Cauchy-Green right dilation tensor ${}^t_0\boldsymbol{C}$ and the Green-Lagrange strain tensor ${}^t_0\boldsymbol{E}$ is applied.

Hyperelasticity. If the second Piola-Kirchhoff stress tensor ${}^t_0\boldsymbol{S}$ in a medium can be determined by derivation from a scalar strain energy density function ${}^t_0W$, the medium is said to be hyperelastic [29]:

$$ {}^t_0S_{ij} = \frac{\partial\, {}^t_0W\left({}^t_0\boldsymbol{E}\right)}{\partial\, {}^t_0E_{ij}} $$

In this definition the strain energy density W is a function of the Green-Lagrange strain tensor ${}^t_0\boldsymbol{E}$. Other descriptions of strain, e.g. the Cauchy-Green right dilation tensor ${}^t_0\boldsymbol{C}$, are also used as parameters for strain energy density functions.

Mooney-Rivlin Model. A representative of hyperelastic models is the Mooney-Rivlin model, whereby the strain energy density function is defined by:

$$ {}^t_0W = C_1({}^t_0I_1 - 3) + C_2({}^t_0I_2 - 3) $$

with the material specific constants $C1$ and $C2$, as well as the invariants of the Cauchy-Green right dilation tensor ${}^t_0I_1$ and ${}^t_0I_2$. Furthermore, incompressibility of the medium is assumed by including the condition ${}^t_0I_3 = 1$ (Sect. 4.2.1).

A variant of the Mooney-Rivlin model reduces the condition of total incompressibility and includes the reduced condition into the definition of the strain energy function [29]:

$$ {}^t_0W = C_1({}^t_0\overline{I}_1 - 3) + C_2({}^t_0\overline{I}_2 - 3) + \frac{1}{2}\kappa({}^t_0\overline{I}_3 - 1)^2 $$

with the bulk modulus κ and the reduced invariants:

$$
\begin{aligned}
{}^t_0\overline{I}_1 &= {}^t_0I_1({}^t_0\overline{I}_3)^{-1/3} \\
{}^t_0\overline{I}_2 &= {}^t_0I_2({}^t_0\overline{I}_3)^{-2/3} \\
{}^t_0\overline{I}_3 &= ({}^t_0\overline{I}_3)^{1/2}
\end{aligned}
$$

The Mooney-Rivlin model was developed to reconstruct the mechanical behavior of rubber-like materials. Further representatives of hyperelastic models specifically for the description of cardiac tissue are listed in Sect. 8.2.2.

Hypoelasticity. If the stress increments $d\boldsymbol{\tau}$ are determined by the strain increments $d\,{}^t_0\boldsymbol{\epsilon}$, the medium is said to be hypoelastic [29]:

$$d\tau_{ij} = C_{ijkl}\; d\,{}^t_0\epsilon_{kl}$$

Commonly, the material tensor $\boldsymbol{C}$ is nonlinearly dependent on the strain, stress or other parameters. Hypoelastic material models are used to reproduce the mechanical behavior of concrete and metals.

Viscoelasticity. If the description of the stress-strain relationship includes derivatives with respect to time, a medium is said to be viscoelastic. Linear viscoelasticity results in the following stress-strain relationship:

$$\left(\boldsymbol{A}_0 + \boldsymbol{A}_1\frac{\partial}{\partial t} + \boldsymbol{A}_2\frac{\partial}{\partial t} + \dots\right){}^t\boldsymbol{\tau} = \left(\boldsymbol{B}_0 + \boldsymbol{B}_1\frac{\partial}{\partial t} + \boldsymbol{B}_2\frac{\partial}{\partial t} + \dots\right){}^t_0\boldsymbol{\epsilon}$$

with the parameter matrices $\boldsymbol{A}_i$ and $\boldsymbol{B}_i$.

Viscoelastic behavior leads to phenomena like [30]:

- Stress relaxation. A body is suddenly strained and afterwards the strain is sustained. The resulting stress decreases over time.
- Creep. A body is suddenly stressed and afterwards the stress sustained. The resulting deformation is a time dependent process.
- Hysteresis. Cyclic stress of a body leads to differences in the stress-strain relationship for loading and unloading phases.

4.3 Numerical Solution

4.3.1 Principle

The finite element method is the primary numerical technique to discretize equations resulting from the principle of virtual displacements. The principle allows the analysis of large displacements, strains and rotations with nonlinear, anisotropic material properties.

The finite element method necessitates a subdivision of the spatial domain Ω in finite elements (Sect. 2.7.3). In each element's domain $\Omega^{(m)}$ the solution as well as stress and strain functions are interpolated starting from node

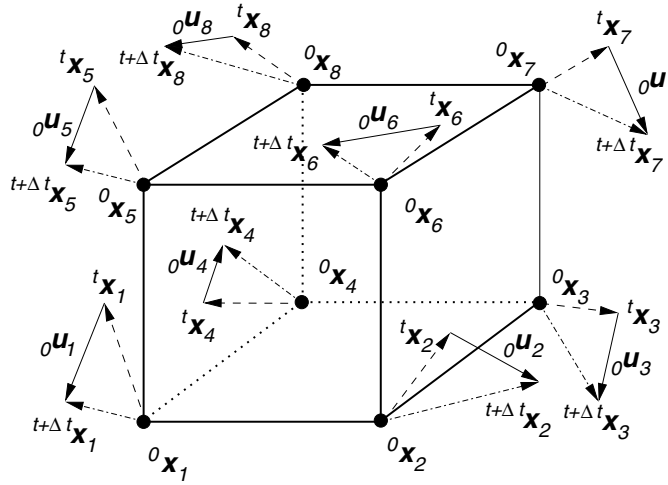

Fig. 4.7. Deformation and incremental displacements in hexahedron. The coordinates of node points ${}^0\boldsymbol{x}_i$ in the Lagrangian configuration are changed to the coordinates ${}^t\boldsymbol{x}_i$ at time t. The incremental displacement ${}_0\boldsymbol{u}_i$ leads to the coordinates ${}^{t+\Delta t}\boldsymbol{x}_i$ at time $t + \Delta t$.

points. For each element an equations system can be created, wherefore in this work primarily the total Lagrangian formulation (Sect. 4.2.4) in conjunction with hyperelastic description of materials (Sect. 4.2.5) is applied. The creation of the equations system is performed applying the displacement function ${}^t\boldsymbol{u}$ at time t. The solution function ${}^{t+\Delta t}\boldsymbol{u}$ describes displacements at time $t+\Delta t$. The evaluation of integral equations delivers element- and time-step-wise systems of linear equations. These equations are assembled into the system equations, which are modified by boundary conditions. The system of equations is solved with iterative techniques (Sect. 2.4.3). The solving is repeatedly performed, both, to determine displacements at different times, e.g. with distance Δt, and to cope the nonlinearity of material and geometry.

4.3.2 Interpolation via Shape-Functions

Interpolation of Displacement Functions. An interpolation of the displacement function ${}^t\boldsymbol{u}$ starting from node variables can be performed via shape-functions, which are selected dependent on the element's geometry and the order of interpolation. In the following – similar to the sections introducing the finite element method (Sect. 2.7.3) and its application in electromagnetism (Sect. 3.3.1) – the shape-functions are arranged to the vector $\boldsymbol{H}^{(m)}$, whereby the superscript m indicates the element.

In other works, displacement- and strain-interpolation matrices are alternatively created for the interpolation [29]. The shape-functions are components of a matrix.

In the three-dimensional domain $\Omega^{(m)}$ of the m-th element the displacement function ${}^t\boldsymbol{u}$ is given at any time t by:

$$ {}^t\boldsymbol{u} = \begin{pmatrix} {}^tu_1 \\ {}^tu_2 \\ {}^tu_3 \end{pmatrix} = \boldsymbol{H}^{(m)\,T}\, {}^t\boldsymbol{U}^{(m)} $$

with the N-dimensional vector of displacement vectors at node variables ${}^t\boldsymbol{U}^{(m)}$:

$$ {}^t\boldsymbol{U}^{(m)} = \begin{pmatrix} \boldsymbol{U}_1^{(m)} \\ \vdots \\ \boldsymbol{U}_N^{(m)} \end{pmatrix} = \begin{pmatrix} \begin{pmatrix} U_{1,1}^{(m)} \\ U_{1,2}^{(m)} \\ U_{1,3}^{(m)} \end{pmatrix} \\ \vdots \\ \begin{pmatrix} U_{N1}^{(m)} \\ U_{N2}^{(m)} \\ U_{N3}^{(m)} \end{pmatrix} \end{pmatrix} $$

and the N-dimensional vector of shape-functions $\boldsymbol{H}^{(m)}$:

$$ \boldsymbol{H}^{(m)} = \begin{pmatrix} H_1^{(m)} \\ \vdots \\ H_N^{(m)} \end{pmatrix} $$

The function of incremental displacements ${}_0\boldsymbol{u}$ is interpolated by:

$$ {}_0\boldsymbol{u} = \boldsymbol{H}^{(m)\,T}\, {}_0\boldsymbol{U}^{(m)} $$

with the vector of incremental displacements at node variables ${}_0\boldsymbol{U}^{(m)}$.

The shape-functions allow furthermore the interpolation of coordinates of points ${}^t\boldsymbol{x}$ and temporal derivatives of displacements, e.g. velocity and acceleration. Additionally force densities and surface tensions can be interpolated.

Interpolation of Deformation Gradient. Similarly, an interpolation is applied for the deformation gradient and variant strain tensors starting from node variables. Therefore, specific derivatives of the shape-functions are developed. The deformation gradient ${}^t_0\boldsymbol{X}$ (Sect. 4.2.1) is interpolated in the domain $\Omega^{(m)}$ by:

$$ {}^t_0\boldsymbol{X} = \nabla \boldsymbol{H}^{(m)\,T}\, {}^t\boldsymbol{U}^{(m)} + \boldsymbol{I} $$

with the identity matrix $\boldsymbol{I}$ and the gradient of the shape-function's vector $\nabla \boldsymbol{H}^{(m)}$:

$$\nabla \boldsymbol{H}^{(m)} = \begin{pmatrix} \nabla H_1^{(m)} \\ \vdots \\ \nabla H_N^{(m)} \end{pmatrix} = \begin{pmatrix} \begin{pmatrix} \frac{\partial H_1^{(m)}}{\partial {}^0x_1} \\ \frac{\partial H_1^{(m)}}{\partial {}^0x_2} \\ \frac{\partial H_1^{(m)}}{\partial {}^0x_3} \end{pmatrix} \\ \vdots \\ \begin{pmatrix} \frac{\partial H_N^{(m)}}{\partial {}^0x_1} \\ \frac{\partial H_N^{(m)}}{\partial {}^0x_2} \\ \frac{\partial H_N^{(m)}}{\partial {}^0x_3} \end{pmatrix} \end{pmatrix}$$

Interpolation of Green-Lagrange Strain Tensor. The Green-Lagrange strain tensor ${}^t_0\boldsymbol{E}$ is determined with the definition of the deformation gradient ${}^t_0\boldsymbol{X}^{(m)}$:

$$\begin{aligned} {}^t_0\boldsymbol{E} &= \frac{1}{2}\left({}^t_0\boldsymbol{X}^2 - \boldsymbol{I}\right) \\ &= \frac{1}{2}\left(\left(\nabla \boldsymbol{H}^{(m)\,T}\,{}^t\boldsymbol{U}^{(m)} + \boldsymbol{I}\right)^2 - \boldsymbol{I}\right) \\ &= \frac{1}{2}\left(\left(\nabla \boldsymbol{H}^{(m)\,T}\,{}^t\boldsymbol{U}^{(m)}\right)^2 + \left(\nabla \boldsymbol{H}^{(m)\,T}\,{}^t\boldsymbol{U}^{(m)}\right)^T + \nabla \boldsymbol{H}^{(m)\,T}\,{}^t\boldsymbol{U}^{(m)}\right) \end{aligned}$$

The decomposition of Green-Lagrange strain tensor ${}^{t+\Delta t}_0\boldsymbol{E}$ at time $t+\Delta t$ into the Green-Lagrange strain tensor ${}^t_0\boldsymbol{E}$ at time t as well as a linear part ${}_0\boldsymbol{e}$ and a nonlinear part ${}_0\boldsymbol{\eta}$ of the incremental Green-Lagrange strain tensor ${}_0\boldsymbol{E}$ (equations 4.4 and 4.5):

$${}^{t+\Delta t}_0\boldsymbol{E} = {}^t_0\boldsymbol{E} + {}_0\boldsymbol{E} = {}^t_0\boldsymbol{E} + {}_0\boldsymbol{e} + {}_0\boldsymbol{\eta} \tag{4.7}$$

can be expressed via shape-functions by:

$$\begin{aligned} {}^{t+\Delta t}_0\boldsymbol{E} &= \frac{1}{2}\left({}^{t+\Delta t}_0\boldsymbol{X}^2 - \boldsymbol{I}\right) \\ &= \frac{1}{2}\left(\left(\nabla \boldsymbol{H}^{(m)\,T}\left({}^t\boldsymbol{U}^{(m)} + {}_0\boldsymbol{U}^{(m)}\right) + \boldsymbol{I}\right)^2 - \boldsymbol{I}\right) \\ &= \frac{1}{2}\left(\left(\nabla \boldsymbol{H}^{(m)\,T}\,{}^t\boldsymbol{U}^{(m)}\right)^2 + \left(\nabla \boldsymbol{H}^{(m)\,T}\,{}^t\boldsymbol{U}^{(m)}\right)^T + \nabla \boldsymbol{H}^{(m)\,T}\,{}^t\boldsymbol{U}^{(m)}\right. \\ &\quad + \left(\nabla \boldsymbol{H}^{(m)\,T}\,{}^t\boldsymbol{U}^{(m)}\right)^T\left(\nabla \boldsymbol{H}^{(m)\,T}\,{}_0\boldsymbol{U}^{(m)}\right) + \left(\nabla \boldsymbol{H}^{(m)\,T}\,{}_0\boldsymbol{U}^{(m)}\right)^T \\ &\quad \left. + \left(\nabla \boldsymbol{H}^{(m)\,T}\,{}_0\boldsymbol{U}^{(m)}\right)^T\left(\nabla \boldsymbol{H}^{(m)\,T}\,{}^t\boldsymbol{U}^{(m)}\right) + \nabla \boldsymbol{H}^{(m)\,T}\,{}_0\boldsymbol{U}^{(m)}\right. \end{aligned}$$

$$+ \left(\nabla \boldsymbol{H}^{(m)\,T}\ {}_0\boldsymbol{U}^{(m)} \right)^2 \Bigg)$$

Comparison with equation 4.7 leads to the definition of the linear part ${}_0\boldsymbol{e}$:

$$\begin{aligned} {}_0\boldsymbol{e} = \frac{1}{2} \Bigg(& \left(\nabla \boldsymbol{H}^{(m)\,T}\ {}^t\boldsymbol{U}^{(m)} \right)^T \left(\nabla \boldsymbol{H}^{(m)\,T}\ {}_0\boldsymbol{U}^{(m)} \right) + \left(\nabla \boldsymbol{H}^{(m)\,T}\ {}_0\boldsymbol{U}^{(m)} \right)^T \\ & + \left(\nabla \boldsymbol{H}^{(m)\,T}\ {}_0\boldsymbol{U}^{(m)} \right)^T \left(\nabla \boldsymbol{H}^{(m)\,T}\ {}^t\boldsymbol{U}^{(m)} \right) + \nabla \boldsymbol{H}^{(m)\,T}\ {}_0\boldsymbol{U}^{(m)} \Bigg) \end{aligned} \tag{4.8}$$

and the nonlinear part ${}_0\boldsymbol{\eta}$ of the incremental Green-Lagrange strain tensor ${}_0\boldsymbol{E}$:

$${}_0\boldsymbol{\eta} = \frac{1}{2} \left(\nabla \boldsymbol{H}^{(m)\,T}\ {}_0\boldsymbol{U}^{(m)} \right)^2 \tag{4.9}$$

Interpolation of Stress Tensors. Stress tensors can be interpolated with the vector of shape-functions $\boldsymbol{H}^{(m)}$ starting from stress tensors at node variables. In other cases stress tensors are described by a function of strain and can therefore be determined after interpolation of the strain.

4.3.3 Determination of Element Equations

The section focuses on the discretization of the total Lagrangian incremental formulation with hyperelastic materials (Sect. 4.2.5). Hence, the equilibrium at any time is given by [29]:

$$\begin{aligned} & \int_{{}_0V} {}_0C_{ijkl}\ {}_0e_{rs}\,\delta\,{}_0e_{ij}\ d^0V + \int_{{}_0V} {}^t_0S_{ij}\,\delta\,{}_0\eta_{ij}\ d^0V \\ & = \int_{{}_0V} {}^{t+\Delta t}_0 f_i^B\,\delta\,u_i\ d^0V + \int_{{}_0S_f} {}^{t+\Delta t}_0 f_i^S\,\delta\,u_i^S\ d^0S_f - \int_{{}_0V} {}^t_0S_{ij}\,\delta\,{}_0e_{ij}\ d^0V \end{aligned} \tag{4.10}$$

with the incremental stress-strain tensor ${}_0\boldsymbol{C}$, a linear part ${}_0\boldsymbol{e}$ and a nonlinear part ${}_0\boldsymbol{\eta}$ of the incremental Green-Lagrange strain tensor ${}_0\boldsymbol{E}$, the second Piola-Kirchhoff stress tensor ${}^t_0\boldsymbol{S}$, the applied force density ${}^{t+\Delta t}_0 f_i^B$ and the surface tension ${}^{t+\Delta t}_0 f_i^S$. The incremental stress-strain tensor ${}_0\boldsymbol{C}$ is of fourth order. The strain and stress tensors are of second order.

System of Equations for Static Analysis. The equation 4.10 can be used to describe the displacements ${}^{t+\Delta t}\boldsymbol{U}$ at time $t + \Delta t$ with given displacements ${}^t\boldsymbol{U}$ for time t. Therefore, an iterative procedure is applied (Fig. 4.8), which is necessary to incorporate nonlinear phenomena. The phenomena result from material properties, which can vary with strain or stress.

In each step a system of linear equations is constructed and solved whereby the unknowns describe incremental displacements ${}_0\boldsymbol{U}^{(i)}$. The system of linear equations is created by the substitution of the strain tensors with the

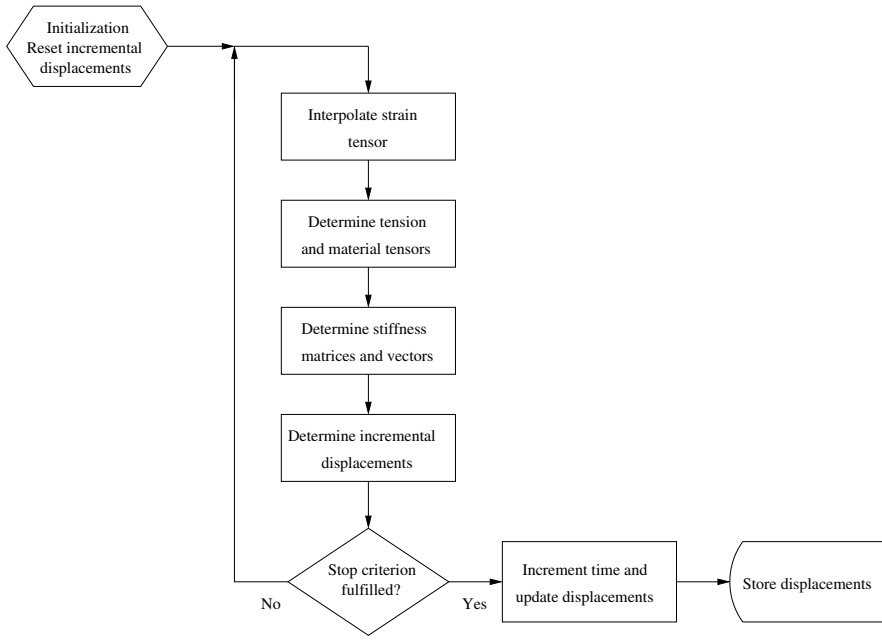

Fig. 4.8. Calculation scheme of total Lagrangian incremental formulation. Incremental displacements are determined starting from initial displacements. The incremental displacements are determined iteratively and serve finally to update the initial displacements. In each step the incremental displacements are the unknowns of a system of linear equations, which is built up by different stiffness matrices and vectors. The matrices and vectors are a function of strain, stress and material tensors.

interpolation starting from node points and the knowledge of the incremental stress-strain tensor ${}_0\boldsymbol{C}$:

$$({}^t_0\boldsymbol{K}_L^{(i)} + {}^t_0\boldsymbol{K}_{NL}^{(i)})\,{}_0\boldsymbol{U}^{(i)} = {}^{t+\Delta t}_0\boldsymbol{R} + {}^t_0\boldsymbol{F}^{(i)} \tag{4.11}$$

with the vector of forces at node points ${}^t_0\boldsymbol{F}^{(i)}$, the unknown incremental displacements ${}_0\boldsymbol{U}^{(i)}$ and the external virtual work ${}^{t+\Delta t}_0\boldsymbol{R}$ as well as the linear incremental stiffness matrix ${}^t_0\boldsymbol{K}_L^{(i)}$ and the nonlinear incremental stiffness matrix ${}^t_0\boldsymbol{K}_{NL}^{(i)}$. The superscript (i) of same quantities denotes the iteration step. The iteration can be stopped, if some norm of the residuum of equation 4.11 becomes smaller than a given threshold.

Determination of Matrices and Vectors. The determination of the matrices and vectors resulting from the total Lagrangian incremental formulation is generally performed with numerical techniques (Sect. 2.5). A frequently used technique is the Gauss quadrature.

The linear incremental stiffness matrix ${}^{t}_{0}\boldsymbol{K}^{(i)}_{L}$ is given by:

$$ {}^{t}_{0}\boldsymbol{K}^{(i)}_{L} = \int_{{}_0V} {}^{t}_{0}\boldsymbol{B}^{T}_{L}\, {}_0\boldsymbol{C}^{(i)}\, {}^{t}_{0}\boldsymbol{B}_{L}\; d\,{}^0V $$

whereby the differential operator ${}^{t}_{0}\boldsymbol{B}_{L}$ is determined with equation 4.8. The incremental stress-strain tensor ${}_0\boldsymbol{C}^{(i)}$ is assumed to be a function of the strain and stress, but can also result from a description of the material properties with generalized Hooke's law for large deformations. The incremental stress-strain tensor ${}_0\boldsymbol{C}^{(i)}$ can be derived from the second Piola-Kirchhoff stress tensor ${}^{t}_{0}\boldsymbol{S}^{(i)}$:

$$ {}_0C^{(i)}_{ijkl} = \frac{\partial\, {}^{t}_{0}S^{(i)}_{ij}}{\partial\, {}^{t}_{0}E_{kl}} $$

whereby the superscript of the tensor ${}_0\boldsymbol{C}^{(i)}$ denotes the i-th step of the incremental procedure and the subscript refers to indices of the tensor. In case of hyperelastic materials the tensor ${}_0\boldsymbol{C}$ can be determined directly from the strain energy density W:

$$ {}_0C^{(i)}_{ijkl} = \frac{\partial^2\, W}{\partial\, {}^{t}_{0}E_{ij}\;\partial\, {}^{t}_{0}E_{kl}} $$

The linear operator ${}^{t}_{0}\boldsymbol{B}_{L}$ allows the determination of the linear part ${}_0\boldsymbol{e}$ of the incremental Green-Lagrange strain tensor ${}_0\boldsymbol{E}$ starting from the vector of incremental displacements at node variables ${}_0\boldsymbol{U}^{(m)}$:

$$ {}_0\boldsymbol{e} = {}^{t}_{0}\boldsymbol{B}_{L}\; {}_0\boldsymbol{U}^{(m)} $$

The nonlinear incremental stiffness matrix ${}^{t}_{0}\boldsymbol{K}_{NL}$ results from:

$$ {}^{t}_{0}\boldsymbol{K}_{NL} = \int_{{}_0V} {}^{t}_{0}\boldsymbol{B}^{T}_{NL}\, {}^{t}_{0}\boldsymbol{S}^{(i)}\, {}^{t}_{0}\boldsymbol{B}_{NL}\; d\,{}^0V $$

whereby the differential operator ${}^{t}_{0}\boldsymbol{B}_{NL}$ is determined with equation 4.9. This nonlinear operator describes the relationship:

$$ {}_0\boldsymbol{\eta} = \left({}^{t}_{0}\boldsymbol{B}_{NL}\; {}_0\boldsymbol{U}^{(m)} \right)^2 $$

The vector of external virtual work ${}^{t+\Delta t}\boldsymbol{R}$ at time $t+\Delta t$ is constructed starting from the vector of applied force densities ${}^{t+\Delta t}_{0}\boldsymbol{f}^{B}_{i}$ and of surface tensions ${}^{t+\Delta t}_{0}\boldsymbol{f}^{S}_{i}$ at node points:

$$ {}^{t+\Delta t}_{0}\boldsymbol{R} = \int_{{}_0V} \boldsymbol{H}^{T}\; {}^{t+\Delta t}_{0}\boldsymbol{f}^{B}_{i}\; d\,{}^0V + \int_{{}_0S_f} \boldsymbol{H}^{T}_{S}\; {}^{t+\Delta t}_{0}\boldsymbol{f}^{S}_{i}\; d\,{}^0S_f $$

with the volume shape-function $\boldsymbol{H}$ and the surface shape-function $\boldsymbol{H}_S$ as well as the surface ${}^0S_f$.

The vector of forces at node points ${}^{t}_{0}\boldsymbol{F}^{(i)}$ is obtained by evaluating:

$$ {}^{t}_{0}\boldsymbol{F}^{(i)} = \int_{{}_0V} {}^{t}_{0}\boldsymbol{B}^{T}_{L}\, {}^{t}_{0}\boldsymbol{S}^{(i)}\; d\,{}^0V $$

System of Equations for Dynamic Analysis. The inclusion of inertia can be achieved by extending of equation 4.11:

$$\boldsymbol{M}\,{}^{t}\boldsymbol{a} + ({}^{t}_{0}\boldsymbol{K}^{(i)}_{L} + {}^{t}_{0}\boldsymbol{K}^{(i)}_{NL})\,{}_{0}\boldsymbol{U} = {}^{t+\Delta t}_{0}\boldsymbol{R} + {}^{t}_{0}\boldsymbol{F}^{(i)}$$

with the vector of acceleration ${}^{t}\boldsymbol{a}$ and the mass matrix $\boldsymbol{M}$ given by:

$$\boldsymbol{M} = \int_{{}_{0}V} {}^{0}\rho\ \boldsymbol{H}^{T}\boldsymbol{H}\ d\,{}^{0}V$$

Here, the mass density ${}^{0}\rho$ and mass matrix $\boldsymbol{M}$ are assumed to be constant over time.

5

Digital Image Processing

5.1 Overview

Digital image processing is applied to extract and measure features and structures in images. Different stages of processing can be distinguished (Fig. 5.1). The image data is transformed in each processing step.

The first steps, imaging, sampling and quantization, lead to digital images [32]. The imaging is commonly performed with physical devices transforming a band of the electromagnetic spectrum into an imaging function, which is then digitized spatially and concerning its amplitude. The spatial digitization is frequently called sampling. The digitization of the amplitude is referred to as quantization.

Subsequently, the digital images are commonly preprocessed to enhance the image quality for further processing. The images are segmented, which means subdivided into enclosed components. These components are assigned to classes by the classification step. All of these stages require the extraction of features in the images. The results of the digital image processing are interpreted, whereby a meaning is attributed to image components.

Different levels of processing can be associated with the digital image processing. Low-level processing involves automatic methods, which can be applied without knowledge concerning the image content. Imaging, sampling, quantization and preprocessing are low-level processing steps. Intermediate-level processing, i.e. segmentation and feature extraction, requires some background knowledge of the image content. High-level processing like classification and interpretation is strongly dependent on the availability of detailed knowledge.

In the context of modeling cardiac anatomy, physiology and mechanics digital image processing is frequently applied in conjunction with medical imaging systems, e.g. ultrasonic (US), magnetic resonance (MRT), and X-ray computed tomography (CT). Furthermore, photographic imaging systems are utilized. A photographic system is applied e.g. in the Visible Human Project of

F.B. Sachse: LNCS 2966, pp. 91–118, 2004.

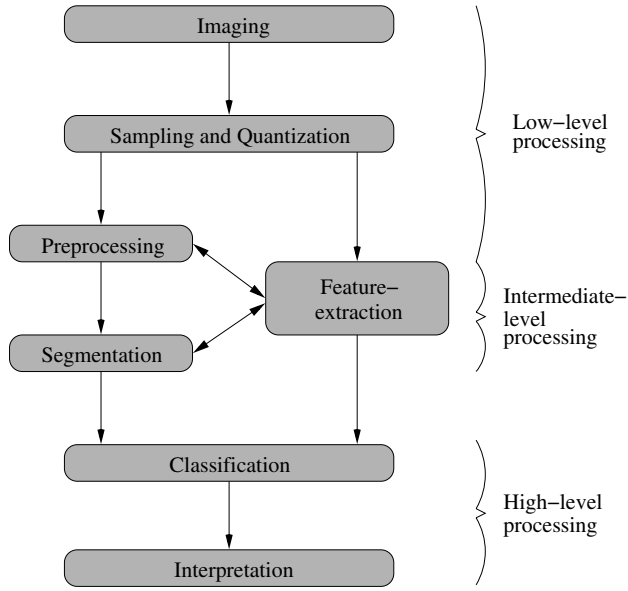

Fig. 5.1. Structure of digital image processing. Starting with imaging, sampling and quantization the image data passes through the preprocessing, segmentation and classification steps. The feature extraction is their common element. The data is finally interpreted e.g. by a human observer. Results of all steps can be applied for succeeding processing steps.

the National Library of Medicine, Bethesda, Maryland (USA) [33], which provides a large source of images from inside of human body (Sect. 6.4.5). Generally, imaging data can have different dimensions, e.g. two-dimensional photos, three-dimensional X-ray computed tomographies and four-dimensional MR tomographies.

In the following sections a survey of numerous pragmatic image processing methods is given. A representation of images suitable for computerized analysis is described. The topics preprocessing and segmentation are introduced. The topics representation, detection and interpolation of orientation in images are presented. These are of importance for modeling fibered structures, e.g. skeletal and heart muscle.

5.2 Digital Representation of Images

Commonly, digitized images are described as a k-dimensional array of $N_1 \times \cdots \times N_k$ discrete elements $v(i_1, \ldots, i_k)$ with $i_j \in \{1, \ldots, N_j\}$ for all $j \in \{1, \ldots, k\}$. Here, the elements represent isotropic equidistant samples of the original image obtained by an imaging device. In two-dimensions the elements of an image are called pixels, in three dimensions voxels.

The elements contain values representing physical quantities, e.g. grey levels in photos, proton densities in MR, and attenuation coefficients in CT tomographies. The value range of the elements is limited. Typical ranges are 0–255 and 0–65535, which can be efficiently stored in 1 byte and 2 bytes, respectively.

Example. A two-dimensional image $\boldsymbol{I}$ with isotropic equidistant elements can be represented by the $N_1 \times N_2$ array:

$$\boldsymbol{I} = \begin{pmatrix} v(1,1) & v(1,2) & \dots\ \dots & v(1,N_1-1) & v(1,N_1) \\ v(2,1) & v(2,2) & \dots\ \dots & v(2,N_1-1) & v(2,N_1) \\ \dots & \dots & \dots\ \dots & \dots & \dots \\ v(N_2-1,1) & v(N_2-1,2) & \dots\ \dots & v(N_2-1,N_1-1) & v(N_2-1,N_1) \\ v((N_2,1) & v(N_2,2) & \dots\ \dots & v(N_2,N_1-1) & v(N_2,N_1) \end{pmatrix}$$

5.3 Preprocessing

5.3.1 Overview

The preprocessing consists of image transformations aiming at simplifying of further processing steps. Transformations are applied to correct errors resulting from imaging conditions and imaging devices. Further transformations are performed to enhance the applicability and quality of an image. Different areas of preprocessing techniques can be distinguished:

- Transformation of coordinates
- Filtering methods
- Matching of images

5.3.2 Transformation of Coordinates

Introduction. Many image processing tasks necessitate the geometrical transformation of images as well as of points and objects. These tasks include matching and warping of images, stereo image analysis, and re-sampling techniques. Further applications of the geometrical transformations are found in computer visualization and computer aided design.

The transformation of coordinates can be defined as:

$$\boldsymbol{x}' = T(\boldsymbol{x})$$

with the transformation T, the coordinate vectors $\boldsymbol{x}$ and $\boldsymbol{x}'$. Commonly, the coordinate vectors $\boldsymbol{x}$ and $\boldsymbol{x}'$ are real and their dimension is equal.

In the following sections a variety of transformations are introduced, which are frequently applied in image processing. The transformations are defined in such a way, that points in a three-dimensional cartesian coordinate system are transferred into a three-dimensional cartesian coordinate system. The transformations can be simplified to two-dimensional and extended to four-dimensional coordinate systems.

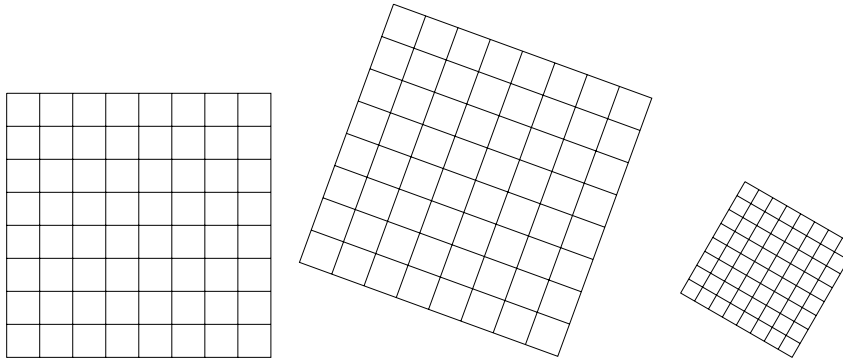

Fig. 5.2. An example of affine transformations of images. Points of (a) the original, two-dimensional image are transferred via (b) rigid transformation consisting of translation and rotation and (c) affine transformation including scaling. The transformation leads to a two-dimensional image.

Affine Transformations. An affine transformation T_A is defined by [34, 35]:

$$T_A(\boldsymbol{x}) = \boldsymbol{A}\boldsymbol{x} + \boldsymbol{b}$$

with the matrix $\boldsymbol{A}$, the translation vector $\boldsymbol{b} = (b_1, b_2, b_3)^T$ and the original vector $\boldsymbol{x}$. The matrix $\boldsymbol{A}$ is used to describe rotation, scaling and shear (Fig. 5.2). Several transformations can be combined in a single matrix $\boldsymbol{A}$ by concatenation of rotation, scaling and shear matrices.

Specific cases of affine transformations are the rigid transformations, whereby angles between lines and distances between points are preserved. The matrix $\boldsymbol{A}$ of a rigid transformation is restricted to be a concatenation of rotation matrices. No restrictions are made concerning the vector $\boldsymbol{b}$.

A rotation with the angle α in the xy-plane is given by the matrix $\boldsymbol{A_{xy}}$:

$$\boldsymbol{A_{xy}} = \begin{pmatrix} cos\ \alpha & sin\ \alpha & 0 \\ -sin\ \alpha & cos\ \alpha & 0 \\ 0 & 0 & 1 \end{pmatrix}$$

A scaling of s_x in x-direction, of s_y in y-direction and of s_z in z-direction is obtained with the matrix $\boldsymbol{A_{scale}}$:

$$\boldsymbol{A_{scale}} = \begin{pmatrix} s_x & 0 & 0 \\ 0 & s_y & 0 \\ 0 & 0 & s_z \end{pmatrix}$$

Reflections can be produced by using negative values for s_x, s_y or s_z. Projections are achieved by setting s_x, s_y or s_z to zero.

A x-shear is created by the matrix $\boldsymbol{A_{shear}}$:

$$\boldsymbol{A_{shear}} = \begin{pmatrix} 1 & a & b \\ 0 & 1 & 0 \\ 0 & 0 & 1 \end{pmatrix}$$

with the parameters a and b.

Homogeneous Transformations. Homogeneous transformations incorporate a larger degree of freedom than affine transformations. A property of homogeneous transformations is that lines are transferred to lines, but that parallelism of lines is not preserved.

A homogeneous transformation is performed in three steps. In the first step the point $\boldsymbol{x} = (x_1, x_2, x_3)^T$ is transferred to a point $\boldsymbol{x}_{hom}$ in the four-dimensional space:

$$\boldsymbol{x}_{hom} = \begin{pmatrix} x_1 \\ x_2 \\ x_3 \\ 1 \end{pmatrix}$$

In the second step the intrinsic transformation T_{hom} is performed:

$$T_{hom}(\boldsymbol{x}_{hom}) = \boldsymbol{A}\boldsymbol{x}_{hom}$$

with the 4×4 matrix $\boldsymbol{A}$.

In the final step the result of the transformation T_{hom}, the point $\boldsymbol{x}'_{hom}$, is transferred to the three-dimensional point $\boldsymbol{x}'$:

$$\boldsymbol{x}' = \frac{1}{x'_{hom,4}} \begin{pmatrix} x'_{hom,1} \\ x'_{hom,2} \\ x'_{hom,3} \end{pmatrix} \quad \text{with} \quad \boldsymbol{x}'_{hom} = \begin{pmatrix} x'_{hom,1} \\ x'_{hom,2} \\ x'_{hom,3} \\ x'_{hom,4} \end{pmatrix}$$

The matrix $\boldsymbol{A}$ is used to describe translation, rotation, scaling, shear and perspective [32]. Similarly to affine transformations, several homogeneous transformations can be combined in a single matrix $\boldsymbol{A}$ by concatenation of matrices.

A translation with the vector $\boldsymbol{b} = (b_1, b_2, b_3)^T$ is determined by the matrix $\boldsymbol{A_{translation}}$:

$$\boldsymbol{A_{translation}} = \begin{pmatrix} 1 & 0 & 0 & b_1 \\ 0 & 1 & 0 & b_2 \\ 0 & 0 & 1 & b_3 \\ 0 & 0 & 0 & 1 \end{pmatrix}$$

A rotation with the angle α in the xy-plane is given by the matrix $\boldsymbol{A_{xy}}$:

$$\boldsymbol{A_{xy}} = \begin{pmatrix} cos\ \alpha & sin\ \alpha & 0 & 0 \\ -sin\ \alpha & cos\ \alpha & 0 & 0 \\ 0 & 0 & 1 & 0 \\ 0 & 0 & 0 & 1 \end{pmatrix}$$

A scaling of s_x in x-direction, of s_y in y-direction and of s_z in z-direction is obtained with the matrix $\boldsymbol{A_{scale}}$:

$$\boldsymbol{A_{scaling}} = \begin{pmatrix} s_x & 0 & 0 & 0 \\ 0 & s_y & 0 & 0 \\ 0 & 0 & s_z & 0 \\ 0 & 0 & 0 & 1 \end{pmatrix}$$

Projections and reflections are created by setting appropriate scaling factors, in a similarl way as described for affine transformations.

A perspective transformation is determined by the matrix $\boldsymbol{A_{perspective}}$:

$$\boldsymbol{A_{perspective}} = \begin{pmatrix} 1 & 0 & 0 & 0 \\ 0 & 1 & 0 & 0 \\ 0 & 0 & 1 & 0 \\ 0 & 0 & -\frac{1}{\lambda} & 1 \end{pmatrix}$$

with the parameter λ.

Polynomial Transformations. Polynomial transformations can be regarded as extension of the linear affine transformation. The transformation of the point $\boldsymbol{x} = (x_1, x_2, x_3)^T$ into the point $\boldsymbol{x'} = (x'_1, x'_2, x'_3)^T$ is given by:

$$\begin{aligned} x'_1 &= a_0 + a_1x_1 + a_2x_2 + a_3x_3 \\ &\quad + a_4x_1^2 + a_5x_2^2 + a_6x_3^2 + a_7x_1x_2 + a_8x_1x_3 + a_9x_2x_3 \\ &\quad + \dots \\ x'_2 &= b_0 + b_1x_1 + b_2x_2 + b_3x_3 \\ &\quad + b_4x_1^2 + b_5x_2^2 + b_6x_3^2 + b_7x_1x_2 + b_8x_1x_3 + b_9x_2x_3 \\ &\quad + \dots \\ x'_3 &= c_0 + c_1x_1 + c_2x_2 + c_3x_3 \\ &\quad + c_4x_1^2 + c_5x_2^2 + c_6x_3^2 + c_7x_1x_2 + c_8x_1x_3 + c_9x_2x_3 \\ &\quad + \dots \end{aligned}$$

with the parameters a_i, b_i and c_i.

Radial Basis Function Transformations. Transformations of images can also be performed using the radial basis function transformation. In contrast to the previously described techniques the transformation shows a scalable local behavior, which can be of advantage in specific applications e.g. image warping (Fig. 5.3).

The transformation T_{RBF} is composed of an affine T_A and a radial transformation T_R:

$$T_{RBF}(\boldsymbol{x}) = T_A(\boldsymbol{x}) + T_R(\boldsymbol{x})$$

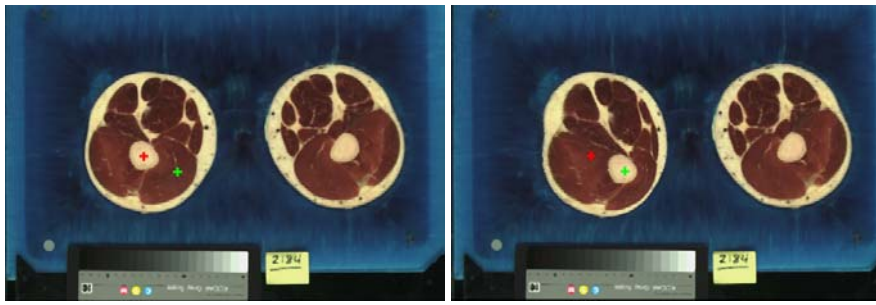

(a) (b)

Fig. 5.3. Exemplary radial basis function transformation (from [26]). (a) The original image is transformed to (b) the result image. Given are a point (red cross) and its transformation (green cross). Obviously, the transformation is local. Distant areas are not transformed.

The affine transformation T_A is responsible for the global behavior and is given by:

$$T_A(\boldsymbol{x}) = \boldsymbol{A}\boldsymbol{x} + \boldsymbol{b}$$

with the matrix $\boldsymbol{A}$ and the vector $\boldsymbol{b}$.

The radial transformation T_R in cooperates local behavior and is determined by:

$$T_R(\boldsymbol{x}) = \begin{pmatrix} T_{RX}(\boldsymbol{x}) \\ T_{RY}(\boldsymbol{x}) \\ T_{RZ}(\boldsymbol{x}) \end{pmatrix}$$

with the radial functions T_{RX}, T_{RY} and T_{RZ}. The radial functions are constructed equal to the function R:

$$R(\boldsymbol{x}) = \sum_{i=1}^{N} a_i g(|\boldsymbol{x} - \boldsymbol{x}_i|)$$

with the scalar parameters a_i, the points $\boldsymbol{x}_i$ and the radial basis function g. The argument of g describes the distance between the point $\boldsymbol{x}$ and the point $\boldsymbol{x}_i$. Different types of radial basis functions were proposed [36]:

$$g(t) = e^{\frac{-t^2}{\sigma^2}}$$

$$g(t) = \begin{cases} 1 - (\frac{t}{\sigma})^2(3 - \frac{2t}{\sigma})^2 & 0 \leq t \leq \sigma \\ 0 & \text{otherwise} \end{cases}$$

$$g(t) = \begin{cases} 6(\frac{t}{\sigma})^2(\frac{t}{\sigma} - 1)^2 + 1 & 0 \leq t < \frac{1}{2}\sigma \\ 2(\frac{1-t}{\sigma})^3 & \frac{1}{2}\sigma \leq t \leq \sigma \\ 0 & \text{otherwise} \end{cases}$$

with the parameter σ. The parameter determines characteristics of the transformation, particularly the radial decrease of influence.

Parameter determination. The parameters of the radial basis function transformation T_{RBF}, i.e. the matrix $\boldsymbol{A}$ and the vector $\boldsymbol{b}$ of the affine transformation T_A, as well as the parameters a_i of the radial transformation T_R are determined with the given parameter σ, points $\boldsymbol{x}_i$ and their corresponding points $\boldsymbol{x}'_i$. In a first step the parameters of the affine transformation T_A are determined, e.g. by least squares methods [5] with a subset of the given points $\boldsymbol{x}_i$ and $\boldsymbol{x}'_i$. In the second step the parameters of the radial transformation T_R are calculated by solving the following equation system:

$$\sum_{j=1}^{N} a_{jk} g(|x_i - x_j|) = x'_{ik} - (T_A(x_i))_k$$

5.3.3 Filtering Methods

Introduction. The task of filtering is the enhancement of image quality and the extraction of features. Filtering serves to simplify and support subsequent processing steps. Commonly, filters modify the image elements taking neighboring elements into account.

Different types of filters are distinguished depending on their domain: spatial and frequency domain filters. Filters can be grouped into linear and nonlinear filters. Hybrid filters can be constructed consisting of a sequence of filters. Filters are called global or local, if the filter operator is equal or not equal, respectively, over the whole image.

In the following sections different filters are introduced, which are of importance for typical image processing applications. The filters are formulated to work in a three-dimensional domain.

Linear Filtering. Linear filtering is performed by convolution of the image $\boldsymbol{I}$ with the filter mask $\boldsymbol{M}$:

$$\boldsymbol{I}' = \boldsymbol{M} * \boldsymbol{I}$$

The operation leads to the image $\boldsymbol{I}'$. The operator $*$ denotes a convolution.

Linear filters have properties, which simplify their application and theoretical study: linearity, additivity, commutativity and associativity. Further filter properties, particularly dependence on spatial frequencies, can be studied by transforming the filter mask $\boldsymbol{M}$ in the frequency domain.

Linearity. The linearity of a filter is guaranteed if the following equation is fulfilled:

$$\boldsymbol{M} * (\alpha \boldsymbol{I}_1 + \beta \boldsymbol{I}_2) = \alpha(\boldsymbol{M} * \boldsymbol{I}_1) + \beta(\boldsymbol{M} * \boldsymbol{I}_2)$$

with the filter mask M, the images $\boldsymbol{I}_1$ and $\boldsymbol{I}_2$ as well as the factors α and β.

Additivity. The additivity of filters is guaranteed if

$$(\boldsymbol{M}_1 + \boldsymbol{M}_2) * \boldsymbol{I} = \boldsymbol{M}_1 * \boldsymbol{I} + \boldsymbol{M}_2 * \boldsymbol{I}$$

with the filter masks $\boldsymbol{M}_1$ and $\boldsymbol{M}_2$

Table 5.1. Exemplary linear, three-dimensional filters and their $3 \times 3 \times 3$ masks [26]. The given filter mask for the simple and Sobel gradient allows the extraction of the image gradient in x-direction. The masks for the y- and z-direction can be created by rotation about the $\boldsymbol{z}$- and $\boldsymbol{y}$-axis.

Filter	Mask
Average	$\frac{1}{27}\left(\begin{pmatrix}1&1&1\\1&1&1\\1&1&1\end{pmatrix}\begin{pmatrix}1&1&1\\1&1&1\\1&1&1\end{pmatrix}\begin{pmatrix}1&1&1\\1&1&1\\1&1&1\end{pmatrix}\right)$
Simple gradient in x-direction	$\frac{1}{10}\left(\begin{pmatrix}0&0&0\\1&0&-1\\0&0&0\end{pmatrix}\begin{pmatrix}1&0&-1\\1&0&-1\\1&0&-1\end{pmatrix}\begin{pmatrix}0&0&0\\1&0&-1\\0&0&0\end{pmatrix}\right)$
Sobel gradient in x-direction	$\frac{1}{12}\left(\begin{pmatrix}0&0&0\\1&0&-1\\0&0&0\end{pmatrix}\begin{pmatrix}1&0&-1\\2&0&-2\\1&0&-1\end{pmatrix}\begin{pmatrix}0&0&0\\1&0&-1\\0&0&0\end{pmatrix}\right)$
Laplace	$\left(\begin{pmatrix}0&0&0\\0&1&0\\0&0&0\end{pmatrix}\begin{pmatrix}0&1&0\\1&-6&1\\0&1&0\end{pmatrix}\begin{pmatrix}0&0&0\\0&1&0\\0&0&0\end{pmatrix}\right)$

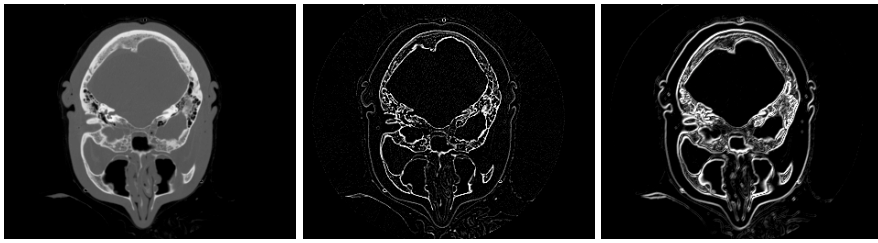

(a) (b) (c)

Fig. 5.4. First and second order derivative filters applied on CT data (from [26]). (a) The original image is filtered with the (b) Sobel- and (c) Laplace-filter. The Sobel-filter approximates the magnitude of the gradient in the image. The Laplace-filter approximates the Laplace-operator applied to the image.

Commutativity. Filters are called commutative if

$$\boldsymbol{M}_1 * (\boldsymbol{M}_2 * \boldsymbol{I}) = \boldsymbol{M}_2 * (\boldsymbol{M}_1 * \boldsymbol{I})$$

Associativity. Filter are called associative if

$$\boldsymbol{M}_1 * (\boldsymbol{M}_2 * \boldsymbol{I}) = (\boldsymbol{M}_1 * \boldsymbol{M}_2) * \boldsymbol{I}$$

Typical linear filters are average, gradient, and Laplace-filters (table 5.1). Average filters perform a low-pass filtering of the image and are applied for noise reduction and blurring. Small objects and structures consisting of high frequency components are erased. Gradient and Laplace-filters perform high-pass filtering of the image and are used for example to detect edges in images (Fig. 5.4).

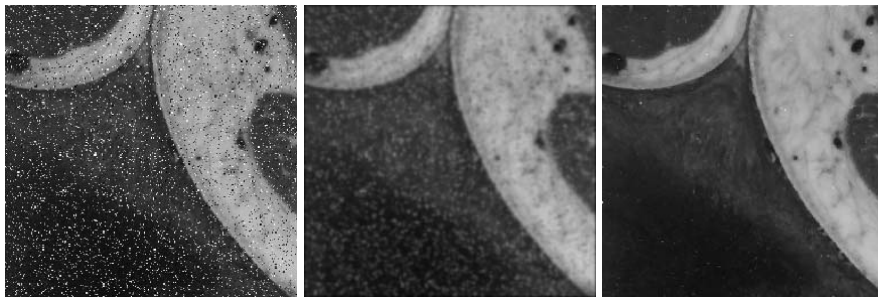

(a) (b) (c)

Fig. 5.5. Comparison of average and median filter (from [37]). (a) An image filled partly with noise. The image after application of (b) average and (c) median filter. The average filter shows blurring and noise reduction properties. The median filter reduces noise, while preserving edges.

Gradient filters approximate the first derivative or so-called gradient of an image $\nabla \boldsymbol{I}$ by applying three unidirectional gradient masks $\boldsymbol{M}_x$, $\boldsymbol{M}_y$, and $\boldsymbol{M}_z$:

$$\nabla \boldsymbol{I} \approx \begin{pmatrix} \boldsymbol{M}_x \\ \boldsymbol{M}_y \\ \boldsymbol{M}_z \end{pmatrix} * \boldsymbol{I}$$

Different types of gradient masks can be derived, e.g. the simple gradient and the Sobel-filter masks (table 5.1). Commonly, the magnitude of the image gradient $\nabla \boldsymbol{I}$ is determined and used as filter response:

$$\boldsymbol{I'} = |\nabla \boldsymbol{I}|$$

Laplace filters approximate the Laplace-operator Δ, i.e. divergence of gradient, by convolution with an appropriate mask $\boldsymbol{M}$. The Laplace-operation applied to the image $\boldsymbol{I}$ is given by:

$$\boldsymbol{I'} = \Delta \boldsymbol{I} \approx \boldsymbol{M} * \boldsymbol{I}$$

Rank-Order Filters. Rank-order filters replace an element's value with the value of an element inside of a given area. The shape of the area is commonly cubic or spherical. The replaceable element is located centrally in the area. The values of all elements in the given area are collected and sorted by size. Rank-order filters are nonlinear. Typical three-dimensional rank-order filters are median, erosion and dilation filters.

Median. The median filter uses the middle value in the sorting of element values. The filter reduces noise and preserves edges. Blurring phenomena similar to linear average filter are not observed (Fig. 5.5).

Erosion. The smallest value in the sorting of element values is selected by the erosion filter. The choice leads to the reduction of high value areas. Single elements with relatively high values regarding the neighborhood are erased.

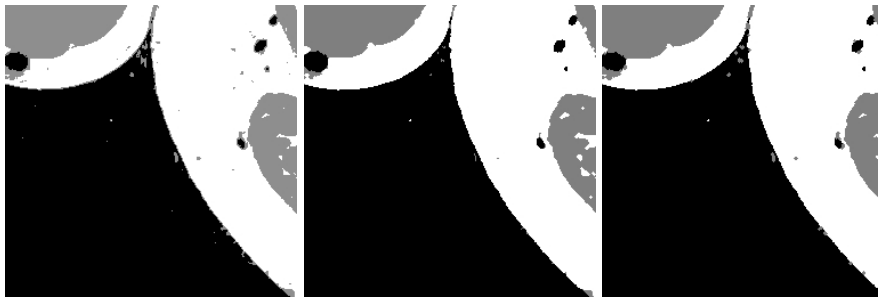

(a) (b) (c)

Fig. 5.6. Opening operator applied to grey level image (from [37]). (a) Original image. The image resulting from application of (b) erosion filter and (c) opening operator. The opening operator consists of an erosion followed by a dilation. Small artifacts are erased and the object's area is reduced by the erosion filter. The object's area is preserved by the opening operator.

Dilation. The dilation filter uses the largest value in the sorting of element values. High value areas are extended. Isolated low value elements are removed.

Hybrid Filters. Hybrid filters are constructed by the concatenation of two and more filters. Partly, the filters are parameterized by feature extraction. In the following important hybrid filters, i.e. the opening and closing operators as well as the Canny-Deriche-Monga filter, are introduced.

Opening. The opening operator consists of a sequence of rank-order filters. The application of $n\times$erosion is followed by $n\times$dilation. The operator allows the reduction of small junctions and bulges (Fig. 5.6).

Closing. The closing operator consists of a sequence of rank-order filters. The application of $n\times$dilation is followed by $n\times$erosion. Small gaps are deleted and objects close to one another are connected.

Canny-Deriche-Monga Filter. The Canny-Deriche-Monga filter was specifically developed for edge detection. The filter is based on the definition of different criteria for the computation of edge points [38], which were originally formulated for one- and two-dimensional data. The criteria are:

- Good detection. The probability of fail and missing detections should be small.
- Good localization. The detected edge points should be near to the true edge.
- Single response. Multiple detection responses corresponding to the same edge point should be avoided.

The algorithm consists of three steps: In a first step gradient filters are applied to detect edges. The second step serves to remove multiple edge points.

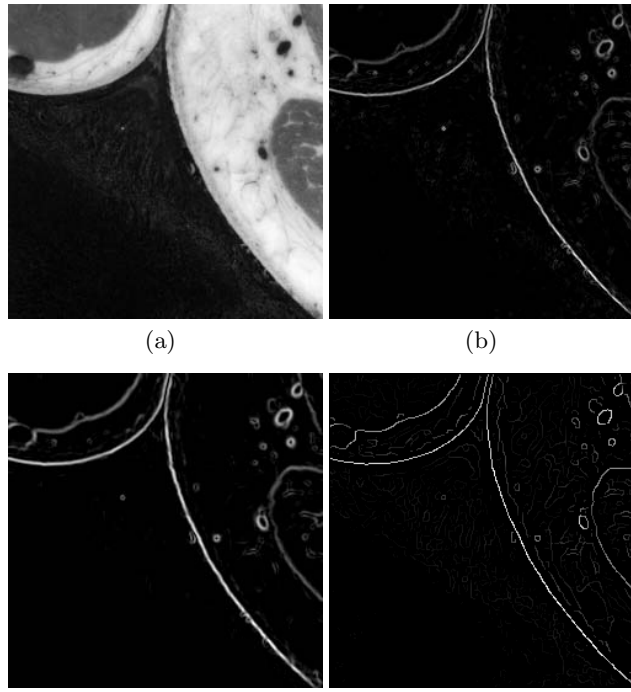

Fig. 5.7. Comparison of different edge detection filters (from [37]). (a) The original image. The image after application of (b) simple gradient, (c) Sobel-, and (d) Canny-Deriche-Monga-filter.

A non-maxima suppression of points perpendicular to the edge is performed. With the final step, missing edge points leading to the so-called streaking were attached to the edge using adaptive thresholding with hysteresis.

Deriche and Monga extended the approach to three-dimensional domains. They implemented an efficient version [39], whereby the computational expense is linearly dependent on the image size.

A comparison of different edge detectors is illustrated in Fig. 5.7. The filter is utilized amongst other things in conjunction with the subsequently introduced active contour models for image segmentation.

5.4 Segmentation Techniques

5.4.1 Introduction

Segmentation is defined as the division of an image into objects or regions [32]. The objects are represented by homogeneous regions. The homogeneity

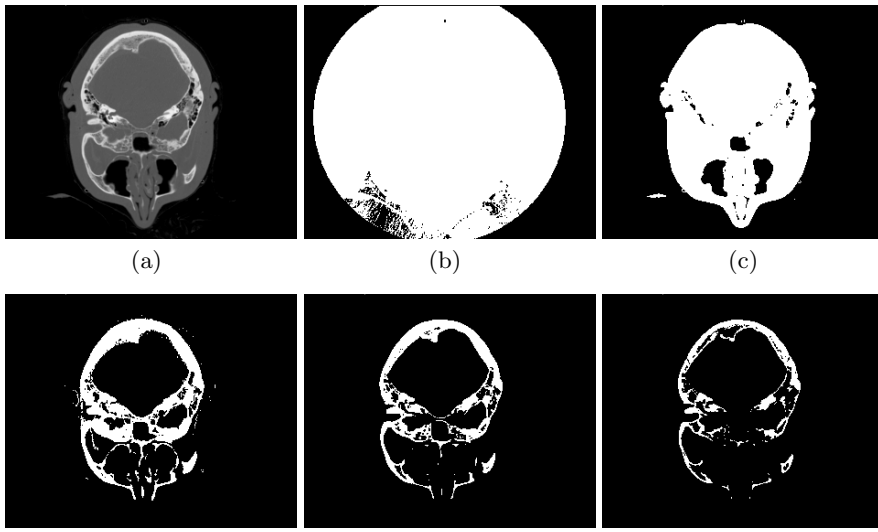

Fig. 5.8. Segmentation of two-dimensional image of CT with thresholding (from [26]). (a) The original image. The result of a segmentation with relation '$\geq$' and threshold (b) 1, (c) 40, (d) 60, (e) 80, and (f) 100.

is assessed by attributes like color intensity and gray level in images as well as the absorption coefficient in CT scans.

Segmentation methods can be classified into automatic, semi-automatic and manual methods. Automatic methods perform an image segmentation without any user intervention. Semi-automatic methods need a parameterization by the user to guide the segmentation process. Manual methods require the highest level of user interaction. Commonly, the user defines the segments interactively.

Segmentation methods can be divided in point, region and edge based methods. Point based methods use only the attributes of an image element for its segmentation. With region based methods image elements are attached to segments in the context of their neighborhood. Edge based methods are based on the extraction of edges in the image data.

In the following sections different segmentation techniques are described and their exemplary application with medical images is illustrated. The techniques are pragmatic for segmentation of medical images. Further applications of these techniques are described in Sect. 6.4.

5.4.2 Thresholding

Thresholding is a point based approach to image segmentation. A voxel is assigned to a region if the image element's characteristics are in a relation,

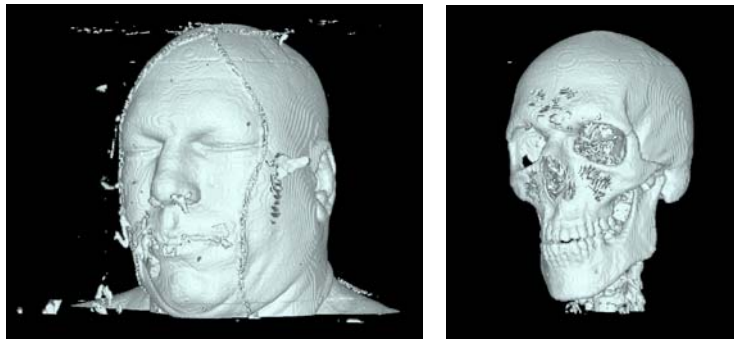

(a) (b)

Fig. 5.9. Segmentation of three-dimensional CT with thresholding (from [26]). The result of a segmentation with relation '$\geq$' and threshold (a) 40 and (b) 80. The first threshold is chosen to segment tissue, the second to segment bone and marrow. Outlying artifacts are caused by noise.

e.g. '$<$', '$\leq$', '$\geq$' and '$>$', to a threshold value. Both, relation and threshold value are given parameters and commonly kept constant while processing. Parameters can be determined by image analysis, e.g. histogram evaluation. The created segments are commonly not contiguous.

An extension of thresholding allows the assignment of an image element at coordinates $\boldsymbol{x}$ to regions by a function T:

$$T = T(\boldsymbol{x}, p(\boldsymbol{x}), \boldsymbol{I}(\boldsymbol{x}))$$

with the characteristic of the adjacent region $p(\boldsymbol{x})$ and the image value $\boldsymbol{I}(\boldsymbol{x})$. The return value of function T identifies the region.

Thresholding can be directly applied e.g. to segment bone structures in CT (Fig. 5.8 and 5.9). A preprocessing by median filtering is of advantage to reduce artifacts caused by noise. An efficient implementation uses precalculated boolean look-up tables, which use the element's value as the index.

5.4.3 Region Growing

Region growing is a region based technique for image segmentation. Region growing means that image elements are collected starting from a set of seed points (Fig. 5.10). If their neighboring elements match the region characteristics, they are included within this region and are chosen to be new seed points. Commonly, in three-dimensional image processing, neighborhoods of 6, 18 or 26 elements are used. In two-dimensional segmentation neighborhoods of 4 or 8 elements are often applied. The match of region characteristics can be checked by thresholding techniques. Region growing is an iterative process, terminating if no neighboring voxels fit in the region characteristics. Each seed point creates a contiguous segment.

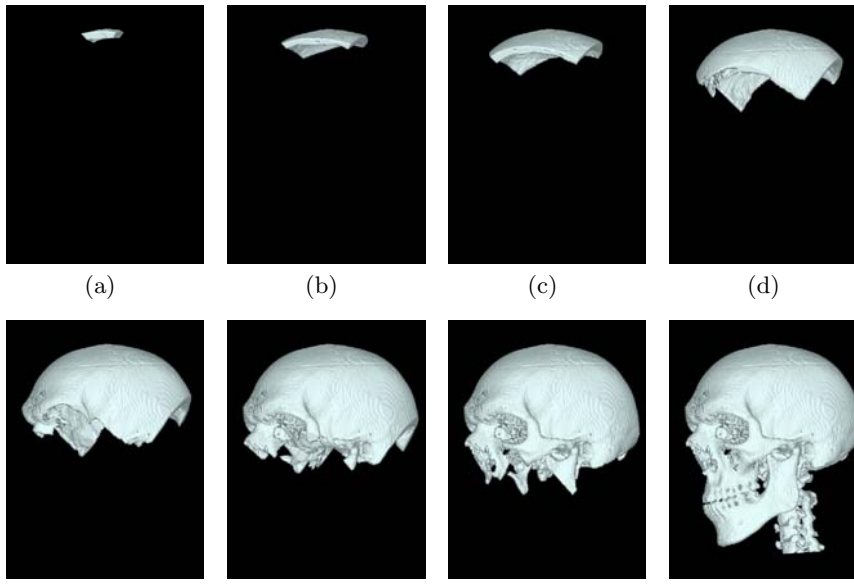

Fig. 5.10. Segmentation of three-dimensional CT with region growing (from [26]). Region growing is initiated by setting a seed point at upper skullcap using a 6-neighborhood and given threshold. The image sequence (a-h) shows different stages of the region growing process. In contrast to the application of threshold techniques a single region without outlying artifacts is constructed.

Region growing can be employed e.g. to segment bone structures in CT (Fig. 5.10). Commonly, preprocessing of the image data is performed.

An efficient implementation provides the usage of a special data structure, the so-called ring buffer, for the management of the seed point set. A ring-buffer provides fast insertion and removal of seed points using a first-in-first-out strategy. The ring-buffer consists of a static array of elements, which has to be chosen sufficiently large, and of two indices, one for insertion and one for removal of elements. Initially, the indices are set to zero. The insertion and removal indices are incremented by insertion and removal, respectively. Index overflows are handled by setting the index to zero. The number of elements is determined by the distance of the insertion and removal index.

5.4.4 Watershed

The watershed algorithm is an edge based segmentation technique. In the first step the magnitude of the image gradient $I_g = |\nabla \boldsymbol{I}|$ is determined. In the second step all image elements are scanned and segmented.

Image elements are assigned to a region, which have a continuous descending path to a common minimum. The path is iteratively constructed starting

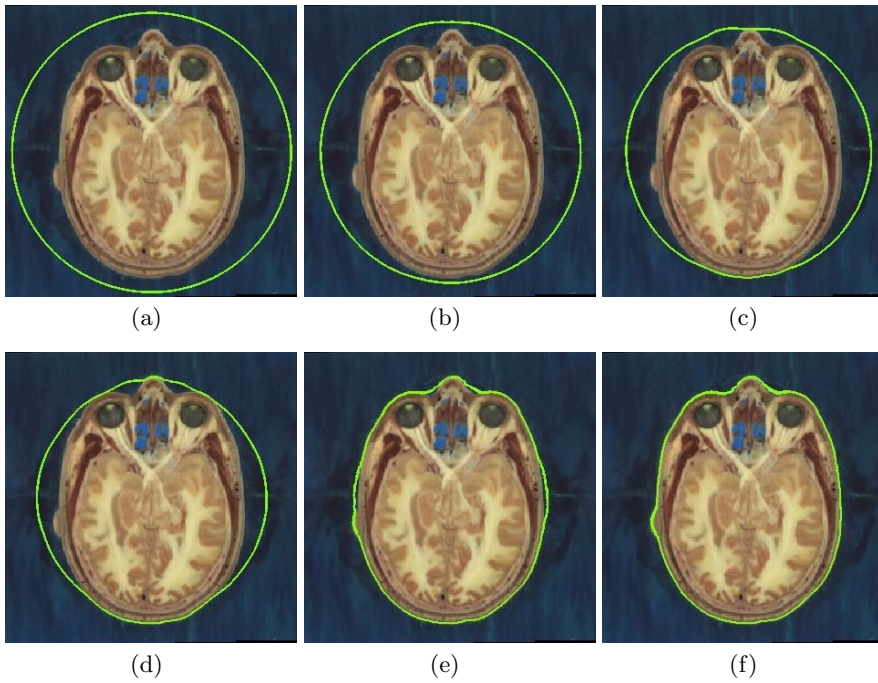

Fig. 5.11. Image segmentation with active contour model (from [37]). (a) Two-dimensional image with initial contour. Assigned to the contour is an energy, which is minimized concerning the geometry. The resulting advance of the contour is shown in (b)-(f). The energy includes stretch and image energies.

at the position of the image element $\boldsymbol{p}$. Here, the image gradient $\nabla I_g(\boldsymbol{p})$ is determined, e.g. by applying the Sobel-filter. If the gradient is zero, a minimum is found and the image elements are assigned to a region. Otherwise, a step in gradient direction is performed leading to a new position $\boldsymbol{p}'$ and the next iteration step is executed setting $\boldsymbol{p} = \boldsymbol{p}'$. The step size is chosen in such a way that an adjacent image element is hit.

Commonly, the segmentation achieved with the watershed algorithm leads to a large number of regions. The fusion of elements can be performed with manual and automatic methods [40].

5.4.5 Deformable Models

Traditional Active Contour Models. Active contour models are edge based methods for image segmentation by iterative adaptation of a surface to edges of an object (Fig. 5.11 and 5.13). The method benefits from knowledge concerning surface characteristics of objects. The application also requires knowledge of the position and the shape of the objects.

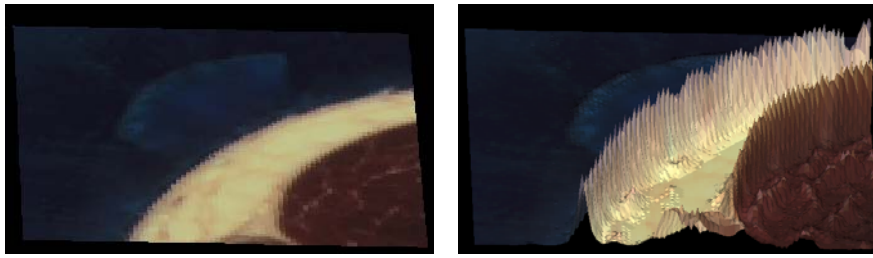

(a) (b)

Fig. 5.12. Potential function for active contour models (from [26]). (a) The original image with red, green and blue channels. (b) Image with height information derived from gradient magnitude of red-channel $|\nabla I(\boldsymbol{x})|$. The potential function used in active contour models is the negative gradient magnitude weighted by a parameter.

Two-dimensional active contour models. In two-dimensional space the geometry of an active contour model can be described by the function $\boldsymbol{v}$ [41, 42, 43]:

$$\boldsymbol{v}(s) = \begin{pmatrix} v_x(s) \\ v_y(s) \end{pmatrix} \tag{5.1}$$

with the parameter $s \in [0, 1]$. Commonly, the contour is closed, i.e. $\boldsymbol{v}(0) = \boldsymbol{v}(1)$.

Attributed to the contour is an energy E:

$$E(\boldsymbol{v}) = E_{internal}(\boldsymbol{v}) + E_{external}(\boldsymbol{v})$$

which is divided in an internal and external energy, $E_{internal}$ and $E_{external}$, respectively.

The internal energy $E_{internal}$ is the sum of the stretch and bending energy. The stretch energy $E_{stretch}$ is defined as:

$$E_{stretch}(\boldsymbol{v}) = \omega_{stretch} \int_0^1 \left| \frac{\partial \boldsymbol{v}}{\partial s} \right|^2 ds$$

with the weighting parameter $\omega_{stretch}$. The parameter controls the tension of the active contour. The bending energy E_{bend} is given by:

$$E_{bend}(\boldsymbol{v}) = \omega_{bend} \int_0^1 \left| \frac{\partial^2 \boldsymbol{v}}{\partial s^2} \right|^2 ds$$

with the weighting parameter ω_{bend}. The parameter controls the bending rigidity, which influences the contour's smoothness.

The external energy $E_{external}$ can consist of image energy E_{image}, balloon energy, gravitation energy, attractor energy etc.. Variant formulations and combinations of these energies are reported [44, 45, 46, 47].

The image energy connects the active contour with the image $\boldsymbol{I}$ via the potential function p:

$$E_{image}(\boldsymbol{v}) = \int_0^1 p(\boldsymbol{v}(s))ds$$

The potential function p uses the negative magnitude of the image gradient (Fig. 5.12):

$$p(\boldsymbol{x}) = -\omega_p |\nabla \boldsymbol{I}(\boldsymbol{x})|$$

with the weighting parameter ω_p. The potential function p provides minima at edges. Alternatively, the potential function can be constructed after smoothing of the image [48]:

$$p(\boldsymbol{x}) = -\omega_p |\nabla \boldsymbol{G} * \boldsymbol{I}(\boldsymbol{x})|$$

with the Gaussian mask $\boldsymbol{G}$.

The advance of a contour is resulting from iterative minimization of the energy E concerning the geometry $\boldsymbol{v}$. The minimization can be performed e.g. with finite element methods (Sect. 2.7.3) and finite differences methods (Sect. 2.7.4) by discretization of the Lagrange equation of motion:

$$\mu \frac{\partial^2 \boldsymbol{v}}{\partial t^2} + \gamma \frac{\partial \boldsymbol{v}}{\partial t} - \frac{\partial}{\partial s}\left(\omega_{stretch} \frac{\partial \boldsymbol{v}}{\partial s}\right) + \frac{\partial^2}{\partial s^2}\left(\omega_{bend} \frac{\partial^2 \boldsymbol{v}}{\partial s^2}\right) = -\nabla p(\boldsymbol{v}(s))$$

with the mass density μ and the damping density γ. The application of the numerical methods requires a discretization of the contour's geometry e.g. with linear, quadratic and cubic functions.

A minimum is found if the gradient of the contour's energy, i.e. forces, is constant zero:

$$\nabla E = \boldsymbol{0}$$

Correspondingly, the so-called Euler-Lagrange equation is fulfilled:

$$-\frac{\partial}{\partial s}\left(\omega_{stretch} \frac{\partial \boldsymbol{v}}{\partial s}\right) + \frac{\partial^2}{\partial s^2}\left(\omega_{bend} \frac{\partial^2 \boldsymbol{v}}{\partial s^2}\right) + \nabla p(\boldsymbol{v}(s)) = 0$$

Three-dimensional active contour models. Active contour models can be applied in three-dimensional space and image data [49]. The geometry of the contour is given by:

$$\boldsymbol{v}(\boldsymbol{s}) = \begin{pmatrix} v_x(\boldsymbol{s}) \\ v_y(\boldsymbol{s}) \\ v_z(\boldsymbol{s}) \end{pmatrix} \tag{5.2}$$

with the parameter $\boldsymbol{s} \in [0,1][0,1]$.

The application in three-dimensional space requires the reformulation of some energies, e.g. of stretch and bending. The three-dimensional stretch energy $E_{stretch}$ is defined as:

$$E_{stretch}(\boldsymbol{v}) = \int_0^1 \int_0^1 \omega_{stretch,1} \left|\frac{\partial \boldsymbol{v}}{\partial s_1}\right|^2 + \omega_{stretch,2} \left|\frac{\partial \boldsymbol{v}}{\partial s_2}\right|^2 dv_1 dv_2$$

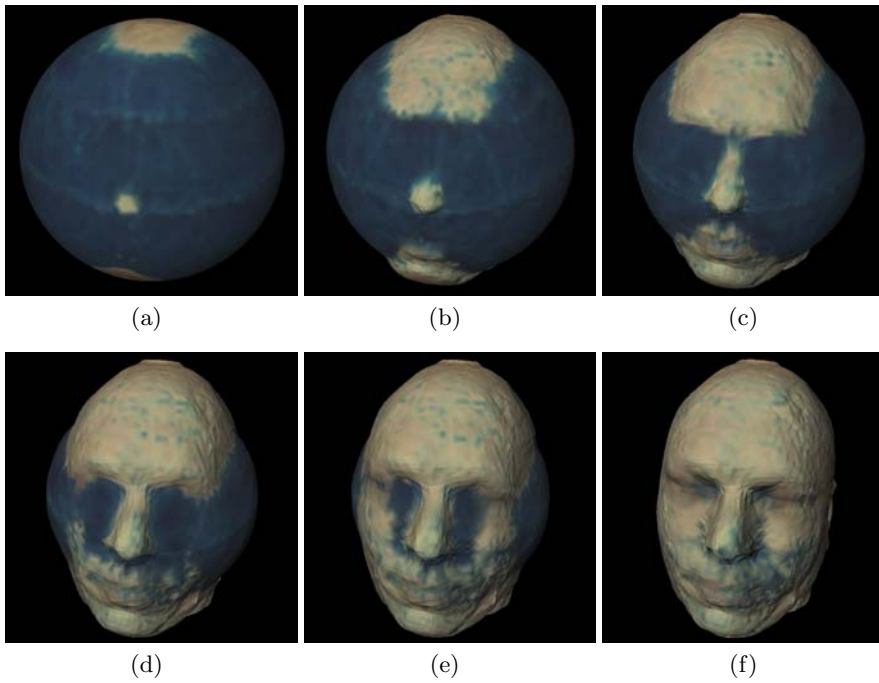

Fig. 5.13. Three-dimensional image segmentation with active contour model (from [37]). (a) The initial contour is a sphere. The resulting advance of the contour is shown in (b)-(f). The energy includes stretch and image energies. The triangle mesh is dyed with colors from the image.

with the weighting parameters $\omega_{stretch,1}$ and $\omega_{stretch,2}$. The parameters control the tension of the active contour in s_1 and s_2 direction, respectively.

The three-dimensional bending energy E_{bend} is given by:

$$E_{bend}(\boldsymbol{v}) = \int_0^1 \int_0^1 \omega_{bend,1} \left| \frac{\partial^2 \boldsymbol{v}}{\partial s_1^2} \right|^2 + \omega_{bend,2} \left| \frac{\partial^2 \boldsymbol{v}}{\partial s_2^2} \right|^2 + \omega_{bend,3} \left| \frac{\partial^2 \boldsymbol{v}}{\partial s_1 \partial s_2} \right|^2 dv_1 dv_2$$

with the weighting parameters $\omega_{bend,1}$, $\omega_{bend,2}$ and $\omega_{bend,3}$. The parameters control the bending rigidity in s_1 and s_2 direction as well as the twisting rigidity, respectively.

Topologically Adaptable Active Contours. Topologically adaptable active contours are an extension of the traditional contours, which have a constant topology [51, 52, 53]. The extension allows splitting and merging of contours (Fig. 5.14 and 5.15).

While advance of the contour its discretization is adapted. The re-discretization respects overlapping and separations of contour parts. The re-discretization can be performed locally [51] or globally [52, 53].

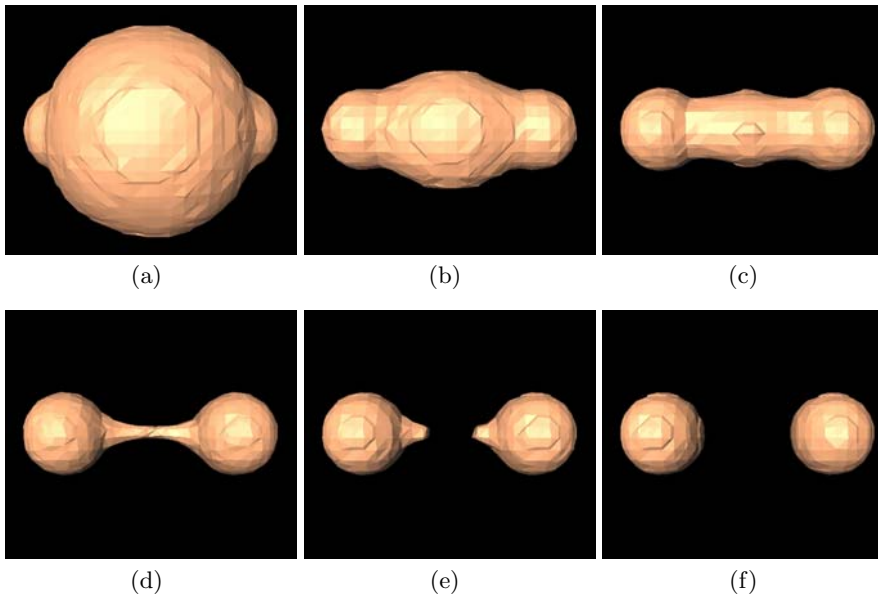

Fig. 5.14. Splitting of active contour model (from [50]). Two spheres are segmented starting with an infolding single spherical contour. The images (a)-(f) show the advance of the contour.

The techniques take advantage of discretization of the active contour with a triangle mesh. Triangle meshes allow efficient management and implementation of operations, e.g. crop and distance measurement.

A local re-discretization is performed after assessment of contour elements and relations between these elements [51]. The distance between node points is used to separate and melt local regions.

A global re-discretization scans information concerning the inside and outside of contours. The information is collected in the node points of tetrahedrons [52] or hexahedrons [53]. The contour can be reconstructed using the information by generating triangles in the polyhedrons. Triangles are created at borders between inside and outside node points. A triangulation in hexahedrons is performed efficiently with the so-called marching cube algorithm [54, 55].

Level Set Methods. Level set methods are a type of active contour models, which allow implicit topological adaptation [56]. The methods showed to have advantages in medical image processing due to their ability to extract the shapes of divers anatomical structures [57].

In level set methods the contour $\boldsymbol{v}$ given in equation 5.1 and 5.2 is represented as zero level set:

$$\Phi = 0$$

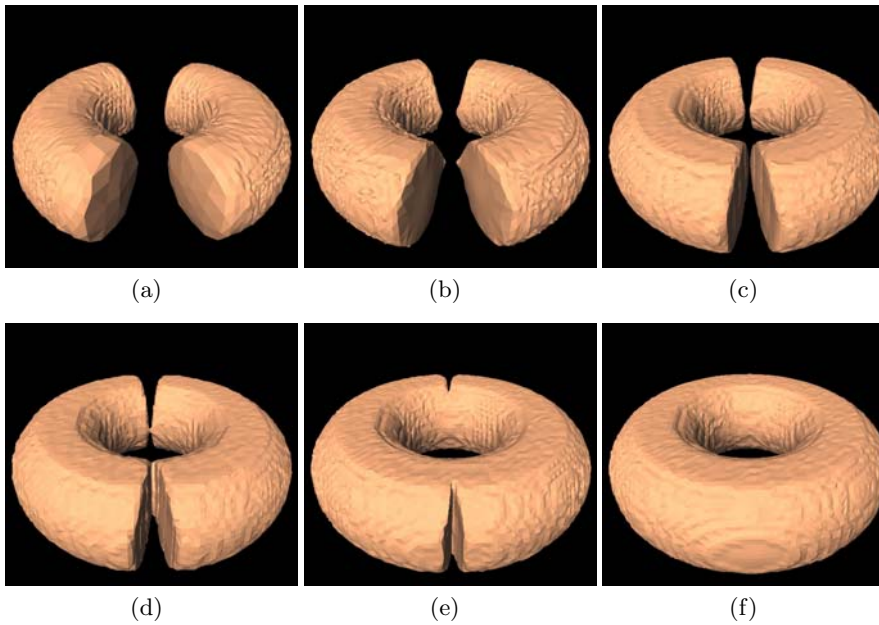

Fig. 5.15. Melting of active contour model (from [50]). A torus is segmented starting with two enclosed spherical contours. The images (a)-(f) show the advance of the contour.

of a higher dimensional function Φ. The function Φ maps positions $\boldsymbol{x}$ at a given time t to a signed distance d to the closed contour $\boldsymbol{v}$:

$$\Phi(\boldsymbol{x}, t) = d$$

A positive and negative distance indicates positions inside and outside of the contour $\boldsymbol{v}$, respectively. An initial contour $\boldsymbol{v}(t = 0)$ is defined by:

$$\boldsymbol{v}(t = 0) = (\boldsymbol{x} | \Phi(\boldsymbol{x}, t = 0) \equiv 0)$$

An evolution of the function Φ at the positions of the contour $\boldsymbol{v}$ is derived starting with:

$$\Phi(\boldsymbol{x}, t) = 0$$

Applying the chain rule leads to:

$$\frac{\partial \Phi}{\partial t} + \sum_{i=1}^{N} \frac{\partial \Phi}{\partial x_i} \frac{\partial x_i}{\partial t} = 0$$

The summation term can be expressed with a speed function F. At a position $\boldsymbol{x} \in \boldsymbol{v}$ the function F has the property that the vector $\boldsymbol{x}_t = F(\boldsymbol{x}, t)$ is normal to the surface $\boldsymbol{v}(t)$. The function F can be influenced by bending, stretch, image properties etc..

Herewith, the summation term is transformed to:

$$\sum_{i=1}^{N} \frac{\partial \Phi}{\partial x_i} \frac{\partial x_i}{\partial t} = F(\boldsymbol{x}(t))|\nabla \Phi|$$

The evolution of the function Φ is expressed by:

$$\frac{\partial \Phi}{\partial t} + F(\boldsymbol{x}(t))|\nabla \Phi| = 0$$

A multitude of level set variants exist, which can be classified by the definition of the speed function F and the numerical implementation [57]. Particularly, the inclusion of anatomical knowledge via regularization of level sets is a topic of active research.

5.4.6 Manual Methods

Manual methods are commonly applied in cases which are not successfully segmentable by automatic or semi-automatic methods. These cases may arise if images are damaged, show an insufficiently contrast, or more automated methods are not available.

A multitude of manual methods were developed, partly based on the previously described techniques. E.g. pixel-wise painting can be supported with the thresholding and watershed techniques. Attractors allow the user interaction with active contour models. Frequently, manual methods are followed by an application of further segmentation techniques. The user creates masks or modifies the image data in such a way that further processing is simplified.

The interactive construction of surfaces proved as an efficient method for separating or enclosing of objects [58, 59] (Fig. 5.16 and 5.17). The method is related with the three-dimensional active contour models. The deformation of an initial contour is controlled by the user, who picks and moves contour elements. The moving of an element affects the elements of a selectable adjacent area. The deformation is controlled by usage of radial basis function transformation (Sect. 5.3.2).

5.5 Principal Component Transform

The determination of principal axes is the main step of the principal component transform, which can be applied in the area of digital image processing to characterize objects and image areas. The transform is also known in literature as discrete Karhunen-Loeve, eigenvector and Hotelling transform [60].

The principal component transform is built on the fundamentals of statistics. It works based on a population $\boldsymbol{X}$ of N random vectors of the following notation:

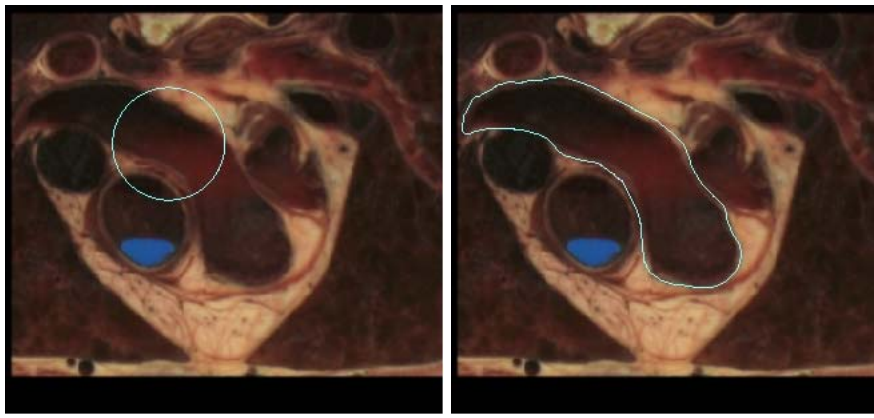

(a) (b)

Fig. 5.16. Interactive deformation of triangle mesh for segmentation of aorta. (a) The image overlayed with an initial triangle mesh and (b) manually adapted triangle mesh. The user adapts the mesh by picking and moving of mesh elements. The moving leads to a local deformation with controllable area of influence. The user interaction is performed in two-dimensional slices of selectable orientation and position. The resulting mesh deformation is three-dimensional.

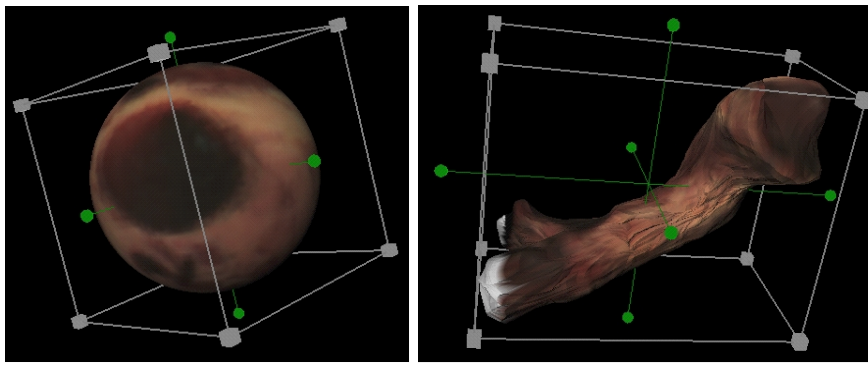

(a) (b)

Fig. 5.17. Interactive deformation of triangle mesh in three-dimensional visualization. (a) The triangle mesh is initially spherical. (b) The manually adapted triangle mesh representing the aorta. The triangle mesh is dyed with colors from the image.

$$\boldsymbol{X} = (\boldsymbol{x}_1, \boldsymbol{x}_2, \ldots, \boldsymbol{x}_N)^T$$

The vectors $\boldsymbol{x}_i$ with $i \in \{1, \ldots, N\}$ are M-dimensional and can be described in the following notation:

$$\boldsymbol{x}_i = (x_1^i, x_2^i, \ldots, x_M^i)^T$$

In digital image processing the vectors $\boldsymbol{x}_i$ are commonly 2–4 dimensional depending on the dimension of the image data. The image elements are taken into account for the generation of the vector population. The elements of the vector population describe the center of gravity of image elements. In black and white pictures, with image elements coded by 0 for black and 1 for white, a single vector is created for each white image element. In gray value pictures a number of vectors is created for each image element. Here, the number is determined by the gray value.

The mean vector $\boldsymbol{m}_{\boldsymbol{X}}$ of a population $\boldsymbol{X}$ is defined as $\boldsymbol{m}_{\boldsymbol{X}} = \boldsymbol{E}(\boldsymbol{X})$, where $\boldsymbol{E}(\boldsymbol{X})$ is the expected value. The mean vector can be approximated from N vector samples of the population:

$$\boldsymbol{m}_{\boldsymbol{X}} \approx \frac{1}{N} \sum_{i=1}^{N} \boldsymbol{x}_i$$

The covariance matrix $\boldsymbol{C}_{\boldsymbol{X}}$ of a population $\boldsymbol{X}$ is defined as:

$$\boldsymbol{C}_{\boldsymbol{X}} = E((\boldsymbol{X} - \boldsymbol{m}_{\boldsymbol{X}})(\boldsymbol{X} - \boldsymbol{m}_{\boldsymbol{X}})^T))$$

The covariance matrix can be approximated from N vector samples of the population:

$$\boldsymbol{C}_{\boldsymbol{X}} \approx \frac{1}{N} \sum_{i=1}^{N} \boldsymbol{x}_i \boldsymbol{x}_i^T - \boldsymbol{m}_{\boldsymbol{X}} \boldsymbol{m}_{\boldsymbol{X}}^T$$

One way to determine the principal axes is the diagonalization of the covariance matrix. A diagonal matrix $\boldsymbol{D}$ and a rotation matrix $\boldsymbol{R}$ can be determined, which fulfill the following condition:

$$\boldsymbol{C}_{\boldsymbol{X}} = \boldsymbol{R}^T \boldsymbol{D} \boldsymbol{R}$$

This can be achieved by calculation of eigenvalues λ_i and eigenvectors $\boldsymbol{e}_i$ (Sect. 2.4.4), which are determined by:

$$\boldsymbol{C}_{\boldsymbol{X}} \boldsymbol{e}_i = \lambda_i \boldsymbol{e}_i$$

The eigenvalues are real, because the covariance matrix is symmetric [8]. They can be notated in descending order:

$$\lambda_1 \geq \lambda_2 \geq \cdots \geq \lambda_M$$

The diagonal matrix $\boldsymbol{D}$ has the following form:

$$\boldsymbol{D} = \begin{pmatrix} \lambda_1 & \cdots & 0 \\ \vdots & \ddots & \vdots \\ 0 & \cdots & \lambda_M \end{pmatrix}$$

The rotation matrix $\boldsymbol{R}$ consists of the eigenvectors:

$$\boldsymbol{R} = (\boldsymbol{e}_1, \ldots, \boldsymbol{e}_M)$$

The first eigenvector $\boldsymbol{e}_1$ is referred to as the first principal axis, the i-th eigenvector $\boldsymbol{e}_i$ is called the i-th principal axis.

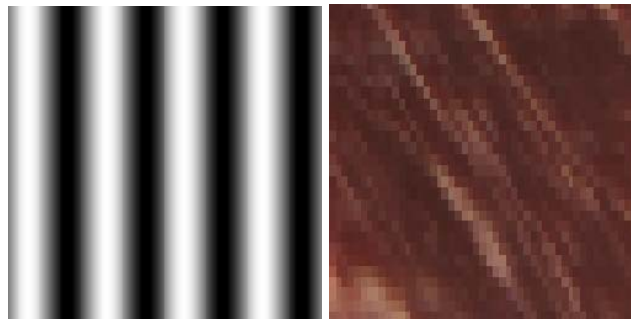

(a) (b)

Fig. 5.18. Examples of textures with orientation (adapted from [61]). (a) Gray level image with unidirectional sine waves. (b) Photography from Visible Human project showing abdominal muscle structures.

5.6 Texture Orientation

5.6.1 Introduction

Techniques of digital image processing can be used to characterize image areas, so-called textures, concerning the orientation of enclosed objects and structures (Fig. 5.18). Commonly, orientation at a position can be represented by a vector. The vector's magnitude describes the strength or reliability of orientation. Some representations use unit vectors, which allow to describe orientation by two angles, each in the range $[0, \pi]$.

An application of knowledge concerning orientation is found in anatomical modeling of skeletal and cardiac muscle structures. The macroscopic orientation of fibers is of importance for the assignment of anisotropic physical properties, e.g. electrical conductivity and mechanical material tensors.

In the following sections different methods are described for the detection and assignment of texture orientation. Rule-based methods are presented, which allow to create orientation fields by definition of problem specific functions. A manual method is introduced, which allows the interactive definition of orientation in three-dimensional datasets. Furthermore, techniques for the interpolation of orientation are presented starting from boundary conditions. The interpolation techniques are similar to techniques for solution of electrical field and mechanical problems.

5.6.2 Detection and Assignment

Texture Analysis. In the literature different techniques are proposed for detection of orientation, e.g. gradient extraction, quadrature filters, eigenvalues of inertia tensor and of covariance matrix [62, 63, 61].

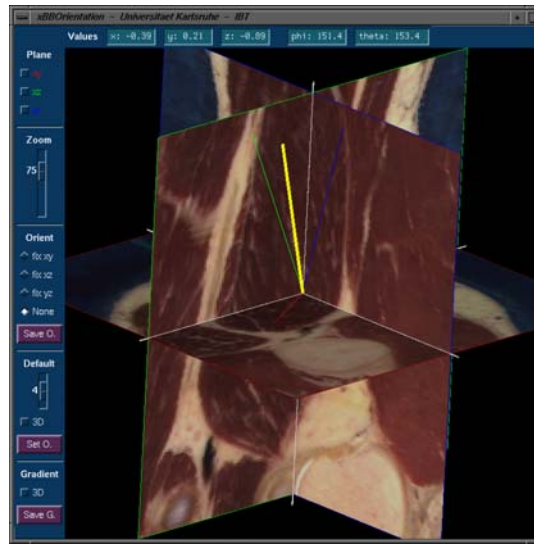

Fig. 5.19. Three-dimensional editor for manual assignment of orientations and their normals. Displayed are transversal, sagittal and frontal cuts in the photographs of the Visible Man dataset from different perspectives.

An obvious technique is the extraction of image gradient and using its normal as orientation. An utilization of this technique is possible only in two-dimensional images.

A detection with quadrature filters requires the construction of a set of linear filters. Each filter corresponds to a direction. The orientation is determined by averaging the vectors corresponding to the response of filters applied in the texture.

The detection techniques basing on extraction of inertia tensor and covariance matrix are similar in proceeding: The tensor and matrix, respectively, are determined in the texture. The eigenvectors and -values are determined (Sect. 2.4.4). If the smallest eigenvalue is multiple, texture orientation is indefinite. Otherwise orientation is defined by the eigenvector corresponding to the smallest eigenvalue.

Rule-Based Methods of Assignment. Rule-Based methods are commonly applied, if images provide insufficient information for texture analysis. These cases can arise e.g. if image resolution is small or if images show an insufficient contrast.

Manual Methods of Assignment. Manual methods can be applied in cases, which show a small reliability of the orientation detection, particularly if the complexity of the orientation field is too high for rule-based assignment.

A three-dimensional editor allows the interactive, manual assignment of orientations and their normals (Fig. 5.19). The editor displays transversal,

sagittal and frontal cuts in image datasets from different perspectives. Default values for the orientation and normals are created automatically by the upper detection technique basing on texture analysis. The covariance matrix is determined in a spherical region of the image and the eigenvector corresponding to the smallest eigenvalue serves a default orientation. The user has the option to manipulate the default values.

5.6.3 Interpolation

Commonly, after point-wise detection, rule-based and manual assignment an interpolation is performed. The interpolation serves to assign orientation in areas, which no orientation is a-priori known.

An efficient technique for interpolation utilizes two sets of restrictions [64, 61]:

- a set $\boldsymbol{R}_O$, which consists of points and their associated orientation
- a set $\boldsymbol{R}_T$, which consists of points and their associated normal of orientation

These sets of restrictions can be determined by detection, rule-based and manual assignment.

The interpolation starts with an initialization of the orientation dataset. The orientation of each voxel in this dataset is initialized with the orientation of the nearest point in the set $\boldsymbol{R}_O$.

The interpolation continues with averaging orientations in the 6-neighborhood. The average of neighboring orientations is calculated determining of their principal axis. The calculation is repeated until the changes of orientations between successive steps are negligible.

Attention is paid to the restrictions in each iteration. The orientation of voxels with restrictions represented by set $\boldsymbol{R}_O$ is unchanged during the interpolation. The orientation of voxels with restrictions represented by set $\boldsymbol{R}_T$ is determined by calculating the average orientation in the 6-neighborhood. The result is projected into the plane perpendicular to the given normal of the orientation.

The results of the interpolation with different sets of test data are shown in Fig. 5.20, 5.21, and 5.22. For each interpolation the number of iterations, orientations and normals of orientations are given.

(a) (b)

Fig. 5.20. Exemplary one-dimensional interpolations of orientations (adapted from [64]). (a) The interpolation was determined based on the given orientations O1 and O2. (b) The interpolation was calculated using the given orientation O3 and normal of orientation N1. The number of iterations amounted to 10.

(a) (b) (c) (d)

Fig. 5.21. Exemplary two-dimensional interpolations of orientations (adapted from [64]). The interpolation was calculated using as restrictions (a) two orientations and (b,c) four orientations. (d) The interpolation was determined using an orientation and a normal of orientation. The number of iterations was 20.

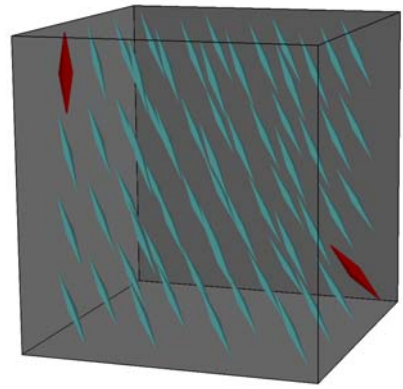

Fig. 5.22. Exemplary three-dimensional interpolation of orientations (adapted from [64]). The interpolation was determined from two given orientations. The number of iterations amounted to 20.

6

Cardiac Anatomy

6.1 Overview

The heart constitutes together with the blood vessels the cardiovascular system, which has the task of transporting blood in the body. In this system the heart acts as a cyclically working pump and as a blood reservoir.

The anatomy is closely coupled with its physiology. Depending on the stage of development, the species, the gender, and pathologies differences can be found in the anatomy as well as in the physiology. The differences concern the microscopic and macroscopic structures as well as the mechanical behavior. Anatomical differences of the mammalian heart are found depending on the posture of a species. The human heart is trapezoidal in silhouette, whereas in pigs a "Valentine heart" shape can be attributed [66]. The attachment of blood vessels is species dependent and interindividual variations are reported.

The anatomy of the heart can be described from different viewpoints, e.g. spatial, embryologic and physiologic. From a macroscopic spatial view a mammalian heart is located inside of the thorax and near to the lungs embedded by the pericardial sac (Fig. 6.1). Large blood vessels are connected to the heart. The heart itself is separated in two functionally and anatomically similar structures, the right and left halves, which represents the division of the blood circulation system in two different parts. The right half collects the deoxygenated blood from the body and pumps it to the lungs. The left half receives the oxygenated blood from the lungs to deliver it to the body. The left half has to generate a higher power, so it is the larger one.

The halves can be further divided into an upper and lower part, the so-called atria and ventricles, respectively. Therefore, a mammalian heart comprises of a left and right atrium, and a left and right ventricle. The atria collect the incoming blood, which is then transported to the ventricles. From these the blood is moved to supply the body and the heart itself. The ventricles are the primary generator of power resulting in relatively large muscular structures.

F.B. Sachse: LNCS 2966, pp. 119–155, 2004.

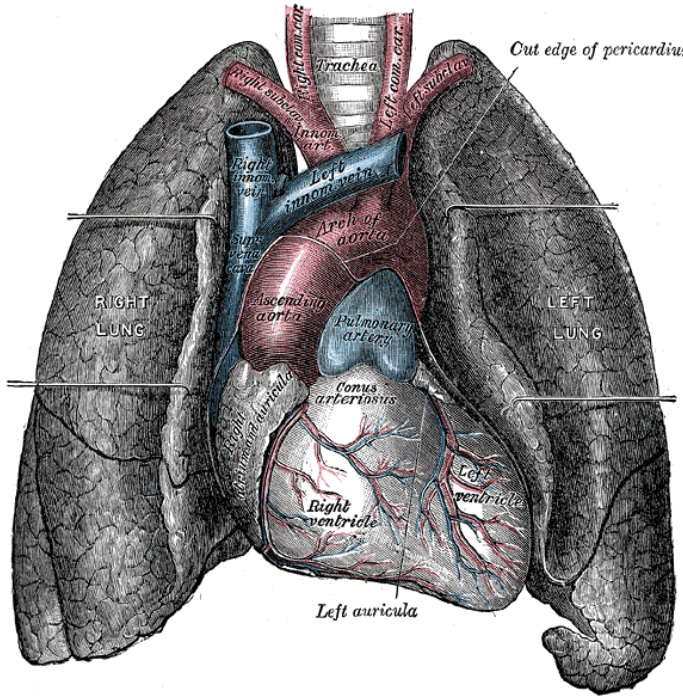

Fig. 6.1. Historical outline of human heart with vessels, lungs and spine (from [65]). The lungs were torn side wards to allow the sight onto the heart. The heart lies in between the lungs in the middle mediastinum and is enclosed by the pericardium.

The atria and ventricles are composed of walls surrounding a cavity, which is normally filled with blood. The walls consist primarily of a muscle structure, the myocardium, which is covered inside and outside by layers, the endocardium and epicardium, respectively. Therefore, a region in the myocardium can be classified in the three groups: subepicardial, midwall and subendocardial. The epicardium is part of the pericardial sac. The atrial myocardium is much thinner than the ventricular, with the myocardium of the left ventricle as the biggest structure of the heart.

The atria and ventricles are connected with blood vessels. Valves are located at different places in the cavities, which fulfill a controlling function for the blood flow.

The contraction of the myocardium causes the blood flow. The myocardium is built up by a muscular tissue richly pervaded by nerve fibers, blood vessels, capillaries, and lymphatic vessels.

From a microscopic view the myocardium consists primarily of discrete myocytes surrounded by a membrane. Aside from these fibroblasts, pericytes, nerve cells etc. are found. Fibroblasts make up the majority of cells of non-myocyte cells and reside in the interstitium [67].

Fig. 6.2. Isolated canine left ventricular myocyte (from [71]). The myocyte is stained with an antibody for the gap junction protein to visualize the distribution of the gap junctions.

The membrane of myocytes includes pores of different types, which allow the transport of diverse substances into and out of the cell. The shape and arrangement of myocytes are dependent on their location and type. The myocardium is surrounded by connective tissue structures forming the epi- and endocardium. Furthermore, connective tissue links mechanically the different cells in the myocardium. The connective tissue includes collagen and elastin fibers.

In the following sections a description of the microscopic and macroscopic structures of the heart is given. The cardiac myocytes, their connection by intercalated disks and connective tissue, their oriented and laminated arrangement as well as the gross anatomy of the heart focusing blood vessels, muscle and nervous structures are presented with respect to their role in electrophysiology and mechanics.

6.2 Microscopic Structures and Molecular Organization

6.2.1 Myocytes

Myocytes are commonly distinguished by their function, which is closely coupled with their anatomy. Resulting from functional reasons the volume, surface area and distribution of cellular components are differing, e.g. for atrial and ventricular myocytes. Differences can also be found depending on the pathologies, age and species [68, 69].

Myocytes assigned to the working myocardium produce primarily mechanical tension. The functions result in an increase of the volume ratio of the involved intracellular structures, i.e. contractile elements and providers of energy. Myocytes of the mammalian working myocardium are of irregular cylinder shape and branching processes are frequently occurring (Fig. 6.2 and 6.3) [70]. The length of myocytes is in the range between 50 and 120 μm and the diameter between 5 and 25 μm.

Specialized myocytes in the myocardium have the task of initiating and transmitting an electrical excitation. These functions result in an adaptation of the cellular shape and the involved cellular structures, e.g. the distribution and density of ionic channels. In the initiator of electrical excitation, the sinus node, different types of cells are observed, spider and spindle shaped, irregular cells [72]. In humans the spider cells have an extension of $92 - 102$ μm with a

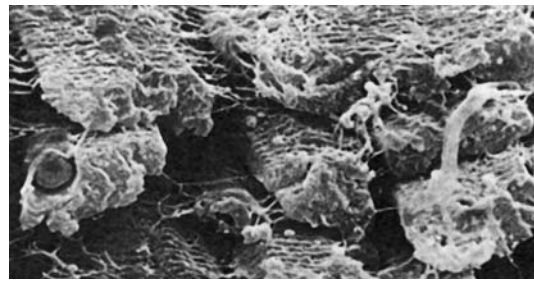

Fig. 6.3. Myocytes with connective tissue and capillaries in the myocardium of hamster (from [70]). The picture shows an area with a width of 42 μm and a height of 21 μm created with scanning electron micrography.

central body diameter of $7-9$ μm. The spindle shaped cells of the sinus node have a central body diameter of $5-7$ μm and an extension of $115-130$ μm.

In many locations the arrangement of myocytes is ordered and the cellular form leads to a macroscopic anisotropic electrical and elastomechanical behavior. Hence, many approximations for numerical simulation purposes describe myocytes by cylinders or bricks. Principal axes are assigned to determine the cellular orientation.

This section is focused on the mammalian cardiac myocytes of the working myocardium. Partly, comparisons with skeletal myocytes are carried out.

The myocytes are enclosed by the sarcolemma, which delimits the extracellular from the intracellular space. Myocytes are surrounded by the extracellular space, which contains e.g. collagen fibers, water, and electrolytes. In the intracellular space reside the nucleus, the mitochondria, the myofibrils, the sarcoplasmic reticulum and the cytoskeleton. The intracellular space is filled up with the sarcoplasm (myoplasm, cytoplasm) containing water, lipids, carbon hydrates, salts, and proteins, e.g. calcium binding calmodulin.

Sarcolemma. The sarcolemma represents a semi-permeable barrier, which is built up primarily by a phospholipid bilayer with a thickness of $3-5$ nm. Each phospholipid consists of two hydrophobic tails adhered to a hydrophilic head (Fig. 6.4). The hydrophobic tails are aligned and located inside. The hydrophilic head is found superficially of the bilayer (Fig. 6.5 and 6.6). The phospholipids can move laterally in the sarcolemma.

The bilayer contains peripheral proteins attached to the surface of the sarcolemma and transmembrane proteins spanning over the sarcolemma. The proteins are responsible are responsible e.g. for signaling and cell-adhesion. Important transmembrane proteins are ionic channels, exchangers, and pump proteins as well as gap junctions and receptors. Proteins relevant for cell-adhesion are cadherins, integrins, selectins, and immunoglobulins. These transmembrane and membrane-attached proteins are partly floating in the bilayer, but can also be fixed to elements of the cytoskeleton.

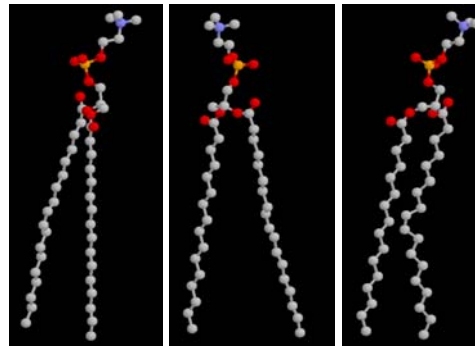

(a) (b) (c)

Fig. 6.4. Molecular structure of phospholipid from different view points (data from [73]). A phospholipid consists of two hydrophobic tails attached to a hydrophilic head. Atoms are color-coded (blue: nitrogen, red: oxygen, brown: phosphorus, dark grey: carbon and light grey: hydrogen).

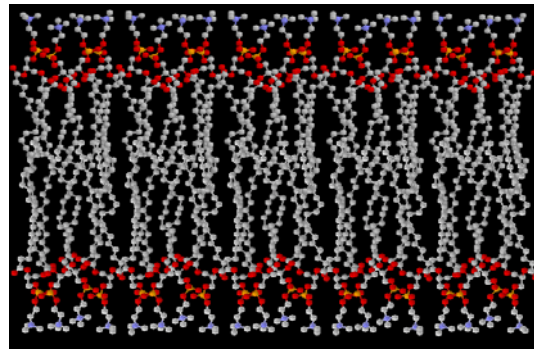

Fig. 6.5. Molecular structure of phospholipid bilayer with two-dimensional alignment (data from [73]). The phospholipids align itself in water such that the hydrophilic head is found superficially and the hydrophobic tails are located inside. Atoms are color-coded.

Specializations of the sarcolemma are the so-called transversal tubuli, which intrude into the myocyte primarily at the adjacencies of the Z disks [74]. The transversal tubuli infold the myofibrils and end near to the sarcoplasmic reticulum. Despite their name the transversal tubuli show not only transversal, but also horizontal components. The transversal tubuli feature differences in concentrations of transmembrane proteins, particularly responsible for calcium handling. In many species transversal tubuli are prevalent in ventricular, but absent or reduced in atrial myocytes and Purkinje cells. Myocytes from birds, reptiles and amphibians show no incidence of transversal tubuli.

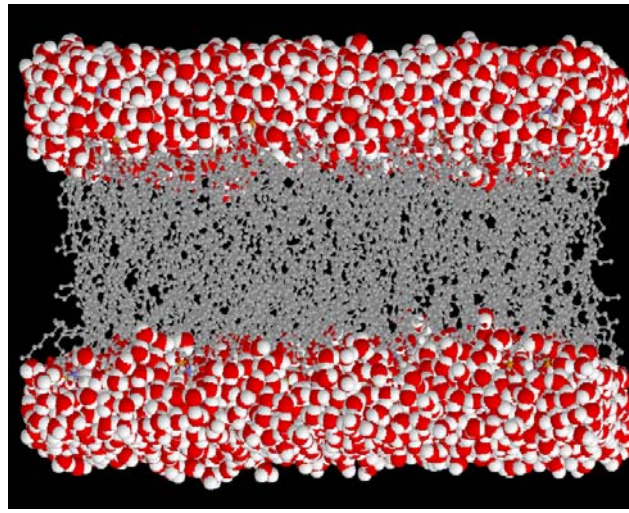

(a)

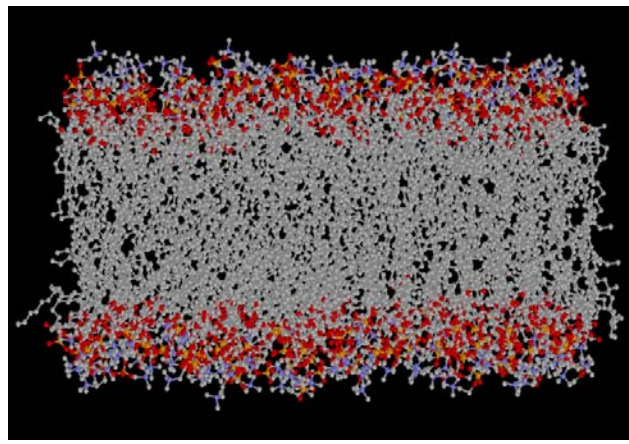

(b)

Fig. 6.6. Molecular structure of phospholipid bilayer in three dimensional alignment viewed (a) with and (b) without water molecules (data from [73]). Atoms are color-coded.

In mammalian ventricular cells transversal tubuli take commonly a large area of the sarcolemma. Depending on species 11 % to 51 % are occupied. The percentage volume of myocyte taken by the transversal tubuli ranges from 0.8 % for mouse to 3.6 % in rat. A smaller area of the sarcolema and of the volume is occupied in mammalian atrial cells.

Intercalated Disks. A further specialization of the sarcolemma is found at the intercalated disks, which are regions, where adjacent cells are mechanically

coupled. Here, intercellular channels, so-called gap junctions (Sect. 6.2.2), form a coupling of the intracellular space, which is of large significance for intercellular signalling. Further components of the intercalated discs are desmosomes and fasciae adherentes, which provide intercellular mechanical connection. In the intracellular space, Desmosomes and fasciae adherentes anchor intermediate filaments of the cytoskeleton and bundles of sarcomeric myofibers, respectively [75, 76].

Nucleus. The nucleus takes a small amount of the volume of myocytes, e.g. approximately $2-4$ % of atrial and ventricular myocytes. It has an ellipsoid shape, is centrally located and surrounded by a membrane.

Mitochondria. Mitochondria belong to the cellular organelles and are surrounded by a double-layered membrane. The outer membrane contains the protein porin, which allows passage of ions and small molecules up to 10 kD. The inner membrane, so-called cristae, is nearly impermeable and highly folded. The inner membrane includes ionic channel, pump and exchanger proteins, i.e. hydrogen pumps, calcium ionic channels, sodium-calcium, and hydrogen-sodium exchangers.

Mitochondria occupy approximately $14-20$ % of the volume of atrial and $25-36$ % of ventricular myocytes. They are cylinder shaped with a length of $0.3-1.7$ μm and a diameter of $0.2-1$ μm. The mitochondria are found near to the sarcolemma and between myofibrils, which results from their task as provider of energy for the myofilaments as well as the sarcolemmal and sarcoplasmic ion pumps. The cellular supply of energy is performed by components of the inner membrane of the mitochondria, which generate adenosine triphosphate (ATP) via oxygenation of nutrients.

Myofibrils. The myofibrils are tube shaped contractile elements taking a high part of the cellular volume, i.e. approximately $41-53$ % of the volume of atrial and $45-54$ % of ventricular myocytes (Fig. 6.7). The myofibrils have an approximate thickness of 1 μm and are divided every 2.5 μm by the Z disk into the sarcomeres.

Sarcomere. The sarcomeres contain the myofilaments (Fig. 6.8), which are of importance for the mechanical contraction. Furthermore, elongated proteins, i.e. titin and nebulin, are found in the sarcomeres [76].

Titin spans parallel to the myofilaments from the Z disks nearly to the center of the sarcomeres with a length of approximately 1 μm. Titin shows a large number of isoforms, e.g. heart muscle N2B isoform with a molecular weight of 2970 kD, soleus skeletal muscle isoform with 3700 kD, and novex-3 titin isoform with ≈ 700 kD. Titin is the third most abundant protein after myosin and actin in myocytes [78].

Nebulin with a molecular weight of $750-850$ kD regulates the assembly and specifies the lengths of the actin filaments [79]. Nebulin can be divided in three parts:

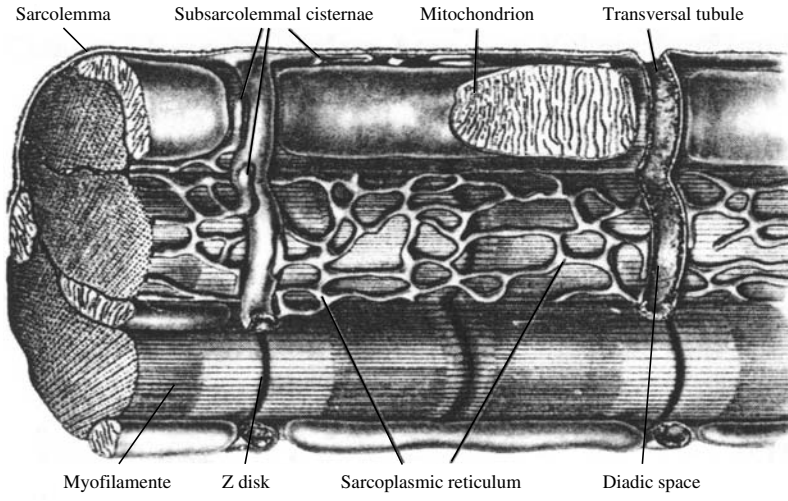

Fig. 6.7. Schematic diagram of intracellular structures of mammalian cardiac muscle (adapted from [77]).

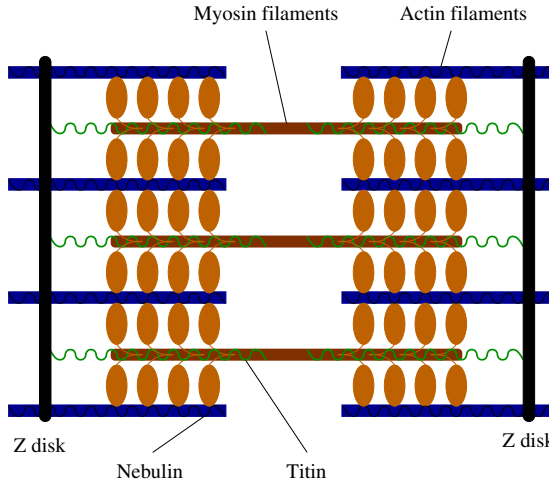

Fig. 6.8. Schematic view of sarcomere. The sarcomere includes myofilaments, titin and nebulin. Myofilaments are composed of actin and myosin filaments. The actin filaments, titin and nebulin are attached to the Z disks.

- Central part with a molecular weight of $\approx 700\ kD$. It associates with actin over the whole filament.
- N-terminal part. It extends form the central part to the ends of the actin filament in the sarcomere's center.
- C-terminal part with a molecular weight of $\approx 80\ kD$. It integrates with the Z-disk.

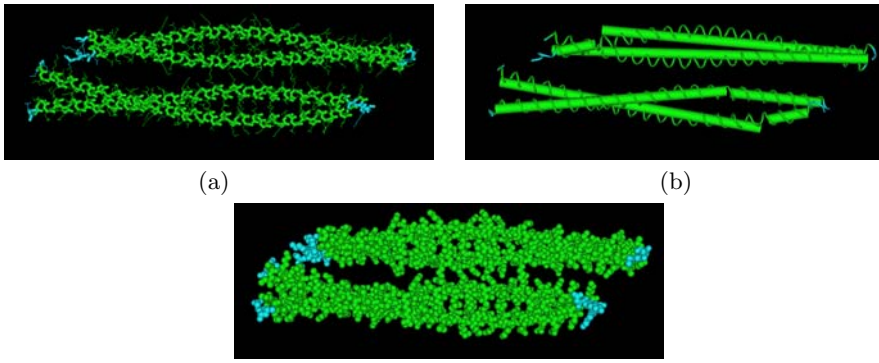

Fig. 6.9. Molecular structure of tropomyosin (data from [81]). The tropomyosin of species gallus gallus (chicken) is visualized from perpendicular to the filaments. The protein is composed of different amino acids, which are indicated by spheres. Different techniques are used for the visualization: (a) Hierarchic visualization, showing components dependent on the rank, (b) secondary structure, whereby only protein backbones are drawn, side chains and bases are off, (c) space filling, whereby the amino acids are shown as spheres.

These proteins provide - in conjuction with several further proteins - mechanical support for the myofilaments and influence the passive mechanical properties of myocytes [80].

Myofilaments. The myofilaments are composed of so-called actin (thin) and myosin (thick) filaments [68] (Fig. 6.8). The thin filaments lead from the Z disks approximately 1 μm towards the center of the sarcomere. The backbone of thin filaments is built up by two actin helices twined with concatenated long, flexible, coiled coil molecules, i.e. tropomyosin (Fig. 6.9). Tropomyosin is a rope-like protein with a length of $\approx 42\ nm$. A homo- and a heterodimer type of tropomyosin exist.

Monomer actin (G-actin) is a plate-shaped protein with a molecular weight of 42 kD and a size of approximately $5,5\ nm$ x $5,5\ nm$ x $3,5\ nm$. G-actin polymerizes forming helices (F-actin). In human six genes code the isoforms of actin, which is the most abundant protein in eukaryotic cells. Tropomyosin has a length of 40 nm and possesses seven actin binding sites. One binding site is found for troponin. Commonly, seven actin molecules and one troponin molecule are attached to each tropomyosin.

Troponin consists of three components: troponin T, troponin I, and troponin C. Troponin T is connected to the tropomyosin and the two further components. Troponin I inhibits interactions between actin and myosin. Troponin C is of importance for the initiation of mechanical contraction by binding of calcium.

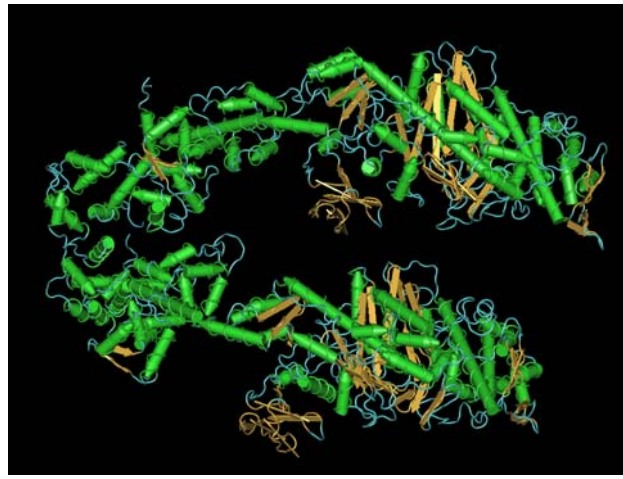

Fig. 6.10. Molecular structure of myosin II (data from [83]). The protein can be divided in a head, neck and tail region. The chains of the head and neck region of species gallus gallus are visualized.

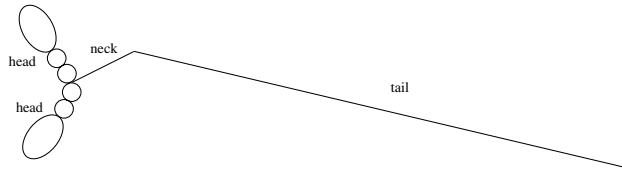

Fig. 6.11. Schematic view of myosin II. The protein myosin can be decomposed into two head, neck and tail regions.

The actin-tropomyosin arrangement is influenced by the binding of calcium to troponin. The arrangement of thin filaments is thought to be maintained by the protein nebulin [76].

The thick filaments have a length of approximately 1.6 μm and are centered in the sarcomere. They are arranged parallel to and between the thin filaments. The thick filament is composed primarily of the myosin molecule, which has a length of approximately 160 nm. A few hundreds of myosin molecules per thick filament are reported [82]. Thirteen types of myosin are distinguished by genome analysis, e.g. myosin I, myosin II, and myosin V, which are found in eukaryotic cells. All kinds of myosin can be subdivided into a head, neck and tail region (Fig. 6.11 and 6.10). Component of the thick filaments and therefore responsible for the contraction of cardiac, skeletal and smooth muscle is myosin II. Myosin II includes two pear-shaped heads showing an ATP and an actin binding site. The neck region with a length of circa 8 nm connects the heads with the two tails. The tails are coiled coil molecules and form the

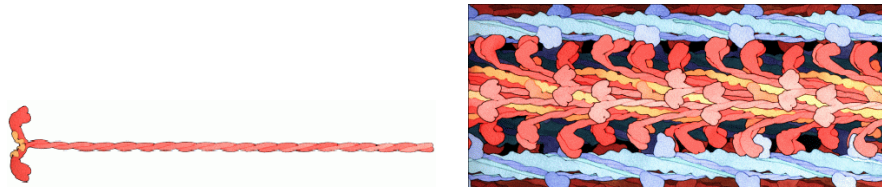

(a) (b)

Fig. 6.12. Schematic view of single myosin and actin-myosin filaments (adapted from [84]). (a) The myosin head and tail is shown in red, its light chains in orange and yellow. (b) The myosin filament is central and surrounded by actin filaments. The actin filaments consist of F-actin, tropomyosin and troponin.

main axis of the thick filaments. The thick filaments are bound via the protein titin to the Z disks [76].

Sarcoplasmic reticulum. The sarcomeres are enfolded by the sarcoplasmic reticulum, which can be divided into the longitudinal tubuli forming a mesh between the Z disks and the terminal cisternae (junctional sarcoplasmic reticulum, subsarcolemmal cisternae) located at the Z disks (Fig. 6.7). The space between the sarcolemma and the terminal cisternae is referred to as diadic space for cardiac myocytes and as triadic space for skeletal myocytes.

The volume occupied by the terminal cisternae and by the system of longitudinal tubuli is commonly smaller in cardiac than in skeletal myocytes [68]. The volume ratios of the terminal cisternae and the system of longitudinal tubuli are in the range of $0.03 - 0.5$ % and $0.62 - 9.47$ %, respectively, for mammalian myocytes of different species [68].

The sarcoplasmic reticulum is enclosed by a membrane containing calcium, potassium, chlorine and hydrogen ionic channel proteins as well as calcium pump proteins. 10-200 calcium release channels (ryanodine receptors) are thought to form a cluster of diameters up to 200 *nm*. This cluster is located where the junctional sarcoplasmic reticulum comes into close contact with the sarcolemma [85] and sarcolemmal L-type calcium channels. In rabbit ventricular myocytes it was demonstrated that more than one sarcolemmal L-type calcium channels is associated to each cluster of release channels [86]. Calcium release channels are regulated by various proteins, e.g. calmodulin, FK-506 binding protein, and sorcin. The other ionic channel and pump proteins are distributed throughout the membrane. The protein calsequestrin with high affinity and high capacity for calcium is found inside, primarily in the terminal cisternae.

Sarcolemmal Ionic Channels, Exchangers and Pumps. The sarcolemma includes pore forming proteins, i.e. ionic channels, exchangers and pumps, which are specified by the ion type, which can pass through, by their specificity for these ions, and by their opening and closing characteristics (Sect. 7.2.1). Exemplary ionic channels are the sodium, potassium, calcium, and chlorine channels with the different variants. The ionic channels, exchangers and pumps are

dynamically expressed by activation of their corresponding genes due to aging and physiological parameters.

Sodium channels are found in the cell membrane of all excitable tissue of vertebrates, e.g. myocytes and neurons, but not in monads [87]. In myocytes they are located primarily on the surface sarcolemma and not in the transversal tubuli. The mammalian genome includes minimally six voltage-dependent sodium channel genes. Three of these genes are found in humans. The density of sodium channels ranges from 100,000 per ventricular myocyte to 1,000,000 per Purkinje fiber. A molecular weight of 240 kD is reported [88]. The domain of the channels is not restricted to the membrane region, but they extend significantly in the intra- and extracellular space.

Ionic channels in the sarcolemma with a high specificity for calcium are divided into two types, discriminated by their electrophysiological behavior: L- and T-type [89]. L-type calcium channels (dihydropyridines receptors) are expressed in all cardiac myocytes. The density of L-type channels is approximately 30,000 per ventricular myocyte. L-type calcium channels consist of 5 subunits with a summary molecular weight of 410 kD. The density in the transversal tubuli is four times higher than on the surface sarcolemma. T-type channels are found in atrial, nodal, Purkinje, and smooth muscle cells. In ventricular myocytes T-type channels are expressed at low or undetectable levels [90].

Potassium channels in the sarcolemma show a large variety [91]. Twenty different variants are known only for voltage dependent channels. The molecular structure of a potassium channel is illustrated in Fig. 6.13.

Furthermore, the sarcolemma includes ion exchanger proteins, e.g. the Na-Ca exchangers, which are located at the openings of the transversal tubuli [92]. A Na-Ca exchanger consists of approximately 1000 amino acids with an approximate weight of 120 kD. An average density of up to 500 exchangers/μm^2 is reported. The mammalian genome includes minimally three Na-Ca exchanger genes.

Pumps in the sarcolemma are e.g. the Na-K and calcium pump, which consume ATP to transport ions. The Na-K pumps of myocytes are primarily located on the surface sarcolemma and not in the transversal tubuli. The calcium pump protein has a weight of 138 kD [68].

Cytoskeleton. The cytoskeleton pervades the intracellular space anchoring the myofibrils, nucleus, mitochondria, and sarcolemma. The cytoskeleton consists primarily of microfilaments, microtubules, and intermediate filaments [76]. The microfilaments are built up of G-actin, which polymerizes as helix-shaped F-actin. The microtubules are composed of the protein tubulin, the intermediate filaments of lamin and desmin. The desmin containing intermediate filaments are linked to the desmosomes of the intercalated disks.

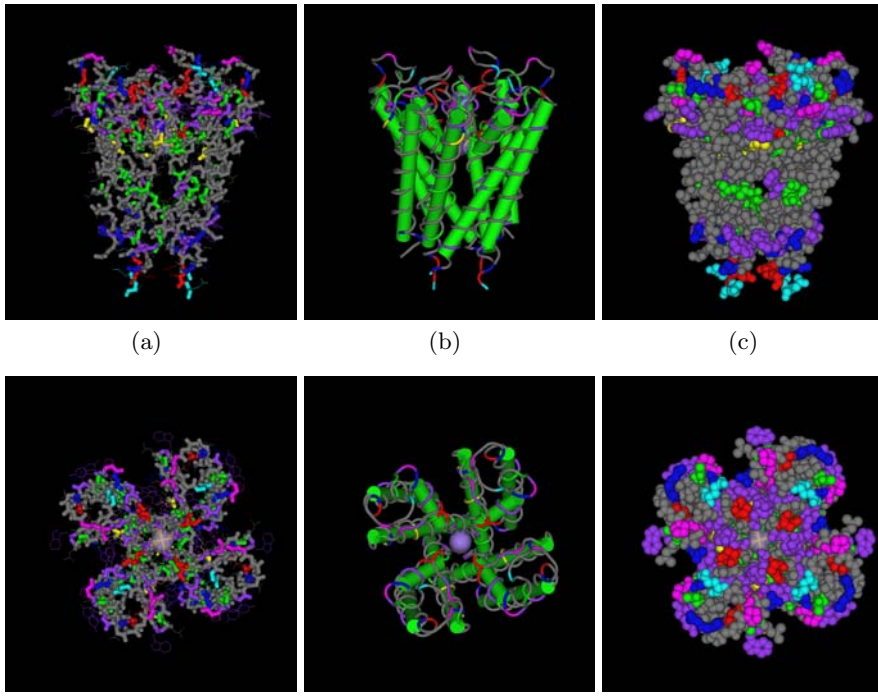

Fig. 6.13. Molecular structure of potassium channel (data from [81]). The so-called Kcsa potassium channel of the bacterium Streptomyces Lividans consists of four identical domains forming a pore. The channel is visualized (upper row) from perpendicular to the ion channel and (lower row) from extracellular in direction of the channel. The channel protein is composed of different amino acids, which are color-coded. Different techniques are used for the visualization: (a,d) Hierarchic visualization, showing components dependent on the rank, (b,e) secondary structure, whereby only protein backbones are drawn, side chains and bases are off, (c,f) space filling, whereby the amino acids are shown as spheres. The central located, large sphere indicates a potassium ion inside of the channel.

6.2.2 Gap Junctions

The intracellular space of adjacent myocytes is coupled by gap junctions (nexus), which are located by bundle at the intercalated disks [94, 95] (Fig. 6.14). Intercalated disks are disk shaped segments, which mechanically couple cells [96]. Mainly, the disks can be found at or near to the ends of myocytes [97] (Fig. 6.2).

A gap junction is cylinder or barrel shaped with a diameter of $1.5-2.0\ nm$ and a length of approximately $2-12\ nm$. A molecule of atomic weight of up to $1\ kD$ can pass through the gap junction [98, 99], e.g. nutrients, metabolites, and ions.

Fig. 6.14. Microscopic section of 1 μm thickness in canine left ventricular myocardium (from [93]). The arrangement of myocytes and the distribution of gap junctions are illustrated. The arrows depict intercalated disks, where the gap junctions are located by bundle. Longitudinal gap junctions are marked by horizontal arrows, transversal gap junctions by vertical arrows.

A gap junction is built up by two hemi-channels, so-called connexons, piercing the sarcolemma of the involved cells. The connexons are formed by six integral membrane proteins, so-called connexins. More than one dozen of connexins have been cloned, which are named by their atomic weight ranging from 25 to 50 kD. The permeability of gap junctions is dependent on their assembly.

The most abundant connexin in the mammalian myocardium is connexin43, which is also expressed in ovary, uterus, kidney, and lens epithelium. Connexin43 was found to be not expressed in atrioventricular node and bundle branches of rats [100]. Further members of the connexin family expressed in the heart are: connexin37, connexin40, and connexin45. Connexin45 is found abundantly in embryonic hearts. In adult hearts connexin45 is expressed mostly in atrial, His bundle and Purkinje cells, but only in a small amount in the ventricular cells. Connexin32 is found in liver, stomach, kidney, and brain, but not in any part of the heart [100].

A half-life of $\approx 1.3\ h$ was determined for cardiac connexin43 [101]. Down-regulation of connexin43 and up-regulation of connexin45 is demonstrated in heart failure [102]. In ischemic cardiomyopathy down-regulation of connexin43 and up-regulation of connexin40 is reported.

In the myocardium each myocyte is coupled by gap junctions non-uniformly with other myocytes, e.g. in canine a myocyte is coupled with 9.1 ± 2.2 myocytes [103]. A distinction can be made between longitudinal and transversal gap junctions. A longitudinal gap junction is oriented in approximately the same direction as the first principal axis of adjacent myocytes, a transversal gap junction is oriented perpendicular thereto. The density and distribution of orientations of gap junctions differ depending on the tissue, e.g. the den-

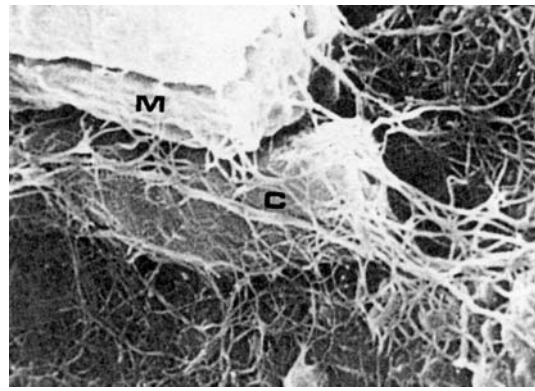

Fig. 6.15. Cardiac collagen network in the rabbit left ventricle (from [70]). The interconnection between a myocyte (M) and capillary (C) is visualized with scanning electron micrography. The picture shows an area with a width of 1.3 μm and a height of 0.95 μm.

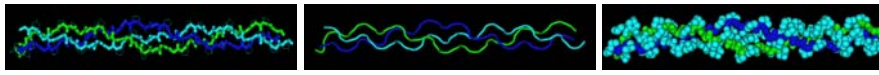

(a) (b) (c)

Fig. 6.16. Molecular structure of collagen (data from [81]). The protein collagen consists of three chains forming a triple helix. Each chain is over 1400 amino acids long, only 20 are shown. Different techniques are used for the visualization: (a) Hierarchic visualization, showing components dependent on the rank, (b) secondary structure, whereby only protein backbones are drawn, side chains and bases are off, (c) space filling, whereby the amino acids are shown as spheres.

sity in the sinus and atrioventricular node is smaller than in the ventricular myocardium. The average density of gap junctions in longitudinal orientation is larger than in transversal orientation [103]. The average length of longitudinal gap junctions is smaller than the length of transversal gap junctions. Both circumstances lead to a macroscopic anisotropic, electrical intracellular conductivity.

6.2.3 Connective Tissue Structures

The myocardium is pervaded and surrounded by a mesh of extracellular collagen fibers, which are composed of a multitude of collagen fibrils. Collagen takes $2-5$ % of the weight of the heart. Collagen is a protein consisting of over 1400 amino acids (Fig. 6.16) and is synthesized by the cardiac fibroblasts. Furthermore, fibers of elastin draw through the myocardium. The content and the structure of the connective tissue are dependent on age, pathologies and species.

Both, collagen and elastin are fibrous proteins of the extracellular matrix, which is a determinant for the viscoelastic behavior of the myocardium. The network serves for the mechanical coupling of the myocytes, capillaries, and lymphatic vessels (Fig. 6.15).

Collagen fibrils have a thickness ranging from 30 to 70 nm [70]. The fiber thickness is in physiologic cases between 120 and 150 nm. An increase up to $250-300$ nm is possible in pathophysiologic cases, e.g. in case of hypertrophy, hypertension and myocardial infarction [104, 105].

The density of collagen fibers is depending on the tissue. E.g. a small density can be found in papillary muscles and trabeculae, a high density in the left ventricular myocardium, the endo- and epicardium [70, 106].

The connective tissue can be divided, according to the classification in skeletal muscles, into three different groups:

- Endomysium. The collagenous network surrounding a single myocyte as well as interconnecting a myocyte with neighboring myocytes or capillaries is referred to as endomysium. Often the connections are starting near to the Z disks perpendicular to the membrane [107]. The length of the connections is in the range $120-150$ nm.
- Epimysium. A layer of collagen and elastin fibers forming the epimysium covers the subendo- and subepicardial myocardium. The layers are named endocardium and epicardium, respectively.
- Perimysium. Bundles of perimysal collagen fibers couple the endomysium with the epimysium and envelop groups of myocytes. The grouping of myocytes resulting from the enveloping leads to a lamination of the myocardium. The perimysal collagen fibers connecting a myocyte inside of a group with a myocyte outside are less frequently occurring. Furthermore, a larger distance can be ascertained. The fiber length is depending on the location, e.g. in canine a fiber length of 31 ± 9 μm can be found in subendocardial ventricular myocardium, a length of 27 ± 10 μm in the midwall and of 17 ± 3 μm in the subepicardial myocardium [108]. Perimysial collagen fibers showed in a study of ventricular trabeculae of rat to be wavy in a two-dimensional manner rather than coiled [109]. The fibers straighten by increased strain. Extension of fibers is limited at sarcomere length of 2.3 ± 0.04 μm.

6.3 Macroscopic Structures

6.3.1 Ventricles

The mammalian heart includes two ventricles, where the atria and different blood vessels are attached (Fig. 6.17 and 6.18). The right and in particular the left ventricle are the anatomically and functionally dominant structures of the heart. Each ventricle consists of walls with openings, so-called ostia,

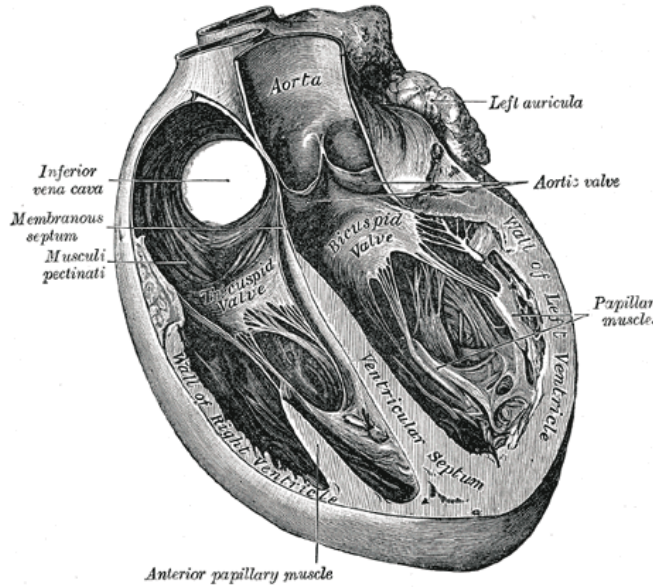

Fig. 6.17. Historical outline of the opened human heart with the atria and ventricles (from [65]).

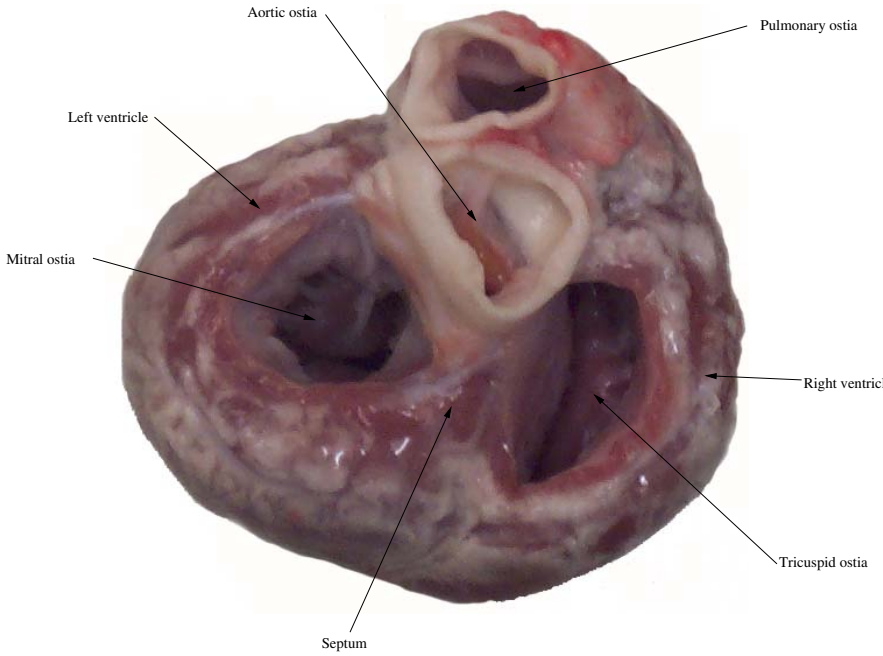

Fig. 6.18. Superior view on ventricles and ostia of pig heart.

surrounding a cavity [110]. The walls are primarily built up of myocardium enclosed by the epicardium and endocardium.

The weight, shape and size of the ventricles and the topology of their internal components is depending on the species. Furthermore, differences can be found e.g. addicted to sex, age, and pathologies. The walls and the cavity of a right ventricle are commonly smaller than a left resulting from the difference in power requirements.

The ostia are the major points of attachment. The left ventricle has two ostia, the mitral and the aortic ostium. Also, the right ventricle has two ostia, the tricuspid and the pulmonary ostium. The ostia are named by the attributed valve.

Attached to the wall are intracaval structures, i.e. the papillary muscles and trabeculae. The papillary muscles can be compared with pillars basing with one end in the wall. At the other end they are connected with tendons leading to the atrioventricular valves. In humans three papillary muscles can be found in the right ventricle and two in the left. The trabeculae are composed of branching small muscle bundles, which pervade the ventricular cavities similar to a mesh.

In the working myocardium of the ventricles an oriented and laminated structure can be found [111, 112, 113, 114, 108, 115]. The orientation and lamination of the myocytes should be interpreted with a macroscopic, averaged perspective, neglecting branching structures and irregular cellular shapes. This perspective is often taken for cardiac modeling, e.g. continuum modeling of electrophysiology and structure mechanics taking anisotropy into account. The orientation and lamination can be determined by histological studies of surfaces of tissue sections and by recently developed imaging techniques (Sect. 6.4.4).

The orientation of myocytes in the ventricular wall is dependent on the depth [111, 112]. The orientation can be quantitatively described by the helix angle of a fiber path through the myocardium parallel to the local epicardium. Alternatively, the orientation is determined by angles in a local coordinate system in surface layers of ellipsoids approximating the ventricles. Hereby, the orthogonal local coordinate system for the assignment of angles at a given point is constructed by a vector parallel to the principal axis of the ellipsoid and a second vector, orthogonal to the principal axis and the surface normal. An angle of $\pm$ 90° denotes an orientation towards the base of the heart, an angle of 0° stands for an equatorial orientation.

An angle of approximately −90° was measured for the orientation of myocytes in the plane of the left ventricular epicardial myocardium of pig and canine in systole, an angle of 90° for the endocardial myocardium. In human left ventricular myocardium an angle of −75° was measured epicardially, 70° endocardially. In the right ventricular myocardium of guinea pig an angle of −45° and 90° was measured epicardially and endocardially, respectively. An angle of 0° was reported in the midwall of all these species. Commonly, a smooth transition of the angle from epicardium to endocardium is measured.

Fig. 6.19. Crista terminalis and musculi pectinati in opened right atrium of pig.

In the apex cordis the orientation leads to two vortices, one for each ventricle. The dorsal and anterior interventricular sulcus show a bifurcation of myocardial fibers. In the papillary muscles a longitudinal orientation of myocytes was found, i.e. in direction of the first principal axis.

The lamination of the myocardium results from the grouping of myocytes. The grouping is caused by the enveloping of groups of myocytes by the perimysal collagenous network. In canine the thickness of a layer amounts to 4 ± 2 myocytes [108]. No significant variation is found through the wall depth. In the papillary muscles a lamination was nowhere observed in anatomical studies.

6.3.2 Atria

The mammalian heart includes two atria, which are attached above the ventricles and are connected with blood vessels of different types (Fig. 6.17 and 6.19). Between the atria and the ventricles resides the atrioventricular septum, which consists of fibrous connective tissue. The atrioventricular septum is punctuated only at the His bundle. The cavities of the atria and ventricles are separated by the atrioventricular valves.

An atrium can be divided into an ear shaped, conical part, the auriculum, and a further part, the atrium proper. The two atria are separated by the atrial septum, which includes the fossa ovalis. The fossa ovalis consists of fibrous tissue and is formed post natal by closing of the foramen ovalis, which

acts before as an open connection for the blood flow between the right and left atrial cavity.

The atrial walls consist primarily of muscle bundles, which are arranged in a complex manner. The orientation of the myocytes follows the local orientation of the muscle bundles. The averaged thickness of the bundles is larger in the left atrium, but some bundles of the right atrium are the strongest. The dominant muscle structure, the crista terminalis or right atrium terminal crest, can be found subendocardial of the right atrium. In humans a thickness of $5 - 8\ mm$ was measured. The walls measure about $2\ mm$. The crista terminalis forms a bow starting at the orifice of the superior vena cava near the sinus node. Attached to the crista terminalis are the musculi pectinati, which branch off nearly perpendicular and progress like a fan. In humans the area of maximal thickness in the left atrium is the frontal wall [116]. A structure similar to the crista terminalis is not found in the left atrium. Furthermore, the musculi pectinati of the left atrium are smaller developed. The interatrial bundle, the so-called Bachmann bundle, connects the two atria as strong muscle structure with a subepicardial and anterior course [117]. Its root can be found near to the sinus node. In the left atrium the bundle surrounds the auriculum and ends up in the musculi pectinati [118]. The Bachmann bundle plays an important role in the interatrial electrical excitation propagation. Circumferential muscle bundles can be found at the ventricular ostia.

The orientation of myocytes in the mammal atria was examined in a large number of anatomical studies [117, 118, 110, 119, 120, 116, 121]. The results show a relatively species independent arrangement, reflecting the configuration of the muscle bundles:

- circumferential orientation in the mitral and tricuspidal ostia
- longitudinal orientation in the vena cava superior and inferior
- longitudinal orientation in the crista terminalis
- circumferential orientation at the atriocaval junctions of the pulmonary veins
- longitudinal orientation of the Bachmann bundle

A lamination of the atrial myocardium similar to the ventricular lamination is not reported in anatomical studies.

The triangle of Koch is a region of high importance for the clinical atrial anatomy. The borders of the triangle are the tendons of Todaro, the septal leaf of the tricuspid valve and the opening of the sinus coronarius. The tendons of Todaro are commonly found between the eustachian and thebesian valve. Because of significant individual variations of the tendons of Todaro, i.e. absent or multiple, the concept of triangle of Koch as a clinical landmark is subject of recent controversy [122, 123].

6.3.3 Blood Vessels

The blood vessels attached to the heart are named by the direction of the transported blood. Vessels with a blood flow in direction to the heart are called veins; those with a flow away from the heart are called arteries.

In the atria and ventricles blood is collected and pumped. The atria receive blood from the veins, which is then transferred to the ventricles. The ventricles pump the blood in the arteries.

The right atrium is attached to the vena cava superior and inferior. Furthermore, the sinus coronarius and the thebesian veins of the vascular system of the heart end in the right atrium. Attached to the left atrium are the venae pulmonalis. In humans commonly four veins are found.

The right ventricle transports blood through the arteria pulmonalis to the lungs. The left ventricle is attached to the aorta to transfer the blood in the body.

The anatomy of the cardiac vessel system is subject to species dependent and inter individual variations. In humans the arteria coronaria sinister and dexter start at the root of the aorta. The coronary arteries supply the atrial and ventricular walls with blood. Commonly, the arteria coronaria dexter transports blood to the right ventricle, in septal regions and the left ventricular dorsal wall. The other regions are supplied by the arteria coronaria sinister.

6.3.4 Valves

Valves are found in different areas of the heart. The valves control the blood transport by opening and closing. Variations of their attachment and their configuration are found depending on species and inter individually. The valves are primarily built up by collagen.

The atrioventricular valves are located between the atrium and ventricle. They are attached through the chordae tendinae with papillary muscles. The free borders of the leaflets atrioventricular valves are directed into the ventricles. The valve between the left atrium and ventricle is named mitral or bicuspid valve, which consists in humans of two leaflets, anterior and posterior. The tricuspid valve is located between the right atrium and ventricle. In humans this valve consists of three leaflets, antero-superior, septal and inferior.

The aortic valve is located in the aorta near to the left ventricular aortic ostium. In humans three leaflets are distinguished: posterior, anterior left and right. The pulmonary valve is attached in the pulmonary artery near to the right ventricular pulmonary ostium, which shows as the aortic valve three leaflets in humans: posterior, anterior left and right. The aortic and pulmonary valve are semilunatic shaped. The free borders of their leaflets are directed into the vessel.

Furthermore, valves in the right atrium are known, which however are not present in all species and individuums. In humans the eustachian and

thebesian valve are reported. The eustachian valve is located between the vena cava inferior and the right atrium over spanning approximately half of the vein. The thebesian valve, which is also labeled valvula foraminis ovalis, is found between the sinus coronarius and the right atrium.

6.3.5 System of Excitation Conduction and Initiation

The cardiac system of excitation conduction and initiation consists of specialized myocytes. The specialization concerns the cellular anatomy, the intercellular coupling and the cellular electrophysiology.

The sinus node as the initiator of the physiologic electrical excitation is found in the human heart at the orifice of the superior vena cava [124]. Variations of position, shape and size are found in humans, among other things the node size is depending on the heart size. A flat, half oval and beet shape is reported. An averaged length of 30 mm, width of 3 mm and thickness of 2 mm is measured [125].

In the rabbit, the node is located in the posterior right atrium, medial to the crista terminals [72]. A length of $4-5$ mm, a width of $1-2$ mm and a thickness of 200 μm is reported. A similar position of the sinus node is found in dogs. A length of $15-20$ mm, a width of $5-7$ mm and a thickness of 200 μm is observed.

The sinus node consists of interweaving cells, which is obvious e.g. in photomicrographs. Two principally distinct types of myocytes were identified in the sinus node, i.e. spider and spindle shaped cells (Sect. 6.2.1). The myocytes are packed in a matrix of connective tissue, which takes 40 to 50 % of the volume. Furthermore, the sinus node is richly innervated.

The myocytes of the sinus node are connected via gap junctions with the myocytes of the atrial working myocardium. The crista terminalis and the Bachmann bundle serve as conduction pathways to the atrioventricular node and left atrium, respectively [121].

The atrioventricular node is located in the right atrium and at the interatrial septum near to the opening of the sinus coronarius. In humans the apex of the triangle of Koch is used as a landmark. Three different types of cells were found in the atrioventricular node: transitional cells as well as in the distal segment located mid-nodal and lower nodal cells [127]. The histologically motivated distinction is further confirmed by electrophysiological differences. The atrioventricular node can be divided into an atrial and distal segment. The atrial part of the node is attached via transitional cells with the atrial myocardium. The distal part is surrounded by fibrous tissue and descends in the His bundle. The distal nodal cells are continuous with the cells of the His bundle.

The His bundle is insulated by sheaths of fibrous tissue and penetrates the heart skeleton between the atria and ventricles. The His bundle is the root of the Tawara bundle branches, which subdivides first into the left and right bundle branch located in the left and right subepicardial myocardium,

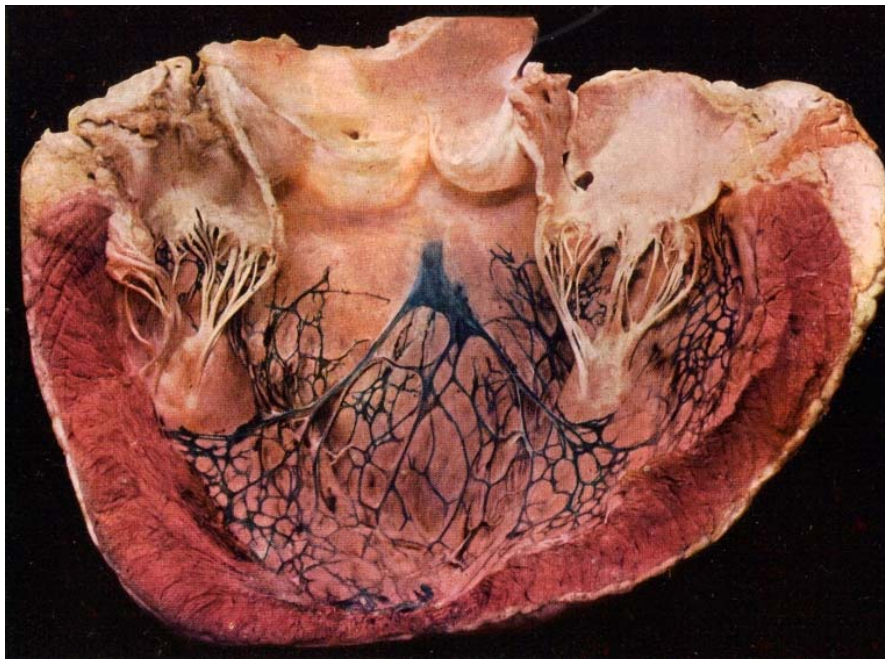

Fig. 6.20. Historical photography of an opened left ventricle from cow with the valves, papillary muscles, and the system of excitation conduction (from [126]). The system is colored with blue ink.

respectively [128, 121]. The branching takes place several fold (Fig. 6.20) resulting in a fan like distribution. The branches are isolated from the working myocardium by fibrous tissue. The ends of the branches are connected with the medial and apical subendocardial located Purkinje cells, which are linked with myocytes from the working myocardium by gap junctions. In humans the right Tawara bundle branch penetrates in the ventricular septum dividing commonly in three branches, which progress in the right septum as well as in the right ventricular latero-ventral and dorsal papillary muscles. The left branch progresses primarily endocardially in the left ventricular, frontal and dorsal papillary muscles. Some fibers pass through the left cavity.

6.3.6 Nervous System

The heart is innervated by sympathetic and parasympathetic nerves stemming from the truncus sympathicus and nervus vagus, respectively [125]. The cardiac nervous structures include efferent and afferent fibers as well as ganglions.

Partly, the nerves are located extracardial, e.g. at the superficial coronary arteries. Furthermore, nerves are found intracardial, e.g. in the myocardium,

at the coronary arteries in the myocardium, in the endocardium and the valves.

Efferent nerves influence large parts of the cardiac conduction system, i.e. the sinus and atrioventricular node, His bundle and Tawara bundle branches [129]. Regional differences of the innervation are reported, e.g. the innervation in the central part of the sinus node and in the transitional part of the atrioventricular node is significantly larger than in the peripheral parts and in the compact region, respectively [129].

Afferent fibers transport information concerning ischemia and pressure. Normally, the fibers are found in contiguity with the efferent fibers of the same root. Fibers responsible for detecting ischemia are reported primarily in the sympathetic nerves. Fibers with the task of measuring pressure are located near to the aorta, the Purkinje fibers, the right atrium and the left ventricle.

6.4 Modeling of Anatomy

6.4.1 Overview

Detailed modeling of the macroscopic cardiac anatomy is commonly performed on base of medical imaging systems, which are used in clinical routine and research. The resulting data is transformed with methods of digital image processing to obtain a representation of anatomy, which is suitable for the target application.

Different levels of spatial description can be distinguished ranging from analytical, comprehensive approaches to detailed descriptions on base of millions of volume elements. In the next sections exemplary analytical models are described, an introduction to the modeling sources is given and some models created by digital image processing are demonstrated.

6.4.2 Analytical models

Model of left ventricle. An example of analytical description is the approximation of left ventricle by crop of two confocal truncated ellipsoids [130]. The ellipsoid's focus length d is defined as $d = \sqrt{a^2 - b^2}$ with the ellipsoid's minor radius b and major radius a. The truncation of an ellipsoid is quantified by a truncation factor f_b specified by $f_b = l_{be}/l_{ea}$ with the distance from basal plane to equator plane l_{ab} and the distances from equator plane to apex l_{ea}. Commonly, a truncation factor f_b of 0.5 is chosen. This analytical approach can be transformed to a description on base of volume elements (Fig. 6.21). A description of the macroscopic orientation and lamination of myocytes can be added taken into account results from anatomical studies (sect. 6.3.1).

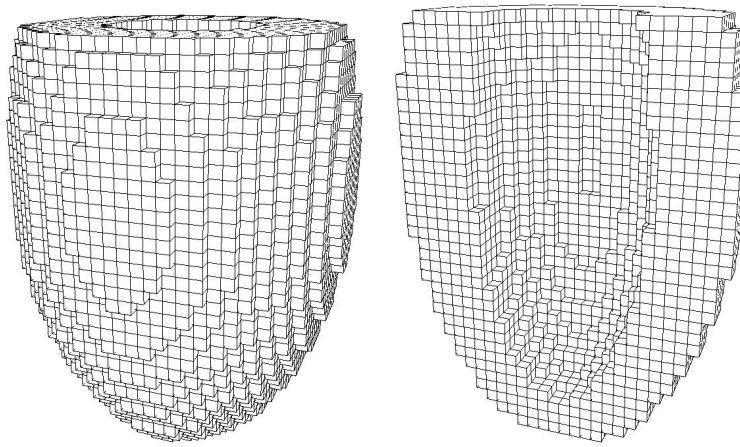

Fig. 6.21. Model of left ventricular anatomy by crop of two confocal truncated ellipsoids. The (a) full and (b) sectioned model is shown in wire frame representation. The model consists of 30 x 30 x 38 cubic elements.

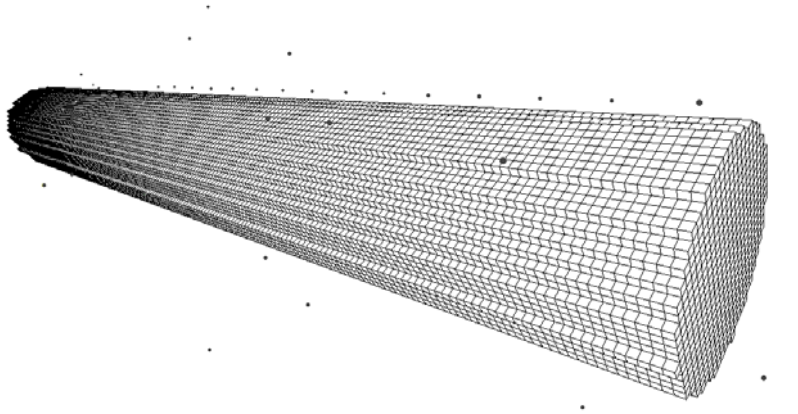

Fig. 6.22. Cylinder model of papillary muscle in wire frame representation. Surface and further points are shown, which were localized using a computer-controlled micromanipulator. The model is created based on points at the surface of the muscle using numerical minimization techniques.

Biventricular model. Analytical biventricular models can be created by extension of the analytical left ventricular model in such a manner that a description of the right ventricle is added [131]. The geometry of the right ventricular model is approximated by crop of two confocal truncated ellipsoids, which are then cropped with the left ventricular model. Similar strategies and parameters for determining the orientation of myocytes in the two ventricles can be applied as in the left ventricular model.

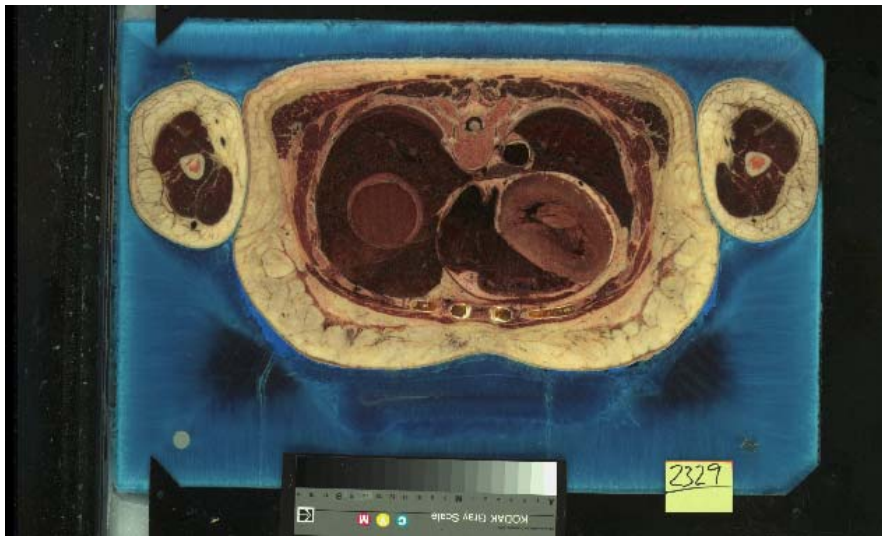

Fig. 6.23. Exemplary cryosection of the Visible Female data set with a transversal view of the thoracic region. The section was performed after freezing of the corpse. The blue gel was used to fix the body and is furthermore necessary for the cryosection to image only in plane information.

Model of papillary muscle. The anatomy of a papillary muscle can be approximated by a cylinder [131]. Parameters of the cylinder were determined by surface points. These points were acquired with a computer-controlled micro-manipulator. The parameterization of the cylinder was performed by numerical minimization of an error function, which uses distances between the cylinder's surface and the given points. The model was extended by incorporation of macroscopic fiber orientation. In accordance to anatomical studies of papillary muscles a fiber orientation parallel to the muscle's first principal axis was included. A lamination was neglected, because it was not observed in anatomical studies. This analytical description was transformed to a description on base of volume elements (Fig. 6.22).

6.4.3 Imaging Systems and Data Sources

Commonly, ultrasonic (US), magnetic resonance (MRT), and computed tomography (CT) are used for the imaging of the heart. These imaging systems use the tissue dependent variations of the acoustic impedance leading to reflection of ultrasonic waves and of their scattering, of the absorption of X-rays, and of the resonance behavior of nuclei to get information of the tissue distribution inside a body.

An alternative data source for the macroscopic modeling of human anatomy provides the Visible Human Project of the National Library of Medicine,

Bethesda, Maryland (USA) [33]. The ongoing project started 1990 and aims at the computerized representation of human bodies, which should be made available as standard for the medical and technical research. In a first approach selected corpses were imaged by CT and MRT as well as by specific photographic techniques. The selection of corpses was made by different criteria, e.g. normal height and weight, no pathologic changes in anatomy, and age between 20 and 60.

The Visible Human Project forms a base of the MEET Man Project (Models for Simulation of Electromagnetic, Elastomechanic and Thermic Behavior of Man) of the Institut für Biomedizinische Technik, Universität Karlsruhe (TH) [26, 132]. The project aims at the generation of anatomical and physical models of the human body suitable for numerical calculation of physical fields. A focus of the MEET Man project is the computerized reconstruction of the anatomy, electrophysiology and mechanics of the human heart.

The following sections present some models of the cardiac anatomy on base of MRT and from the data of the Visible Human Project. Special focus was taken on the applicability of the models in the area of numerical field calculation.

6.4.4 Modeling of Orientation and Lamination of Myocytes

In the following sections the modeling of the orientation and lamination of myocytes is restricted to a macroscopic, averaged perspective onto the cellular geometry. This perspective is often taken in the modeling of complex, inhomogeneous structures, e.g. continuum modeling of electrophysiology and structure mechanics, and allows a simplified treatment, especially, if the microscopic inhomogeneity of attributes can be neglected.

In the macroscopic perspective the orientation and lamination of myocytes is defined by averaging and interpolation. The local attributes can be viewed as averaged macroscopic quantities, e.g. the spatial averaged principal axis of the myocytes and orientations of the lamination.

The strategies for the modeling of the orientation and lamination of myocytes can be divided into two groups. The first group includes methods, which base on the measurement of the attributes, i.e. histological studies of surfaces of tissue sections and recently developed imaging techniques. The second group consists of rule-based methods, which apply rules constructed from anatomical studies.

A representative of the first group is the diffusion weighted magnetic resonance tomography, which allows a measurement of the macroscopic, averaged orientation of myocytes in vitro [133, 134, 135, 136] and in vivo [137, 138, 139]. Hereby, the assignment of the orientation of myocytes is based on the assumption, that the diffusion of water molecules by Brownian motion is larger in the direction of the cells than transversal to it. The cellular membrane is considered as a barrier, which restricts diffusion. The ratio of transversal to overall membrane area is in particular for myocytes from the working myocardium

significantly larger than the ratio of longitudinal to overall membrane area resulting from the cellular shape (Fig. 6.2).

The assumption was verified, e.g. by comparison with histological measurements of paraffin-embedded and sectioned probes of rabbit left ventricles [135, 140] and right ventricular free wall of mongrel dog [134]. Hereby, for the orientations a RMS difference of 5.3° and an averaged difference of $-2.3° \pm 0.98°$ was reported in [135] and [134], respectively.

Different rule-based strategies can be used to assign the myocyte orientation and lamination. A strategy consists of a manual assignment of the attributes by a human expert at specific points [141, 142]. A further strategy uses knowledge delivered by anatomical studies (sections 6.3.1 and 6.3.2) [143, 144, 145]. The knowledge is used in computer programs and allows the automatic assignment of attributes. In both strategies an interpolation of the orientation and lamination can follow in order to determine the attributes in the remaining myocardial volume.

6.4.5 Models from the Visible Human Project

Data of the Visible Human Project. The corpses of a 38-year-old man and a 59-year-old woman form the basis of the Visible Human Project in conjunction with specific processing and imaging techniques. The male data set is available since 1994, the female since 1996, each of them after more than one year of processing. The processing of the corpses was structured as follows:

- Conservation
- Imaging with MRT
- Fixation
- Imaging with CT
- Freezing
- Imaging with CT (only Visible Man)
- Cryosection

The conservation of a corpse was performed 1.5 h post mortem by injection of 19 l of 1 % formalin and anticoagulant into the right femoral artery and dorsum of each forearm. The conservation delayed a deterioration of tissue, which was reported by earlier studies especially for willed corpses from persons, who were subjected to court ordered lethal injection. Then the cadaver underwent MRT with an in clinical routine used scanner. Imaging with CT was performed after a fixation of the corpse by a foaming agent. The imaging took place with a conventional CT scanner and in the non-frozen state of the corpse, because pilot studies showed minor contrast in the frozen state. The freezing of the corpse was achieved in two days as reported by earlier studies. In the frozen state a CT imaging and the cryosection were performed.

The cryosection images are the essential component of the Visible Human Project. They were created by iterative mill cutting of frozen corpses and

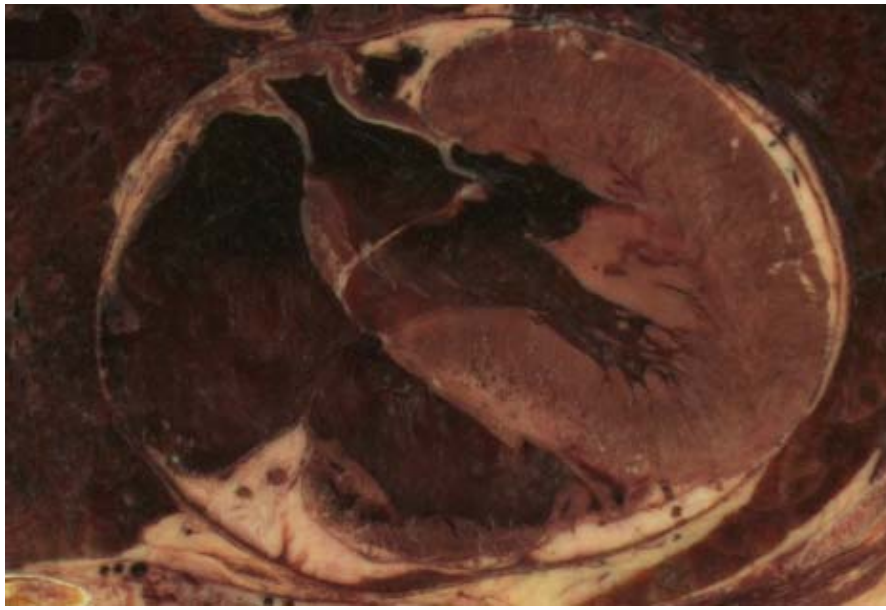

Fig. 6.24. Clipping of a cryosection from the Visible Female data set with a transversal view of the cardiac region. All atrial and ventricular cavities are visible. Parts of the lungs and fat are surrounding the heart.

photographing of the uncovered area (Fig. 6.23). Special attention was cared for air filled cavities. The cavities were filled by blue colored gel, to restrict the view to plane surface of the uncovered area.

The cryosection was performed by a cryomacrotom, which was developed at the Department of Anatomy at the University of Colorado Medical School. The cryomacrotom consists of computer controlled milling cutter and an adjustable table, on which the corpse was mounted. The photographing was done digitally and analog. Hereby, the digital images were used after image processing for the production of the digital database.

Each cryosection shows a transversal view onto the uncovered area of a corpse and consists of 2048 x 1280 pixels with 24 bit color information and a pixel size of 0.33 mm x 0.33 mm. Between the cryosections a distance of 1 mm and 0.33 mm was selected for the Visible Man and Visible Female data set leading to 1871 and 5189 images, respectively.

Preprocessing of Digital Images. The stack of two dimensional cryosections and CT scans from the Visible Man and Visible Female data set was preprocessed to obtain three dimensional data sets [146, 147, 148, 149]. Therefore, the images (Fig. 6.24) were converted and combined with homogeneous transformations. Missing areas in the cryosection data sets were interpolated using radial basis functions [148]. The CT scans were registered with the

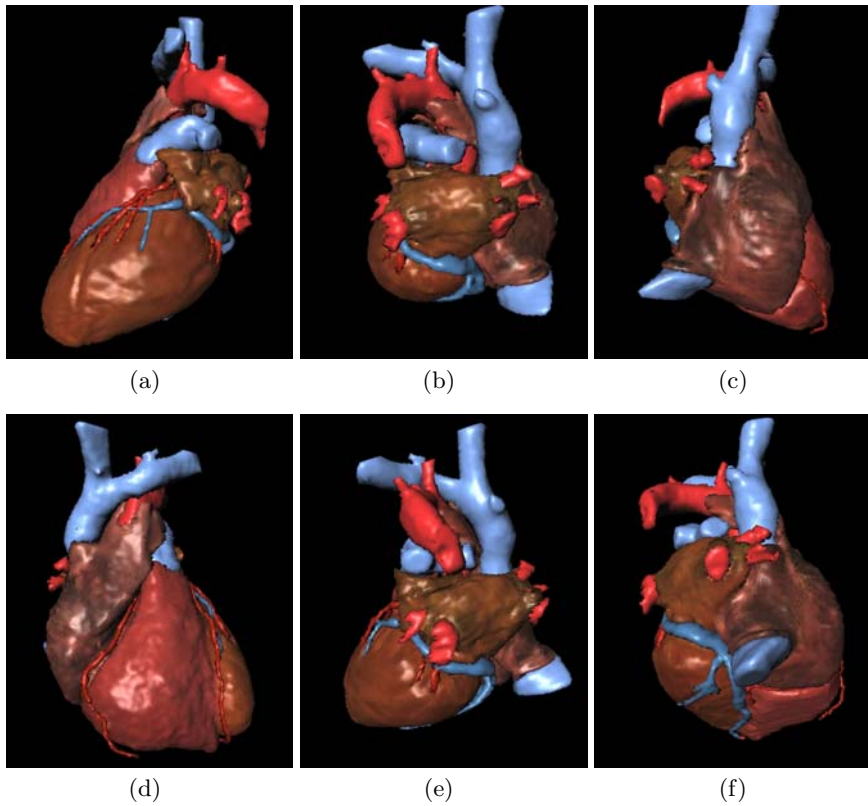

Fig. 6.25. Model of human heart from (a) left, (b) dorsal left, (c) dorsal right, (d) frontal, (e) right, and (f) dorsal caudal (from [37]). The model was constructed on base of the Visible Man data set with techniques of digital image processing.

cryosection images by point-based methods. The result of the preprocessing were four data sets representing the red, green, and blue channel of the cryosection images as well as the Hounsfield values of the CT.

Classification of Tissues. The three dimensional data sets were segmented and classified using different techniques of digital image processing, e.g. interactively deformable meshes, thresholding, region growing, and morphological operators [150, 144, 37]. The boundaries of the atria, ventricles, aorta and truncus pulmonalis were constructed using interactively deformable two-dimensional splines [150] and triangle meshes [58]. The initial meshes were manually placed, oriented, scaled and afterwards deformed.

The boundaries of the atria and ventricles served as a mask for thresholding in the 3D-data sets to classify blood, myocardium and other tissue. Further anatomical structures, e.g. the coronary vessels, the blood in the cavities and large vessels, are segmented with region growing techniques. Minor fail assign-

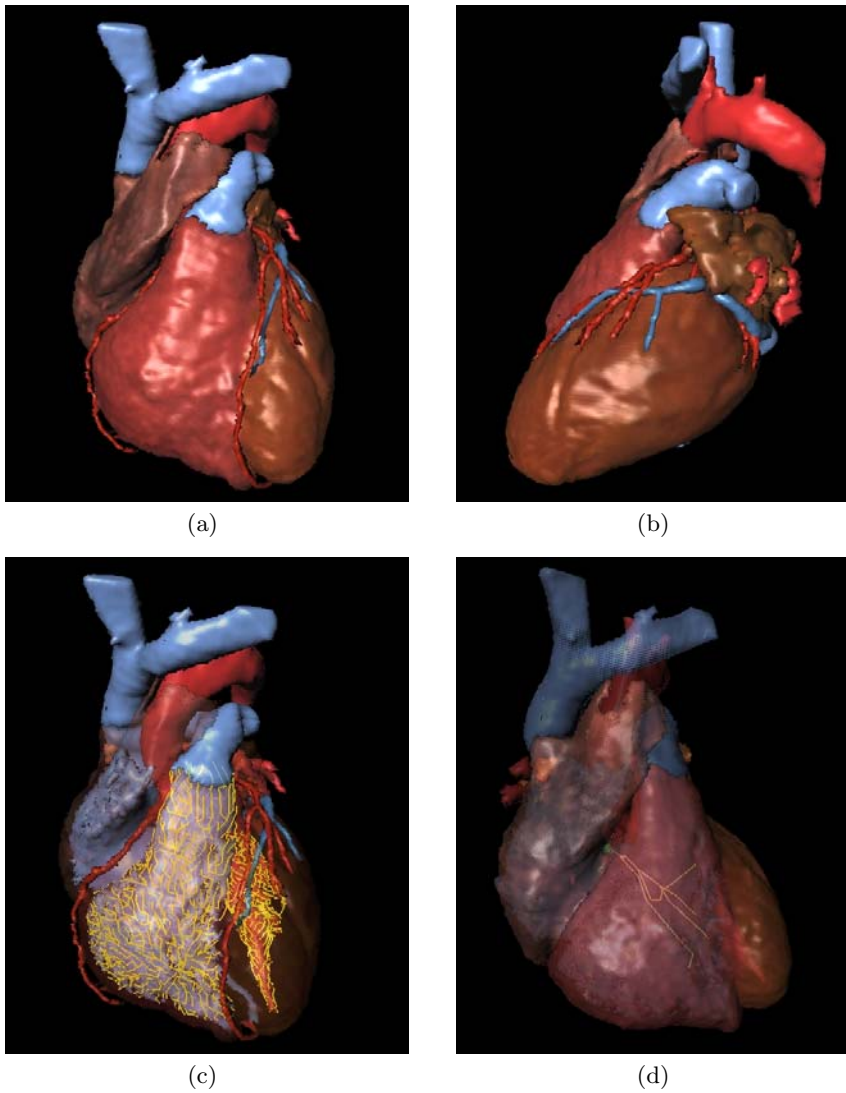

Fig. 6.26. Model of visible man heart (adapted from [37]): (a,b) anatomy and (c,d) conduction system. The different tissue classes are color-coded visualized.

ments were eliminated with morphological operators. Therefore, sequences of median filtering as well as opening and closing operators were executed.

The excitation conduction and initiation system was constructed manually and with rule-based methods in the Visible Man data set [37]. The valves were created from suitable triangle meshes in the Visible Female data set.

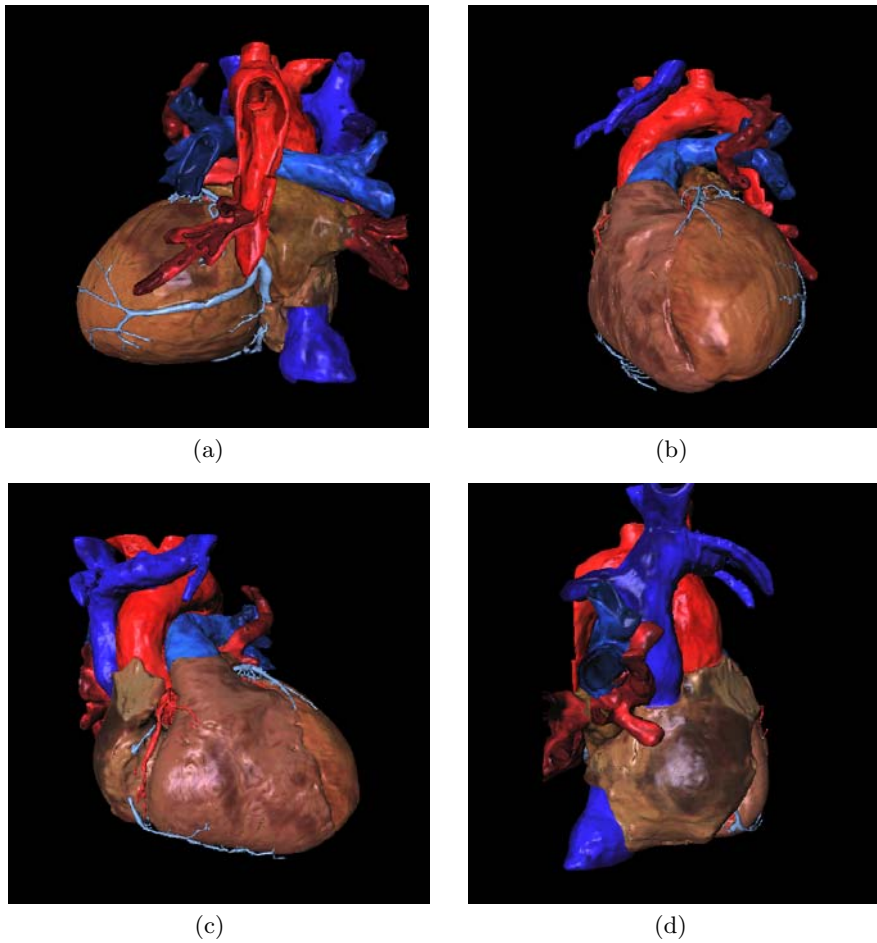

Fig. 6.27. Model of human heart from (a) left, (b) frontal, (c) right, and (d) dorsal. The model was constructed on base of the Visible Female data set with techniques of digital image processing.

The resulting anatomical models are illustrated in Fig. 6.25, and 6.27. The anatomical models were validated by human experts.

The model of the Visible Man heart was stored in a three dimensional data set consisting of approximately 360,000 cubic voxels with a size of 1 *mm* x 1 *mm* x 1 *mm*. Each voxel was assigned to one out of 16 different tissue classes, e.g. left and right ventricle, left and right atrium, arterial and venous blood, and fat as well as different kinds of vessels. Special focus was given to the excitation conduction system (Fig. 6.26), which is partly represented in a tree like data structure.

The model of the Visible Female heart was stored in a three dimensional data set, which consists of approximately 80 million cubic voxels. Each voxel has a size of 0.33 mm x 0.33 mm x 0.33 mm and was assigned to one out of 20 different tissue classes.

Assignment of Myocyte Orientation and Lamination. The assignment of the macroscopic orientation and lamination of myocytes in the heart model was performed by a sequence of steps [64]:

- point-wise definition of restrictions with manual and rule-based methods
- interpolation of orientation and lamination by iterative averaging
- validation by human experts

In all these steps the cryosections and the tissue-classified data sets were used in conjunction with methods of digital image processing (Chap. 5, particularly Sect. 5.6) and of tensor algebra (Sect. 2.3).

The restrictions define point-wise a myocyte or sheet orientation. Furthermore, they can limit the degree of freedom of an orientation.

Restrictions for orientations were determined with automatic methods on the epi- and endocardial surface of myocardial structures. For some structures an individual rule-based method using knowledge from anatomical studies was chosen to derive restrictions (Sect. 6.3.1 and 6.3.2). Furthermore, restrictions were created by the detection of orientations (Sect. 5.6.2) followed by manual editing by human experts.

The orientation of myocytes and their arrangement in layers was interpolated based on the created sets of restrictions. The interpolation was performed by iterative averaging in the six-neighborhood of a voxel. The averaging was performed by accumulation of tensors constructed from the orientation and lamination, followed by singular value decomposition. The direction of the first and second principal component was used as orientation and sheet direction, respectively (Sect. 2.3).

The methods were applied to the Visible Man and Visible Female data set [64, 143, 151, 144, 145]. For the atria the methods delivered the orientations of myocytes, for the ventricles the method delivered the orientation and lamination (Fig. 6.28). The resulting data sets have the same resolution and geometrical dimension as the corresponding tissue classified data sets. The orientation and lamination are described by three bytes, encoding three angles, ϕ, θ, and γ, in the range of $[0, \pi]$. The encoding of the angle can be efficiently used in conjunction with methods of numerical field calculation e.g. in electromagnetics and structure mechanics. The results were compared visually by human experts with anatomical studies.

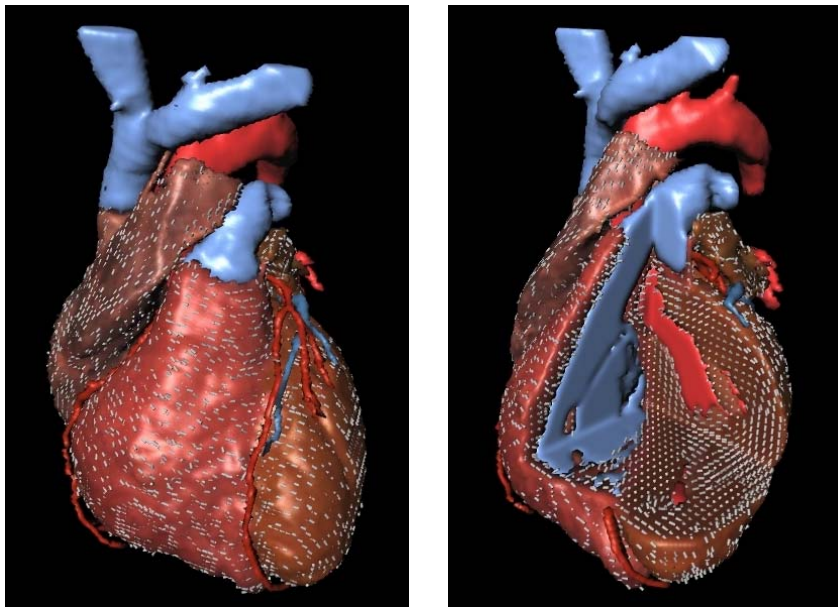

(a) (b)

Fig. 6.28. Model of human heart with averaged orientation of myocytes projected on (a) epicardial surface and (b) cutting planes. The orientation was constructed on base of the Visible Man data set, manual editing and interpolation.

6.4.6 Models from Magnetic Resonance Imaging

Imaging of Heart. An extracorporated canine heart was fixed and scanned with MRT[1]. Images of the proton density and diffusion weighted scans were performed (Fig. 6.29). The images were stored in three dimensional data sets, consisting of 256 x 128 x 128 voxels with a size of 0.4 *mm* x 0.8 *mm* x 0.6 *mm*. The proton density of each voxel was coded by a float value (4 *bytes*), the diffusion tensor by its three principal axes (3 x 3 x 4 *bytes*) and its three eigenvalues (3 x 4 *bytes*).

Preprocessing of Digital Images. The MRT data sets were preprocessed primarily regarding the simplification of the following image segmentation and classification process. The proton density scans showed a significant decrease of signal intensity in apical and basal regions, which was detected and compensated by scaling operations. In addition, the proton density images were preprocessed by a sequence of morphological filtering to reduce measurement noise. The data format of the proton density scans was reduced to 1 *byte*.

[1] The imaging was performed by Prof. C. Henriquez, Prof. E. Hsu, and their work groups at the Department of Biomedical Engineering, Duke University, Durham (USA). Special pulse sequences were developed for the diffusion weighting.

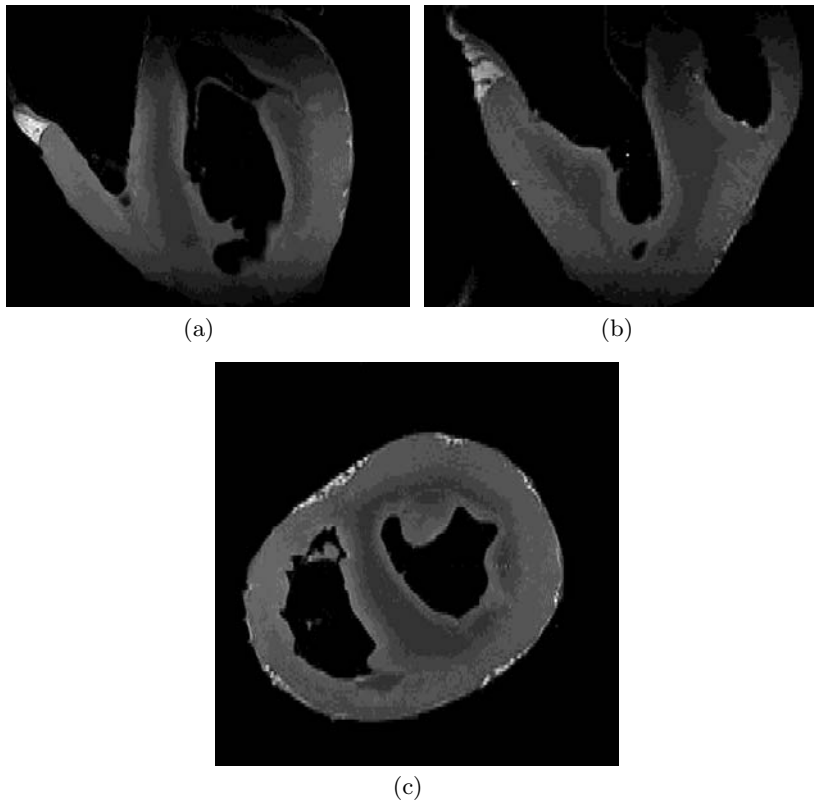

Fig. 6.29. Slices of proton density weighted, three dimensional MRT data set of extracorporated canine heart with (a) frontal, (b) lateral, and (c) transversal.

The decrease of signal intensity in apical and basal regions was also found in the diffusion weighted images. The images show gaps of different size in the regions, which were filled by interpolation techniques taking neighboring values into account. Additional small artifacts in the diffusion-weighted images were detected, erased and filled up by an interpolation.

Segmentation and Classification of Tissues. The segmentation and classification of the three dimensional data sets were performed using different techniques of digital image processing, e.g. interactively deformable meshes, thresholding, region growing, and morphological operators (Sect. 5.3.3 and 5.4.1).

The boundaries of the epicardial and endocardial myocardium as well as the septum were constructed using interactively deformable triangle meshes [58]. Therefore, the initial meshes were manually placed, oriented, scaled and afterwards deformed. The boundaries of the epicardial and endocardial myocardium as well as the septum served as a mask for thresholding and region

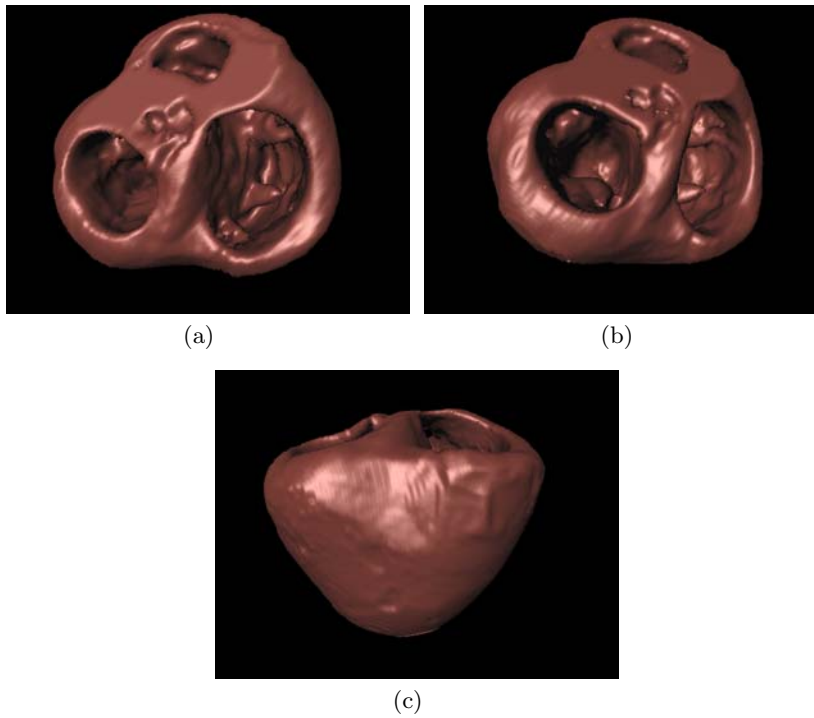

Fig. 6.30. Anatomical model of canine heart viewed from the base of (a) the right ventricle and (b) the left ventricle as well as from (c) frontal. The ventricles and papillary muscles are segmented with interactively deformable meshes and thresholding techniques.

growing in the three dimensional data sets to classify blood and papillary muscles as well as left and right ventricular myocardium. Sequences of morphological operators, i.e. median filtering as well as opening and closing, eliminated minor fail assignments. The tissue-classified data set is illustrated in Fig. 6.30.

Myocyte Orientation. The eigenvector of the measured diffusion tensor with the highest eigenvalue served as a basis for the assignment of the orientation. An averaging filter was applied to reduce noise and artifacts in the measurement data.

The resulting data set has the same resolution and size as the tissue classified data set. Each voxel in the orientation data set includes 2 bytes, encoding two angles, ϕ, and θ, in the range of $[0, \pi]$. An exemplary slice of the anatomical model in conjunction with the assigned fiber orientation is shown in Fig. 6.31.

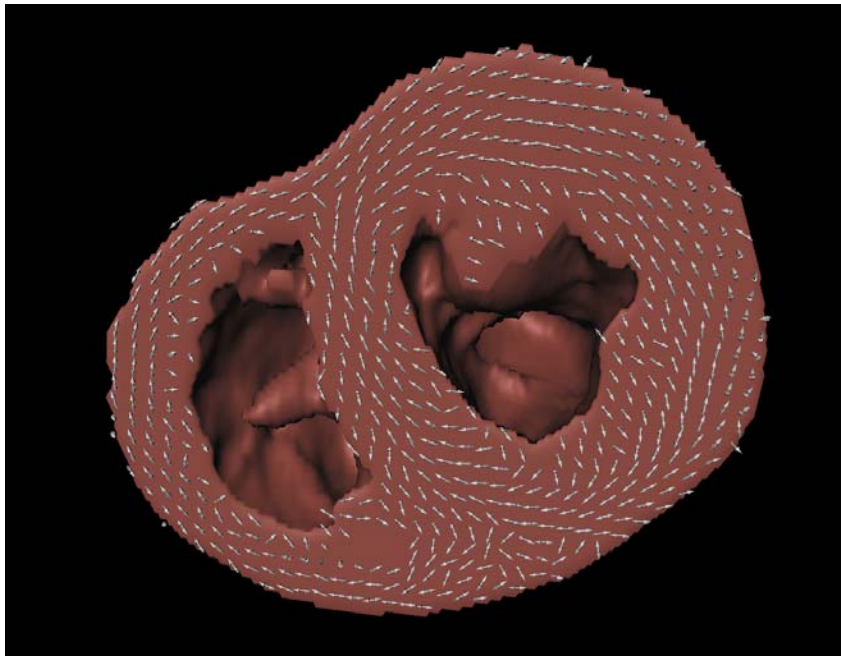

Fig. 6.31. Anatomical model of canine heart with myocyte orientation.

7

Cardiac Electrophysiology

7.1 Overview

Knowledge concerning the electrophysiology of the heart is necessary for the understanding of many aspects of the physiological and pathophysiological cardiac behavior. The electrophysiology is tightly coupled with the mechanic deformation and the pump function of the heart by controlling the development of tension. Furthermore, various mechano-electrical feedback mechanisms influence the cardiac electrophysiology.

The origin of the electrical activity of the heart are the myocytes, which show like nerve cells an electrical excitability. The electrical excitation of a myocyte is tightly coupled with its mechanical contraction. A propagation of electrical excitation from a myocyte to neighboring myocytes is primarily achieved by intercellular transport of ions via the gap junctions. Additionally, extracellular potentials resulting from the electrical activity of cells or from an external current flow can modulate the propagation and initiate an excitation.

A large amount of experiments was performed to achieve knowledge concerning the cardiac electrophysiology, delivering data of the intra-, extra- and intercellular electrophysiological quantities from specific functional regions and from the heart as an integrated whole. The quantities obtained by the experiments are e.g. voltages across membranes and in the different spatial domains as well as flow and concentrations of ions. The experiments range from the measurement of opening states of single ion channels to the extracorporal registration of electrograms. The hereby discovered phenomena can be attributed e.g. to changes of the electrophysiological states of cellular components and the intercellular electrical coupling. Relevant components are the cell membrane, its ionic channels, pumps and exchangers, as well as intracellular structures, e.g. the sarcoplasmic reticulum.

The measurement data were partly used to create mathematical models of different levels of abstraction. The models of membrane patches, of single cells and of cell clusters describe the electrophysiological status commonly in a spatially averaged sense by regionally varying concentrations of different

F.B. Sachse: LNCS 2966, pp. 157–219, 2004.

kinds of ions, by the conductivity of ionic channels, and by the activity of ionic pumps and exchangers. The transport of ions through the channels and exchangers is determined from gradients of ionic concentrations and electrical forces. The models allow the simulation of the electrophysiological behavior with numerical methods. A reconstruction of the previously measured data and furthermore the discovery of unknown phenomena can be achieved.

In the following sections different electrophysiological experiments and modeling approaches are described. The description starts with the measuring and modeling approaches of phenomena of cellular components, followed by the whole cell electrophysiological behavior and mechanisms of the intercellular excitation propagation. The description of the electrophysiology of cellular components concerns primarily the phenomena resulting from the behavior of the cell membrane and the sarcoplasmic reticulum.

In this context the classical work of Hodgkin and Huxley is presented, who delivered quantitative data of the electrophysiology of a squid axon and constructed a mathematical model. Most electrophysiological models of nerve and muscle cells base on their mathematical formulation.

Special focus is given to experiments delivering quantitative data and physically motivated models. In addition, mechano-electrical feedback mechanisms are described for the different levels of measurement and modeling.

7.2 Cellular Electrophysiology

7.2.1 Experimental Studies

Cell Membrane. The cell membrane consists of a phospholipid bilayer, which is perforated by pores formed by proteins (Sect. 6.2.1). The membrane suppresses the diffusion of ions and molecules into and out of the cell. The membrane separates the intra- and extracellular space with different ionic concentrations. The gradient of ionic concentrations is resulting from transport mechanisms and the cellular metabolism.

The electrical behavior of a cellular membrane can be measured in vivo and in situ with two intracellular electrodes. One of the electrodes is used for applying current and one for the registration of the transmembrane voltage. A third electrode is located in the extracellular space near to the cell. The measurement procedure is relatively insensitive with regard to the placement of the electrodes, resulting from the high resistivity of the membrane in contrast to the high conductivity of the extra- and intracellular space. The application of a conveniently chosen current allows the measurement of an action voltage, whereby different phases can be distinguished (Fig. 7.1). The action voltage differs depending on the stimulus frequency, tissue type and location in the heart (Fig. 7.2).

An alternative procedure is the patch clamp technique, whereby the electrical behavior of a membrane patch restricted by the opening of a glass pipette

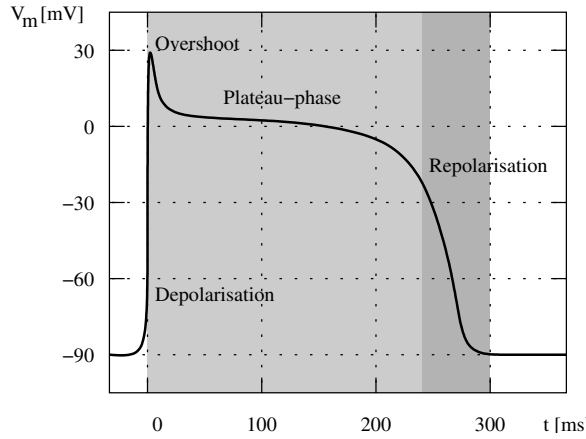

Fig. 7.1. Schematic illustration of action voltage V_m measured at membrane of cardiac myocyte (adapted from [152]). A stimulus current is applied in a myocyte with its membrane at resting voltage. After a fast depolarization the transmembrane voltage reaches positive values. Followed by a fast decrease the relatively long plateau phase is passed through. At their end the repolarization leads to a decrease commonly until the resting voltage is reached.

is registered. The patch is sealed to the glass pipette. Only two electrodes are used, one inside of the pipette and the other outside, near to the patch.

The most common used protocol for these measurements is the voltage clamp technique. Hereby, the voltage over the membrane is kept constant by supplying a convenient current. The voltage and the course of the current are registered. Commonly, in these measurements the voltage is varied stepwise, e.g. from $-90\ mV$ to $20\ mV$ in steps of $10\ mV$.

The measurements are often performed in conjunction with the application of drugs and toxins, which allows the discrimination of the involved currents and channels. E.g. tetradotoxin and tetraethylammonium block specifically sodium and potassium channels, respectively [154]. Furthermore, the variation of ionic concentrations and of the mechanical load offers additional insights [155].

A fundamental step in describing the electrophysiology of a cell membrane was performed by Hodgkin and Huxley, who measured and described quantitatively the active and passive electrical behavior of the axon membrane of giant squids [156]. Hereby, voltage clamp techniques as well as the variation of ionic concentrations and temperature were used to measure and discriminate currents through the membrane.

The measurements by Hodgkin and Huxley of the electrical behavior of the membrane as well as the numerous following experiments show significant nonlinearities of the membrane resistivity [156]. The nonlinearities can be attributed to the behavior of pores in the membrane, i.e. ionic channels

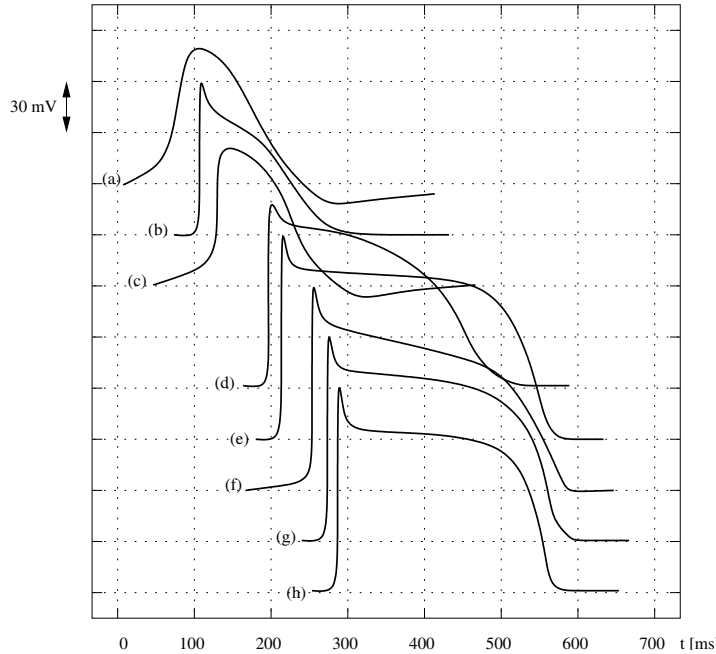

Fig. 7.2. Action voltages measured at membrane of human cardiac myocytes. The voltages at the membrane of myocytes from the (a) sinus node, (b) atrium, (c) atrioventricular node, (d) His bundle, (e) Tawara bundle branch, (f) Purkinje fibers, (g) subendocardial and (h) subepicardial ventricular myocardium are illustrated [153].

and pumps. Furthermore, concentration gradients over the membrane and ion specific permeabilities lead to measurable voltages, which can be dedicated to the behavior of semi-permeable membranes.

Ionic Channels of the Cell Membrane. Ionic channels exist in a wide variety in cell and intracellular membranes (Sect. 6.2.1). Their electrophysiological behavior can be measured with voltage clamp techniques of the whole cell, a membrane patch and a single channel. The observations show that a single channel flips randomly between a conducting and non-conducting state. Measurements of the stochastic opening and closing over a time period allow the assignment of channel specific probabilities of opening and closing. The transitions are performed in dependence of voltage, ionic concentrations, stretch and neurotransmitters. Often, a time influenced transition between the states can be found. A population of these channels acts in unison with the probabilities assigned to the single channel. The behavior of the population can be measured as the sum of the single channel behaviors.

Sodium Channels. Sodium channels are found to be responsible for the fast depolarization in myocytes of all vertebrates [87]. Measurements of sodium

channels with voltage clamp techniques show a fast transition to the high conductivity state if the voltage exceeds a threshold [156, 88]. Furthermore, the conductivity is found to be significantly time dependent. The conductivity decreases rapidly after activation. Sodium channels can be blocked specifically and reversibly by tetradotoxin and saxitoxin [154].

Potassium Channels. Potassium channels show a large diversity in their molecular arrangement and in their electrophysiology. They are responsible for the repolarization of myocytes and neurons. Several types with a different time- and voltage-activated behavior are found in the heart [157]. Twenty different types are known only for voltage dependent channels, e.g. channels responsible for the ultra-rapid delayed rectifier current, the rapidly activating delayed rectifier current, the slowly activating delayed rectifier current, and the inward rectifier current. Furthermore, specific types of potassium channels are regulated by ATP [158] and cAMP [159]. Potassium channels can be blocked reversibly by tetraethylammonium, cesium, barium and dendrotoxins [154]. Heterogeneity of properties and densities of several potassium channels in the ventricular wall is reported for many species, e.g. cat, canine, and human [160, 161, 162, 163].

Calcium Channels. The sarcolemmal ionic channels with a high specificity for calcium show a voltage- and time-dependent behavior. They are discriminated by their electrophysiological behavior [89]. L-type calcium channels (dihydropyridines receptors) show relatively large and long lasting ion flow after activation. T-type channels show a tiny and transient ion flow. L-type channel blocking by magnesium, nickel, cadmium, and cobalt as well as regulation of the T-type channels by extracellular ATP was observed [154].

Ionic Pumps of the Cell Membrane. Pumps in the sarcolemma are e.g. the Na-K and calcium pump. The Na-K pump maintains the ionic gradients, which are largely influencing the transmembrane voltage. In a single procedure the Na-K pump transports three sodium ions out of and two potassium ions into the cell consuming ATP. The transport is found to be dependent on the intra- and extracellular sodium and potassium concentration as well as on transmembrane voltage and on temperature. The pump can be blocked specifically by quabain (strophantin).

The sarcolemmal calcium pump transports calcium out of the cell dependent on the concentration of the intracellular calcium. The pump consumes ATP.

Na-Ca Exchanger in the Cell Membrane. Na-Ca exchangers are predominantly responsible for the transport of calcium out of the cell, which passed into the cell via the sarcolemmal calcium channels and leak currents [92]. In a single procedure three extracellular sodium ions are exchanged with a single intracellular calcium ion. A Na-Ca exchanger can also work in the

opposite direction, which is primarily found in the initial phase of excitation. Measurements show a dependence of the exchange capacity on the concentration of intra- and extracellular calcium and sodium as well as on the transmembrane voltage [164, 165]. The contribution of Na-Ca exchangers to the raise of intracellular calcium concentration during voltage clamp steps to 30 mV is reported to be ca. 10 % of the contribution of the L-type calcium channels [166]. A block is reported for small pH-values, flunarizine, and inorganic cations, e.g. cadmium, strontium and barium [68].

Sarcoplasmic Reticulum. The sarcoplasmic reticulum is an intracellular structure, which is enclosed by a membrane (Sect. 6.2.1). Studies, e.g. with antibodies, showed that the membrane contains calcium, potassium, chlorine and hydrogen ionic channel proteins as well as calcium pump proteins. The sarcoplasmic reticulum has a significant influence to the intracellular calcium handling. Calcium is pumped into the sarcoplasmic reticulum by the sarcoplasmic calcium pump and is released by the calcium release channels. Furthermore, leak calcium currents through the membrane are demonstrated. Insights in the electrophysiological behavior were primarily obtained by voltage clamp techniques of isolated vesicles.

Calcium Release Channel. The calcium release channel (ryanodine receptor) shows a high specificity for divalent cations [85]. The release channel is activated by approximately micro-molar cytoplasmic concentration of calcium and releases calcium buffered in the sarcoplasmic reticulum into the cytoplasma. This positive feedback mechanism is called calcium induced calcium release (CICR) [167]. An inhibition is reported by approximately milli-molar concentration of calcium. The channel is regulated by ryanodine and caffeine.

The activation of release channels is commonly result of calcium flux from the extracellular space into the cytoplasm through L-type calcium channels. The sarcoplasmic release and sarcolemmal L-type channels are located in close neighborhood. The summary calcium release occurs by concerted activation of many single channel release, leading to so-called calcium sparks [168, 86]. A refractory period of release channels is reported after their coherent and simultaneous activation. This refractoriness of circa 1 s is attributed to the entire sarcoplasmic reticulum and not found in small groups of functional units.

Sarcoplasmic Calcium Pump. The sarcoplasmic calcium pump, known also as sarcoplasmic Ca^{2+}-ATPase and SERCA (sarco-endoplasmatic reticulum calcium ATPase), transports calcium ions into the sarcoplasmic reticulum by usage of ATP. Two calcium ions are transported for each hydrolyzed ATP molecule. The sarcoplasmic calcium is buffered by the protein calsequestrin. The transport is regulated by the concentration of calcium, magnesium, ATP and the protein phospholamban as well as by pH-value [68, 169].

Mitochondrion. Mitochondria are intracellular organelles enclosed by a membrane (Sect. 6.2.1). The membrane contains calcium ionic channel and

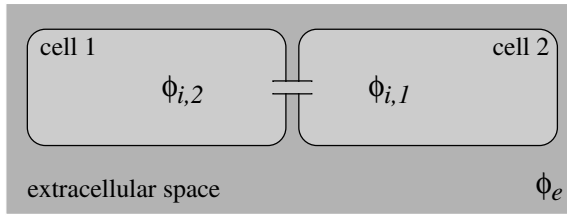

Fig. 7.3. Double cell voltage clamp technique. The conductivity of the gap junctions, which couple the intracellular space of adjacent myocytes, can be measured by clamping the potentials $\phi_{i,1}$ and $\phi_{i,2}$ of two adjacent cells. The voltages are clamped by two voltage sources with common reference potential ϕ_e. The difference of the potentials delivers the voltage over the gap junction.

hydrogen pump proteins as well as sodium-calcium and hydrogen-sodium exchanger. Furthermore, hydrogen pumps are included. The sodium-calcium pump transports two sodium ion inside, while bringing one calcium ion to the cytosol. The hydrogen-sodium pump transports a hydrogen ion inside, while hauling one sodium ion outside.

Gap Junctions. Gap junctions are found to be the most important components of the electrical coupling between myocytes [94]. The gap junctions serve as a pathway, which transport electrical current from one cell to adjacent cells depending on the intracellular potentials. Hence, the gap junctions play a determinant role for the propagation of the electrical excitation through the myocardium.

The electrophysiological behavior of gap junctions can be determined by measurements with a variation of the before described voltage clamp methods, the so-called double cell voltage clamp technique (Fig. 7.3). The intracellular potential of each cell is clamped by a voltage source. The intercellular voltage is controlled by the two voltage sources with common reference potential. The voltages are registered in conjunction with the applied current, which offers the possibility to calculate the conductivity. The measurements show that the conductivity of gap junctions is dependent on their type and on the intercellular voltage. In the range between -50 and 50 mV the variation is small for connexin43, which is the most abundant connexin in the mammalian myocardium.

Experiments were performed, which reveal that the gap junctions uncouple in the case of acute ischaemia and that the homogeneity and ordering of the gap junction distribution is decreased by chronic ischaemia. Also, chronic atrial arrhythmia and infective heart diseases changes the distribution pattern.

The conductivity of gap junctions can be decreased by halothane, heptanol and carbon dioxide [98]. A blocking is reported for low pH-values [95].

Fig. 7.4. Cell membrane and its approximation by resistor-capacitor circuit. The circuit consists of a nonlinear resistor R_m and a capacitor C_m. The voltage over the membrane V_m is hereby defined as the difference between the extracellular potential ϕ_e and the intracellular potential ϕ_i

7.2.2 Modeling of Cellular Components

Cell Membrane as Resistor-Capacitor Circuit. The electrical behavior of a cell membrane can be approximated by a resistor-capacitor circuit with the nonlinear resistor R_m and the capacitor C_m (Fig. 7.4) [154]. The voltage over the membrane V_m is dependent on the charge Q:

$$V_m = \frac{Q}{C_m}$$

A change of the transmembrane voltage V_m can be described by the current flow I_C:

$$\frac{dV_m}{dt} = \frac{d}{dt}\frac{Q}{C_m} = \frac{I_C}{C_m}$$

assuming that the capacity C_m is constant over time. This equation is - adapted by definition of a summary current through the membrane - foundation of most electrophysiological models of membranes and cells.

The capacity of the sarcolemma is depending on its surface. A specific capacitance of approximately 1 $\mu F/cm^2$ is found in biological membranes.

The membrane resistor R_m is responsible for the discharge of the membrane by the current I_C. Using Ohm's law the resistor is determined by:

$$R_m = -\frac{V_m}{I_C}$$

Equilibrium Voltages of Cell Membrane. The description of the cell membrane as resistor-capacitor circuit neglects the phenomenon, that a voltage is generated across a semipermeable membrane between to regions with different ionic concentrations. Different equations, e.g. the Nernst and Goldman-Hodgkin-Katz equation, describe this voltage, which results from electrical and chemical forces. The equations are applied in the area of cellular electrophysiology. Hereby, the regions are the intra- and extracellular space with the semi-permeable cell enclosing membrane as border.

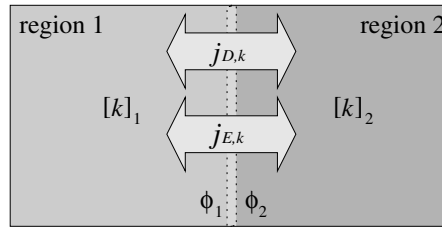

Fig. 7.5. Fluxes, potentials, and ionic concentrations of the Nernst equation. The equation describes the equilibrium voltage $\phi_2 - \phi_1$ across the border of the two adjacent regions resulting from the ionic concentrations $[k]_1$ and $[k]_2$. In equilibrium the flux of the ion k due to electrical forces $\boldsymbol{j_{E,k}}$ and due to diffusion $\boldsymbol{j_{D,k}}$ sums up to zero.

Nernst Equation. The Nernst equation describes the equilibrium voltage across the border of two regions resulting from gradients of ionic concentrations [154] (Fig. 7.5).

The Nernst equation determines the equilibrium voltage U by:

$$U = -\frac{RT}{z_k F} ln \frac{[k]_1}{[k]_2}$$

with the gas constant R, Faraday's constant F, the concentrations in region 1 $[k]_1$ and in region 2 $[k]_2$ as well as the valence of the ion z_k. Furthermore, the equilibrium voltage U is linearly depending on the absolute temperature T.

The equilibrium is achieved when the total flux $\boldsymbol{j}_k$ of the ion k through the border is zero. The Nernst equation takes into account two different fluxes: the ionic flux caused by diffusion $\boldsymbol{j}_{D,k}$ and the ionic flux $\boldsymbol{j}_{E,k}$ due to electrical forces (Fig. 7.5). Hence, the equilibrium is achieved if

$$\boldsymbol{j}_k = \boldsymbol{j}_{D,k} + \boldsymbol{j}_{E,k} = 0$$

is fulfilled. The ionic flux caused by diffusion $\boldsymbol{j}_{D,k}$ is determined by the diffusion constant D_k and the gradient of the concentration $[k]$:

$$\boldsymbol{j}_{D,k} = -D_k \nabla [k]$$

Hereby, the diffusion coefficient is expressed as:

$$D_k = \frac{u_k RT}{|z_k| F}$$

The flux due to electrical forces $\boldsymbol{j}_{E,k}$ is given by the ionic mobility u_k, the valence of the ion z_k, and the electrical potential ϕ:

$$\boldsymbol{j}_{E,k} = -u_k \frac{z_k}{|z_k|} [k] \nabla \phi$$

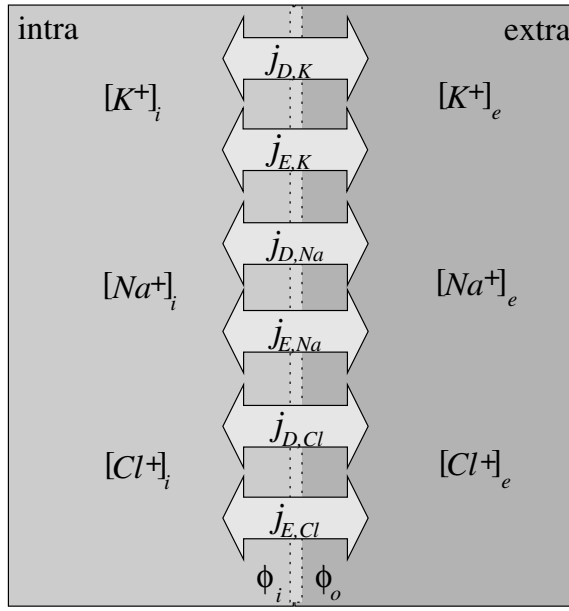

Fig. 7.6. Fluxes, potentials, and ionic concentrations of the Goldman-Hodgkin-Katz equation. The equation describes the equilibrium voltage $\phi_i - \phi_o$ across a cellular membrane between the intra- and extracellular space resulting from the concentrations of potassium, sodium, and chlorine. In equilibrium the flux of the ions due to electrical forces $\boldsymbol{j_E}$ and due to diffusion $\boldsymbol{j_D}$ sums up to zero.

The flux due to electrical forces $\boldsymbol{j}_{E,k}$ can also be described by:

$$\boldsymbol{j}_{E,k} = -D_k \frac{[k] z_k F}{RT} \nabla \phi$$

which leads to the Nernst-Planck equation delivering the total ionic flux $\boldsymbol{j}_k$:

$$\boldsymbol{j}_k = \boldsymbol{j}_{D,k} + \boldsymbol{j}_{E,k} = -D_k \left(\nabla [k] + \frac{[k] z_k F}{RT} \nabla \phi \right)$$

A restriction of the Nernst equation is caused by the inclusion of only one kind of ions. The approach is justifiable if the mobility of further kinds of ions is restricted or their concentrations are negligible.

Goldman-Hodgkin-Katz Equation. The Goldman-Hodgkin-Katz equation was developed to describe the equilibrium voltage U of a cellular membrane separating the intra- and extracellular space. The equation extends the Nernst equation by allowing the occurrence of multiple kinds of ions, which are determinants in cellular electrophysiology, i.e. potassium, sodium, and chlorine. A concentration for each kind of ions is assigned to the intra- and extracellular space as well as fluxes for each kind of ions caused by diffusion and electrical forces are allowed through the membrane (Fig. 7.6).

With the Goldman-Hodgkin-Katz equation the equilibrium voltage U is determined by:

$$U = -\frac{RT}{F} ln \frac{P_K[K^+]_i + P_{Na}[Na^+]_i + P_{Cl}[Cl^-]_o}{P_K[K^+]_o + P_{Na}[Na^+]_o + P_{Cl}[Cl^-]_i}$$

from intra- and extracellular ionic concentrations, ionic permeabilities and the absolute temperature T. The permeability of the membrane for the potassium, Sodium, and Chloride ions is depicted by P_K, P_{Na}, and P_{Cl}, respectively. The permeability of an ion k is expressed by:

$$P_k = \frac{D_k \beta_k}{h}$$

with the membrane thickness h, the diffusion coefficient D_k and the water-membrane partition coefficient β_k. The diffusion coefficient as well as the water-membrane partition coefficient are dependent on the type of membrane and kind of ion k.

A restriction of the Goldman-Hodgkin-Katz equation is that the membrane is presumed to be homogeneous, planar, and infinite as well as the distribution of the extra- and intracellular concentration is homogeneous. Further assumptions are that the electric field in the membrane is constant and the ions pass through the membrane independently [154].

Ionic Channels. The behavior of a single ionic channel can be modeled with states and functions describing the transition between the states. In the simplest case two states are assumed: an opened and a closed state. Assigned to these states is an opened probability O_i and a closed probability C_i, respectively, reflecting that the transition between the states is stochastic. The probabilities sum up to one. They are in the range between 0 and 1.

The change of the open probability O is determined by:

$$\frac{dO_i}{dt} = \alpha C_i - \beta O_i$$

with the rate constant α, responsible for the transition from the closed to the opened state: $C_i \Rightarrow O_i$, and the rate constant β, concerned with the transition from the opened to the closed state: $O_i \Rightarrow C_i$. The rate constants depend on the type of ionic channel, transmembrane voltage, ionic concentration, stretch etc.. In equilibrium the change is zero:

$$\frac{dO_i}{dt} = 0$$

The macroscopic conductivity of a population of similar channels is specified by:

$$g_i = N_i \; O_i \; g_{i,max}$$

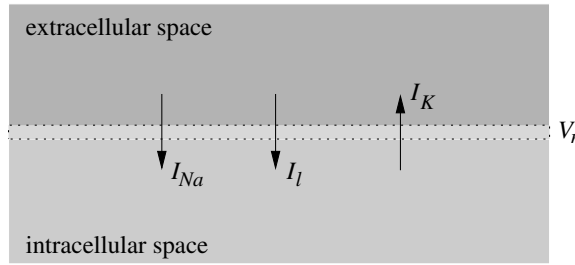

Fig. 7.7. Schematic diagram of the Hodgkin-Huxley model. The model calculates the currents I_{Na}, I_K, and I_l as well as the transmembrane voltage V_m.

with the number of channels N_i and the maximal conductivity of the channel $g_{i,max}$.

The total current through a population of ionic channels is resulting from the difference between the transmembrane voltage V_m and the Nernst voltage E_i:

$$I_i = g_i(V_m - E_i)$$

with the conductivity g_i.

Regional Concentrations and Current. The time derivative of a regional concentration $[k]$ for the ion k is calculated with:

$$\frac{\partial[k]}{\partial t} = -\frac{I_k}{z_k F V}$$

with the current I_k carrying ion k, the valence of the ion z_k, Faraday's constant F and the volume V of the region, where k is distributed.

Model of Hodgkin and Huxley (1951). The Hodgkin-Huxley model describes the dynamic electrophysiology of a giant squid axon membrane from measurements of the active and passive electrical behavior [156]. A foundation of the mathematical description is the Nernst Equation (7.2.2). Using the measurement data an equivalent circuit consisting of resistors, a capacity, and voltage sources was parameterized. Partly, the resistors were nonlinear time and voltage dependent.

The model allows to calculate ionic currents of different type passing through the axon membrane and the transmembrane voltage (Fig. 7.7 and Fig. 7.8). The transmembrane voltage V_m is defined as intracellular minus extracellular potential and the time derivative of V_m is described by:

$$\frac{\partial V_m}{\partial t} = -\frac{1}{C_m}\left(I_m + I_{stim}\right)$$

with the membrane capacity C_m, the transmembrane current I_m and the stimulus current I_{stim}. The transmembrane current I_m reconstructed by the Hodgkin-Huxley model consists of

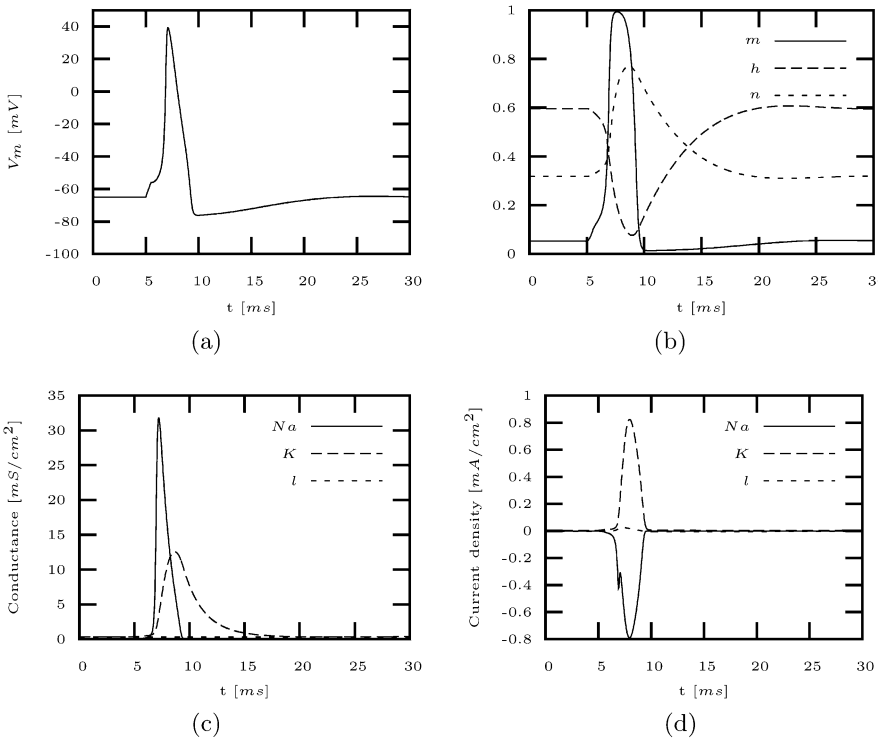

Fig. 7.8. Simulations with the Hodgkin-Huxley model. A stimulus current density of 0.02 mA/cm^2 is injected at $t = 5$ ms with a length of 0.5 ms. The stimulus leads to significant changes in (a) the transmembrane voltage, (b) the state variables for sodium and potassium channels, (c) the conductances, and (d) the transmembrane current densities of sodium, potassium and leakage.

$$I_m = I_{Na} + I_K + I_l$$

with the sodium current I_{Na}, the potassium current I_K, and the leakage current I_l. The leakage current I_l summarizes different ionic currents, primarily chloride ions. The currents are determined by the conductances g_{Na}, g_K, and g_l, respectively, as well as by the difference between the transmembrane voltage and the equilibrium voltages E_{Na}, E_K, and E_l, respectively:

$$\begin{aligned} I_{Na} &= g_{Na}(V_m - E_{Na}) \\ I_K &= g_K(V_m - E_K) \\ I_l &= g_l(V_m - E_l) \end{aligned}$$

The conductance g_l is assumed to be constant, the other conductances vary with time and are voltage dependent. The ionic concentrations are supposed to be invariant leading to non-varying equilibrium voltages.

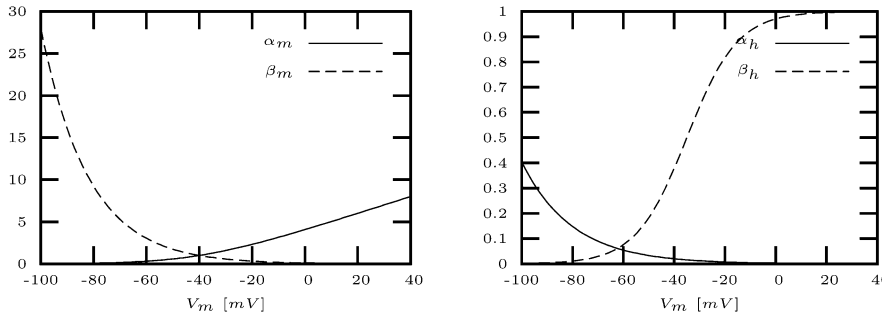

Fig. 7.9. Rate coefficients of sodium channels of the Hodgkin-Huxley model. The coefficients describe the voltage and time dependent changes of the state variables responsible for (a) the activation and (b) the inactivation of sodium channels.

The sodium conductivity g_{Na} is time and voltage dependent:

$$g_{Na} = m^3 h \overline{g}_{Na}$$

with the maximal conductance for sodium ions $\overline{g}_{Na}$, the dimensionless activation variable m, and inactivation variable h. The voltage dependent rate constants α_m, β_m, α_h, and β_h control the activation and inactivation variable:

$$\frac{dm}{dt} = \alpha_m(1-m) - \beta_n m$$
$$\frac{dh}{dt} = \alpha_h(1-n) - \beta_n h$$

Fig. 7.9 shows the dependency on the rate constants α_m, β_m, α_h, and β_h to the transmembrane voltage V_m.

The biophysical motivated assumption of the weighting of the conductance g_{Na} by the state variables m and h was, that sodium ions can only flow through a sodium channel, if three similar, independent events lead to an opening and no blocking event occurred.

The potassium conductivity g_K is time and voltage dependent:

$$g_K = \overline{g}_K n^4$$

with the maximal conductance for potassium ions $\overline{g}_K$ and the dimensionless state variable n, which is regulated by the voltage dependent rate constants α_n and β_n:

$$\frac{dn}{dt} = \alpha_n(1-n) - \beta_n n$$

Fig. 7.10 depicts the dependence of the rate constants α_n and β_n to the transmembrane voltage V_m.

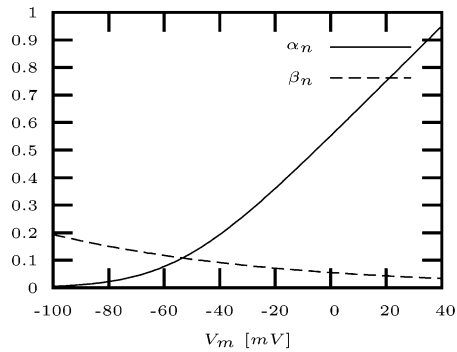

Fig. 7.10. Rate coefficients of potassium channels of the Hodgkin-Huxley model. The coefficients describe the voltage and time dependent changes of the state variables responsible for the activation of potassium channels.

The biophysical motivation of the weighting of the conductance g_K with the state variable n was the assumption, that potassium ions can only flow through a potassium channel, if four similar, independent events are involved in the opening process.

7.2.3 Models of Cardiac Myocytes

Overview. In the last years a large number of models of myocytes was constructed (table 7.1), with increasing abilities to describe the different electrophysiological mechanisms. Primarily, the models are produced from animal experiments using the mathematical formulations of Hodgkin and Huxley. The modeling approaches of the cell membrane, ionic channels and pumps, exchanger and intracellular components are combined to describe the behavior of a whole cell.

Modern models include detailed descriptions of the behavior of intracellular structures as well as of the influence of pharmaceuticals, neurotransmitters and mechanics. Some recently published models describe the human cellular electrophysiology.

In the following some electrophysiological models of cardiac cells are described. Their assumptions, principles and advances are presented. The overview is focused to models of ventricular myocytes. A model of Purkinje fibers and of cells from the sinoatrial node extend the overview. Special attention was attended to the handling of intracellular calcium, because of its importance for the coupling between electrical excitation and mechanical contraction.

Model of Noble (1962). The Noble model describes the electrophysiology of a Purkinje fiber by modifications of the Hodgkin-Huxley equations (Fig. 7.11) [170]. The selection of this cell type was caused by the relatively

Table 7.1. Electrophysiological models of cardiac cells.

Date	Publisher	Cell Type	Species	Reference
1962	Noble	Purkinje fiber	-	[170]
1975	McAllister, Noble, Tsien	Purkinje fiber	-	[171]
1977	Beeler, Reuter	ventricular myocardium	mammal	[172]
1980	Yanagihara, Noma, Irisawa	sinus node	rabbit	[173]
1982	Bristow, Clark	sinus node	rabbit	[174]
1983	Bristow, Clark	sinus node	rabbit	[175]
1984	Noble, Noble	sinus node	rabbit	[176]
1985	DiFrancesco, Noble	Purkinje fiber	mammal	[177]
1987	Hilgemann, Noble	atrial myocardium	rabbit	[178]
1990	Earm, Noble	atrial myocardium	rabbit	[179]
1991	Luo, Rudy	ventricular myocardium	mammal	[180]
1994	Luo, Rudy	ventricular myocardium	guinea pig	[181, 182]
1994	Demir, Clark, Murphey, Giles	sinus node	mammal	[183]
1996	Dokos, Celler, Lovell	sinus node	mammal	[184]
1996	Demir, O'Rourke, Tomaselli, Marban, Winslow	ventricular myocardium	canine	[185]
1996	Lindblad, Murphey, Clark, Giles	atrial myocardium	rabbit	[186]
1998	Courtemanche, Ramirez, Nattel	atrial myocardium	human	[187]
1998	Jafri, Rice, Winslow	ventricular myocardium	guinea pig	[188]
1998	Noble, Varghese, Kohl, Noble	ventricular myocardium	guinea pig	[189]
1998	Nygren, Fiset, Firek, Clark, Lindblad, Clark, Giles	atrial myocardium	human	[190]
1998	Priebe, Beuckelmann	ventricular myocardium	human	[191]
1999	Winslow, Rice, Jafri, Marbán, O'Rourke	ventricular myocardium	canine	[192, 193]
2000	Ramirez, Nattel, Courtemanche	atrial myocardium	canine	[194]
2000	Zhang, Holden, Kodama, Honjo, Lei, Varghese, Boyett	sinus node	rabbit	[195]
2002	Bernus, Wilders, Zemlin, Verschelde, Panfilov	ventricular myocardium	human	[196]
2003	Sachse, Seemann, Chaisaowong, Weiß	ventricular myocardium	human	[197]
2003	Seemann, Sachse, Weiß, Dössel	ventricular myocardium	human	[198]
2003	Ten Tusscher, Noble, Noble, Panfilov	ventricular myocardium	human	[199]

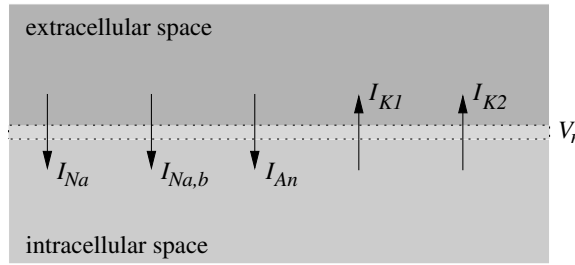

Fig. 7.11. Schematic diagram of the Noble model. The model calculates the currents I_{Na}, $I_{Na,b}$, I_{K1}, I_{K2}, and I_{An} as well as the transmembrane voltage V_m.

large cellular size simplifying measurements and by the apparent resemblance of the electrophysiological behavior to nervous cells. A novel quality of the model was the decomposition of the sodium and potassium currents as well as the reconstruction of the pace-maker property in cells. As in the Hodgkin-Huxley model all ionic concentrations are supposed to be invariant. The conductances and the rate constants are adapted to fit to measurements and to take into account the decompositions.

The transmembrane current I_m reconstructed by the Noble model consists of

$$I_m = I_{Na} + I_{Na,b} + I_{K1} + I_{K2} + I_{An}$$

with the inward sodium current I_{Na}, the background sodium current $I_{Na,b}$, the outward potassium currents I_{K1} and I_{K2}, and the anion current I_{An} corresponding to the leak current of the Hodgkin-Huxley model.

The sodium current equations are similar to those from the Hodgkin-Huxley equations:

$$\begin{aligned} I_{Na} &= g_{Na}(V_m - E_{Na}) \\ g_{Na} &= m^3 h \overline{g}_{Na} \end{aligned}$$

with the time and voltage dependent conductance for sodium g_{Na}, the equilibrium sodium voltage E_{Na}, the dimensionless activation variable m and inactivation variable h. The sodium current is the principal determinant during the rising phase of the action voltage.

A background sodium current $I_{Na,b}$ controlled by the constant background conductance $g_{Na,b}$ is introduced:

$$I_{Na,b} = g_{Na,b}(V_m - E_{Na})$$

The outward potassium current is composed of two currents I_{K1} and I_{K2}. The current I_{K1} is time independent and decreases instantaneously when the membrane voltage increases:

$$I_{K1} = g_{K1}(V_m - E_K)$$
$$g_{K1} = 1.2e^{-\frac{V_m}{50}} + 0.015e^{\frac{V_m+90}{60}}$$

with the potassium conductance g_{K1} and the equilibrium potassium voltage E_K. The current I_{K2} is time and voltage dependent. Its description is similar to the Hodgkin-Huxley model:

$$I_{K2} = g_{K_2}(V_m - E_K)$$
$$g_{K2} = \overline{g}_{K2} n^4$$

with the conductance for potassium g_{K2}, the maximal conductance for potassium $\overline{g}_{K2}$, and the dimensionless activation variable n. The voltage dependent rate constants α_n and β_n specify the activation by

$$\frac{dn}{dt} = \alpha_n(1 - n) - \beta_n n$$

Their values are two order of magnitude smaller than in the Hodgkin-Huxley model, because of the slower onset of this current in Purkinje fibers.

The anion current equations are similar to those from Hodgkin-Huxley:

$$I_{An} = g_{An}(V_m - E_{An})$$

with the constant anion conductance g_{An} and the anion equilibrium voltage E_{An}.

Model of Beeler and Reuter (1977). The Beeler-Reuter model describes the electrophysiology of a mammalian ventricular myocyte based on measurements with the voltage-clamp method on multicellular preparations of cardiac muscle (Fig. 7.12) [172]. Variables of the model are the transmembrane voltage V_m and the intracellular calcium concentration $[Ca^{2+}]_i$ as well as six activation and inactivation parameters m, h, j, d, f, and $x1$ controlling the conductance of the membrane. Each of these parameters is governed by a Hodgkin-Huxley equation with specifically chosen transfer rate coefficients.

The transmembrane current I_m reconstructed by the Beeler-Reuter model consists of

$$I_m = I_{Na} + I_{Na,b} + I_{K1} + I_{X1} + I_S$$

with:

Fast inward sodium current	I_{Na}
Background sodium current	$I_{Na,b}$
Outward potassium current	I_{K1}
Non-specific outward current, primarily potassium	I_{X1}
Non-specific inward current, primarily calcium	I_S

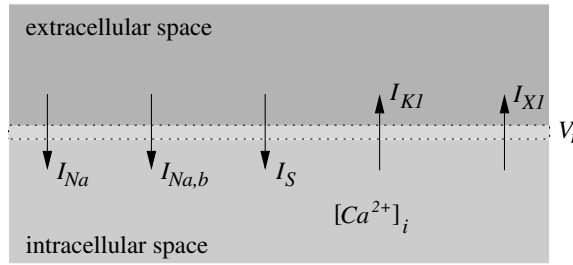

Fig. 7.12. Schematic diagram of the Beeler-Reuter model. The model calculates the transmembrane voltage V_m, the currents I_{Na}, $I_{Na,b}$, I_{K1}, I_{X1}, and I_S, and the intracellular calcium concentration $[Ca^{2+}]_i$.

The time- and voltage-dependent inward sodium current I_{Na} is in particular responsible for the fast upstroke of the action voltage. The formulation is in parts adopted from the Hodgkin-Huxley and the Noble model:

$$I_{Na} = g_{Na} m^3 h j (V_m - E_{Na})$$

with the Nernst voltage of sodium $E_{Na} = 50\ mV$, the maximal sodium conductance g_{Na}, the activation parameter m, and the inactivation parameters h and j.

The sodium background current $I_{Na,b}$ is time independent:

$$I_{Na,b} = g_{Na,b}(V_m - E_{Na})$$

with the background sodium conductance $g_{Na,b}$ chosen to reproduce the measured steady sodium leakage current.

The time-independent and voltage-dependent outward potassium current I_{K1} is obtained by:

$$I_{K1} = 0.35 \left(\frac{4e^{0.04(V_m+85)-1}}{e^{0.08(V_m+53)} + e^{0.04(V_m+53)}} + \frac{0.2(V_m+23)}{1-e^{-0.04(V_m+23)}} \right)$$

A large contribution of this current to the transmembrane current can be found at the plateau phase of the action voltage. The current is slowly deactivated and a determinant for the shape of the plateau phase of the action voltage.

The time-dependent and voltage-dependent outward current I_{X1} is mainly dedicated to the flow of potassium ions:

$$I_{X1} = 0.8\ x1\ \frac{e^{0.04(V_m+77)} - 1}{e^{0.04(V_m+35)}}$$

with the parameter $x1$. The current is slowly activated and responsible for the repolarization of the cell membrane.

The time- and voltage-dependent inward current I_S reflects the summary flow of different types of ions, but is primarily attributed to calcium ions:

$$I_S = g_s df(V_m - E_s)$$

with the Nernst voltage of calcium $E_s = -82.3 - 13.0287\ ln\ [Ca^{2+}]_i$, the maximal conductance g_s, the activation parameter d, and the inactivation parameter f. As the outward current I_{K1} the current I_S is slowly deactivated and a determinant for the shape of the plateau phase of the action voltage.

The concentration of the intracellular calcium $[Ca^{2+}]_i$ is initially set to 0.2 μM. The time derivative of $[Ca^{2+}]_i$ is calculated with the inward current I_S by

$$\frac{\partial [Ca^{2+}]_i}{\partial t} = -10^{-7} I_S + 0.07(10^{-7} - [Ca^{2+}]_i)$$

Fig. 7.13 (a) shows the transmembrane voltage calculated with the Beeler-Reuter model in dependency on different stimulus frequencies. An increase of the stimulus frequency in the range of $[0.5Hz \ldots 3Hz]$ leads to an decrease of the plateau voltage as well as of the action voltage duration. Simulations with lower frequencies lead to insignificant changes in the shape and duration of the action voltage. Simulations with higher frequencies using stimuli in the relative and absolute refractory period lead commonly to irregular shapes and durations.

Fig. 7.13 (b) depicts the intracellular calcium concentration $[Ca^{2+}]_i$ resulting from simulations with different stimulus frequencies. An increase of the stimulus frequency in the range $[0.5Hz \ldots 3Hz]$ leads to a decreasing duration of the action voltage and of the calcium enhancement. Furthermore, the potential in and after the plateau phase is reduced.

The model of Beeler-Reuter reconstructs successfully the transmembrane voltage of ventricular myocytes. Major drawback is the neglect of important ionic channels, pumps and exchangers leading to deficiencies for the reconstruction of many phenomena. Furthermore, the model overestimates the intracellular calcium concentration $[Ca^{2+}]_i$ significantly, which can be attributed e.g. to the neglect of buffering mechanisms by troponin and calmodulin.

Model of Luo and Rudy Phase-1 (1991). The Luo-Rudy phase-1 model describes the electrophysiology of a ventricular cell from guinea pig based primarily on data from single-cell and single-channel measurements (Fig. 7.14) [180]. The model is a succession of the Beeler-Reuter model using similar formulations e.g. for the fast sodium current and the slow inward current. Variables of the model are the transmembrane voltage V_m and the intracellular calcium concentration $[Ca^{2+}]_i$ as well as seven activation and inactivation parameters m, h, j, d, f, x, and $k1$. Each of these parameters is governed by a Hodgkin-Huxley equation with specifically chosen transfer rate coefficients.

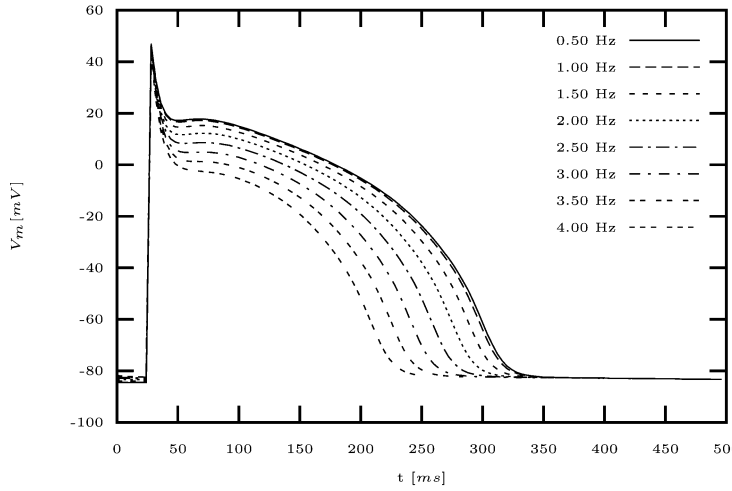

(a)

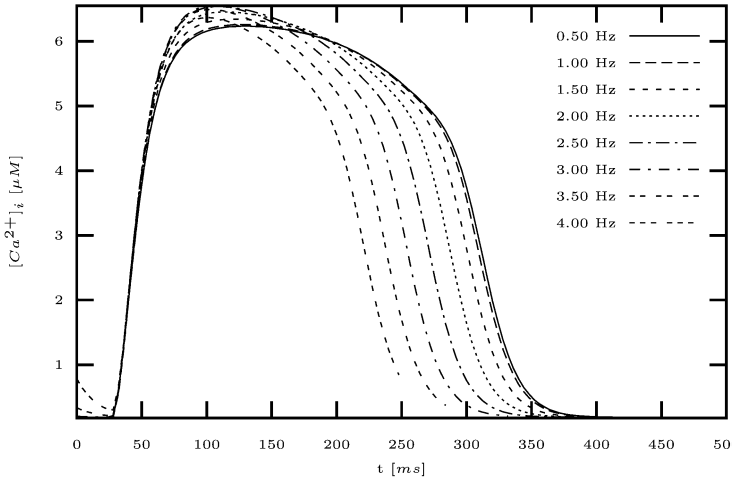

(b)

Fig. 7.13. Simulations with the Beeler-Reuter model. (a) Transmembrane voltage V_m and (b) intracellular calcium concentration $[Ca^{2+}]_i$ are dependent on the stimulus frequency. For each frequency a single course is visualized. The cell is activated by applying a current at $t = 25\ ms$ with a length of 3 ms.

The transmembrane current I_m of the Luo-Rudy phase-1 model consists of

$$I_m = I_{Na} + I_{si} + I_K + I_{K1} + I_{Kp} + I_b$$

with:

Fast inward sodium current	I_{Na}
Slow inward current	I_{si}
Time-dependent potassium current	I_K
Time-independent potassium current	I_{K1}
Plateau potassium current	I_{Kp}
Background potassium current	I_b

The transfer rate coefficients for the activation of the fast inward sodium current I_{Na} were adjusted to achieve an upstroke velocity $\frac{\partial V_m}{\partial t}$ of 400 $\frac{mV}{s}$. A novelty of the model was the introduction of the plateau potassium current I_{Kp} activated at high potentials.

The model allows the reproduction of supernormal activity, defined as larger than normal excitability during or after the repolarization phase, and of Wenckebach periodicity, defined as periodic, stimulus frequency dependent activation failure.

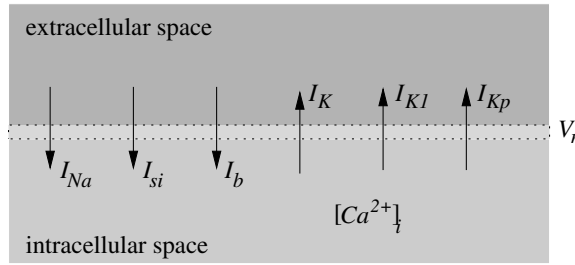

Fig. 7.14. Schematic diagram of the Luo-Rudy phase-1 model. The model calculates the transmembrane voltage V_m, the currents I_{Na}, I_{si}, I_K, I_{K1}, I_{Ko}, and I_b, and the intracellular calcium concentration $[Ca^{2+}]_i$.

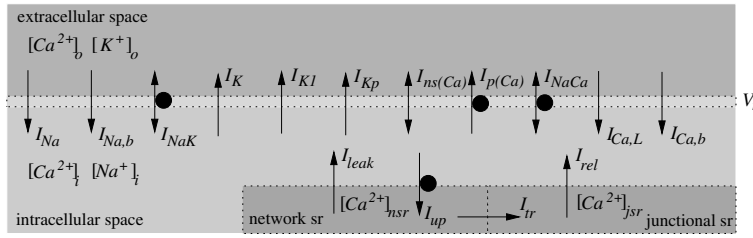

Fig. 7.15. Schematic diagram of the original Luo-Rudy phase-2 model. The model calculates the transmembrane voltage V_m, eleven currents through the sarcolemma and four currents of the sarcoplasmic reticulum (sr). Furthermore, two extracellular and four intracellular concentrations are updated.

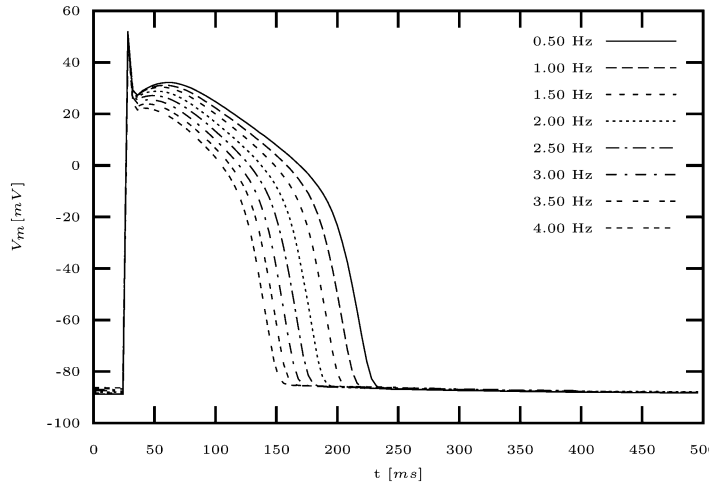

(a)

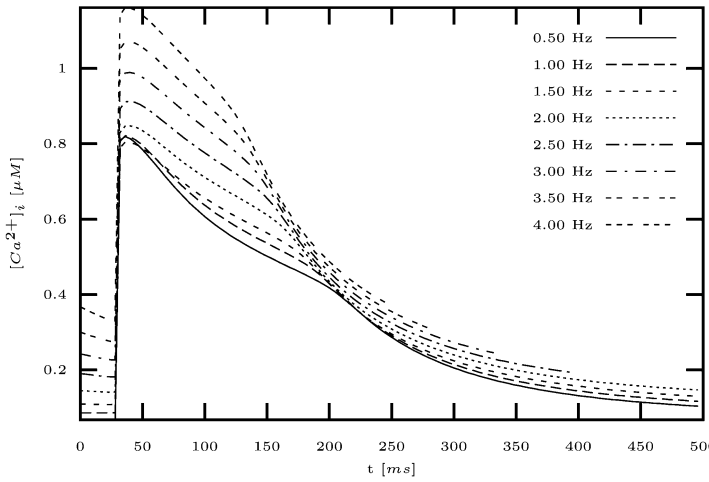

(b)

Fig. 7.16. Simulations with an enhanced Luo-Rudy phase-2 model. (a) Transmembrane voltage V_m and (b) intracellular calcium concentration $[Ca^{2+}]_i$ are dependent on the stimulus frequency. For each frequency a single course of the transmembrane voltage and intracellular calcium concentration, respectively, is visualized.

Model of Luo and Rudy Phase-2 (1994). The Luo-Rudy phase-2 model is an extension of the phase-1 model and describes the electrophysiology of a ventricular cell (Fig. 7.15) [181, 182]. The model is constructed primarily from single-cell and single-channel measurements of guinea pig ventricular cells. The extension consists mainly of a reformulation of the calcium handling, i.e. the intracellular currents describing quantitatively the calcium mechanics of the

sarcoplasmic reticulum. Different enhancements and adaptations of the model exist.

The transmembrane current I_m of the original phase-2 model consists of

$$I_m = I_{Na} + I_{Ca,L} + I_K + I_{K1} + I_{Kp} + I_{NaCa} + I_{NaK} + I_{ns(Ca)} + I_{p(Ca)} + I_{Ca,b} + I_{Na,b}$$

with:

Fast inward sodium current	I_{Na}
Currents through L-type calcium channel (Ca^{2+}, Na^+, K^+)	$I_{Ca,L}$
Time-dependent potassium current	I_K
Time-independent potassium current	I_{K1}
Plateau potassium current	I_{Kp}
Na-Ca exchanger current	I_{NaCa}
Na-K pump current	I_{NaK}
Non-specific calcium-activated current	$I_{ns(Ca)}$
Sarcolemmal calcium pump	$I_{p(Ca)}$
Background calcium current	$I_{Ca,b}$
Background sodium current	$I_{Na,b}$

The model includes a representation of the sarcoplasmic reticulum by two subcompartements, the network and the junctional sarcoplasmic reticulum. The subcompartements serve for the buffering of calcium ions. The intracellular calcium mechanisms are governed by four currents:

inward calcium current to network sarcoplasmic reticulum	I_{up}
outward calcium current from network sarcoplasmic reticulum	I_{leak}
calcium current between network and junctional sarcoplasmic reticulum	I_{tr}
outward calcium current from junctional sarcoplasmic reticulum	I_{rel}

The current I_{up} represents a pump mechanism transporting calcium ions from the cytoplasm to the network sarcoplasmic reticulum. The calcium ions are transferred via a leak current I_{leak} back to the cytoplasm and via the current I_{tr} to the junctional sarcoplasmic reticulum. Thenceforth, the calcium is released to the cytoplasm with a calcium activated current I_{rel}.

The model allows the reconstruction of early (EAD) and delayed afterdepolarization (DAD) as well as triggered and rhythmic activity, which are arrhythmogenic single cell phenomena [200]. The EAD is defined as a depolarizing after-voltage beginning before the completion, the DAD as a depolarizing after-voltage beginning after the completion of the repolarization.

Model of Demir, Clark, Murphey and Giles (1994). The Demir-Clark-Murphey-Giles model describes the electrophysiology of a rabbit sinoatrial node cell (Fig. 7.17) [183]. The model is based on whole cell recordings from enzymatically isolated single cells of the border zone of the sinus node. The

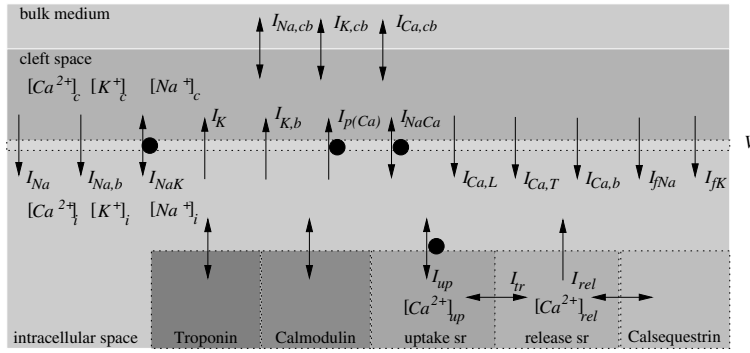

Fig. 7.17. Schematic diagram of the Demir-Clark-Murphey-Giles model. The model calculates the transmembrane voltage V_m, twelve currents through the sarcolemma, three current from the cleft space to the bulk medium, and three currents of the sarcoplasmic reticulum (sr). Furthermore, three cleft and five intracellular concentrations are updated.

internal concept is derived from the work of DiFrancesco and Noble [177] as well as Hilgeman and Noble [178].

The transmembrane currents I_m of the Demir-Clark-Murphey-Giles model are described by:

$$\begin{aligned} I_m = {} & I_{Na} + I_{Ca,T} + I_{Ca,L} + I_K + I_{fK} \\ & + I_{fNa} + I_{Na,b} + I_{K,b} + I_{Ca,b} + I_{NaK} + I_{NaCa} + I_{p(Ca)} \end{aligned}$$

with:

Inward sodium current	I_{Na}
Transient calcium current	$I_{Ca,T}$
Long-lasting calcium current	$I_{Ca,L}$
Time- and voltage dependent delayed rectifier potassium current	I_K
Hyper-polarization-activated potassium current	I_{fK}
Hyper-polarization-activated sodium current	I_{fNa}
Background sodium current	$I_{Na,b}$
Background potassium current	$I_{K,b}$
Background calcium current	$I_{Ca,b}$
Na-K pump current	I_{NaK}
Na-Ca exchanger current	I_{NaCa}
Calcium pump current	$I_{p(Ca)}$

The activation rate coefficients of the inward sodium currents are adapted to consider the low upstroke velocity $\frac{\partial V_m}{\partial t}$ of sinoatrial node cells. The model includes two hyper-polarization-activated currents I_{fK} and I_{fNa}. Hyper-polarization-activated currents are of importance for any model of pacemaker

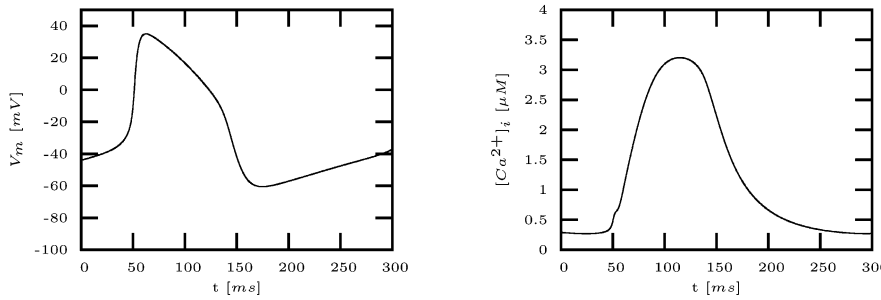

(a) (b)

Fig. 7.18. (a) Transmembrane voltage V_m and (b) intracellular calcium concentration $[Ca^{2+}]_i$ calculated with Demir-Clark-Murphey-Giles model.

activity. The currents increase the transmembrane voltage after a repolarization. An automatic depolarization process is initiated after exceeding of the threshold voltage (Fig. 7.18).

Model of Priebe and Beuckelmann (1998). The Priebe-Beuckelmann model describes the electrophysiology of a human ventricular myocyte [191]. The model was used as a tool to explore therapeutic interventions on the electrical excitability of myocardium. The model is a descendant of the Luo-Rudy phase-2 model, which was parameterized with data from measurements of transmembrane voltage, ionic currents and concentrations in human myocytes [201].

The transmembrane currents I_m of the Priebe-Beuckelmann model are described by:

$$\begin{aligned} I_m = {} & I_{Na} + I_{Ca,L} + I_{to} + I_{Kr} + I_{Ks} \\ & + I_{K1} + I_{NaCa} + I_{NaK} + I_{Na,b} + I_{Ca,b} \end{aligned}$$

with:

Inward sodium current	I_{Na}
Long-lasting calcium current	$I_{Ca,L}$
Transient outward potassium current	I_{to}
Time- and voltage dependent delayed rectifier potassium current	I_{Kr}
Time- and voltage dependent delayed rectifier potassium current	I_{Ks}
Inward rectifier potassium current	I_{K1}
Na-Ca exchanger current	I_{NaCa}
Na-K pump current	I_{NaK}
Background potassium current	$I_{Na,b}$
Background calcium current	$I_{Ca,b}$

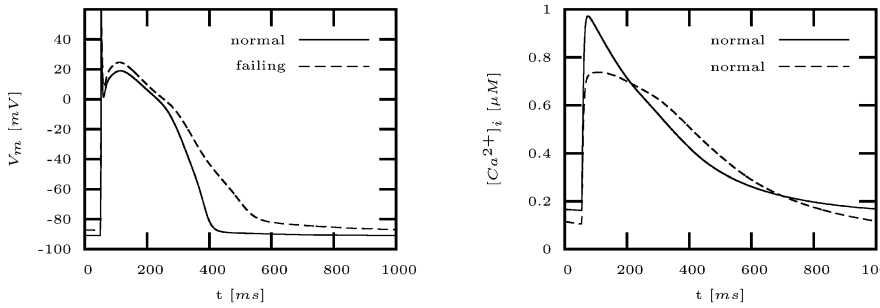

Fig. 7.19. Simulations with the Priebe-Beuckelmann model of human ventricular myocytes. The reconstructed course of (a) transmembrane voltage V_m and (b) intracellular calcium concentration $[Ca^{2+}]_i$ show differences in normal and failing myocytes. Failing myocytes feature prolonged duration of action voltage and intracellular calcium transients.

Models exist for normal and failing myocytes (Fig. 7.19). The model of failing myocytes differs in several parameters from the model of normal myocytes: reduced conductivity for transient output potassium current $g_{to,max}$, reduced conductivity for inward rectifier current $g_{K1,max}$, increased conductivity for calcium background current $\overline{G}_{Ca,b}$, reduced conductivity of sodium background current $\overline{G}_{Na,b}$, down-regulation of Na-K pump $\overline{I}_{NaK}$, up-regulation of Na-Ca exchanger k_{NaCa}, down-regulation of network sarcoplasmic reticulum calcium pump $\overline{I}_{up}$, and decreased calcium leak of network sarcoplasmic reticulum K_{leak}.

A variant of the model exists using only six state variables, which allows an efficient calculation of excitation propagation [196]. The models shows significant numerical advantages, but neglects intracellular calcium handling and several further components.

The Priebe-Beuckelmann model was adapted in subsequent work to take recent measurement data from humans into account and to integrate it with tension development models [197, 198]. Adaptations were made for both normal and failing myocytes concerning the intracellular calcium handling, i.e. NSR Ca^{2+} uptake, Ca^{2+} background current, and Na-Ca exchanger. Further adaptations were made to reconstruct the heterogeneity of several components over the ventricular wall, i.e. transient outward potassium current I_{to}, the delayed rectifier potassium currents I_{Kr} and I_{Ks}, and inward rectifier potassium current I_{K1}.

Model of Noble, Varghese, Kohl and Noble (1998). The Noble-Varghese-Kohl-Noble model describes the electrophysiology of a ventricular cell of guinea pig (Fig. 7.20). The model includes effects on ionic channels by the concentration of ATP and acetylcholine (ACh) as well as by stretching. Furthermore, a force generation model is included. A description of the diadic

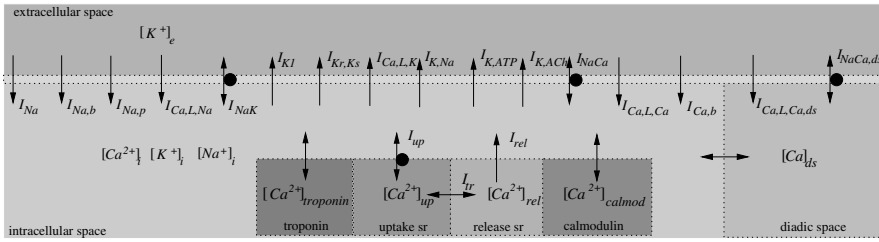

Fig. 7.20. Schematic overview of the Noble-Varghese-Kohl-Noble model. The model calculates the transmembrane voltage V_m, the currents through the sarcolemma to the intracellular space and the currents of the sarcoplasmic reticulum (sr). Furthermore, intra- and extracellular concentrations are updated.

space is incorporated. Different variants and configurations of the model exist. The following description is based on [189, 202, 203] and focused on the electrophysiological part of the model.

Hereby, the transmembrane currents are described by:

$$\begin{aligned} I_m = & I_{Na} + I_{Na,b} + I_{Na,p} \\ & + I_{K1} + I_{Kr} + I_{Ks} + I_{K,ATP} + I_{K,ACh} \\ & + I_{Ca,b} + I_{Ca,L,K} + I_{Ca,L,Na} + I_{Ca,L,Ca} \\ & + I_{Ca,L,K,ds} + I_{Ca,L,Na,ds} + I_{Ca,L,Ca,ds} \\ & + I_{NaK} + I_{NaCa} + I_{NaCa,ds} \\ & + I_{stretch} \end{aligned}$$

with:

Fast sodium current	I_{Na}
Background sodium current	$I_{Na,b}$
Voltage dependent sodium current	$I_{Na,p}$
Time-independent potassium current (background)	I_{K1}
Time-dependent, delayed potassium currents	I_{Kr}, I_{Ks}
Sodium dependent potassium current	$I_{K,Na}$
ATP-dependent potassium current	$I_{K,ATP}$
ACh-dependent potassium current	$I_{K,ACh}$
Background calcium current	$I_{Ca,b}$
Currents through L-type calcium channels	$I_{Ca,L,Ca}$, $I_{Ca,L,Na}$, $I_{Ca,L,K}$
L-type calcium current into the diadic space	$I_{Ca,L,Ca,ds}$
Na-K pump current	I_{NaK}
Na-Ca exchanger current	I_{NaCa}
Na-Ca exchanger current for diadic space	$I_{NaCa,ds}$
Stretch activated currents	$I_{stretch}$

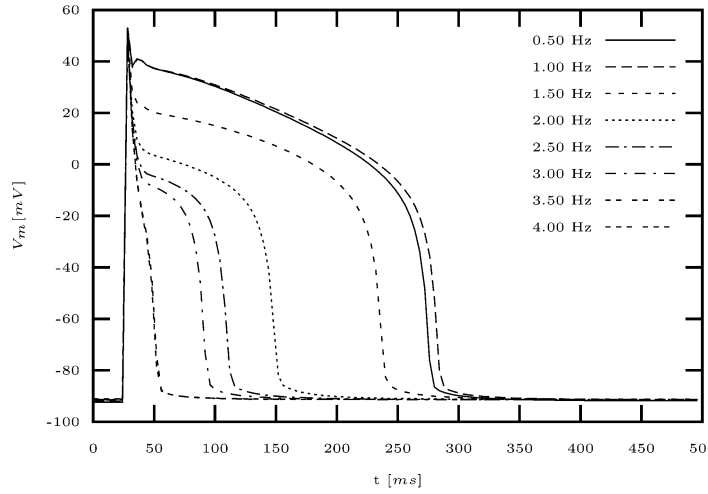

(a)

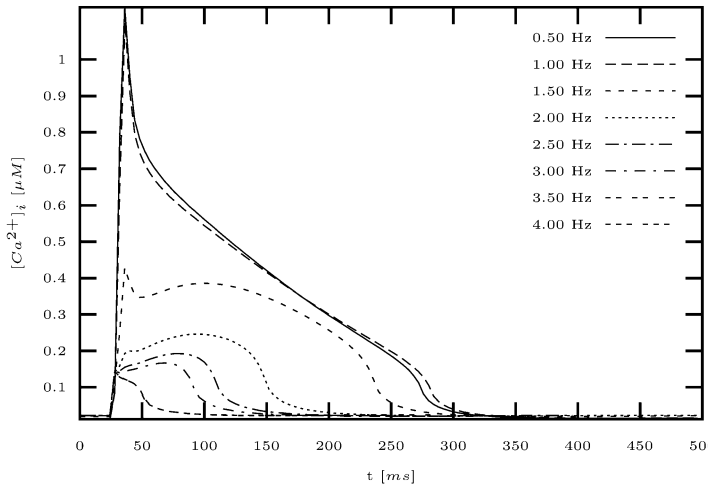

(b)

Fig. 7.21. Simulations with the Noble-Varghese-Kohl-Noble model. (a) Transmembrane voltage V_m and (b) intracellular calcium concentration $[Ca^{2+}]_i$ are dependent on the stimulus frequency. For each frequency a single course of the transmembrane voltage and the calcium concentration is visualized.

Fig. 7.21 shows the influence of stimulus frequency to the course of the transmembrane voltage V_m and intracellular calcium concentration $[Ca^{2+}]_i$. Hereby, stretch activated currents are neglected. With higher stimulus frequency the resting voltage is increased and the duration of the action voltage is decreased.

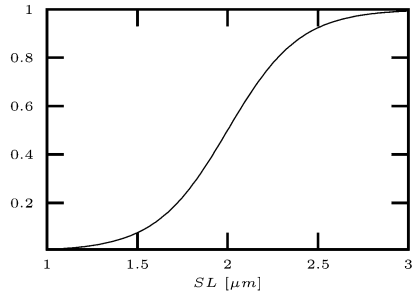

Fig. 7.22. Stretch function for weighting of ion conductances in dependence of sarcomere length SL. The sarcomere length $SLHST$ of half maximal activation is set to 2 μm, the steepness parameter $SACSL$ to 2.

Intracellular Mechano-Electric Feedback. The Noble-Varghese-Kohl-Noble model includes dependencies of electrophysiological parameters on the length or tension of the sarcomere. The mechano-electric feedback is realized by introducing

- selective and non selective stretch-activated ion conductances
- a modulation of calcium binding to troponin
- a modulation of sarcoplasmic leak current

The following description of the mechanisms is restricted to the length dependencies of the electrophysiological parameters. The length or stretch dependent formulation is of advantage for the coupling with deformation models.

Stretch-activated ion conductances. Two models are proposed to calculate stretch-activated ion conductances and to reconstruct stretch activated currents. In both models the ion conductances are weighted by the sarcomere length SL with the stretch function

$$fstretch(SL) = \frac{1}{1 + e^{-2SACSL(SL-SLHST)}}$$

with the steepness parameter $SACSL$ and the sarcomere length $SLHST$ at which half maximal activation occurs (Fig. 7.22).

The first model describes the summary stretch current $I_{stretch}$ with a nonspecific $I_{Ns-stretch}$ and an anion stretch current $I_{An-stretch}$:

$$I_{stretch} = I_{Ns-stretch} + I_{An-stretch}$$

The currents $I_{Ns-stretch}$ and $I_{An-stretch}$ are determined by the stretch function $fstretch$ dependent on the sarcomere length SL, the maximal conductivities $g_{Ns-stretch}$ and $g_{An-stretch}$, respectively, and the equilibrium voltages $E_{Ns-stretch}$ and $E_{An-stretch}$, respectively:

$$I_{Ns-stretch} = fstretch(SL)\ g_{Ns-stretch}\ (V_m - E_{Ns-stretch})$$
$$I_{An-stretch} = fstretch(SL)\ g_{An-stretch}\ (V_m - E_{An-stretch})$$

The second model subdivides the summary stretch current $I_{stretch}$ in a sodium $I_{Na-stretch}$, a potassium $I_{K-stretch}$, a calcium $I_{Ca-stretch}$, and an anion stretch current $I_{An-stretch}$:

$$I_{stretch} = I_{Na-stretch} + I_{K-stretch} + I_{Ca-stretch} + I_{An-stretch} \tag{7.1}$$

Hereby, the stretch currents are calculated as described in the simple model with the stretch function $fstretch$, the maximal conductivities and the equilibrium voltages:

$$\begin{aligned} I_{Na-stretch} &= fstretch(SL)\ g_{Na-stretch}\ (V_m - E_{Na}) \\ I_{K-stretch} &= fstretch(SL)\ g_{K-stretch}\ (V_m - E_K) \\ I_{Ca-stretch} &= fstretch(SL)\ g_{Ca-stretch}\ (V_m - E_{Ca}) \\ I_{An-stretch} &= fstretch(SL)\ g_{An-stretch}\ (V_m - E_{An-stretch}) \end{aligned}$$

The second model describes the stretch current obviously more detailed regarding the different types of ions and herewith offers the advantage to update quantitatively the sodium, potassium and calcium concentrations.

Modulation of calcium binding to troponin C. The binding of intracellular calcium to troponin C is modulated by stretch:

$$\begin{aligned} \frac{\partial [Ca^{2+}]_{troponin}}{\partial t} = {} & \alpha_{troponin} e^{\gamma_{trop,SL} SL} ([troponin] - [Ca^{2+}]_{troponin})[Ca^{2+}]_i \\ & - \beta_{troponin} [Ca^{2+}]_{troponin} \end{aligned}$$

with the concentration of calcium bound to troponin C $[Ca^{2+}]_{troponin}$, the total troponin concentration $[tropronin]$, the intracellular calcium concentration $[Ca^{2+}]_i$, the transfer rates $\alpha_{troponin}$ and $\beta_{troponin}$, and the parameter $\gamma_{trop,SL}$. The stretch is defined by the sarcomere length SL.

Modulation of sarcoplasmic reticulum leak current. The calcium leak current I_{rel} from the sarcoplasmic reticulum to the cytoplasm is divided in a stretch dependent and an independent part:

$$I_{rel} = \left(\frac{f_{activator}}{f_{activator} + 0.25} \right)^2 k_{mca2} [Ca^{2+}]_{rel} + J_{SR-leak} e^{\gamma_{SR,SL} SL}$$

The current is controlled independently of stretch by the state variable $f_{activator}$, the parameter k_{mca2} and the sarcoplasmic calcium concentration $[Ca^{2+}]_{rel}$. The stretch dependent part is calculated with the sarcomere length SL, the experimentally determined parameters $\gamma_{SR,SL}$ and $J_{SR-leak}$.

Simulations. Two sets of simulations were performed to examine the influence of static and dynamic stretch [204]. The influence of static stretch of different strength was tested by initiation of excitation via injection of a convenient current with a duration of 3 ms. The phenomena of dynamic stretch were

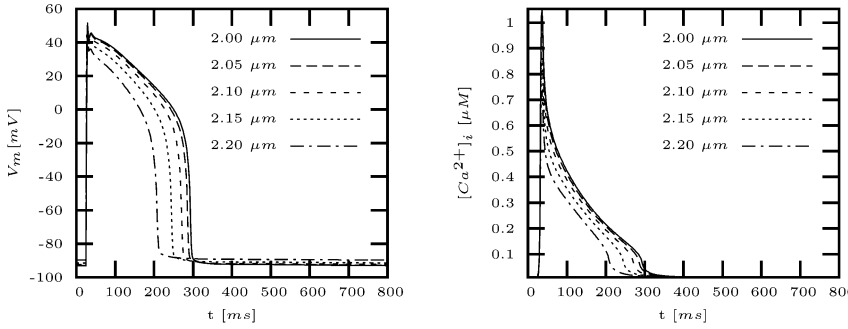

Fig. 7.23. Simulations with varied static length of sarcomere. (a) Transmembrane voltage and (b) calcium concentration in the cytoplasm dependent on length of sarcomere calculated with Noble-Varghese-Kohl-Noble model. The cell is excited by applying a stimulus current at $t = 25\ ms$ with a length of 3 ms. The sarcomere length ranges from 2.0 to 2.2 μm. The default length of the sarcomere is 2 μm. The stimulus frequency was set to 1 Hz.

examined with different stretch impulses and durations. The application of stretch starts in the diastolic phase. In both sets of simulations the calculated model variables were stored and processed.

The complex stretch model (equation 7.1) is parameterized and used in the following simulations. The parameterization was performed by fitting data measured in single guinea pig ventricular myocytes [155] with methods similar to those presented in [205]. The parameters are $SACSL = 7$, $SLHST = 2.4\ \mu m$, $g_{Na-stretch} = 15\ nS$, $g_{K-stretch} = 30\ nS$, $g_{Ca-stretch} = 0.1\ nS$, $g_{An-stretch} = 15\ nS$, and $E_{An-stretch} = -20\ mV$. The simulations deliver information concerning the mechanisms of mechano-electric feedback.

The influence of static stretch on the course of the transmembrane voltage and the intracellular calcium concentration is illustrated in Fig. 7.23 and Fig. 7.24. Hereby, the stretch amplitude is specified by the length of the sarcomere with a default of 2 μm. The resting voltage as well as the progression of the action voltage are dependent on the length of the sarcomere ranging from 1.6 to 2.2 μm. The resting voltage as well as the course of the action voltage are dependent on the length of the sarcomere ranging from 2.0 to 2.2 μm. The resting voltage increases and the duration of the action voltage decreases with larger sarcomere length. Both effects can be attributed to the raise of the sarcolemmal conductances. The maxima of the transmembrane voltage are independent of stretch.

The influence of mechanical stretch impulses is depicted in Fig. 7.25 and Fig. 7.26. In the presented simulations the stretch amplitude and duration were varied. Once again, the stretch amplitude was specified by the length of the sarcomere with a default of 2 μm. Depending on the amplitudes and

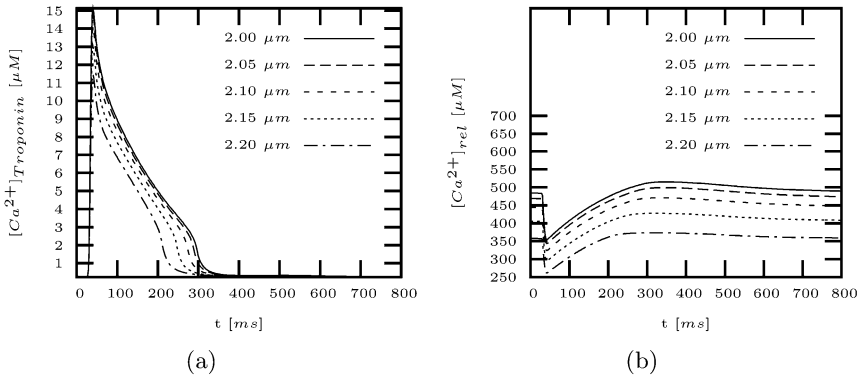

Fig. 7.24. Simulations with varied static length of sarcomere (continued). (a) concentration of calcium bound to troponin C and (b) concentration of calcium in the release part of the sarcoplasmic reticulum dependent on length of sarcomere calculated with Noble-Varghese-Kohl-Noble model. The cell is excited by applying a stimulus current at $t = 25\ ms$ with a length of 3 ms. The sarcomere length ranges from 2.0 to 2.2 μm. The default length of the sarcomere is 2 μm. The stimulus frequency was set to 1 Hz.

the length an effect ranging from a small change of the resting voltage to an excitation of the cell was achieved.

The simulation presented in Fig. 7.25 (a) shows the initiation of an action impulse by a relatively small stretch duration only for large sarcomere length. The simulations with sarcomere length 2.5 μm show an increase in the duration of the action impulse with the exception of the results with a relatively long stretch duration depicted in Fig. 7.26 (a) and (b).

The initiation of early afterdepolarizations (EAD) is apparent in Fig. 7.25 (d) and 7.26 (a) for sarcomere lengths 2.4 and 2.5 μm, and for length 2.4 μm, respectively. The classification of the EADs was performed using the description of [206] by examination of the activation and inactivation gates of the L-type calcium channels during the plateau phase.

All these effects are primarily attributed to the raise of the sarcolemmal conductances by stretch. The stretch dependence of intracellular structure influences the course of the transmembrane voltage only to a small degree.

7.3 Excitation Propagation

7.3.1 Experimental Studies

Measurement Systems. The propagation of electrical excitation in the heart is commonly measured by temporal and spatial registration of voltages resulting from cardiac current flow. Cellular processes generate the current

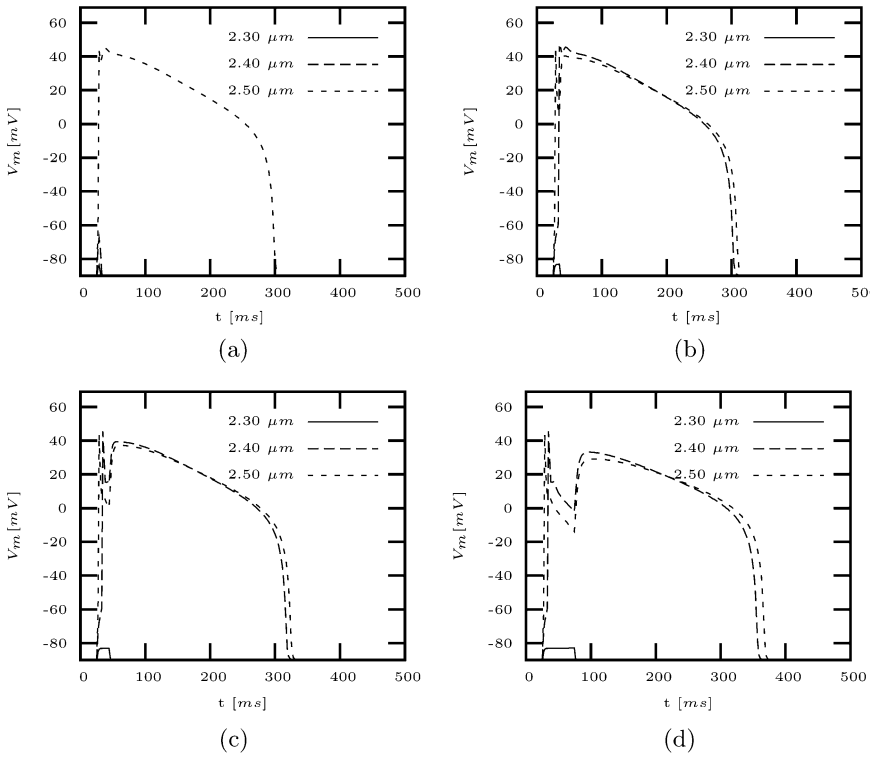

Fig. 7.25. Simulation of initiation of action impulse by dynamic stretch simulated with Noble-Varghese-Kohl-Noble model. At $t = 25\ ms$ a mechanical stretch of (a) 5 ms, (b) 10 ms, (c) 20 ms, and (d) 50 ms was performed delivering a sarcomere length from 2.3 to 2.5 μm. The default length of the sarcomere is 2 μm. Some combinations of stretch and length lead to action impulses, others increase the transmembrane voltage insufficiently for activation.

flow, i.e. the transmembrane current responsible for the de- and repolarization of myocytes (Sect. 7.2.1). Electrocardiographic, magnetocardiographic and optical systems were developed to register the propagation of electrical excitation.

Electrocardiographic systems measure so-called electrocardiograms, which are registered via electrodes and amplified for further processing [207]. An electrocardiogram consists of voltages, which are assigned to different points in time. These voltages can be alluded to the intra- and extracellular domain as well as over the membrane.

Magnetocardiographic systems produce magnetocardiograms, whereby the magnetic field resulting from the electrical current flow is registered [208]. This current flow is composed of intracellular, extracellular and transmembrane currents.

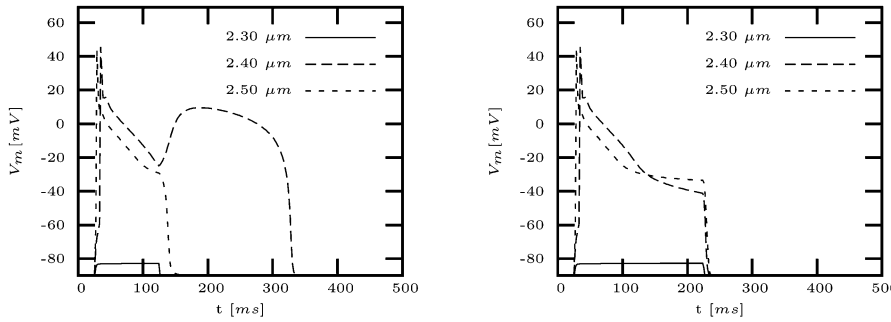

Fig. 7.26. Simulation of initiation of action impulse by dynamic stretch simulated with Noble-Varghese-Kohl-Noble model (continued). At $t = 25\ ms$ a mechanical stretch of (a) 100 ms, and (b) 200 ms was performed delivering a sarcomere length from 2.3 to 2.5 μm. The default length of the sarcomere is 2 μm.

Optical systems work in conjunction with voltage sensitive dyes, video recordings and image processing. Commonly, the course of transmembrane voltage is scanned at surfaces of extracorporated hearts and multicellular preparations.

The electrocardiography is the primary tool in clinical diagnosis. Hereby, the electrocardiograms are registered via electrodes, amplified and commonly visualized for visual analysis. A distinction commonly made for medical measurement systems concerns the placement of the registration. Hereby, extra- and intracorporal systems are distinguished.

Of diagnostic importance is the extracorporal registration via electrodes at the body surface, whereby different arrangements of electrodes are used to produce e.g. the leads of Einthoven, Goldberger and Wilson. The extracorporal registration delivers voltages resulting from the distribution of current sources in the heart and the conductivity distribution in the body (Fig. 7.27). A spatial discrimination of the excitation process is possible by analysis with numerical methods and by usage of background knowledge concerning the electrophysiology of the heart. Nevertheless, an automated, computer-based analysis is still topic of research.

Alternatively, in clinical diagnosis intracorporal methods allow a simplified spatial discrimination and deliver additional information. Hereby, voltages are measured e.g. at the subepicardial myocardium via multi-electrode socks [209] and in the endocardial cavity via multi-electrode catheters [210, 211].

Furthermore, the propagation can be observed directly at cellular and multicellular level, e.g. by registration of the

- transmembrane voltages with voltage clamp techniques (Sect. 7.2.1)
- intercellular current flow through gap junctions with double cell voltage clamp techniques (Sect. 7.2.1)
- extracellular voltages in the near-by of an excited structure (Fig. 7.28).

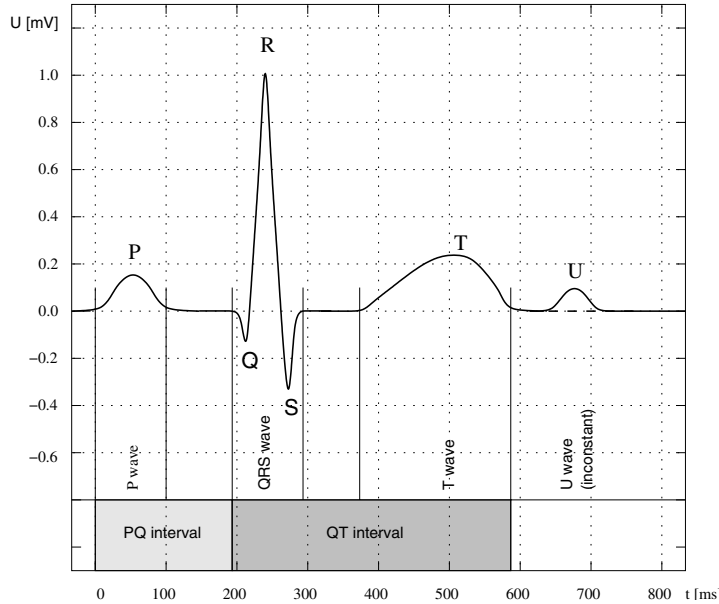

Fig. 7.27. Exemplary electrocardiogram for physiological excitation propagation in normal, adult humans. Commonly, the P wave takes less than 100 ms, the PQ interval less than 200 ms, and the QRS wave less than 100 ms. The duration of the QT interval is dependent on the cycle rate. E.g. for a cycle rate of 70 min^{-1} a duration of $320 - 390$ ms is observed [152].

The registration, analysis and automatic classification of electrocardiograms is a basic function of many biomedical instruments and software packages. E.g. the stimulus delivery of pacemakers as well as external and implanted defibrillators are controlled by features extracted from electrocardiograms. Also, the measurement of excitation propagation velocity necessitates the detection of activation times in electrograms.

Mechanisms. The mechanisms of macroscopic excitation propagation through the heart was examined by various studies since the begin of the twentieth century [128, 124, 117, 126]. The studies showed, that the normal electrical excitation is cyclical and precedes the mechanical contraction. The chronological order of activation was found to be similar in hearts of mammals.

As initiator of the physiological excitation serves the sinus node. Then, the excitation propagates over the right atrium to the atrioventricular node and via the Bachmann bundle to the left atrium. The atrioventricular node delays the propagation. Afterwards, the His bundle, the fast conducting Tawara bundle branches and the subendocardially located Purkinje fibers are activated. Subsequently, the excitation passes to the subendocardial ventricular myocardium, wherefrom the excitation traverses the ventricles to their epicardial surface.

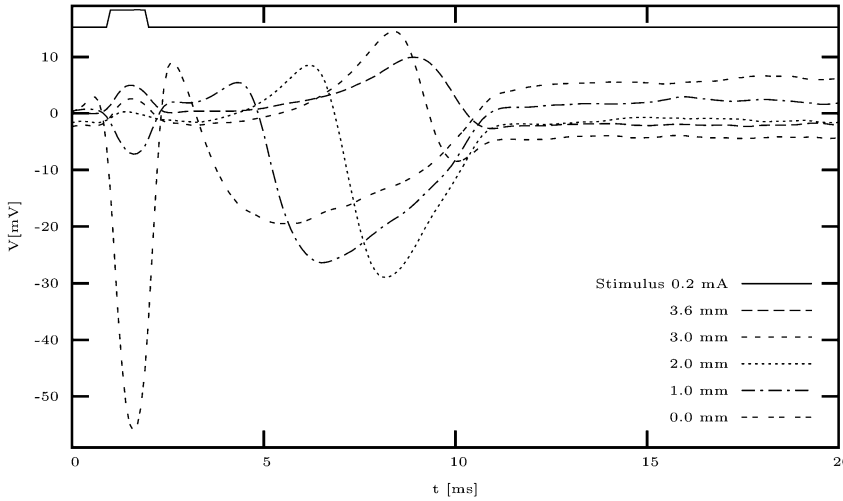

Fig. 7.28. Electrograms measured at surface of papillary muscle. The papillary muscle was excised from a rabbit's right ventricle and placed in a flow-through bath. The musle is fixed at both ends, i.e. the onset of the tendon and proximal to its former attachment to the ventricle wall. A stimulus was given at t=1 *ms* with a length of 1 *ms* proximal to the former attachment. Electrograms were measured at several positions along the muscle, i.e. near to the stimulus electrode, indicated by 0 *mm*, and in a distance of 1, 2, 3, and 3.6 *mm*. Activation times can be detected by analysing the electrograms, e.g. by searching for maximal negative slopes in the region after the stimulus artefact.

The excitation propagation process can be registered with extracorporal electrodes (Fig. 7.27). The propagation through the atria corresponds to the P wave. The propagation through the ventricles is reflected by the QRS wave, their repolarization by the T wave.

Further studies of different types, e.g. with double cell voltage clamp techniques (Sect. 7.2.1) and genetically modified cells [97], showed that the intercellular excitation propagation is resulting from a flow of current primarily through gap junctions. The current flow is depending on the differences of the intracellular potential. Hence, the cellular electrophysiology, i.e. the upstroke velocity of the transmembrane voltage, determines the excitation velocity. Primarily, sodium and potassium ions serve as charge carrier.

Coupling via gap junctions between cardiac myocytes and fibroblasts is reported, e.g. by connexin45 in the sinoatrial node and connexin43 in rat ventricular cell cultures [212, 213]. The electrophysiological implications of this coupling are still topic of research.

Experimental studies of the mechanisms of microscopic propagation of electrical excitation through the myocardium showed different phenomena depending on the scale of observation [214, 215]. In the scale of single cells a discontinuous, stochastic propagation is found resulting from the irregular

cellular shape and the inhomogeneous gap junction distribution. In a larger scale a continuous, anisotropic propagation is observed. The anisotropy is resulting from the myocyte orientation dependent, averaged distribution of gap junctions.

A variety of phenomena can be initiated by experiments, whereby specifically timed and located electrical stimulus sequences are applied [216, 217, 218]. Similar stimulus sequences applied via endocardial catheter electrodes are used in clinical electrophysiological examinations for an evaluation of the heart.

An important arrhythmogenic phenomenon is the unidirectional block for excitation propagation, which can be found in excitable media commonly resulting from static or dynamic inhomogeneities. A unidirectional block can be generated with a suitably located and timed stimulus of the excitable media, e.g. of the atrial and ventricular myocardium. The stimulus is suitably located and timed, if the stimulus is located with one part in a non-excitable area, with the other in an excitable area. The non-excitability of the area results from an electrophysiological cellular status in which the cell cannot be activated by an early secondary stimulus. In this case the excitation propagates in the direction opposite to the blocked area.

Depending on the dimension of the excitable media, different phenomena resulting from a unidirectional block can be observed: In a one-dimensional domain the block leads to a propagation in the opposite direction, while normally a stimulus is followed by two propagation fronts in each direction. A block in a non-homogeneous two-dimensional area can lead to a rotating wave around obstacles, which is reported e.g. in the right and left atrium [217, 218]. The block can also lead to single or multiple spiral waves. The spiral waves can rotate freely, no obstacles or channels of muscle structures are necessary. The three-dimensional equivalent for spiral waves are scroll waves.

7.3.2 Modeling Approaches

Different modeling approaches of the excitation propagation in the myocardium can be distinguished depending on the representation of the microscopic and macroscopic anatomy as well as depending on the approximation of the cellular electrophysiology.

Modeling approaches that use only macroscopic information allow the combining of cells and their common treatment. In contrast, models using microscopic anatomical information at a cellular level split cells in components, which are separately treated.

In the last years different approaches for the macroscopic excitation propagation were developed:

- cellular automata
- reaction diffusion systems

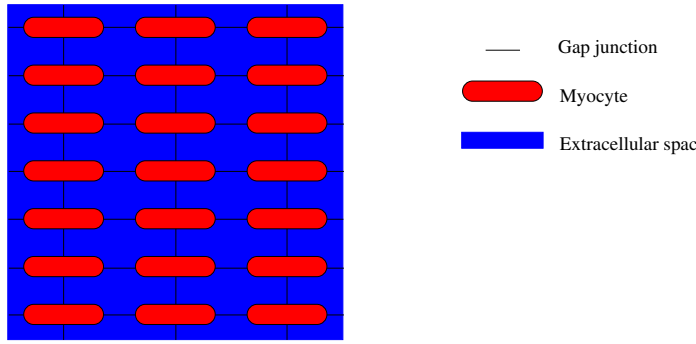

Fig. 7.29. Modeling of electrical intercellular coupling. Adjacent myocytes are coupled via gap junctions and through the extracellular space.

Microscopic and macroscopic models allow the inclusion of anisotropic effects resulting from the orientation of myocytes, e.g. by using conductivity tensors. Commonly, the methods are applied on a one-, two- or three-dimensional lattice (Fig. 7.29), whereby each cell's intracellular space is coupled directly only with the intracellular space of adjacent cells.

Microscopic Models. Microscopic models use anatomical information of the cellular architecture acquired with microscopy to reconstruct the excitation propagation in a region of the myocardium [219, 214]. The region is divided in different areas, which are assigned to the intra- and extracellular space, the membrane of myocytes and capillaries. The membrane areas include an electrophysiological description, i.e. the sarcolemmal ionic currents from a cell model. The current flow between the areas is modeled with Ohm's law using resistors.

The approach allows the inclusion of irregularities of the cellular architecture as well as inhomogeneities of the orientation and distribution of gap junctions. Hence, anisotropic effects are implicitly included.

Microscopic models allow the reconstruction of experimental results, whereby the inhomogeneous microstructure of the myocardium is of importance. An example therefore is the discontinuous excitation propagation found at cellular level [214, 215]. The microscopic modeling of the myocardium is restricted to a small volume, because of the high expense to describe each single cell with a number of complex and coupled elements.

7.3.3 Cellular Automata

Cellular automata are applied as models of natural processes in various disciplines, e.g. in physics, chemistry, biology, and medicine. A large number of different cellular automata were developed to model the excitation process in the heart [220, 221, 222, 223, 224, 225, 226, 227, 228, 142, 37]. Cellular models

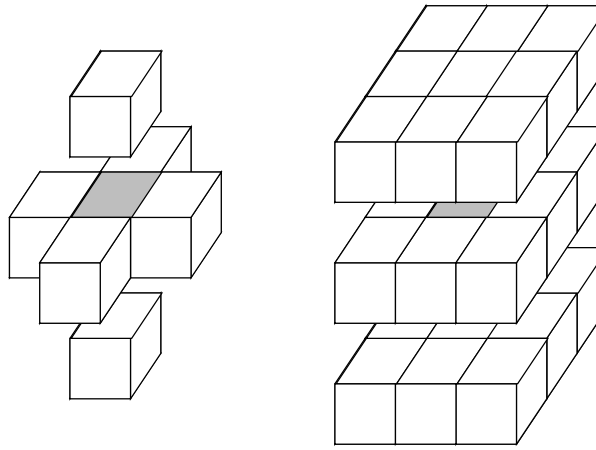

Fig. 7.30. Three-dimensional neighborhood of cells in cellular automaton. The grey labeled central cell communicates with (a) 6 and (b) 26 neighbors (from [37]).

were used in the early work of Wiener and Rosenblueth (1946) to describe phenomena of excitation propagation in two-dimensional sheets of cardiac muscle [220] and of Moe et al. (1964) to model atrial fibrillation [221]. Recently published works showed that cellular automata are capable of efficient simulation of excitation propagation in the whole heart. Furthermore, tissue specific and stimulus frequency dependent courses of the transmembrane voltage as well as tissue specific anisotropy of excitation velocities are taken into account in these simulations [225, 228, 142].

A cellular automaton can be divided in two components [229, 230]:

- regular, discrete, infinite network representing the underlying spatial structure.
- finite automaton working at each node (so-called cell) of the network.

Each cell communicates with a finite set N of other cells. The number and the arrangement of the cells with which a cell communicates determines the neighborhood of the cellular automaton. Classical neighborhoods are the nearest neighbors neighborhoods of von Neumann or Moore. In case of three-dimensional cellular automata these are the 6- and 26-neighborhood, respectively (Fig. 7.30). The neighborhood determines the shape of the wave front (Fig. 7.31). The set N is usually fixed and is an ordered subset of the set of all cells Z.

The communication between cells is performed in a local, deterministic, uniform and synchronous way. Hence, the global evolution of the system is predetermined running the cellular automaton along discrete time steps [229].

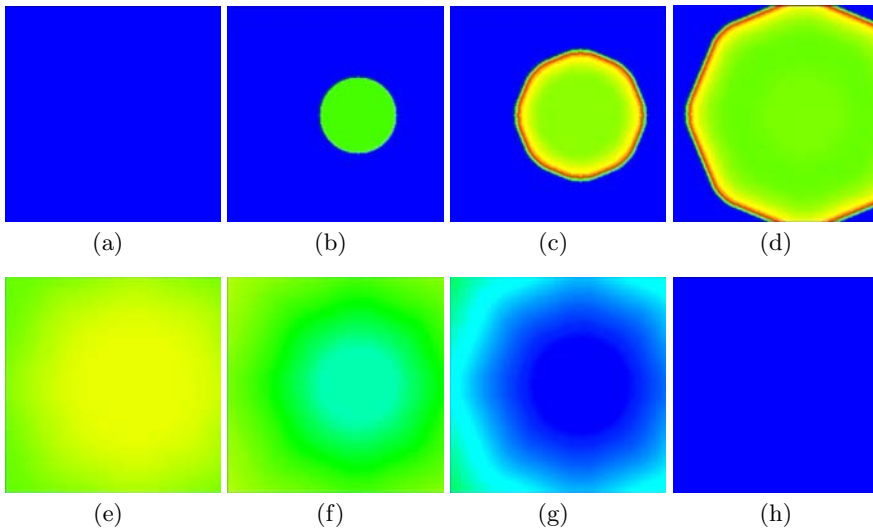

Fig. 7.31. Excitation wave simulated with a cellular automaton in a three-dimensional slice of 256 x 256 x 3 elements with a size of 0.2 *mm* x 0.2 *mm* x 0.2 *mm* modeling the electrophysiology of atrial cells. The simulated transmembrane voltage is color coded illustrated at different time steps. (a) Initially, the area is in the resting state with all cells at resting voltage. (b) A stimulus was applied followed by (c-g) a wave propagating over the area. The shape of the wave front is resulting from the 26-neighborhood used in the cellular automaton for the communication between cells. (h) Finally, the area is returned to the resting state with all cells at resting voltage.

Model of Werner, Sachse, Seemann, and Dössel. The three-dimensional automaton simulates the propagation of electrical excitation with models ranging from areas of myocardium up to the whole heart [227, 231, 142, 37]. Anisotropy of the myocardium and frequency dependent changes of the course of the transmembrane voltages are taken into account.

As underlying spatial structure anatomical models of the myocardium and of the whole heart can be used. E.g. the whole heart model used in the subsequently described simulations consists of a classified anatomical tissue data set (section 6.4.5) derived from the Visible Man data set, a myocyte orientation data set and a specialized cardiac conduction system tree. While the myocyte orientation data set has only an impact on the local transition function, the conduction system tree varies the neighborhood of the cells located at the nodes of the tree. Hence, unlike classical cellular automata, the neighborhood N varies. For cells located at the nodes of the tree the 26 fixed neighbors are extended by the set of successors and one predecessor defined by the conduction system tree. However, most of the cells have a fixed set N_{fixed} of 26 neighbors, whereas only for a very small number of the cells, approximately 0.01 %, the neighborhood N varies.

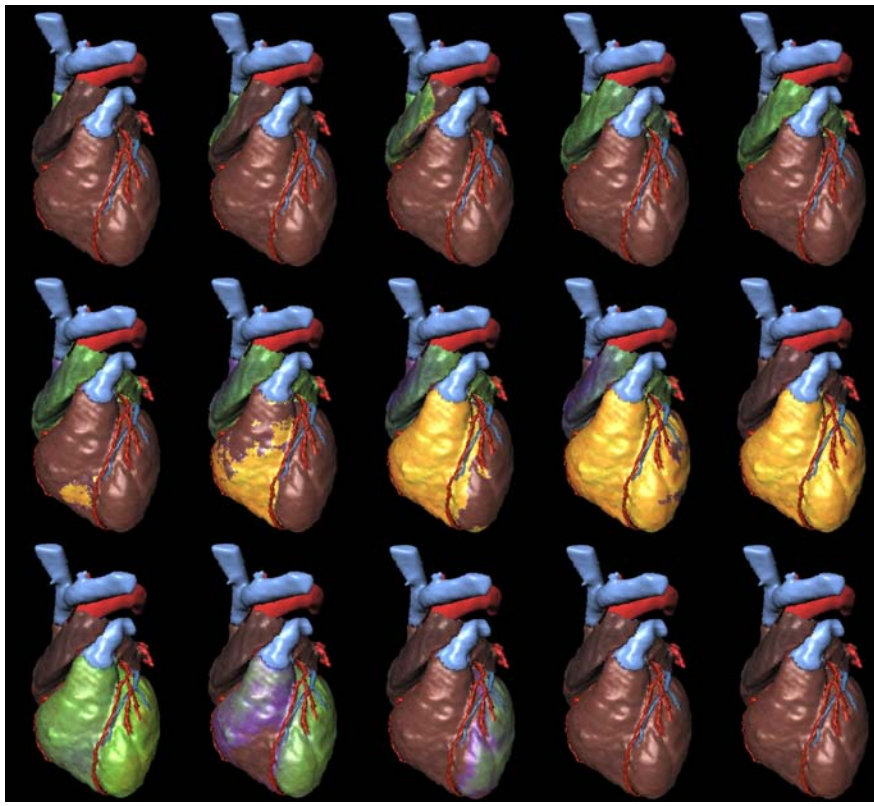

Fig. 7.32. Color coded transmembrane voltage distribution of subepicardial myocardium resulting from the simulation of a sinus rhythm (from [37]). The simulation is performed with a cellular automaton. Tissue specific variations of the maxima and duration of the transmembrane voltage are visible. Different time steps of the excitation process are visualized. The excitation starts in the sinus node located in the upper right atrium and propagates over the atrial myocardium. The atrioventricular node delays the propagation, which continues then spreading over the Tawara branches to the subendocardial Purkinje fibers. Finally, the excitation propagates over the ventricular myocardium.

The finite automaton at each node is configured with results from published measurements [23] and from simulations with electrophysiological cell models, e.g. simulations similar to those shown in Fig. 7.21. For that purpose, a large number of simulations was performed varying the cell model and the stimulus frequency. The simulations deliver tissue and stimulus frequency specific courses of the transmembrane voltage and of the excitation velocity.

The result of a simulation with the cellular automaton is the temporal and spatial distribution of the transmembrane voltage for each cell (Fig. 7.31, Fig. 7.32 and Fig. 7.33). This distribution can be used in subsequent numer-

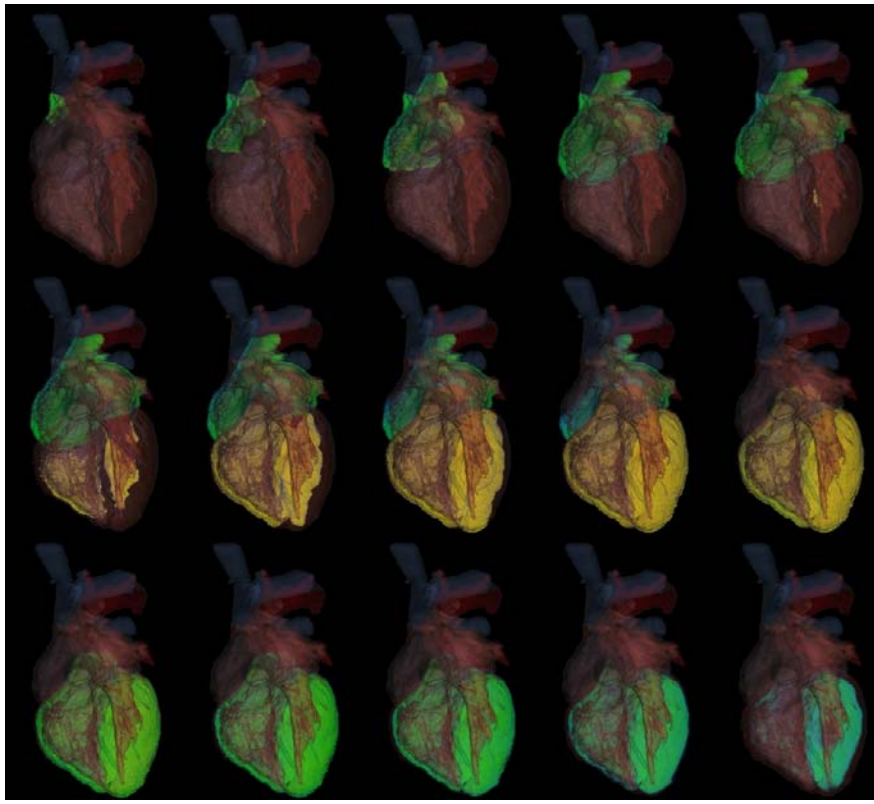

Fig. 7.33. Volume visualization of color coded transmembrane voltage distribution resulting from the simulation of a sinus rhythm (from [37]). The figure shows the same time steps as Fig. 7.32. The propagation through the volume of the heart, e.g. from the subendocardial located Purkinje fibers to the ventricular myocardium, is observable.

ical calculations of physical fields in the human body (Sect. 7.3.4), e.g. the calculation of the current source distribution in the heart (Fig. 7.34) and of the extracellular potentials in the whole body (Fig. 7.35). The potentials at the body surface can be used to determine electrocardiograms (Fig. 7.36). Hereby, for each time step the potentials at different points on the body surface are read out. The electrocardiograms of different type, e.g. Einthoven, Goldberger and Wilson leads, are calculated by their differences and averages.

Simulation of unidirectional blocks, spiral and scroll waves. A unidirectional block can be simulated with the cellular automaton for a suitably located and timed stimulus in the repolarization phase of the excitable media, e.g. atrial and ventricular myocardium [221, 224, 228, 232, 233]. In this case the excitation propagates in the direction opposite to the block. A stimulus is

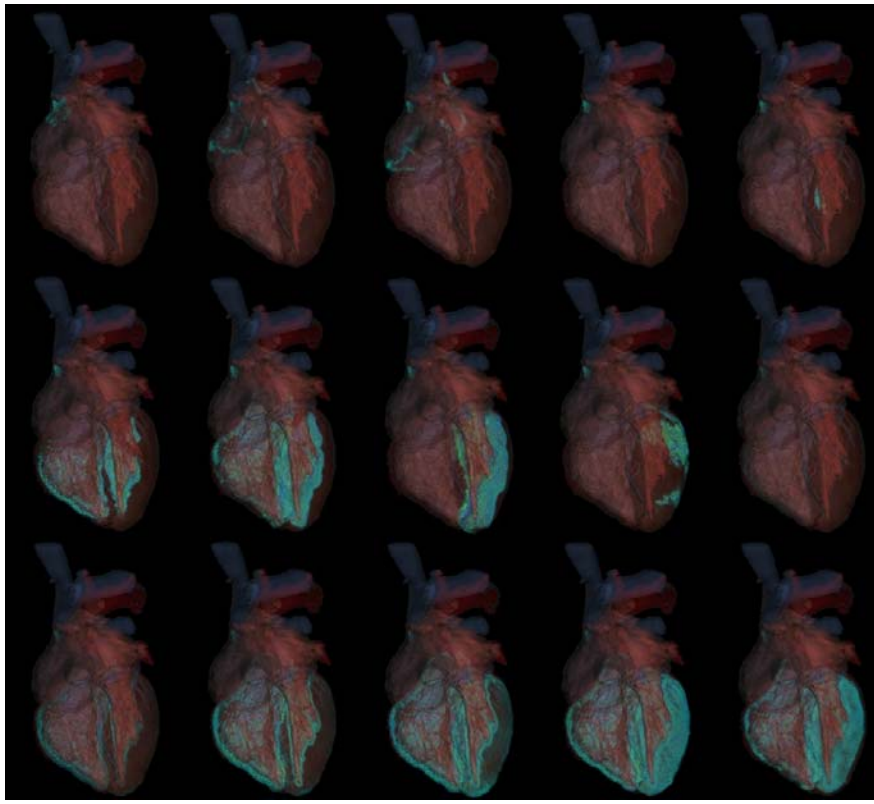

Fig. 7.34. Volume visualization of color coded current source density distribution of simulated sinus rhythm (from [37]). Different time steps of the excitation process are visualized. The sources are calculated with the bidomain model. They occur at places with a gradient of the transmembrane voltage, primarily at the front of the excitation propagation. No sources are found in the fully activated atrial and ventricular myocardium.

suitably located and timed, if it is located with one part in a non-excitable area, with the other in an excitable area.

Depending on the dimension of the simulated area, different phenomena of excitable media resulting from a unidirectional block can be reconstructed in simulations with the cellular automaton. The reconstructability is depending on the specific implementation of the automaton.

While normally a stimulus in a one-dimensional domain is followed by two propagation fronts in each direction, a block leads to a propagation in the opposite direction. In an inhomogeneous two-dimensional domain a block can lead to a wave rotating around obstacles (Fig. 7.37). The block can produce single and multiple spiral waves, too. The spiral waves can rotate freely. No obstacles or specifically arranged geometrical structures are necessary. In sim-

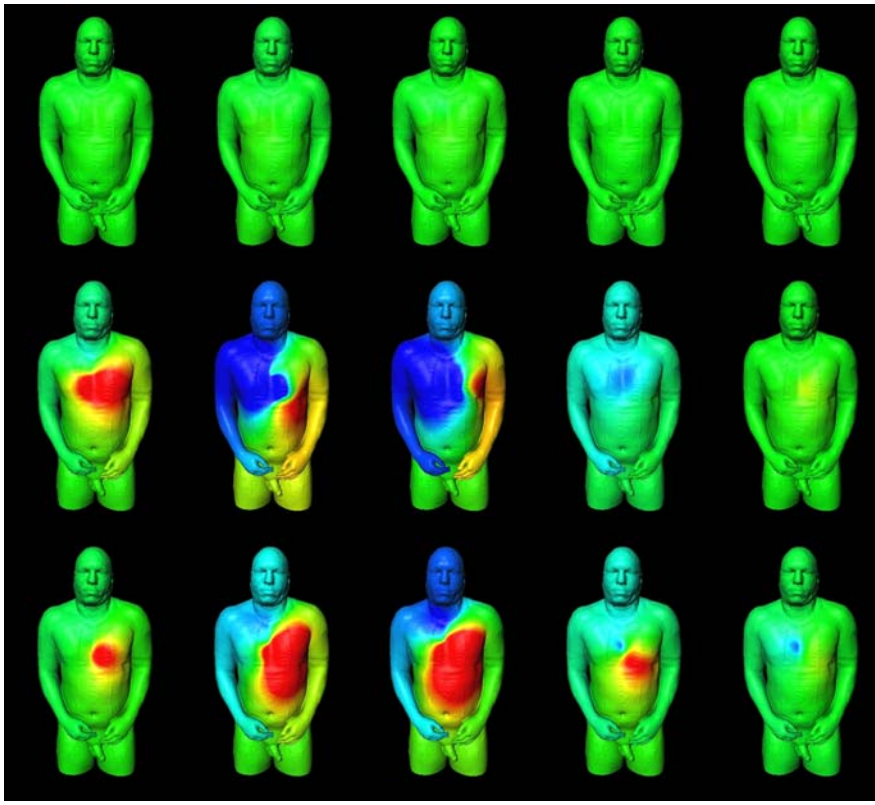

Fig. 7.35. Color coded body surface potential map of sinus rhythm (from [37]). Different time steps are visualized. The voltages at the body surface resulting from the cardiac sources are calculated with the finite difference method and a conductivity model of the whole body [26].

ulations with three-dimensional domains scroll waves can be reconstructed. The cellular automaton allows an efficient simulations in large and complex models, e.g. atrial and ventricular flutter can be simulated with models of the whole heart (Fig. 7.38 and Fig. 7.39).

Simulated radiofrequency (RF) ablation in right human atrium. A clinical option for the treatment of chronical atrial flutter is the catheter ablation therapy with radiofrequency current [234]. The applied current destroys cells in areas of the atrial myocardium, so that an excitation propagation through the area is suppressed. Commonly, lines of myocardium are ablated with endpoints at the ostia of the atrium, e.g. to the vena cava superior and inferior. The location of the lines has to be chosen so, that a propagation from the sinus node to the atrioventricular node is still possible and the atrial flutter is permanently terminated.

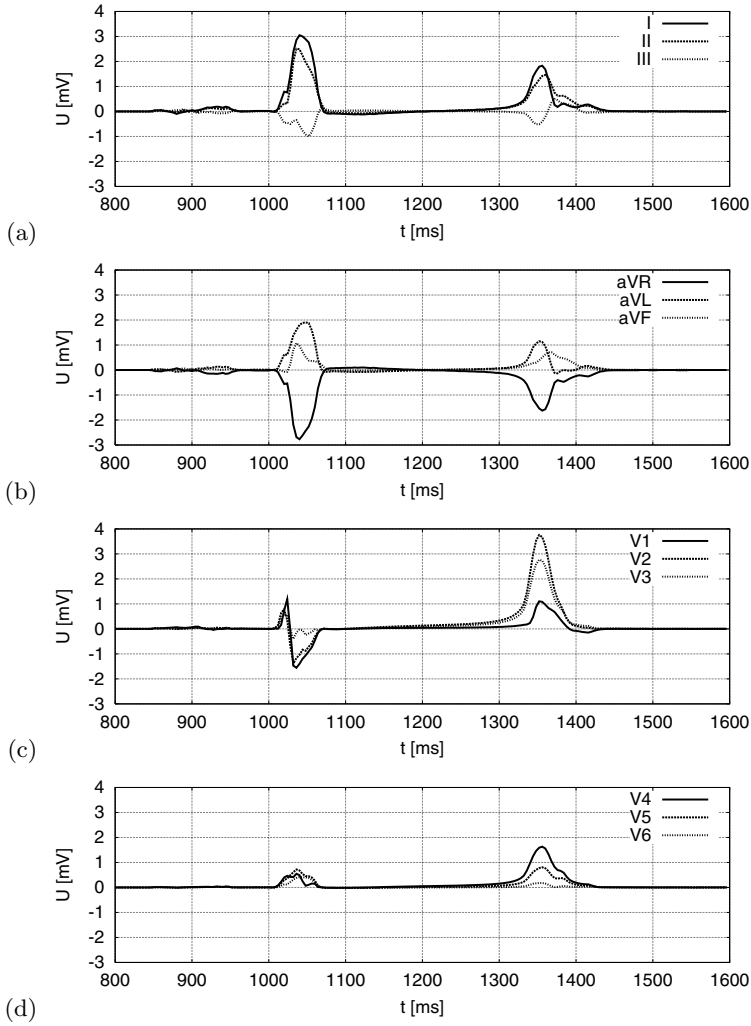

Fig. 7.36. Simulated electrocardiograms of sinus rhythm (from [37]). (a) Einthoven lead I, II and III, (b) Goldberger leads aVR, aVL and aVF, (c) Wilson leads V1, V2 and V3, (d) Wilson leads V4, V5 and V6.

The cellular automaton is capable of simulating the atrial flutter and the electrophysiological effects of an ablation therapy. In the exemplary simulation illustrated in Fig. 7.40 the atrial flutter is represented by a rotating wave around the vena cava inferior.

The rotation wave is terminated after execution of two ablation lines. A first line is set in the dorsal right atrial wall from the vena cava inferior to the vena cava superior. The first line results in a rotating wave around the

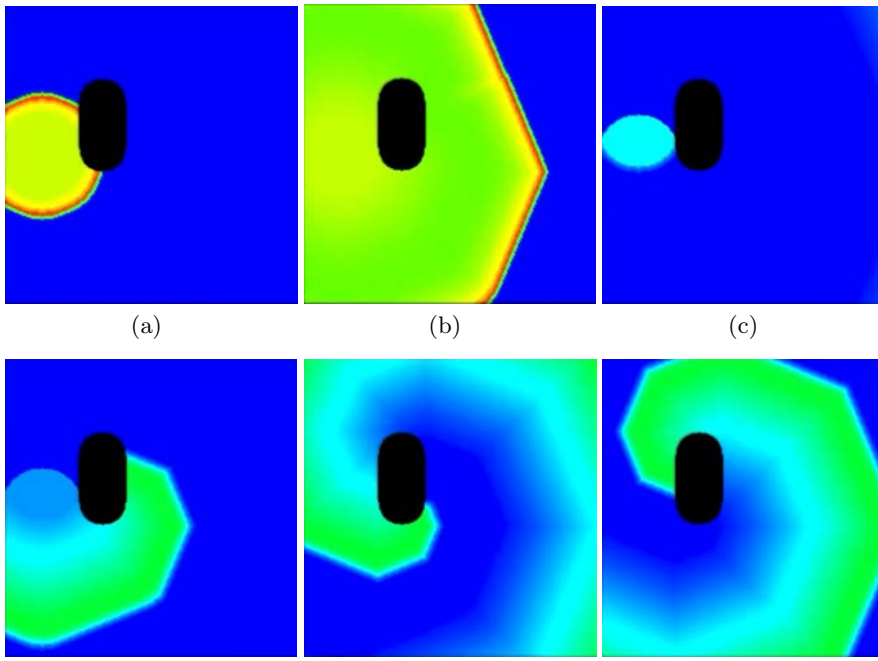

Fig. 7.37. Rotation of wave around an obstacle simulated with cellular automaton in a three-dimensional slice of 256 x 256 x 3 elements with a size of 0.2 *mm* x 0.2 *mm* x 0.2 *mm* modeling the electrophysiology of atrial cells. The simulated transmembrane voltage is color coded illustrated at different time steps. (a) A first stimulus was applied followed by (b) a wave propagating over the obstacle. (c) A second stimulus in the repolarization phase leads through a unidirectional block to an excitation propagation in the opposite direction. (d-f) The excitation propagates around the obstacle.

vena cava inferior and the ablation line, which leads to an increase of the cycle duration of the flutter. A second line is set orthogonal in the right area of the right atrium leading to a termination of the flutter. The ablation still permits the propagation from sinus node to the ventricles via the atrioventricular node, but a reinitiation of flutter with the same stimulus sequence is not possible.

7.3.4 Reaction Diffusion Systems

Overview. Reaction diffusion systems, which are also known as excitable dynamics equations, use a system of non-linear partial differential equations to describe the excitation and propagation process in excitable media [235]. The system consists of n equations of the following type:

$$\frac{\partial u_i}{\partial t} = f_i(u_1, \ldots, u_n) + \nabla \cdot (\mathbf{D_i} \nabla u_i) \qquad i = 1, \ldots, n$$

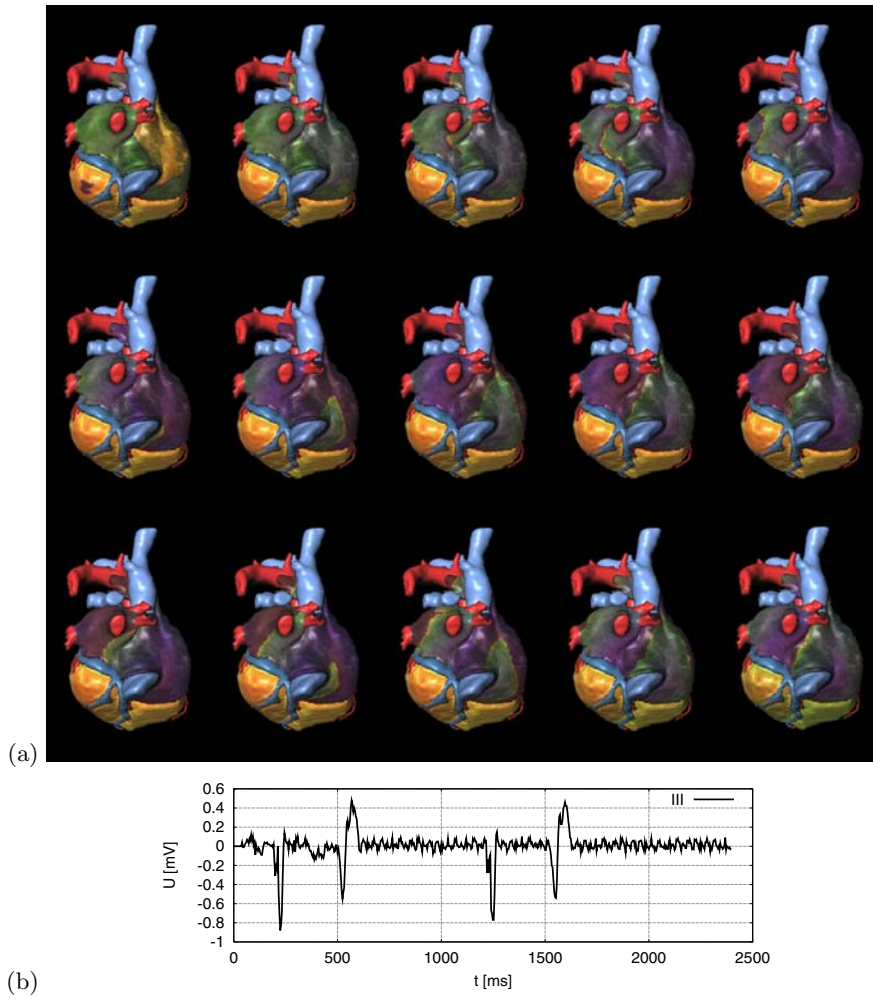

Fig. 7.38. Atrial flutter simulated with cellular automaton (from [37]). (a) A stimulus in the repolarization phase of the atrial myocytes leads through a unidirectional block to an excitation propagation in the opposite direction. The excitation propagates unidirectionally along the musculi pectinati. The reentry takes place at the dorsal right atrium near to the vena cava inferior. The excitation rotates around the ostium of the vena cava inferior. (b) The electrocardiogram shows a high frequency pattern for the atrial flutter in conjunction with normal QRS-complexes.

with the state variables u_i, the excitation term f_i and the diffusion tensor $\mathbf{D_i}$. In the context of cardiac excitation propagation, the state variables u_i correspond to the cellular status, e.g. transmembrane voltage, ionic channel

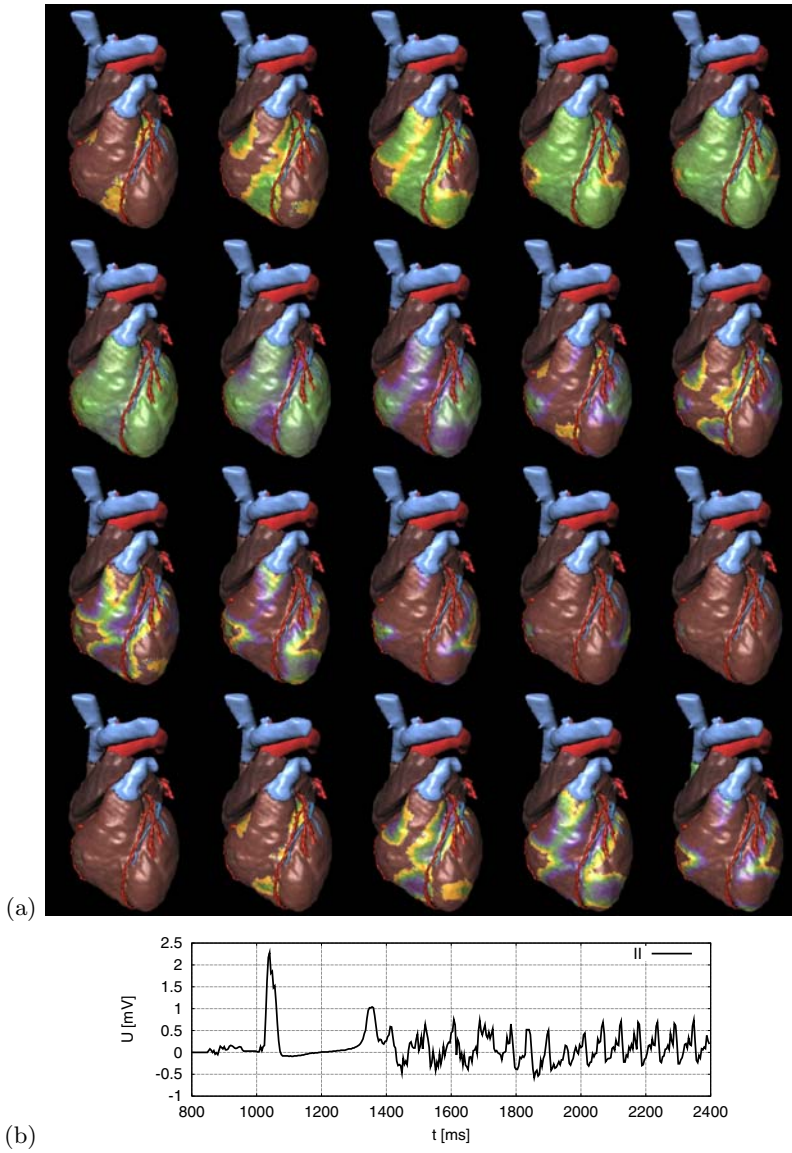

Fig. 7.39. Ventricular flutter simulated with cellular automaton (from [37]). (a) A stimulus in the repolarization phase of the left ventricular myocytes leads to a unidirectional block followed by ventricular flutter. (b) The electrocardiogram shows a high frequency pattern for the ventricular flutter.

conductivity and ionic concentrations. The change of the state variables is determined by the excitation term f_i and the diffusion term $\nabla \cdot (\mathbf{D_i} \nabla u_i)$.

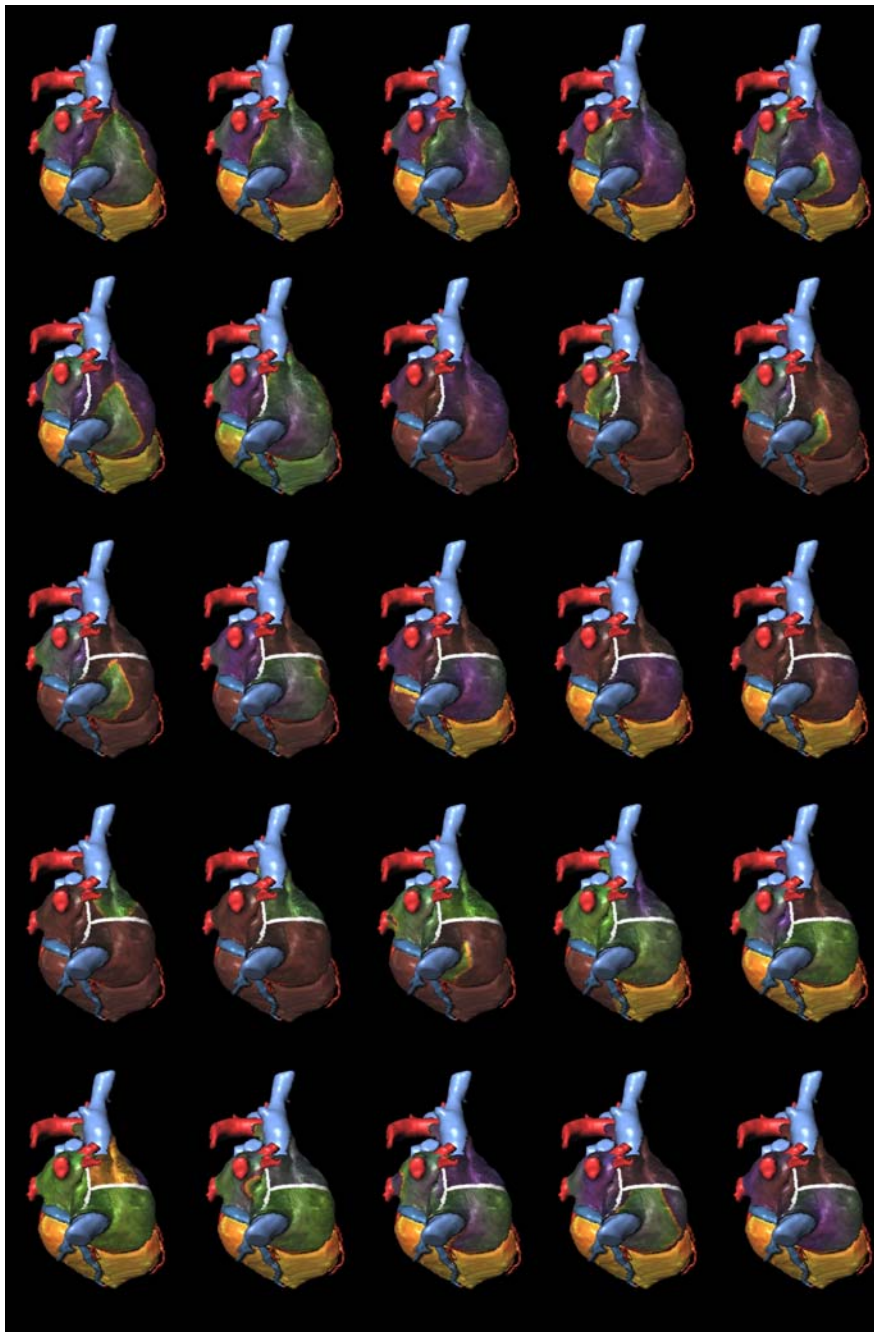

Fig. 7.40. Simulation of RF ablation in human right atrium with flutter (from [37]). The ablation lines are labeled in white.

Depending on the dimension n of the equation system as well as on the formulation of the excitation and diffusion terms different types of models can be distinguished:

- simplified approaches
- combinations of electrophysiological cell models with electrical current flow models
  - monodomain models with resistor networks or Poisson's equation
  - bidomain models with Poisson's equation

Simplified Approaches

Model of FitzHugh and Nagumo. An early representation of the simplified approaches for excitation propagation is the two state FitzHugh-Nagumo model [236]:

$$\frac{\partial u}{\partial t} = \frac{u - \frac{u^3}{3} - v}{\epsilon} + D\nabla^2 u$$
$$\frac{\partial v}{\partial t} = \epsilon(u + \beta - \gamma v)$$

with the state variable u for the transmembrane voltage and the state variable v for inhibition. The diffusion term is formulated for isotropic media with the scalar diffusion coefficient D. Typical parameters are $0 < |\beta| < \sqrt{3}$, $0 < \gamma < 1$ and $\epsilon \ll 1$.

Model of Rogers and McCulloch. A modification of the FitzHugh-Nagumo equations allows a more realistic description of the propagation in the myocardium [237, 238]:

$$\frac{\partial u}{\partial t} = c_1 u(u - a)(1 - u) - c_2 uv + \nabla \cdot (\mathbf{D}\nabla u)$$
$$\frac{\partial v}{\partial t} = b(u - dv)$$

with the diffusion tensor $\mathbf{D}$, and the membrane parameters a, b, $c1$, $c2$, and d. The additional parameters are used to reconstruct the course of the transmembrane voltage of ventricular myocytes. The state variables u and v describe as in the FitzHugh-Nagumo equations the transmembrane voltage and the inhibition. The boundary condition

$$\frac{\partial u}{\partial \mathbf{n}} = 0$$

is added, which allows to define the derivative of the transmembrane voltage at borders with normal n. The equations were used in conjunction with finite element techniques to simulate the excitation propagation in two-dimensional sheets of myocardium.

Further adaptations of the FitzHugh-Nagumo equation in the area of cardiac electrophysiology are found in [239, 240, 241].

Combinations of Electrophysiological Cell Models with Electrical Current Flow Models. A biophysically well-founded approach consists of combining detailed electrophysiological models of single myocardial cells with models of the electrical current flow through the intra- and extracellular space as well as the gap junctions. The electrophysiological cell models describe the concentration and flow of ions as well as the conductivity of cellular structures and the transmembrane voltage by a set of coupled differential equations.

Two main representatives of these combined models were developed differing in the number of domains for the electrical current flow: mono- and bidomain models. The combined models are further distinguished depending on the representation of the conductivity used for the electrical current flow model. Hereby, approximations with isotropic and anisotropic conductivities represented by resistors as well as conductivity tensors of first or second rank are known.

Monodomain Models. The monodomain models incorporate the effect of coupled intracellular space with gap junctions by resistors [242, 243, 244] or conductivity tensors. In each time step and for each cell two calculations are performed:

- computation of the summary intracellular current source density f_i using a model of intercellular current flow
- updating of the status of the electrophysiological cell model using the current source densities f_{si}

The summary intracellular current source density f_i can be calculated outgoing from Poisson's equation:

$$\nabla \cdot (\sigma_i \nabla V_m) = f_i \tag{7.2}$$

with the transmembrane voltage V_m and the intracellular conductivity tensor σ_i, describing conductivities for intracellular space and gap junctions. The summary intracellular current source density f_i consists of two different components:

$$f_i = \beta I_{tm} - f_{si} \tag{7.3}$$

with the intracellular current source density f_{si}, the transmembrane current I_{tm}, and the myocytes per volume ratio β, allowing the conversion from currents to current source densities. The current I_{tm} describes the summary flow through the membrane given by the electrophysiological model:

$$I_{tm} = C_m \frac{\partial V_m}{\partial t} + I_m \tag{7.4}$$

with the membrane capacitor C_m and the ionic current I_m, which is a function of the transmembrane voltage V_m. Additional stimulus currents are neglected. The inclusion of these definitions (equations 7.2-7.4) delivers the complete equation:

$$\nabla \cdot (\sigma_i \nabla V_m) = \beta \left(C_m \frac{\partial V_m}{\partial t} + I_m \right) - f_{si}$$

Numerically motivated the complete equation can be transformed to:

$$\frac{\partial V_m}{\partial t} = \frac{1}{C_m} \left(\frac{f_{si} + \nabla \cdot (\sigma_i \nabla V_m)}{\beta} - I_m \right)$$

The transformed equation is commonly solved with the finite-difference or finite-element method for the underlying generalized Poisson equation (Sect. 3.3) and the Euler or Runge-Kutta methods for the underlying ordinary differential equation (Sect. 2.5).

Bidomain Models. The bidomain models are an extension of monodomain models including the effects of the extracellular space [245, 246, 247, 248, 249]. The bidomain model treats the electrical behavior of tissue in two domains, in the intracellular and extracellular space, which are separated by the cell membrane. In each domain Poisson's equation for fields of stationary electrical current is fulfilled:

$$\nabla \cdot (\sigma_i \nabla \phi_i) = \beta I_{tm} - f_{si}$$
$$\nabla \cdot (\sigma_e \nabla \phi_e) = -\beta I_{tm} - f_{se}$$

with the intracellular potential ϕ_i, the extracellular potential ϕ_e, the intracellular conductivity tensor σ_i, the extracellular conductivity tensor σ_e, the intracellular stimulus current source density f_{si}, the extracellular stimulus current source density f_{se}, and the myocyte per volume ratio β. The intracellular conductivity tensor σ_i consists of conductivities for the intracellular space and for the gap junctions. The domains are coupled by the summary current I_{tm} through the cell membrane and by the definition of the transmembrane voltage:

$$V_m = \phi_i - \phi_e$$

The summary membrane current I_{tm} vanishes in the summation of the two Poisson's equations:

$$\nabla \cdot (\sigma_i \nabla \phi_i) + \nabla \cdot (\sigma_e \nabla \phi_e) = -f_{si} - f_{se} \tag{7.5}$$

The following method can be chosen to couple the bidomain equations with the electrophysiological cell models (Fig. 7.41) [250]. The method uses a decomposition of the intracellular Poisson's equation:

$$\nabla \cdot (\sigma_i \nabla \phi_i) = \nabla \cdot (\sigma_i \nabla (V_m + \phi_e)) = \nabla \cdot (\sigma_i \nabla V_m) + \nabla \cdot (\sigma_i \nabla \phi_e)$$

and of the summation equation (equation 7.5):

$$\nabla \cdot (\sigma_i \nabla \phi_i) + \nabla \cdot (\sigma_e \nabla \phi_e) = \nabla \cdot (\sigma_i \nabla V_m) + \nabla \cdot ((\sigma_i + \sigma_e) \nabla \phi_e)$$

The method bases on the iterative solving of Poisson's equations with numerical techniques:

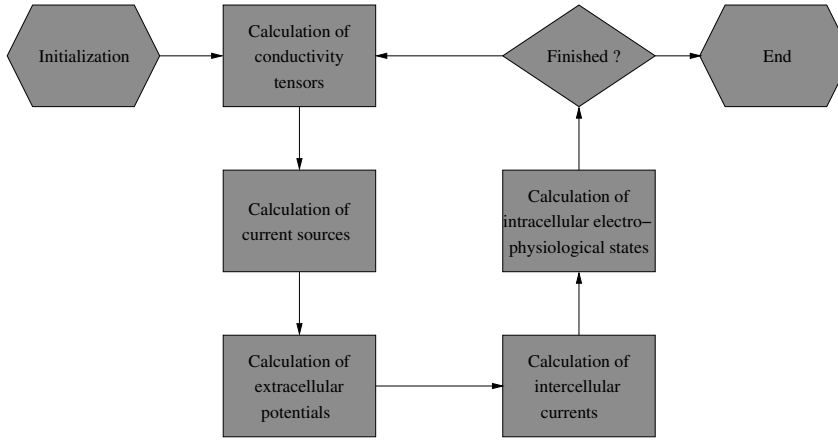

Fig. 7.41. Bidomain modeling of cardiac electrophysiology. The depicted modeling includes the possible adaption of conductivity, e.g. to incorporate deformation, which is neglected in traditional bidomain formulations.

- calculation of extracellular current sources f_e with the transmembrane voltage V_m delivered by the electrophysiogical model
- computation of extracellular potentials ϕ_e with the extracellular current source densities f_e
- calculation of summary intracellular stimulus current source density f_i with the transmembrane voltage V_m and the extracellular potentials ϕ_e
- updating of the status of the electrophysiological cell model using the current source densities f_{si}

The formulation neglects the extracellular stimulus current f_{se} for simplicity of description.

In a first step the extracellular current source density f_e delivered by the transmembrane voltage V_m is determined:

$$\nabla \cdot (\sigma_i \nabla V_m) = f_e$$

In a second step the extracellular potential ϕ_e is calculated from the current source density f_e:

$$\nabla \cdot ((\sigma_i + \sigma_e) \nabla \phi_e) = -f_e$$

The calculation of ϕ_e is commonly numerically expensive, because the solving of a large system of linear equations is necessary.

In a third step the summary intracellular current source density f_i is determined:

$$\nabla \cdot (\sigma_i \nabla V_m) + \nabla \cdot (\sigma_i \nabla \phi_e) = f_i$$

The incooperation of the electrophysiological model's equation (equation 7.4) and the separation of the intracellular current source density f_i (equation 7.3) lead to a combined equation:

$$\nabla \cdot (\sigma_i \nabla V_m) + \nabla \cdot (\sigma_i \nabla \phi_e) = \beta \left(C_m \frac{\partial V_m}{\partial t} + I_m \right) - f_{si}$$

with the membrane capacitor C_m and the ionic current I_m delivered by the electrophysiogical model. The combined equation is numerically motivated transformed to:

$$\frac{\partial V_m}{\partial t} = \frac{1}{C_m} \left(\frac{f_{si} + \nabla \cdot (\sigma_i \nabla V_m) + \nabla \cdot (\sigma_i \nabla \phi_e)}{\beta} - I_m \right)$$

Commonly, the finite-difference or finite-element method is applied to solve the underlying generalized Poisson equations (Sect. 3.3). The Euler or Runge-Kutta methods is used to solve the underlying ordinary differential equation (Sect. 2.5).

Simulations. A set of simulations was performed to illustrate the excitation propagation model consisting of a combination of electrophysiological cell models with electrical current flow models. The simulations aim at the gain of knowledge, which is of importance for the construction of whole heart electromechanical models. Furthermore, they allow a comparison with cellular automata models.

As electrophysiological cell models served the Courtemanche-Ramirez-Nattel and Noble-Varghese-Kohl-Noble model [187, 189], which were solved with the Euler method. As current flow model the bidomain model was applied in conjunction with isotropic and anisotropic conductivities as well as with the finite-difference method to solve Poisson's equation. A time step of 0.025 ms was used for the repeated calculation of the electrophysiological and electrical current flow model.

Two-Dimensional Simulations. Spiral waves of different types were initiated in simulations with thin, plane slices approximating atrial myocardium. The slices consisted of 128 x 128 x 3 voxels with a size of 0.2 mm x 0.2 mm x 0.2 mm. Hereby, the bidomain model with isotropic extra- and intracellular conductivities was utilized in conjunction with the Courtemanche-Ramirez-Nattel model for atrial myocytes.

Stimulus sequences as described in Sect. 7.3.3 were used to create a unidirectional block with an excitation wave propagating in the opposite direction. The generation and evolution of freely rotating spiral waves are shown in Fig. 7.42. A wave rotating around an obstacle is illustrated in Fig. 7.43.

Three-Dimensional Simulations. In further simulations the physiologic and pathophysiologic excitation propagation in an area of the ventricular free wall was explored (Fig. 7.44). Hereby, an adapted Noble-Varghese-Kohl-Noble

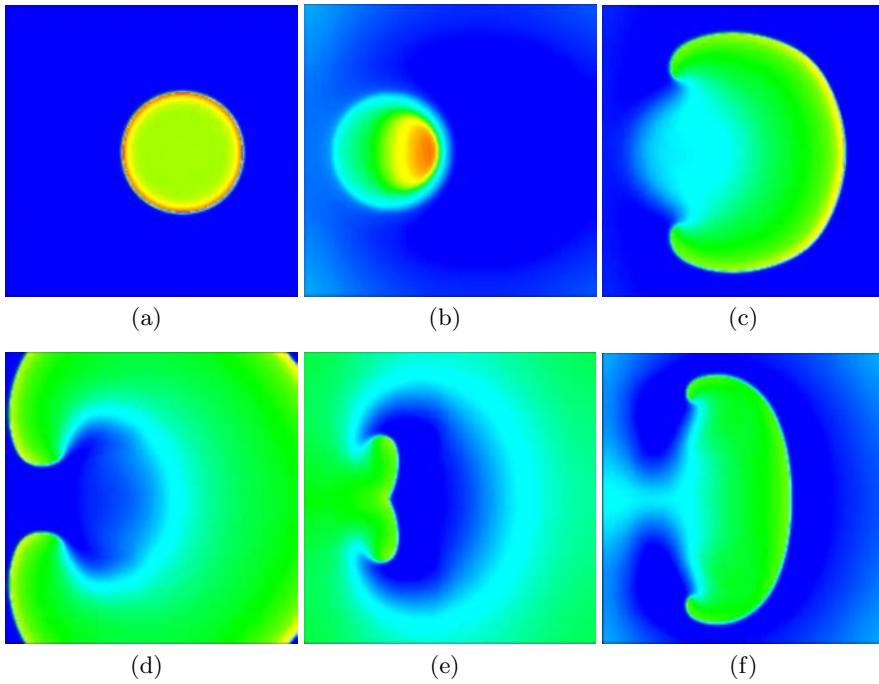

Fig. 7.42. Freely rotating spiral waves simulated with the bidomain model in a three-dimensional slice of 128 x 128 x 3 elements with a size of 0.2 *mm* x 0.2 *mm* x 0.2 *mm* modeling the electrophysiology of atrial cells. The simulated transmembrane voltage is color coded illustrated at different time steps. (a) A first stimulus was applied followed by a wave propagating over the whole area. (b) A second stimulus in the repolarization phase leads through a unidirectional block to an excitation propagation in the opposite direction. The timing and geometry of the stimulus create two mirrored rotors. (c-f) The two rotors generate spiral shaped wave fronts. The further behavior is primarily determined by the velocity of the excitation wave in the core of the rotors. Various effects were observed, e.g. meandering of the rotors as well as extinction, generation and detachment of wavelets.

model for ventricular myocytes was applied. The adaptation concerns the integration of a potassium current I_{to}, which was found to be dependent on the depth in the wall [160, 251, 252]. The bidomain model with anisotropic conductivities published in [248] was used. The area was described with 150 x 150 x 125 voxels, each with a size of 0.2 *mm* x 0.2 *mm* x 0.2 *mm*.

The myocyte orientation was incorporated varying from the subepicardial to the subendocardial myocardium. An angle of -70° is assigned for the orientation at the ventricular subepicardial myocardium, an angle of 70° at the subendocardial myocardium [111][112]. The orientation in the space lying in between is interpolated outgoing from these boundary conditions by iterative averaging [64].

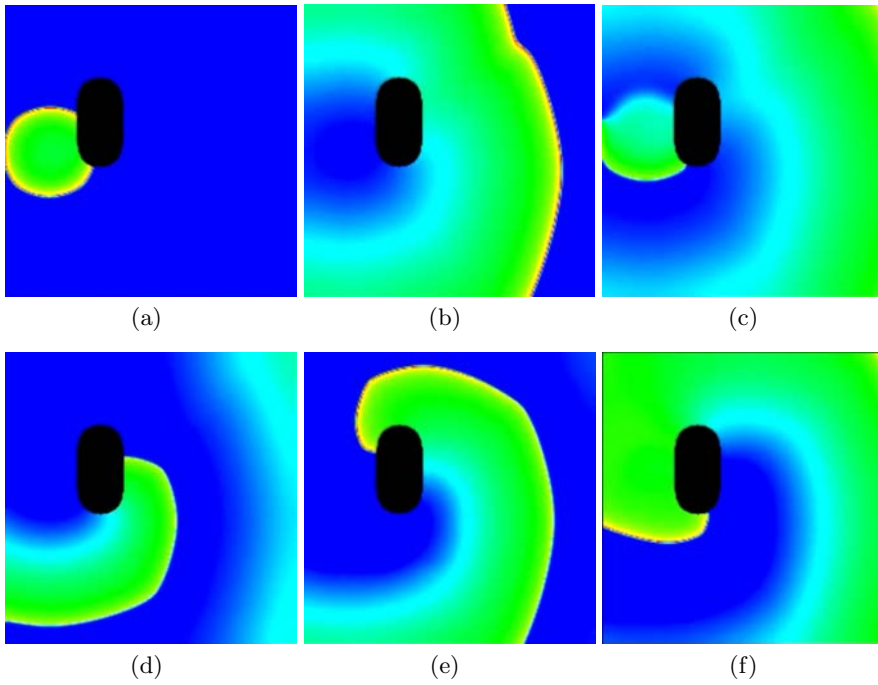

Fig. 7.43. Rotation of wave around an obstacle simulated with the bidomain model in a three-dimensional slice of 128 x 128 x 3 elements with a size of 0.2 *mm* x 0.2 *mm* x 0.2 *mm* modeling the electrophysiology of atrial cells. The obstacle consists of inactive cells with no intercellular coupling. The simulated transmembrane voltage is color coded illustrated at different time steps. (a) A first stimulus was applied followed by (b) a wave propagating over the obstacle. (c) A second stimulus in the repolarization phase leads through a unidirectional block to an excitation propagation in the opposite direction. (d-f) The excitation propagates around the obstacle. The further behavior is determined by the velocity of the excitation wave in relation to the geometry of the obstacle. An extinction as well as a detachment of the wave from the obstacle is possible.

The excitation of the heart wall is initiated at the subendocardial myocardium by applying pointwise a sufficiently large intracellular current. The points model location of myocytes with connections to Purkinje fibers. The applying of current starts at apical points and wanders in basal direction.

The physiologic excitation propagation in the ventricular free wall is visualized by evolution of the transmembrane voltage V_m (Fig. 7.45 (a) and Fig. 7.46). The propagation from the subendocardial to the subepicardial myocardium is reconstructed as well as the evolution of the repolarization. The evolution of the repolarization is found to be not similar to the depolarization. This behavior is observed in measurements. The differences are attributed to the variation of the potassium current I_{to}. Similar differences are found for the

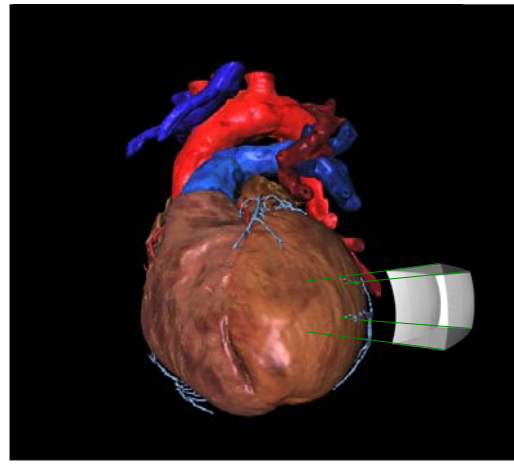

Fig. 7.44. Model of heart wall in anatomical context of whole heart. The model consists of 150 x 150 x 125 elements with a size of 0.2 mm x 0.2 mm x 0.2 mm modeling the electrophysiology of ventricular cells. The orientation of myocytes and the contribution of the ionic current I_{to} are varying in the cells from endocardium to epicardium. The cells are electrically coupled via the bidomain model using anisotropic conductivities.

evolution of the concentration of intracellular calcium $[Ca^{2+}]_i$ (Fig. 7.45 (b) and Fig. 7.47). These differences lead to a non-homogeneity of the force development, which is not only depending on the process of excitation propagation, but also on the position in the heart wall.

A scroll wave is a representative of pathophysiologic excitation propagation (Fig. 7.48 (a)). The scroll wave is linked with significant changes of the concentration of intracellular calcium $[Ca^{2+}]_i$ (Fig. 7.48 (b)).

7.3.5 Comparison of Macroscopic Models of Excitation Propagation

A comparison of traditional cellular automata and the reaction diffusion systems shows differences in the characteristics of the wave front and the reconstructability of cellular phenomena. These differences are observable in physiologic and pathophysiologic cases of the excitation propagation. Furthermore, significant distinctions are found concerning the demand of computing and main memory resources.

As characteristics of the wave front are considered its curvature and velocity. The wave front curvature of the reaction diffusion models is less obviously influenced by the neighborhood relationship of cells as of the traditional cellular automata [216]. An extreme case of influence can be found using the 6-neighborhood in cellular automata, which delivers rectangular propagation patterns. The velocity of the wave front is found to be dependent on

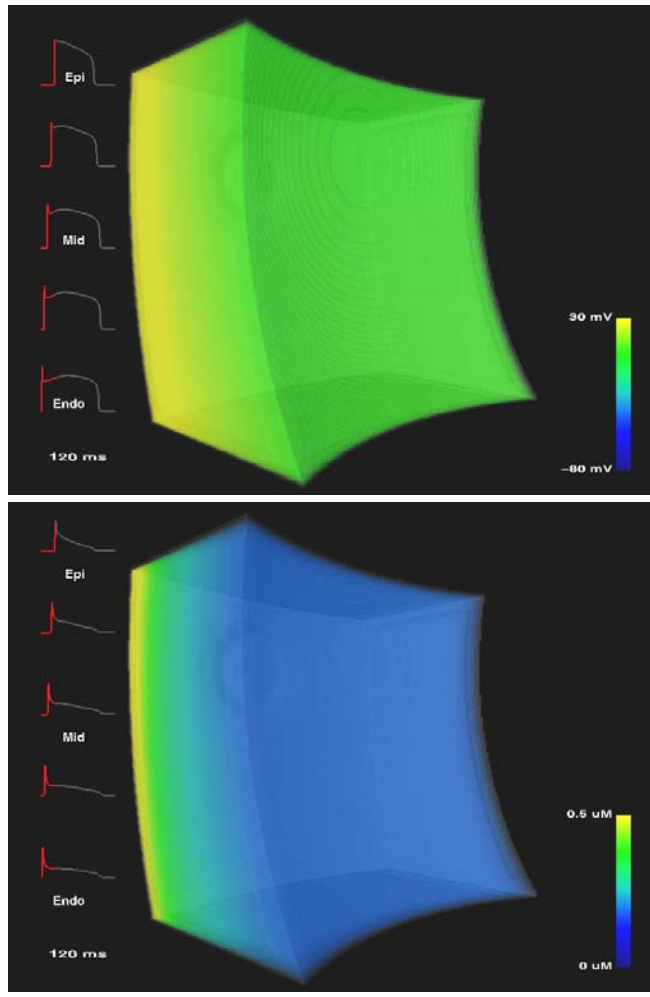

Fig. 7.45. Simulation of electrophysiology in static model of heart wall. (a) The transmembrane voltage V_m and (b) intracellular calcium concentration $[Ca^{2+}]_i$ are visualized with volume based techniques at the exemplary point in time 120 ms. The corresponding color palette is located at the right side. At the left side the course of the transmembrane voltage V_m and the intracellular calcium concentration $[Ca^{2+}]_i$ in different regions of the wall are illustrated.

its curvature in simulations with the reaction diffusion systems as well as in experiments with excitable media. Furthermore, the velocity varies with the stimulus frequency if the reaction term is suitably chosen. In contrast, the velocity is constant with traditional cellular automata. Whereas spirals and scroll waves generated with traditional cellular automata are stable and fixed, the phenomena are commonly instable in reaction diffusion systems caused

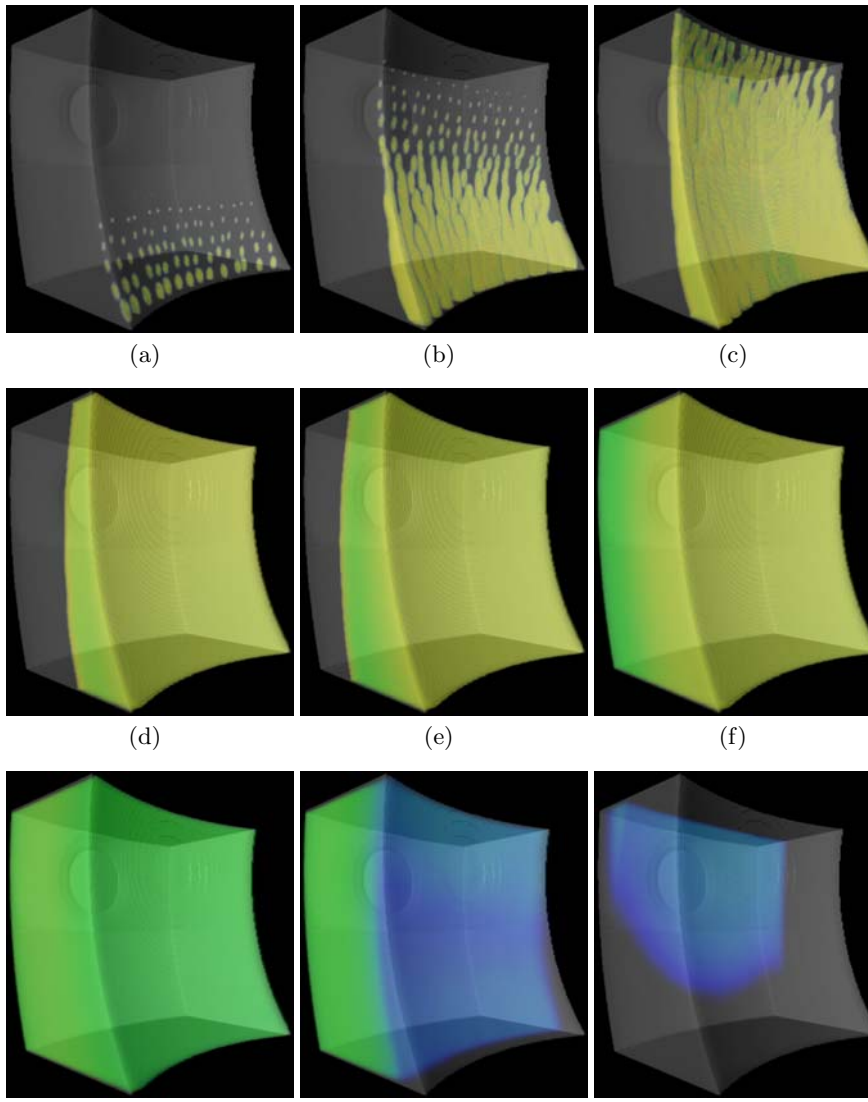

Fig. 7.46. Excitation propagation in static model of heart wall at different points in time. The simulated transmembrane voltage is visualized with volume based techniques at (a) 5 *ms*, (b) 10 *ms*, (c) 15 *ms*, (d) 30 *ms*, (e) 65 *ms*, (f) 130 *ms*, (g) 290 *ms*, (h) 340 *ms*, and (i) 410 *ms*.

by meandering, extinction and detachment of wavelets. These facts regarding the characteristics of the wave front apply for the simplified reaction diffusion systems as well as for the combined systems. Different approaches were chosen

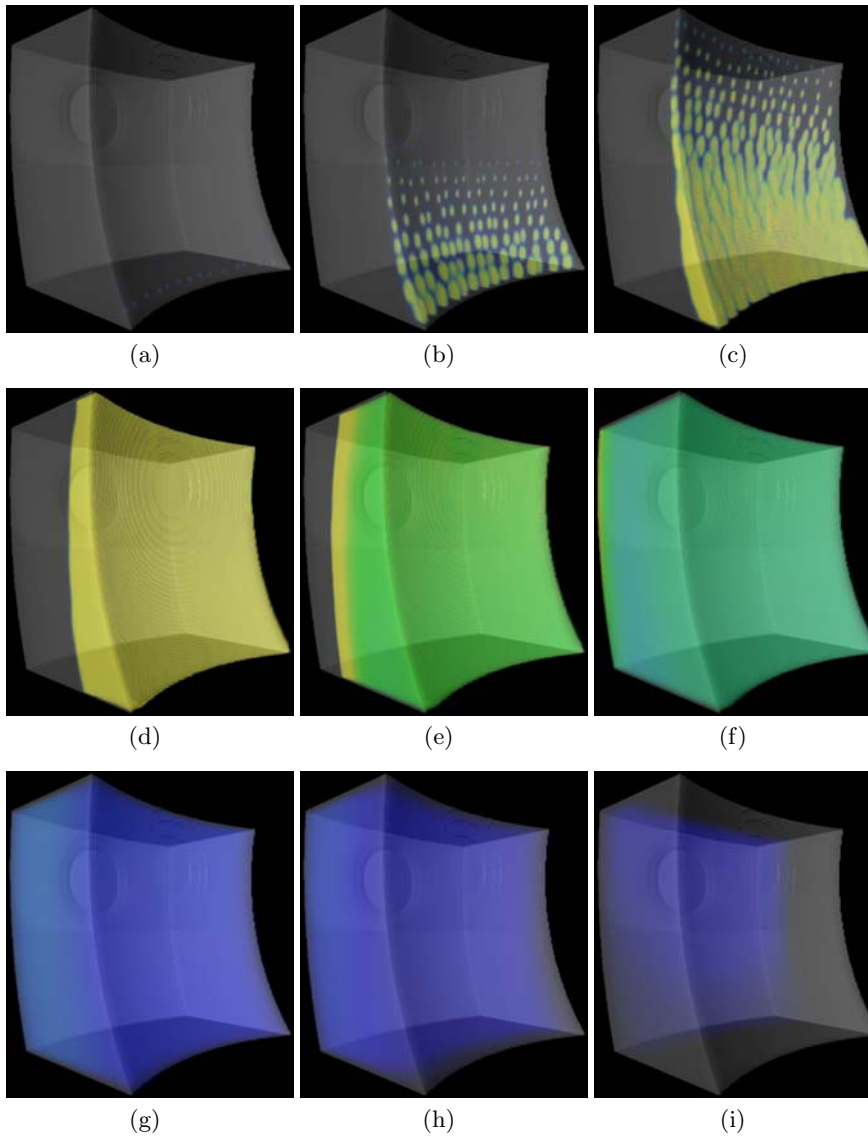

Fig. 7.47. Intracellular calcium concentration $[Ca^{2+}]_i$ in static model of heart wall at different points in time. The simulated concentration is visualized with volume based techniques at (a) 5 ms, (b) 10 ms, (c) 15 ms, (d) 30 ms, (e) 65 ms, (f) 130 ms, (g) 290 ms, (h) 340 ms, and (i) 410 ms.

to approximate and reconstruct these characteristics with extended cellular automata.

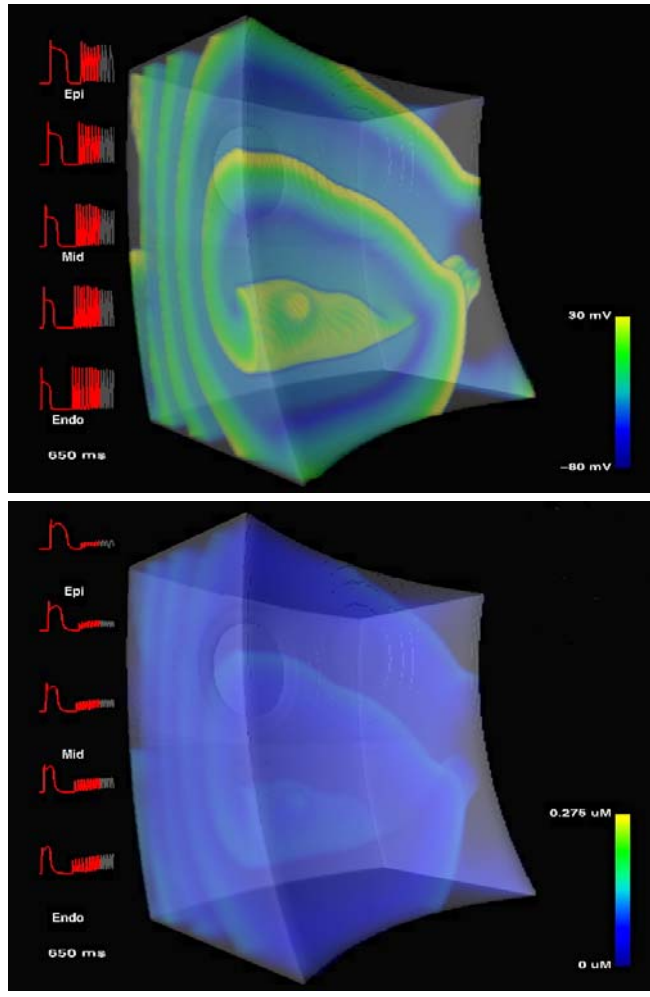

Fig. 7.48. Simulation of scroll wave in static model of heart wall. (a) The transmembrane voltage V_m and (b) intracellular calcium concentration $[Ca^{2+}]_i$ are visualized with volume based techniques at the exemplary point in time 650 ms. The corresponding color palette is located at the right side. At the left side the course of the transmembrane voltage V_m and the intracellular calcium concentration $[Ca^{2+}]_i$ in different regions of the wall are illustrated.

Cellular phenomena, e.g. EADs, DADs, and triggered activity, are commonly not reconstructed by cellular automata, although an inclusion is principally possible. The inclusion of complex cellular phenomena can be achieved by a modification of the finite automata working at each node of the cellular automaton.

The traditional cellular automata and the simplified reaction diffusion systems make the least demands on compute and storage resource. The demands of the combined models are primarily determined by the electrophysiological cell models and the numerical method to solve Poisson's equation. Nevertheless, these demands are strongly depending on the specific implementation and compute platform.

8

Cardiac Mechanics

8.1 Overview

The heart acts as a cyclically working pump with the task of transporting blood in the body. Primarily responsible for this transport is the contraction of the heart's dominant structures, the left and right ventricle, which are composed of myocardial walls surrounding a cavity. The cavities are normally filled with blood and change their volume by the contraction. Resulting from this change of volume is the pumping of blood through vessels into the body. The returning blood is collected in the left and right atrium, which are built up similar to the ventricles, but with less pronounced myocardial walls. Afterwards, the blood is transported to the ventricles. The blood transport in the atria is supported by active suction of the ventricles. Different valves control the blood flow and prevent re-flow.

Like all types of muscle structures the myocardium consumes chemical energy to develop forces. The myocardial force development is a sub-cellular process controlled by electrophysiological parameters and depending on the availability of energy sources. Concerned with the force development are the myofilaments, which are found inside of the sarcomeres and composed of actin and myosin.

The forces in the ventricular wall can create a sufficiently high pressure to distribute the blood in the body. Multiple electro-mechanical and mechano-electrical feedback mechanisms are integrated in the heart. These mechanisms allow an automaticity and an implicit adaptation to power demands without control by super-ordinate structures.

The topics of this section are the passive mechanical properties and the active force development of the myocardium. Whereas the passive mechanical properties are ascribed primarily from a macroscopic view with the continuum mechanics as foundation, the active force development is considered on cellular base in strong relationship to the sub-cellular components. In both sections experimental studies are described followed by modeling approaches. The descriptions are restricted to experiments delivering quantitative data

F.B. Sachse: LNCS 2966, pp. 221–266, 2004.

and to biophysically motivated modeling approaches. Special focus is given to numerically efficient models, which can be combined with computer-based anatomical and electrophysiological models.

8.2 Mechanical Properties of Myocardium

8.2.1 Experimental Studies

A majority of initial experiments to acquire mechanical properties of myocardium was carried out with trabecular and papillary muscles of animals [30]. Alternatively, mechanical properties were determined with specimens from different regions in the atrial and ventricular wall [253] as well as with whole ventricles [254, 255]. Furthermore, cellular mechanical properties were quantified by measurements with single or small groups of myocytes [256].

Commonly, the specimens are taken from exposed hearts. The studies were performed with the species canine, cat, rabbit, ferret and rat (table 8.1).

Macroscopic and microscopic measurement devices can be distinguished dependent on the specimens size ranging from large papillary muscles to single myocytes. Uni-, bi- and triaxial measurement devices were used to measure the relationship between strain and stress, the so-called constitutive law, in myocardium. Hereby, strain is varied and the corresponding stress is measured. As well, a vice versa procedure is possible. The measurement of strain can be performed with displacement transducers, e.g. Hall effect and liquid metal strain gauges, and optical systems consisting of camera and image analysis tools [274].

Partly, the devices allow the measurement of specimens inlaid in a tempered fluid, which keeps the metabolism of the specimens at work despite interrupted blood perfusion. The metabolism is performed via diffusion, which implies a small specimens size. Hereby, the specimens are surrounded with the fluid, e.g. Ringer-Tyrode and Krebs-Ringer solution, which is conveniently composed similar to blood. The temperature of the solution is often set to low values, which reduces degradation of specimens. The measurement at body temperature proves to be of advantage, because a temperature dependence of material properties is observed. The usage of noncytotoxic materials, which are also resistant to chemical degradation by the fluid, is recommended for all device components, which come in contact with specimens and fluids.

A major difficulty in many studies is the attachment of specimens particularly to mechanical transducers [275]. Desirable is a uniform stress distribution with the attachment and a small compliance of the attachment.

Historically, the first measurements were made with uniaxial devices [257, 258], which are of restricted usability e.g. concerning the registration of shear and volume changes [276]. The usage of biaxial devices allowed the measurement of further components of the relationship useful to reduce indeterminateness of the stress-strain relationship [265]. A recently developed

Table 8.1. Measurements of mechanical properties of myocardium.

Date	Publisher	Tissue	Species	Reference
1964	Sonnenblick	papillary muscle	cat	[257]
1973	Pinto, Fung	papillary muscle	rabbit	[258, 30]
1973/74	Janz, Kubert, Moriarty, Grimm	papillary muscle	rat	[259, 260]
1974	Alpert, Hamrell, Halpern	ventricular muscle	rabbit	[261]
1975	Kane, McMahon, Wagner, Abelmann	ventricular muscle	hamster	[262]
1976	Rankin, Arentzen, McHale, Ling, Anderson	ventricular muscle	canine	[263]
1988	Hunter, Smaill	ventricular muscle	canine	[264, 265]
1991	Guccione, McCulloch, Waldman	ventricular muscle	canine, rat	[266]
1994	Novak, Yin, Humphrey	ventricular muscle	canine	[267]
1995	Hunter, Nash, Sands	ventricular muscle	canine	[268, 253]
1995	Moulton, Creswell, Actis, Myers, Vannier, Szabó, Pasque	ventricular muscle	canine	[269]
1997	Miller, Vanni, Keller	ventricular muscle	chicken	[270]
1998	Omens, Vaplon, Fazeli, McCulloch	ventricular muscle	rat	[271]
1998	Zile, Cowles, Buckley, Richardson, Cowles, Baicu, Cooper, Gharpuray	ventricular myocytes	cat	[256]
2000	Dokos, LeGrice, Smaill, Kar, Young	septal muscle	rat	[272]
2000	Okamoto, Moulton, Pasque, Peterson, Li, Guccione	ventricular muscle	canine	[255]
2003	Dokos, Smaill, Young, LeGrice	ventricular muscle	pig	[273]

triaxial device permits the application of two-dimensional shear and the measurement of three-dimensional force (Fig. 8.1) [272, 273].

Alternatively, mechanical tissue properties were measured with experiments, where suction or pressure is applied to the heart (Fig. 8.2) [269, 255]. The resulting deformation is quantified using medical imaging systems, e.g. magnetic resonance tagging, in conjunction with image processing techniques. The mechanical properties were determined with finite element models, which were adapted by nonlinear optimization techniques.

Experimental studies revealed that the mechanical properties of myocardium depend strongly on the composition and arrangement of the extracellular matrix. Its dominant components are fibrous proteins, i.e. collagen and elastin. A cellular component of resistance to extension was found, which was primarily attributed to cytoskeleton elements, i.e. titin and desmin [275].

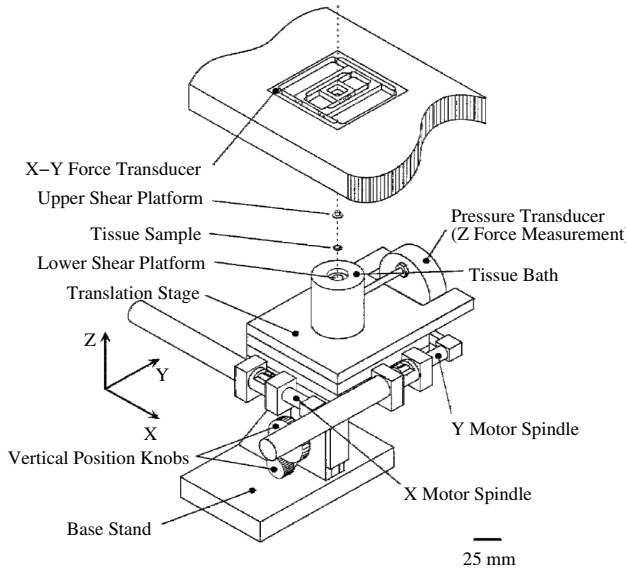

Fig. 8.1. Triaxial-measurement shear-test devices for soft tissue (adapted from [272]). The device can impose shear deformation in X- and Y-direction with two linear motors. The forces in X-, Y- and Z-direction can be measured. The tissue sample is located in a bath between two circular platforms. The shear-test device is controlled and its data recorded using a computer. A shear test is performed by moving the bottom surface of the tissue sample in X- and Y-direction, while three-dimensional forces are measured.

The mechanical properties are found to be nonlinear, anisotropic and viscoelastic [263]. These characteristics are common in many biological tissues [28]. Furthermore, the volume change resultant by deformation was found to be small and significant residual stresses are present [277, 278, 271]. Material properties of myocardium are reported to be dependent on the intracellular calcium concentration and state of active contraction [279, 256] as well as on the pressure produced by the coronary perfusion [280].

The studies by Kane et al. looked into the age dependency of the elastic modulus of ventricular myocardium [262]. An analysis of left and right ventricular pressure-volume curves of Syrian golden hamsters was performed showing no significant age dependent variation of elastic modulus. The analysis suggested that structural changes with regard to the passive properties of myocardium are not associated with age.

8.2.2 Modeling Approaches

Overview. The results of many experimental studies were used to model the relationship between strain and stress by assumption of a convenient template

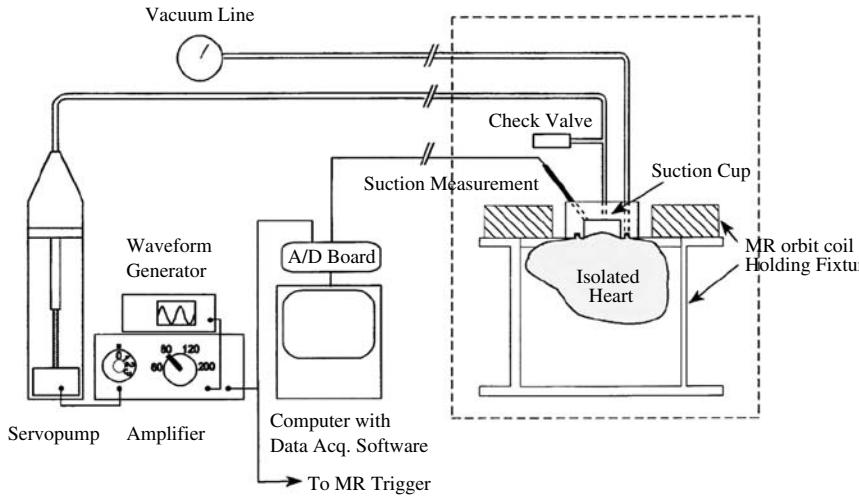

Fig. 8.2. Measurement system with epicardial suction (adapted from [255]). The isolated arrested heart is located in cold saline and cardioplegic solution. The borders of an epicardially placed suction cup are attached to the left ventricular free wall epicardium by continuously applied vacuum pressure. The cup orifice with an opening of 2.5 *cm* x 2.5 *cm* is connected to a servo-pump providing cyclic suction. The suction is controlled with a waveform generator and recorded with a computer system. The check valve prevents large positive pressures in the suction orifice, which would detached the heart and cup. A deformation of the heart is performed through pressure in the orifice created in the servo-pump. The deformed heart is imaged with a MRT system triggered with the signals of the waveform generator. The images are analyzed and used in conjunction with finite element models to determine mechanical parameters.

strain energy function and parameter fitting procedures (table 8.2). The parameters were determined by numerical experiments reconstructing the measurements.

In the following sections some modeling approaches are described. The development of models and the inclusion of different properties are illustrated. The properties are e.g. inhomogeneity, anisotropy, and multiple domains. In multiple domain approaches different strain energy functions, each defined on a domain, contribute to the summary strain energy. Commonly, the energy density function does not comprise plasto- and viscoelastic effects.

Demiray 1972. The strain energy density function proposed by Demiray aims at the resembling of the energy function of biological tissue [281] (Fig. 8.3), which was found to be entirely different from former described materials, e.g. rubber. The biological tissue was assumed to be isotropic, homogeneous, and incompressible as wells as non-visco- and hyperelastic. The

Table 8.2. Models of mechanical properties of myocardium.

Date	Publisher	Tissue	Species	Reference
1972	Demiray	papillary muscle	cat	[281]
1973/74	Janz, Kubert, Moriarty, Grimm	papillary muscle	rat	[259, 260]
1974	Glantz	papillary muscle	cat	[282]
1976	Rankin, Arentzen, McHale, Ling, Anderson	ventricular muscle	canine	[263]
1983	Needleman, Rabinowitz, Bogen, McMahon	ventricular muscle	canine	[283]
1987	Humphrey, Yin	ventricular and papillary muscle	canine	[284]
1988	Horowitz, Lanir, Yin, Perl, Sheinman, Strumpf	ventricular muscle	canine	[285, 286]
1989	Nevo, Lanir	ventricular muscle	-	[287]
1990	Humphrey, Strumpf, Yin	ventricular muscle	canine	[288, 289]
1991	Huyghe, van Campen, Arts, Heethaar	divers	divers	[290]
1991	Yang, Tabber	papillary muscle	rabbit, frog, turtle	[291]
1991	Guccione, McCulloch, Waldman	ventricular muscle	canine, rat	[266, 254]
1993	Sacks, Chuong	ventricular muscle	canine	[292]
1994	Nevo, Lanir	ventricular muscle	-	[278]
1994	Novak, Yin, Humphrey	ventricular muscle	canine	[267]
1995	Guccione, Costa, McCulloch	ventricular muscle	canine	[293]
1995	Hunter, Nash, Sands	ventricular muscle	canine	[268, 253]
1998	May-Newman, McCulloch	ventricular muscle	canine	[280]
2000	Okamoto, Moulton, Pasque, Peterson, Li, Guccione	ventricular muscle	canine	[255]
2000	Usyk, Mazhari, McCulloch	left ventricle	canine	[294]

strain energy density function W was defined as a function of the first invariant I_1 of the Cauchy-Green left dilation or Finger strain tensor:

$$W = \frac{\beta}{2\alpha}\left(e^{\alpha(I_1-3)} - 1\right)$$

with the parameters α and β. The function was constructed to resemble studies of cat papillary muscle [257]. No explicit values were given for the parameters α and β.

Janz-Kubert-Moriarty-Grimm 1974. The strain energy density function proposed by Janz et al. was constructed using uniaxial measurement data from left ventricular papillary muscles of adult Sprague-Dawley albino male rats [260]. The function is depending on the principal components of strain ϵ_i:

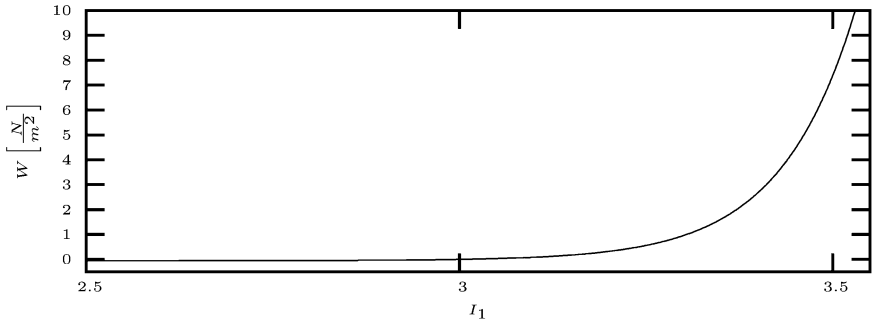

Fig. 8.3. Strain energy density W proposed by Demiray for biological tissue dependent on first invariant I_1 of the Cauchy-Green left dilation tensor. The parameters α and β are set to 10 and 1, respectively.

$$W = \frac{E}{\beta^2(1+\nu)}\left(\sum_{i=1}^{3} e^{\beta\epsilon_i} + \frac{1-2\nu}{\nu} e^{-\frac{\beta\nu}{1-2\nu}\sum_{i=1}^{3}\epsilon_i} - \frac{1+\nu}{\nu}\right)$$

with Young's modulus E, Poisson's ratio ν, and the additional parameter β. The function assumes isotropy of myocardium.

Young's modulus E was obtained with measurement data, whereby the slope of the stress-extension at small strain is evaluated. The evaluation delivers a spatial inhomogeneous Young's modulus E, which was found to be $5886\,\frac{N}{m^2}$ in the outer two-thirds and $2943\,\frac{N}{m^2}$ in the inner third of the myocardial wall. Poisson's ratio ν was set to 0.49 to approximate incompressibility of the papillary muscles. The parameter β was set according to measurement data to 15 by curve fitting procedures.

Rankin-Arentzen-McHale-Ling-Anderson 1976. The work of Rankin et al. aimed at the assessment of the viscoelastic properties of myocardium [263]. The properties of normal left ventricular myocardium of dogs were measured with micromano- and sonomicrometry. The ultrasonic transmitters were sewed at different locations at the epi- and endocardial wall. The micromanometers were located in the left ventricle and pleura. The measurement of pressure and geometry was performed in diastole. Increases of the systolic and diastolic loading were performed using inflating occluders implanted in the aorta as well as in the vena cava superior and inferior. The determination of the mechanical properties was performed by an ellipsoid shell theory neglecting anisotropy and inertia.

The so-called natural strain was calculated at the midwall circumference by:

$$\epsilon = ln\frac{l}{l_0}$$

with the minimal midwall circumference l_0 and the instantaneous midwall circumference l.

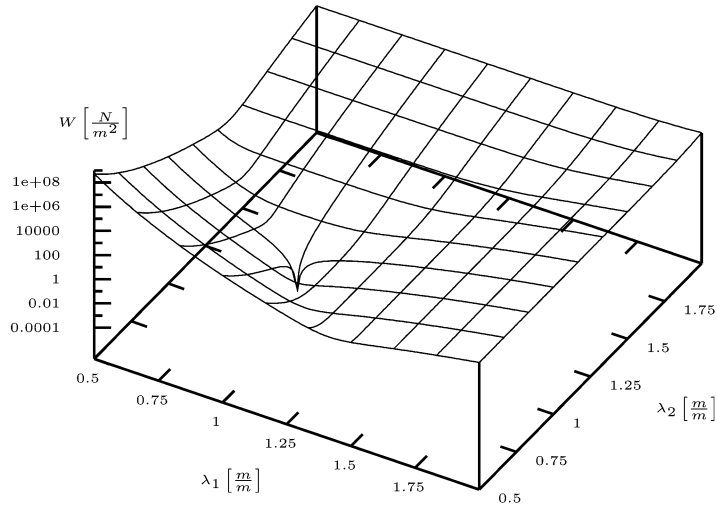

Fig. 8.4. Strain energy density W proposed by Needleman et al. for normal left ventricular myocardium of canine in diastole. The strain energy density W is dependent on the principal stretches λ_1 and λ_2. The third principal stretch λ_3 is set to $(\lambda_1\lambda_2)^{-1}$ assuming incompressibility.

The uniaxial connection between stress τ and strain ϵ was evaluated for different functions. The most precise approximation was achieved by a function including viscoelasticity:

$$\tau = \alpha(e^{\beta\epsilon} - 1) + \eta\,\dot{\epsilon}$$

with the nonlinear elastic constants α and β, the viscous constant η, and the strain time derivative $\dot{\epsilon}$. Mean values of the parameters, derived from measurements of 10 animals, were given by $\alpha = 7.3 \cdot 10^{-6}\frac{1}{m^2}$, $\beta = 12.3$, and $\eta = 34.7 \cdot 10^{-6}\frac{s}{m^2}$.

Needleman-Rabinowitz-Bogen-McMahon 1983. The material properties given by Needleman et al. were used to represent normal and infarcted left ventricular myocardium of canine [283]. Differences of the material properties were reflected by appropriate parameterization of strain energy density functions.

Two different configurations for material descriptions were examined, i.e. diastole and end-systole. For each configuration a specific strain energy density function was defined. At diastole the material was described as incompressible, isotropic and hyperelastic with the strain energy density function W_d:

$$W_d = \frac{\mu_p}{k_p}\left(\lambda_1^{k_p} + \lambda_2^{k_p} + \lambda_3^{k_p} - 3\right)$$

with the principal stretches λ_1, λ_2, and λ_3 as well as the parameters μ_p and k_p. Incompressibility was ensured by:

$$\lambda_3 = \frac{1}{\lambda_1 \lambda_2}$$

The parameters μ_p and k_p were chosen partly dependent on measurement data. Normal myocardium was characterized by $k_p = 16$ and $\mu_p = 2$ (Fig. 8.4). Infarcted myocardium was described by $k_p = 16$ and $\mu_p = \{1, 16\}$.

At end-systole the upper strain energy density function W_d was extended by an additional strain energy function W_s:

$$W_s = \frac{\mu_s}{k_s} \left(\overline{\lambda}_1^{k_s} + \overline{\lambda}_2^{k_s} + \overline{\lambda}_3^{k_s} - 3 \right)$$

with the stretches $\overline{\lambda}_1$, $\overline{\lambda}_2$, and $\overline{\lambda}_3$ as well as the parameters μ_s and k_s. The stretches of the diastolic and end-systolic configuration are related by:

$$\begin{aligned} \overline{\lambda}_1 &= \lambda_c \lambda_1 \\ \overline{\lambda}_2 &= \lambda_c \lambda_2 \\ \overline{\lambda}_3 &= \lambda_c^{-2} \lambda_3 \end{aligned}$$

with the parameter $\lambda_c = 1.18$. The parameters μ_s and k_s were not explicitly given in [283].

Humphrey-Yin 1987. The approach of Humphrey at el. attempted to describe tissue behavior by the interaction and properties of the tissue constituents [284]. The formulation of the strain density energy function reflects histological observations [70, 107], which showed that the tissue consists of a homogeneous matrix and non-interacting families of fibers, which are densely distributed, thin and hyperelastic. Therefore, the proposed strain density energy function W consists of two parts, a function W_m, describing the homogeneous matrix, and a function W_f, representing the fiber behavior and anisotropic properties of the tissue:

$$W = W_m + W_f$$

The definition of the homogeneous matrix function W_m follows the approach by Demiray et al. (Sect. 8.2.2) for isotropic material:

$$W_m = c \left(e^{b(I_1 - 3)} - 1 \right)$$

with the first invariant I_1 of the Cauchy-Green deformation tensor $\boldsymbol{C}$, and the parameters c and b.

The definition of the fiber behavior function W_f is exponential:

$$W_f = A \left(e^{a(\alpha - 1)^2} - 1 \right)$$

with the fiber stretch α, and the parameters A and a. The fiber stretch was calculated by:

$$\alpha = \sqrt{\boldsymbol{n}^T \boldsymbol{C} \boldsymbol{n}}$$

with the unit fiber direction $\boldsymbol{n}$.

The parameters A, a, b and c were determined by fitting procedures using uniaxial measurements from canine papillary muscle and biaxial measurements of thin slabs of canine subepicardial left ventricular free wall. Parameter fitting with data from uniaxial measurements of papillary muscles led to a significant underestimation of the stresses. Parameter fitting with data from biaxial measurements, whereby the ratio of fiber- and crossfiber-strain was varied as well as different specimens scanned, showed large variations of the parameters.

Horowitz-Lanir-Yin-Perl-Sheinman-Strumpf 1988. The model of mechanical properties introduced by Horowitz et al. is motivated by histological studies of myocardium. Different models for thin myocardial strips [285] and full three-dimensional areas of canine myocardium [286] were proposed. The myocardium is treated as a hyperelastic, non-viscoelastic, incompressible material.

The strain energy in a unit volume is assumed to be the sum of the strain energies of different fibers, i.e. enclosed myocytes and collagen struts. The myocytes are tethered by the collagen struts.

The three-dimensional strain energy density function W of the domain Ω of spatial directions $\boldsymbol{n}$ is given by [295]:

$$W = \sum_k s_k \int_\Omega R_k(\boldsymbol{n}) w_k^*(E'_{11}) \, d\Omega$$

with the volumetric fraction of fibers s_k, the fiber specific density distribution function R_k, the integral fiber specific strain energy density function w_k^*, and the Green-Lagrange strain in fiber direction E'_{11}. Two fiber types k were defined: collagen struts and myofibers.

The function R_k describes stochastically the spatial arrangement of the fibers, such that the relative portion p_{rk} of type k fibers in the volume $\Delta\Omega$ is determined by:

$$p_{rk} = R_k(\boldsymbol{n}) \Delta\Omega$$

The integral fiber specific strain energy density function w_k^* is depending on the strain in fiber direction E'_{11}:

$$w_k^* = \int_0^{E'_{11}} D_{k,n}(x) w_k(E'_{11t}) dx$$

with the fiber specific waviness distribution function $D_{k,n}$, the fiber specific strain energy density function w_k and the true strain E'_{11t} given by:

$$E'_{11t} = \frac{E'_{11} - x}{1 + 2x}$$

The fiber specific waviness distribution function $D_{k,n}$ describes the waviness of type k fibers, such that these fiber's portion p_{dk} aligned with $\boldsymbol{n}$ and having a strain in $[x, x + \Delta x]$ is given by:

$$p_{dk} = D_{k,n}\Delta x$$

Humphrey-Strumpf-Yin 1990. The strain energy density function proposed by Humphrey et al. describes the mechanical properties of passive myocardium [288] [289] [276]. In a general form the function is given by:

$$W = \sum_{i=0}^{n}\sum_{j=0}^{n} c_{ij}(I_1 - 3)^i(\alpha - 1)^j$$

with the parameters c_{ij}, the first invariant I_1 of the right Cauchy-Green deformation tensor $\boldsymbol{C}$ and the strain $\alpha = \sqrt{\boldsymbol{N}^T\boldsymbol{C}\boldsymbol{N}}$. The function describes anisotropic behavior in the case of transversal isotropy. Restrictions on the parameters lead to the strain energy density function:

$$W = c_1(\alpha - 1)^2 + c_2(\alpha - 1)^3 + c_3(I_1 - 3) + c_4(I_1 - 3)(\alpha - 1) + c_5(I_1 - 3)^2$$

with the parameters c_1, c_2, c_3 ,c_4, and c_5.

The strain energy density function was parameterized with data from biaxial measurements on excised midwall myocardium of canine. The parameters were calculated applying nonlinear optimization techniques.

Yang-Tabber 1991. The constitutive equations proposed by Yang and Taber are applied to investigate the role of extracellular fluid for the viscoelastic properties of passive myocardium [291]. The total stress $\boldsymbol{\tau}_{total}$ is composed of the stress $\boldsymbol{\tau}_{solid}$ for the solid and the stress $\tau_{fluid}\boldsymbol{I}$ for the fluid:

$$\boldsymbol{\tau}_{total} = \boldsymbol{\tau}_{solid} + \tau_{fluid}\boldsymbol{I}$$

The stress for the fluid τ_{fluid} is dependent on the hydrostatic pressure p and the ratio of fluid to bulk volume ϕ:

$$\tau_{fluid} = -\phi p$$

The stress for the solid is given by:

$$\boldsymbol{\tau}_{solid} = 2\mu\epsilon^s + \lambda\epsilon^s\boldsymbol{I} - (1 - \phi)p\boldsymbol{I}$$

with the Lamé constants λ and μ and the strain of solid ϵ^s. Hence, the total stress $\boldsymbol{\tau}_{total}$ is determined by:

$$\boldsymbol{\tau}_{total} = 2\mu\epsilon^s + \lambda\epsilon^s\boldsymbol{I} - p\boldsymbol{I}$$

The Lamé constants λ and μ were determined starting from a strain energy density function W:

$$W = \frac{C}{\alpha} e^{\alpha\left(\sqrt{I_3}+\frac{nI_2}{2I_3}+\frac{(n-1)I_1}{2}-3n+0.5\right)}$$

with the invariants of the strain tensor I_1, I_2, and I_3, as well as the parameters C, n and α. The function W was used only for mathematical convenience, because experimental work concerning the poroelastic properties of myocardium is missing. For small strain the following approximations were identified:

$$\begin{aligned}\lambda &= C \\ \mu &= C(2n-1) \\ \nu &= \frac{1}{4n}\end{aligned}$$

with the Poisson's ratio ν.

Uniaxial simulations were performed and compared with measurements of rabbit, frog and turtle cardiac muscle. The results indicate that some observed biomechanical phenomena can be explained with extracellular flow, but that further experimental work is requisite.

Guccione-McCulloch-Waldman 1991. The strain energy density function W proposed by Guccione et al. was constructed on the base of constitutive laws for arteries assuming orthotrophic material properties [254]. The function is exponential:

$$W = \frac{C}{2}\left(e^{Q}-1\right) \tag{8.1}$$

with the parameter C and the function Q, depending on the Green-Lagrange strain tensor $\boldsymbol{E}$. Two variants of the function Q were investigated: an isotropic function Q_{iso} and an anisotropic, transversal isotropic function Q_{aniso} with respect to the fiber orientation:

$$\begin{aligned}Q_{iso} &= 2b_1(E_{RR}+E_{FF}+E_{CC}) \\ Q_{aniso} &= 2b_1(E_{RR}+E_{FF}+E_{CC}) \\ &\quad + b_2E_{FF}^2 + b_3(E_{CC}^2+E_{RR}^2+E_{CR}^2+E_{RC}^2) \\ &\quad + b_4(E_{RF}^2+E_{FR}^2+E_{FC}^2+E_{CF}^2)\end{aligned}$$

with the parameters b_1, b_2, b_3, b_4, and the components of the Green-Lagrange strain tensor $\boldsymbol{E}$. The indices F, C, and R depict the fiber axis, cross-fiber in-plane axis, and the radial direction, respectively.

The strain energy density function was parameterized by comparison of measurements performed with canine ventricles and results of numerical simulation. The measurements delivered epicardial strains and left ventricular volumes in dependence of ventricular pressure. A thick-walled cylindrical model was used to describe the equatorial ventricular geometry. In the isotropic case the parameter C was set to 0.765 kPa and the parameter b_1 to 4.24. For the anisotropic case the parameter b_3 was set to 0. Different parameterizations were determined depending on the assumption of transmural distribution of fiber orientation and residual stress in the ventricular wall.

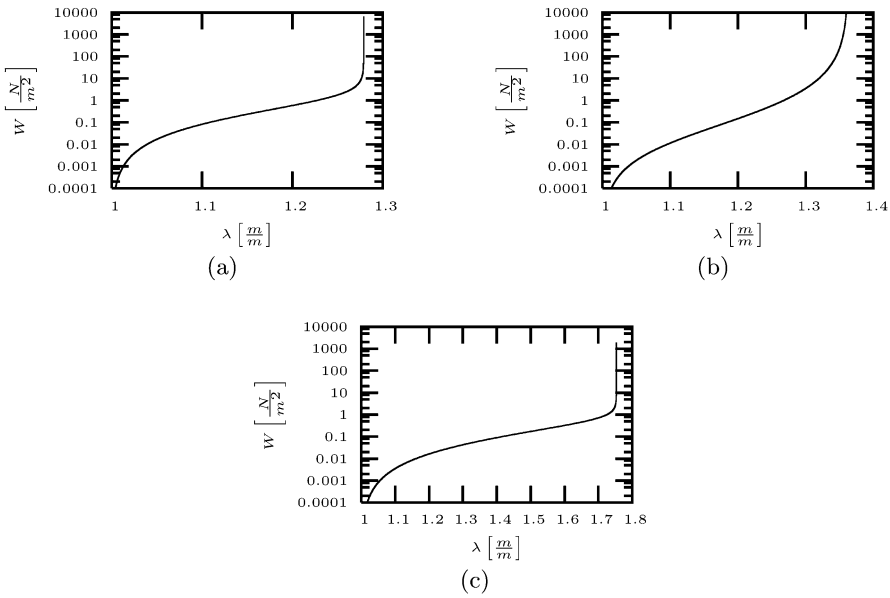

Fig. 8.5. Unidirectional strain energy densities W proposed by Hunter-Nash-Sands for epicardial canine myocardium. The energy density is shown versus the stretch ration λ and dependent on three orthogonal axes, i.e. (a) fiber orientation, (b) sheet orientation and (c) sheet normal.

Hunter-Nash-Sands 1995. The strain energy density function W proposed by Hunter et al. takes the anisotropic and inhomogeneous behavior of myocardium into account [268, 253, 296, 297] (Fig. 8.5, 8.6 and 8.7). Three microstructural justified, orthogonal axes were distinguished: the fiber, sheet and sheet normal axis. The energy density function is named pole-zero law. The summary strain energy density is composed of energy densities for different strains with axes $i = 1, 2, 3$ and $j = 1, 2, 3$:

$$W = \frac{k_{11}E_{11}^2}{(a_{11} - |E_{11}|)^{\beta_{11}}} + \frac{k_{22}E_{22}^2}{(a_{22} - |E_{22}|)^{\beta_{22}}} + \frac{k_{33}E_{33}^2}{(a_{33} - |E_{33}|)^{\beta_{33}}} + \frac{k_{12}E_{12}^2}{(a_{12} - |E_{12}|)^{\beta_{12}}} + \frac{k_{13}E_{13}^2}{(a_{13} - |E_{13}|)^{\beta_{13}}} + \frac{k_{23}E_{23}^2}{(a_{23} - |E_{23}|)^{\beta_{23}}} \tag{8.2}$$

with the components of the Green-Lagrange strain tensor E_{ij} as well as the parameters, k_{ij}, a_{ij}, and β_{ij}. The parameter k_{ij} is set to zero, if E_{ij} is negative. The energy density attributed to a strain is zero in case of compression in the direction. The strain energy density function W is defined for $|E_{ij}| < a_{ij}$. The function shows large values for strain E_{ij} approaching its 'pole' a_{ij}, reflecting the steep rise in tension coming upon a strain limit.

The energy densities and their parameters are divided into an axial and a shear group. The parameters of the two groups are assumed to be inter-

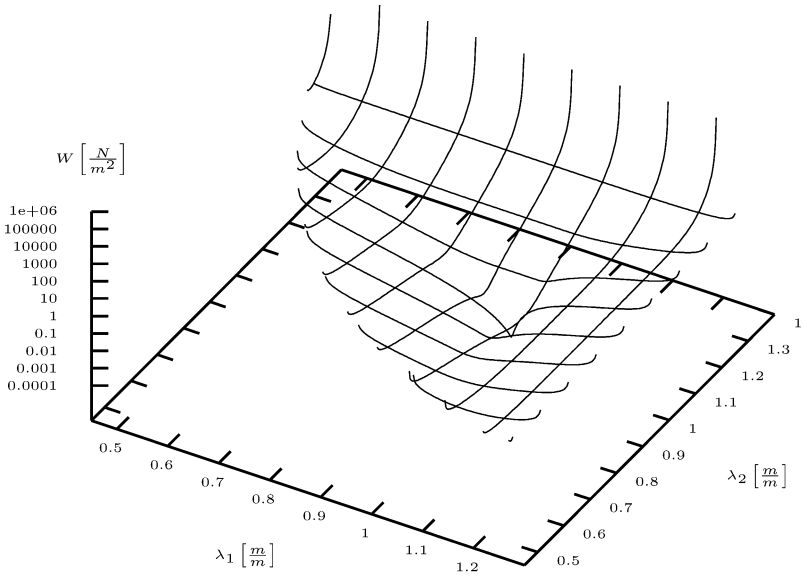

Fig. 8.6. Strain energy density W proposed by Hunter-Nash-Sands for epicardial canine myocardium. The strain energy density W is visualized dependent on the principal stretches λ_1 and λ_2 corresponding to fiber and sheet directions, respectively. The third principal stretch λ_3 corresponding to the sheet normal is set to $(\lambda_1\lambda_2)^{-1}$ assuming incompressibility.

Table 8.3. Exemplary parameter set of strain energy density function proposed by Hunter et. al. [297]. The parameters of each line serve to parameterize a single component of the summary function. The shear parameters are result of microstructurally based assumptions.

Strain energy term	Group	k	a	b
11	axial	1.937	0.523	1.351
22	axial	0.028	0.681	5.991
33	axial	0.310	1.037	0.398
12	shear	1.000	0.731	2.000
13	shear	1.000	0.731	2.000
23	shear	1.000	0.886	2.000

dependent, because the same anatomical microstructures are involved in the deformation. Therefore, only 9 free parameters are attributed (table 8.3).

The parameterization of the function W was performed by uniaxial measurements of canine ventricle in the different directions of the axes. Hereby, the parameters of different regions in myocardium were collected, i.e. epicardium and midwall.

The strain energy density function was extended by terms representing the incompressibility of myocardium. High demands must be made concerning the

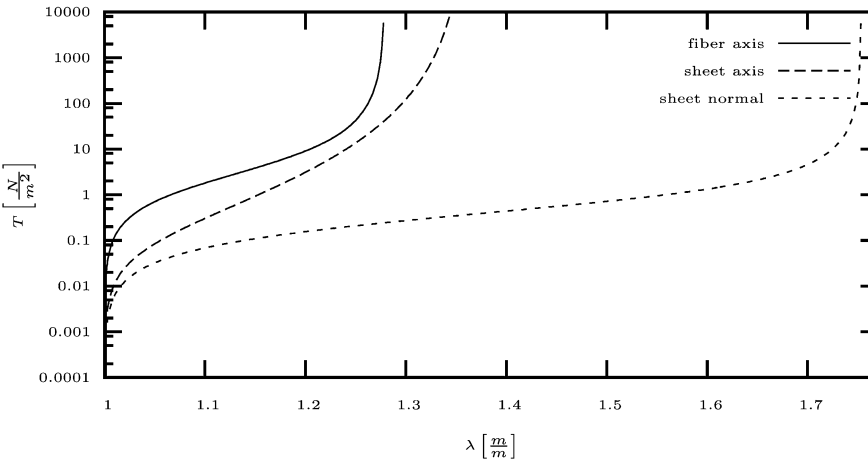

Fig. 8.7. Unidirectional second Piola-Kirchhoff stress $\boldsymbol{T}$ derived from hyperelastic material law of Hunter-Nash-Sands for epicardial canine myocardium. The stress is shown versus the stretch ration λ and is dependent on three orthogonal axes.

compliance of incompressibility in numerical calculation if strains are near to the poles. Extensions for in-cooperation of more complex stress-strain relationships can use a polynomial expansion of the single strain energy densities in equation 8.2 [268].

Okamoto-Moulton-Peterson-Li-Pasque-Guccione 2000. The energy density function W proposed by Okamoto et al. follows the approach of an exponential, anisotropic, transversely isotropic constitutive relation given by equation 8.1. Hereby, the function W is defined as [255]:

$$W = \frac{C}{2}\left(e^{Q} - 1\right)$$

with parameter C and the strain dependent function Q. The function Q is dependent on the components of the Green-Lagrange strain tensor $\boldsymbol{E}$ and is defined as:

$$\begin{aligned} Q = {} & b_F E_{FF}^2 + b_T(E_{CC}^2 + E_{RR}^2 + E_{CR}^2 + E_{RC}^2) \\ & + b_{FS}(E_{FC}^2 + E_{CF}^2 + E_{FR}^2 + E_{RF}^2) \end{aligned}$$

with the parameters b_F, b_T, and b_{FS} as well as the fiber strain E_{FF}, the cross-fiber in-plane strain E_{CC}, the radial strain E_{RR}, the shear strains E_{CR}, E_{RC}, E_{FC}, E_{CF}, E_{RF}, and E_{FR}.

The parameterization was performed by experiments, whereby suction was applied to the left ventricular epicardium of dogs. Therefore, the heart was exposed by median sternotomy. The suction produced a deformation, which

was measured using magnetic resonance tagging and image processing techniques. A finite element model was adapted to the measured deformation by variation of the parameterization.

Usyk-Mazhari-McCulloch 2000. The energy density function W proposed by Usyk et al. extends the transversely isotropic constitutive, incompressible approach given by equation 8.1 by taking orthotropy and compressibility of myocardium into account. Hereby, the function W is defined as [294]:

$$W = \frac{C}{2}\left(e^{Q} - 1\right) + C_{compr}\left(J\ lnJ - J + 1\right)$$

with parameters C and C_{compr}, the strain dependent function Q, and the Jacobian J. The function Q is dependent on the components of the Green-Lagrange strain tensor $\boldsymbol{E}$:

$$\begin{aligned} Q = {} & b_{FF}E_{FF}^2 + b_{SS}E_{SS}^2 + b_{NN}E_{NN}^2 + b_{FS}(E_{FS}^2 + E_{SF}^2) \\ & + b_{FN}(E_{FN}^2 + E_{NF}^2) + b_{NS}(E_{NS}^2 + E_{SN}^2) \end{aligned}$$

with the parameters b_{FF}, b_{SS}, b_{NN}, b_{FS}, b_{FN}, and b_{NS}. The indices F, S, and N of the components of the strain tensor $\boldsymbol{E}$ indicate fiber, sheet and sheet-normal axes, respectively. The parameterization was performed by comparison of distributions of three-dimensional diastolic and systolic strains obtained by numerical experiments in a prolate spheroidal model and by measurements in the dog heart.

8.3 Tension Development

8.3.1 Mechanisms

Cardiac, smooth and skeletal muscles are not only passively reacting to external forces but can create internal tension resulting in deformation and movement. Some first, out-dated theories explained these internal tensions by folding or coiling of long protein filaments [298, 299], e.g. the lactid acid theory. Experimental evidence for a different mechanism achieved by different microscopic techniques lead to the theories of sliding filaments, which were proposed in the year 1953 by A. F. Huxley and N. Niedergerke as well as H. E. Huxley and J. Janson. The sliding filament theory was subsequently confirmed by a multitude of experiments. E.g. it was found by microscopy that whilst sarcomere contraction, i.e. the distance between the Z disks is decreased, the length of thick and thin filaments is kept constant. Enhancements of the theory are resulting from improvements of measurement techniques. Despite many parts of the tension development are clarified as far as to the molecular level, some details are still under exploration.

Responsible structures for the sliding of myofilaments are different proteins arranged in the sarcomeres of myocytes (Sect. 6.2.1). The interplay of these proteins is enabled by different reversible chemical reactions primarily controlled by electrophysiological processes.

Motor Proteins. So-called motor proteins, e.g. myosin, transform chemically bound energy to mechanical energy. Energy source is adenosine triphosphate (ATP) produced in the mitochondria by oxygenation of nutrients and transferring its energy by hydrolysis. Already the binding of ATP to myosin results in a change of its configuration.

The hydrolysis consists of splitting the ATP into adenosine diphosphate (ADP), phosphate P_i, and the hydrogen ion H^+, whereby water H_2O is incorporated into the ATP:

$$ATP + H_2O \longrightarrow ADP + P_i + H^+$$

The chemical reaction is conjuncted with a release of energy $\Delta G = -7.3 \frac{kcal}{mol}$, which is used to modify chemical bindings of myosin.

Members of the myosin family drive not only muscle contraction, but also intracellular transport process, cytokinesis and cell locomotion [76]. In muscle contraction the myosin II is involved. However, the mechanisms of energy transfer and mechanical behavior are similar in other types of myosin.

Myofilaments in Sarcomeres. The sarcomeres include an arrangement of thick and thin myofilaments (Fig. 6.8). Ordered myosin forms the thick filaments, which are surrounded by the thin filaments. The thin filaments, formed by the proteins tropomyosin, troponin and actin, act as passive mechanical counterpart of myosin. The spatial arrangement of thick and thin filaments is maintained by the proteins titin and nebulin.

Excitation-Contraction Coupling and Intracellular Calcium Handling. The development of tension in the sarcomeres is provoked by an increase of the concentration of cytoplasmic calcium. Commonly, the increase of the concentration is result of electrical excitation. The concentration is affected primarily by sarcolemmal and sarcoplasmic proteins, which control the flow of calcium from and to spatial microdomains within the cell [300]. The sarcolemmal Na-Ca exchangers and calcium pumps can remove calcium ions from the cytoplasm into the extracellular space. Voltage gated calcium ion channels allow the controlled influx of calcium. In mammalian myocytes a high density of Na-Ca exchangers and of L-type calcium ion channels is reported at the end of transversal tubuli, which intrude into the myocyte as a specialization of the sarcolemma and end at adjacencies of Z disks.

The intracellular calcium handling is carried out in large parts by the sarcoplasmic reticulum, which is decomposed in the terminal cisternae and longitudinal tubuli (Sect. 6.2.1). The longitudinal tubuli surround mesh-like the sarcomeres. The terminal cisternae located at the Z disks act primarily as buffer for calcium resulting from a high density of the protein calsequestrin. The sarcoplasmic reticulum includes different proteins controlling the calcium flux through the membrane (Sect. 7.2.1). Sarcoplasmic calcium pumps remove calcium ions from the cytoplasm into the sarcoplasmic reticulum consuming ATP. Sarcoplasmic calcium release channels are gated by cytoplasmic calcium concentration and allow the efflux of calcium from the junctional sarcoplasmic reticulum into the cytoplasm.

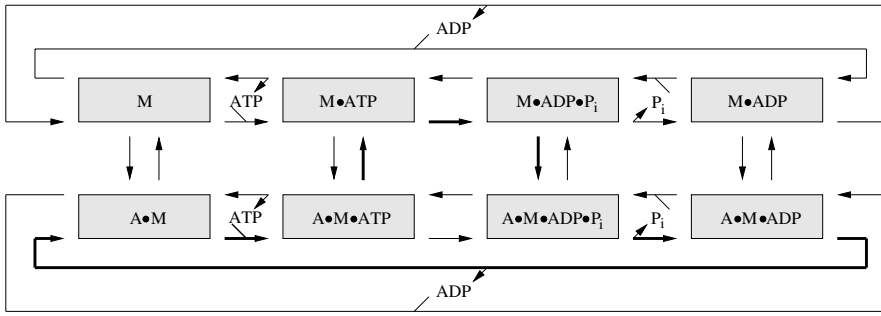

Fig. 8.8. States and transitions of actin-activated myosin II ATPase cycle (adapted from [68, 301]). M and A symbolize Myosin and actin, respectively. ATP, ADP and P_i represent adenosine triphosphate, adenosine diphosphate and phosphate, respectively. Arrows indicate possible transitions. The bold arrows signify the normal transitions.

Physiological Operating Sequence. The physiological initiation of tension development is performed by electrical excitation of the myocyte. The excitation propagates over the sarcolemma, particularly the transversal tubuli, where in consequence the sarcolemmal voltage-gated L-type calcium ion channels open initiating a positive feed back mechanism. The influx of calcium ions through the L-type calcium ion channels and to a smaller amount through Na-Ca exchangers triggers the opening of sarcoplasmic calcium release channels leading to calcium sparks. Numerous calcium sparks sum up to a significant increase of the concentration of cytoplasmic calcium. The release channels show a refractory period, which stops the positive feed back mechanism. The calcium is reuptaken by calcium specific pumps into the sarcoplasmic reticulum. Smaller amounts are transported extracellularly via the sarcolemmal Na-Ca exchangers and calcium pumps.

The calcium binds to troponin C resulting in shifting of the troponin-tropomyosin complex followed by structural changes of the tropomyosin-actin configuration [68]. The changes allow the binding of a myosin head to actin, the so-called cycling of cross bridges or actin-activated myosin II ATPase cycle (Fig. 8.8).

In absence of ATP the actin-myosin binding is arrested. By binding and hydrolysis of ATP the motor protein performs four steps (Fig. 8.9):

- Binding of ATP to myosin head resulting in its unbinding from actin
- Rebinding of myosin head at adjacent actin while ATP hydrolysis
- Changing of the angle of myosin heads to neck and tails (Fig. 8.10), whereby phosphate P_i is released into the cytoplasm
- Unbinding of ADP from myosin and its release into the cytoplasm

If ATP is available, a binding to the myosin is occurring. If the calcium concentration is sufficiently large, the procedure can be repeated.

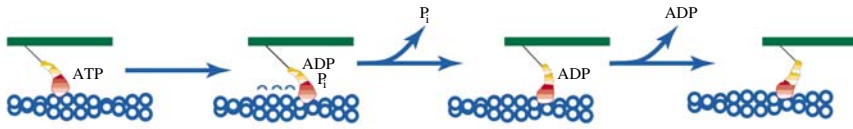

Fig. 8.9. Sliding of myosin and actin filament (adapted from [302]). The sliding starts with the binding of ATP to the myosin head, followed by its unbinding and rebinding to actin. The distance between the binding positions is a multiple of a minimal length. The ATP is hydrolyzed and the metabolites, P_i and ADP, are released sequentially into the cytoplasm. Between the second and third step a so-called power stroke is performed, developing tension and/or changing the relative position of the myofilaments. The illustrated processing presumes, that a formation of cross bridges is possible. Commonly, structural changes of the tropomyosin-actin configuration resulting from calcium binding to troponin C are necessary to allow the formation.

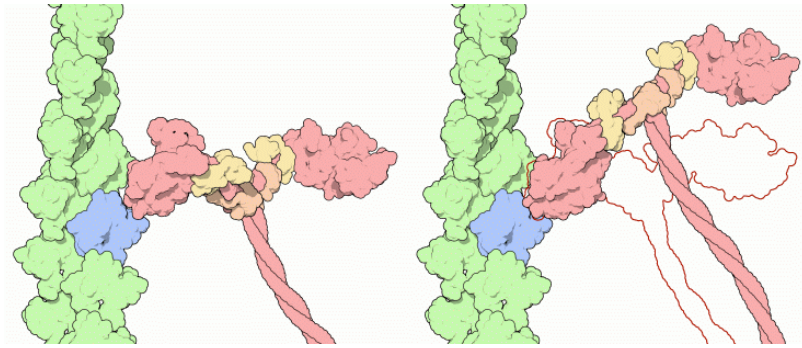

Fig. 8.10. Attachment of actin to myosin and its folding (from [84]). The myosin head and tail is shown in red, its light chains in orange and yellow. The actin filament is visualized in green and blue. The left hand illustration shows a myosin head attached to actin, the right hand the folding of the myosin head.

Different step lengths and tensions are reported for the variant types of myosin and myocytes. Step lengths, which are multiple of a minimal length, and back steps are reported in recent experimental works. These works change the deterministic view point to a stochastical.

For myosin II several sub-steps per hydrolyzed ATP are performed by folding of the head-neck junction [302]. Each folding leads to sub-steps with a length of circa n x 2.7 nm in direction of the actin filament with n as positive or negative integer [303]. Commonly, n is reported to be in the range -5 to +5. Frequently, a sub-step length of 5.4 nm is measured, which is equal to the monomer repeat along an actin filament [304]. Each folding of myosin II leads to a summary force of $1 - 5$ pN [76].

8.3.2 Experimental Studies

A large number of experiments of active muscular behavior was performed starting with experiments of A. V. Hill in 1938 [305], who measured, analyzed and described in a mathematical manner the interdependencies between speed of shortening, tension and heat production in skeletal muscles of frog. In these experiments the muscle load was varied. The muscle was clamped at both ends, its length was fixed and noted. The muscle was tetanized isometrically by electrical stimulation. After quick release of the fixation the muscle shortened and the shorting velocity was measured. The measurement data was used to parameterize an equation, which is now known as Hill's equation.

As for acquisition of passive mechanical properties the specimens for the measurement of active muscular behavior are primarily from the species rat, rabbit and cat (tables 8.4 and 8.5). The specimens size varies between large papillary muscles, differently shaped blocks of myocardial tissue, small cellular clusters of myocytes to single myocytes [275].

The development of force in myocardial tissue and myocytes is measured with devices similar to those for acquisition of passive mechanical properties. In contrast thereto specific extensions are included in the devices to activate a force development, either indirectly by electrical stimuli or directly by an increase of the concentration of intracellular calcium $[Ca^{2+}]_i$. Miscellaneous macroscopic and microscopic measurement devices were applied to record the active mechanics. Commonly, the devices were specifically developed dependent on the specimens size and geometrical properties. A system for measurement of force in single myocytes is shown in Fig. 8.11 and 8.12.

The early works involved in measurement of active mechanics of cardiac muscle followed the experimental and conceptual approaches of Hill. The relationships between force, stretch and stimulus frequency as well as the underlying mechanisms, e.g. electro-mechanic coupling, were focus of interest. The primary specimens used in the early works were ventricular trabeculae obtained after rapid removal of the heart. The specimens were suspended in an appropriate fluid. Electrical stimulation of the muscles was performed by applying current via electrodes.

Already in these early works, e.g. of Sonnenblick [257] and Parmley et al. [306], and similar to measurements of skeletal muscle a stretch dependence of the tensions developed in myocardium was reported. This phenomenon can be regarded as the underlying principle of the Frank-Starling mechanism, which leads to an increase of contractile force and ejection of blood by increase of the end-diastolic volume of the ventricular cavity. The phenomenon provides evidence for the sliding filament theory, whereby the overlapping of the myofilaments determines the recruitment and formation of cross bridges. The early works were validated by various subsequent experiments. E.g. it was found in experiments with constant or sinusoidally pertubated [307] sarcomere length, that the overlap of the thick and thin filaments is a significant determinant of the force amplitude.

Table 8.4. Force measurements of cardiac muscle.

Date	Publisher	Tissue/Cell type	Species	Reference
1964	Sonnenblick	papillary muscle	cat	[257]
1973	Parmley, Chuck	papillary muscle	cat	[306]
1976	Ingebretsen, Becker, Friedman, Mayer	papillary muscle	cat rat	[308]
1980	ter Keurs, Rijnsburger, Heuningen, Nagelsmit	trabeculae	rat	[309]
1984	Eisner, Lederer, Vaughan-Jones	Purkinje fibers	sheep	[310]
1986	Wier, Yue	papillary muscle	ferret	[311]
1986	Kentish, ter Keurs, Ricciardi, Bucx, Noble	intact and skinned trabeculae	rat	[312]
1987	Hofmann, Fuchs	skinned ventricular muscle bundles	cow	[313]
1991	Peterson, Hunter, Berman	papillary muscle	New Zealand White rabbit	[314]
1991	Nassar, Malouf, Kelly, Oakely, Anderson	ventricular myocardium	New Zealand White rabbit	[315]
1994	Gao, Backx, Azan-Backx, Marban	ventricular myocardium	rat	[316]
1995	Bluhm, Lew	right ventricular papillary muscle	rabbit	[317]
1995	Wang, Fuchs	divers	divers	[318]
1995	Janssen, Hunter	trabeculae	rat	[319]
1997	Janssen, de Tombe	trabeculae	rat	[320]
1998	Baker, Figueredo, Keung, Camacho	ventricular muscle	rat	[321]
1998	Maier, Brandes, Pieske, Bers	ventricular muscle	rat	[322]
1998	Saeki, Kurihara, Komukai, Ishikawa, Takigiku	papillary muscle	ferret	[323]
1999	Layland, Kentish	ventricular trabeculae	rat	[324]
2000	Allan, Xu, Kerrick	skinned ventricular fiber strips	rat	[325]
2000	Bluhm, Kranias, Dillmann, Meyer	left ventricular papillary muscle	wild-type and phospholamban knockout mice	[169]
2000	Maier, Barckhausen, Weisser, Aleksic, Baryalei, Pieske	right atrial trabeculae fiber strips	human	[326]
2000	ter Keurs, Hollander, ter Keurs	right ventricular trabeculae	rat	[327]
2000	Wannenburg, Heijne, Geerdink, van den Dool, Janssen, de Tombe	right ventricular trabeculae	rat	[307]
2002	Konhilas, Irving te Tombe	right ventricular skinned trabeculae	rat	[328]

Table 8.5. Force measurements of cardiac myocytes.

Date	Publisher	Tissue/Cell type	Species	Reference
1975	Fabiato, Fabiato	ventricular myocytes skinned	rat	[167]
1977	De Clerck, Claes, Brutsaert	myocytes	rat	[329]
1989/90	Harrison, Bers	ventricular myocytes skinned	rabbit, frog, guinea pig, rat	[68]
1993	White, Guennec, Nigretto, Gannier, Argibay, Garnier	ventricular myocytes	guinea-pig	[155]
1993	Gannier, Bernengo, Jacquemond, Garnier	ventricular myocytes	guinea-pig	[330]
1995	White, Boyett, Orchard	ventricular myocytes	guinea-pig	[331]
1995	Bluhm, McCulloch, Lew	left ventricular myocytes	rabbit	[332]
1998	Brandt, Colomo, Piroddi, Poggesi, Tesi	skinned atrial and ventricular	frog	[333]
1999	O'Rourke, Kass, Tomaselli, Kaab, Tunin, Marbán	left ventricular myocytes	canine	[193]
2001	Yasuda, Sugiura, Kobayakawa, Fjita, Yamashita, et al.	ventricular myocytes	rat	[334]

Careful observation revealed that the performing of length switches leads to transitions of tensions, which were time dependent [306]. E.g. a quick shortening to 90 % of the resting length leads an immediate decrease of force to circa 50 %. The subsequent transient rise of force by 10 % was followed by a slow asymptotic fall. The asymptotic force was 55 % of the force at resting length.

In further studies it was reported that the progression of tension is modulated by the progression of intracellular calcium concentration $[Ca^{2+}]_i$. E.g. a graded effect of the intracellular calcium concentration $[Ca^{2+}]_i$ on the cross bridge kinetics was found in studies of chemically permeabilized ventricular trabeculae, whereby the calcium concentration was varied as well as the muscle length was sinusoidal pertubated [307]. The regulation of the tension development kinetics by the extracellular calcium concentration $[Ca^{2+}]_i$ was reported in tetanized ventricular trabeculae [321]. Therefore, it can be concluded that also the progression of an electrical excitation influences the progression of the force development.

Table 8.6. Mathematical models of force development in muscle and myocytes. The focus is on cardiac models, but early skeletal muscle models are also included.

Date	Publisher	Tissue/Cell type	Species	Reference
1938	Hill	skeletal muscle	frog	[305]
1957	Huxley	skeletal muscle	-	[298]
1971	Huxley, Simmons	striated muscle	-	[338]
1971/72	Wong	cardiac muscle	-	[339, 340]
1980	Panerai	papillary muscle	mammalian	[341]
1991	Peterson, Hunter, Berman	papillary muscle	New Zealand White rabbit	[314]
1994	Landesberg, Sideman	skinned cardiac myocytes	-	[342]
1994	Landesberg, Sideman	cardiac muscle	-	[343, 344]
1997	Hunter, Nash, Sands	cardiac muscle	mammalian	[253]
1998	Noble, Varghese, Kohl, Noble	ventricular myocardium	guinea pig	[189]
1998	Guccione, Motabar-Zadeh, Zahalak	cardiac myocytes	-	[345]
1998	Hunter, McCulloch, ter Keurs	cardiac myocytes	-	[296]
1998	Winslow, Rice, Jafri	ventricular myocytes	guinea pig	[346]
1999	Rice, Winslow, Hunter	papillary muscle	New Zealand White rabbit	[347]
2000	Rice, Jafri, Winslow	cardiac muscle	ferret	[348]
2001	Mlcek, Neumann, Kittnar, Novak	cardiac myocytes	-	[349]
2001	Nickerson, Smith, Hunter	cardiac myocytes	-	[350]
2002	Glänzel, Sachse, Seemann	cardiac myocytes	-	[351, 352]

The relationship between force and intracellular calcium is frequency dependent. Most studies with isolated myocardial preparations under physiologic conditions report a positive relationship, i.e. increasing the calcium frequency leads to higher force [324]. The positive relationship is attributed to a higher uptake of extracellular calcium into the myocyte by increasing stimulus frequency leading to a higher uptake and release of calcium in the sarcoplasmic reticulum. Under non-physiologic conditions the relationship can have a negative slope or show an U-shape as well as species and specimens dependent variations of the relationship were found [323, 169].

Variant measurements were performed with skinned myocytes, which permit directly the control of the environment inside of the cells. E.g. calcium can be applied into the intracellular space and to the contractile elements. A removal of sarcolemma can be achieved chemically as well as by mechanical homogenization and manual micro-dissection. A disadvantage of this kind of

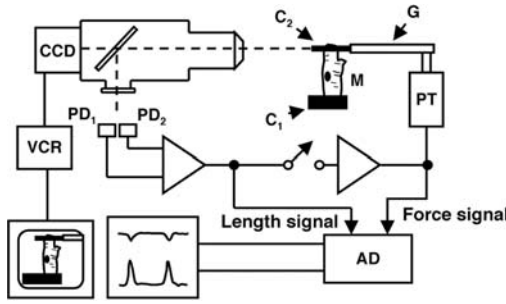

Fig. 8.11. System for measurement of force in single myocytes (from [334]). The myocyte (M) is clamped between two carbon graphite fibers. The first fiber (C1) is fixed, the second (C2) connected via a glass rode (G) to a piezoelectric transducer (PT). The image of myocyte and the second fiber is projected through a half mirror onto a CCD camera and a pair of photo-diodes (PD_1 and PD_2). The photo-diode arrangement allows in conjunction with a feedback system the correction of the second fiber's compliance. The force and length signals are fed into the data acquisition system (AD). The camera is connected with a video recorder (VCR) and a display.

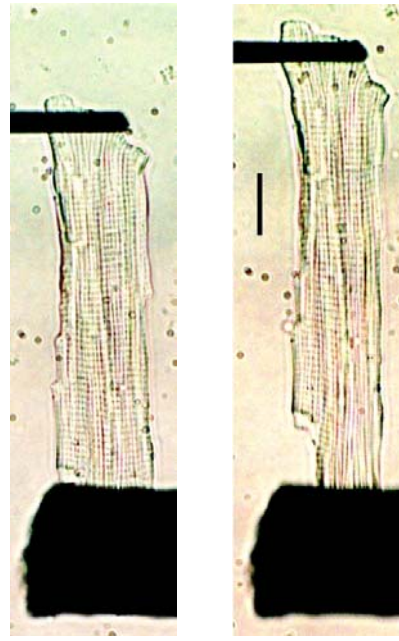

(a) (b)

Fig. 8.12. Myocyte held clamped between two carbon graphite fibers (from [334]). The lower, thicker fiber is fixed. The second fiber connected to a piezoelectric transducer. Forces are measured by variation of the myocyte stretch leading to different lengths of the sarcomere, e.g. (a) 1.9 μm and (b) 2.1 μm. The bar indicates a length of 20 μm.

preparation is that cellular constituents may be lost which affect the calcium sensitivity of myofilaments [68].

A classical work was carried out by Fabiato and Fabiato [167], who measured the tension of skinned myocytes and its interdependencies with calcium release and re-sequestrations by the sarcoplasmic reticulum. A single skinned myocyte was located in a perfusion chamber with the two ends of the cell attached to glass micro-needles. One micro-needle was fixed, the other connected to the lever of a force transducer. Force as well as length and width of the cell were measured. Furthermore, a mean sarcomere length was determined.

Several conclusions were drawn from the measurements of Fabiato and Fabiato: Cellular tension is a direct effect of the concentration of free calcium, where the tension is developed regardless the deletion of the sarcoplasmic reticulum. A significant calcium sink exists in the cell, which was identified as the sarcoplasmic reticulum. Physiologically, calcium is re-sequestrated after contraction. The release of calcium from the sarcoplasmic reticulum is triggered by concentration of free calcium. The amplitude of contraction is increased when the triggering concentration of free calcium is increased.

Further studies were performed to elucidate cooperativity mechanisms for force development. Three different cooperativity mechanisms were demonstrated:

- cross-bridges increase affinity for binding of calcium to troponin C (XB-TN) [335]
- cross-bridges support the building of cross-bridges in the neighborhood (XB-XB) [336]
- shifting of tropomyosin leads to shifting of attached tropomyosins (TM-TM) [337]

Topics of recent studies are the effects of specific proteins and pathologies onto force and calcium handling. The role of the protein phospholamban, a inhibiting regulator of the sarcoplasmic calcium pump (SERCA), was studied with wild-type and phospholamban knockout mice [169]. The effects of hypertrophy and tachycardia were acquired in single myocytes as well as in myocardium [322, 193].

8.3.3 Mathematical Modeling Approaches

Overview. A first attempt to describe mathematically active tensions developed in muscle was published 1938 by A. V. Hill [305]. He developed the model on base of his work concerning heat production in striated muscle, wherefore he received a Nobel prize in 1922. The description refers to the force-velocity relationship of tetanized skeletal muscle of frog upon quick release from isometric condition. In the context of a mathematical modeling of the heart Hill's equation is primarily of pedagogical value, because the general framework is differing between the two muscle types. A tetanized contraction is physiologically not common for cardiac muscle. The coupling to electrophysiological

quantities is not included in Hill's equation but is of fundamental importance for cardiac force development. Hill's equation can be regarded as an empirical equation [30], which gives macroscopic information and neglects biophysical phenomena on microscopic and molecular level.

A biophysically, microscopic anatomically based mathematical description, i.e. the theory of sliding filaments, was proposed in 1953 by A. F. Huxley and N. Niedergerke as well as H. E. Huxley and J. Janson. This description of force development in striated muscle and derived models are introduced in the following sections.

Of special interest for biophysically motivated modeling are descriptions of cellular force development, which base on electrophysiological quantities delivered e.g. by electrophysiological cell models (Sect. 7.2.3). The concentration of intracellular calcium $[Ca^{2+}]_i$ is used to define rate coefficients, which depict the interaction between states of actin and myosin. The states describe e.g. the binding of intracellular Ca^{2+} to the troponin complex and the cross bridge cycling. Further parameters influencing the rate coefficients are the sarcomere length and the state variables.

Hill. Hill's equation describes the shortening velocity of frog skeletal muscle in dependence on load [305]. The muscle is initially fixed by clamping of its ends and tetanized by electrical stimulation. Velocity of contraction is measured after quick release. The interdependencies are described by:

$$(v + b)(P + a) = b(P_0 + a)$$

with the velocity of contraction v, the tension P, and the constants a, b and P_0.

Sliding Filament Theory. During contraction the length of the thick and thin filaments is kept constant while the distance between the Z disks is decreased. This observation forms the motivation for the so-called sliding filament theory, which was proposed independently by two groups in the year 1953, i.e. A. F. Huxley and N. Niedergerke as well as H. E. Huxley and J. Janson.

The sliding filament theory assumes that the forming of cross bridges by actin A and myosin M can be described by:

$$A + M \underset{g}{\overset{f}{\rightleftharpoons}} A - M \tag{8.3}$$

with the attached cross bridges $A-M$, the binding rate f and the dissociation rate g. The binding rate f quantifies the probability, that a myosin side-piece binds to an actin monomer. The dissociation rate g specifies the probability, that an attached cross bridge breaks down.

Applying the sliding filament theory the tension developed in muscle can be derived starting with the definition of a function $n(x, t)$ [298], which describes the proportion of bound actin to summary actin sites with displacement x at time t. Therewith, the proportion of bound actin sites at time t

with displacements in the range $[x_0, x_0 + \Delta x]$ is given by:

$$\int_{x_0}^{x_0+\Delta x} n(x,t)\ dx$$

The material derivative of the function n is decomposed into a local rate of change and a convective rate of change:

$$\frac{Dn}{Dt} = \frac{\partial n}{\partial t} - v(t)\frac{\partial n}{\partial x}$$

with the shortening velocity v [30]. The convective rate of change is resulting from the sliding of filaments. Actin sites are presented to a myosin site with frequency v/l, whereby l refers to the distance between successive actin binding sites.

The upper rates (equation 8.3), the binding rate f and the dissociation rate g, must be redefined as functions of displacement, $f(x)$ and $g(x)$, respectively. Using these definitions the material derivative is described by:

$$\frac{Dn}{Dt} = (1-n)f - ng$$

Assuming that Hooke's law can be applied for description of the mechanical properties of myofilaments, the average work done W at one myosin site by filament sliding is calculated by:

$$W = \int_{-\infty}^{\infty} nkx\ dx$$

with the stiffness k.

The total tension S results from summing up all single tensions generated by contraction sites within one half-sarcomere:

$$S = \frac{ms}{2l}\int_{-\infty}^{\infty} nkx\ dx$$

with the sarcomere length s and the density of myosin sites m.

Landesberg-Sideman Model. The force model of Landesberg and Sideman is based on a description of binding of Ca^{2+} to troponin C and configuration of cross bridges [342, 343, 344, 353]. Different physiologically motivated assumptions are made for the modeling, e.g. cross bridges can cycle between weak, non-force generating to strong, force-generating conformations, calcium binding to troponin leads to actin-myosin ATPase, and calcium can dissociate from troponin before cross bridges return to their weak conformation.

The mathematical specification of force generation is made by time, calcium and length dependent transitions of states. Four different state variables, describing the amount of troponin in different configurations, are distinguished

Table 8.7. State variables of Landesberg-Sideman force model. The state variables represent the amount of troponin in different configurations. The state variable R describes the amount of troponin in resting state with weak cross bridges, i.e. calcium is not bound to troponin C. The variable A represents the amount of troponin with weak cross bridges available for turning to strong conformation because calcium was bound to troponin C. The state variable T describes the amount of troponin with strong cross bridges while calcium is bound to troponin C. The variable U represents the amount of troponin with strong cross bridges after calcium is released from troponin C.

State variable	Ca^{2+} bound to troponin C	Cross bridge conformation
R	released	weak
A	bound	weak
T	bound	strong
U	released	strong

(table 8.7). The change of the amount of differently configured troponin is specified by a set of first order ordinary differential equations [353]:

$$\frac{\partial}{\partial t}\begin{pmatrix}\bar{R}\\ \bar{A}\\ \bar{T}\\ \bar{U}\end{pmatrix} = \boldsymbol{M}\begin{pmatrix}\bar{R}\\ \bar{A}\\ \bar{T}\\ \bar{U}\end{pmatrix}$$

with the 4 x 4 matrix $\boldsymbol{M}$ consisting of rate coefficients. The variables $\bar{R}$, $\bar{A}$, $\bar{T}$, and $\bar{U}$ correspond to the spatial density of the amount of troponin in different configurations.

The matrix $\boldsymbol{M}$ is a function of myofilament overlap:

$$\boldsymbol{M} = \begin{pmatrix} -k_l[Ca^{2+}]_i & k_{-l} & 0 & g_0 + g_1 V \\ k_l[Ca^{2+}]_i & -f - k_{-l} & g_0 + g_1 V & 0 \\ 0 & f & -g_0 - g_1 V - k_{-l} & k_l[Ca^{2+}]_i \\ 0 & 0 & k_{-l} & -k_l[Ca^{2+}]_i - g_0 - g_1 V \end{pmatrix}$$

with the calcium to troponin binding rate k_l, the calcium to troponin dissociation rate k_{-l}, and the cross bridge kinetics parameters f, g_0 and g_1. The parameter V quantifies the ratio of change of myofilament overlap to thick filament length:

$$V = \frac{1}{L_m}\frac{\partial L_s}{\partial t}$$

with the overlap length L_s and the thick filament length L_m.

The force of a contractile element is generated by cross bridges in strong conformation and therefore proportional to the state variables T and U. The force per unit filament cross section F_{CE} is given by:

$$F_{CE} = (\bar{F} - \eta V)(T + U)$$

with the force of a single cross bridge $\bar{F}$ and the viscous element property η.

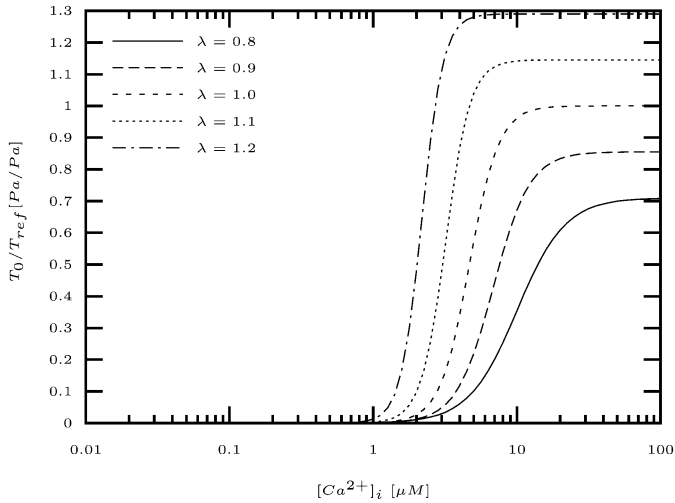

Fig. 8.13. Steady state simulations with Hunter-McCulloch-ter Keurs model by variation of stretch ratio and calcium concentration. The steady state tension T_0 is dependent on the stretch ratio λ ranging from 0.8 to 1.2 and the intracellular calcium concentration $[Ca^{2+}]_i$. The tension T_0 is normalized with the maximal tension $T_{ref} = 100\ kPa$ developed at stretch ration $\lambda = 1$.

Hunter-McCulloch-ter Keurs Model. The Hunter-McCulloch-ter Keurs model describes the kinetics of calcium binding to troponin C, of the tropomyosin and of the cross bridges binding [296]. The model was in parts parameterized using measurement data from skinned rat right ventricular muscle [312]. The model is capable of reproducing phenomena observed in length step, constant velocity and frequency response experiments.

The concentration of calcium bound to the calcium specific site of troponin C $[Ca^{2+}]_b$ is reconstructed by:

$$\frac{d[Ca^{2+}]_b}{dt} = \rho_0 [Ca^{2+}]_i \left([Ca^{2+}]_{b,max} - [Ca^{2+}]_b\right) - \rho_1 \left(1 - \frac{T}{\gamma T_0}\right) [Ca^{2+}]_b$$

with the rate constants for binding ρ_0 and for unbinding ρ_1, the intracellular calcium concentration $[Ca^{2+}]_i$, the tension T, the maximal tension value γT_0, and the maximal calcium concentration $[Ca^{2+}]_{b,max}$ at maximal tension.

The calcium concentration $[Ca^{2+}]_b$ determines the portion of actin sites z available for cross bridge binding:

$$\frac{dz}{dt} = \alpha_0 \left(\left(\frac{[Ca^{2+}]_b}{C_{50}} \right)^n (1 - z) - z \right)$$

with the rate constant of tropomyosin movement α_0, the Hill parameters C_{50} and n. The parameter C_{50} defines the intracellular calcium concentration nec-

essary for half maximal availability of actin sites portion in steady state. The Hill parameters are found to be stretch dependent:

$$n = n_{ref}(1 + \beta_1(\lambda - 1))$$
$$C_{50} = 10^{6 - pC_{50ref}(1+\beta_2(\lambda-1))}$$

with the stretch ratio λ, the parameters β_1, β_2, n_{ref}, and pC_{50ref}.

In steady state, i.e. $dz/dt = 0$ and $[Ca^{2+}]_b = const$, the portion of actin sites z_{ss} available for cross bridge binding is calculated by

$$z_{ss} = \frac{[Ca^{2+}]_b^n}{[Ca^{2+}]_b^n + C_{50}^n}$$

Under the assumption that all available actin sites are used for cross bridge binding the steady state tension T_0 is defined by

$$T_0 = T_{ref}(1 + \beta_0(\lambda - 1))z$$

with reference tension $T_{ref} = 125\ kPa$ as the reference tension at stretch ratio $\lambda = 1$. The portion of actin sites z available for cross bridge binding is determined by either equation 8.4 or - for steady state - equation 8.4. The constant $\beta_0 = 1/T_{ref}\ d\ T_0/d\ \lambda = 1.45$ describes the slope of the steady state tension T_0 as function of stretch ration λ. The reference tension T_{ref} and constant β_0 are determined from experiments with skinned rat right ventricular muscle [312].

The description of steady state tension is extended by a so-called fading memory model to take changes of stretch into account. The steady state tension T_0 is modulated by a nonlinear function Q to determine the developed tension T:

$$T = T_0 \frac{1 + aQ}{1 - Q}$$

with the curvature parameter a. The function Q is given by:

$$Q\left(\frac{T}{T_0}\right) = \sum_{i=1}^{3} A_i \int_{-\infty}^{t} e^{-\alpha_i(t-\tau)} \lambda'(\tau) d\tau$$

with $\lambda = \lambda(t)$, $\lambda' = d\lambda/dt$, and the parameters A_i and α_i. These parameters are determined by length step and constant velocity experiments.

Rice-Winslow-Hunter Model. The Rice-Winslow-Hunter models consist of 5 models reproducing the force development in cardiac muscle [347]. The models differ in the number of state variables and the definition of rates. Simulations allow the evaluation of reproducibility of length dependencies and dynamic behavior by the different models. As examples of the modeling a description of the 1st and 3rd model is given.

Table 8.8. Tropomyosin and cross bridge state variables of Rice-Winslow-Hunter model of cardiac cells. The variable $N0$ indicates the resting state with no strongly bound cross bridges and non permissive tropomyosin. The variable $P0$ is associated with no strongly bound cross bridges and permissive tropomyosin. The variable $P1$ and $N1$ describes the force generating states, i.e. the cross bridges are strongly bound.

State variable	Tropomyosin	Number of cross bridges
$N0$	non permissive	0
$N1$	non permissive	1
$P0$	permissive	0
$P1$	permissive	1

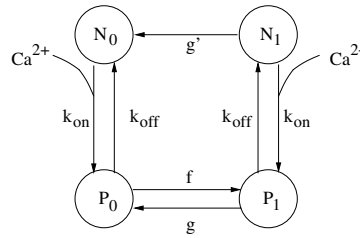

Fig. 8.14. State diagram of 1st Rice-Winslow-Hunter model. The states are described in table 8.8.

Model 1. The model is similar to the Landesberg-Sideman model and applies 4 state variables, i.e. $N0$, $N1$, $P0$, and $P1$ with $N0 + N1 + P0 + P1 = 1$ to characterize the configuration of tropomyosin and cross bridges (table 8.8, Fig. 8.14). The interaction between the state variables of the model is described by a system of first order differential equations:

$$\frac{\partial}{\partial t}\begin{pmatrix} N0 \\ P0 \\ P1 \\ N0 \end{pmatrix} = \boldsymbol{M}\begin{pmatrix} N0 \\ P0 \\ P1 \\ N0 \end{pmatrix}$$

with the 4 x 4 matrix $\boldsymbol{M}$ consisting of rate coefficients. The matrix $\boldsymbol{M}$ is a function of the cytosolic calcium concentration $[Ca^{2+}]_i$:

$$\boldsymbol{M} = \begin{pmatrix} -k_{on}[Ca^{2+}]_i & k_{off} & 0 & g' \\ k_{on}[Ca^{2+}]_i & -k_{off} - f & g & 0 \\ 0 & f & -g - k'_{off} & k'_{on}[Ca^{2+}]_i \\ 0 & 0 & k'_{off} & -k'_{on}[Ca^{2+}]_i - g' \end{pmatrix}$$

with the constants k_{on}, k_{off}, f, g, k'_{on}, k'_{off}, and g'.

The normalized force F is determined by the force generating state variables $N1$ and $P1$:

$$F = \frac{\alpha(P1 + N1)}{F_{max}}$$

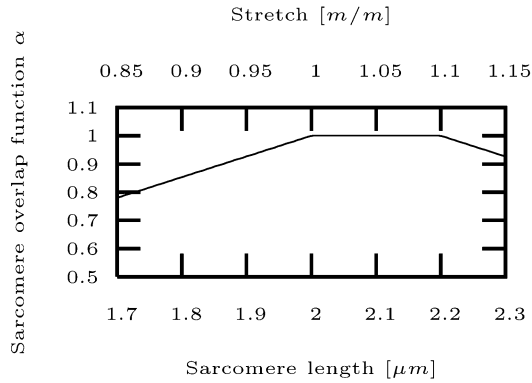

Fig. 8.15. Sarcomere overlap function. The function quantifies the fraction of myosin heads that are capable to interact with actin in such a way that force is produced. The overlap function is dependent on stretch. The scaling of the lower axis assumes a default sarcomere length of 2 μm.

Table 8.9. State variables of Rice-Winslow-Hunter model of cardiac cells describing the Ca^{2+} binding to troponin C.

State variable	Ca^{2+} binding to troponin C
T	no
TCa	yes

with the sarcomere overlap function $\alpha = \alpha(SL)$ and the maximal force F_{max}. The force F is in the range $[0, 1]$ representing no force and maximal possible force, respectively. The sarcomere overlap function α describes the fraction of myosin heads capable to interact with actin in such a way that force is produced (Fig. 8.15).

The static behavior of the model in dependence of the calcium concentration is depicted in Fig. 8.16. The dynamic behavior resulting from a given course of the intracellular calcium concentration is shown in Fig. 8.17.

Model 3. The model consists of 6 state variables, $N0$, $N1$, $P0$, $P1$, T, and TCa with $N0 + N1 + P0 + P1 = 1$ and $T + TCa = 1$ (tables 8.8 and 8.9, Fig. 8.18). In addition to the 1st model the configuration of tropomyosin is described. The interaction between the state variables is characterized by a system of 1st order differential equations:

$$\frac{\partial}{\partial t}\begin{pmatrix} T \\ TCa \\ N0 \\ P0 \\ P1 \\ N1 \end{pmatrix} = \boldsymbol{M}\begin{pmatrix} T \\ TCa \\ N0 \\ P0 \\ P1 \\ N1 \end{pmatrix}$$

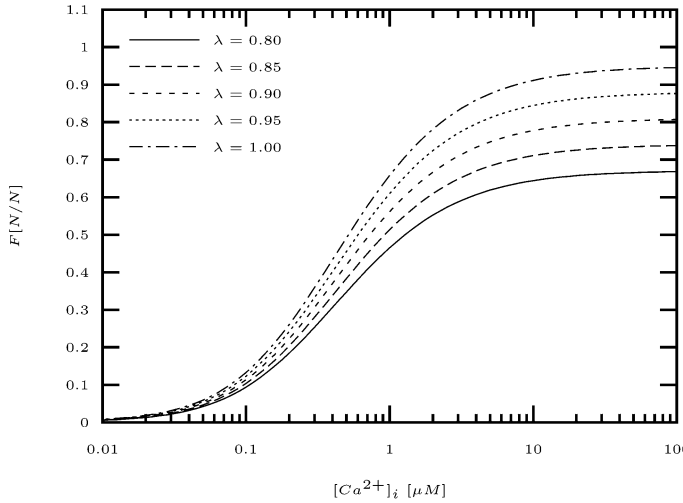

Fig. 8.16. Steady state simulations with 1st Rice-Winslow-Hunter model for different sarcomere lengths and calcium concentrations. The steady state force F is dependent on the stretch ranging from 0.8 to 1 and the intracellular calcium concentration $[Ca^{2+}]_i$. A stretch of 0.8 corresponds to a sarcomere length of 1.6 μm, a stretch of 1 to a sarcomere length of 2.0 μm. The steady state force F for larger stretches can be determined with the sarcomere overlap function. The force F is normalized with the maximal force F_{max}.

with the 6 x 6 matrix $\boldsymbol{M}$ consisting of rate coefficients. The matrix $\boldsymbol{M}$ is a function of the cytosolic calcium concentration $[Ca^{2+}]_i$ and of the sarcomere length SL:

$$\boldsymbol{M} = \begin{pmatrix} -k_{on}[Ca^{2+}]_i & k_{off} & 0 & 0 & 0 & 0 \\ k_{on}[Ca^{2+}]_i & -k_{off} & 0 & 0 & 0 & 0 \\ 0 & 0 & -k_1 & k_{-1} & 0 & g \\ 0 & 0 & k_1 & -k_{-1} - f & g & 0 \\ 0 & 0 & 0 & f & -g - k_{-1} & k_1 \\ 0 & 0 & 0 & 0 & k_{-1} & -k_1 - g \end{pmatrix}$$

with the constants k_{-1}, f, g, k_{on}. The rate coefficient k_1 describing the interaction between the troponin and tropomyosin configuration, i.e. the transfer from $N0$ to $P0$ and from $N1$ to $P1$, is a function of the variable TCa and the sarcomere length. The rate coefficient k_{off} is a function of force.

The static behavior of the model in dependence of the calcium concentration is shown in Fig. 8.19. The dynamic behavior resulting from a given course of the intracellular calcium concentration is illustrated with Fig. 8.20.

Glänzel-Sachse-Seemann Model. The so-called hybrid model combines a description of the binding of intracellular calcium $[Ca^{2+}]_i$ to troponin C, the configuration change of tropomyosin, and the interaction of actin and myosin

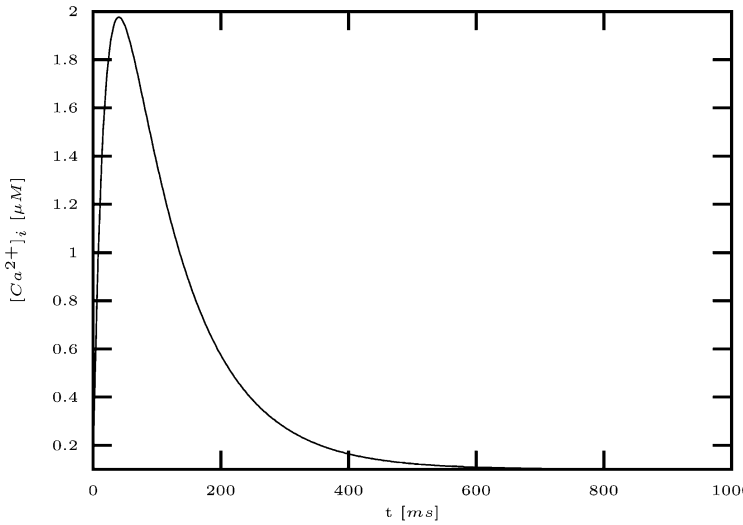

(a)

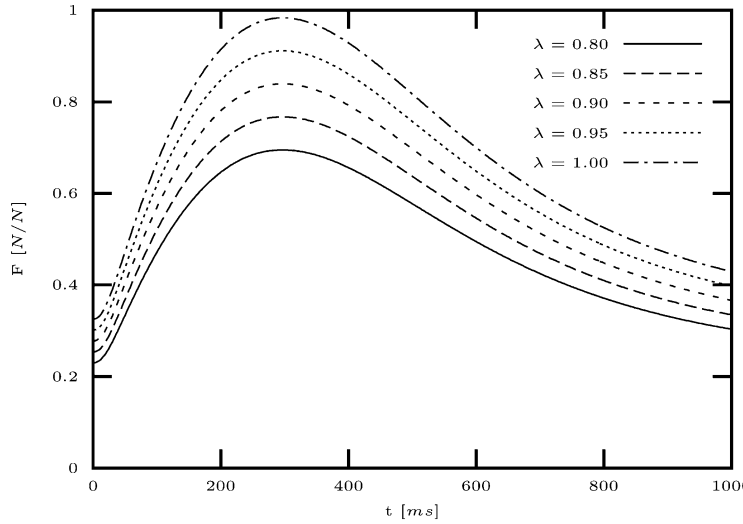

(b)

Fig. 8.17. Simulations with 1st Rice-Winslow-Hunter model by variation of the stretch ratio. (a) An exemplary course of the intracellular calcium concentration $[Ca^{2+}]_i$ is used in the simulations. (b) The development of force F is dependent on the stretch ratio λ ranging from 0.8 to 1.2. The force F is normalized with the maximal force F_{max} developable in these simulations.

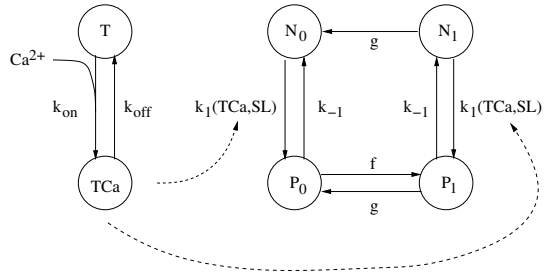

Fig. 8.18. State diagram of 3rd Rice-Winslow-Hunter model. The states are described in tables 8.8 and 8.9.

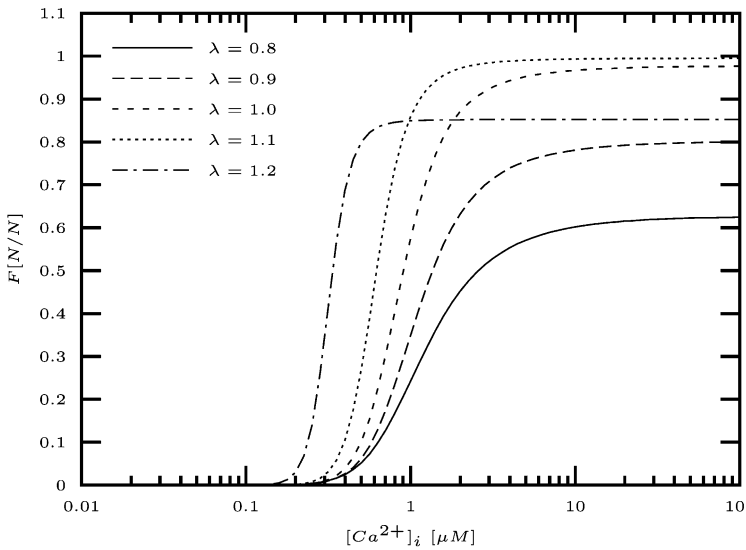

Fig. 8.19. Steady state simulations with 3rd Rice-Winslow-Hunter model for different sarcomere lengths and calcium concentrations. The steady state force F is dependent on stretch ranging from 0.8 to 1.2 and the intracellular calcium concentration $[Ca^{2+}]_i$. A stretch of 1 corresponds to a sarcomere length of 2 μm. The force F is normalized with the maximal force F_{max}.

[354]. The calcium binding to troponin C is similarly described as in the 3rd Rice-Winslow-Hunter model [347]. The interaction of actin and myosin is adopted from Gordon et al. [355], Bers et al. [68], and Spudich [301]. The cooperativity mechanisms XB-TN, XB-XB, and TM-TM are incorporated in the hybrid model. The model uses as input the concentration of intracellular calcium $[Ca^{2+}]_i$, the sarcomere stretch λ, and the sarcomere stretch velocity v. As alternative to the intracellular calcium $[Ca^{2+}]_i$ the calcium bound to troponin C can be provided as input. The model delivers as output a nor-

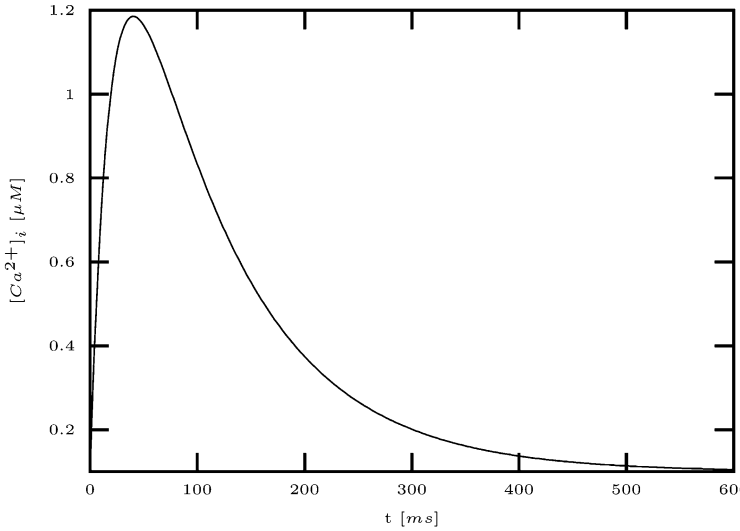

(a)

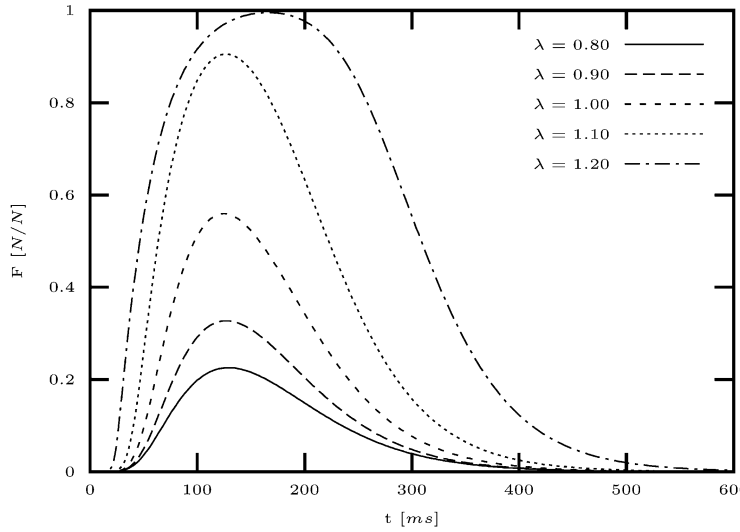

(b)

Fig. 8.20. Simulations with 3rd Rice-Winslow-Hunter model by variation of the stretch ratio. (a) An exemplary course of the intracellular calcium concentration $[Ca^{2+}]_i$ is used in the simulations. (b) The development of force F is dependent on the stretch ratio λ ranging from 0.8 to 1.2. The force F is normalized with the maximal force F_{max} developable in these simulations.

Table 8.10. Rate coefficients of Glänzel-Sachse-Seemann model (adapted from [351]). Rate coefficients, which are modulated by further parameters, are indicated with a star.

Rate coefficient	Model	Measurement	Reference
k_1^*	1000	$\approx 1\ \mu M^{-1}$[ATP] s^{-1}	[356]
		fast, nearly irreversible	[357]
k_{-1}	10		
k_2	1000	≥ 1000	[355]
k_3	150	$k_3 - k_{-3} = 125\ s^{-1}$	[358]
		$k_3 - k_{-3} = 168\ s^{-1}$	[359]
k_{-3}	15	$K_3 = \frac{k_3}{k_{-3}} \approx 10$	[355, 357]
k_4	1000	≥ 1000	[355]
k_5^*	25	$30\ s^{-1} \leq k_5 + k_{-5} \leq 50\ s^{-1}$	[355]
k_{-5}	8	$3 \leq K_5 = \frac{k_5}{k_{-5}} \leq 5$	
k_6	50	$45\ s^{-1}$	[360]
		$77\ s^{-1}$	[361]
k_{-6}	20	$20 - 30\ s^{-1}$	[355]
k_7^*	30	$3 - 10\ s^{-1}$ due to high force	[355]
		$\geq 500\ s^{-1}$ for fast contraction	
k_8	200	$\geq 100\ s^{-1}$	[355]
		$200\ s^{-1}$	[362]
		$325\ s^{-1}$	[360]
k_{-8}	5	$K_8 = \frac{k_8}{k_{-8}} \approx 100$	[355]

malized tension and optionally the intracellular calcium $[Ca^{2+}]_i$ modified by calcium bound to troponin C (Fig. 8.22).

The model uses 14 state variables, which are coupled by rate coefficients. Two state variables, T and TCa, detail the binding of intracellular calcium Ca^{2+} to troponin C (Fig. 8.21a). The state variable T describes the normalized concentration of troponin C with no bound calcium, TCa the normalized concentration of troponin C with bound calcium. The normalization leads to:

$$T + TCa = 1$$

Two further state variables, TM_{on} and TM_{off}, quantify the configuration of tropomyosin (Fig. 8.21b). The state variable TM_{on} describes the concentration of tropomyosin in permissive configuration, TM_{off} the normalized concentration in non permissive. The normalization leads to:

$$TM_{on} + TM_{off} = 1$$

Ten state variables are used to quantify the interaction between actin and myosin, particularly the cross-bridge cycling (Fig. 8.21c). The ten variables describe normalized concentrations of myosin. The condition, that the variables sum up to 1, is used as normalization:

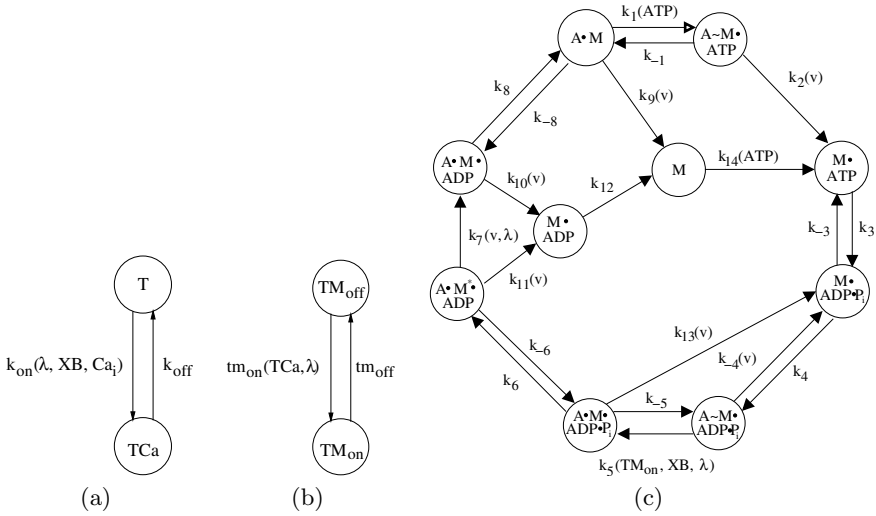

Fig. 8.21. State diagram of hybrid model of force development. (a) Two state variables, T and TCa, quantify the calcium binding to troponin C. (b) Two further state variables, TM_{on} and TM_{off}, describe the configuration of tropomyosin. (c) Ten state variables detail the interaction of actin and myosin as well as the hydrolysis of ATP. M and A symbolize myosin and actin, respectively. ATP, ADP, and P_i represent adenosine triphosphate, adenosine diphosphate, and phosphate, respectively. The transition between states is depicted by an arrow, strong binding by a closed circle, and weak binding by a tilde. The arrows are labeled with constants k_x, which are parameters of the rate coefficients functions. Further parameters, e.g. ATP, cross-bridge density XB and stretch velocity v, are in brackets.

$$\begin{aligned} M \bullet ATP + M \bullet ADP \bullet P_i + M \bullet ADP + M \\ + A \sim M \bullet ATP + A \sim M \bullet ADP \bullet P_i \\ + A \bullet M \bullet ADP \bullet P_i + A \bullet M^* \bullet ADP + A \bullet M \bullet ADP + A \bullet M = 1 \end{aligned}$$

The power stroke is performed during transition from $A \bullet M \bullet ADP \bullet P_i$ to $A \bullet M^* \bullet ADP$. The normalized concentration of myosin strongly bound to actin $S_{A \bullet M}$ is quantified by:

$$S_{A \bullet M} = A \bullet M \bullet ADP \bullet P_i + A \bullet M^* \bullet ADP + A \bullet M \bullet ADP + A \bullet M$$

The interaction between the states of the model is described by a system of first order differential equations:

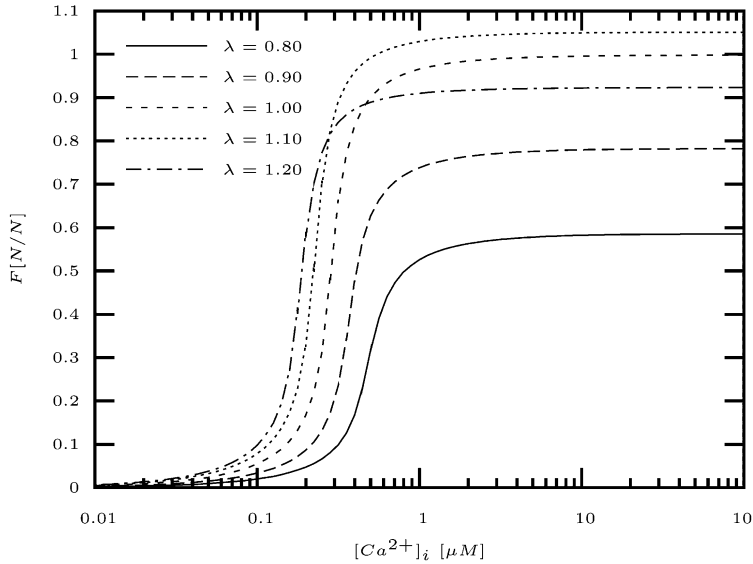

Fig. 8.22. Steady state simulations with Glänzel-Sachse-Seemann model for different sarcomere lengths and calcium concentrations. The steady state force F is dependent on stretch ranging from 0.8 to 1.2 and the intracellular calcium concentration $[Ca^{2+}]_i$. A stretch of 1 corresponds to a sarcomere length of 2 μm. The force F is normalized with the maximal force F_{max}.

$$\frac{\partial}{\partial t}\begin{pmatrix} T \\ TCa \\ TM_{off} \\ TM_{on} \\ M \bullet ATP \\ M \bullet ADP \bullet P_i \\ A \sim M \bullet ADP \bullet P_i \\ A \bullet M \bullet ADP \bullet P_i \\ A \bullet M^* \bullet ADP \\ A \bullet M \bullet ADP \\ A \bullet M \\ A \sim M \bullet ATP \\ M \\ M \bullet ADP \end{pmatrix} = \boldsymbol{R} \begin{pmatrix} T \\ TCa \\ TM_{off} \\ TM_{on} \\ M \bullet ATP \\ M \bullet ADP \bullet P_i \\ A \sim M \bullet ADP \bullet P_i \\ A \bullet M \bullet ADP \bullet P_i \\ A \bullet M^* \bullet ADP \\ A \bullet M \bullet ADP \\ A \bullet M \\ A \sim M \bullet ATP \\ M \\ M \bullet ADP \end{pmatrix}$$

with the 14 x 14 matrix $\boldsymbol{R}$ consisting of rate coefficients. Partly, the rate coefficients are dependent on the sarcomere stretch velocity v, the sarcomere stretch λ, and the concentration of intracellular calcium $[Ca^{2+}]_i$. The matrix $\boldsymbol{R}$ is sparse indicating that transitions between states are only partly possible. The initial values and coefficients are given in [352].

The sum of tension generating states T_{AM} is given by:

$$T_{AM} = A \bullet M + A \bullet M \bullet ADP + A \bullet M^* \bullet ADP$$

The normalized force F is determined by

$$F = \frac{\alpha \, T_{AM}}{F_{max}}$$

with the sarcomere overlap function $\alpha = \alpha(\lambda)$ (Fig. 8.15), which is tissue and species specific [68, 347], and maximal tension F_{max}, which is dependent on the rate coefficients. The normalized force F can be multiplied by a tissue and species specific factor f_{T0} to quantify force development of myocardium.

The hybrid model was applied e.g. to elucidate cooperativity mechanisms by simulations [363], whereby the calcium concentration was varied and a stretch of $\lambda = 1$ was applied. Results with and without incorperation of the mechanisms are shown in Fig. 8.23. The influence of the different cooperativity mechanisms is quantified by the Hill parameters Ca_{50} and N. All mechanisms lead to a left shift and steepening of the calcium-force relationship, which is indicated by a decrease of the parameter Ca_{50} and an increase of the parameter N.

8.4 Mechanics in Anatomical Models

Descriptions of mechanical properties of myocardium can be applied in conjunction with anatomical models (Sect. 6.4) and numerical methods of mechanics to simulate the mechanical behavior of the heart [264, 266, 254, 364, 365, 366]. Different modeling and simulation environments were developed allowing this kind of reconstruction of the cardiac behavior:

- **CMISS** developed at Bioengineering Institute, Auckland, NZ [367].
- **Continuity** developed of the cardiac mechanics research group, Department of Bioengineering and the Whitaker Institute for Biomedical Engineering, UCSD, USA [368].
- **MEET Man tools** developed at the Institut für Biomedizinische Technik, Universität Karlsruhe (TH) [132].

All these environments apply primarily the finite element method for continuum mechanics modeling (Sect. 4.3) .

Coupling of Passive Mechanics and Force Development. In continuum mechanics based modeling the coupling between force development and passive mechanics models is performed via definition of summary stress. In incompressible, hyperelastic solids the summary second Piola-Kirchhoff stress tensor $\boldsymbol{S}$ is composed of:

$$S_{ij} = \frac{\partial W}{\partial E_{ij}} - p\delta_{ij} + S_{active,ij}$$

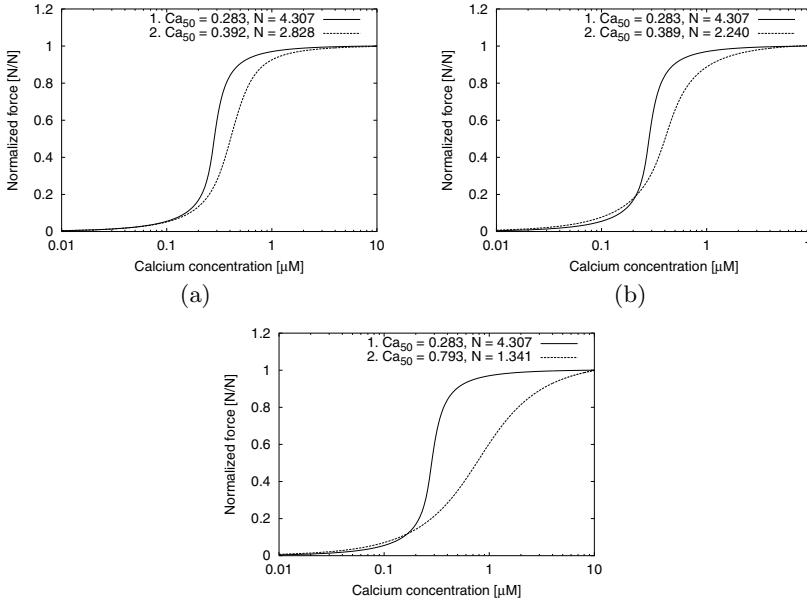

Fig. 8.23. Evaluation of cooperativity mechanisms (adapted from [354]). Simulations are performed (1) with and (2) without the mechanisms (a) XB-TN, (b) XB-XB, and (c) TM-TM. The Hill parameters Ca_{50} and N quantify the differences resulting from incorporating the different mechanisms.

with the strain energy density function W, the Green-Lagrange strain tensor $\boldsymbol{E}$, the Kronecker delta δ, the hydrostatic pressure p, and the active tension tensor $\boldsymbol{S}_{active}$.

In a local, cartesian coordinate system the active tension tensor $\boldsymbol{S}_{local,active}$ is given by:

$$\boldsymbol{S}_{local,active} = \begin{pmatrix} s_{fiber,active} & 0\,0 \\ 0 & 0\,0 \\ 0 & 0\,0 \end{pmatrix}$$

with the scalar tension in fiber direction $s_{fiber,active}$, which is commonly set using data from measurements or simulations. In the local coordinate system the $\boldsymbol{x}$-axis is aligned with the fiber orientation.

Alternatively, the active tension tensor $\boldsymbol{S}_{local,active}$ may be defined as:

$$\boldsymbol{S}_{local,active} = \begin{pmatrix} s_{fiber,active} & 0 & 0 \\ 0 & s_{sheet,active} & 0 \\ 0 & 0 & s_{normal,active} \end{pmatrix}$$

with the scalar tension in fiber direction $s_{fiber,active}$, in sheet direction $s_{sheet,active}$, and in sheet normal direction $s_{normal,active}$. This definition al-

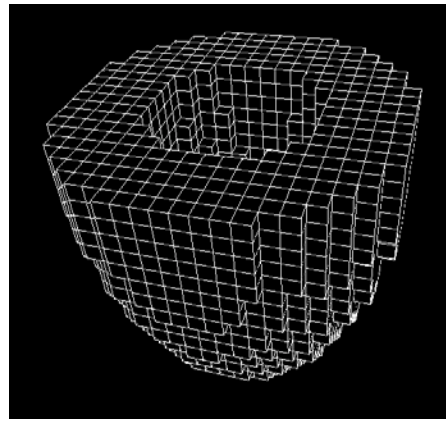

Fig. 8.24. Left ventricle approximated with 3752 cubic elements.

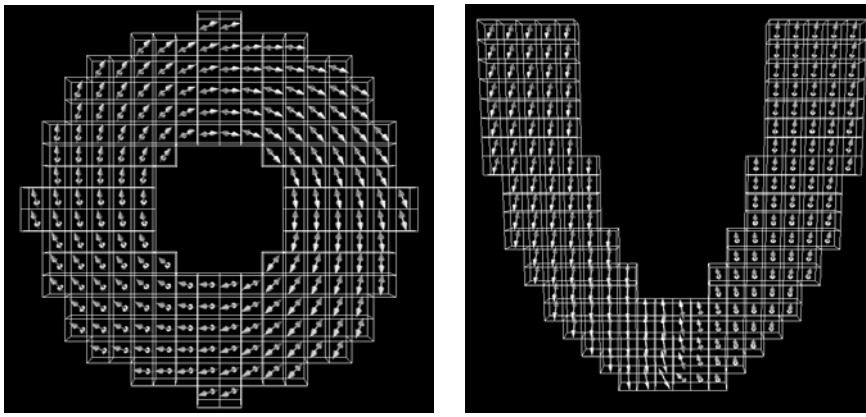

(a) (b)

Fig. 8.25. Myocyte orientation in (a) central short and (b) central long axis slice. The endocardial, midwall and epicardial myocyte orientation is set to $-45°$, $-45°$, and $-45°$, respectively.

lows the inclusion of active tension transversal to the fiber direction resulting e.g. from inhomogeneities of sarcomere orientation and microstructural considerations of the cross-bridge cycling.

The active tension tensor in local coordinate system $\boldsymbol{S}_{local,active}$ is transferred in the global coordinate system by:

$$S_{active,ij} = R_{ik}\ R_{jl}\ S_{local,active,kl}$$

with the rotation matrix $\boldsymbol{R}$ describing the transform from local to global coordinate system.

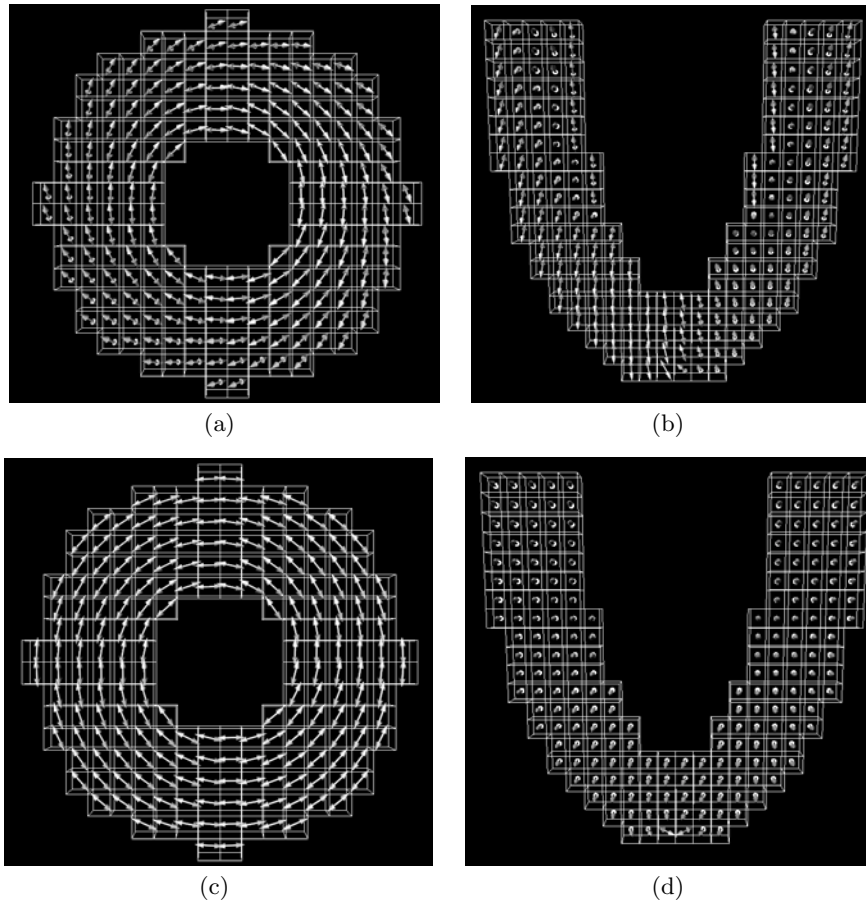

Fig. 8.26. Myocyte orientation in (a,c) central short and (b,d) central long axis slice. (a,b) The endocardial, midwall and epicardial orientation is set to -45°, 0°, and 45°, respectively. (c,d) The orientation is to 0°, 0°, and 0°, respectively.

Exemplary Simulations. Simulations were performed to illustrate the mechanical effects of myocyte orientation in the left ventricular wall. The orientation of myocytes is reported to be dependent on the depth [111, 112].

The left ventricle is approximated by a truncated, thick ellipsoid. The half ellipsoid is discretized with 3752 cubic elements (Fig. sfi8.24). Assigned to the elements vertices are node variables, which describe a displacement vector. The displacement, tension and strain is trilinearly interpolated inside of an element.

In the simulations three different orientations are assigned to the endocardial, midwall, and epicardial layer (Fig. 8.25 and 8.26). The orientation in the regions in between is interpolated with the techniques described in Sect. 5.6.3.

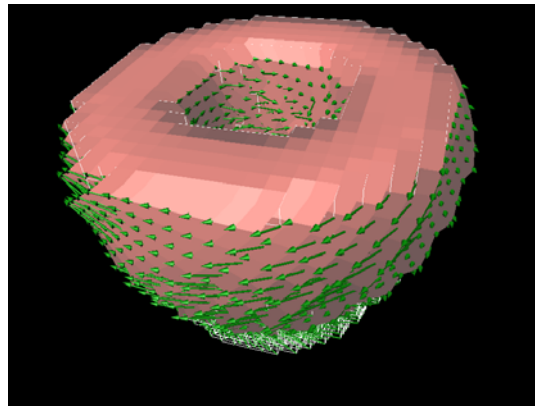

(a)

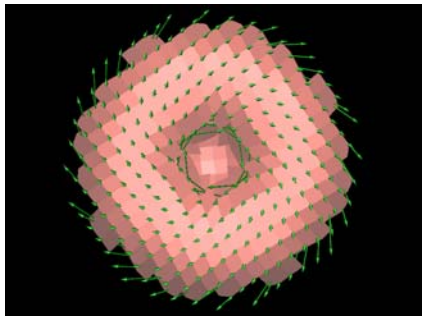

(b)

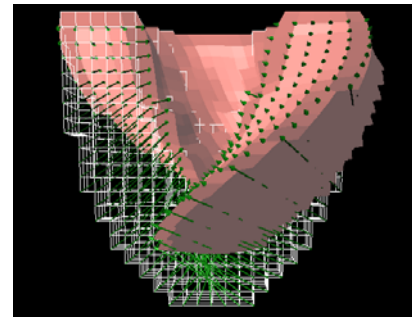

(c)

Fig. 8.27. Deformation of ventricle model. The endocardial, midwall and epicardial myocyte orientation is set to $-45°$, $-45°$, and $-45°$, respectively. The deformation is visualized in (a) full, (b) short axis cutted, and (c) long axis cutted ventricle. Green arrows indicate the displacement of a vertex. The white lattice represents the initial configuration.

Attributed to each element of the ellipsoid is a hyperelastic anisotropic material description assuming incompressibility. The material law of Guccione et al. is used, which reconstructs orthotrophic properties (Sect. 8.1) [254]:

$$W = \frac{C}{2}\left(e^{Q} - 1\right)$$
$$Q = 2b_1(E_{RR} + E_{FF} + E_{CC}) + b_2 E_{FF}^2 + b_3(E_{CC}^2 + E_{RR}^2 + E_{CR}^2 + E_{RC}^2) + b_4(E_{RF}^2 + E_{FR}^2 + E_{FC}^2 + E_{CF}^2)$$

with the parameter C, b_1, b_2, b_3, b_4, and the components of the Green-Lagrange strain tensor $\boldsymbol{E}$. As parameters are chosen: $C = 0.6\ kPa$, $b_1 = 0$, $b_2 = 26.7$, $b_3 = 2.0$, and $b_4 = 14.7$.

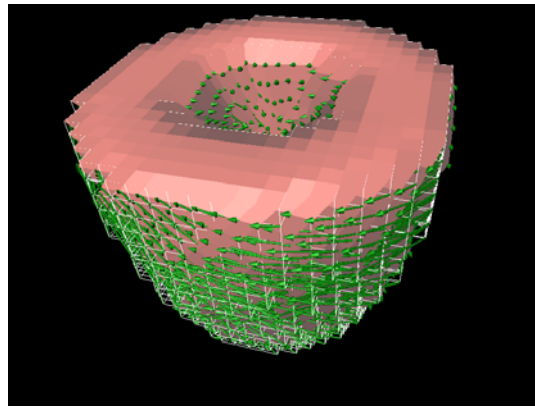

(a)

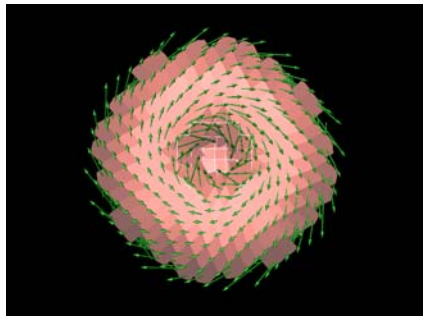

(b)

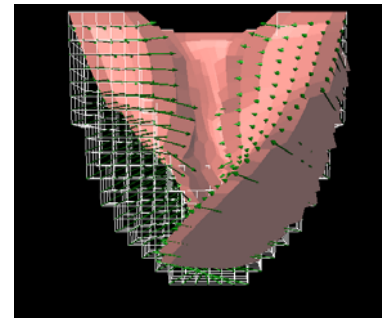

(c)

Fig. 8.28. Deformation of ventricle model. The endocardial, midwall and epicardial myocyte orientation is set to $-45°$, $0°$, and $45°$, respectively. The deformation is visualized in (a) full, (b) short axis cutted, and (c) long axis cutted ventricle. Green arrows indicate the displacement of a vertex. The white lattice represents the initial configuration.

The finite element method is applied to determine the mechanical deformation in the ventricle resulting from given forces (Sect. 4.3). A numerical evaluation of integral equations resulting from the principal of virtual displacements is performed delivering element- and time-step-wise linear systems of equations. These equations are assembled into the system equations, which are modified by boundary conditions. The system of equations is solved by the conjugate gradient method (Sect. 2.4.3).

Anatomically motivated boundary conditions are chosen. The half ellipsoid is fixed at its top layer with the opening. A tension $s_{fiber,active}$ of 1 kPa is applied in fiber direction homogeneously in each element.

Results of simulations are illustrated in the Fig. 8.27, 8.28, and 8.29. The simulation with orientations equal to $0°$ shows a significant long axis stretch-

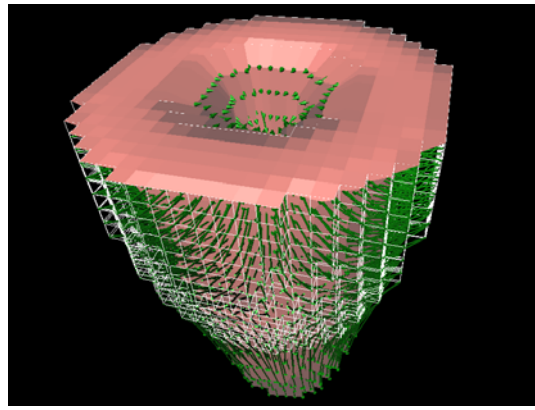

(a)

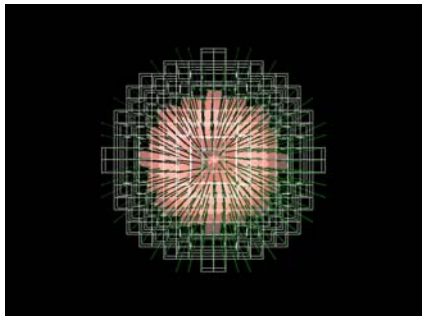

(b)

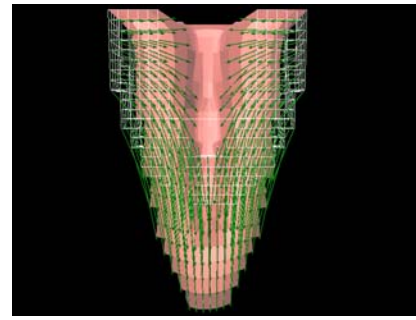

(c)

Fig. 8.29. Deformation of ventricle model. The endocardial, midwall and epicardial myocyte orientation is set to 0°, 0°, and 0°, respectively. The deformation is visualized in (a) full, (b) short axis cutted, and (c) long axis cutted ventricle. Green arrows indicate the displacement of a vertex. The white lattice represents the initial configuration.

out and shrinking in short axes direction. Orientations of -45° lead to a long axis shortening and short axes stretch. The model with endocardial, midwall and epicardial orientation set to -45°, 0°, and 45°, respectively, maintains its shape.

9

Modeling of Cardiac Electro-Mechanics

9.1 Introduction

Efficient working of the heart necessitates an adaptation to suddenly emerging demands and loads. The adaptation is performed by a well ordered interplay between cellular electrophysiology, intercellular excitation propagation and cellular force development. Different feedback mechanisms, i.e. mechano-electrophysiological and mechano-force development feedbacks, support the interplay. A reconstruction of this interplay can be achieved by coupled models of different type, particularly anatomical, electrophysiological, force development and deformation models.

In this chapter strategies for reconstruction of heart's electro-mechanic function are introduced. The modeling includes intra-cardiac, short-term adaptation phenomena. Middle-term transients are neglected, e.g. stimulus frequency dependence of intracellular concentration of calcium and of calcium loading of sarcoplasmic reticulum. Long-term adaptations, e.g. by macroscopic anatomical adaptation and varying densities of transmembrane proteins, are not on target. Also, metabolic and hormonal effects are not considered.

In the following sections electro-mechanic models at cellular, macroscopic and whole heart level are presented, which result from a coupling of diverse models. The electro-mechanic models are illustrated by simulations. Electro-mechanic models of different levels and applied techniques are shown:

- Models of electrophysiology and force development at level of single cell. The models are described by systems of coupled ordinary differential equations. The models include geometric descriptions. The resultant stretch is derived.
- Excitation propagation and cardiac force development at whole heart level. A rule-based method, a cellular automaton, is working in the spatial domain of a realistic anatomical heart model.

F.B. Sachse: LNCS 2966, pp. 267–289, 2004.

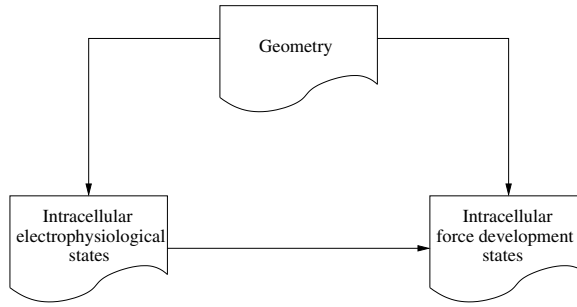

Fig. 9.1. Modeling of coupled cellular electro-mechanics. Changes in geometry can lead to stretch of sarcomere, which influences the cellular electrophysiology and force development. Electrophysiological models determine the course of intracellular calcium concentration, which is used as input for the force development model.

- Electro-mechanics in areas of myocardium. Cellular models of electrophysiology and force development are coupled with excitation propagation and deformation models. The excitation propagation is reconstructed with the bidomain model. For simulation of deformation the mechanical material properties are described as hyperelastic.

9.2 Electrophysiology and Force Development of Single Cells

Muscle cells control the development of force in the myofilaments via the intracellular calcium concentration and stretch of sarcomere. The coupling of electrophysiology and force development can be simulated with combined cell models, which reconstruct the binding of cytosolic calcium to troponin C and the calcium release from troponin C into the cytosol.

Only some recently developed electrophysiological cell models include explicitly the calcium interaction with troponin, e.g. the Demir-Clark-Murphey-Giles and Noble-Varghese-Kohl-Noble model (Fig. 7.24). The therewith achieved knowledge concerning the concentration of calcium bound to troponin C allows the determination of actin sites available for cross-bridge binding.

Alternatively, calcium-troponin interaction can be formulated explicitly by a force model, e.g. Landesberg-Sideman, Hunter-McCulloch-ter Keurs and 3rd Rice-Winslow-Hunter model. A further alternative are models, which neglect an explicit description of calcium-troponin interaction, e.g. 1st Rice-Winslow-Hunter model. Input parameter for both types of model is the cytosolic concentration of calcium.

Simulations with combined electrophysiology and force development models are shown in Fig. 9.3, 9.2, 9.4, and 9.5. The cytosolic concentration of

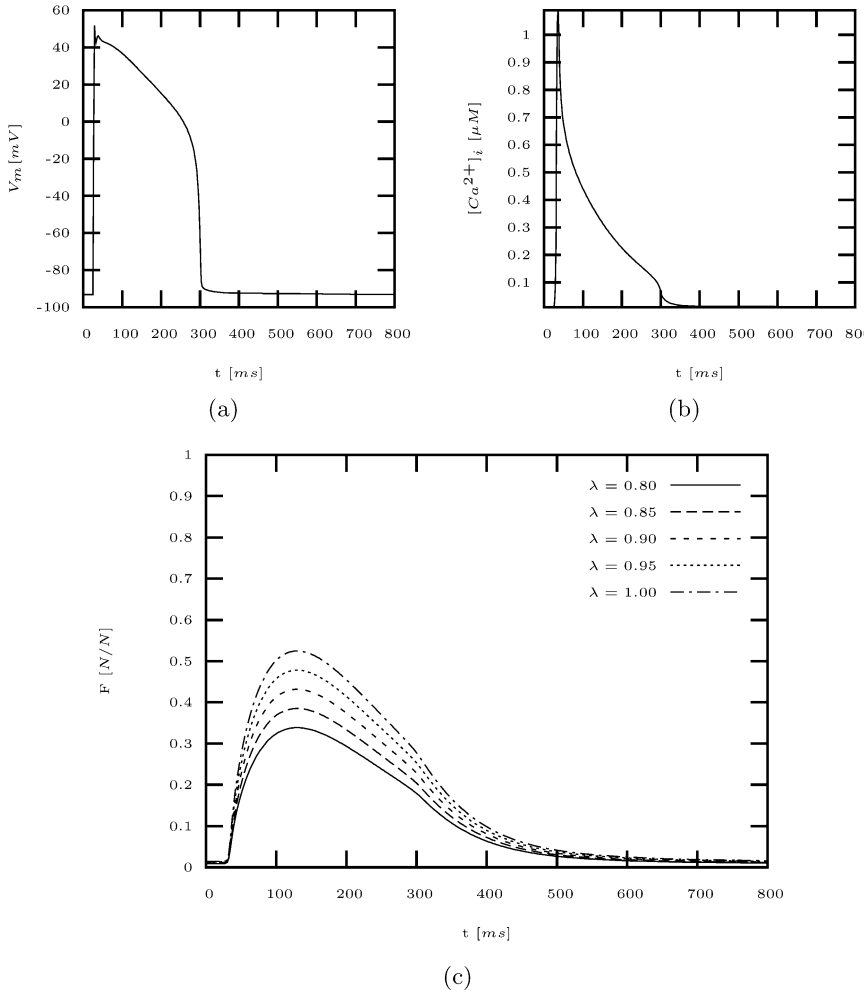

Fig. 9.2. Simulations with Noble-Varghese-Kohl-Noble and 1st Rice-Winslow-Hunter model. The cell is excited by applying a stimulus current at $t = 25\ ms$ with a length of 3 ms. The course of (a) transmembrane voltage V_m and (b) calcium concentration $[Ca^{2+}]_i$ is typical for a ventricular myocyte of guinea pig. (c) The development of force F is dependent on static stretch ranging from 0.8 to 1. The force F for larger stretches can be determined with the sarcomere overlap function. The force F is normalized with the maximal force F_{max}.

calcium serves in conjunction with the sarcomere stretch as input parameter for the force models. The data following the 100th excitation at a frequency of 1 Hz were used for visualization to avoid artifact resulting from imprecise initial values. The underlying system of ordinary differential equation was solved with the Euler method.

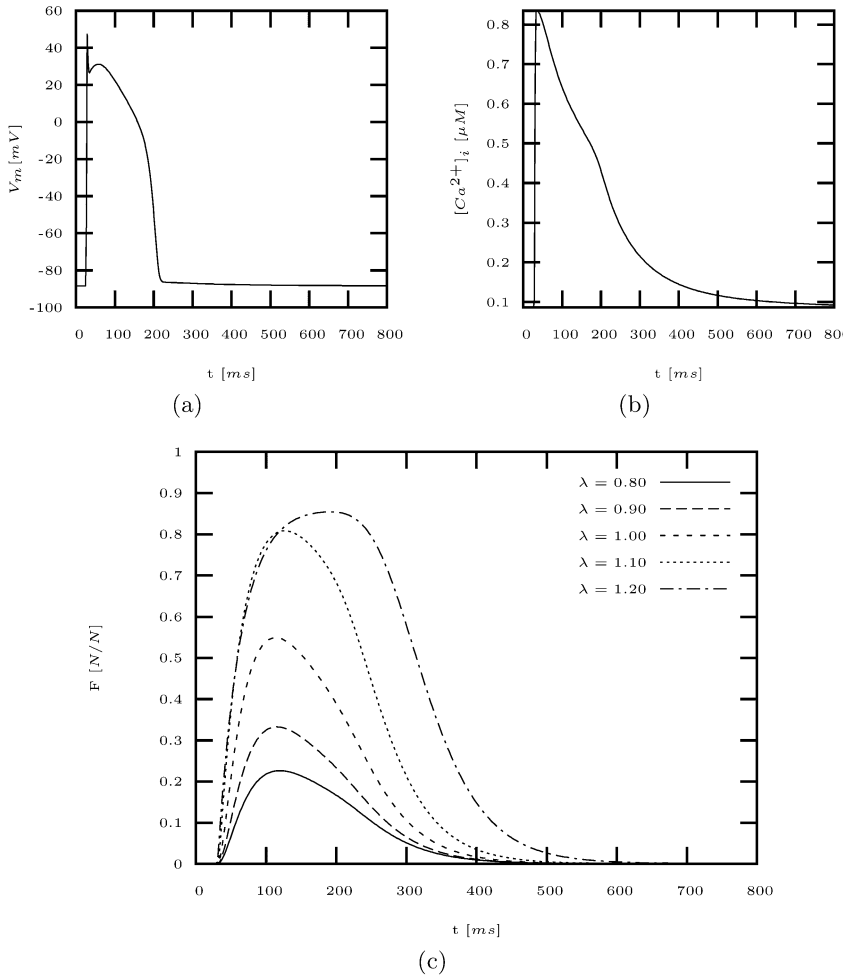

Fig. 9.3. Simulations with Luo-Rudy and 3rd Rice-Winslow-Hunter model. The cell is excited by applying a stimulus current at $t = 25\ ms$ with a length of 3 ms. The course of the (a) transmembrane voltage V_m and (b) calcium concentration $[Ca^{2+}]_i$ is reconstructed for ventricular myocytes of guinea pig.. (c) The development of force F is dependent on static stretch ranging from 0.8 to 1.2. The force F is normalized with the maximal force F_{max}.

The simulations with the combined Noble-Varghese-Kohl-Noble and 1st Rice-Winslow-Hunter model show non-realistic lengths and offsets of developed force (compare Fig. 8.16 and 8.17), which can be reduced by careful parameterization.

The simulations with the 3rd Rice-Winslow-Hunter model (Fig. 9.3 and 9.4) reveal consistent shapes of the developed cellular force. Differences of

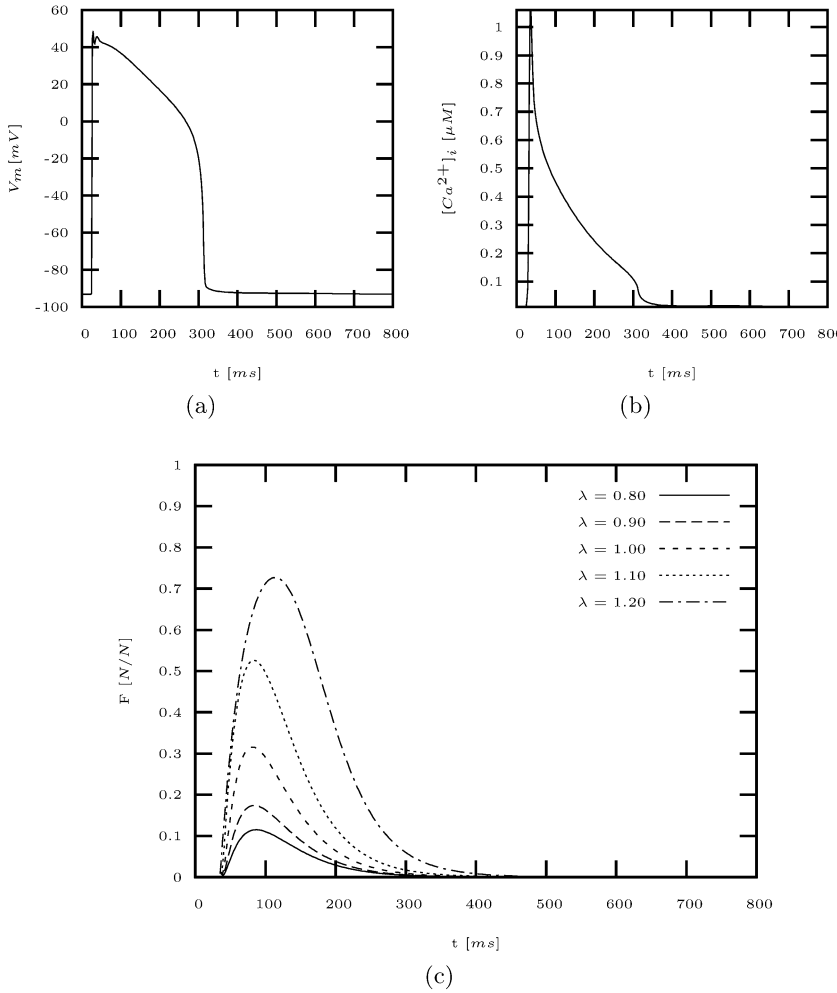

Fig. 9.4. Simulations with Noble-Varghese-Kohl-Noble and 3rd Rice-Winslow-Hunter model. The cell is excited by applying a stimulus current at $t = 25\ ms$ with a length of 3 ms. The course of (a) transmembrane voltage V_m and (b) calcium concentration $[Ca^{2+}]_i$ is typical for ventricular myocytes of guinea pig. (c) The development of force F is dependent on static stretch ranging from 0.8 to 1.2. The force F is normalized with the maximal force F_{max}.

length and amplitude can be attributed to differences in the reconstruction of the intracellular calcium concentration by the electrophysiological Luo-Rudy phase-2 and Noble-Varghese-Kohl-Noble models. The calcium-troponin interaction is described explicitly by the 3rd Rice-Winslow-Hunter model and the Noble-Varghese-Kohl-Noble model. The calcium binding to troponin C is neglected in the Luo-Rudy phase-2 model.

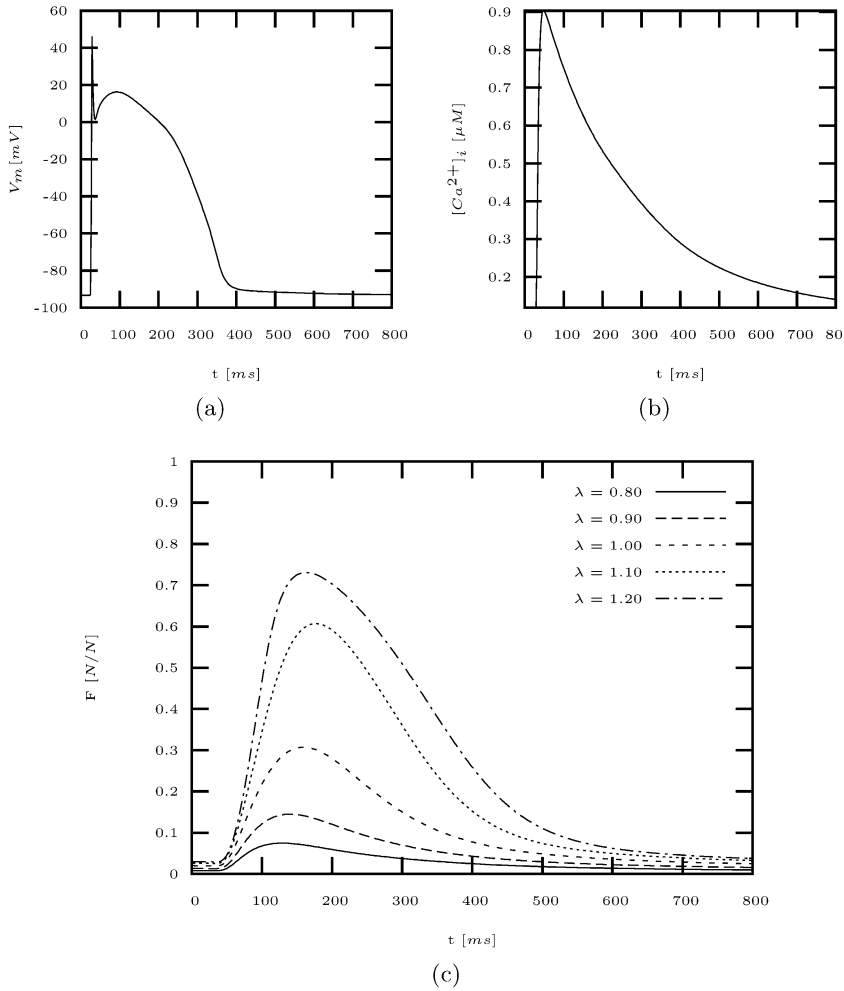

Fig. 9.5. Simulations with Priebe-Beuckelmann and Glänzel-Sachse-Seemann model. The cell is excited by applying a stimulus current at $t = 25\ ms$ with a length of 3 ms. The course of (a) transmembrane voltage V_m and (b) calcium concentration $[Ca^{2+}]_i$ is typical for normal human ventricular myocytes. (c) The development of force F is dependent on static stretch ranging from 0.8 to 1.2. The force F is normalized with the maximal force F_{max}.

The simulations with the Glänzel-Sachse-Seemann and a modified Priebe-Beuckelmann model aimed at reconstruction of electro-mechanics of human ventricular cells [197]. These models allow the quantitative reconstruction of various electro-mechanical phenomena at cellular level. The modification of the Priebe-Beuckelmann model concerned the calcium handling of myocytes, which was adapted to data obtained by recent studies [369]. The

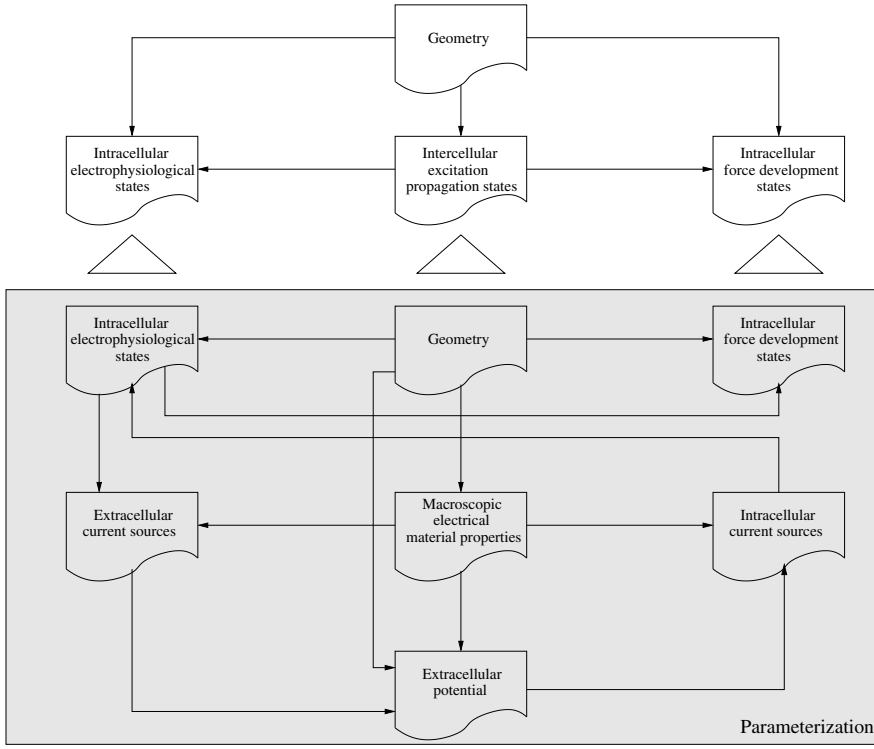

Fig. 9.6. Modeling of cardiac force development with cellular automaton at whole heart level. The cellular automaton is illustrated in the upper part. The automation is parameterized by prior simulations. The simulations are performed at cellular level with electrophysiological and force development models as well as with an excitation propagation model.

Glänzel-Sachse-Seemann model was parameterized in such a way that the static calcium-force relationship is similar to measurements in human myocardium.

Human myocytes show significantly prolonged durations of action potential and calcium transient in comparison to myocytes of guinea pigs. The resulting force transient is as well prolonged.

9.3 Cellular Automaton of Cardiac Force Development

A cellular automaton can be used to simulate force development in areas of myocardium and in the whole heart [370, 371, 372, 373]. The automaton, introduced in Sect. 7.3.3 for simulation of cardiac electrophysiology, allows to calculate force distributions on base of anisotropic electrical excitation propagation in anatomical models (Fig. 9.6).

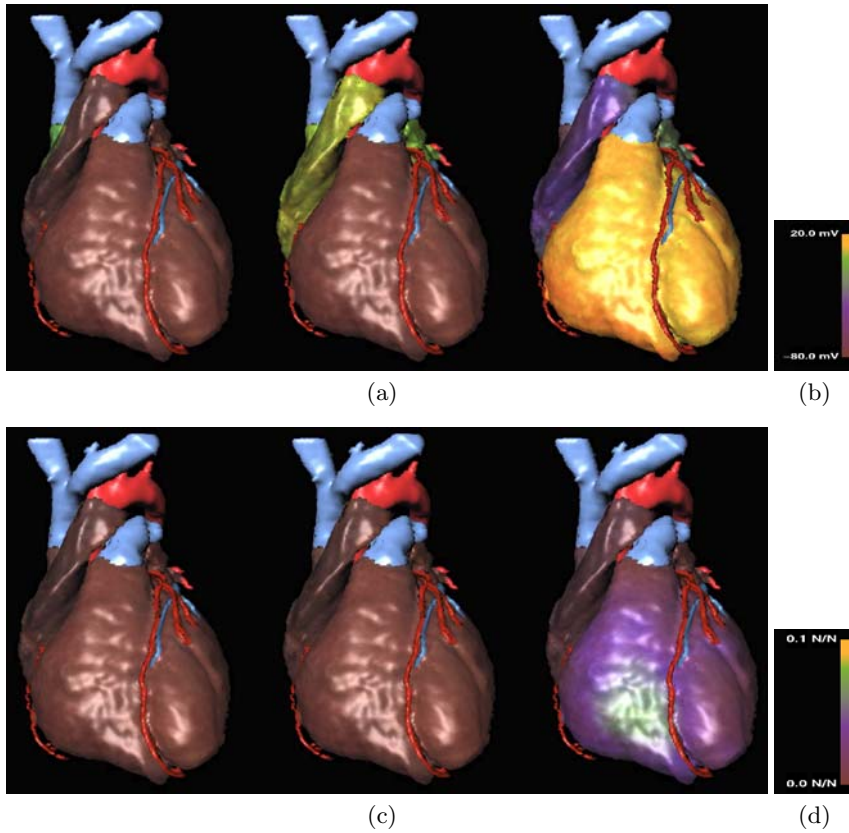

Fig. 9.7. Simulation of force development with cellular automaton. (a) The images sequence shows the transmembrane voltage at heart surface for time 16 ms, 76 ms, and 136 ms after activation of sinus node. (c) The sequence represents force at corresponding times. (b) Transmembrane voltage and (d) force are color coded using a palette.

The finite automaton at each node is parameterized with results from numerical simulations with cellular electrophysiologic, force development and excitation propagation models, e.g. simulations similar to those shown in Fig. 9.4. For that purpose, a large number of simulations was performed varying the cell model and the stimulus frequency. The simulations deliver tissue and stimulus frequency specific courses of the cellular force. The stretch dependence of force development can be included as a further parameter of the simulations for parameterization. Alternatively, some force models allow an a-posteriori scaling of the calculated force by stretch. E.g. the a-posteriori scaling of the 1st Rice-Winslow-Hunter model is achieved by applying the sarcomere overlap function (equation 8.15).

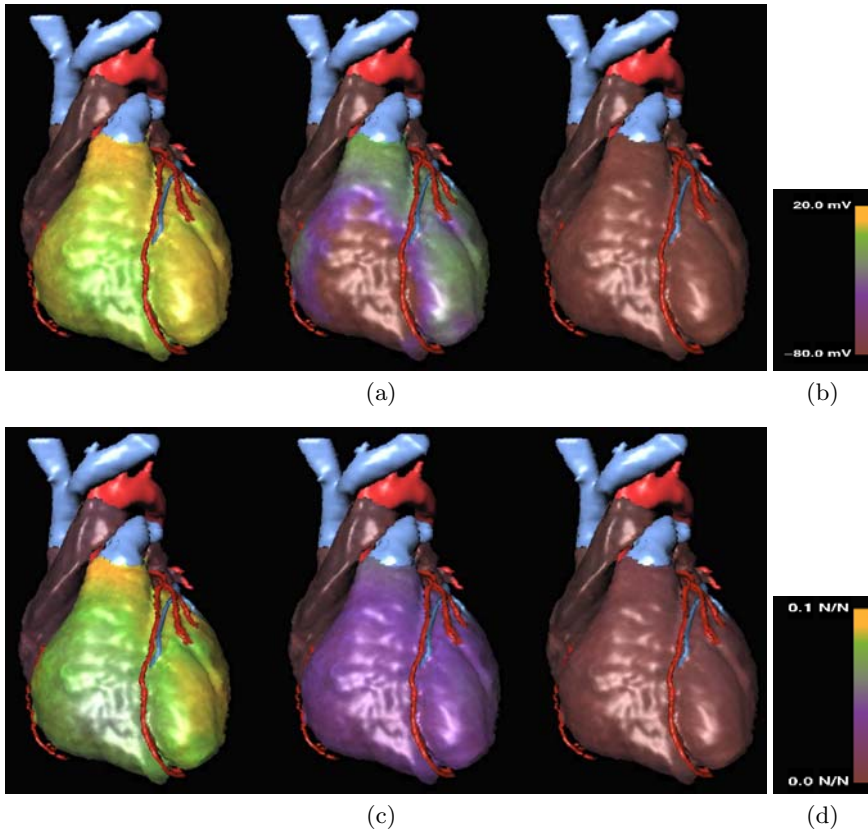

(a) (b)

(c) (d)

Fig. 9.8. Simulation of force development with cellular automaton. (a) The images sequence shows the transmembrane voltage at heart surface for time 376, 436 ms, and 556 ms after activation of sinus node. (c) The sequence represents force at corresponding times. (b) Transmembrane voltage and (d) force are color coded using a palette.

Result of a simulation with the cellular automaton is the temporal and spatial distribution of the force development for each cell (Fig. 9.7, 9.8, 9.9 and 9.10). The distributions can be applied in subsequent calculations of cardiac mechanical deformation, e.g. in conjunction with methods of continuum mechanics.

9.4 Electro-Mechanics of the Myocardium

9.4.1 Overview

A simulation environment was developed [374, 375, 376, 377, 252, 378], which has the purpose to achieve knowledge concerning the cardiac deformation

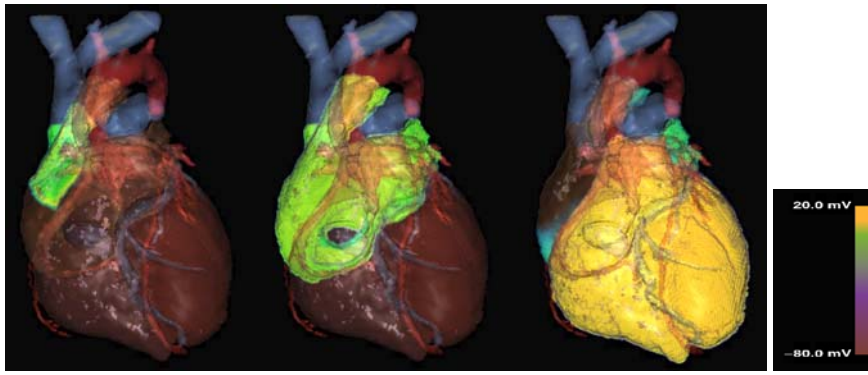

(a) (b)

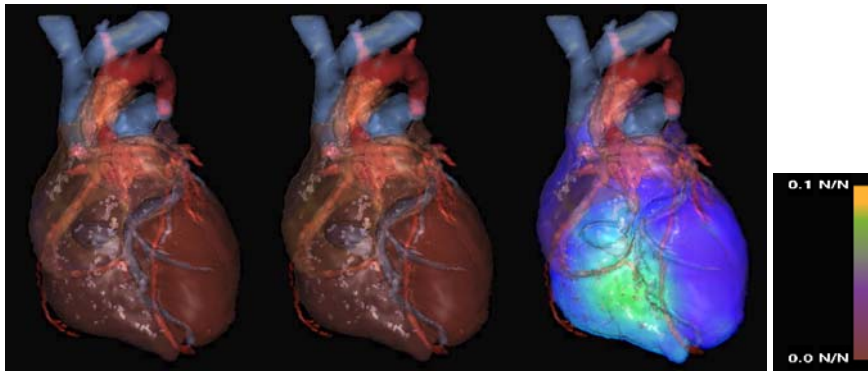

(c) (d)

Fig. 9.9. Simulation of force development with cellular automaton. (a) The images sequence shows the transmembrane voltage in heart surface for time 16 ms, 76 ms, and 136 ms after activation of sinus node. (c) The sequence represents force at corresponding times. (b) Transmembrane voltage and (d) force are color coded using a palette.

and its influence to the initiation and propagation of electrical excitation and to the force development. The environment combines and extends the cellular electrophysiological and force development models as well as macroscopic propagation models, which were presented in previous chapters. The environment consists of

- a cellular electrophysiological model with possibly stretch dependent behavior
- a bidomain model for excitation propagation taking stretch into account
- a cellular model of the force development with inclusion of stretch
- an elastomechanical model

The interdependencies of the different data are depicted in Fig. 9.11.

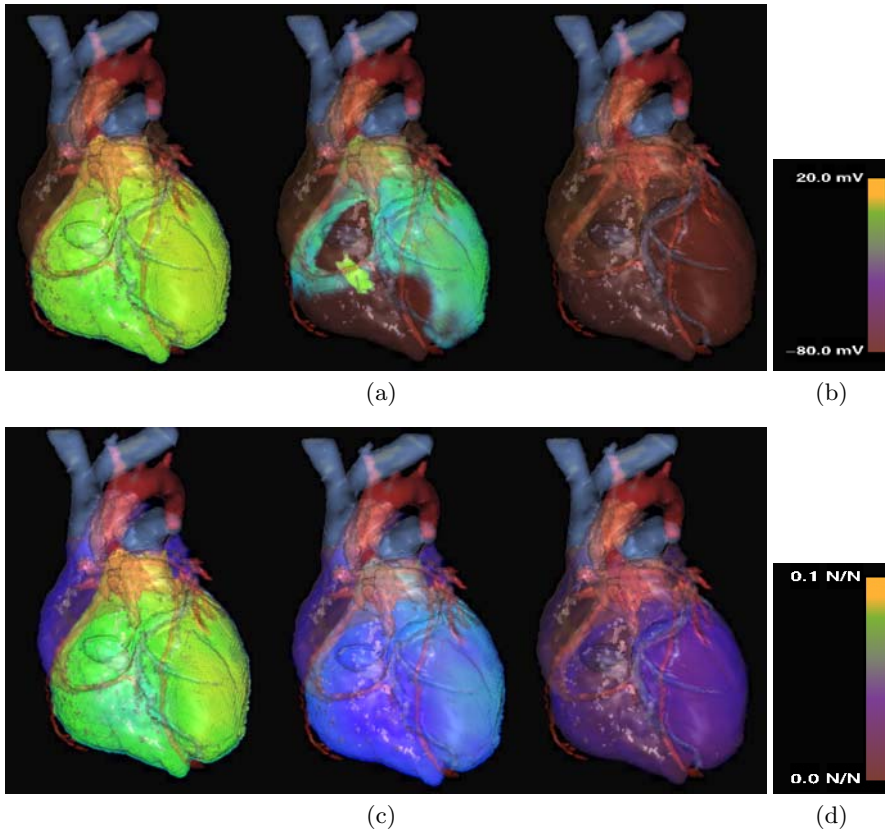

Fig. 9.10. Simulation of force development with cellular automaton. (a) The images sequence shows the transmembrane voltage in heart surface for time 376, 436 ms, and 556 ms after activation of sinus node. (c) The sequence represents force at corresponding times. (b) Transmembrane voltage and (d) force are color coded using a palette.

Influence of Stretch to Intra- and Extracellular Conductivity Tensors. An extension of the mono- and bidomain model was proposed (Sect. C), which allows to take the deformation of tissue into account for the calculation of electrical conductivities (Fig. 9.12). This extension delivers conductivity tensors σ_i and σ_e for the intra- and extracellular space, respectively. The conductivity tensors follow the rules of model assumptions.

In the following simulations a different behavior due to stretch of the extra- and intracellular conductivity tensor is assumed [374]:

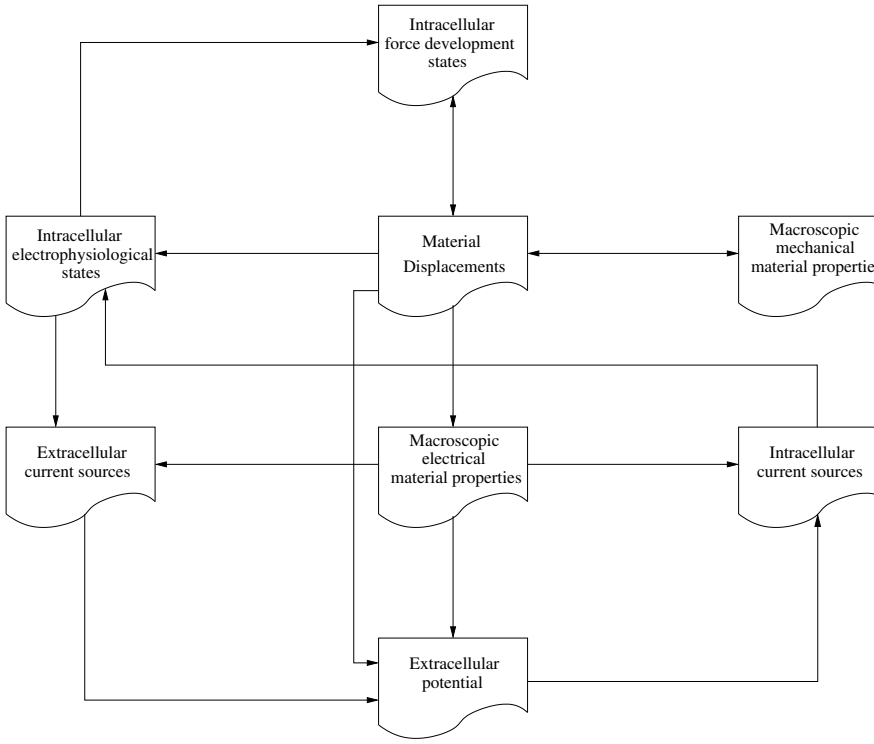

Fig. 9.11. Modeling of electro-mechanics in myocardium. Models of electrophysiology and force development at cellular level are coupled with excitation propagation and deformation models.

- The intracellular conductivity tensor σ_i is primarily influenced by the resistors R_{gj} of the gap junctions. These resistors R_{gj} are stretch independent.
- The extracellular space behaves like an incompressible fluid. The extracellular conductivity tensor σ_e is not influenced by stretch.

These physically motivated assumptions simplify the behavior of the conductivity tensors and allow their efficient calculation.

9.4.2 Simulations

Static Model of Heart Wall. The simulation serves to explore the propagation of excitation and force development in a static area of ventricular free wall (Fig. 7.44) [252]. The wall area was modeled as described in Sect. 7.3.4 and consists of 150 x 150 x 125 elements with a size of 0.2 mm x 0.2 mm x 0.2 mm reconstructing the electrophysiology and force development of ventricular cells.

In each cell the Noble-Varghese-Kohl-Noble and 3rd Rice-Winslow-Hunter model were coupled. Both cellular models were calculated by the Euler method

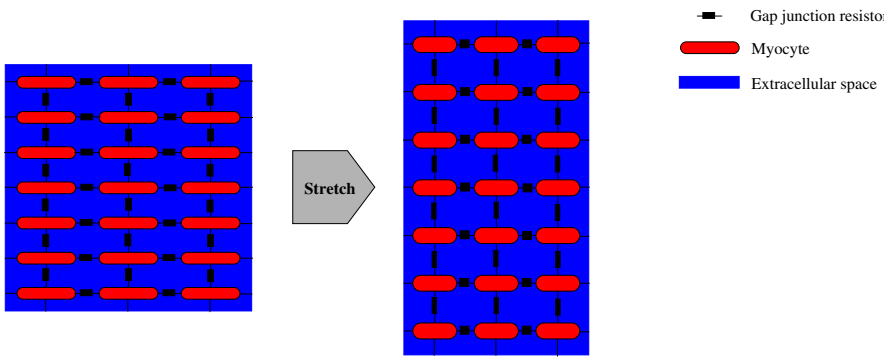

Fig. 9.12. Coupling of myocytes with gap junctions and through the extracellular space. The deformation of a region changes the intra- and extracellular conductivity. The resistor yielded by the gap junction is not changed.

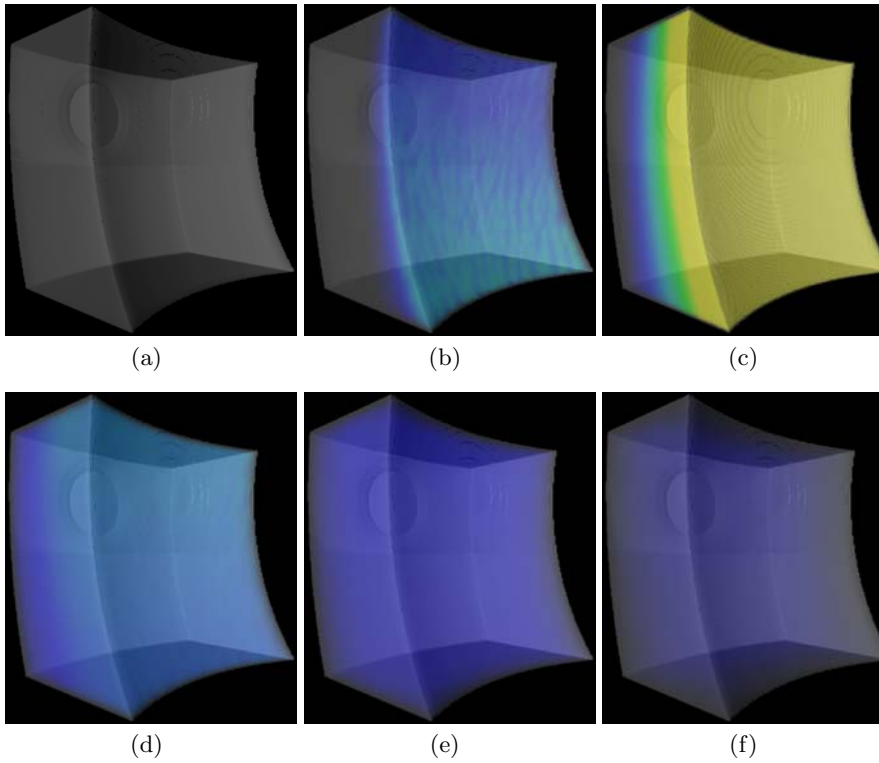

Fig. 9.13. Force development in static model of heart wall at different points in time. The simulated normalized force is visualized with volume based techniques at (a) 30 *ms*, (b) 65 *ms*, (c) 130 *ms*, (d) 290 *ms*, (e) 340 *ms*, and (f) 410 *ms*.

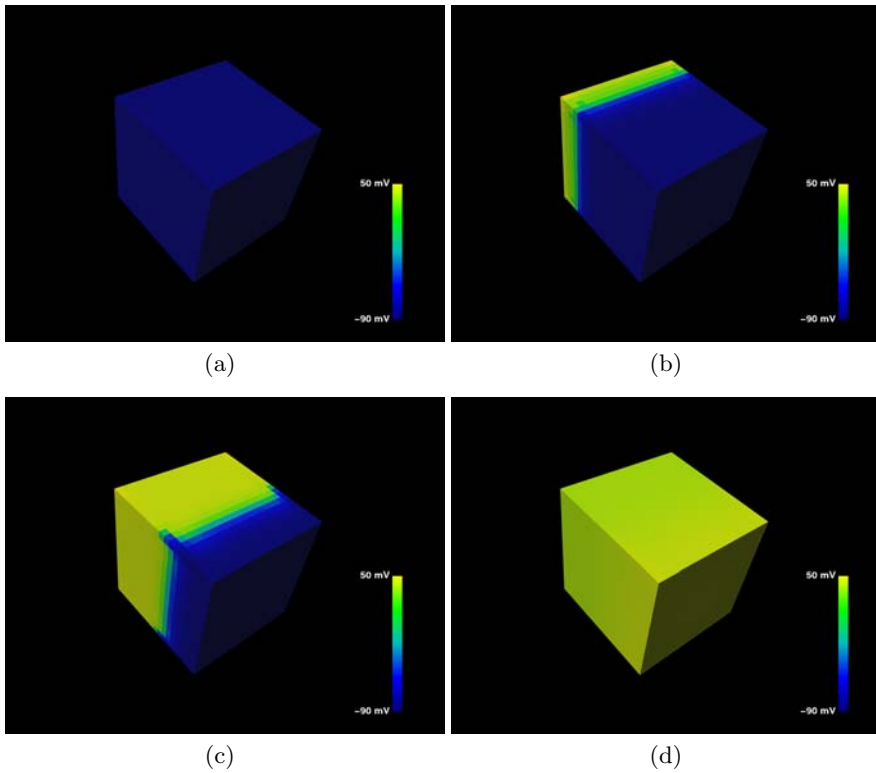

Fig. 9.14. Transmembrane voltage at time (a) 0 ms, (b) 3 ms, (c) 5 ms, and (d) 8 ms in an anisotropic model of myocardial area. The model consists of 20 x 20 x 20 cubic voxels with a size of 0.1 mm x 0.1 mm x 0.1 mm.

with a time step of 20 μs to solve the underlying ordinary differential equations.

The traditional bidomain model was applied to interconnect the electrophysiological cell models. Poisson's equations as parts of the bidomain model were solved with the finite-differences method. A Gauss-Seidel iteration at every 20 μs was carried out to solve these differential equations.

The excitation propagation at different points is shown in Fig. 7.46. Correspondingly, the propagation of force development is illustrated with Fig. 9.13. The propagation of force development follows the propagation of electrical excitation with a delay, which is found similarly in single cell simulations. The developed force is inhomogeneously distributed in the wall resulting from differences of the underlying electrophysiology.

Electro-Mechanical Model of Myocardium Block. Simulations were performed with fully coupled electro-mechanical models of a myocardial area. The applied anatomical model consisted of 20 x 20 x 20 cubic voxels, each

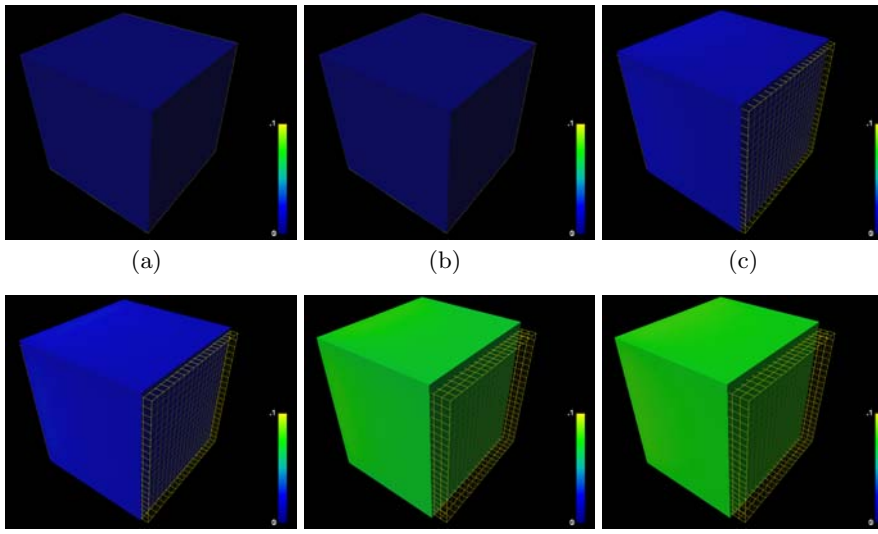

(a) (b) (c)

(d) (e) (f)

Fig. 9.15. Color-coded normalized force and deformation at time (a) 0 ms, (b) 50 ms, (c) 100 ms, (d) 150 ms, (e) 200 ms, and (f) 250 ms in an anisotropic model of myocardial area. The model consists of 20 x 20 x 20 cubic voxels with a size of 0.1 mm x 0.1 mm x 0.1 mm. Central positions in the plane $z = 0$ were fixed, i.e. the displacements were set to zero. The wire frame shows the reference configuration.

with a size of 0.1 mm x 0.1 mm x 0.1 mm. The activation was initiated at time 0 ms by application of a sufficient electrical current at plane $z = 0$. The principal axis of myocytes was chosen parallel to the $\boldsymbol{z}$-axis.

Transversal isotropy of the electrical conductivities was set. Anisotropy of the elastomechanical parameters and incompressibility was assumed. Central positions of the plane $z = 0$ were fixed, i.e. the displacements were set to zero.

The simulations were performed applying the Euler method with a time step of 20 μs to solve the ordinary differential equations of the electrophysiological and force development model, i.e. the Noble-Varghese-Kohl-Noble and 3rd Rice-Winslow-Hunter model, respectively. Differential equations of the bidomain model were solved using the finite element method with a Gauss-Seidel iteration every 20 μs.

The material law of Hunter-Nashs-Sands was employed to describe the passive mechanics of the myocardium. The deformation was calculated with a time step of 1 ms. The system of linear equations resulting from the elastomechanical model was solved by the conjugate gradient method.

The results were visualized with surface and volume based techniques (Fig. 9.14 and 9.15). The simulations with the combined model show processes of different time scale. The process of excitation propagation is rapidly spreading over the myocardium (Fig. 9.14). The force development and the resulting

deformation follow with a significant delay (Fig. 9.15). In contrast to static simulations, e.g. those presented in the previous paragraph, a decrease of force can be found, which is primarily attributed to stretch dependence of force development models.

Electro-Mechanical Model of Left Ventricle. An integrated electro-mechanical ventricular model was investigated by exemplary simulations. The environment of the model was similar to those of the classical Langendorff studies [379]. The simulations represented a cardiac cycle including electrical de- and repolarization as well as mechanical contraction and relaxation.

The ventricle was approximated by crop of two confocal truncated ellipsoids (Sect. 6.4.2). The size of these ellipsoids was chosen in such a manner, that the resulting model has similar size as a small animal's left ventricle. The ventricle's geometry and fiber orientation was rendered in lattices of 40 x 40 x 50 and 20 x 20 x 25 cubic elements with a length of 200 and 400 μm, respectively. The macroscopic orientation of myocytes was included by interpolation starting from boundary conditions in three depths of the myocardium. The orientation was set subepicardial to $-70°$, midwall $0°$, and subendocardial $70°$ reflecting knowledge from anatomical studies [111].

The lattice with high resolution was applied for simulation of cellular electrophysiology, excitation propagation, and force development. The low resolution lattice served for simulation of passive mechanics. An intracellular conductivity tensor was assigned to all cells of the high resolution lattice taking tissue, material and fiber orientation into account. The Noble-Varghese-Kohl-Noble, the hybrid model of force development and a monodomain model of intercellular current flow [380] were attributed to all cells of the high resolution lattice, which were assigned to myocardium. In all cells of the low resolution lattice a model of passive mechanics was assigned. The orthotropic material law of Guccione et al. was attributed to cells containing myocardium (Sect. 8.1) [254], a linear law to the other cells.

Basal positions of the ventricular model were fixed in such a manner that displacements in direction of the ellipsoid's long axis were impossible and radial displacements were preferred. The maximal tension T_{max} was set to 10 kPa in the first simulations. In further simulations it was set to 5, 10, and 20 kPa.

An exemplary simulation had a duration of 800 ms started by applying an electrical stimulus at all voxels in the apical third of the subendocardial myocardium. Only voxels bordering directly to the endocardial cavity were taken into account. The stimulus applied a current of 10 μA at time $t = 0$ ms for a duration of 1 ms.

Every 20 μs a calculation of the electrophysiological, excitation propagation, and tension development model assigned to each voxel was performed. The displacements were determined every 5 ms and delivered to the electrophysiological, excitation propagation, and tension development model.

Table 9.1. Parameters extracted from simulation results (from [381]). The maximal slope of transmembrane voltage V_m and tension T was used to characterize onset of electrical excitation and tension development, respectively. The value APD_{90} identifies the duration between onset of electrical excitation and repolarization to 90 % of amplitude. The value TD_{90} is determined by duration between onset of tension development and return to 90 % of amplitude. Simulation results were stored with a temporal discretization of 5 ms. The parameter extraction was performed applying linear interpolation.

Position	time Max $\frac{\partial V_m}{\partial t}$ $[ms]$	APD_{90} $[ms]$	time Max $\frac{\partial T}{\partial t}$ $[ms]$	TD_{90} $[ms]$
epicardial apex	2.5	328.7	87.5	440.1
equatorial midwall	27.5	325.0	97.5	430.6
basal midwall	37.5	318.5	117.5	444.1

The simulations with the integrated model showed a rapid spread of electrical excitation characterized by depolarisation of cell membrane from apical-endocardial to basal-epicardial (table 9.1). A homogeneous distribution of transmembrane voltage was found during the plateau phase, whereby the homogeneity decreased over time. The spread of repolarisation followed the same patterns as found for depolarisation.

The spread of tension development occurred with delay similar to the spread of electrical excitation (table 9.1). The tension development was found to be homogeneous in the early stages, but inhomogeneity was significant for later stages. The inhomogeneity was resulting from an inhomogeneous distribution of strain and intracellular calcium after initial static stages of simulation.

The deformation of the ventricle, described by displacements of node points, is illustrated in Fig. 9.16 and 9.17. The deformation led to a significant decrease of endocardial volume and increase of wall thickness. The apical and equatorial regions showed a torsion as well as a significant radial and a minor displacement in basal direction. Regions at the basal border moved radial.

In a further set of simulations, the maximal tension T_{max} was varied. The endocardial volume was decreased during the contraction to maximal 84, 74, and 61 % of its reference volume for a maximal tension of 5, 10, and 20 kPa, respectively. The course of volume decrease was similar for the different tension factors (Fig. 9.18).

The transmembrane voltages and intracellular calcium concentrations vary only slightly for different tension factors and measurement positions (Fig. 9.19 a,b). Significant differences are found for tension development (Fig. 9.20). Normalized developed tensions T were larger for small tension factors. The differences can be attributed to the decrease in stretch by increase of tension factors. This decrease leads to reduced calcium-troponin C binding and small values in the sarcomere overlap function.

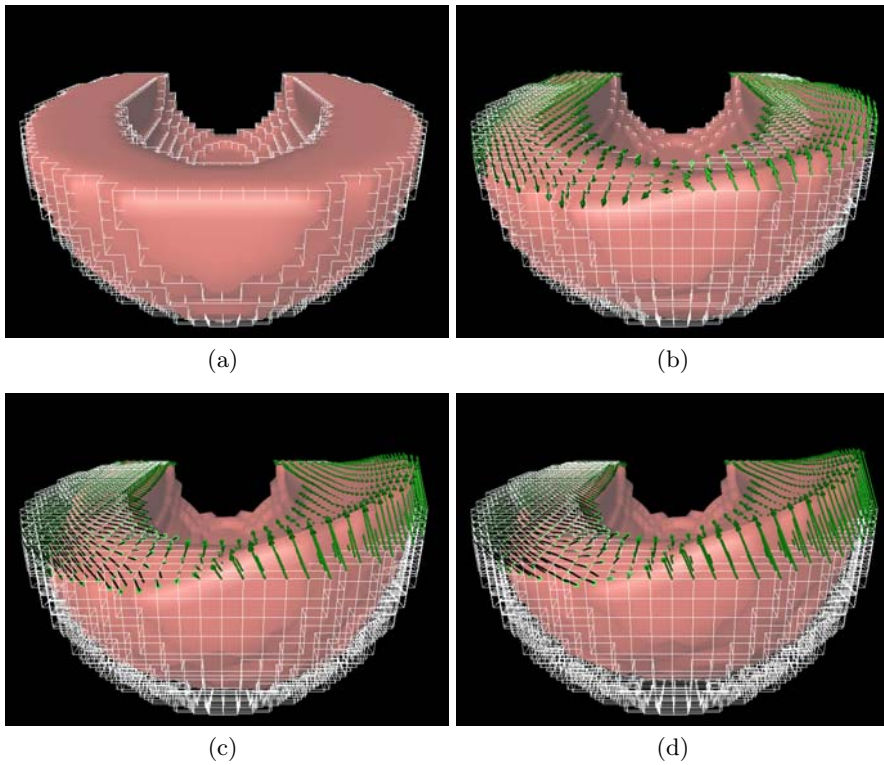

Fig. 9.16. Apical view on deformation at time (a) 0 ms, (b) 100 ms, (c) 200 ms, and (d) 300 ms in electro-mechanical model of left ventricle (from [381]). A half of the ventricle's model is shown with a bright wire-frame as reference configuration. Arrows indicate displacements at node points.

Electro-Mechanical Biventricular Model. The ventricles' geometry and fiber orientation were rendered as described in Sect. 6.4.2 and 9.4.2 in two lattices of 48 x 36 x 44 and 24 x18 x22 cubic elements with a length of 200 and 400 μm, respectively. An exemplary simulation was performed as described in section 9.4.2 applying models of electrophysiology, tension development, and passive mechanics. Electrical boundary conditions were added for the right ventricle. Mechanical boundary conditions were assigned only for the left ventricle. Results of the simulation are presented in Fig. 9.21.

Electro-Mechanical Biventricular Model Based on Diffusion Weighted MRT. The geometry and fiber orientation of the canine's ventricles were modeled as described in Sect. 6.4.6) and stored as depicted in Sect. 9.4.2 in two lattices of 128 x 128 x 96 and 32 x 32 x 24 cubic elements with a length of 800 and 3200 μm, respectively. The lattice for modeling electrophysiology and tension development is illustrated in Fig. 6.30 and 6.31.

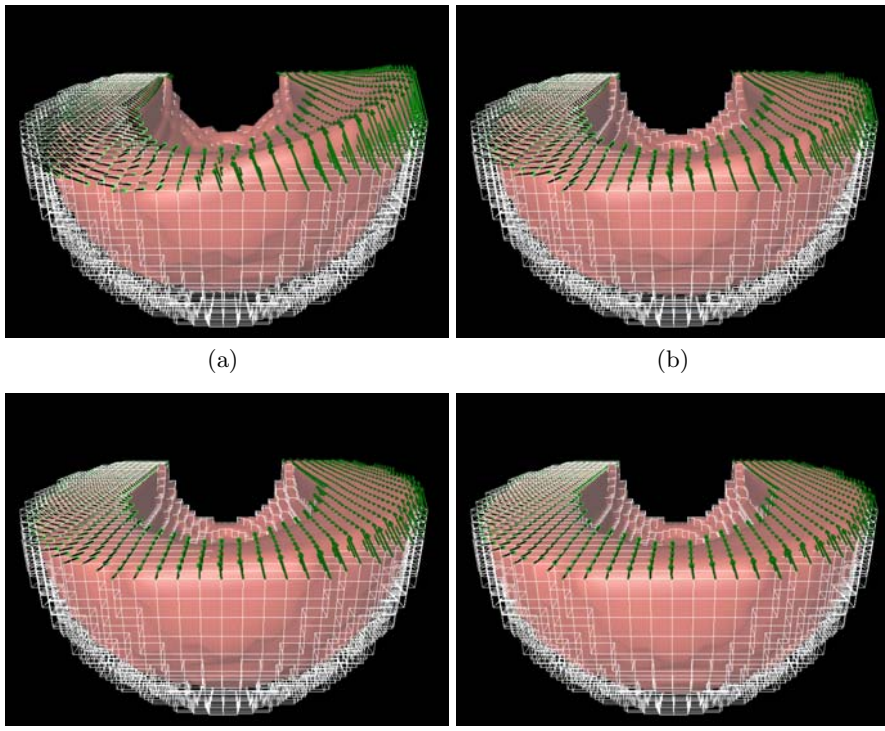

Fig. 9.17. Apical view on deformation at time (a) 400 ms, (b) 500 ms, (c) 600 ms, and (d) 700 ms (from [381]).

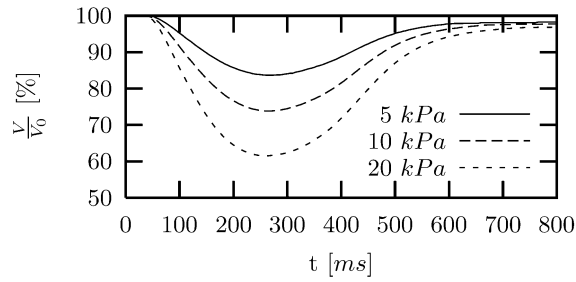

Fig. 9.18. Ratio of endocardial volume. The ratio between the volume of left ventricular cavity in deformed and undeformed configuration is dependent on the tension produced by contractile units. The course of the volume ratio is shown calculated by simulations with a maximal tension T_{max} of 5, 10 and 20 kPa.

An exemplary simulation was performed as detailed in section 9.4.2. Mechanical boundary conditions fixed the myocardium in the basal endocardial rim of the left ventricle. Results of the simulation are shown in Fig. 9.22.

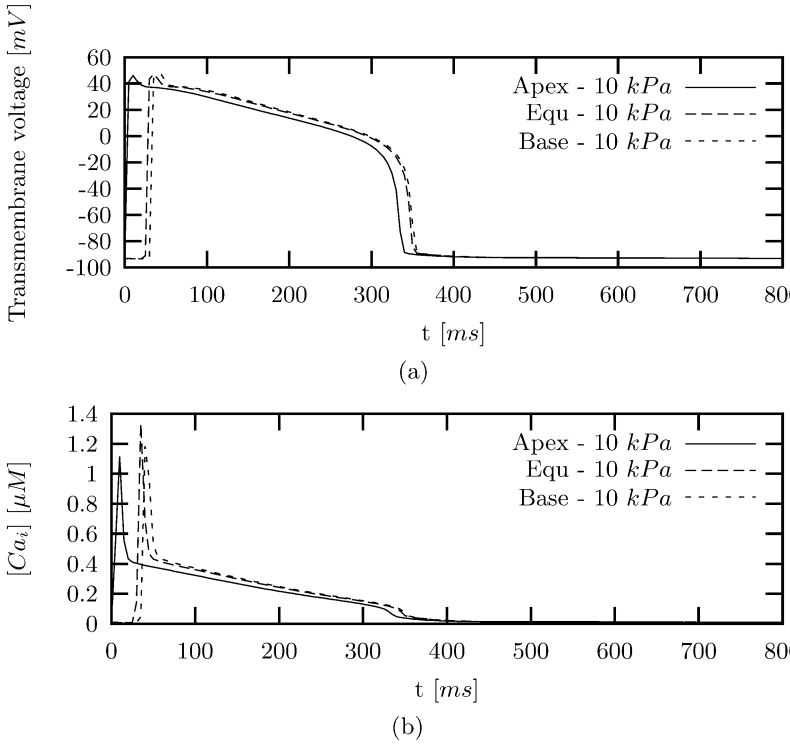

Fig. 9.19. (a) Transmembrane voltage V_m and (b) concentration of intracellular calcium $[Ca^{2+}]_i$ at different positions and for different maximal tensions T_{max}. Maximal tensions of 5, 10 and 20 kPa were assigned to the contractile units. Positions at the epicardial apex, equatorial midwall, and basal midwall were selected.

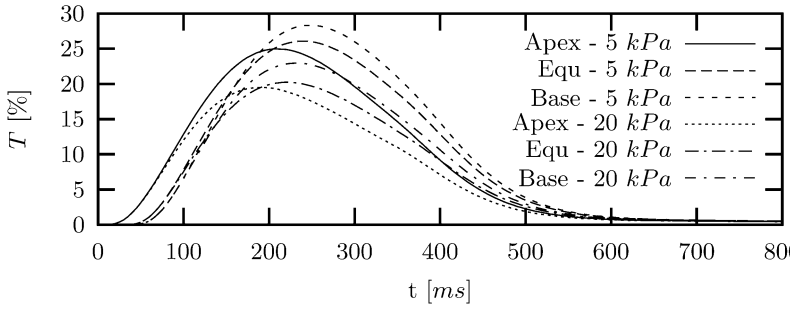

Fig. 9.20. Normalized tension at different positions and for different maximal tensions T_{max}. Maximal tensions of 5, 10 and 20 kPa were assigned to the contractile units. Positions at the epicardial apex, equatorial midwall, and basal midwall were selected.

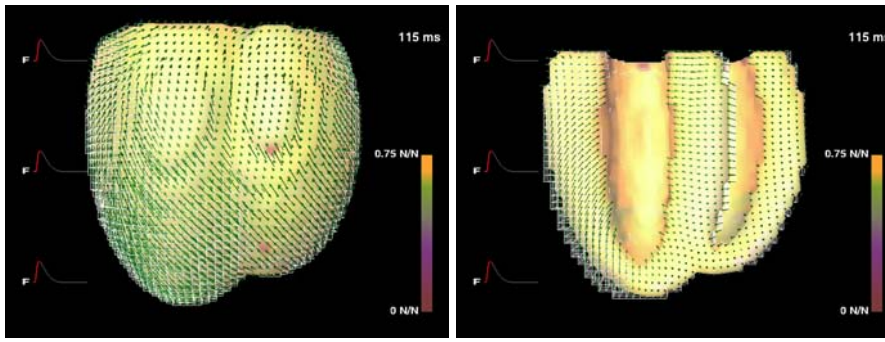

(a) (b)

Fig. 9.21. Results of simulation with analytical biventricular model (from [131]). (a) Full and (b) halved model are shown at time of maximal developed tension. The displacement of vertices is indicated by arrows. The white wire frame describes the initial configuration. The course of developed tension at apical, equatorial, and basal midwall positions is depicted on the left side.

9.4.3 Limitations and Perspectives

Different limitations of the simulations with the electro-mechanical models can be assigned, which aim at reconstruction of short-term phenomena.

The applied anatomical model approximated the cardiac tissue and fiber distribution in parts. Further anatomical structures were not included, e.g. papillary muscles, pericardium, and atria. Transmural inhomogeneities of myocardium [382] and lamination of ventricular myocardium [108] were not represented by the anatomical model, but the electrophysiological and mechanical models are capable of reconstructing of inhomogeneity and full anisotropic effects. More detailed anatomical models can be generated e.g. using medical imaging systems [136].

The application of mechano-electrical feedback mechanisms in the integrated models was restricted to incorporation of modulation of calcium binding to troponin C and modulation of sarcoplasmic leak current. Stretch activated sarcolemmal ion channels were deactivated.

Mechanical and electrical boundary conditions were simplified in the presented simulations. Endocardial pressure and valve mechanics were not taken into account in the presented simulations. Nevertheless, interfaces for incorporation various boundary conditions are provided in the integrated model, e.g. pressure at endocardial surfaces and residual stress. Mechanical boundary conditions can be determined by coupling of the integrated model to model of fluid and valve mechanics.

The models showed to be challenging concerning computing resources. Particularly the modeling of deformation demands significant parts of calculation time. Exploiting of new numeric methods, e.g. meshless techniques for solving

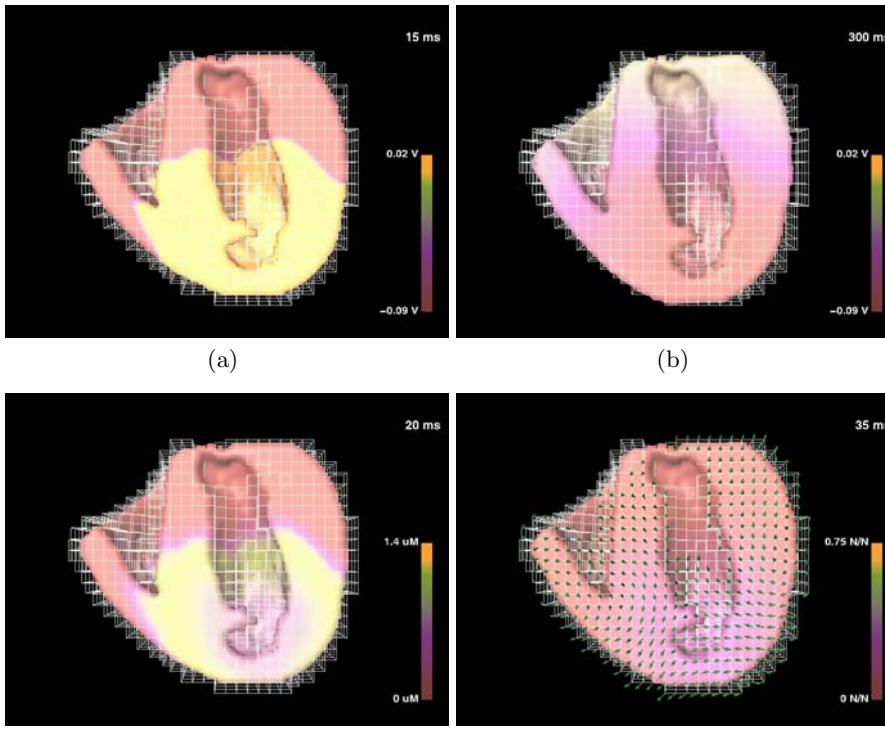

Fig. 9.22. Results of simulation with diffusion weighted MRT biventricular model (from [131]). Several aspects of electrophysiology and mechanics in halved model are illustrated: distribution of transmembrane voltage V_m at time (a) 15 and (b) 300 ms, (c) the distribution of intracellular calcium $[Ca^{2+}]_i$ at time 20 ms, and (d) tension developed at 35 ms, i.e. an initial phase of contraction. The displacement of vertices is indicated by arrows. All times are referenced to the time of application of stimulus.

of differential equations [383], and software development, e.g. Grid technologies for computing, seems to be a chance to satisfy these demands.

The presented ventricular simulation was performed on a shared memory computing server of type SGI Origin 2000 with 8 processors of type R10000 195 MHz claiming 7 processors each for a time 120 h. The simulations with the analytical and MRT based biventricular model were performed on a shared memory computing server of type SGI Origin 3000 using 16 of 64 processors of type R14000 600 MHz each for a time 32 and 72 h, respectively. Parallelization of computationally expensive tasks was achieved on basis of the OpenMP API [384].

Demands of extendability can be defined concerning the further development of the presented framework for modeling of cardiac electro-mechanics,

i.e. providing interfaces to external modeling, simulation and numerical environments, e.g. to CellML for storage and exchange of computer-based biological models [385] and SCIRun/BioPSE [386]. Upcoming specifications and formalizations of information in biology, medicine and mathematics have to be taken into account for further development, e.g. AnatML for exchanging information at organ level and FieldML for describing field information using finite elements.

Despite the limitations of the models characteristic micro- and macroscopic phenomena of cardiac electro-mechanics were reconstructed. The presented methods show a strategy, which can be adapted e.g. for improvement of biomedical instrumentation and pharmaceuticals as well as of clinical cardiologic diagnosis and planning of therapies. The inclusion of patient specific data ranging from genetic scans to medical images is possible and offers the adaptation of models to patient specific characteristics.

Appendix

A Physical Units and Constants

Table A.1. Physical units.

Quantity	Symbol	Unit
Capacity	C	F
Charge	Q	C
Current	I	A
Current density	J	$A\ m^{-2}$
Energy	W	$W\ s$
Electric conductivity	σ	$(\Omega\ m)^{-1}$
Electric field	$\boldsymbol{E}$	$V\ m^{-1}$
Electric flux density	$\boldsymbol{D}$	$A\ s\ m^{-2}$
Electric potential	ϕ	V
Electric resistor	R	Ω
Electric voltage	ϕ	V
Force	$\boldsymbol{F}$	N
Frequency	f	s^{-1}
Length	l	m
Magnetic field	$\boldsymbol{H}$	$A\ m^{-1}$
Magnetic flux density	$\boldsymbol{B}$	$V\ s\ m^{-2}$
Mass	m	kg
Power	P	W
Time	t	s

Table A.2. Physical constants.

Symbol	Description	Value	Dimension
ϵ_0	Permittivity in vacuum	$8.8542 \cdot 10^{-12}$	$A\ s\ V^{-1}\ m^{-1}$
μ_0	Permeability in vacuum	$1.2566 \cdot 10^{-6}$	$V\ s\ A^{-1}\ m^{-1}$
c	Velocity of light	$2.99792456 \cdot 10^{8}$	$m\ s^{-1}$
e	Elementary charge	$1.6021773 \cdot 10^{-19}$	C
F	Faraday's constant	$9.64853 \cdot 10^{4}$	$C\ mol^{-1}$
N	Avogadro's number	$6.022 \cdot 10^{23}$	mol^{-1}
R	Gas constant	8.31451	$J\ K^{-1}\ mol^{-1}$
D	Dalton, atomic unit of mass	$1.66 \cdot 10^{-27}$	kg

F.B. Sachse: LNCS 2966, pp. 291–298, 2004.

B Differential Operators

The definition of the following operators simplifies the notation of differential equations with vectorial components. These equations are frequently occurring describing phenomena in electromagnetics. The operators are illustrated with three-dimensional operands, but a generalization for arbitrary dimensions is straightforward possible.

The gradient or so-called nabla operator ∇ consists of spatial derivatives and is defined in a Cartesian coordinate system as:

$$\nabla \equiv \begin{pmatrix} \frac{\partial}{\partial x} \\ \frac{\partial}{\partial y} \\ \frac{\partial}{\partial z} \end{pmatrix}$$

whereby the variables x, y and z describe commonly coordinates in a three-dimensional domain.

The operator $\cdot$ indicates a scalar or inner product:

$$\boldsymbol{a} \cdot \boldsymbol{b} \equiv a_1 b_1 + a_2 b_2 + a_3 b_3$$

with the three-dimensional vectors $\boldsymbol{a}$ and $\boldsymbol{b}$.

The composite operator $\nabla\cdot$ is named divergence:

$$\nabla \cdot \boldsymbol{a} \equiv \frac{\partial a_1}{\partial x} + \frac{\partial a_2}{\partial y} + \frac{\partial a_3}{\partial z}$$

The cross product operator $\times$ is given by:

$$\boldsymbol{a} \times \boldsymbol{b} \equiv \begin{pmatrix} a_2 b_3 - a_3 b_2 \\ a_3 b_1 - a_1 b_3 \\ a_1 b_2 - a_2 b_1 \end{pmatrix}$$

The composite operator $\nabla\times$ is termed curl operator:

$$\nabla \times \boldsymbol{a} \equiv \begin{pmatrix} \frac{\partial a_3}{\partial y} - \frac{\partial a_2}{\partial z} \\ \frac{\partial a_1}{\partial z} - \frac{\partial a_3}{\partial x} \\ \frac{\partial a_2}{\partial x} - \frac{\partial a_1}{\partial y} \end{pmatrix}$$

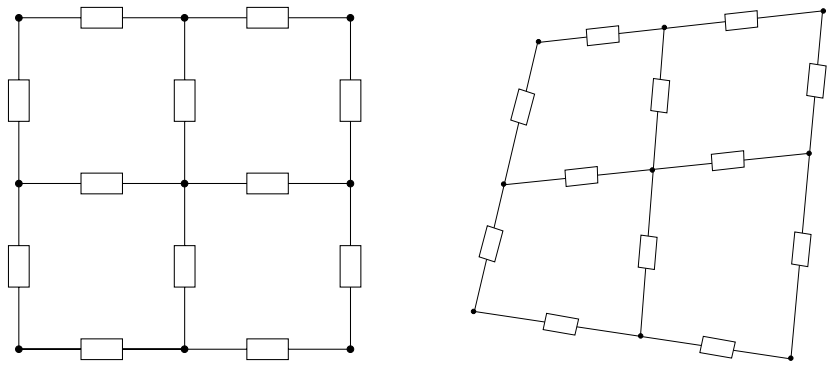

Fig. C.1. Deformation of two-dimensional grid of resistors with (a) reference configuration and (b) deformed configuration.

C Model of Stretch-Dependent Conductivity

C.1 Model Assumptions

A model of stretch-dependence of electrical conductivities was proposed describing transformations of conductivity attributed to a medium, which is deformed starting from the reference configuration [374]. Motivated is the model by two types of possible conductivity changes:

- Conductivity is unchanged and independent of deformation.
- The associated resistor between two arbitrary points remains the same in reference and deformed configuration.

The first type can be understood as a fluid-like behavior. The second type represents a behavior as shown by a grid of electrical resistors (Fig. C.1). The resistor between arbitrary node points is independent of the deformation. Also, the potential at node points resulting from applied current is independent of the deformation.

In principal the model of stretch-dependence of electrical conductivities is based on extracting stretch of regions resulting from an arbitrary deformation. The extracted stretch is used to transform a conductivity tensor attributed to the reference configuration. Different weights allow choosing a specific behavior of the conductivity.

Two formulations of stretch-dependence of electrical conductivities were proposed: a general and a restricted formulation. The general formulation is capable of handling full anisotropic material properties and arbitrary continuous deformations. The restricted formulation serves primarily for demonstration of the method and is only applicable if the deformation gradient is restricted in such a way, that the decomposition of the deformation gradient in a rotation and diagonal stretch tensor is possible.

C.2 General Formulation

Assumption. A conductivity tensor σ is modified by stretch to the conductivity tensor σ_s:

$$\sigma_s = \frac{1}{det\boldsymbol{W}}\boldsymbol{W}\sigma\boldsymbol{W}^T$$

with the second order weighting tensor $\boldsymbol{W}$. The tensor allows the transformation of the conductivity in such a way, that the upper two cases of conductivity changes and in between lying cases are selectable by a weighting parameter.

The weighting tensor $\boldsymbol{W}$ is a function of the weighting parameter θ:

$$\boldsymbol{W} = \boldsymbol{R}(\boldsymbol{I} + \theta(\boldsymbol{U} - \boldsymbol{I}))$$

with the unit tensor $\boldsymbol{I}$, the right stretch tensor $\boldsymbol{U}$ and rotation tensor $\boldsymbol{R}$. The weighting parameter θ is in the range $[0, 1]$. The tensors $\boldsymbol{U}$ and $\boldsymbol{R}$ are resulting from a polar decomposition of the deformation gradient $\boldsymbol{F}$ (Sect. 4.2.1):

$$\boldsymbol{F} = \boldsymbol{R}\,\boldsymbol{U}$$

Examples for Weighting Parameter. Two exemplary cases are examined to illustrate the influence of the weighting parameter θ.

Case 1: $a = 0$. The influence of stretch is neglected:

$$\boldsymbol{W} = \boldsymbol{R}$$

resulting in stretch independence of the conductivity:

$$\sigma_s = \boldsymbol{R}\sigma\boldsymbol{R}^T$$

Case 2: $a = 1$. The conductivity is weighted by the deformation gradient:

$$\boldsymbol{W} = \boldsymbol{R}\boldsymbol{U} = \boldsymbol{F}$$

The conductivity σ is transformed to the conductivity σ_s by:

$$\sigma_s = \frac{1}{det\boldsymbol{F}}\boldsymbol{F}\sigma\boldsymbol{F}^T$$

Proof. Aim of the following derivation is the definition of a transformation rule for electrical conductivity tensors [387]. In conjunction with Poisson's equations for fields of stationary electrical current the transformation rule leads to potentials functions, which are independent of material deformation. Different domains are distinguished: The domain Ω_0 is interpreted as reference. The domain Ω_t is resulting from deformation, i.e. coordinate transformation, of the reference.

Poisson's equation can be solved indirectly by minimizing an equivalent integral Π defined in a domain Ω concerning the unknown potential function

ϕ [4]. Commonly, boundary conditions are added to assure uniqueness of the solution.

The equivalent integral $\mathit{\Pi}_0$ describes the electrical power in the reference domain Ω_0:

$$\mathit{\Pi}_0 = \int_{\Omega_0} \frac{1}{2}(\nabla\phi_0)^T \sigma_0 (\nabla\phi_0) + f_0\phi_0 \; d\Omega_0 \tag{C.1}$$

with the conductivity tensor σ_0, the electrical source density current f_0 and the electrical potential function ϕ_0. A Dirichlet condition specifies the values at some part of the boundary $\Gamma_{0,D} \subset \Gamma_0$ with the function u_0:

$$\phi_0(\boldsymbol{x}) = u_0(\boldsymbol{x}) \text{ for } \boldsymbol{x} \in \Gamma_{0,D}$$

Equivalently, an integral $\mathit{\Pi}_t$ can be constructed in the deformed domain Ω_t:

$$\mathit{\Pi}_t = \int_{\Omega_t} \frac{1}{2}(\nabla\phi_t)^T \sigma_t (\nabla\phi_t) + f_t\phi_t \; d\Omega_t$$

with the conductivity tensor σ_t, the electrical source density current f_t and the electrical potential function ϕ_t. A Dirichlet condition specifies the values at some part of the boundary $\Gamma_{t,D} \subset \Gamma_t$ with the function u_t:

$$\phi_t(\boldsymbol{x}) = u_t(\boldsymbol{x}) \text{ for } \boldsymbol{x} \in \Gamma_{t,D}$$

The searched transformation rule for conductivity tensors necessitates equality of the potential functions at corresponding points:

$$\phi_0({}^0\boldsymbol{x}) = \phi_t({}^t\boldsymbol{x})$$

with the coordinate vectors ${}^0\boldsymbol{x}$ and ${}^t\boldsymbol{x}$ as defined in Sect. 4.2.1. This equality is valid also at the boundaries $\Gamma_{0,D}$ and $\Gamma_{t,D}$.

The integral $\mathit{\Pi}_t$ can be transformed into domain Ω_0:

$$\begin{aligned}\mathit{\Pi}_t &= \int_{\Omega_0} \left(\frac{1}{2}(\boldsymbol{G}\nabla\phi)^T \sigma_t (\boldsymbol{G}\nabla\phi) + f_t\phi\right) J \, d\Omega_0 \\ &= \int_{\Omega_0} \left(\frac{1}{2}\nabla\phi^T (\boldsymbol{G}^T\sigma_t\boldsymbol{G})\nabla\phi + f_t\phi\right) J \, d\Omega_0 \end{aligned} \tag{C.2}$$

with the Jacobian J and the reverse deformation gradient $\boldsymbol{G}$ determined by the coordinate transformation.

Comparison of equation C.1 and C.2 is applied to derive the transformation rule for conductivity tensors concerning deformation. The minimization of the integrals $\mathit{\Pi}_0$ and $\mathit{\Pi}_t$ concerning ϕ delivers:

$$\begin{aligned}\nabla \cdot (\sigma_0 \nabla\phi_0) &= f_0 \\ \nabla \cdot \left((\boldsymbol{G}^T\sigma_t\boldsymbol{G})\nabla\phi_t\right) &= f_t\end{aligned}$$

Equal potential functions are resulting from:

$$\sigma_0 = \boldsymbol{G}^T \sigma_t \boldsymbol{G}$$
$$f_0 = f_t$$

delivering a transformation rule:

$$\sigma_t = \boldsymbol{F} \sigma_0 \boldsymbol{F}^T$$

with the deformation gradient $\boldsymbol{F} = \boldsymbol{G}^{-1}$.

If the current per reference volume is assumed to be equal in the original and deformed configuration, the current source densities are determined by:

$$f_0({}^0\boldsymbol{x}) = \frac{1}{J} f_t({}^t\boldsymbol{x})$$

Thus, the transformation rule is given by:

$$\sigma_t = \frac{\boldsymbol{F} \sigma_0 \boldsymbol{F}^T}{J} \tag{C.3}$$

Usage of the with equation C.3 transformed conductivity and of the unmodified conductivity leads to the cases 1 and 2, respectively. Intermediate behavior can be defined by an using an appropriate weighting function W instead of the deformation gradient F.

Extension. Anisotropic behavior of the transformation rule can be defined by substitution of the weighing parameter θ with an appropriate weighting parameter tensor of higher order, e.g. the second order diagonal tensor Θ:

$$\Theta = \begin{pmatrix} \theta_x & 0 & 0 \\ 0 & \theta_y & 0 \\ 0 & 0 & \theta_z \end{pmatrix}$$

C.3 Restricted Formulation in Material Coordinate System

Extraction of Stretch. The stretch of myofibers in a voxel is determined by applying the deformation gradient $\boldsymbol{F}$ to the base of the material coordinate system $\boldsymbol{M}$:

$$\boldsymbol{M}' = \boldsymbol{F}\boldsymbol{M}$$

Base vectors of the material coordinate system M are the fiber orientation M_x, the sheet orientation M_y, and the sheet normal M_z:

$$\boldsymbol{M} = (M_x | M_y | M_z)$$

The stretch s_x, s_y, and s_z in direction of the fiber, the sheet and the sheet normal, respectively, are the lengths of the transformed corresponding base vectors $\boldsymbol{M}'_x$, $\boldsymbol{M}'_y$, and $\boldsymbol{M}'_z$:

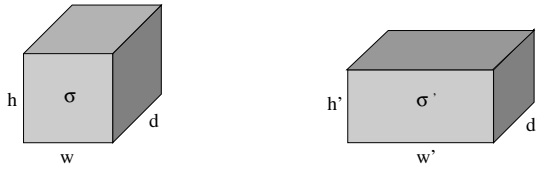

Fig. C.2. Cube and deformed cube. The undeformed cube is parameterized by a conductivity σ, width w, height h, and depth d. The deformed cube's parameters are a conductivity σ', width w', height h', and depth d'.

$$s_x = \sqrt{\boldsymbol{M}_x'^2}$$
$$s_y = \sqrt{\boldsymbol{M}_y'^2}$$
$$s_z = \sqrt{\boldsymbol{M}_z'^2}$$

Construction and Scaling of Conductivity Tensor. The conductivity tensor influenced by stretch in a local coordinate system is determined by:

$$\sigma_{s,local} = \begin{pmatrix} ((\frac{s_x}{s_y s_z} - 1)\theta + 1)\sigma_x & 0 & 0 \\ 0 & ((\frac{s_y}{s_x s_z} - 1)\theta + 1)\sigma_y & 0 \\ 0 & 0 & ((\frac{s_z}{s_x s_y} - 1)\theta + 1)\sigma_z \end{pmatrix}$$

with the conductivity σ_x in direction of the fiber, σ_y in direction of the sheet, and σ_z in direction of the sheet normal. The weighting parameter θ allows to select a specific material behavior.

For isovolumetric deformations, $s_x s_y s_z = 1$, the conductivity tensor reduces to:

$$\sigma_{s,local} = \begin{pmatrix} ((s_x^2 - 1)\theta + 1)\sigma_x & 0 & 0 \\ 0 & ((s_y^2 - 1)\theta + 1)\sigma_y & 0 \\ 0 & 0 & ((s_z^2 - 1)\theta + 1)\sigma_z \end{pmatrix}$$

Examples for Weighting Parameters. To illustrate the influence of the weighting parameter θ, two cases are exemplary examined. The examples base on a cube with a conductivity σ (in x-direction), a height h, a width $w = h$, and a depth $d = h$ (Fig. C.2). Hereby, the resistor R (in x-direction) of the cube is determined by

$$R = \frac{1}{h\sigma}$$

The cube is isovolumetric, transversal isotropic deformed with a stretch s, which delivers a deformed cube of width $w' = hs$, height $h' = \frac{h}{\sqrt{s}}$, and depth $d' = \frac{h}{\sqrt{s}}$. The conductivity of the deformed cube σ' is scaled with the weighting factor θ to

$$\sigma' = ((s^2 - 1)\theta + 1)\sigma$$

The resistor of the deformed cube R' is calculated by:

$$R' = \frac{s^2}{h\sigma'} = \frac{s^2}{h((s^2 - 1)\theta + 1)\sigma}$$

Case 1: $\theta = 0$. The influence of stretch is inhibited:

$$R'_{\theta=0} = \frac{s^2}{h\sigma}$$

resulting in a quadratic dependency of a corresponding resistor with respect to the stretch.
Case 2: $\theta = 1$. The corresponding resistor is independent on stretch:

$$R'_{\theta=1} = \frac{1}{h\sigma}$$

C.4 Coordinate System Transformation

A polar decomposition of the deformation gradient $\boldsymbol{F}$ delivers the rotation matrix $\boldsymbol{R}_F$, which is needed in conjunction with the rotation of the material coordinate system $\boldsymbol{R}_M$ to construct a summary rotation matrix $\boldsymbol{R}$:

$$\boldsymbol{R} = \boldsymbol{R}_M \boldsymbol{R}_F$$

The summary rotation matrix $\boldsymbol{R}$ is applied to transform the conductivity tensor $\sigma_{s,local}$ from the local coordinate into the global coordinate system $\sigma_{s,global}$:

$$\sigma_{s,global} = \boldsymbol{R}\sigma_{s,local}\boldsymbol{R}^T$$

References

1. L. da Vinci, "Drawing of a woman's torso," Anatomical Notebooks.
2. L. da Vinci, "The heart as a furnace," Codex Arundel, folder 24r.
3. D. C. Kay, *Schaum's Outline of Theory and Problems of Tensor Calculus*, McGraw-Hill, New York, San Francisco, Washington, 1988.
4. H. R. Schwarz, *Methode der finiten Elemente*, Teubner, Stuttgart, 3 edition, 1991.
5. W. H. Press, S. A. Teukolsky, W. T. Vetterling, and B. P. Flannery, *Numerical Recipes in C*, Cambridge University Press, Cambridge, New York, Melbourne, 2 edition, 1992.
6. W. Hackbusch, *Iterative Lösung großer schwachbesetzter Gleichungssysteme*, Teubner, Stuttgart, 2 edition, 1993.
7. W. Hackbusch and U. Trottenberg, *Lecture Notes in Mathematics, Multigrid Methods*, vol. 960, Springer, New York, 1982.
8. I. N. Bronštejn and K. A. Semendjaev, *Taschenbuch der Mathematik*, B. G. Teubner, Stuttgart; Leipzig, 1991.
9. H. R. Schwarz, *Numerische Mathematik*, Teubner, Stuttgart, 3 edition, 1993.
10. G. B. Buchanan, *Schaum's Outline of Theory and Problems of Finite Element Analysis*, McGraw-Hill, New York, San Francisco, Washington, 1994.
11. K. S. Yee, "Numerical solution of initial boundary value problems involving maxwell's equations in isotropic media," *IEEE Trans. Antennas Propagat.*, vol. AP-17, pp. 585–589, 1966.
12. J. A. Edminister, *Schaum's Outline: Elektromagnetismus - Theorie und Anwendung*, McGraw-Hill, Hamburg, 1984.
13. J. D. Jackson, *Klassische Elektrodynamik*, Walter de Gruyter, Berlin, New York, 2 edition, 1983.
14. R. Plonsey and D. B. Heppner, "Considerations of quasi-stationarity in electrophysiological systems," *Bulletin of mathematical biophysics*, vol. 29, pp. 657–664, 1967.
15. H. P. Schwan, "Electrical properties of tissue and cell suspensions," *Adv. Biol. Med. Phys.*, vol. 5, pp. 147–209, 1957.
16. R. Pethig, "Dielectrical properties of biological material: Biophysical and medical applications," *IEEE Trans. Elec. Ins.*, vol. EI-19, no. 5, pp. 453–474, 1984.
17. K. R. Foster and H. P. Schwan, "Dielectric properties of tissues and biological materials: A critical review," *Critical Reviews in Biomedical Engineering*, vol. 17, no. 1, pp. 25–104, 1989.

F.B. Sachse: LNCS 2966, pp. 299–322, 2004.

18. E. T. McAdams and J. Jossinet, "Tissue impedance: A historical overview," *Physiol. Meas.*, vol. 16, pp. A1–A13, 1995.
19. C. Gabriel, S. Gabriel, and E. Corthout, "The dielelectric properties of biological tissues: I. literature survey," *Phys. Med. Biol.*, vol. 41, pp. 2231–2249, 1996.
20. S. Gabriel, R. W. Lau, and C. Gabriel, "The dielelectric properties of biological tissues: II. measurements in the frequency range 10 Hz to 20 GHz," *Phys. Med. Biol.*, vol. 41, pp. 2251–2269, 1996.
21. S. Gabriel, R. W. Lau, and C. Gabriel, "The dielelectric properties of biological tissues: III. parametric models for the dielectric spectrum of tissues," *Phys. Med. Biol.*, vol. 41, pp. 2271–2293, 1996.
22. C. S. Henriquez, "Simulating the electrical behaviour of cardiac tissue using the bidomain model," *Critical Reviews in Biomedical Engineering*, vol. 21, no. 1, pp. 1–77, 1993.
23. J. Malmivuo and R. Plonsey, *Bioelectromagnetism*, Oxford University Press, New York; Oxford, 1995.
24. B. J. Roth, "Electrical conductivity values used with the bidomain model of cardiac tissue," *IEEE Transactions on Biomedical Engineering*, vol. 44, no. 4, pp. 326–327, Apr. 1997.
25. K.-J. Bathe, *Finite Element Procedures in Engineering Analysis*, Prentice Hall, Englewood Cliffs/NJ, 1982.
26. F. B. Sachse, *Modelle des menschlichen Körpers zur Berechnung von physikalischen Feldern*, Shaker, Aachen, 1998.
27. G. E. Mase, *Schaum's Outline of Theory and Problems of Continuum Mechanics*, McGraw-Hill, New York, San Francisco, Washington, 1970.
28. W. Maurel, Y. Wu, N. Magnenat Thalmann, and D. Thalmann, *Biomechanical Models for Soft Tissue Simulation*, Springer, Berlin, 1998.
29. K.-J. Bathe, *Finite Element Procedures*, Prentice Hall, Upper Saddle River, New Jersey, 1996.
30. Y. C. Fung, *Biomechanics: Mechanical Properties of Living Tissues*, Springer, New York, Berlin, Heidelberg, 1993.
31. H. Vogel, *Gerthsen Physik*, Springer Verlag, Berlin Heidelberg, 20 edition, 1999.
32. R. C. Gonzalez and R. E. Woods, *Digital Image Processing*, Addison-Wesley, Reading, Massachusetts; Menlo Park, California, 1992.
33. M. J. Ackerman, "Viewpoint: The Visible Human Project," *J. Biocommunication*, vol. 18, no. 2, pp. 14, 1991.
34. P. Haberäcker, *Digitale Bildverarbeitung: Grundlagen und Anwendungen*, Hanser, München; Wien, 1991.
35. R. C. Gonzalez and R. E. Woods, "Digital image fundamentals," in *Digital Image Processing*, chapter 2, pp. 21–80. Addison-Wesley, Reading, Massachusetts; Menlo Park, California, 1992.
36. N. Arad and D. Reisfeld, "Image warping using few anchor points and radial functions," *Computer Graphics Forum*, vol. 14, no. 1, pp. 35–46, 1995.
37. C. D. Werner, *Simulation der elektrischen Erregungsausbreitung in anatomischen Herzmodellen mit adaptiven zellulären Automaten*, Ph.D. thesis, Universität Karlsruhe (TH), Institut für Biomedizinische Technik, Berlin, 2001.
38. J. Canny, "A computational approach to edge detection," *IEEE Transactions on Pattern Analysis and Machine Intelligence*, vol. 8, no. 6, pp. 679–698, 1986.

39. O. Monga, R. Deriche, G. Malandain, and J. P. Cocquerez, "Recursive filtering and edge tracking: Two primary tools for 3-D edge detection," *Image and Vision Computing*, vol. 9, no. 4, pp. 203–214, Aug. 1991.
40. F. Maes, D. Vandermeulen, P. Suetens, and G. Marchal, "Computer-aided interactive delineation using an intelligent paintbrush technique," in *Computer Vision, Virtual Reality and Robotics in Medicine, Proc. First International Conference*. 1995, pp. 77–83, Springer.
41. M. Kass, A. Witkin, and D. Terzopoulos, "Snakes: Active contour models," *Int. J. Comput. Vision*, vol. 1, no. 4, pp. 321–331, 1988.
42. T. McInerney and D. Terzopoulos, "A finite element based deformable model for 3D biomedical image segmentation," in *SPIE*, 1993, vol. 1905, pp. 254–269.
43. T. J. McInerney and D. Terzopoulos, "Deformable models in medical image analysis: A survey," *Medical Image Analysis*, vol. 1, no. 2, pp. 91–108, 1996.
44. K. Mühlmann, "Modellbasierte Segmentation des menschlichen Thorax basierend auf klinischen tomographischen Aufnahmen," Diploma Thesis, Institut für Biomedizinische Technik, Universität Karlsruhe (TH), Jan. 1997.
45. N. H. Busch, F. B. Sachse, C. D. Werner, and O. Dössel, "Segmentation klinischer vierdimensionaler magnetresonanztomographischer Aufnahmen mittels Aktiver Kontur Modelle und haptischer Interaktion," in *Biomedizinische Technik*, Sep. 1998, vol. 43-1, pp. 526–529.
46. N. H. Busch, "Segmentation klinischer vierdimensionaler magnetresonanztomographischer Aufnahmen mittels Aktiver Kontur Modelle und haptischer Interaktion," Diploma Thesis, Institut für Biomedizinische Technik, Universität Karlsruhe (TH), Aug. 1998.
47. C. D. Werner, F. B. Sachse, K. Mühlmann, and O. Dössel, "Modellbasierte Segmentation klinischer MR-Aufnahmen," in *Bildverarbeitung für die Medizin 1998*, T. Lehmann, V. Metzler, K. Spitzer, and T. Tolxdorff, Eds., Berlin Heidelberg New York, 1998, pp. 274–278, Springer.
48. T. J. McInerney, *Topologically Adaptable Deformable Models for Medical Image Analysis*, Ph.D. thesis, University of Toronto, 1997.
49. L. D. Cohen, "On active contour models and balloons," *CVGIP: Image Understanding*, vol. 53, no. 2, pp. 211–218, Mar. 1991.
50. L. Thomas, F. B. Sachse, C. D. Werner, and O. Dössel, "Topologisch veränderbare dreidimensionale Aktive Konturen in der medizinischen Bildverarbeitung," in *Biomedizinische Technik*, Sep. 2000, vol. 45-1, pp. 509–510.
51. J.-O. Lachaud and A. Montanvert, "Deformable meshes with automated topology changes for coarse-to-fine 3D surface extraction," *Medical Image Analysis*, vol. 3, no. 2, pp. 187–207, 1999.
52. T. McInerney and D. Terzopoulos, "Medical image segmentation using topologically adaptable surfaces," in *CVRMed-MRCAS'97*. 1996, pp. 23–32, Springer.
53. L. Thomas, "Topologisch veränderbare dreidimensionale Aktive Konturen in der medizinischen Bildverarbeitung," Diploma Thesis, Institut für Biomedizinische Technik, Universität Karlsruhe (TH), Mar. 2000.
54. W. E. Lorensen and H. E. Cline, "Marching cubes: A high resolution 3D surface construction algorithm," *Computer Graphics*, vol. 21, no. 4, pp. 163–169, 1987.
55. W. Heiden, T. Goetze, and J. Brickmann, "'Marching-Cube'-Algorithmen zur schnellen Generierung von Isoflächen auf der Basis dreidimensionaler Datenfelder," in *Visualisierung von Volumendaten*, M. Frühauf and Martina G"obel, Eds., pp. 112–117. Springer, Berlin, Heidelberg, New York, 1991.

56. R. Malladi, J. A. Sethian, and B. C. Vemuri, "Shape modeling with front propagation: A level set approach," *IEEE Transactions on Pattern Analysis and Machine Intelligence*, vol. 17, no. 2, pp. 158–175, Feb. 1995.
57. J. S. Suri, K. Liu, S. N. Laxminarayan, and X. Zeng, "Shape recovery algorithms: Using level sets in 2-D/3-D medical imagery: A state-of-the-art review," *IEEE Trans. Inform. Techn. Biomed.*, vol. 6, no. 1, pp. 8–28, 2002.
58. P. Zerfass, F. B. Sachse, C. D. Werner, and O. Dössel, "Deformation of surface nets for interactive segmentation of tomographic data," in *Biomedizinische Technik*, Sep. 2000, vol. 45-1, pp. 483–484.
59. P. Zerfass, "Interaktive Deformation von Dreiecksnetzen zur Segmentation tomographischer Aufnahmen," Diploma Thesis, Institut für Biomedizinische Technik, Universität Karlsruhe (TH), Mar. 2000.
60. R. C. Gonzalez and R. E. Woods, "Image transforms," in *Digital Image Processing*, chapter 3, pp. 81–160. Addison-Wesley, Reading, Massachusetts; Menlo Park, California, 1992.
61. M. Wolf, "Detektion der Orientierung von Muskelfasern im Visible Man Datensatz," Diploma Thesis, Institut für Biomedizinische Technik, Universität Karlsruhe (TH), Apr. 1997.
62. R. C. Gonzalez and R. E. Woods, "Representation and description," in *Digital Image Processing*, chapter 8, pp. 483–570. Addison-Wesley, Reading, Massachusetts; Menlo Park, California, 1992.
63. B. Jähne, "Einfache Bildstrukturen," in *Orientierung und adaptive Filterung*, pp. 128–141. Springer, Berlin; Heidelberg; New York; London; Paris; Tokyo; Hong Kong; Barcelona; Budapest, 3 edition, 1993.
64. F. B. Sachse, M. Wolf, C. D. Werner, and K. Meyer-Waarden, "Extension of anatomical models of the human body: Three dimensional interpolation of muscle fiber orientation based on restrictions," *Journal of Computing and Information Technology*, vol. 6, no. 1, pp. 95–101, 1998.
65. H. Gray and W. H. Lewis, *Anatomy of the human body*, Lea & Febiger, Philadelphia, 20 edition, `http://www.bartleby.com/107/` 1918.
66. S. J. Crick, M. N. Sheppard, S. Y. Ho, L. Gebstein, and R. H. Anderson, "Anatomy of the pig heart: Comparisons with normal human cardiac structure," *J. Anat.*, vol. 193, pp. 105–119, 1998.
67. A. Agocha, A. V. Sigel, and M. Eghbali-Webb, "Characterization of adult human heart fibroblasts in culture: A comparative study of growth, proliferation and collagen production in human and rabbit cardiac fibroblasts and their response to transforming growth factor-beta$_1$," *Tissue Cell Res*, vol. 288, pp. 87–93, 1997.
68. D. M. Bers, *Excitation-Contraction Coupling and Cardiac Contractile Force*, Kluwer Academic Publishers, Dordrecht, Netherlands, 1991.
69. S. E. Campbell, A. M. Gerdes, and T. D. Smith, "Comparison of regional differences in cardiac myocyte dimensions in rats, hamsters, and guinea pigs," *The anatomical record*, vol. 219, pp. 53–59, 1987.
70. J. B. Caulfield and T. K. Borg, "The collagen network of the heart," *Laboratory Investigation*, vol. 40, no. 3, pp. 364–372, 1979.
71. R. A. Luke, E. C. Beyer, R. H. Hoyt, and J. E. Saffitz, "Quantitative analysis of intercellular connections by immunohistochemistry of the cardiac gap junction protein connexin43," *Circ Res.*, vol. 65, pp. 1450–1457, 1989.

72. R. B. Schuessler, J. P. Boineau, J. E. Saffitz, B. I. Bromberg, and K. F. Kwong, "Cellular mechanisms of sinuatrial activity," in *Cardiac Electrophysiology. From Cell to Bedside*, D. P. Zipes and J. Jalife, Eds., chapter 22, pp. 187–196. W. B. Saunders Company, Philadelphia, 2 edition, 1999.
73. H. Heller, M. Schaefer, and K. Schulten, "Molecular dynamics simulation of a bilayer of 200 lipids in the gel and in the liquid-crystal phases," *J. Phys. Chem.*, vol. 97, pp. 8343–8360, 1993.
74. F. Brette and C. Orchard, "T-tubule function in mammalian cardiac myocyte," *Circ Res.*, vol. 92, pp. 1182–1192, 2003.
75. B. M. Gumbiner, "Cell adhesion: The molecular basis of tissue architecture and morphogenesis," *Cell*, vol. 84, pp. 345–357, Feb. 1996.
76. H. Lodish, A. Berk, P. Matsudaira, C. A. Kaiser, M. Krieger, M. P. Scott, S. L. Zipursky, and J. Darnell, *Molecular Cell Biology*, W. H. Freeman and Company, New York, 2003.
77. D. W. Fawcett and N. S. McNutt, "The ultrastructure of cat myocardium. I. ventricular papillary muscle," *Cell Biol.*, vol. 42, pp. 1–45, 1969.
78. M.-L. Bang, T. Centner, F. Fornoff, A. J. Geach, M. Gotthardt, M. McNabb, C. C. Witt, D. Labeit, C. C. Gregorio, H. Granzier, and S. Labeit, "The complete gene sequence of titin, expression of a unusual ≈700-kDa titin isoform, and its interaction with obscurin identify a novel Z-line to I-band linking system," *Circ. Res.*, vol. 89, pp. 1065–1072, 2001.
79. S. T. Kazmierski, P. B. Antin, C. C. Witt, N. Huebner, A. S. McElhinny, S. Labeit, and C. C. Gregorio, "The complete mouse nebulin gene sequence and the identification of cardiac nebulin," *J. Mol. Bio.*, vol. 328, pp. 835–846, 2003.
80. P. E. Marszalek, H. Lu, H. Li, M. Carrion-Vazquez, A. F. Oberhauser, K. Schulten, and J. M. Fernandez, "Mechanical unfolding intermediates in titin modules," *Nature*, vol. 402, pp. 100–103, Nov. 1999.
81. National Center for Biotechnology Information, National Library of Medicine, National Institutes of Health, Bethesda, MD 20894, USA, "Molecular Modelling Database,"
`http://www.ncbi.nlm.nih.gov/entrez/query.fcgi?db=Structure`
82. J. Howard, "Molecular motors: Structural adaptations to cellular functions," *Nature*, vol. 389, pp. 561–567, 1997.
83. L. F. Chen, H. Winkler, M. K. Reedy, M. C. Reedy, and K. A. Tayler, "Molecular modeling of averaged rigor crossbridges from tomograms of flight muscle," *J Struct Biol*, vol. 138, no. 1-2, pp. 92–104, 2002.
84. David S. Goodsell, "Protein data bank. molecule of the month: Myosin," 2001.
`http://www.rcsb.org/pdb/molecules/pdb18_3.html`
85. G. Meissner, "Sarcoplasmic reticulum ion channels," in *Cardiac Electrophysiology. From Cell to Bedside*, D. P. Zipes and J. Jalife, Eds., chapter 6, pp. 51–58. W. B. Saunders Company, Philadelphia, 2 edition, 1999.
86. M. Inoue and J. H. B. Bridge, "Ca^{2+} sparks in rabbit ventricular myocytes evoked by action potentials," *Circ Res.*, vol. 92, pp. 532–538, 2003.
87. E. Marbán and G. F. Tomaselli, "Molecular biology of sodium channels," in *Cardiac Electrophysiology. From Cell to Bedside*, D. P. Zipes and J. Jalife, Eds., chapter 1, pp. 1–8. W. B. Saunders Company, Philadelphia, 2 edition, 1999.

88. P. B. Bennett and H.-G. Shin, "Biophysics of cardiac sodium channels," in *Cardiac Electrophysiology. From Cell to Bedside*, D. P. Zipes and J. Jalife, Eds., chapter 8, pp. 67–78. W. B. Saunders Company, Philadelphia, 2 edition, 1999.
89. C. W. Balke, E. Marbán, and B. O'Rourke, "Calcium channels: Structure, function, and regulation," in *Cardiac Electrophysiology. From Cell to Bedside*, D. P. Zipes and J. Jalife, Eds., chapter 2, pp. 8–21. W. B. Saunders Company, Philadelphia, 2 edition, 1999.
90. T. J. Kamp, Z. Zhou, S. Zhang, J. C. Makielski, and C. T. January, "Pharmacology of L- and T-type calcium channels in the heart," in *Cardiac Electrophysiology. From Cell to Bedside*, D. P. Zipes and J. Jalife, Eds., chapter 17, pp. 141–156. W. B. Saunders Company, Philadelphia, 2 edition, 1999.
91. R. L. Rasmusson, "Pharmacology of potassium channels," in *Cardiac Electrophysiology. From Cell to Bedside*, D. P. Zipes and J. Jalife, Eds., chapter 18, pp. 156–167. W. B. Saunders Company, Philadelphia, 2 edition, 1999.
92. P. Lipp and Martin D. Bootman, "The physiology and molecular biology of cardiac Na/Ca exchange," in *Cardiac Electrophysiology. From Cell to Bedside*, D. P. Zipes and J. Jalife, Eds., chapter 5, pp. 41–51. W. B. Saunders Company, Philadelphia, 2 edition, 1999.
93. R. A. Luke and J. E. Saffitz, "Remodeling of ventricular conduction pathways in healed canine infarct border zones," *J. Clin. Invest.*, vol. 87, pp. 1594–1602, 1991.
94. S. Dhein, *Cardiac Gap Junctions*, Karger, 1998.
95. M. Dellmar, G. E. Morley, J. F. Ek-Vitorin, D. Francis, N. Homma, K. Stergiopoulos, A. Lau, and S. M. Taffet, "Intracellular regulation of the cardiac gap junction channel connexin43," in *Cardiac Electrophysiology. From Cell to Bedside*, D. P. Zipes and J. Jalife, Eds., chapter 15, pp. 126–132. W. B. Saunders Company, Philadelphia, 2 edition, 1999.
96. M. S. Forbes and N. Sperelakis, "Intercalated discs of mammalian heart: A review of structure and function," *Tissue and Cell*, vol. 17, no. 5, pp. 605–648, 1985.
97. J. E. Saffitz and K. A. Yamada, "Gap junction distribution in the heart," in *Cardiac Electrophysiology. From Cell to Bedside*, D. P. Zipes and J. Jalife, Eds., chapter 21, pp. 271–277. W. B. Saunders Company, Philadelphia, 2 edition, 1999.
98. H. J. Jongsma and M. B. Rook, "Biophysics of cardiac gap junction channels," in *Cardiac Electrophysiology. From Cell to Bedside*, D. P. Zipes and J. Jalife, Eds., chapter 14, pp. 119–125. W. B. Saunders Company, Philadelphia, 2 edition, 1999.
99. Mark Yeager, "Molecular biology and structure of cardiac gap junction intercellular channels," in *Cardiac Electrophysiology. From Cell to Bedside*, D. P. Zipes and J. Jalife, Eds., chapter 4, pp. 31–40. W. B. Saunders Company, Philadelphia, 2 edition, 1999.
100. M. J. A. van Kempen, C. Fromaget, A. F. M. Moorman, and W. H. Lamers, "Spatial distribution of connexin43, the major gap junction protein, in the developing and adult heart," *Circ. Res.*, vol. 68, pp. 1638–1651, 1991.
101. J. E. Saffitz, J. G. Laing, and K. A. Yamada, "Connexin expression and turnover: Implications for cardiac excitability," *Circ. Res.*, vol. 86, pp. 723–728, 2000.

102. K. A. Yamada, J. G. Rogers, R. Sundset, T. H. Steinberg, and J. E Saffitz, "Up-regulation of connexin45 in heart failure," *J. Cardiovasc. Electrophysiol.*, vol. 14, pp. 1205–1212, 2003.
103. R. H. Hoyt, M. L. Cohen, and J. E. Saffitz, "Distribution and three-dimensional structure of intercellular junctions in canine myocardium," *Circ Res.*, vol. 64, pp. 563–574, 1989.
104. C. Abrahams, J. S. Janicki, and K. T. Weber, "Myocardial hypertrophy in macaca fascicularis: Structural remodeling of the collagen matrix," *Laboratory Investigation*, vol. 56, pp. 676–683, 1987.
105. H. Ju and I. M. C. Dixon, "Extracellular matrix and cardiovascular diseases," *Can. J. Cardiol.*, vol. 12, no. 12, pp. 1259–1267, 1996.
106. K. T. Weber, Y. Sun, S. C. Tyagi, and J. P. M. Cleutjens, "Collagen network of the myocardium: Function, structural remodeling and regulatory mechanisms," *J. Mol. Cell. Cardiol.*, vol. 26, pp. 279–292, 1994.
107. Thomas F. Robinson, Leona Cohen-Gould, and Stephen M. Factor, "Skeletal framework of mammalian heart muscle: Arrangement of inter- and pericellular connective tissue structures," *Laboratory Investigation*, vol. 49, no. 4, pp. 482–498, 1983.
108. I. J. LeGrice, B. H. Smaill, L. Z. Chai, S. G. Edgar, J. B. Gavin, and P. J. Hunter, "Laminar structure of the heart: Ventricular myocyte arrangement and connective tissue architecture in the dog," *Am J Physiol.*, vol. 269, pp. H571–H582, 1995.
109. P. J. Hanley, A. A. Young, I. J. LeGrice, S. G. Edgar, and D. S. Loiselle, "3-dimensional configuration of perimysial collagen fibres in rat cardiac muscle at resting and extended sarcomere lengths," *J. Physiol.*, vol. 517.3, pp. 831–837, 1999.
110. W. A. McAlpine, *Heart and Coronary Arteries*, Springer, Berlin, 1976.
111. D. D. Streeter, jr. and D. L. Bassett, "An engineering analysis of myocardial fiber orientation in pig's left ventricle in systole," *Anatomical Record*, vol. 155, pp. 503–512, 1966.
112. D. D. Streeter, "Gross morphology and fiber geometry of the heart," in *Handbook of Physiology: The Cardiovascular System*, Berne Bethesda, Ed., vol. I, pp. 61–112. American Physiology Society, 1979.
113. M. A. Fernandez-Teran and J. M. Hurle, "Myocardial fiber architecture of the human heart ventricles," *The Anatomical Record*, vol. 204, pp. 137–147, 1982.
114. A. F. Grimm, K. V. Katele, and H.-L. Lin, "Fiber bundle direction in the mammalian heart," *Basic Res. Cardiol.*, vol. 71, pp. 381–388, 1976.
115. A. A. Young, L. J. LeGrice, M. A. Young, and B. H. Smaill, "Extended confocal microscopy of myocardial laminae and collagen network," *J. Microscopy*, vol. 192, pp. 139–150, Nov. 1998.
116. K. Wang, S. Y. Ho, D. G. Gibson, and R. H. Anderson, "Architecture of atrial musculature in humans," *Brit. Heart J.*, , no. 73, pp. 559–565, 1995.
117. G. Bachmann, "The inter-auricular time interval," *Am J Physiol.*, vol. 41, pp. 309–320, 1916.
118. J. W. Papez, "Heart musculature of the atria," *Am J Anatomy*, vol. 27, pp. 255–286, 1920.
119. R. H. Anderson and A. E. Becker, *Anatomie des Herzens*, Georg Thieme Verlag, Stuttgart, 1982.

120. D. K. Racker, P. C. Ursell, and B. F. Hoffmann, "Anatomy of the tricuspid annulus: Circumferential myofibers as the structural basis for atrial flutter in a canine model," *Circ.*, vol. 84, pp. 841–851, 1991.
121. R. H. Anderson and S. Y. Ho, "The architecture of the sinus node, the atrioventricular conduction axis, and the internodal atrial myocardium," *J. Cardiovasc. Electrophysiol.*, vol. 9, pp. 1233–1248, 1998.
122. T. N. James, "The tendons of todaro and the "triangle of Koch"," *J. Cardiovasc. Electrophysiol.*, vol. 10, pp. 1478–1496, Nov. 1999.
123. M. A. McGuire, "Koch's triangle: Useful concept or dangerous mistake," *J. Cardiovasc. Electrophysiol.*, vol. 10, pp. 1497–1500, Nov. 1999.
124. W. Koch, "Weitere Mitteilungen über den Sinusknoten des Herzens," *Verhandlungen der Dt. Pathologischen Anatomie*, vol. 13, pp. 85–92, 1909.
125. W. Bargmann, "Bau des Herzens," in *Das Herz des Menschen*, W. Bargmann and W. Doerr, Eds., pp. 88–164. Georg Thieme Verlag, Stuttgart, 1963.
126. T. Lewis, *The Mechanism and Graphic Registration of the Heart Beat*, Shaw & Sons Ltd., London, 3 edition, 1925.
127. R. H. Anderson, M. J. Janse, F. J. L. van Capelle, J. Billette, A. E. Becker, and D. Durrer, "A combined morphological and electrophysiological study of the atrioventricular node of the rabbit heart," *Circ Res.*, vol. 35, pp. 909–922, Dec. 1974.
128. S. Tawara, *Das Reitzleitungssystem des Säugetierherzen*, G. Fischer, Jena, 1906.
129. S. J. Crick, J. Wharton, M. N. Sheppard, D. Royston, M. H. Yacoub, R. H. Anderson, and J. M. Pok, "Innervation of the human cardiac conduction system," *Circ.*, vol. 89, no. 4, pp. 1697–1708, 1994.
130. A. D. McCulloch, "Cardiac biomechanics," in *The Biomedical Engineering Handbook*, J. D. Bronzino, Ed., pp. 28–1–28–26. CRC Press, 2 edition, 2000.
131. F. B. Sachse, G. Seemann, and M. B. Mohr, "Multilevel integrative description of cardiac electro-mechanics," *Medical Image Analysis*, 2004, submitted.
132. Institut für Biomedizinische Technik, Universität Karlsruhe, Germany, "MEET Man project," . `http://www-ibt.etec.uni-karlsruhe.de/MEETMan`
133. A. van Doorn, P. H. M. Bovendeerd, K. Nicolay, M. R. Drost, and J. D. Janssen, "Determination of muscle fibre orientation using diffusion-weighted MRI," *European J. Morphology*, vol. 34, no. 1, pp. 5–10, 1996.
134. E. W. Hsu, A. L. Muzikant, S. A. Matulevicius, R. C. Penland, and C. S. Henriquez, "Magnetic resonance myocardial fiber-orientation mapping with direct histological correlation," *Am J Physiol.*, vol. 274, no. 43, pp. H1627–H1634, 1998.
135. D. F. Scollan, A. A. Holmes, R. L. Winslow, and J. Forder, "Histological validation of myocardial microstructure obtained from diffusion tensor magnetic resonance imaging," *Am J Physiol.*, vol. 275, no. 44, pp. H2308–H2318, 1998.
136. F. B. Sachse, C. Henriquez, G. Seemann, C. Riedel, C. D. Werner, R. C. Penland, B. Davis, and E. Hsu, "Modeling of fiber orientation in the ventricular myocardium with MR diffusion imaging," in *Proc. Computers in Cardiology*, Sep. 2001, vol. 28, pp. 617–620.
137. T. G. Reese, V. J. Wedeen, and R. M. Weisskoff, "Measuring diffusion in the presence of material strain," *J. Magnetic Resonance*, vol. 112, pp. 253–258, 1996.

138. W.-Y. I. Tseng, T. G. Reese, R. M. Weisskoff, and V. J. Wedeen, "Cardiac diffusion tensor MRI in vivo without strain correction," *J. MRM*, vol. 42, pp. 393–403, 1999.
139. W.-Y. I. Tseng, T. G. Reese, R. M. Weisskoff, T. J. Brady, and V. J. Wedeen, "Myocardial fiber shortening in humans: Initial results of MR imaging," *Radiology*, vol. 216, no. 1, pp. 128–139, 2000.
140. D. F. Scollan, A. A. Holmes, J. Zhang, and R. L. Winslow, "Reconstruction of myocardial architecture at high resolution using diffusion tensor MRI," in *Proc. 21th Conf. IEEE Eng. in Med. and Biol.*, 1999, p. 1071.
141. O. Abdallah, C. D. Werner, F. B. Sachse, and O. Dössel, "Zellulärer Automat zur Simulation der Erregungsausbreitung unter Berücksichtigung der Anisotropie," in *Biomedizinische Technik*, 1998, vol. 43, 1, pp. 490–491.
142. C. D. Werner, F. B. Sachse, and O. Dössel, "Electrical excitation propagation in the human heart," *Int. J. Bioelectromagnetism*, vol. 2, no. 2, 2000. `http://ee.tut.fi/rgi/ijbem/volume2/number2/werner/ paper_ijbem.htm`
143. F. B. Sachse, R. Frech, C. D. Werner, and O. Dössel, "A model based approach to assignment of myocardial fibre orientation," in *Proc. Computers in Cardiology*, 1999, vol. 26, pp. 145–148.
144. F. B. Sachse, C. D. Werner, M. H. Stenroos, R. F. Schulte, P. Zerfass, and O. Dössel, "Modeling the anatomy of the human heart using the cryosection images of the Visible Female dataset," in *Proc. Third Users Conference of the National Library of Medicine's Visible Human Project*, 2000. `http://www.nlm.nih.gov/research/visible/vhpconf2000/AUTHORS/SACHSE/SACHSE.HTM`
145. R. Schulte, F. B. Sachse, C. D. Werner, and O. Dössel, "Rule based assignment of myocardial sheet orientation," in *Biomedizinische Technik*, 2000, vol. 45-2, pp. 97–102.
146. C. D. Werner, "Vorverarbeitung des Visible Man Datensatzes," Diploma Thesis, Institut für Biomedizinische Technik, Universität Karlsruhe (TH), Apr. 1996.
147. C. D. Werner, M. Müller, F. B. Sachse, and K. Meyer-Waarden, "Vorverarbeitung des Visible Man Datensatzes," in *Biomedizinische Technik*, 1996, vol. 41, pp. 602–603.
148. F. B. Sachse, C. D. Werner, M. Müller, and K. Meyer-Waarden, "Preprocessing of the Visible Man dataset for the generation of macroscopic anatomical models," in *Proc. First Users Conference of the National Library of Medicine's Visible Human Project*, 1996. `http://www.nlm.nih.gov/research/visible/vhp_conf/sachse/vh1.htm`
149. S. Binhack, C. D. Werner, F. B. Sachse, and O. Dössel, "Vorverarbeitung des Visible Female Datensatzes," in *Biomedizinische Technik*, 1998, vol. 43, 1, pp. 528–529.
150. F. B. Sachse, M. Glas, M. Müller, and K. Meyer-Waarden, "Segmentation and tissue-classification of the Visible Man dataset using the computertomographic scans and the thin-section photos," in *Proc. First Users Conference of the National Library of Medicine's Visible Human Project*, 1996. `http://www.nlm.nih.gov/research/visible/vhp_conf/sachse/vh2.htm`
151. F. B. Sachse, C. D. Werner, and O. Dössel, "Knowledge based assignment of ventricular muscle fibre orientation," in *Proc. CARS 1999*, 1999, p. 1028.

152. H. Antoni, "Erregungsphysiologie des Herzens," in *Physiologie des Menschen*, R. F. Schmidt, G. Thews, and F. Lang, Eds., chapter 23, pp. 472–497. Springer, Berlin, Heidelberg, New York, 2000.
153. J. Malmivuo and R. Plonsey, "The heart," in *Bioelectromagnetism*, chapter 6, pp. 119–130. Oxford University Press, New York; Oxford, 1995.
154. B. Hille, *Ionic channels of excitable membranes*, Sinauer Associates, 2 edition, 1992.
155. E. White, J.-Y. Le Guennec, J. M. Nigretto, F. Gannier, J. A. Argibay, and D. Garnier, "The effects of increasing cell length on auxotonic contractions; membrane potential and intracellular calcium transients in single guinea-pig ventricular myocytes," *Exp Physiol.*, vol. 78, no. 1, pp. 65–78, 1993.
156. A. L. Hodgkin and A. F. Huxley, "A quantitative description of membrane current and its application to conduction and excitation in nerve," *J. Physiol*, vol. 177, pp. 500–544, 1952.
157. M. C. Sanguinetti and M. Tristani-Firouzi, "Delayed and inward rectifier potasium channels," in *Cardiac Electrophysiology. From Cell to Bedside*, D. P. Zipes and J. Jalife, Eds., chapter 9, pp. 79–86. W. B. Saunders Company, Philadelphia, 2 edition, 1999.
158. K. Shivkumar and J. N. Weiss, "Adenosine triphospate-sensitive potassium channels," in *Cardiac Electrophysiology. From Cell to Bedside*, D. P. Zipes and J. Jalife, Eds., chapter 10, pp. 86–93. W. B. Saunders Company, Philadelphia, 2 edition, 1999.
159. R. S. Kass and W. Wang, "Regulatory and molecular properties of delayed potassium channels in the heart: Relationship to human disease," in *Cardiac Electrophysiology. From Cell to Bedside*, D. P. Zipes and J. Jalife, Eds., chapter 12, pp. 104–112. W. B. Saunders Company, Philadelphia, 2 edition, 1999.
160. D.-W. Liu, G. A. Gintant, and C. Antzelevitch, "Ionic bases for electrophysiological distinctions among epicardial, midmyocardial, and endocardial myocytes from the free wall of the canine left ventricle," *Circ Res.*, vol. 72, no. 3, pp. 671–687, 1993.
161. D.-W. Liu and C. Antzelevitch, "Characteristics of the delayed rectifier current (i_{Kr} and i_{Ks}) in canine ventricular epicardial, midmyocardial and endocardial myocytes: a weaker i_{Ks} contributes to the longer action potential of the M cell," *Circ Res.*, vol. 76, pp. 351–365, 1995.
162. D. L. Weiß, G. Seemann, F. B. Sachse, and O. Dössel, "Investigation of electrophysiological heterogeneity and anisotropy across the human ventricular wall," in *Biomedizinische Technik*, 2003, vol. 48-1, pp. 228–229.
163. D. L. Weiß, "Charakterisierung der Ventrikelwand durch anatomische und elektrophysiologische Modellierung," Diploma Thesis, Institut für Biomedizinische Technik, Universität Karlsruhe (TH), Sep. 2003.
164. C. R. Weber, V. Piacentino III, K. S. Ginsburg, S. R. Houser, and D. M. Bers, "$Na^+ - Ca^{2+}$ exchange current and submembrane $[Ca^{2+}]$ during the cardiac action potential," *Circ. Res.*, vol. 90, pp. 182–189, 2001.
165. C. R. Weber, V. Piacentino III, K. B. Margulies, D. M. Bers, and S. R. Houser, "Calcium influx via I_{NCX} is favored in failing human ventricular myocytes.," *Ann. N. Y. Sci.*, vol. 976, pp. 478–479, 2002.
166. S. E. Litwin, J. Li, and J. H. B. Bridge, "Na-Ca exchange and the trigger for sarcoplasmic reticulum Ca release: Studies in adult rabitt ventricular myocytes," *Biophys J*, vol. 75, pp. 359–371, 1998.

167. A. Fabiato and F. Fabiato, "Contractions induced by a calcium-triggered release of calcium for the sarcoplasmic reticulum of single skinned cardiac cells," *J. Physiol. Lond.*, vol. 249, pp. 469–495, 1975.
168. F. DelPrincipe, M. Egger, and E. Niggli, "Calcium signalling in cardiac muscle: Refractoriness revealed by coherent activation," *Nature Cell Biology*, vol. 1, pp. 323–329, Oct. 1999.
169. W. F. Bluhm, E. G. Kranias, W. H. Dillmann, and M. Meyer, "Phospolamban: A major determinant of the cardiac force-frequency relationship," *Am J Physiol.*, vol. 278, pp. H249–H255, 2000.
170. D. Noble, "A modification of the Hodgkin-Huxley equation applicable to Purkinje fibre action and pacemaker potentials," *J. Physiol.*, vol. 160, pp. 317–352, 1962.
171. R. E. McAllister, D. Noble, and R. W. Tsien, "Reconstruction of the electrical activitity of cardiac purkinje fibres," *J. Physiol.*, vol. 251, pp. 1–59, 1975.
172. G. W. Beeler and H. Reuter, "Reconstruction of the action potential of ventricular myocardial fibres," *J. Physiol.*, vol. 268, pp. 177–210, 1977.
173. K. Yanagihara, A. Noma, and H. Irisawa, "Reconstruction of sino-atrial node pacemaker potential based on the voltage clamp experiments," *Jpn. J. Physiol.*, vol. 30, no. 6, pp. 841–857, 1980.
174. D. G. Bristow and J. W. Clark, "A mathematical model of primary pacemaker cell in sa node of the heart," *Am J Physiol.*, vol. 243, no. 2, pp. H207–18, 1982.
175. D. G. Bristow and J. W. Clark, "A mathematical model of the vagally driven primary pacemaker," *Am J Physiol.*, vol. 244, no. 1, pp. H150–61, 1983.
176. D. Noble and S. J. Noble, "A model of sino-atrial node electrical activity based on a modification of the DiFrancesco-Noble (1984) equations," *Proc. R. Soc. Lond. B. Biol. Sci.*, vol. 222, pp. 295–304, 1984.
177. D. DiFrancesco and D. Noble, "A model of cardiac electrical activity incorporating ionic pumps and concentration changes," *Phil. Trans. R. Soc. Lond.*, vol. 307, pp. 353–398, 1985.
178. D. W. Hilgemann and D. Noble, "Excitation-contraction coupling and extracellular calcium transients in rabbit atrium: Reconstruction of basic cellular mechanisms," *Proc. R. Soc. Lond.*, vol. 230, pp. 163–205, 1987.
179. Y. E. Earm and D. Noble, "A model of single atrial cell: Relation between calcium current and calcium release," *Proc. R. Soc. Lond.*, vol. 240, pp. 83–96, 1990.
180. C.-H. Luo and Y. Rudy, "A model of the ventricular cardiac action potential," *Circ Res.*, vol. 68, no. 6, pp. 1501–1526, 1991.
181. C.-H. Luo and Y. Rudy, "A dynamic model of the ventricular cardiac action potential: I. simulations of ionic currents and concentration changes," *Circ Res.*, vol. 74, no. 6, pp. 1071–1096, 1994.
182. C.-H. Luo and Y. Rudy, "A dynamic model of the ventricular cardiac action potential: II. afterdepolarizations, triggered activity, and potentiation," *Circ Res.*, vol. 74, no. 6, pp. 1097–1113, 1994.
183. S. S. Demir, J. W. Clark, C. R. Murphey, and W. R. Giles, "A mathematical model of a rabbit sinoatrial node cell," *Am J Physiol.*, vol. 35, pp. 832–852, 1994.
184. S. Dokos, B. G. Celler, and N. H. Lovell, "Vagal control of sinoatrial rhythm: A mathematical model," *J. of theor. Biol.*, vol. 182, pp. 21–44, Sep. 1996.

185. S. S. Demir, B. O'Rourke, G. F. Tomaselli, E. Marbán, and R. L. Winslow, "Action potential variation in canine ventricle: A modeling study," in *Proc. Computers in Cardiology*, 1996, vol. 23, pp. 221–224.
186. D. S. Lindblad, C. R. Murphey, J. W. Clark, and W. R. Giles, "A model of the action potential and underlying membrane currents in a rabbit atrial cell," *Am J Physiol.*, vol. 271, no. 4 Pt 2, pp. 1666–96, 1996.
187. M. Courtemanche, R. J. Ramirez, and S. Nattel, "Ionic mechanisms underlying human atrial action potential properties: Insights from a mathematical model," *Am J Physiol.*, vol. 275, no. 44, pp. H301–H321, 1998.
188. M. S. Jafri, J. J. Rice, and R. L. Winslow, "Cardiac Ca^{2+} dynamics: The roles of ryanodine receptor adapation and sarcoplasmic reticulum load," *Biophysical J*, vol. 74, pp. 1149–1168, Mar. 1998.
189. D. Noble, A. Varghese, P. Kohl, and P. Noble, "Improved guinea-pig ventricular cell model incorporating a diadic space, I_{Kr} and I_{Ks}, and length- and tension-dependend processes," *Can. J. Cardiol.*, vol. 14, no. 1, pp. 123–134, Jan. 1998.
190. A. Nygren, C. Fiset, L. Firek, J. W. Clark, D. S. Lindblad, R. B. Clark, and W. R. Giles, "Mathematical model of an adult human atrial cell," *Circ Res.*, vol. 82, pp. 63–81, 1998.
191. L. Priebe and D. J. Beuckelmann, "Simulation study of cellular electric properties in heart failure," *Circ Res.*, vol. 82, pp. 1206–1223, 1998.
192. R. L. Winslow, J. J. Rice, S. Jafri, E. Marbán, and B. O'Rourke, "Mechanisms of altered excitation-contraction coupling in canine tachycardia-induced heart failure, II model studies," *Circ Res.*, vol. 84, pp. 571–586, 1999.
193. B. O'Rourke, D. A. Kass, G. F. Tomaselli, S. Kaab, R. Tunin, and E. Marbán, "Mechanisms of altered excitation-contraction coupling in canine tachycardia-induced heart failure, I experimental studies," *Circ. Res*, vol. 84(5), pp. 562–570, 1999.
194. R. J. Ramirez, S. Nattel, and M. Courtemanche, "Mathematical analysis of canine atrial action potentials: Rate, regional factors, and electrical remodeling," *Am. J. Physiol. Heart Circ. Physiol.*, vol. 279, pp. H1767–H1785, 2000.
195. H. Zhang, A. V. Holden, I. Kodama, H. Honjo, M. Lei, T. Varghese, and M. R. Boyett, "Mathematical models of action potentials in the periphery and center of the rabbit sinoatrial node," *Am J Physiol.*, vol. 279, no. 1, pp. 397–421, 2000.
196. O. Bernus, R. Wilders, C. W. Zemlin, H. Verschelde, and A. V. Panfilov, "A computationally efficient electrophysiological model of human ventricular cells," *Am J Physiol.*, vol. 282, pp. H2296–H2308, 2002.
197. F. B. Sachse, G. Seemann, K. Chaisaowong, and D. Weiß, "Quantitative reconstruction of cardiac electromechanics in human myocardium: assembly of electrophysiological and tension generation models," *J Cardiovasc Electrophysiol*, vol. 14, no. S10, pp. S210–S218, Oct. 2003.
198. G. Seemann, F. B. Sachse, D. L. Weiß, and O. Dössel, "Quantitative reconstruction of cardiac electromechanics in human myocardium: regional heterogeneity," *J Cardiovasc Electrophysiol*, vol. 14, no. S10, pp. S219–S228, Oct. 2003.
199. K. H. W. J. Ten Tusscher, D. Noble, P. J. Noble, and A. V. Panfilov, "A model for human ventricular tissue," *Am J Physiol. Heart Circ. Physiol.*, 2003, Epub ahead of print.

200. J. Zeng, K. R. Laurita, D. S. Rosenbaum, and Y. Rudy, "Two components of the delayed rectifier K^+ current in ventricular myocytes of the guinea pig type: Theoretical formulation and their role in repolarization," *Circ Res.*, vol. 77, pp. 140–152, 1995.
201. D. J. Beuckelmann, M. Nabauer, and E. Erdmann, "Intracellular calcium handling in isolated ventricular myocytes from patients with terminal heart failure," *Circ.*, vol. 85, pp. 1046–1055, 1992.
202. P. Kohl, K. Day, and D. Noble, "Cellular mechanisms of cardiac mechanoelectric feedback in a mathematical model," *Can. J. Cardiol.*, vol. 14, no. 1, pp. 111–119, 1998.
203. P. Noble, "-," personal communication, 2000.
204. F. B. Sachse, C. Riedel, C. D. Werner, and G. Seemann, "Stretch activated ion channels in myocytes: Parameter estimation, simulations and phenomena," in *Proc. 23rd Conf. IEEE Eng. in Med. and Biol.*, Oct. 2001, vol. 1, pp. 52–55.
205. F. Sachs, "Modeling mechanical-electrical transduction in the heart," in *Cell Mechanics and Cellular Engineering*, C. Mow, F. Guilak, R. Tran-Son-Tay, and R. M. Hochmuth, Eds., pp. 308–328. Springer, New York, 1994.
206. J. Zeng and Y. Rudy, "Early afterdepolarizations in cardiac myocytes: Mechanism and rate dependence," *Biophys J*, vol. 68, pp. 949–964, Mar. 1995.
207. J. Malmivuo and R. Plonsey, "12-lead ECG system," in *Bioelectromagnetism*, chapter 15, pp. 277–289. Oxford University Press, New York; Oxford, 1995.
208. J. Malmivuo and R. Plonsey, "Magnetocardiography," in *Bioelectromagnetism*, chapter 20, pp. 336–360. Oxford University Press, New York; Oxford, 1995.
209. J. E. Burnes, B. Taccardi, R. S. MacLeod, and Y. Rudy, "Noninvasive ecg imaging of electrophysiologically abnormal substrates in infarcted hearts: A model study," *Circ.*, vol. 8, pp. 533–540, Feb. 2000.
210. M. R. Franz, "Monophasic action potential recording," in *Cardiac Electrophysiology. From Cell to Bedside*, D. P. Zipes and J. Jalife, Eds., chapter 26, pp. 763–770. W. B. Saunders Company, Philadelphia, 3 edition, 1999.
211. R. J. Schilling, N. S. Peters, and D. W. Davies, "Simultaneous endocardial mapping in the human left ventricle using a noncontact catheter," *Circ.*, vol. 98, pp. 887–898, 1998.
212. P. Kohl, "Heterogeneous cell coupling in the heart: An electrophysiological role for fibroblasts," *Circ. Res.*, vol. 93, pp. 381–383, 2003.
213. G. Gaudesius, M. Miragoli, S. P. Thomas, and S. Rohr, "Coupling of cardiac electrical activity over extended distances by fibroblasts of cardiac origin," *Circ. Res.*, vol. 93, pp. 421–428, 2003.
214. M. S. Spach, J. F. Heidlage, and P. C. Dolber, "The dual nature of anisotropic discontinous conduction in the heart," in *Cardiac Electrophysiology. From Cell to Bedside*, D. P. Zipes and J. Jalife, Eds., chapter 25, pp. 213–222. W. B. Saunders Company, Philadelphia, 2 edition, 1999.
215. A. G. Kléber, V. G. Fast, and S. Rohr, "Continuous and discontinuous propagation," in *Cardiac Electrophysiology. From Cell to Bedside*, D. P. Zipes and J. Jalife, Eds., chapter 24, pp. 213–222. W. B. Saunders Company, Philadelphia, 2 edition, 1999.
216. A. T. Winfree, *When Time Breaks Down*, Princeton University Press, Princeton, 1987.

217. R. A. Gray, K. Takkellapati, and J. Jalife, "Dynamics and anatomical correlations of atrial flutter and fibrillation," in *Cardiac Electrophysiology. From Cell to Bedside*, D. P. Zipes and J. Jalife, Eds., chapter 41, pp. 356–263. W. B. Saunders Company, Philadelphia, 2 edition, 1999.
218. M. J. Janse, "Mechanisms of atrial fibrillation," in *Cardiac Electrophysiology. From Cell to Bedside*, D. P. Zipes and J. Jalife, Eds., chapter 55, pp. 476–481. W. B. Saunders Company, Philadelphia, 2 edition, 1999.
219. M. S. Spach and J. F. Heidlage, "The stochastic nature of cardiac propagation at a microscopic level," *Circ Res.*, vol. 76, no. 3, pp. 118–130, 1995.
220. N. Wiener and A. Rosenblueth, "The mathematical formulation of the problem of conduction of impulses in a network of connected excitable elements, specifically in cardiac muscle," *Arch. Del. Instit. De Cardiologia De Mexico*, vol. 16, pp. 205–265, 1946.
221. G. K. Moe, W. C. Rheinboldt, and J. A. Abildskov, "A computer model of atrial fibrillation," *Am. Heart J*, vol. 67, pp. 200–220, 1964.
222. W. J. Eifler and R. Plonsey, "A cellular model for the simulation of activation in the ventricular myocardium," *J. Electrocardiology*, vol. 8, no. 2, pp. 117–128, 1975.
223. R. Killmann, P. Wach, and F. Dienstl, "Three-dimensional computer model of the entire human heart for simulation of reentry and tachycardia: Gap phenomenon and Wolff-Parksinson-White syndrome," *Basic Research in Cardiology*, vol. 86, no. 5, pp. 485–501, 1991.
224. B. E. H. Saxberg and R. J. Cohen, "Cellular automata models of cardiac conduction," in *Theory of Heart*, L. Glass, P. Hunter, and A. McCulloch, Eds., pp. 437–476. Springer, Berlin, Heidelberg, New York, 1991.
225. D. Wei, O. Okazaki, K. Harumi, E. Harasawa, and H. Hosaka, "Comparative simulation of excitation and body surface electrocardiogram with isotropic and anisotropic computer heart models," *IEEE Transactions on Biomedical Engineering*, vol. 42, no. 4, pp. 343–357, Apr. 1995.
226. P. Siregar, J. P. Sinteff, M. Chahine, and P. Le Beux, "A cellular automata model of the heart and its coupling with a qualitative model," *Computers and Biomedical Research*, vol. 29, pp. 222–246, 1996.
227. C. D. Werner, F. B. Sachse, and O. Dössel, "Applications of the Visible Man dataset in electrocardiology: Simulation of the electrical excitation propagation," in *Proc. Second Users Conference of the National Library of Medicine's Visible Human Project*, 1998, pp. 69–79.
`http://www.nlm.nih.gov/research/visible/vhpconf98/AUTHORS/WERNER/WERNER.HTM`
228. P. Siregar, J. P. Sinteff, N. Julen, and P. Le Beux, "An interactive 3D anisotropic cellular automata model of the heart," *Computers and Biomedical Research*, vol. 31, pp. 323–347, 1998.
229. M. Delorme, "An introduction to cellular automata," in *Cellular Automata*, M. Delorme and J. Mazoyer, Eds., chapter 1, pp. 5–49. Kluwer, Dordrecht, 1999.
230. T. A. Sudkamp, *Languages and Machines*, Addison-Wesley, Reading, Massachusetts; Menlo Park, California, 2 edition, 1997.

231. F. B. Sachse, C. D. Werner, K. Meyer-Waarden, and O. Dössel, "Applications of the Visible Man dataset in electrocardiology: Calculation and visualization of body surface potential maps of a complete heart cycle," in *Proc. Second Users Conference of the National Library of Medicine's Visible Human Project*, 1998, pp. 47–48.
`http://www.nlm.nih.gov/research/visible/vhpconf98/AUTHORS/SACHSE/SACHSE.HTM`
232. A. L. Bardou, P. M. Auger, R. Seigneuric, and J.-L. Chassé, "Cellular automata models and cardiac arrhythmias," in *Cellular Automata*, M. Delorme and J. Mazoyer, Eds., chapter 10, pp. 279–292. Kluwer, Dordrecht, 1999.
233. D. L. Weiß, F. B. Sachse, C. D. Werner, G. Seemann, and O. Dössel, "Vergleich elektrophysiologischer Modelle bei simulierten atrialen Fibrillationen," in *Biomedizinische Technik*, Sep. 2001, vol. 46-1, pp. 514–515.
234. A. L. Waldo, "Atrial flutter: Mechanisms, clinical features, and management," in *Cardiac Electrophysiology. From Cell to Bedside*, D. P. Zipes and J. Jalife, Eds., chapter 54, pp. 468–476. W. B. Saunders Company, Philadelphia, 2 edition, 1999.
235. M. R. Boyett, A. Clough, J. Dekanski, and A. V. Holden, "Modelling cardiac excitation and excitability," in *Computational Biology of the Heart*, A. Panfilov and A. V. Holden, Eds., chapter 1, pp. 1–48. John Wiley & Sons, Chichester, 1997.
236. R. A. FitzHugh, "Impulses and physiological states in theoretical models of nerve membran," *Biophys J*, vol. 1, pp. 445–466, 1961.
237. J. M. Rogers and A. D. McCulloch, "A collocation-Galerkin finite element model of cardiac action potential propagation," *IEEE Transactions on Biomedical Engineering*, vol. 41, no. 8, pp. 743–757, Aug. 1994.
238. J. Rogers, M. Courtemanche, and A. McCulloch, "Finite element methods for modelling impulse propagation in the heart," in *Computational Biology of the Heart*, A. Panfilov and A. V. Holden, Eds., chapter 7, pp. 217–234. John Wiley & Sons, Chichester, 1997.
239. J. P. Keener and A. V. Panfilov, "The effects of geometry and fibre orientation on propagation and extracellular potentials in myocardium," in *Computational Biology of the Heart*, A. V. Panfilov and A. V. Holden, Eds., pp. 235–258. John Wiley & Sons, Chichester, 1997.
240. A. V. Panfilov, "Three-dimensional wave propagation in mathematical models of ventricular fibrillation," in *Cardiac Electrophysiology. From Cell to Bedside*, D. P. Zipes and J. Jalife, Eds., chapter 31, pp. 271–277. W. B. Saunders Company, Philadelphia, 2 edition, 1999.
241. J. M. Rogers, "Modeling the cardiac action potential using b-spline surfaces," *IEEE Transactions on Biomedical Engineering*, vol. 47, no. 6, pp. 784–791, June 2000.
242. Y. Rudy and W. Quan, "Mathematical model of reentry of cardiac excitation," in *Proc. Computers in Cardiology*, 1989, vol. 16, pp. 135–136.
243. N. Virag, O. Blanc, J. M. Vesin, J. Koerfer, and L. Kappenberger, "Study of the mechanisms of arrhythmias in an anatomical computer model of human atria," in *Proc. Computers in Cardiology*, 1999, vol. 26, pp. 113–116.
244. O. Blanc, N. Virag, J.-M. Vesin, and L. Kappenberger, "A computer model of human atria with reasonable computation load and realistic anatomical properties," *IEEE Transactions on Biomedical Engineering*, vol. 48, no. 11, pp. 1229–1237, Nov. 2001.

245. R. Plonsey and R. C. Barr, "Mathematical modeling of electrical activity of the heart," *J. Electrocardiology*, vol. 20, no. 3, pp. 219–226, 1987.
246. C. S. Henriquez and R. Plonsey, "A bidomain model for simulating propagation in multicellular cardiac tissue," in *Proc. of the Annual International Conference of the IEEE Engineering in Medicine and Biology Society*, 1989, vol. 4, p. 1266.
247. N. G. Sepulveda and J. P. Wikswo, "Bipolar stimulation of cardiac tissue using an anisotropic bidomain model," *J. Cardiovasc. Electrophysiol.*, vol. 5, no. 3, pp. 258–267, May 1994.
248. C. S. Henriquez, A. L. Muzikant, and C. K. Smoak, "Anisotropy, fiber curvature and bath loading effects on activation in thin and thick cardiac tissue preparations: Simulations in a three-dimensional bidomain model," *J. Cardiovasc. Electrophysiol.*, vol. 7, no. 5, pp. 424–444, May 1996.
249. K. Simelius, J. Nenonen, and B. M. Horacek, "Simulation of anisotropic propagation in the myocardium with a hybrid bidomain model," in *Functional Imaging and Modeling of the Heart*, T. Katila, I. E. Magnin, P. Clarysse, J. Montagnat, and J. Nenonen, Eds., pp. 140–147. Springer, 2001.
250. N. Hooke, C. S. Henriquez, P. Lanzkron, and D. Rose, "Linear algebraic transformations of the bidomain equations: Implications to numerical methods," *Crit Rev Biomed Eng*, vol. 120, pp. 127–145, 1992.
251. C. Antzelevitch, G. Yan, W. Shimizu, and A. Burashnikov, "Electrical heterogeneity, the ECG, and cardiac arrhythmias," in *Cardiac Electrophysiology. From Cell to Bedside*, D. P. Zipes and J. Jalife, Eds., chapter 26, pp. 222–238. W. B. Saunders Company, Philadelphia, 3 edition, 1999.
252. G. Seemann, F. B. Sachse, C. Riedel, C. D. Werner, and O. Dössel, "Regional and frequency dependencies of force development in the myocardium: A simulation study," in *Proc. Computers in Cardiology*, Sep. 2001, vol. 28, pp. 345–348.
253. P. Hunter, M. P. Nash, and G. P. Sands, "Computational electromechanics of the heart," in *Computational Biology of the Heart*, A. V. Panfilov and A. V. Holden, Eds., pp. 345–408. John Wiley & Sons, Chichester, 1997.
254. J. M. Guccione, A. D. McCulloch, and L. K. Waldman, "Passive material properties of intact ventricular myocardium determined from a cylindrical model," *J. Biomechanical Engineering*, vol. 113, pp. 42–55, Feb. 1991.
255. R. J. Okamoto, M. J. Moulton, S. J. Peterson, D. Li, M. K. Pasque, and J. M. Guccione, "Epicardial suction: A new approach to mechanical testing of the passive ventricular wall," *J. Biomedical Engineering*, vol. 122, pp. 479–487, Oct. 2000.
256. M. R. Zile, M. K. Cowles, J. M. Buckley, K. Richardson, B. A. Cowles, C. F. Baicu, G. Cooper, and V. Gharpuray, "Gel stretch method: A new method to measure constitutive properties of cardiac muscle cells," *Am J Physiol.*, vol. 274, pp. H2188–H2202, 1998.
257. E. H. Sonnenblick, "Series elastic and contractile elements in heart muscles: Changes in muscle length," *Am J Physiol.*, vol. 207, no. 6, pp. 1330–1338, 1964.
258. J. G. Pinto and Y. C. Fung, "Mechanical properties of the heart muscle in the passive state," *J. Biomechanics*, vol. 6, pp. 597–616, 1973.
259. R. F. Janz and A. F. Grimm, "Deformation of the diastolic left ventricle - I. nonlinear elastic effects," *Biophysical J*, vol. 13, pp. 689–704, 1973.
260. R. F. Janz, B. R. Kubert, and T. F. Moriarty, "Deformation of the diastolic left ventricle - II. nonlinear geometric effects," *J. Biomechanics*, vol. 7, pp. 509–516, 1974.

261. N. R. Alpert, B. B. Hamrell, and W. Halpern, "Mechanical and biochemical correlates of cardiac hypertrophy," *Circ Res.*, vol. 34,35, pp. II71–II82, 1974.
262. R. L. Kane, T. A. McMahon, R. L. Wagner, and W. H. Abelmann, "Ventricular elastic modulus as a function of age in the syrian golden hamster," *Circ Res.*, vol. 38, pp. 74–80, Feb. 1975.
263. J. S. Rankin, C. E. Arentyen, P. A. McHale, D. Ling, and R. W. Anderson, "Viscoelastic properties of the diastolic left ventricle in the conscious dog," *Circ Res.*, vol. 41, pp. 37–45, July 1976.
264. P. J. Hunter and B. H. Smaill, "The analysis of cardiac function: A continuum approach," *Prog. Biophys. Mol. Biol.*, vol. 52, pp. 101–164, 1988.
265. B. H. Smaill and P. J. Hunter, "Structure and function of the diastolic heart," in *Theory of Heart*, L. Glass, P. Hunter, and A. McCulloch, Eds., pp. 1–30. Springer, Berlin, Heidelberg, New York, 1991.
266. J. M. Guccione, "Finite element modeling of ventricular mechanics," in *Theory of Heart*, L. Glass, P. Hunter, and A. McCulloch, Eds., pp. 121–127. Springer, Berlin, Heidelberg, New York, 1991.
267. V. P. Novak, F. C. P. Yin, and J. D. Humphrey, "Regional mechanical properties of passive myocardium," *J. Biomechanics*, vol. 27, no. 4, pp. 403–412, 1994.
268. P. J. Hunter, "Myocardial constitutive laws for continuum mechanics models of the heart," in *Molecular and Subcellular Cardiologgy: Effects of Structure and Function*, S. Sideman and R. Beyar, Eds., chapter 30, pp. 303–318. Plenum Press, New York, 1995.
269. M. J. Moulton, L. L. Creswell, R. L. Actis, K. W. Myers, M. W. Vannier, B. A. Szabó, and M. K. Pasque, "An inverse approach to determining myocardial material properties," *J. Biomechanics*, vol. 28, no. 8, pp. 935–948, 1995.
270. C. E. Miller, M. A. Vanni, and B. B. Keller, "Characterization of passive embryonic myocardium by quasi-linear viscoelasticity theory," *J. Biomechanics*, vol. 30, no. 9, pp. 985–988, 1997.
271. J. H. Omens, S. M. Vaplon, B. Fazeli, and A. D. McCulloch, "Left ventricular geometric remodeling and residual stress in the rat heart," *J. Biomechanical Engineering*, vol. 120, pp. 715–719, 1998.
272. S. Dokos, I. J. LeGrice, B. H. Smaill, J. Kar, and A. A. Young, "A triaxial-measurement shear-test device for soft biological tissues," *J. Biomedical Engineering*, vol. 122, pp. 471–478, Oct. 2000.
273. S. Dokos, B. H. Smaill, A. A. Young, and I. J. LeGrice, "Shear properties of passive ventricular myocardium," *Am J Physiol Heart Circ Physiol*, vol. 283, pp. H2650–H2659, 2003.
274. W. P. Smutz, M. Drexler, L. J. Berglund, E. Growney, and K. N. An, "Accuracy of a video strain measurement system," *J. Biomechanics*, vol. 29, no. 6, pp. 813–817, 1996.
275. A. J. Brady, "Mechanical properties of isolated cardiac myocytes," *Physiological Reviews*, vol. 71, no. 2, pp. 413–428, 1991.
276. J. Humphrey, R. Strumpf, H. Halperin, and F. Yin, "Towards a stress analysis in the heart," in *Theory of Heart*, L. Glass, P. Hunter, and A. McCulloch, Eds., pp. 59–76. Springer, Berlin, Heidelberg, New York, 1991.
277. A. McCulloch and J. H. Omens, "Factors affecting the regional mechanics of the diastolic heart," in *Theory of Heart*, L. Glass, P. Hunter, and A. McCulloch, Eds., pp. 121–144. Springer, Berlin, Heidelberg, New York, 1991.

278. E. Nevo and Y. Lanir, "The effect of residual strain on the diastolic function of the left ventricle as predicted by a structural model," *J. Biomechanics*, vol. 27, no. 12, pp. 1433–1446, 1994.
279. D. H. S. Lin and F. C. P. Yin, "A multiaxial constituive law for mammalian left ventricular myocardium in steady-state barium contracture or tetanus," *J. Biomechanical Engineering*, vol. 120, pp. 504–517, 1998.
280. K. May-Newman and A. McCulloch, "Homogenization modeling for the mechanics of perfused myocardium," *Progress in Biophysics and Molecular Biology*, vol. 69, pp. 463–481, 1998.
281. H. Demiray, "A note on the elasticity of soft biological tissue," *J. Biomechanics*, vol. 5, pp. 309–311, 1972.
282. S. A. Glantz, "A constitutive equation for the passive properties of muscle," *J. Biomechanics*, vol. 7, pp. 137–145, 1974.
283. A. Needleman, S. A. Rabinowitz, D. K. Bogen, and T. A. McMahon, "A finite element model of the infarcted left ventricle," *J. Biomechanics*, vol. 16, no. 1, pp. 45–58, 1983.
284. J. D. Humphrey and F. C. P. Yin, "On constitutive relations and finite deformations of passive cardiac tissue: I a. pseudostrain energy function," *J. Biomechanical Engineering*, vol. 109, pp. 298–304, 1987.
285. A. Horowitz, I. Sheinman, Y. Lanir, M. Perl, and S. Sideman, "Nonlinear incompressible finite elemet for simulating loading on cardiac tissue - part 1: Two dimensional formulation for thin myocardial stripes," *J. Biomechanical Engineering*, vol. 110, pp. 57–61, 1988.
286. A. Horowitz, Y. Lanir, F. C. P. Yin, M. Perl, I. Sheinman, and R. K. Strumpf, "Structural three-dimensional constitutive law for the passive myocardium," *J. Biomechanical Engineering*, vol. 110, pp. 200–207, 1988.
287. E. Nevo and Y. Lanir, "Structural finite deformation model of the left ventricle during diastole and systole," *J. Biomechanical Engineering*, vol. 111, pp. 342–349, 1989.
288. J. D. Humphrey, R. K. Strumpf, and F. C. P. Yin, "Determination of a constitutive relation for passive myocardium: I. a new functional form," *J. Biomechanical Engineering*, vol. 112, pp. 333–339, 1990.
289. J. D. Humphrey, R. K. Strumpf, and F. C. P. Yin, "Determination of a constitutive relation for passive myocardium: II. parameter estimation," *J. Biomechanical Engineering*, vol. 112, pp. 340–346, 1990.
290. J. M. Huyghe, D. H. van Campen, Theo Arts, and R. M. Heethaar, "The constitutive behaviour of passive heart muscle tissue: A quasi-linear viscoelastic formulation," *J. Biomechanical Engineering*, vol. 24, no. 9, pp. 840–849, 1991.
291. M. Yang and L. A. Taber, "The possible role of poroelasticity in the apparent viscoelastic behavior of passive cardiac muscle," *J. Biomechanics*, vol. 24, no. 7, pp. 587–597, 1991.
292. M. S. Sacks and C. J. Chuong, "A constitutive relation for passive right-ventricular free wall myocardium," *J. Biomechanics*, vol. 26, no. 11, pp. 1341–1345, 1993.
293. J. M. Guccione, K. D. Costa, and A. D. McCulloch, "Finite element stress analysis of left ventricular mechanics in the beating dog heart," *J. Biomechanics*, vol. 28, no. 10, pp. 1167–1177, 1995.
294. T. P. Usyk, R. Mazhari, and A. D. McCulloch, "Effect of laminar orthotropic myofiber architecture on regional stress and strain in the canine left ventricle," *J. Elasticity*, vol. 61, pp. 143–165, 2000.

295. A. Horowitz, "Structural considerations in formulating material laws for the myocardium," in *Theory of Heart*, L. Glass, P. Hunter, and A. McCulloch, Eds., pp. 31–58. Springer, Berlin, Heidelberg, New York, 1991.
296. P. J. Hunter, A. D. McCulloch, and H. E. D. J. ter Keurs, "Modelling the mechanical properties of cardiac muscle," *Prog. Biophys. Mol. Biol.*, vol. 69, pp. 289–331, 1998.
297. M. Nash, *Mechanics and Material Properties of the Heart using an Anatomically Accurate Mathematical Model*, Ph.D. thesis, University of Auckland, Dep. of Engineering Science, New Zealand, 1998.
298. A. F. Huxley, "Muscle structures and theories of contraction," *Prog. Biophys. and Biophys. Chem.*, vol. 7, pp. 255–318, 1957.
299. A. F. Huxley, "Cross-bridge action: Present views, prospects and unknowns," *J Biomechanics*, vol. 33, pp. 1189–1195, 2001.
300. D. M. Bers, "Cardiac excitation-contraction coupling," *Nature*, vol. 415, pp. 198–205, 2002.
301. J. A. Spudich, "TIMELINE: The myosin swinging cross-bridge model," *Nature Reviews Molecular Cell Biology*, vol. 2, pp. 387–392, 2001.
302. M. Irving and Y. E. Goldman, "Another step ahead for myosin," *Nature*, vol. 398, pp. 463–465, 1999.
303. O. Yakovenko, F. Blyakhman, and G. H. Pollack, "Fundamental step size in single cardiac and skeletal sarcomeres," *Am J Physiol. Cell Physiol.*, vol. 283, pp. C735–C742, 2002.
304. K. Kitamura, M. Tokunaga, A. H. Iwane, and T. Yanagida, "A single myosin head moves along an actin filament with regular steps of 5.3 nanometeres," *Nature*, vol. 397, pp. 129–134, 1999.
305. A. V. Hill, "The heat of shortening and the dynamic constants of muscle," *Proc. R. Soc. Lond.*, vol. B126, pp. 136–195, 1938.
306. W. W. Parmley and L. Chuck, "Length-dependent changes in myocardial contractile state," *Am J Physiol.*, vol. 224, no. 5, pp. 1195–1199, 1973.
307. T. Wannenburg, G. H. Heijne, J. H. Geerdink, H. W. van den Dool, P. M. L. Janssen, and P. P. de Tombe, "Cross-bridge kinetics in rat myocardium: Effect of sarcomere length and calcium activation," *Am J Physiol.*, vol. 279, pp. H779–H790, 2000.
308. W. R. Ingebretsen, E. Becker, W. F. Friedman, and S. E. Mayer, "Contractile and biochemical responses of cardiac and skeletal muscle to isoproterenol covalently linked to glass beads," *Circ Res.*, vol. 40, no. 5, pp. 474–484, May 1976.
309. H. E. D. J. ter Keurs, W. H. Rijnsburger, R. van Heuningen, and M. J. Nagelsmit, "Tension development and sarcomere length in rat cardiac trabeculae," *Circ Res.*, vol. 46, pp. 703–714, 1980.
310. D. A. Eisner, W. J. Lederer, and R. D. Vaughna-Jones, "The quantitative relationship between twitch tension and intracellular sodium activity in sheep cardiac Purkinje fibers," *J. Physiol.*, vol. 355, pp. 251–266, 1984.
311. W. G. Wier and D. T. Yue, "Intracellular calcium transients underlying the short-term force-interval relationship in ferret ventricular myocardium," *J. Physiol.*, vol. 376, pp. 507–530, 1986.
312. J. C. Kentish, H. E. ter Keurs, L. Ricciardi, J. J. Bucx, and M. I. Noble, "Comparison between the sarcomere length-force relations of intact and skinned trabeculae from rat right ventricle. influence of calcium concentrations on these relations," *Circ. Res*, vol. 58(6), pp. 755–68, 1986.

313. P.A. Hofmann and F. Fuchs, "Evidence for a force-dependent component of calcium binding to cardiac troponin C," *Am J Physiol.*, vol. 253, pp. C541–C546, 1987.
314. J. N. Peterson, W. C. Hunter, and M. R. Berman, "Estimated time course of Ca^{2+} bound to trophononin C during relaxation in isolated cardiac muscle," *Am J Physiol. Circ. Heart.*, vol. 260, pp. H1013–H1024, 1991.
315. R. Nassar, N. N. Malouf, M. B. Kelly, A. E. Oakely, and P. A. W. Anderson, "Force-pCa relation and troponin T isoforms of rabbit myocardium," *Circ Res.*, vol. 69, no. 6, pp. 1470–1475, 1991.
316. W. D. Gao, P. H. Backx, M. Azan-Backx, and E. Marban, "Myofilament Ca^{2+} sensitivity in intact versus skinned rat ventricular muscle," *Circ Res.*, vol. 74, pp. 408–415, 1994.
317. W. F. Bluhm and W. Y. W. Lew, "Sarcoplasmic reticulum in cardiac length-dependent activation in rabbits," *Am J Physiol.*, vol. 269, no. 38, pp. H965–H972, 1995.
318. L. Wang and R. Patterson, "Multiple sources of the impedance cardiogram based on 3-d finite difference human thorax models," *IEEE Transactions on Biomedical Engineering*, vol. 42, no. 2, pp. 141–148, Feb. 1995.
319. P. M. L. Janssen and W. C. Hunter, "Force, not sarcomere length, correlates with prolongation of isosarcometric contaction," *Am J Physiol.*, vol. 269, pp. H676–H685, 1995.
320. P. M. L. Janssen and P. P. de Tombe, "Uncontrolled sarcomere shortening increases the intracellular Ca^{2+} transient in rat cardiac trabeculae," *Am J Physiol.*, vol. 272, pp. H1892–H1897, 1997.
321. A. J. Baker, V. M. Figueredo, E. C. Keung, and S. A. Camacho, "Ca^{2+} regulates the kinetics of tension development in intact cardiac muscle," *Am J Physiol.*, vol. 275, pp. H744–H750, 1998.
322. L. S. Maier, R. Brandes, B. Pieske, and D. M. Bers, "Effect of left ventricular hypertrophy on force and Ca^{2+}-handling in isolated rat myocardium," *Am J Physiol.*, vol. 274, pp. H1361–H1370, 1998.
323. Y. Saeki, S. Kurihara, K. Komukai, T. Ishikawa, and K. Takigiku, "Dynamic relations among length, tension, and intracellular Ca^{2+} in activated ferret papillary muscles," *Am J Physiol.*, vol. 275, pp. H1957–H1962, 1998.
324. J. Layland and J. C. Kentish, "Positve force and $[Ca^{2+}]_i$-frequency relationships in rat ventricular trabeculae at physiological frequencies," *Am J Physiol.*, vol. 276, pp. H9–H18, 1999.
325. K. Allen, Y. Y. Xu, and W. G. L. Kerrick, "Ca^{2+} measurements in skinned cardiac fibers: Effects of Mg^{2+} on Ca^{2+} activation of force and fiber ATPase," *J. Appl. Physiol.*, vol. 88, pp. 180–185, 2000.
326. L. S. Maier, P. Barckhausen, J. Weisser, I. Aleksic, M. Baryalei, and B. Pieske, "Ca^{2+}-handling in isolated human atrial myocardium," *Am J Physiol.*, vol. 279, pp. H952–H958, 2000.
327. H. E. D. J. ter Keurs, E. H. Hollander, and M. H. C. ter Keurs, "The effect of sarcomere length on the force-cytosolic $[Ca^{2+}]$ relationship in intact rat cardiac trabeculae," in *Skeletal muscle mechanics: From Mechanisms to Function*, W. Herzog, Ed., chapter 4, pp. 53–70. John Wiley & Sons, Ltd, Baffins Lane, Chichester, West Sussex P019 1UD, UK, 2000.
328. J. P. Konhilas, T. C. Irving, and P. P. de Tombe, "Myofilament calcium sensitivity in skinned rat cardiac trabeculae - role of interfilament spacing," *Circ Res.*, vol. 90, pp. 59–65, 2002.

329. N. M. de Clerck, V. A. Claes, and D. L. Brutsaert, "Force velocity relations of single cardiac muscle cells," *J. Gen. Physiol.*, vol. 69, pp. 221–241, 1977.
330. F. Gannier, J. C. Bernengo, V. Jacquemond, and D. Garnier, "Measurements of sarcomere dynamics simultaneously with auxotonic force in isolated cardiac cells," *IEEE Transactions on Biomedical Engineering*, vol. 40, no. 12, pp. 1226–1232, Dec. 1993.
331. E. White, M. R. Boyett, and C. H. Orchard, "The effects of mechanical loading and changes to length on single guinea-pig ventricular myocytes," *J. Physiol.*, vol. 482, pp. 93–107, 1995.
332. W. F. Bluhm, A. D. McCulloch, and W. Y. W. Lew, "Active force in rabbit ventricular myocytes," *J. Biomechanics*, vol. 28, no. 9, pp. 1119–1122, 1995.
333. P. W. Brandt, F. Colomo, N. Piroddi, C. Poggesi, and C. Tesi, "Force regulation by Ca^{2+} in skinned single cardiac myocytes of frog," *Biophys J*, vol. 74, pp. 1994–2004, 1998.
334. S. Yasuda, S. Sugiura, N. Kobayakawa, H. Fjita, H. Yamashita, K. Katoh, Y. Seaki, H. Kaneko, Y. Suda, R. Nagai, and H. Sugi, "A novel method to study contraction characteristics of a single cardiac myocyte using carbon fibers," *Am J Physiol.*, vol. 281, pp. H1442–H1446, 2001.
335. D.G. Allen and S. Kurihara, "The effects of muscle length on intracellular calcium transients in mammalian cardiac muscle," *J. Physiol.*, vol. 327, pp. 79–94, 1982.
336. H. Nagashima and S. Asakura, "Studies on co-operative properties of tropomyosin-actin and tropomyosin-troponin-actin complexes by use of N-ethylmaleinide-treated and untreated species of myosin subfragment," *J. Mol. Bio.*, vol. 155, pp. 409–428, 1982.
337. L. S. Tobacman, "Thin filament mediated regulation of cardiac contraction," *Ann. Rev. Physiol.*, vol. 58, pp. 447–481, 1996.
338. A. F. Huxley and R. M. Simmons, "Proposed mechanism of force generation in striated muscle," *Nature*, vol. 233, pp. 533–538, 1999.
339. A. Y. K. Wong, "Mechanics of cardiac muscle, based on Huxley's model: Mathematical simulation of isometric contraction," *J. Biomechanics*, vol. 4, pp. 529–540, 1971.
340. A. Y. K. Wong, "Mechanics of cardiac muscle, based on Huxley's model: Simulation of active state and force-velocity relation," *J. Biomechanics*, vol. 5, pp. 107–117, 1972.
341. R. B. Panerai, "A model of cardiac muscle mechanics and energetics," *J. Biomechanics*, vol. 13, pp. 929–940, 1980.
342. A. Landesberg and S. Sideman, "Coupling calcium binding to troponin C and cross-bridge cycling in skinned cardiac cells," *Am J Physiol.*, vol. 266, pp. H1260–H1271, 1994.
343. A. Landesberg and S. Sideman, "Mechanical regulation of cardiac muscle by coupling calcium kinetics with cross-bridge cycling: A dynamic model," *Am J Physiol.*, vol. 267, pp. H779–H795, 1994.
344. A. Landesberg, R. Beyar, and S. Sideman, "Intracellular control of contraction of the cardiac muscle," in *IFAC Modeling and Control in Biomedical Systems*, 1994, pp. 79–80.
345. J. M. Guccione, I. Motabarzadeh, and G. I. Zahalak, "Finite element stress analysis of left ventricular mechanics in the beating dog heart," *J. Biomechanics*, vol. 31, pp. 1069–1073, 1998.

346. R. L. Winslow, J. Rice, and S. Jafri, "Modeling the cellular basis of altered excitation-contraction coupling in heart failure," *Progress in Biophysics and Molecular Biology*, vol. 69, pp. 497–514, 1998.
347. J. J. Rice, R. L. Winslow, and W. C. Hunter, "Comparison of putative cooperative mechanisms in cardiac muscle: Length dependence and dynamic responses," *Am J Physiol. Circ. Heart.*, vol. 276, pp. H1734–H1754, 1999.
348. J. J. Rice, M. S. Jafri, and R. L. Winslow, "Modeling short-term interval-force relations in cardiac muscle," *Am J Physiol. Circ. Heart.*, vol. 278, pp. H913–H931, 2000.
349. M. Mlcek, J. Neumann, O. Kittnar, and V. Novak, "Mathematical model of the electromechanical heart contractile system - regulatory subsystem physiological considerations," *Physiol. Res.*, vol. 50, pp. 425–432, 2001.
350. D. P. Nickerson, N. P. Smith, and P. J. Hunter, "A model of cardiac cellular electromechanis," *Phil. Trans. R. Soc. Lond.*, vol. 359, pp. 1159–1172, 2001.
351. K. Glänzel, F. B. Sachse, G. Seemann, C. Riedel, and O. Dössel, "Modeling force development in the sarcomere in consideration of electromechanical coupling," in *Biomedizinische Technik*, 2002, vol. 47-1/2, pp. 774–777.
352. F. B. Sachse, K. Glänzel, and G. Seemann, "Modeling of protein interactions involved in cardiac tension development," *Int. J. Bifurc. Chaos*, vol. 13, no. 12, pp. 3561–3578, 2003.
353. A. Landesberg, V. S. Markhasin, R. Beyar, and S. Sideman, "Effect of cellular inhomogeneity on cardiac tissue mechanics based on intracellular control mechanisms," *Am J Physiol.*, vol. 270, pp. H1101–H1114, 1996.
354. K. Glänzel, "Kraftentwicklung im Sarkomer unter Berücksichtigung elektromechanischer Kopplung," Diploma Thesis, Institut für Biomedizinische Technik, Universität Karlsruhe (TH), Sep. 2002.
355. A. M. Gordon, M. Regnier, and E. Homsher, "Skeletal and cardiac muscle contractile activation: Tropomyosin "rocks and rolls"," *News Physiol. Sci.*, vol. 16, pp. 49–55, 2001.
356. A. M. Gordon, E. Homsher, and M. Regnier, "Regulation of contraction in striated muscle," *Physiological Reviews*, vol. 80, pp. 853–924, 2000.
357. M. A. Geeves and K. C. Holmes, "Structural mechanism of muscle contraction," *Annual Review in Biochemistry*, vol. 68, pp. 687–728, 1999.
358. J.D. Johnson and E.W. Taylor, "Intermediate states of subfragment 1 and actosubfragment1 ATPase: Reevaluation of the mechanism," *Biochemistry*, vol. 17, pp. 3432–3442, 1978.
359. M. Regnier, D.M. Lee, and E. Homsher, "ATP analogs and muscle contraction: Mechanics and kinetics of nucleoside triphosphate binding and hydrolysis," *Biophys. J.*, vol. 74, pp. 3044–3058, 1998.
360. M. Brune, J.L. Hunter, J.E. Corrie, and M.R. Webb, "Direct, real-time measurement of rapid inorganic phosphate release using a novel fluorescent probe and its application to actomyosin subfragment 1 atpase," *Biochemistry*, vol. 33, pp. 8262–8271, 1994.
361. H.D. White and E.W. Taylor, "Energetics and mechanism of actomyosin adenosine triphosphatease," *Biochemistry*, vol. 15, pp. 5818–5826, 1976.
362. E.W. Taylor, "Mechanism of actomyosin ATPase and the problem of muscle contraction," *CRC Crit. Rev. Biochem.*, vol. 6, pp. 103–164, 1979.
363. F. B. Sachse, K. Glänzel, and G. Seemann, "Modeling of electro-mechanical coupling in cardiac myocytes: Feedback mechanisms and cooperativity," *LNCS 2674*, pp. 62–71, 2003.

364. A. McCulloch, L. Waldmann, and J. Rogers, "Large-scale finite element analysis of the beating heart," *Critical Reviews in Biomedical Engineering*, vol. 20, no. 5-6, pp. 427–449, 1992.
365. K. D. Costa, P. J. Hunter, J. S. Wayne, L. K. Waldmann, J. M. Guccione, and A. D. McCulloch, "A three-dimensional finite element method for large elastic deformations of ventricular myocardium: II - prolate spheroidal coordinates," *J. Biomedical Engineering*, vol. 118, no. 4, pp. 464–472, Nov. 1996.
366. F. J. Vetter and A. McCulloch, "Three-dimensional analysis of regional cardiac function: A model of rabbit ventricular anatomy," *Progress in Biophysics and Molecular Biology*, vol. 69, pp. 157–183, 1998.
367. "CMISS: An interactive computer program for continuum mechanics, image analysis, signal processing and system identification," Bioengineering Institute, The University of Auckland, New Zealand.
`http://www.bioeng.auckland.ac.nz/cmiss/cmiss.php`
368. A. McCulloch, "Continuity: Continuum modeling for bioengineering and physiology," University of California San Diego, California.
`http://cmrg.ucsd.edu/modelling/software/software.html`
369. V. Piacentino III, C. R. Weber, X. Chen, J. Weisser-Thomas, K. B. Margulies, D. M. Bers, and S. R. Houser, "Cellular basis of abnormal calcium transients of failing human ventricular myocytes," *Circ Res.*, vol. 92, pp. 651–658, 2003.
370. F. B. Sachse, C. D. Werner, and G. Seemann, "Anatomical models of the heart for the simulation of excitation propagation and force development," in *Annals of Biomedical Engineering*, Oct. 2001, p. 48, ISSN 0090-6964.
371. L. G. Blümcke, F. B. Sachse, G. Seemann, C. D. Werner, and O. Dössel, "Entwicklung eines schnellen Verfahrens zur Deformation im Herzen ausgehend von makroskopischen Modellen der Kraftentwicklung," in *Biomedizinische Technik*, Sep. 2001, vol. 46-1, pp. 516–517.
372. L. G. Blümcke, "Entwicklung eines schnellen Verfahrens zur Berechnung der Deformation im Herzen ausgehend von makroskopischen Modellen der Kraftentwicklung," Diploma Thesis, Institut für Biomedizinische Technik, Universität Karlsruhe (TH), Sep. 2001.
373. F. B. Sachse, G. Seemann, M. B. Mohr, L. G. Blümcke, and C. D. Werner, "Models of the human heart for simulation of clinical interventions," in *Proc. CARS 2002*, 2002, pp. 43–48.
374. F. B. Sachse, G. Seemann, C. Riedel, C. D. Werner, and O. Dössel, "Modeling of the cardiac mechano-electrical feedback," *Int. J. Bioelectromagnetism*, vol. 2, no. 2, 2000.
`http://ee.tut.fi/rgi/ijbem/volume2/number2/sachse/paper_ijbem.htm`
375. G. Seemann, "Elektrische Erregungsausbreitung im Herzen ausgehend von elektrophysiologischen Zellmodellen: Erregungsausbreitung im Zellverband, Parametrisierung Zellulärer Automaten," Diploma Thesis, Institut für Biomedizinische Technik, Universität Karlsruhe (TH), Aug. 2000.
376. C. H. Riedel, "Modellierung der Kopplung von elektrischer Erregung und mechanischer Kontraktion von Zellen des Myocardiums," Diploma Thesis, Institut für Biomedizinische Technik, Universität Karlsruhe (TH), Sep. 2000.
377. F. B. Sachse, G. Seemann, C. D. Werner, C. Riedel, and O. Dössel, "Electromechanical modeling of the myocardium: Coupling and feedback mechanisms," in *Proc. Computers in Cardiology*, Sep. 2001, vol. 28, pp. 161–164.

378. F. B. Sachse, G. Seemann, and C. D. Werner, "Combining the electrical and mechanical functions of the heart," *Int. J. Bioelectromagnetism*, vol. 3, no. 2, 2001. http://ee.tut.fi/rgi/ijbem/volume3/number2/sachse/index.htm
379. O. Langendorff, "Untersuchungen am überlebenden Säugetierherzen," *Pflügers Arch. ges. Physiologie*, vol. 61, pp. 291–332, 1895.
380. F. B. Sachse, "Mathematical modeling of the mammalian heart," Universität Karlsruhe (TH), Institut für Biomedizinische Technik, 2002, Habilitationsschrift.
381. F. B. Sachse, G. Seemann, M. B. Mohr, and Arun V. Holden, "Mathematical modeling of cardiac electro-mechanics: From protein to organ," *Int. J. Bifurc. Chaos*, vol. 13, no. 12, pp. 3747–3755, 2003.
382. H.-G. Zimmer, "Some aspects of cardiac heterogeneity," *Basic Res. Cardiol.*, vol. 89, pp. 101–107, 1994.
383. M. Griebel and M. A. Schweitzer, Eds., *LNCS - Meshfree Methods for Partial Differential Equations*, Springer, 2002.
384. "OpenMP: Simple, portable, scalable SMP programming". http://www.openmp.org
385. CellML Project, "What is CellML?," Bioengineering Institute, The University of Auckland, New Zealand. http://www.cellml.org/public/about/what_is_cellml.html
386. Scientific Computing and Imaging Institute, "SCIRun - Software," University of Utah, Utah. http://software.sci.utah.edu/scirun.html
387. F. B. Sachse, G. Seemann, and C. Riedel, "Modeling of cardiac excitation propagation taking deformation into account," in *Proc. BIOMAG 2002*, 2002, pp. 839–841.

Index

F.B. Sachse: LNCS 2966, pp. 323–327, 2004.